Towards stochastic multi-scale methods in continuum solid mechanics

Ludovic Noels[a,]

[a] *Computational & Multiscale Mechanics of Materials, University of Liège, Belgium*

Abstract

The scientific community has realised that non-determinism is a major issue that affects structural and material performance and reliability. Because experimental characterisation alone cannot reliably sample the tails of distributions, virtual stochastic testing has thus become a research field of growing interest. Since the uncertainties at the structural level also result from the variability of the micro-structure, there is a need to develop computationally efficient stochastic multi-scale methods. The purpose of this work is to provide a summary of the different methods that have been developed in the context of micro-structure characterisation and reconstruction, of stochastic homogenisation and of uncertainties up-scaling.

Keywords: Stochastic, Multiscale, Heterogeneous Materials

---

1. Introduction and motivations

The last decades have seen the emergence of more and more accurate and detailed numerical models for predicting material behaviours and structural responses, including when considering several scales, see the reviews by Kanouté et al. (2009); Matous et al. (2017); Yvonnet (2019). However, most of the research considers deterministic models whilst the scientific community has realised that non-determinism is a major issue that affects structural and material performance and reliability. This has motivated the introduction of uncertainty quantification in model developments.

Uncertainties are generally classified in two categories (Rosi and Matthies, 2008; Pivovarov et al., 2018a, *e.g.*). On the one hand, aleatory uncertainties are associated with the inherent randomness of nature, and their effect on the structural responses for a given material system and environment cannot be reduced. Material structure randomness, loading variability, geometrical imperfections are part of the aleatory uncertainties. On the other hand epistemic uncertainties result from a lack of knowledge of the system under consideration due to insufficient measurements, (lack of) accuracy in the experimental measurements, or from model errors. Their effects can be reduced by obtaining more information, *e.g.* by collecting more data, improving the model accuracy *etc.* It is common to handle aleatory

---

Email address: `l.noels ulg.ac.be` (Ludovic Noels)

uncertainties using statistical approaches, whilst epistemic uncertainties can be handled by non-probabilistic uncertainty treatment like Interval and Fuzzy analyses (Moens and Vandepitte, 2005). Models considering both sources of uncertainties are called polymorphic (Pivovarov et al., 2018a). However, following Soize (2017), when considering probability theory and mathematical statistics of uncertainty quantification, the same tools can be used with these two types of uncertainties.

Uncertainties, and probabilistic approaches can also be classified in parametric and non-parametric ones. Following Soize (2017), parametric uncertainties are associated with the parameters of computational models, and non-parametric uncertainties are induced by modelling errors. Parametric probabilistic approaches can handle model-parameter uncertainties for predictive computational models but not the modelling errors. Soize (2017) gave the following example. Assuming one wants to represent the uncertainties in the matrix of a structural model, and that the matrix $\mathbf{b}$ depends on a parameter x, in the parametric approach the uncertainties in the parameter are described by a distribution. As a result, if when spanning the support of this distribution, the region spanned by the matrix $\mathbf{b}$ does not include the experimental observations, the model has a deficiency which cannot be addressed by this parametric approach. The non parametric approach pioneered by Soize (2000) consists in directly building prior probability distribution of a random matrix, *e.g.* using the maximum entropy principle. The non-parametric probabilistic approach can thus handle both the model-parameter uncertainties and the model uncertainties.

In this work we mainly consider the uncertainties which originate from the material itself, whilst remaining at the continuum mechanics scale, and that affect structural responses. This is particularly true in the context of strongly non-linear behaviours and/or fracture (Graham-Brady et al., 2006; McDowell, 2010; Mariani et al., 2011b), in which case the strength of a structure strongly depends on the micro-structure realisation observed in stress concentration parts. For various applications, it is important, not only to be able to estimate the nominal behaviour of a structure and possibly its standard deviation, but it is also important to be able to estimate the probability of rare realisations. However, experimental characterisation alone cannot reliably sample the tails of the distributions, since this would require an excessive number of tests. This has motivated the development of virtual stochastic testing, in which the stochastic description relies on a mathematics model or on database, which are characterised by a quantification of the material uncertainties. Although the stochastic model of macro-scale properties can be built directly from macro-scale measurements as achieved in the context of composite materials by, *e.g.* Mehrez et al. (2012b,a), because of the different involved length scales (Charmpis et al., 2007), there is a growing interest in developing a combined experimental/numerical framework to up-scale the uncertainties by formulating a computationally efficient stochastic scale transition between the material scale and the structural scale. In this context, the uncertainty due to the material heterogeneities has to be described as the spatial variability of the material properties at the micro-structure level and the generated virtual specimens serve as Stochastic Volume Elements (SVEs) in a stochastic multiscale analysis, see the review by Ostoja-Starzewski et al. (2016).

The development of stochastic scale-transition methods is a subject of research which has seen a growing interest in the last decade, but which has still numerous challenges to overcome, even for linear systems, before becoming commonly used in scientific or industrial practices. In particular one can cite, as a non-exhaustive list, the following difficulties

- Characterising the micro-scale uncertainties, both in the micro-structure geometrical description and material behaviours;
- Generating virtual specimens under the form of Stochastic Volume Elements (SVEs) which respect the statistical content of real micro-structures, both in the micro-structure geometrical description and material behaviours, in particular for 3D micro-structure;
- Conducting stochastic analyses in an efficient and accurate way;
- Coupling stochastic micro-scale behaviour to stochastic macro-scale response, which is not achievable by classical multi-scale methods because of the overwhelming cost; Although the evaluation of the stochastic apparent properties of the Stochastic Volume Elements can be decoupled to macro-scale stochastic finite elements analyses in the linear range, the question remains open in the non-linear range.

One can find in the literature extensive reviews on micro-structures generation (Fullwood et al., 2010; Bostanabad et al., 2018, *e.g.*), at least with respect to the geometrical features, on the formulation of stochastic problems (Sudret and Der Kiureghian, 2000; Grimmett and Stirzaker, 2001; Nouy, 1999; Soize, 2017), on stochastic homogenisation (Ostoja-Starzewski et al., 2016), and on conducting stochastic finite element analyses (Stefanou, 2009). It is, however, not always an easy task for a researcher to make the link between the different fields. In particular, the notations are not always uniform, some choices made at one scale constrain the methods that can be used at another scale, the size of the generated virtual micro-structure affects the statistical content of the homogenised properties *etc.* The purpose of this work is to provide a summary of different methods, without pretending to be exhaustive, that have been developed at the different scales and to attempt to make the link between micro-structure generation, stochastic homogenisation and up-scaling of uncertainties. The manuscript is organised as follows. The definitions related to the main concepts of stochastic analyses are provided in Section 2. The problem of virtual micro-structures generation is reviewed in Section 3. Section 4 presents the different stochastic homogenisation methods that have been developed, in both linear and non-linear ranges, in order to predict the stochastic apparent properties of the virtual micro-structures. The representation of these apparent properties, the need of generating pseudo-samples in order to conduct stochastic structural analyses, and accounting for the size of the virtual micro-structures are discussed in Section 5. Finally, details on stochastic and multi-scale algorithms are provided in the appendices. Although these details can be found elsewhere, they are not provided in the same context and the author hopes that it could be useful for the reader to have a self-content review with a unique set of notations and conventions.

2. Definitions and notations

In this section we introduce the notations of some statistics and probability concepts that will be used throughout the work. This section is not a summary of probabilistic theories, for which we refer to the books by Grimmett and Stirzaker (2001); Soize (2017) for a more complete presentation.

2.1. Probability space

Definitions. The probability space $(\mathcal{Q}, \mathcal{F}, \mathbb{P})$ is defined from the sample space $\mathcal{Q}$, which is the set of all possible outcomes, a collection $\mathcal{F}$ of subsets of $\mathcal{Q}$, which is assumed to be a σ-field[1], and the probability measure $\mathbb{P}$ on $(\mathcal{Q}, \mathcal{F})$.

Probability measure. Following Grimmett and Stirzaker (2001), the probability measure $\mathbb{P}$ on $(\mathcal{Q}, \mathcal{F})$ is a function $\mathbb{P} : \mathcal{F} \to [0, 1]$ satisfying (i) $\mathbb{P}(\emptyset) = 0$ and $\mathbb{P}(\mathcal{Q}) = 1$; (ii) for $\mathcal{A}^{(i)}$, $i = 1, 2, ..\infty$ a collection of disjoint members of $\mathcal{F}$, $\mathbb{P}\left(\cup_{i=1}^{\infty}\mathcal{A}^{(i)}\right) = \sum_{i=0}^{\infty} \mathbb{P}(\mathcal{A}^{(i)})$.

Conditional probability. Considering two events $\mathcal{A}$ and $\mathcal{B}$, the conditional probability that $\mathcal{A}$ occurs knowing than $\mathcal{B}$ occurs reads

$$\mathbb{P}(\mathcal{A}|\mathcal{B}) = \frac{\mathbb{P}(\mathcal{A} \cap \mathcal{B})}{\mathbb{P}(\mathcal{B})} . \tag{1}$$

We also have for two events $\mathcal{A}$ and $\mathcal{B}$, with $0 < \mathbb{P}(\mathcal{B}) < 1$ and $\mathcal{B}^c$ the complementary subset of $\mathcal{B}$, that

$$\mathbb{P}(\mathcal{A}) = \mathbb{P}(\mathcal{A}|\mathcal{B})\mathbb{P}(\mathcal{B}) + \mathbb{P}(\mathcal{A}|\mathcal{B}^c)\mathbb{P}(\mathcal{B}^c) . \tag{2}$$

Independence. Two events $\mathcal{A}$ and $\mathcal{B}$ are called independent if

$$\mathbb{P}(\mathcal{A} \cap \mathcal{B}) = \mathbb{P}(\mathcal{A})\mathbb{P}(\mathcal{B}) . \tag{3}$$

2.2. Random variables and vectors

2.2.1. Random variable with values in $\Re$

Definition. The random variable is a function $Q : \mathcal{Q} \to \Re$ with the property that $\{q \in \mathcal{Q} : Q(q) \leq q\} \in \mathcal{F}$ for each $q \in \Re$; such a function is said to be $\mathcal{F}$-measurable (Grimmett and Stirzaker, 2001). We note that the random variable Q is not in $\Re$ but is a mapping; however a realisation $Q(q)$ of a fixed $q \in \mathcal{Q}$ is in $\Re$.

Cumulative distribution function. The cumulative distribution function $F_Q : \Re \to [0, 1]$ is given as the probability to have the random variable Q lower or equal to a value q, *i.e.* $F_Q(q) = \mathbb{P}(Q \leq q)$[2].

The support $\mathcal{S}_Q$ of the probability distribution of the random variable Q is the smallest closed set $\mathcal{S}_Q \subset \Re$ such that $\mathbb{P}(Q \in \mathcal{S}_Q) = 1$ (Anderson et al., 2017).

---

[1] A collection $\mathcal{F}$ of subsets of $\mathcal{Q}$ is called a σ-field if (i) the empty set $\emptyset \in \mathcal{F}$; (ii) for subsets $\mathcal{A}^{(i)} \in \mathcal{F}$, $i = 1, ..\infty$ then $\cup_{i=1}^{\infty}\mathcal{A}^{(i)} \in \mathcal{F}$; and (iii) for a subset $\mathcal{A} \in \mathcal{F}$, the complementary subset $\mathcal{A}^c \in \mathcal{F}$ (Grimmett and Stirzaker, 2001). As examples, $\mathcal{F} = \{\emptyset, \mathcal{Q}\}$ and $\mathcal{F} = \{\emptyset, \mathcal{A}, \mathcal{A}^c, \mathcal{Q}\}$ for any subset $\mathcal{A} \subset \mathcal{Q}$ are both σ-fields.

[2] Following Grimmett and Stirzaker (2001), this last expression is an abbreviation of the more rigorous notation $F_Q(q) = \mathbb{P}(\mathcal{A}(q))$, where $\mathcal{A}(q) = \{q \in \mathcal{Q} : Q(q) \leq q\}$. We will use this abuse of notations all along this work for conciseness.

Discrete random variables. In the case of a discrete random variable Q that can only take values in some countable subset $\{q^{(1)},\, q^{(2)},\, ...\}$ of $\Re$, the probability mass function $\pi_Q : \Re \to [0,\, 1]$ is defined as

$$\pi_Q(q^{(i)}) = \mathbb{P}(Q = q^{(i)})\,. \tag{4}$$

The expectation operator $\mathbb{E}\left[Q\right] \in \Re$ of the random variable Q is then defined as

$$\bar{q} = \mathbb{E}\left[Q\right] = \sum_{q^{(i)};\, \pi_Q(q^{(i)})>0} q^{(i)}\pi_Q(q^{(i)})\,, \tag{5}$$

where the summation is over all the possible $q^{(i)}$.

The definition of the support $\mathcal{S}_Q$ allows defining the support indicator function $\chi_{\mathcal{S}_Q} : \Re \to \{0,\, 1\}$ as

$$\chi_{\mathcal{S}_Q}(q^{(i)}) = \begin{cases} 1 & \text{if } q^{(i)} \in \mathcal{S}_Q\,;\ \text{and} \\ 0 & \text{if } q^{(i)} \notin \mathcal{S}_Q\,. \end{cases} \tag{6}$$

The probability mass function $\pi_Q(q^{(i)})$ can then be expressed as $\pi_Q(q^{(i)}) = \chi_{\mathcal{S}_Q}(q^{(i)})f_Q(q^{(i)})$, with no sum on i intended, where, $f_Q(q^{(i)}) : \mathcal{S}_Q \to [0,\, 1]$ with

$$\sum_{q^{(i)}\in\mathcal{S}_Q} f_Q(q^{(i)}) = 1\,. \tag{7}$$

Continuous random variables. A random variable Q is called continuous if its cumulative distribution function can be expressed in terms of an integrable function $\pi_Q : \Re \to [0,\, \infty[$, called probability density function, following

$$\int_{-\infty}^{q} \pi_Q(u)du = F_Q(q) = \mathbb{P}(Q \leq q)\,. \tag{8}$$

The expectation operator $\mathbb{E}\left[Q\right] \in \Re$ of the random variable Q is then defined as

$$\bar{q} = \mathbb{E}\left[Q\right] = \int_{\Re} q\pi_Q(q)dq\,, \tag{9}$$

whenever it exists.

The definition of the support $\mathcal{S}_Q$ allows defining a similar expression than Eq. (6) for the support indicator $\chi_{\mathcal{S}_Q} : \Re \to \{0,\, 1\}$ with

$$\chi_{\mathcal{S}_Q}(q) = \begin{cases} 1 & \text{if } q \in \mathcal{S}_Q\,;\ \text{and} \\ 0 & \text{if } q \notin \mathcal{S}_Q\,. \end{cases} \tag{10}$$

The probability density function $\pi_Q(q)$ can then be expressed as $\pi_Q(q) = \chi_{\mathcal{S}_Q}(q)f_Q(q)$ where $f_Q(q) : \mathcal{S}_Q \to [0,\, \infty[$ with

$$\int_{\mathcal{S}_Q} f_Q(q)dq = 1\,. \tag{11}$$

Moments. For $k \in \mathbb{N}$[3], the k^{th}-moment m_{k_Q} and the k^{th}-central moment σ_{k_Q} of a random variable Q are defined using the expectation operator

$$m_{k_Q} = \mathbb{E}[Q^k] \ \text{ and } \sigma_{k_Q} = \mathbb{E}[(Q - m_{1_Q})^k] \,. \tag{12}$$

In particular, for $k = 1$, m_{1_Q} is the expectation operator, and for $k = 2$, $\sigma_{2_Q} = m_{2_Q} - m_{1_Q}^2$ corresponds to the variance, whilst $\sigma_Q = \sqrt{\sigma_{2_Q}}$ is called standard deviation.

Considering n^{sample} observations $q^i = Q(q^i)$, $i = 1..n^{\text{sample}}$, of the random vector Q, with $q^i \in \mathcal{Q}$, the expectation operator can be approximated by

$$\mathbb{E}\left[Q\right] \simeq \frac{1}{n^{\text{sample}}} \sum_{i=1}^{n^{\text{sample}}} q^i \,. \tag{13}$$

The variance follows from

$$\sigma_Q^2 \simeq \frac{1}{n^{\text{sample}} - 1} \sum_{i=1}^{n^{\text{sample}}} \left(q^i - \mathbb{E}\left[Q\right]\right)^2 \,. \tag{14}$$

Event indicator function. Let $\mathcal{A} \subset \mathcal{Q}$ be an event, and $\mathcal{A}^c$ its complement, the indicator function $\chi_{\mathcal{A}} : \mathcal{Q} \rightarrow \{0,\, 1\}$ is defined as

$$\chi_{\mathcal{A}}(q) = \begin{cases} 1 & \text{if } q \in \mathcal{A} \,; \text{ and} \\ 0 & \text{if } q \in \mathcal{A}^c \,. \end{cases} \tag{15}$$

The probabilities for the (Bernoulli) random variable $\chi_{\mathcal{A}}$ to take the values 1 and 0 are, respectively, $\mathbb{P}(\mathcal{A})$ and $\mathbb{P}(\mathcal{A}^c)$.

Some distributions. The notation $Q \sim \pi_Q$ means that a random variable Q follows the mass/probability density function $\pi_Q(q)$. Here we present some particular cases of mass/-probability density function $\pi_Q(q)$.

We first consider the case of a discrete random variable Q. A Poisson distribution $\mathcal{P}_\lambda$ with a support $\mathbb{N}_0$ is defined by

$$\mathcal{P}_\lambda(q^{(i)}) = \begin{cases} \frac{\lambda^{q^{(i)}}}{q^{(i)}!} e^{-\lambda} & \text{if } q^{(i)} \in \mathbb{N}_0 \,; \\ 0 & \text{if not } \,, \end{cases} \tag{16}$$

where $\lambda \in]0,\, \infty[$ is the expectation $\mathbb{E}[Q]$ and variance σ_Q^2 is λ.

We now consider a continuous random variable Q. A Gaussian or Normal distribution $\mathcal{N}_{\mu,\,\sigma^2}$ with a support $]-\infty,\, \infty[$ is defined by

$$\mathcal{N}_{\mu,\,\sigma^2}\left(q\right) = \frac{1}{\sigma\sqrt{2\pi}} \exp\left[-\frac{1}{2}\left(\frac{q-\mu}{\sigma}\right)^2\right] , \tag{17}$$

---

[3] $\mathbb{N}$ is the set $\{1,\, 2,\, 3,\, ...\}$ whilst $\mathbb{N}_0$ is the set $\{0,\, 1,\, 2,\, 3,\, ...\}$

where μ and σ are respectively the expectation and standard deviation. A uniform distribution $\mathcal{U}_{a,\,b}$ with a support $[a,\,b]$ is defined by

$$\mathcal{U}_{a,\,b}(q) = \begin{cases} \frac{1}{b-a} & \text{if } q \in [a,\,b]\,; \\ 0 & \text{if } q \notin [a,\,b]\,. \end{cases} \tag{18}$$

A Beta distribution $\beta_{\alpha,\,\beta,\,a,\,b}$ of support $[a,\,b]$ is defined by

$$\beta_{\alpha,\,\beta,\,a,\,b}(q) = \begin{cases} \frac{(q-a)^{\alpha-1}(b-q)^{\beta-1}}{(b-a)^{\alpha+\beta-1}B(\alpha,\,\beta)} & \text{if } q \in [a,\,b]\,; \\ 0 & \text{if } q \notin [a,\,b]\,, \end{cases} \tag{19}$$

where $B(\alpha,\,\beta)$ is the normalisation constant, and $\alpha,\,\beta > 0$ are the shape parameters. The expectation $\mathbb{E}[Q]$ is $a + \frac{(b-a)\alpha}{\alpha+\beta}$ and the standard deviation σ_Q is $\frac{(b-a)\sqrt{\alpha\beta}}{(\alpha+\beta)\sqrt{1+\alpha+\beta}}$. A Gamma distribution $\Gamma_{\alpha,\,\beta,\,a,\,c}$ of support $[a, \infty[$ is defined by

$$\Gamma_{\alpha,\,\beta,\,a,\,c}(q) = \begin{cases} \frac{\left(\frac{q-a}{c}\right)^{\alpha-1}\beta^{\alpha}e^{-\beta\left(\frac{q-a}{c}\right)}}{c\Gamma(\alpha)} & \text{if } q \in [a,\,\infty[\,; \\ 0 & \text{if } q \in]-\infty,\,a[\,, \end{cases} \tag{20}$$

where $\Gamma(\alpha)$ is the normalisation constant, $\alpha > 0$ is the shape parameter, $\beta > 0$ is the rate parameter, and c allows defining the distribution independently of the possible unit of Q. The expectation $\mathbb{E}[Q]$ is $a + \frac{c\alpha}{\beta}$ and the standard deviation σ_Q is $\frac{c\sqrt{\alpha}}{\beta}$.

2.2.2. Random vector with values in $\Re^n$

Definition. The n-dimension random vector $\boldsymbol{Q} = [Q_1\ Q_2\ ...\ Q_n]^T$ is defined as a function $\boldsymbol{Q} : \mathcal{Q} \to \Re^n$, where $\mathcal{Q}$ is a high dimension space. We note that $\boldsymbol{Q}$ is not a vector in $\Re^n$ but a mapping; however a realisation $\boldsymbol{Q}(q)$ for a fixed $q \in \mathcal{Q}$ is a vector in $\Re^n$. The components Q_i are also random variables. Each random variable Q_i is associated to a cumulative distribution function $F_{Q_i} : \Re \to [0,\,1]$, with $F_{Q_i}(q_i) = \mathbb{P}(Q_i \leq q_i)$ the probability for the random variable Q_i to be lower than q_i. The cumulative distribution function $F_{Q_i} : \Re \to [0,\,1]$ is in this context also called marginal cumulative distribution function.

Joint cumulative distribution function. The joint probability $\mathbb{P}(\boldsymbol{Q} \leq \boldsymbol{q})$ is defined on the probability space $(\mathcal{Q},\,\mathcal{F},\,\mathbb{P})$ as the probability $\mathbb{P}(Q_1 \leq q_1,\,\dots,Q_n \leq q_n)$.

The joint cumulative distribution function $F_{\boldsymbol{Q}} : \Re^n \to [0,\,1]$, of a random vector $\boldsymbol{Q}$ on the probability space $(\mathcal{Q},\,\mathcal{F},\,\mathbb{P})$ is thus given by

$$F_{\boldsymbol{Q}}(\boldsymbol{q}) = \mathbb{P}(\boldsymbol{Q} \leq \boldsymbol{q}) \qquad \forall \boldsymbol{q} \in \Re^n\,. \tag{21}$$

Discrete random vectors. In the case of discrete random vectors $\boldsymbol{Q}$ that can only take values in some countable subset $\{\boldsymbol{q}^{(1)},\,\boldsymbol{q}^{(2)},\,...\}$ of $\Re^n$, the probability mass function $\pi_{\boldsymbol{Q}} : \Re^n \to [0,\,1]$ is defined using the previous notations as

$$\pi_{\boldsymbol{Q}}(\boldsymbol{q}^{(i)}) = \mathbb{P}(\boldsymbol{Q} = \boldsymbol{q}^{(i)})\,. \tag{22}$$

Similarly to Eq. (5), the expectation operator $\bar{\boldsymbol{q}} = \mathbb{E}\left[\boldsymbol{Q}\right] \in \Re^n$ of the random vector $\boldsymbol{Q}$ is then defined for its component s as

$$\bar{q}_s = \mathbb{E}\left[Q_s\right] = \sum_{q_s^{(i)};\, \pi_{Q_s}(q_s^{(i)})>0} q_s^{(i)} \pi_{Q_s}(q_s^{(i)}) \quad \forall s = 1..n\,, \tag{23}$$

where the summation is over all the possible $\boldsymbol{q}^{(i)}$, and where no sum on s is intended.

Continuous random vectors. In the case of continuous random vectors $\boldsymbol{Q}$, the probability density function $\pi_{\boldsymbol{Q}} : \Re^n \to [0,\, \infty[$, assuming it exists, is defined using the previous notations such that

$$\int_{]-\infty,\, q_1]\times \ldots \times]-\infty,\, q_n]} \pi_{\boldsymbol{Q}}(\boldsymbol{u})d\boldsymbol{u} = F_{\boldsymbol{Q}}(\boldsymbol{q}) = \mathbb{P}(\boldsymbol{Q} \leq \boldsymbol{q})\,, \tag{24}$$

and, if the joint cumulative distribution function $F_{\boldsymbol{Q}}(\boldsymbol{q})$ is differentiable, it comes

$$\pi_{\boldsymbol{Q}}(\boldsymbol{q}) = \frac{\partial^n}{\partial q_1 \, \ldots \, \partial q_n} F_{\boldsymbol{Q}}(\boldsymbol{q})\,. \tag{25}$$

Similarly to Eq. (9), the expectation operator $\bar{\boldsymbol{q}} = \mathbb{E}\left[\boldsymbol{Q}\right] \in \Re^n$ of the random vector $\boldsymbol{Q}$ is then defined for its component s as

$$\bar{q}_s = \mathbb{E}\left[Q_s\right] = \int_{\Re} q_s \pi_{Q_s}(q_s) dq\,, \tag{26}$$

whenever it exists and where no sum on s is intended.

Second-order random vector & m^{th}-order random vector. $\boldsymbol{Q}$ is a second order random vector if $\mathbb{E}[\boldsymbol{Q}^T\boldsymbol{Q}] < \infty$.

$\boldsymbol{Q}$ is a m^{th}-order random vector of joint probability density $\pi_{\boldsymbol{Q}}(\boldsymbol{q})$ if

$$\mathbb{E}[\|\boldsymbol{Q}\|^m] = \int_{\Re^n} \|\boldsymbol{q}\|^m \, \pi_{\boldsymbol{Q}}(\boldsymbol{q})d\boldsymbol{q} < +\infty\,, \forall m \in \mathbb{N} \tag{27}$$

where $\|\boldsymbol{q}\| = \sqrt{\boldsymbol{q}^T\boldsymbol{q}}$.

Support and support indicator function. The support $\mathcal{S}_{\boldsymbol{Q}}$ of the probability distribution of the random vector $\boldsymbol{Q}$ is the smallest closed set $\mathcal{S}_{\boldsymbol{Q}} \subset \Re^n$ such that $\mathbb{P}(\boldsymbol{Q} \in \mathcal{S}_{\boldsymbol{Q}}) = 1$. As for a random variable, with a similar expression than Eq. (6), the support indicator $\chi_{\mathcal{S}_{\boldsymbol{Q}}} : \Re \to \{0,\, 1\}$ is defined as

$$\chi_{\mathcal{S}_{\boldsymbol{Q}}}(\boldsymbol{q}) = \begin{cases} 1 & \text{if } \boldsymbol{q} \in \mathcal{S}_{\boldsymbol{Q}}\,;\ \text{and} \\ 0 & \text{if } \boldsymbol{q} \notin \mathcal{S}_{\boldsymbol{Q}}\,. \end{cases} \tag{28}$$

The probability mass/density function $\pi_{\boldsymbol{Q}}(\boldsymbol{q})$ can then be expressed as $\pi_{\boldsymbol{Q}}(\boldsymbol{q}) = \chi_{\mathcal{S}_{\boldsymbol{Q}}}(\boldsymbol{q}) f_{\boldsymbol{Q}}(\boldsymbol{q})$ where

$$\sum_{\boldsymbol{q}^{(i)} \in \mathcal{S}_{\boldsymbol{Q}}} f_{\boldsymbol{Q}}(\boldsymbol{q}^{(i)}) = 1 \quad \text{or} \quad \int_{\mathcal{S}_{\boldsymbol{Q}}} f_{\boldsymbol{Q}}(\boldsymbol{q})d\boldsymbol{q} = 1\,, \tag{29}$$

for discrete and continuous random vectors, respectively.

Moments. We note that the moments of a random vector can also be defined for $\boldsymbol{k} = \{k_1,\, ...,\, k_n\} \in \mathbb{N}_0^n$ as

$$m_{\boldsymbol{k}_{\boldsymbol{Q}}} = \mathbb{E}\left[Q_1^{k_1} \times ... \times Q_n^{k_n}\right] \,. \tag{30}$$

Event indicator functions. Finally, the event indicator function (15) $\chi_{\mathscr{A}} : \mathscr{Q} \to \{0,\, 1\}$ is readily generalised for an event $\mathscr{A} \subset \mathscr{Q}$ and $\mathscr{A}^c$ its complement.

2.2.3. *Joint distributions of random vectors with values in* $\Re^n$

Let us consider the n-dimension random vector $\boldsymbol{Q} = [Q_1\; Q_2\; ...\; Q_n]^T : \mathscr{Q} \to \Re^n$ and the m-dimension random vector $\boldsymbol{Y} = [Y_1\; Y_2\; ...\; Y_m]^T : \mathscr{Q} \to \Re^m$.

The joint cumulative distribution function of a pair of random vectors $(\boldsymbol{Q},\, \boldsymbol{Y})$ is the function $F_{\boldsymbol{Q},\boldsymbol{Y}} : \Re^n \times \Re^m \to [0,\, 1]$ such that

$$F_{\boldsymbol{Q},\boldsymbol{Y}}\left(\boldsymbol{q},\, \boldsymbol{y}\right) = \mathbb{P}\left(\boldsymbol{Q} \le \boldsymbol{q} \text{ and } \boldsymbol{Y} \le \boldsymbol{y}\right) \,. \tag{31}$$

Pair of discrete random vectors. The joint probability mass function $\pi_{\boldsymbol{Q},\boldsymbol{Y}} : \Re^n \times \Re^m \to [0,\, 1]$ of a pair of discrete random vectors $(\boldsymbol{Q},\, \boldsymbol{Y})$ reads

$$\pi_{\boldsymbol{Q},\boldsymbol{Y}}\left(\boldsymbol{q}^{(i)},\, \boldsymbol{y}^{(j)}\right) = \mathbb{P}\left(\boldsymbol{Q} = \boldsymbol{q}^{(i)} \text{ and } \boldsymbol{Y} = \boldsymbol{y}^{(j)}\right) \,. \tag{32}$$

The marginal probability mass function $\pi_{\boldsymbol{Q}} : \Re^n \to [0,\, 1]$ is defined as

$$\pi_{\boldsymbol{Q}}\left(\boldsymbol{q}^{(i)}\right) = \mathbb{P}\left(\boldsymbol{Q} = \boldsymbol{q}^{(i)}\right) = \sum_{\boldsymbol{y}^{(j)}} \pi_{\boldsymbol{Q},\boldsymbol{Y}}\left(\boldsymbol{q}^{(i)},\, \boldsymbol{y}^{(j)}\right) \,, \tag{33}$$

for all possible $\boldsymbol{y}^{(j)}$.

The conditional cumulative distribution function of $\boldsymbol{Y}$ knowing $\boldsymbol{Q} = \boldsymbol{q}^{(i)}$, with $\mathbb{P}\left(\boldsymbol{Q} = \boldsymbol{q}^{(j)}\right) > 0$ is defined as

$$F_{\boldsymbol{Y}|\boldsymbol{Q}}\left(\boldsymbol{y}^{(j)}|\boldsymbol{q}^{(i)}\right) = \mathbb{P}\left(\boldsymbol{Y} \le \boldsymbol{y}^{(j)}|\boldsymbol{Q} = \boldsymbol{q}^{(i)}\right) \,, \tag{34}$$

and the conditional probability mass function of $\boldsymbol{Y}$ knowing $\boldsymbol{Q} = \boldsymbol{q}^{(i)}$, with $\mathbb{P}\left(\boldsymbol{Q} = \boldsymbol{q}^{(j)}\right) > 0$ is defined as

$$\pi_{\boldsymbol{Y}|\boldsymbol{Q}}\left(\boldsymbol{y}^{(j)}|\boldsymbol{q}^{(i)}\right) = \mathbb{P}\left(\boldsymbol{Y} = \boldsymbol{y}^{(j)}|\boldsymbol{Q} = \boldsymbol{q}^{(i)}\right) \,. \tag{35}$$

The conditional expectation of $\boldsymbol{Y}$ knowing $\boldsymbol{Q} = \boldsymbol{q}^{(i)}$ reads

$$\boldsymbol{\Psi}\left(\boldsymbol{q}^{(i)}\right) = \mathbb{E}\left[\boldsymbol{Y}|\boldsymbol{Q} = \boldsymbol{q}^{(i)}\right] = \sum_{\boldsymbol{y}^{(j)}} \boldsymbol{y}^{(j)} \pi_{\boldsymbol{Y}|\boldsymbol{Q}}\left(\boldsymbol{y}^{(j)}|\boldsymbol{q}^{(i)}\right) \,, \tag{36}$$

for all possible $\boldsymbol{y}^{(j)}$, and can be seen as a vector dependent on the value $\boldsymbol{q}^{(i)}$ taken by $\boldsymbol{Q}$. $\boldsymbol{\Psi}\left(\boldsymbol{Q}\right)$ is thus another m-dimension random vector called the conditional expectation of $\boldsymbol{Y}$ knowing $\boldsymbol{Q}$ and denoted $\mathbb{E}\left[\boldsymbol{Y}|\boldsymbol{Q}\right]$ (Grimmett and Stirzaker, 2001).

Pair of continuous random vectors. The random vectors $\boldsymbol{Q}$ and $\boldsymbol{Y}$ are jointly continuous with the joint probability density function $\pi_{\boldsymbol{Q},\boldsymbol{Y}} : \Re^n \times \Re^m \to [0, \infty[$ if

$$F_{\boldsymbol{Q},\boldsymbol{Y}}(\boldsymbol{q}, \boldsymbol{y}) = \int_{]-\infty, y_1]\times\ldots]-\infty, y_m]} \int_{]-\infty, q_1]\times\ldots]-\infty, q_n]} \pi_{\boldsymbol{Q},\boldsymbol{Y}}(\boldsymbol{u}, \boldsymbol{v})\, d\boldsymbol{u}d\boldsymbol{v}\,. \tag{37}$$

We define the marginal cumulative distribution $F_{\boldsymbol{Q}} : \Re^n \to [0, 1]$ such that

$$F_{\boldsymbol{Q}}(\boldsymbol{q}) = \mathbb{P}(\boldsymbol{Q} \leq \boldsymbol{q}) = \int_{]-\infty, q_1]\times\ldots]-\infty, q_n]} \left(\int_{\Re^m} \pi_{\boldsymbol{Q},\boldsymbol{Y}}(\boldsymbol{u}, \boldsymbol{y})\, d\boldsymbol{y} \right) d\boldsymbol{u}\,, \tag{38}$$

and the marginal probability density function $\pi_{\boldsymbol{Q}} : \Re^n \to [0, \infty[$ follows as

$$\pi_{\boldsymbol{Q}}(\boldsymbol{q}) = \int_{\Re^m} \pi_{\boldsymbol{Q},\boldsymbol{Y}}(\boldsymbol{q}, \boldsymbol{y})\, d\boldsymbol{y}\,. \tag{39}$$

Finally, the conditional cumulative distribution function of $\boldsymbol{Y}$ knowing $\boldsymbol{Q} = \boldsymbol{q}$, with $\pi_{\boldsymbol{Q}}(\boldsymbol{q}) > 0$ is defined as

$$F_{\boldsymbol{Y}|\boldsymbol{Q}}(\boldsymbol{y}|\boldsymbol{q}) = \frac{1}{\pi_{\boldsymbol{Q}}(\boldsymbol{q})} \int_{]-\infty, y_1]\times\ldots\times]-\infty, y_m]} \pi_{\boldsymbol{Q},\boldsymbol{Y}}(\boldsymbol{q}, \boldsymbol{v})\, d\boldsymbol{v}\,, \tag{40}$$

and the conditional probability density function of $\boldsymbol{Y}$ knowing $\boldsymbol{Q} = \boldsymbol{q}$, with $\pi_{\boldsymbol{Q}}(\boldsymbol{q}) > 0$ is defined as

$$\pi_{\boldsymbol{Y}|\boldsymbol{Q}}(\boldsymbol{y}|\boldsymbol{q}) = \frac{\pi_{\boldsymbol{Q},\boldsymbol{Y}}(\boldsymbol{q}, \boldsymbol{y})}{\pi_{\boldsymbol{Q}}(\boldsymbol{q})}\,. \tag{41}$$

The conditional expectation of $\boldsymbol{Y}$ knowing $\boldsymbol{Q}$ reads

$$\boldsymbol{\Psi}(\boldsymbol{q}) = \mathbb{E}[\boldsymbol{Y}|\boldsymbol{Q} = \boldsymbol{q}] = \int_{\Re^m} \boldsymbol{y}\pi_{\boldsymbol{Y}|\boldsymbol{Q}}(\boldsymbol{y}|\boldsymbol{q})\, d\boldsymbol{y}\,, \tag{42}$$

which can be seen as a vector dependent on the value taken by $\boldsymbol{Q}$. $\boldsymbol{\Psi}(\boldsymbol{Q})$ is another m-dimension random vector called the conditional expectation of $\boldsymbol{Y}$ knowing $\boldsymbol{Q}$ and denoted $\mathbb{E}[\boldsymbol{Y}|\boldsymbol{Q}]$.

2.3. Random vector fields

In order to further characterise the properties distribution over a body, we introduce the notion of random (vector) field.

2.3.1. Discrete and continuous random vector fields

Discrete random vector field. Considering $\Omega = \{\boldsymbol{x}^{(0)}, \boldsymbol{x}^{(1)}, \ldots\}$ a countable set of material points with $\Omega \subset \Re^d$, with $d \in \mathbb{N}$, a discrete random vector field $\boldsymbol{Q}(\Omega)$ is a countable family $\{\boldsymbol{Q}(\boldsymbol{x}^{(i)}) : \boldsymbol{x}^{(i)} \in \Omega\}$ of random vectors which map the sample space $\mathcal{Q}$ in a set $\mathcal{S}_{\boldsymbol{Q}}$. For all fixed $\boldsymbol{x}^{(i)} \in \Omega$, $\boldsymbol{Q}(\boldsymbol{x}^{(i)})$ is a random vector of support $\mathcal{S}_{\boldsymbol{Q}}$. We note that for $d = 1$ the random field is called random process.

Continuous random vector field. Considering $\Omega \subset \Re^d$, $d \in \mathbb{N}$, a space of material points, a continuous random vector field $\boldsymbol{Q}(\Omega)$ is an uncountable family $\{\boldsymbol{Q}(\boldsymbol{x}) : \boldsymbol{x} \in \Omega\}$ of random vectors which map the sample space $\mathcal{Q}$ in a set $\mathcal{S}_{\boldsymbol{Q}}$. For all fixed $\boldsymbol{x} \in \Omega$, $\boldsymbol{Q}(\boldsymbol{x})$ is a random vector of support $\mathcal{S}_{\boldsymbol{Q}}$.

Remarks. The set $\mathcal{S}_{\boldsymbol{Q}}$ can be either countable or uncountable in both cases.

We also use the notations $\{\boldsymbol{Q}(\boldsymbol{x}^{(i)};\, q^{(i)}) : \boldsymbol{x}^{(i)} \in \Omega,\, q^{(i)} \in \mathcal{Q}\}$, $\{\boldsymbol{Q}(\boldsymbol{x}^{(i)};\, q) : \boldsymbol{x}^{(i)} \in \Omega,\, q \in \mathcal{Q}\}$, $\{\boldsymbol{Q}(\boldsymbol{x};\, q^{(i)}) : \boldsymbol{x} \in \Omega,\, q^{(i)} \in \mathcal{Q}\}$ and $\{\boldsymbol{Q}(\boldsymbol{x};\, q) : \boldsymbol{x} \in \Omega,\, q \in \mathcal{Q}\}$ to denote the random field for the cases of discrete/continuous fields and countable/ uncontable supports.

2.3.2. Properties

Realisation path. For a fixed $\boldsymbol{x}$, the evaluation of $\boldsymbol{Q}(\boldsymbol{x})$ at a given $q \in \mathcal{Q}$ yields a point of $\mathcal{S}_{\boldsymbol{Q}}$, defining the mapping $\boldsymbol{Q}(\boldsymbol{x};\, q) : \Omega \to \mathcal{S}_{\boldsymbol{Q}}$.

For a fixed $q \in \mathcal{Q}$, the collection $\{\boldsymbol{Q}(\boldsymbol{x};\, q) : \boldsymbol{x} \in \Omega\}$ is known as the trajectory or sample path.

Stationary and homogeneous random vector fields. The random field $\boldsymbol{Q}(\Omega) = \{\boldsymbol{Q}(\boldsymbol{x}) : \boldsymbol{x} \in \Omega\}$ is said to be (strongly) stationary if for any set $\mathbf{x} = (\boldsymbol{x}^{(1)}, \ldots, \boldsymbol{x}^{(m)})$ of m members of Ω, and for any translation vector $\boldsymbol{\tau} \in \Re^d$ such that $\boldsymbol{x}^{(1)} + \boldsymbol{\tau}, \ldots, \boldsymbol{x}^{(m)} + \boldsymbol{\tau} \in \Omega$, the two families $\{\boldsymbol{Q}\left(\boldsymbol{x}^{(1)}\right), \ldots, \boldsymbol{Q}\left(\boldsymbol{x}^{(m)}\right)\}$ and $\{\boldsymbol{Q}\left(\boldsymbol{x}^{(1)} + \boldsymbol{\tau}\right), \ldots, \boldsymbol{Q}\left(\boldsymbol{x}^{(m)} + \boldsymbol{\tau}\right)\}$ have the same joint cumulative distribution. We refer to (Grimmett and Stirzaker, 2001) for the definition of the joint cumulative distribution function in this context.

The random field $\boldsymbol{Q}(\Omega) = \{\boldsymbol{Q}(\boldsymbol{x}) : \boldsymbol{x} \in \Omega\}$ is said to be weak stationary, or second-order stationary, or again homogeneous, if for any pair $(\boldsymbol{x}^{(1)}, \boldsymbol{x}^{(2)})$ of Ω, and for any translation vector $\boldsymbol{\tau} \in \Re^d$ such that $\boldsymbol{x}^{(1)} + \boldsymbol{\tau}$, $\boldsymbol{x}^{(2)} + \boldsymbol{\tau} \in \Omega$, one has

$$\begin{aligned}
&\mathbb{E}\left[\boldsymbol{Q}(\boldsymbol{x}^{(1)})\right] = \mathbb{E}\left[\boldsymbol{Q}(\boldsymbol{x}^{(1)} + \boldsymbol{\tau})\right]; \quad \text{and}\\
&\mathbb{E}\left[\left(\boldsymbol{Q}(\boldsymbol{x}^{(1)}) - \mathbb{E}[\boldsymbol{Q}(\boldsymbol{x}^{(1)})]\right)\left(\boldsymbol{Q}(\boldsymbol{x}^{(1)} + \boldsymbol{\tau}) - \mathbb{E}[\boldsymbol{Q}(\boldsymbol{x}^{(1)} + \boldsymbol{\tau})]\right)^T\right] =\\
&\mathbb{E}\left[\left(\boldsymbol{Q}(\boldsymbol{x}^{(2)}) - \mathbb{E}[\boldsymbol{Q}(\boldsymbol{x}^{(2)})]\right)\left(\boldsymbol{Q}(\boldsymbol{x}^{(2)} + \boldsymbol{\tau}) - \mathbb{E}[\boldsymbol{Q}(\boldsymbol{x}^{(2)} + \boldsymbol{\tau})]\right)^T\right]. \qquad (43)
\end{aligned}$$

The random field is said to be isotropic and homogeneous, if only the norm τ of $\boldsymbol{\tau}$ and not the direction has importance in the last equation, *i.e.*

$$\begin{aligned}
&\mathbb{E}\left[\boldsymbol{Q}(\boldsymbol{x}^{(1)})\right] = \mathbb{E}\left[\boldsymbol{Q}(\boldsymbol{x}^{(2)})\right]; \quad \text{and}\\
&\mathbb{E}\left[\left(\boldsymbol{Q}(\boldsymbol{x}^{(1)}) - \mathbb{E}[\boldsymbol{Q}(\boldsymbol{x}^{(1)})]\right)\left(\boldsymbol{Q}(\boldsymbol{x}^{(1)} + \tau\boldsymbol{n}^{(1)}) - \mathbb{E}[\boldsymbol{Q}(\boldsymbol{x}^{(1)} + \tau\boldsymbol{n}^{(1)})]\right)^T\right] =\\
&\mathbb{E}\left[\left(\boldsymbol{Q}(\boldsymbol{x}^{(2)}) - \mathbb{E}[\boldsymbol{Q}(\boldsymbol{x}^{(2)})]\right)\left(\boldsymbol{Q}(\boldsymbol{x}^{(2)} + \tau\boldsymbol{n}^{(2)}) - \mathbb{E}[\boldsymbol{Q}(\boldsymbol{x}^{(2)} + \tau\boldsymbol{n}^{(2)})]\right)^T\right],
\end{aligned} \qquad (44)$$

for any unit vectors $\boldsymbol{n}^{(1)}$ and $\boldsymbol{n}^{(2)} \in \Re^d$.

Ergodicity. Finally, if the random field $\boldsymbol{Q}(\Omega) = \{\boldsymbol{Q}(\boldsymbol{x}) : \boldsymbol{x} \in \Omega\}$ is stationary and ergodic[4], with $\mathbb{E}\left[\boldsymbol{Q}(\boldsymbol{x}^{(1)})\right]$ finite, one has

$$\frac{1}{V(\omega)} \int_{\omega} \boldsymbol{Q}(\boldsymbol{x};\, q) d\boldsymbol{x} \rightarrow \mathbb{E}\left[\boldsymbol{Q}(\boldsymbol{x}^{(1)})\right] \,, \tag{45}$$

where ω is a subset of Ω and $V(\omega)$ is the volume of ω, and where the $\rightarrow$ means converges almost surely with the size of ω. This means that analysing one realisation of appropriate size allows extracting the statistical behaviour of the random field. Besides, the expectation obtained from many small samples yields the same value as the expectation of a large one.

2.4. Correlation & covariance matrices

On top of the moments, which characterise some statistical properties of the random vector, the correlation, either between the vector components or between different random vectors, is of particular interest and should be respected when generating stochastic properties. In the case of a random field this correlation evolution in terms of a translation vector in Ω is also bringing more information on the stochastic process.

2.4.1. Random vectors

Let us consider the n-dimension random vector $\boldsymbol{Q} = [Q_1\ Q_2\ ...\ Q_n]^T : \mathfrak{Q} \rightarrow \Re^n$ and the m-dimension random vector $\boldsymbol{Y} = [Y_1\ Y_2\ ...\ Y_m]^T : \mathfrak{Q} \rightarrow \Re^m$.

The covariance matrix $\tilde{\mathbf{R}}_{\boldsymbol{Q}} \in \mathbb{M}^+_{0_n}(\Re)$, where $\mathbb{M}^+_{0_n}(\Re)$ refers to all symmetric semi-positive-definite real matrices of size $n \times n$, is defined by its entries $r\,s$

$$\tilde{R}_{\boldsymbol{Q}_{r\,s}} = \mathbb{E}\left[(Q_r - \mathbb{E}[Q_r])(Q_s - \mathbb{E}[Q_s])\right] \,,\ r,\, s = 1..n\,. \tag{46}$$

Assuming the standard deviations σ_{Q_r} of the random variables Q_r are all strictly positive, then $\tilde{\mathbf{R}}_{\boldsymbol{Q}} \in \mathbb{M}^+_n(\Re)$, where $\mathbb{M}^+_n(\Re)$ refers to all symmetric positive-definite real matrices of size $n \times n$, and the correlation matrix $\mathbf{R}_{\boldsymbol{Q}} \in \mathbb{M}^+_n(\Re)$ is defined by its entries $r\,s$ as

$$R_{\boldsymbol{Q}_{r\,s}} = \frac{\tilde{R}_{\boldsymbol{Q}_{r\,s}}}{\sigma_{Q_r}\sigma_{Q_s}} = \frac{\mathbb{E}\left[(Q_r - \mathbb{E}[Q_r])(Q_s - \mathbb{E}[Q_s])\right]}{\sigma_{Q_r}\sigma_{Q_s}} \,,\ r,\, s = 1..n\,. \tag{47}$$

We note that the diagonal terms correspond to the unity.

We note that in the case for which the random variables Q_s follow a Gaussian distribution, the correlation also brings information on their statistical dependence, an entry $R_{\boldsymbol{Q}_{r\,s}}$ close to zero meaning statistical independence of random variables Q_s and Q_r. However, if the random variables do not follow such a Gaussian distribution, the statistical dependence of the random variables Q_r cannot be assessed by the correlation. An alternative is to consider their distance correlations matrix denoted by $\mathbf{dR}_{\boldsymbol{Q}}$: each entry of $dR_{\boldsymbol{Q}_{r\,s}}$ is the distance covariance divided by the product of their distance standard deviations, whose detailed expressions are given by Székely et al. (2007).

---

[4] We refer to (Chiu et al., 2013) for the definition of ergodicity and here give the consequence.

The cross-covariance matrix $\tilde{\mathbf{R}}_{\boldsymbol{Q},\boldsymbol{Y}} \in \Re^{n\times m}$, is defined by its entries $r\,s$ as

$$\tilde{R}_{\boldsymbol{Q},\boldsymbol{Y}_{r\,s}} = \mathbb{E}\left[(Q_r - \mathbb{E}[Q_r])(Y_s - \mathbb{E}[Y_s])\right]\,,\ r = 1..n,\ s = 1..m\,. \tag{48}$$

Assuming the standard deviations of the random variables Q_r and Y_s are all strictly positive, the cross-correlation matrix $\mathbf{R}_{\boldsymbol{Q},\boldsymbol{Y}} \in \Re^{n\times m}$, is defined by its entries $r\,s$ as

$$R_{\boldsymbol{Q},\boldsymbol{Y}_{r\,s}} = \frac{\tilde{R}_{\boldsymbol{Q},\boldsymbol{Y}_{r\,s}}}{\sigma_{Y_r}\sigma_{Y_s}} = \frac{\mathbb{E}\left[(Q_r - \mathbb{E}[Q_r])(Y_s - \mathbb{E}[Y_s])\right]}{\sigma_{Y_r}\sigma_{Y_s}}\,,\ r = 1..n,\ s = 1..m\,. \tag{49}$$

2.4.2. Random vector fields

Let us consider the random field $\boldsymbol{Q}(\Omega)$ as the collection $\{\boldsymbol{Q}(\boldsymbol{x}) : \boldsymbol{x} \in \Omega\}$ of random vectors $\boldsymbol{Q}(\boldsymbol{x})$, and the translation vector $\boldsymbol{\tau}$ such that $\boldsymbol{x} + \boldsymbol{\tau} \in \Omega$.

The covariance matrix $\tilde{\mathbf{R}}_{\boldsymbol{Q}}(\boldsymbol{x};\,\boldsymbol{\tau}) : \Omega \times \Omega \to \Re^{n\times n}$, is defined by its entries $r\,s$ as

$$\tilde{R}_{\boldsymbol{Q}_{r\,s}}(\boldsymbol{x};\,\boldsymbol{\tau}) \;=\; \mathbb{E}\left[(Q_r(\boldsymbol{x}) - \mathbb{E}[Q_r(\boldsymbol{x})])(Q_s(\boldsymbol{x}+\boldsymbol{\tau}) - \mathbb{E}[Q_s(\boldsymbol{x}+\boldsymbol{\tau})])\right]\,,\ r,\ s = 1..n\,. \tag{50}$$

Assuming the standard deviations $\sigma_{Q_r(\boldsymbol{x})}$ of the random variables $Q_r(\boldsymbol{x})$ are all strictly positive, the correlation matrix $\mathbf{R}_{\boldsymbol{Q}}(\boldsymbol{x};\,\boldsymbol{\tau}) : \Omega \times \Omega \to \Re^{n\times n}$, is defined by its entries $r\,s$ as

$$\begin{aligned} R_{\boldsymbol{Q}_{r\,s}}(\boldsymbol{x};\,\boldsymbol{\tau}) \;&=\; \frac{\tilde{R}_{\boldsymbol{Q}_{r\,s}}(\boldsymbol{x};\,\boldsymbol{\tau})}{\sigma_{Q_r}(\boldsymbol{x})\sigma_{Q_s}(\boldsymbol{x}+\boldsymbol{\tau})} \\ &=\; \frac{\mathbb{E}\left[(Q_r(\boldsymbol{x}) - \mathbb{E}[Q_r(\boldsymbol{x})])(Q_s(\boldsymbol{x}+\boldsymbol{\tau}) - \mathbb{E}[Q_s(\boldsymbol{x}+\boldsymbol{\tau})])\right]}{\sigma_{Q_r}(\boldsymbol{x})\sigma_{Q_s}(\boldsymbol{x}+\boldsymbol{\tau})}\,,\ r,\ s = 1..n\,. \end{aligned} \tag{51}$$

In case of a homogeneous random field, one has $\mathbf{R}_{\boldsymbol{Q}}(\boldsymbol{x};\,\boldsymbol{\tau}) = \mathbf{R}_{\boldsymbol{Q}}(\boldsymbol{\tau})$ and $\tilde{\mathbf{R}}_{\boldsymbol{Q}}(\boldsymbol{x};\,\boldsymbol{\tau}) = \tilde{\mathbf{R}}_{\boldsymbol{Q}}(\boldsymbol{\tau})$. Finally, if the random field is homogeneous and isotropic, one has $\mathbf{R}_{\boldsymbol{Q}}(\boldsymbol{x};\,\boldsymbol{\tau}) = \mathbf{R}_{\boldsymbol{Q}}(\tau)$ and $\tilde{\mathbf{R}}_{\boldsymbol{Q}}(\boldsymbol{x};\,\boldsymbol{\tau}) = \tilde{\mathbf{R}}_{\boldsymbol{Q}}(\tau)$, where τ is the norm of $\boldsymbol{\tau}$.

3. Virtual micro-structures

The concept of virtual stochastic testing strongly relies on the ability to generate virtual micro-structure samples that contain the statistical information of real materials. In this context, the stochastic descriptions, relying on a mathematics model or on database, are characterised by a quantification of the material uncertainties. A generator of virtual micro-structure should then be built from these stochastic descriptions.

Different methods of characterisation and of reconstruction, the latter being strongly linked to the former, exist. However, none of them is universal as pointed out by Bostanabad et al. (2018) and the method should be carefully selected/developed for the studied micro-structure. The different methods however follow a similar methodology as illustrated in Fig. 1

- First data need to be obtained, either from experimental means, *e.g.* Scanning Electron Microscopy (SEM) images from unidirectional (UD) composites, or possibly by simulating the manufacturing process;

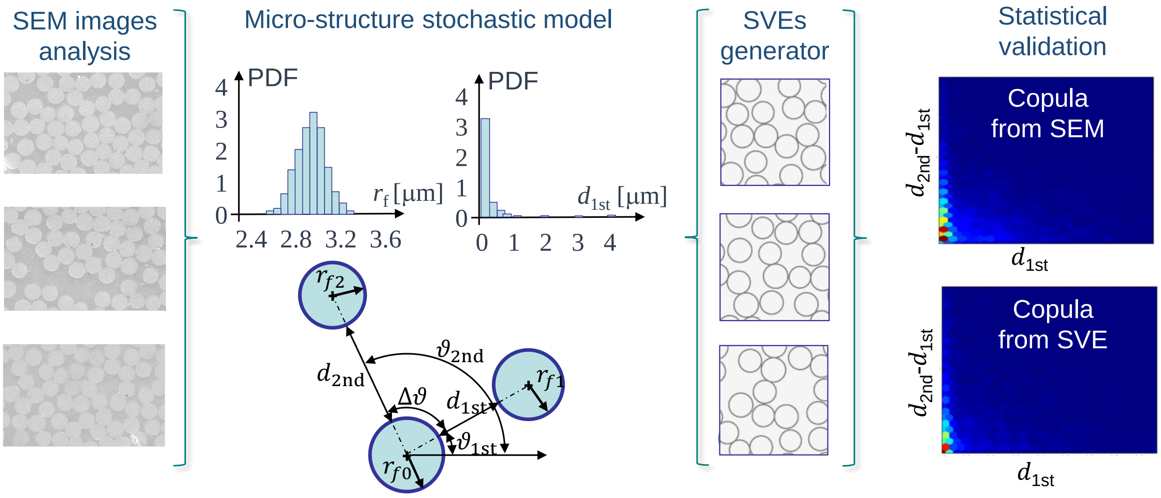

Figure 1: Geometrical characterisation and reconstruction of the microstructure of a unidirectional composite material by Wu et al. (2018a); SEM images are analysed in order to extract (distance) correlated statistical descriptors which are in turn used to generate virtual micro-geometries respecting those statistical descriptors, including their distance correlation.

- A statistical characterisation has then to be performed from the available data, *e.g.* physical descriptors such as neighbouring distances for UD;
- A reconstruction method is developed using the statistical characterisation in order to generate virtual micro-structures;
- The statistical properties of the virtual micro-structures are validated with the ones of the initial data, *e.g.* for UD the copula of two physical descriptors, see further explanations.

We note that the characterisation and reconstruction are not only related to the geometrical properties of the micro-structure, but the material response of the different constituents also ought to be considered in order to generate virtual micro-structures that can be used to predict meso-scale, or homogenised, stochastic material responses. Besides, defects also strongly affect the apparent material behaviours and should thus be characterised as well.

3.1. Statistical geometrical characterisation & Reconstruction

A recent comprehensive review of the statistical geometrical characterisation & reconstruction has been provided by Bostanabad et al. (2018). In this section we will review the existing methodologies with a particular emphasis for the different common micro-structures illustrated in Fig. 2. But before we define the stochastic micro-structure.

3.1.1. Definitions related to the stochastic micro-structure

Description of a local state by a random variable/vector. Considering the probability space $(\mathcal{W}, \mathcal{F}, \mathbb{P})$ and a fixed material point of a micro-structure, the local state of the material point can be represented by a random vector $\boldsymbol{H} : \mathcal{W} \rightarrow \Re^n$, with $\mathcal{S}_{\boldsymbol{H}}$ the support of the

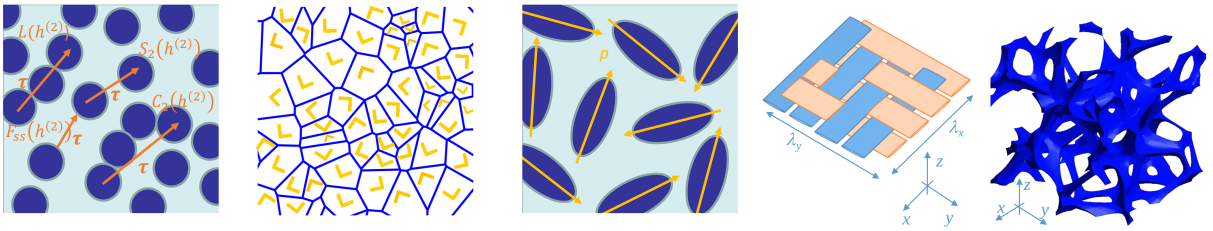

(a) UD (b) Poly-crystal (c) SFRP (d) Woven (e) Foam

Figure 2: Schematics of different micro-structures ω: (a) Cross-section of a unidirectional (UD) fibre reinforced matrix; (b) Single-phase poly-crystal; (c) 2D schematics of short fibre reinforced matrix; (d) 2/2 twill woven textile; and (e) Metallic open foam.

probability distribution function. Some examples are now given for the micro-structures illustrated in 2D in Fig. 2.

Figure 2(a) represents the cross-section of a Unidirectional (UD) fibre reinforced matrix. The matrix phase is represented by the set of material points $\omega_0 \subset \omega$ and the fibre phase by the set of material points $\omega_{\mathrm{I}} \subset \omega$. In that case, the sample space of one material point $\mathscr{W}_{\text{phase}} = \{0,\, \mathrm{I}\}$ lists the two possible phases, 0 for the matrix phase and I for the inclusion phase, of the composite material. For $\mathscr{w} \in \mathscr{W}_{\text{phase}}$, let us define the random variable $H : \mathscr{W}_{\text{phase}} \rightarrow \Re$ as

$$H_{\text{phase}}(\mathscr{w}) = \begin{cases} h^{(1)}_{\text{phase}} = 0 & \text{if } \mathscr{w} = 0\,; \text{ and} \\ h^{(2)}_{\text{phase}} = 1 & \text{if } \mathscr{w} = \mathrm{I}\,. \end{cases} \tag{52}$$

This defines a discrete random variable H_{phase} with the support set $\mathcal{S}_{H_{\text{phase}}} = \{0,\, 1\} \subset \Re$. If the problem is statistically homogeneous, the probability mass function $\pi_{H_{\text{phase}}}\left(h^{(2)}_{\text{phase}}\right) = v_{\mathrm{I}}$, with v_{I} the volume fraction of fibres in the micro-structure ω and the probability mass function $\pi_{H_{\text{phase}}}\left(h^{(1)}_{\text{phase}}\right) = v_0$ with $v_0 = 1 - v_{\mathrm{I}}$ the volume fraction of matrix in the micro-structure ω.

Figure 2(b) illustrates a single-phase poly-crystal in which each grain has a different orientation. Defining the 3D local state by the Euler angles $(\varphi,\, \theta,\, \psi)$, the sample space of one material point is defined by $\mathscr{W}_{\text{Euler}} = \{(\varphi,\, \theta,\, \psi) :\ 0 \leq \varphi < 2\pi,\, 0 \leq \theta \leq \pi,\, 0 \leq \psi < 2\pi\}$. The random vector $\boldsymbol{H}_{\text{Euler}} : \mathscr{W}_{\text{Euler}} \rightarrow \Re^3$ is defined as the collection $\{[\varphi(\mathscr{w})\ \theta(\mathscr{w})\ \psi(\mathscr{w})]^T : \mathscr{w} \in \mathscr{W}_{\text{Euler}}\}$ and the support space of its distribution function reads $\mathcal{S}_{\boldsymbol{H}_{\text{Euler}}} = [0,\, 2\pi[\times [0,\, \pi] \times [0,\, 2\pi[$. We however note that these bounds in the support space do not account for the possible crystal symmetries and are thus only valid for triclinic crystals; Fullwood et al. (2010) have provided the sample space for different crystallographic structures. The probability density function $\pi_{\boldsymbol{H}_{\text{Euler}}}(\boldsymbol{h}_{\text{Euler}})$ characterises the distribution of the grains orientations.

Finally, Fig. 2(c) illustrates the case of a matrix ω_0 reinforced by short fibres ω_{I}. As for the first example, each material point belongs to a given phase, and is characterised by an anisotropy direction of the material behaviour. Most of the time the matrix is considered as isotropic, but is here assumed to be characterised by Euler angles too. In the general case, an anisotropic fibre is characterised by the three Euler angles, but in the case of the existence of a revolution axis, the spin angle ψ is undefined; the revolution body direction is also fully characterised by its direction vector $\boldsymbol{p}$. As a consequence, the Euler sample space can be different for the two phases, and the resulting sample space of one material point reads $\mathscr{W} = \{(0,\, \varphi,\, \theta,\, \psi) : (\varphi,\, \theta,\, \psi) \in \mathscr{W}_{\text{Euler}^0}\} \cup \{(\text{I},\, \varphi,\, \theta,\, \psi) : (\varphi,\, \theta,\, \psi) \in \mathscr{W}_{\text{Euler}^\text{I}}\}$, or under the abbreviation $\mathscr{W} = \mathscr{W}_{\text{phase}^0} \cup \mathscr{W}_{\text{phase}^\text{I}}$. For $\varpi \in \mathscr{W}$, let us define the random vector $\boldsymbol{H}(\varpi) : \mathscr{W} \to \Re^4$ as

$$\boldsymbol{H}(\varpi) = \begin{cases} [1\ \varphi\ \theta\ \psi]^T & \text{if } \varpi \in \mathscr{W}_{\text{phase}^\text{I}}\,;\ \text{and} \\ [0\ \varphi\ \theta\ \psi]^T & \text{if } \varpi \in \mathscr{W}_{\text{phase}^0}\,. \end{cases} \tag{53}$$

We note that $\pi_{\boldsymbol{H}_{\text{Euler}}|H_1}\,(\boldsymbol{h}_{\text{Euler}}|H_1 = 0) : \Re^3 \to [0,\, \infty[$, respectively $\pi_{\boldsymbol{H}_{\text{Euler}}|H_1}\,(\boldsymbol{h}_{\text{Euler}}|H_1 = 1) : \Re^3 \to [0,\, \infty[$, corresponds to the probability density function of the Euler angles distribution $\pi_{\boldsymbol{H}_{\text{Euler}^{(0)}}}\,(\boldsymbol{h}_{\text{Euler}^{(0)}})$ in the matrix phase, respectively the Euler angles distribution $\pi_{\boldsymbol{H}_{\text{Euler}^{(1)}}}$ $(\boldsymbol{h}_{\text{Euler}^{(1)}})$ in the fibre phase. Finally, $\pi_{H_1}(h_1^{(i)}) : \Re \to [0,\, 1]$ is the probability mass function of phase, which corresponds to the volume fraction $v_0 = 1 - v_\text{I}$ of the matrix phase and v_I of the fibre phase for respectively $i = 0$ and $i = 1$.

Description of the micro-structure through a random field. Let us consider micro-structures defined on a set $\omega \in \Re^3$ of material points $\boldsymbol{x}$. It is thus possible to represent the local states of the microstructure by a random field $\boldsymbol{H}(\omega) = \{\boldsymbol{H}(\boldsymbol{x}) : \boldsymbol{x} \in \omega\}$, which is an uncountable family $\{\boldsymbol{H}(\boldsymbol{x}) : \boldsymbol{x} \in \omega\}$ of random vectors $\boldsymbol{H}$ valued in $\Re^n$ which maps the sample space $\mathscr{W}$ in a set $\mathcal{S}_H$. The sample space $\mathscr{W}$ is defined as all the possible outcomes at the different material points; it represents all the possible combinations of micro-structure states, at the different material points, like the phase in the case of a multi-phase heterogeneous material (the random variables are then discrete and can be assigned to an integer in order to have values in $\Re$), the micro-structure orientation in the case of a single-phase poly-crystals (the random variable is then continuous), or their combination in the case of multi-phase poly-crystals *etc.*, see the examples reported in the previous paragraph. We thus work in all generalities in the probability space $(\mathscr{W},\, \mathcal{F},\, \mathbb{P})$.

For a fixed point $\boldsymbol{x} \in \omega$, the evaluation $\boldsymbol{H}(\boldsymbol{x})$ for a given realisation $\varpi \in \mathscr{W}$ yields a point in the support $\mathcal{S}_{\boldsymbol{H}} \subset \Re^n$ for which the probability of the outcomes is positive, thus defining the mapping $\boldsymbol{H}(\boldsymbol{x};\, \varpi) : \omega \to \mathcal{S}_{\boldsymbol{H}}$.

For example, going back to the UD case studied in the previous paragraph, one can define the random field $H_{\text{phase}}(\omega)$ as the family $\{H_{\text{phase}}(\boldsymbol{x}) : \boldsymbol{x} \in \omega\}$ of discrete random variables H_{phase} valued in $\Re$ and of support $\{0,\, 1\}$, whilst for the single-phase poly-crystal micro-structure ω, one can define the random vector field $\boldsymbol{H}_{\text{Euler}}(\omega)$ as the family $\{\boldsymbol{H}_{\text{Euler}}(\boldsymbol{x}) : \boldsymbol{x} \in \omega\}$ of continuous random vectors $\boldsymbol{H}_{\text{Euler}}$ valued in $\Re^3$ and of support $\mathcal{S}_{\boldsymbol{H}_{\text{Euler}}}$.

A micro-structure realisation for a given $\varpi \in \mathscr{W}$ is thus defined by the collection $\{\boldsymbol{H}(\boldsymbol{x};\, \varpi) : \boldsymbol{x} \in \omega\}$, also called realisation path. In this work, we use ω to represent the set of material points, but also, with an abuse of notation, to refer to the micro-structure in itself, and $\omega(\varpi)$ to denote a micro-structure realisation. We assume ergodicity so that if the micro-structure is large enough it is statistically representative: the statistical content of one realisation $\varpi \in \mathscr{W}$ is enough to extract the statistical content. This is not restrictive since, because of ergodicity, one can alternatively consider several realisations $\mathpzc{w} \in \mathpzc{W}$ if the micro-structure ω is not large enough.

3.1.2. Micro-structure representation using micro-structure functions

Micro-structure functions have been defined by Fullwood et al. (2010) and their main concepts are summarised here below.

Local state distribution. The local state distribution function $f(\boldsymbol{h})$ was defined by Fullwood et al. (2010) as the volume density of material points in the micro-structure ω associated to the local state $\boldsymbol{h}$, *i.e.*

$$f(\boldsymbol{h})d\boldsymbol{h} = \frac{V\left(\omega|\boldsymbol{H} \in [\boldsymbol{h},\, \boldsymbol{h}+d\boldsymbol{h}[\right)}{V\left(\omega\right)} \quad \text{and} \quad f\left(\boldsymbol{h}^{(i)}\right) = \frac{V\left(\omega|\boldsymbol{H} = \boldsymbol{h}^{(i)}\right)}{V\left(\omega\right)}\,, \tag{54}$$

for respectively the continuous and discrete random vector cases, where $\omega|\boldsymbol{H} \in [\boldsymbol{h},\, \boldsymbol{h}+d\boldsymbol{h}[$ is the part of ω in a local state belonging to $[h_1,\, h_1+dh_1[\times \ldots \times [h_n,\, h_n+dh_n[$, $\omega|\boldsymbol{H} = \boldsymbol{h}^{(i)}$ is the part of ω in the local state $\boldsymbol{h}^{(i)}$, and where $V(\bullet)$ is the volume operator. Since we are considering a single micro-structure, *i.e.* a realisation $\mathpzc{w} \in \mathpzc{W}$, we are actually considering the collection $\{\boldsymbol{H}(\boldsymbol{x};\, \mathpzc{w}) : \boldsymbol{x} \in \omega\}$ in Eq. (54).

Assuming the micro-structure ω is large enough to be statistically representative and ergodicity, the local state distribution function (54) actually corresponds to the probability density function $f = \pi_{\boldsymbol{H}} : \Re^n \to \Re^+$ in the case of a continuous random vector and probability mass function $f = \pi_{\boldsymbol{H}} : \Re^n \to [0,\, 1]$ in the case of a discrete random vector with, respectively,

$$\int_{\Re^n} \pi_{\boldsymbol{H}}(\boldsymbol{h})d\boldsymbol{h} = 1 \quad \text{and} \quad \sum_{\boldsymbol{h}^{(i)};\, \pi_{\boldsymbol{H}}(\boldsymbol{h}^{(i)})>0} \pi_{\boldsymbol{H}}(\boldsymbol{h}^{(i)}) = 1\,, \tag{55}$$

where the sum stands for all possible $\boldsymbol{h}^{(i)}$.

Some components H_i of the local state can represent a continuous random variable whilst other components H_j a discrete random variable, in which case one should combine the integral and sum operators.

Micro-structure functions definition. Adams et al. (2005) have introduced the micro-structure function $m(\boldsymbol{x},\, \boldsymbol{h}) : \omega \times \Re^n \to \mathbb{R}^+$ to represent the micro-structure in a infinitesimal region $\Delta\omega(\boldsymbol{x})$ around the material point $\boldsymbol{x}$ of the micro-structure ω.

In the case of a discrete random vector, one has

$$m\left(\boldsymbol{x},\, \boldsymbol{h}^{(i)}\right) = \frac{V\left(\Delta\omega(\boldsymbol{x})|\boldsymbol{H} = \boldsymbol{h}^{(i)}\right)}{V\left(\Delta\omega(\boldsymbol{x})\right)}\,, \quad \text{and} \quad \frac{1}{V\left(\omega\right)}\int_{\omega} \sum_{\boldsymbol{h}^{(i)};\, \pi_{\boldsymbol{H}}(\boldsymbol{h}^{(i)})>0} m\left(\boldsymbol{x},\, \boldsymbol{h}^{(i)}\right) d\boldsymbol{x} = 1\,, \tag{56}$$

where $\Delta\omega(\boldsymbol{x})|\boldsymbol{H} = \boldsymbol{h}^{(i)}$ is the part of $\Delta\omega(\boldsymbol{x})$ in a local state $\boldsymbol{h}^{(i)}$, with the following properties

$$\sum_{\boldsymbol{h}^{(i)}} m\left(\boldsymbol{x},\, \boldsymbol{h}^{(i)}\right) = 1 \quad \forall \boldsymbol{x} \in \omega\,, \quad \text{and} \quad \frac{1}{V\left(\omega\right)}\int_{\omega} m\left(\boldsymbol{x},\, \boldsymbol{h}^{(i)}\right) d\boldsymbol{x} = \pi_{\boldsymbol{H}}\left(\boldsymbol{h}^{(i)}\right)\,. \tag{57}$$

One has in the case of a continuous random vector

$$m\left(\boldsymbol{x},\,\boldsymbol{h}\right)d\boldsymbol{h}=\frac{V\left(\Delta\omega(\boldsymbol{x})|\boldsymbol{H}\in[\boldsymbol{h},\,\boldsymbol{h}+d\boldsymbol{h}[\right)}{V\left(\Delta\omega(\boldsymbol{x})\right)}\,,\qquad\text{and}\qquad\frac{1}{V\left(\omega\right)}\int_{\omega}\int_{\Re^{n}}m\left(\boldsymbol{x},\,\boldsymbol{h}\right)d\boldsymbol{h}d\boldsymbol{x}=1\,,\tag{58}$$

where $\Delta\omega(\boldsymbol{x})$ is the infinitesimal spatial neighbourhood of the material point $\boldsymbol{x}\in\omega$, and $\Delta\omega(\boldsymbol{x})|\boldsymbol{H}\in[\boldsymbol{h},\,\boldsymbol{h}+d\boldsymbol{h}[$ is the part of $\Delta\omega(\boldsymbol{x})$ in a local state belonging to $[h_1,\,h_1+dh_1[\times...\times[h_n,\,h_n+dh_n[$. Therefore the following properties arise

$$\int_{\Re^{n}}m\left(\boldsymbol{x},\,\boldsymbol{h}\right)d\boldsymbol{h}=1\quad\forall\boldsymbol{x}\in\omega\,,\qquad\text{and}\qquad\frac{1}{V\left(\omega\right)}\int_{\omega}m\left(\boldsymbol{x},\,\boldsymbol{h}\right)d\boldsymbol{x}=\pi_{\boldsymbol{H}}\left(\boldsymbol{h}\right)\,.\tag{59}$$

3.1.3. Voxelisation

Since the micro-structures are practically analysed using data from images, either experimentally or synthetically obtained, it is convenient to frame the function in a voxel-based formalism.

The micro-structure ω is spatially discretized into $N^{\boldsymbol{x}}$ voxels $\delta\omega^{(j)}$ of uniform volume $V(\delta\omega^{(j)})$, with the spatial indicator function

$$\chi_{\delta\omega^{(j)}}\left(\boldsymbol{x}\right)=\begin{cases}1 & \text{if }\boldsymbol{x}\in\delta\omega^{(j)}\,;\\ 0 & \text{if not}\,;\end{cases}\tag{60}$$

with $\frac{1}{V\left(\delta\omega^{(j)}\right)}\int_{\omega}\chi_{\delta\omega^{(j)}}\left(\boldsymbol{x}\right)\chi_{\delta\omega^{(k)}}\left(\boldsymbol{x}\right)d\boldsymbol{x}=\delta_{jk}$.

Considering first a discrete random vector, the assumed bounded support $\mathcal{S}_{\boldsymbol{H}}$ is the set of $N^{\boldsymbol{h}}$ possible values that can be taken by the random vector. The indicator function (28) is then particularised as

$$\chi_{\boldsymbol{h}^{(i)}}\left(\boldsymbol{h}^{(p)}\right)=\begin{cases}1 & \text{if }\boldsymbol{h}^{(p)}=\boldsymbol{h}^{(i)}\,;\\ 0 & \text{if not}\,;\end{cases}\tag{61}$$

with $\sum_{p=1}^{N^{\boldsymbol{h}}}\chi_{\boldsymbol{h}^{(i)}}\left(\boldsymbol{h}^{(p)}\right)\chi_{\boldsymbol{h}^{(j)}}\left(\boldsymbol{h}^{(p)}\right)=\delta_{ij}$, in which case the micro-structure function (56) can be approximated by

$$m\left(\boldsymbol{x},\,\boldsymbol{h}^{(p)}\right)\simeq\sum_{j=1}^{N^{\boldsymbol{x}}}\sum_{i=1}^{N^{\boldsymbol{h}}}m^{\delta\omega^{(j)},\boldsymbol{h}^{(i)}}\chi_{\delta\omega^{(j)}}\left(\boldsymbol{x}\right)\chi_{\boldsymbol{h}^{(i)}}\left(\boldsymbol{h}^{(p)}\right)\,,\tag{62}$$

where $m^{\delta\omega^{(j)},\boldsymbol{h}^{(i)}}=\frac{1}{V(\delta\omega^{(j)})}\sum_{p=1}^{N^{\boldsymbol{h}}}\int_{\omega}m\left(\boldsymbol{x},\,\boldsymbol{h}^{(p)}\right)\chi_{\delta\omega^{(j)}}\left(\boldsymbol{x}\right)\chi_{\boldsymbol{h}^{(i)}}\left(\boldsymbol{h}^{(p)}\right)d\boldsymbol{x}$. We also note that

$$\sum_{i=1}^{N^{\boldsymbol{h}}}m^{\delta\omega^{(j)},\boldsymbol{h}^{(i)}}\chi_{\boldsymbol{h}^{(i)}}\left(\boldsymbol{h}^{(p)}\right)\simeq\frac{1}{V(\delta\omega^{(j)})}\int_{\omega}m\left(\boldsymbol{x},\,\boldsymbol{h}^{(p)}\right)\chi_{\delta\omega^{(j)}}\left(\boldsymbol{x}\right)d\boldsymbol{x}\,,\tag{63}$$

represents the local probability density function of realisation $\boldsymbol{h}^{(p)}$ in the voxel $\delta\omega^{(j)}$.

In the case of a continuous random vector, the assumed bounded support space $\mathcal{S}_{\boldsymbol{H}}$ is divided into $N^{\boldsymbol{h}}$ independent and uniform bins $\delta\mathcal{S}_{\boldsymbol{H}}^{(i)}$, allowing redefining the indicator functions (61) as

$$\chi_{\delta\mathcal{S}_{\boldsymbol{H}}^{(i)}}\left(\boldsymbol{h}\right) = \begin{cases} 1 & \text{if } \boldsymbol{h} \in \delta\mathcal{S}_{\boldsymbol{H}}^{(i)}\,; \\ 0 & \text{if not}\,; \end{cases} \tag{64}$$

with $\frac{N^{\boldsymbol{h}}}{d(\mathcal{S}_{\boldsymbol{H}})}\int_{\mathcal{S}_{\boldsymbol{H}}} \chi_{\delta\mathcal{S}_{\boldsymbol{H}}^{(i)}}\left(\boldsymbol{h}\right)\chi_{\delta\mathcal{S}_{\boldsymbol{H}}^{(j)}}\left(\boldsymbol{h}\right) d\boldsymbol{h} = \delta_{ij}$, $\int_{\delta\mathcal{S}_{\boldsymbol{H}}^{(i)}} d\boldsymbol{h} = d(\mathcal{S}_{\boldsymbol{H}})/N^{\boldsymbol{h}}$, and with $d(\mathcal{S}_{\boldsymbol{H}}) = \int_{\mathcal{S}_{\boldsymbol{H}}} d\boldsymbol{h}$.

The micro-structure function (58) can then be approximated as

$$m\left(\boldsymbol{x},\,\boldsymbol{h}\right) \simeq \sum_{j=1}^{N^{\boldsymbol{x}}}\sum_{i=1}^{N^{\boldsymbol{h}}} m^{\delta\omega^{(j)},\,\delta\mathcal{S}_{\boldsymbol{H}}^{(i)}} \chi_{\delta\omega^{(j)}}\left(\boldsymbol{x}\right)\chi_{\delta\mathcal{S}_{\boldsymbol{H}}^{(i)}}\left(\boldsymbol{h}\right)\,, \tag{65}$$

where $m^{\delta\omega^{(j)},\,\delta\mathcal{S}_{\boldsymbol{H}}^{(i)}} = \frac{N^{\boldsymbol{h}}}{V\left(\delta\omega^{(j)}\right)d(\mathcal{S}_{\boldsymbol{H}})}\int_{\mathcal{S}_{\boldsymbol{H}}}\int_{\omega} m\left(\boldsymbol{x},\,\boldsymbol{h}\right)\chi_{\delta\omega^{(j)}}\left(\boldsymbol{x}\right)\chi_{\delta\mathcal{S}_{\boldsymbol{H}}^{(i)}}\left(\boldsymbol{h}\right) d\boldsymbol{x}d\boldsymbol{h}$. The local probability function in voxel $\delta\omega^{(j)}$ thus reads

$$\sum_{i=1}^{N^{\boldsymbol{h}}} m^{\delta\omega^{(j)},\,\delta\mathcal{S}_{\boldsymbol{H}}^{(i)}} \chi_{\delta\mathcal{S}_{\boldsymbol{H}}^{(i)}}\left(\boldsymbol{h}\right) \simeq \frac{1}{V(\delta\omega^{(j)})}\int_{\omega} m\left(\boldsymbol{x},\,\boldsymbol{h}\right)\chi_{\delta\omega^{(j)}}\left(\boldsymbol{x}\right) d\boldsymbol{x}\,. \tag{66}$$

Besides, since $\int_{\mathcal{S}_{\boldsymbol{H}}} m\left(\boldsymbol{x},\,\boldsymbol{h}\right) d\boldsymbol{h} = 1\;\forall\boldsymbol{x}\in\omega$, one has $\sum_{i=1}^{N^{\boldsymbol{h}}} m^{\delta\omega^{(j)},\,\delta\mathcal{S}_{\boldsymbol{H}}^{(i)}} = \frac{N^{\boldsymbol{h}}}{d(\mathcal{S}_{\boldsymbol{H}})}$ in all cell $\delta\omega^{(j)}$, and $\sum_{j=1}^{N^{\boldsymbol{x}}}\sum_{i=1}^{N^{\boldsymbol{h}}} m^{\delta\omega^{(j)},\,\delta\mathcal{S}_{\boldsymbol{H}}^{(i)}} = \frac{N^{\boldsymbol{x}}N^{\boldsymbol{h}}}{d(\mathcal{S}_{\boldsymbol{H}})}$.

3.1.4. n-point statistical functions

Whilst the local state distributions defined in Section 3.1.2 provides statistical information for the whole micro-structure, information on the spatial distribution also needs to be provided. To this end, several n-point statistical functions have been developed.

n-point correlation function. Corson (1974a,b) has developed the concept of the n-point correlation function, see also the reviews by Fullwood et al. (2010); Bostanabad et al. (2018).

Let us consider N^{ω} independent micro-structure realisations ω^j. Considering a spatial vector $\boldsymbol{\tau}$, Fullwood et al. (2010) have defined the independent spatial regions $\omega^j|\boldsymbol{\tau}^2, ..., \boldsymbol{\tau}^n$ as the set of material points

$$\omega^j|\boldsymbol{\tau}^2, ..., \boldsymbol{\tau}^n = \left\{\boldsymbol{x} : \boldsymbol{x}\in\omega^j \text{ and } \boldsymbol{x}+\boldsymbol{\tau}^k\in\omega^j \quad \forall\, k = 2..n\right\}\,. \tag{67}$$

For discrete random vectors $\boldsymbol{H}$ taking values in $\Re^m$, the n-point correlation function $f_n\left(\boldsymbol{h}^{(1)}, ..., \boldsymbol{h}^{(n)};\, \boldsymbol{\tau}^2, ..., \boldsymbol{\tau}^n\right)$ is defined as the joint probability mass function of occurrence of $\boldsymbol{h}^{(k)}$ at the end extremity of the spatial vector $\boldsymbol{\tau}^k$ and of $\boldsymbol{h}^{(1)}$ at the start extremity of $\boldsymbol{\tau}^k$, for $k = 2..n$, or in the mathematical notation:

$$\begin{aligned} f_n\left(\boldsymbol{h}^{(1)}, ..., \boldsymbol{h}^{(n)};\, \boldsymbol{\tau}^2, ..., \boldsymbol{\tau}^n\right) \;&=\; \mathbb{E}\left[\frac{1}{V\left(\omega^j|\boldsymbol{\tau}^2, ..., \boldsymbol{\tau}^n\right)}\int_{\omega^j|\boldsymbol{\tau}^2,...,\boldsymbol{\tau}^n} m\left(\boldsymbol{x},\,\boldsymbol{h}^{(1)}\right)\times\right. \\ &\left. m\left(\boldsymbol{x}+\boldsymbol{\tau}^2,\,\boldsymbol{h}^{(2)}\right)\times ... \times m\left(\boldsymbol{x}+\boldsymbol{\tau}^n,\,\boldsymbol{h}^{(n)}\right) d\boldsymbol{x}\right]\,, \end{aligned} \tag{68}$$

where the expectation operator $\mathbb{E}\left[\bullet^j\right]$ is here used as the spatial expectation on the different micro-structures, *i.e.* $\mathbb{E}\left[\bullet^j\right] = \frac{1}{\sum_{l=1}^{N^\omega} V\left(\omega^l|\boldsymbol{\tau}^2,...,\boldsymbol{\tau}^n\right)} \sum_{j=1}^{N^\omega} V\left(\omega^j|\boldsymbol{\tau}^2,...,\boldsymbol{\tau}^n\right)\bullet^j$. Assuming ergodicity allows considering a single, large-enough, micro-structure realisation ω that contains all the relevant statistical information and which is usually called Representative Volume Element (RVE). In that case, Eq. (68) reads

$$\begin{aligned} f_n\left(\boldsymbol{h}^{(1)},...,\boldsymbol{h}^{(n)};\,\boldsymbol{\tau}^2,...,\boldsymbol{\tau}^n\right) &= \frac{1}{V\left(\omega|\boldsymbol{\tau}^2,...,\boldsymbol{\tau}^n\right)}\int_{\omega|\boldsymbol{\tau}^2,...,\boldsymbol{\tau}^n} m\left(\boldsymbol{x},\,\boldsymbol{h}^{(1)}\right)\times \\ & \qquad m\left(\boldsymbol{x}+\boldsymbol{\tau}^2,\,\boldsymbol{h}^{(2)}\right)\times...\times m\left(\boldsymbol{x}+\boldsymbol{\tau}^n,\,\boldsymbol{h}^{(n)}\right)d\boldsymbol{x}\,. \end{aligned} \tag{69}$$

In case of continuous random vectors, the n-point correlation function is defined as the joint probability density function and reads

$$\begin{aligned} f_n\left(\boldsymbol{h}^1,...,\boldsymbol{h}^n;\,\boldsymbol{\tau}^2,...,\boldsymbol{\tau}^n\right) &= \frac{1}{V\left(\omega|\boldsymbol{\tau}^2,...,\boldsymbol{\tau}^n\right)}\int_{\omega|\boldsymbol{\tau}^2,...,\boldsymbol{\tau}^n} m\left(\boldsymbol{x},\,\boldsymbol{h}^1\right)\times \\ & \qquad m\left(\boldsymbol{x}+\boldsymbol{\tau}^2,\,\boldsymbol{h}^2\right)\times...\times m\left(\boldsymbol{x}+\boldsymbol{\tau}^n,\,\boldsymbol{h}^n\right)d\boldsymbol{x}\,. \end{aligned} \tag{70}$$

Although the evaluation of high-order correlation functions is not straightforward, the two-point correlation function, here given for a discrete random vector,

$$f_2\left(\boldsymbol{h}^{(1)},\,\boldsymbol{h}^{(2)};\,\boldsymbol{\tau}\right) = \frac{1}{V\left(\omega|\boldsymbol{\tau}\right)}\int_{\omega|\boldsymbol{\tau}} m\left(\boldsymbol{x},\,\boldsymbol{h}^{(1)}\right)\times m\left(\boldsymbol{x}+\boldsymbol{\tau},\,\boldsymbol{h}^{(2)}\right)d\boldsymbol{x}\,, \tag{71}$$

is widely used to characterise the spatial distribution of micro-structures, see (Torquato, 2002; Huang, 2005; Gao et al., 2006; Niezgoda et al., 2008) among others.

The case of a poly-crystal illustrated in Fig. 2(b) was exemplified by Huang (2005): in that case, the two-point correlation function $f_2\left(\boldsymbol{h}_{\text{Euler}},\,\boldsymbol{h}'_{\text{Euler}};\,\boldsymbol{\tau}\right)$ represents the joint probability density function of having an orientation $\boldsymbol{h}'_{\text{Euler}}$ at the end extremity of the spatial vector $\boldsymbol{\tau}$ and of $\boldsymbol{h}_{\text{Euler}}$ at the start extremity of $\boldsymbol{\tau}$. Combining this formalism with the digitisation (65), opens the way to a representation in the Fourier space as detailed by Adams et al. (2005) in the context of a poly-crystal.

n-point probability function. We consider the definition of the n-point probability function given by Torquato (2002); MacSleyne et al. (2008); Fullwood et al. (2010); however some authors use the terminology n-point correlation function for this concept.

Let us again consider N^ω independent micro-structure realisations ω^j. Assuming a discrete random vector $\boldsymbol{H}$ valued in $\Re^m$, the indicator function of n-material points $\boldsymbol{x}^i$ is defined as

$$\chi_{\omega^j,\boldsymbol{h}^{(i)}}\left(\boldsymbol{x}^1,\,...,\,\boldsymbol{x}^n,\,\boldsymbol{h}^{(p)}\right) = \begin{cases} 1 & \text{if } \boldsymbol{h}^{(p)} = \boldsymbol{h}^{(i)} \text{ at } \boldsymbol{x}^k \in \omega^j \quad k = 1..n; \\ 0 & \text{if not}\,. \end{cases} \tag{72}$$

Considering N^ω independent realisations of the micro-structure ω^j, we define the n-point probability function as

$$S_n\left(\boldsymbol{h}^{(i)};\,\boldsymbol{x}^1,\,...,\,\boldsymbol{x}^n\right) = \mathbb{E}\left[\chi_{\omega^j,\boldsymbol{h}^{(i)}}\left(\boldsymbol{x}^1,\,...,\,\boldsymbol{x}^n,\,\boldsymbol{h}^{(p)}\right)\right]\,, \tag{73}$$

where the expectation operator stands for the expectation on the different micro-structures, *i.e.* $\mathbb{E}\left[\bullet^j\right] = \frac{1}{N^\omega}\sum_{j=1}^{N^\omega}\bullet^j$. The n-point probability $S_n\left(\boldsymbol{h}^{(i)};\, \boldsymbol{x}^1,\, ...,\, \boldsymbol{x}^n\right)$ is interpreted as the probability to have the local state $\boldsymbol{h}^{(i)}$ at points $\boldsymbol{x}^1$, ..., $\boldsymbol{x}^n$.

One particular case is the 1-point probability function $S_1\left(\boldsymbol{h}^{(i)};\, \boldsymbol{x}\right)$ that represents the probability to be in a local state $\boldsymbol{h}^{(i)}$ at position $\boldsymbol{x}$. If the micro-structure is statistically homogeneous, $S_1\left(\boldsymbol{h}^{(i)}\right)$ is independent on the material point and corresponds to the volume fraction v_i of local state $\boldsymbol{h}^{(i)}$ of the micro-structure. Another particular case arises when assuming statistically homogeneous micro-structures, in which case the dependency on $(\boldsymbol{x}^1,\, ...,\, \boldsymbol{x}^n)$ reduces to a dependency on $(\boldsymbol{\tau}^2 = \boldsymbol{x}^2 - \boldsymbol{x}^1,\, ...,\, \boldsymbol{\tau}^n = \boldsymbol{x}^n - \boldsymbol{x}^1)$, yielding $S_n\left(\boldsymbol{h}^{(i)};\, \boldsymbol{\tau}^2,\, ...,\, \boldsymbol{\tau}^n\right)$. In that case, $S_n\left(\boldsymbol{h}^{(i)};\, \boldsymbol{\tau}^2,\, ...,\, \boldsymbol{\tau}^n\right)$ corresponds to a particular case of the n-point correlation function (69) for $\boldsymbol{h}^{(1)} = ... = \boldsymbol{h}^{(n)} = \boldsymbol{h}^{(i)}$, *i.e.* $f_n\left(\boldsymbol{h}^{(i)}, ..., \boldsymbol{h}^{(i)};\, \boldsymbol{\tau}^2, ..., \boldsymbol{\tau}^n\right)$, which is called auto-correlation function.

One of the most commonly used function is the two-point probability function $S_2\left(\boldsymbol{h}^{(i)};\, \boldsymbol{\tau}\right)$, which can be particularised in the case of an isotropic material, for which the direction of the vector $\boldsymbol{\tau}$ does not affect the function, as $S_2\left(\boldsymbol{h}^{(i)};\, \tau\right)$, where τ is the norm of $\boldsymbol{\tau}$.

Examples and other path functions. Taking as example the case of the UD two-phase composite of Fig. 2(a), the discrete random variable $h^{(i)}_{\text{phase}}$ can take only two values $h^{(1)}_{\text{phase}} = 0$ or $h^{(2)}_{\text{phase}} = 1$, see Section 3.1.1. Clearly $S_1(h^{(1)}_{\text{phase}}) = v_0$ is the volume fraction of the matrix phase, and $S_1(h^{(2)}_{\text{phase}}) = v_{\text{I}} = 1 - v_0$ is the volume fraction of the fibre phase. However, additional information is brought on the micro-structure by $S_2\left(h^{(2)}_{\text{phase}};\, \boldsymbol{\tau}\right)$ as the probability to have two material points separated by the vector $\boldsymbol{\tau}$ to be in the fibre phase, as illustrated in Fig. 2(a).

Nevertheless, for non-periodic micro-structure, see the discussion by Bostanabad et al. (2018), $S_2\left(h^{(i)}_{\text{phase}};\, \boldsymbol{\tau}\right)$ does not fully characterise a micro-structure since different statistical configurations can possibly yield the same function. Additional information related to the clustering are needed. Lu and Torquato (1992) have introduced the concept of lineal path function $L(h^{(i)}_{\text{phase}};\, \boldsymbol{\tau})$, which gives the probability for a linear segment supported by the vector $\boldsymbol{\tau}$ to lie entirely within the same phase, see Fig. 2(a). A more general representation of the clusteredness that has been introduced by Torquato (2002); Jiao et al. (2009) is the two-point cluster correlation function $C_2(h^{(i)}_{\text{phase}};\, \boldsymbol{\tau})$ that quantifies the probability for two material points separated by the vector $\boldsymbol{\tau}$ to lie within the same cluster, see Fig. 2(a). Finally Torquato (2002); Jiao et al. (2009) have also considered $F_{ss}(h^{(i)};\, \boldsymbol{\tau})$ the equivalent of $S_2\left(h^{(i)};\, \boldsymbol{\tau}\right)$ but for points $\boldsymbol{x}^1$ and $\boldsymbol{x}^2$, with $\boldsymbol{\tau} = \boldsymbol{x}^2 - \boldsymbol{x}^1$, belonging to the "dilated" interface at the two phases. $F_{ss}(h^{(i)};\, \boldsymbol{\tau})$ is thus interpreted as the probability of finding two points separated by $\boldsymbol{\tau}$ at the two-phase inter-phase.

3.1.5. Data acquisition

The two main features to be characterised are, on the one hand, the grain size and grain shape distributions, and on the other hand the crystallographic texture defined by the orientation distribution functions, as it will be explained in more details in Section 3.2.4. We refer to the review by Segurado et al. (2018) for a review of the data acquisition related to these two aspects. Because of the convenience of using voxelisation to represent the micro-structure as illustrated by Eq. (65), imaging techniques are a popular way to extract the information.

Optical microscopy of polished sections allows extracting grain size and shape distributions after chemical etching has revealed the grain boundary structures.Transformation from 2D surfaces to 3D information then requires particular treatment. Automated serial-sectioning by means of a micro-tome combined with reconstruction algorithm yield 3D images of the micro-structures. A non-destructive alternative is the use X-ray micro-focus Computed Tomography (μ-CT) (Segurado et al., 2018).

Grain orientation has been extracted for single-phase poly-crystals by Gao et al. (2006) using orientation imaging microscopy (OIM), which images the microstructure using the electron back-scattered diffraction probe (EBSD); 3D information was recovered by considering different cut orientations, see also the work by Saylor et al. (2004); high resolution segmented back-scatter electron micro-graphs were used by Salem et al. (2014) to extract the bi-modal microstructure statistical information of $\alpha - \beta$ titanium alloy with primary and secondary α phases, as a non-exhaustive list.

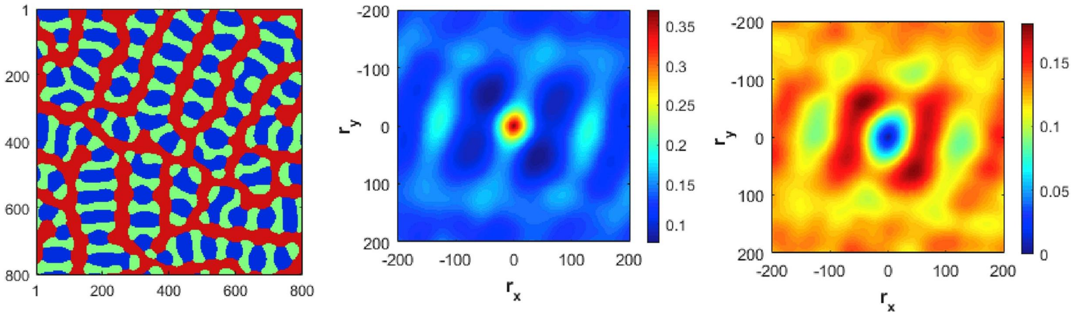

(a) Micro-structure (b) $f_2(h^{(1)}, h^{(1)}; \boldsymbol{r})$ (c) $f_2(h^{(1)}, h^{(3)}; \boldsymbol{r})$

Figure 3: Statistical study of a Al-Ag-Cu ternary eutectic alloy microstructure obtained via phase-field simulations by Yabansu et al. (2017): (a) Micro-structure obtained by phase-field simulation; (b) two-point auto-correlation $f_2(h^{(1)}, h^{(1)}; \boldsymbol{r})$ of the red phase; and (c) two-point cross-correlation $f_2(h^{(1)}, h^{(3)}; \boldsymbol{r})$ between the red and blue phases; Reprinted from Acta Materialia, 124, Yabansu, Y.C., Steinmetz, P., Hötzer, J., Kalidindi, S.R., Nestler, B., Extraction of reduced-order process-structure linkages from phase-field simulations, 182-194, Copyright (2017), with permission from Elsevier.

The "images" can also result from numerical simulations. MacSleyne et al. (2008) have extracted "γ'" precipitates in nickel-base alloys from textures predicted by several 2D phase-field simulations. Yabansu et al. (2017) have used the phase-field approach, see also the work by Krill III and Chen (2002), in order to simulate the solidification of ternary eutectic alloys, before extracting the two-point spatial correlation. The resulting statistical analysis using the two-point correlation function (71) is illustrated in Fig. 3 for two points separated by a vector $\boldsymbol{r}$.

3.1.6. Reconstruction

Practically the micro-structures are constructed under the form of voxels $\delta\omega^j$ associated to a local state $\boldsymbol{h}^{(i)}$ (or centred on $\delta\mathcal{S}_{\boldsymbol{H}}^{(i)}$ depending on the sample space). The voxels are then optimised in order to minimise a cost function built using the statistical functions $g_l\left(\{\boldsymbol{\tau}^{j,k}\},\, \{\boldsymbol{h}^{(i)}\}\right)$ of the generated micro-structure for the set of vectors $\{\boldsymbol{\tau}^{j,k}\}$, whose number depends on the statistical function considered, separating the voxels $\delta\omega^j$ and $\delta\omega^k$, and for the set of local states $\{\boldsymbol{h}^{(i)}\}$, whose number depends on the statistical function considered. The cost function can be built as

$$C = \sum_{l=1}^{N_g}\sum_{j=1}^{N^{\boldsymbol{x}}}\sum_{k=1}^{N^{\boldsymbol{x}}} w_l \left[\hat{g}_l\left(\{\boldsymbol{\tau}^{j,k}\},\, \{\boldsymbol{h}^{(i)}\}\right) - g_l\left(\{\boldsymbol{\tau}^{j,k}\},\, \{\boldsymbol{h}^{(i)}\}\right)\right]^2 , \tag{74}$$

where $\hat{g}_l\left(\{\boldsymbol{\tau}^{j,k}\},\, \{\boldsymbol{h}^{(i)}\}\right)$ is the target function, N_g is the number of functions considered and w_l their associated weight and $N^{\boldsymbol{x}}$ is the number of voxels. The current techniques used to optimise the micro-structure using this cost function have been reviewed by Bostanabad et al. (2018).

Jiao et al. (2009) have used the so-called Yeong and Torquato (1998) stochastic optimisation with different two-point functions in Eq. (74) to reconstruct a concrete micro-structure, see Fig. 4. Clearly the two-point probability function $S_2(h^{(2)};\, \boldsymbol{r})$ is not enough to characterise the micro-structure and another function related to the clusteredness is required to get closer to the targeted micro-structure features.

3.1.7. Wang tiles

Because it can be time consuming to generate large structures of arbitrary sizes when several realisations are required, the concept of Wang tiles to generate aperiodic micro-structures was developed by Novák et al. (2012); Doškář et al. (2014). In this approach, domains of reduced sizes are assumed to be fast to be generate and constraints are put on the edges patterns so that an assembly can be readily achieved. A number of n_x possible vertical edge patterns and a number of n_y possible horizontal edge patterns are defined. It is thus possible to generate maximum of $n_x^2 n_y^2$ tiles of different edges combinations. In practice one can chose to limit the number of tiles by assigning a number $n = 2..n_x n_y$ with the same top-left combination. In this case the total number of tiles is $n n_x n_y$. Figure 5(a) represents the case of $n_x = 2$ possible vertical edges of key either “blue” or “orange” and $n_y = 2$ possible horizontal edges of key either “red” or “green”. The value n is selected to be 2, meaning that we have two different tiles of the top-left keys “red-blue”, 2 tiles for the top-left keys “green-blue”, 2 tiles for the top-left keys “red-oranges” and 2 tiles for the top-left keys “green-oranges”. Under these conditions, a random assembly can proceed by respecting *vis-à-vis* edge keys, as depicted in Fig. 5(b), whilst aperiodicity is guaranteed (Novák et al., 2012).

Assuming known target statistical functions $\hat{g}_l\left(\{\boldsymbol{\tau}^{j,k}\},\, \{\boldsymbol{h}^{(i)}\}\right)$, see Section 3.1.6 for the notations, it is possible to generate the micro-structure distribution of the $n n_x n_y$ tiles. To this end the difference between the statistical functions $g_l\left(\{\boldsymbol{\tau}^{j,k}\},\, \{\boldsymbol{h}^{(i)}\}\right)$ of a generated large enough tiles-assembly (and not by considering single tiles) with the target statistical

(a) Micro-structure (b) Using $S_2(h^{(2)}; \boldsymbol{r})$ (c) Using $S_2(h^{(2)}; \boldsymbol{r})$ & $F_{ss}(h^{(2)}; \boldsymbol{r})$

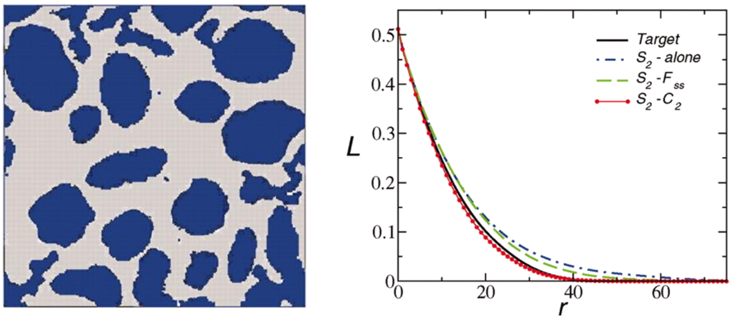

(d) Using $S_2(h^{(2)}; \boldsymbol{r})$ & $C_2(h^{(2)}; \boldsymbol{r})$ (e) Comparison in terms of $L(h^{(2)}; \boldsymbol{r})$

Figure 4: Stochastic reconstruction of a concrete micro-structure by Jiao et al. (2009): (a) Digitalised target micro-structure; and reconstructions (b) Using the two-point probability function $S_2(h^{(2)}; \boldsymbol{r})$; (c) Using the two-point probability function $S_2(h^{(2)}; \boldsymbol{r})$ and the surface-surface correlation function $F_{ss}(h^{(2)}; \boldsymbol{r})$; (d) Using the two-point probability function $S_2(h^{(2)}; \boldsymbol{r})$ and the cluster correlation function $C_2(h^{(2)}; \boldsymbol{r})$; and (e) Comparison of the reconstructed micro-structures in terms of the lineal path function $L(h^{(2)}; \boldsymbol{r})$; Reprinted from Proceedings of the National Academy of Sciences, 106, Jiao, Y., Stillinger, F.H., Torquato, S., A superior descriptor of random textures and its predictive capacity, 17634-17639, 2009, with permission from PNAS.

functions $\hat{g}_l\left(\{\boldsymbol{\tau}^{j,k}\}, \{\boldsymbol{h}^{(i)}\}\right)$ is minimised, see Section 3.1.6. An additional constraint is to avoid the existence of inclusions at the corners. The two-point probability function $S_2(h^{(2)}; \boldsymbol{r})$ was considered by Novák et al. (2012) and it was found that the method reduces long-range artefacts in the $S_2(h^{(2)}; \boldsymbol{r})$ as compared to a periodic micro-structures. Besides, the long-range artefacts were found to be mainly due to the tile interiors and it was concluded that the discrete nature of Wang tiling can be almost eliminated by a proper morphology optimisation.

Doškář et al. (2014) have extended the method using image fusion techniques in order to define the tiles directly from micro-structure images. In this approach, diamond shapes are cut out from the aggregate of four overlapping square reference samples extracted from a micro-structure image, see Fig. 6(a), and placed according to the edge keys of the tiles. These four samples are merged within their overlapping regions using a quilting algorithm,

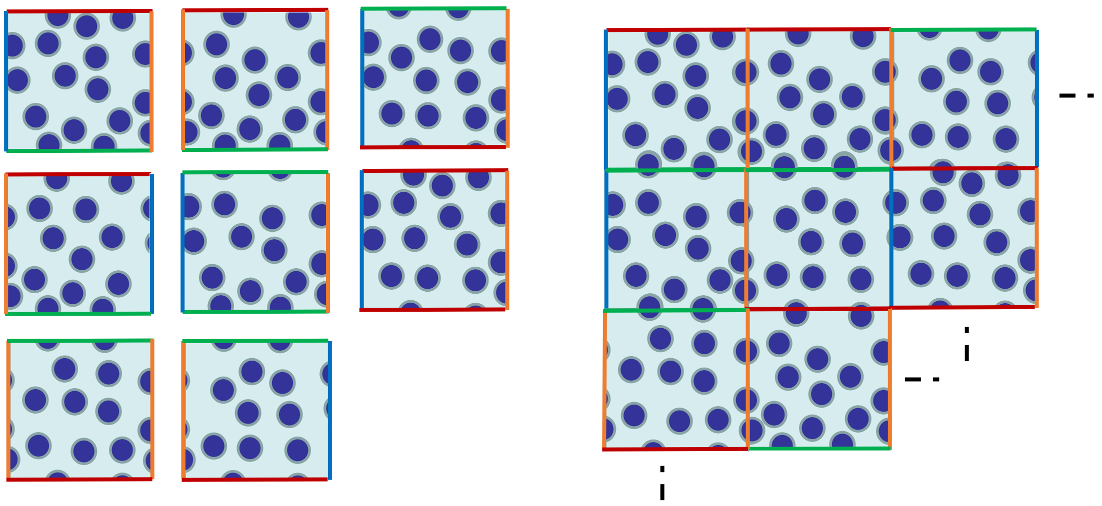
(a) Tiles with edge keys

(b) Tiles assembly

Figure 5: Concept of Wang tiles following the presentation by Novák et al. (2012); Doškář et al. (2014): (a) Definition of $nn_xn_y = 8$ tiles with a combination of $n_y = 2$ different horizontal edge keys (red or green) and $n_x = 2$ different vertical edge keys (orange or blue) ; and (b) An aperiodic assembly realisation of the tiles.

see Fig. 6(b). It was noted that weakly packed dispersion brings less complexity to perform this automatic tile design. This quilting method also induces short-range artefacts which were investigated by the two-point cluster correlation function $C_2(h^{(i)}_{\text{phase}}; \boldsymbol{\tau})$ by Doškář et al. (2014).

A review of the method has been conducted by Budarapu et al. (2019).

3.2. *Physical descriptors*

Another methodology to construct virtual micro-structures is to generate geometries that respect, in a statistical way, some *a priori* selected features of experimental observations. Clearly, the physical descriptors and the reconstruction algorithms are strongly linked to the material system under investigation. In the following we summarise methodologies developed for commonly studied materials.

3.2.1. *Unidirectional composites*

The spatial arrangement of fibres, see Fig. 2(a), in a Unidirectional (UD) composite micro-structure is normally not periodic, which affects significantly the failure/damage initiation and evolution under certain loading conditions as discussed by Maligno et al. (2009); Hobbiebrunken et al. (2008); Hojo et al. (2009); Bhuiyan et al. (2020).

Besides, because of coefficients mismatch affecting the manufacturing process, fibres exhibit a waviness along their principal orientation, as reviewed by Kugler and Moon (2002), which largely affects the compression failure behaviour by micro-buckling (Jelf and Fleck, 1992). However the wavelength is above the mm size, and is thus several orders of magnitude larger than the distribution scatter of the fibres organisation in the cross-section; this stochastic effect can thus be studied at the level of the ply as done by Sepahvand (2016). We

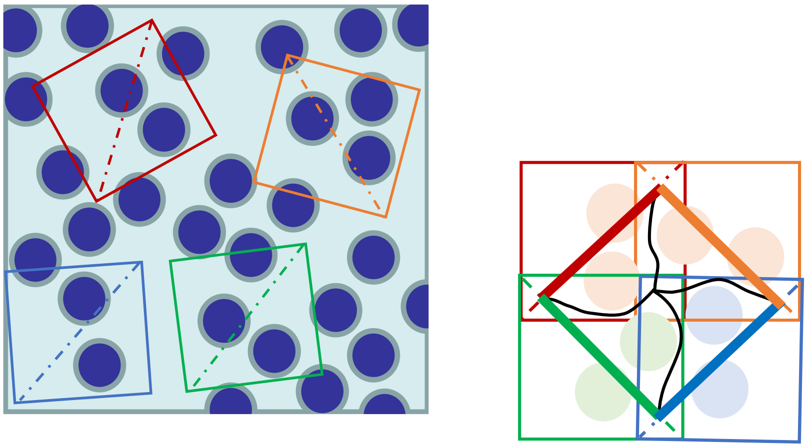

(a) Reference squares (b) Merge by quilting

Figure 6: Construction of Wang tiles following the presentation by Cohen et al. (2003); Doškář et al. (2014): (a) Extraction of 4 reference square samples from a micro-structure; and (b) Assembly of the reference samples in a diamond shape with quilting performed in the overlapping regions and the final definition of the tile edges.

note that Huang et al. (2021) have conducted a stochastic analysis by considering the correlated volume fraction distribution on a 10-ply laminate cross-section and the fibre waviness along the laminate length.

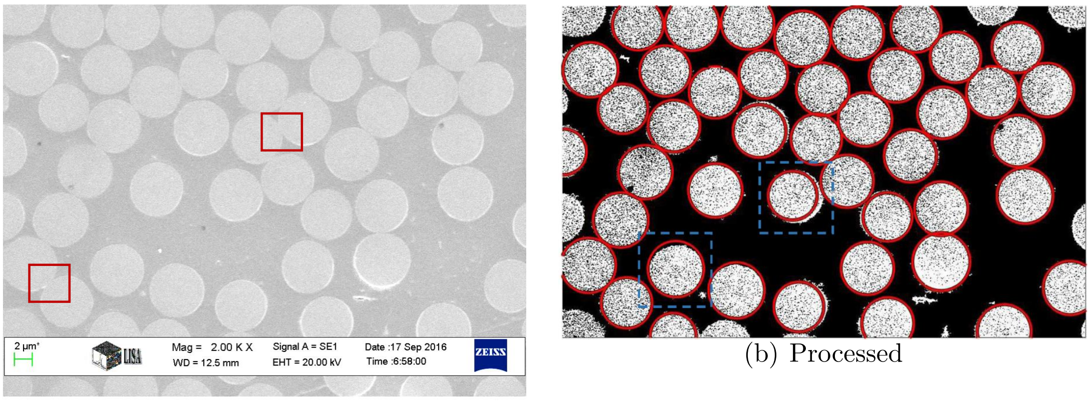

(a) Original SEM (b) Processed

Figure 7: Experimental characterisation of a UD composite material: (a) Original SEM image of a polished cross-section sample with an amplification ratio of 2000× obtained by Wu et al. (2018a), the squares represent zero-distance fibres; and (b) Processed image by Wu et al. (2018a) with the detected fibres, the dashed squares represent the over/under-estimated fibre circles; Reprinted from Composite Structures 189, Wu, L., Chung, C.N., Major, Z., Adam, L., Noels, L., From SEM images to elastic responses: A stochastic multiscale analysis of UD fiber reinforced composites, 206-227, Copyright (2018), with permission from Elsevier.

Data acquisition. The spatial characterisation of UD cross-sections is achieved from two-dimensional images acquired via the Scanning Electron Microscope (SEM) technique in scales ranging from a few to hundreds of micrometers (Vaughan and McCarthy, 2010; Hojo et al., 2009). An example of an image treated by Wu et al. (2018a) is illustrated in Fig. 7(a). Since a single image does not include enough fibres in order to conduct a statistical characterisation, assuming ergodicity, Wu et al. (2018a) have processed 103 SEM images of amplification ratios 3000× and 2000× in order to identify the fibres with a circles detection tool as illustrated in Fig. 7(b). Considering round fibres was justified by Wu et al. (2018a) by evaluating the roundness, from the perimeter p and the cross-section area A with roundness $= \frac{p^2}{4\pi A}$, of a few hundreds of fibres, yielding an average value of 1.045 with a standard deviation of 0.011.

Fibre waviness can by characterised by optical microscopy, see the review by Kugler and Moon (2002). Huang et al. (2021) have characterised the weaviness from binary image segments followed by a linear texture regression.

Features. In this work we focus on the fibres distribution within the cross-section, which can be statistically analysed using the circles identified in Fig. 7(b).

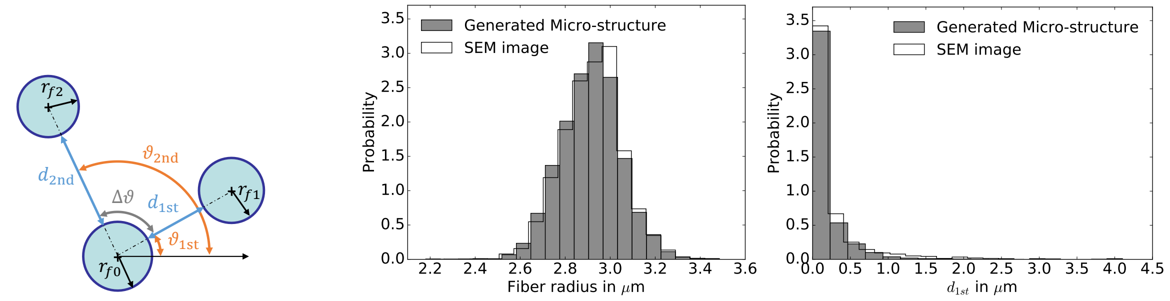

(a) Features (b) $\pi_{R_f}(r_f)$ (c) $\pi_{D_{1\text{st}}}(d_{1\text{st}})$

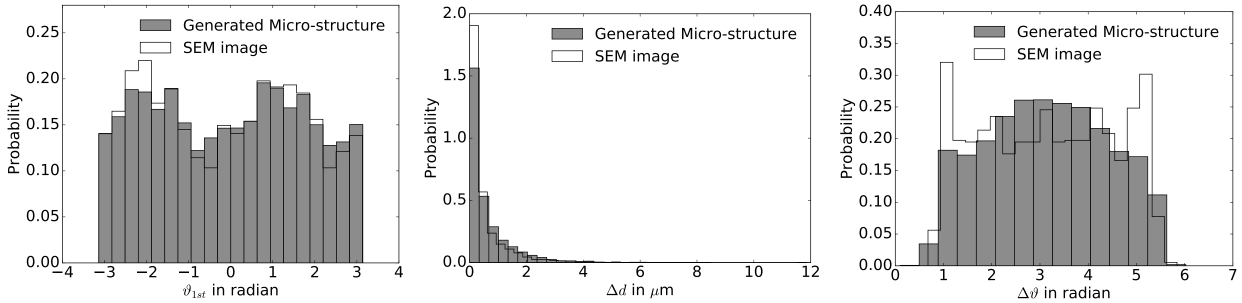

(d) $\pi_{\Theta_{1\text{st}}}(\vartheta_{1\text{st}})$ (e) $\pi_{\Delta D}(\Delta d)$ (f) $\pi_{\Delta\Theta}(\Delta\vartheta)$

Figure 8: Comparison of histograms extracted by Wu et al. (2018a) from probability density functions of the statistical descriptors evaluated from the experimental data and from the reconstructed micro-structures: (a) Illustration of the statistical descriptors; (b) Fibre radius R_f distributions; (c) Nearest-neighbour net distance $D_{1\text{st}}$ distributions; (b) Nearest-neighbour orientation $\Theta_{1\text{st}}$ distributions; (c) Difference between the net distances to the second and to the first nearest-neighbours ΔD distributions; and (d) Difference between nearest-neighbour orientations $\Delta\Theta$ distributions; Reprinted from Composite Structures 189, Wu, L., Chung, C.N., Major, Z., Adam, L., Noels, L., From SEM images to elastic responses: A stochastic multiscale analysis of UD fiber reinforced composites, 206-227, Copyright (2018), with permission from Elsevier.

Statistical functions of the fibre radius r_f, 1st and 2nd closest neighbours distance, d_{1st} and d_{2nd} etc. were extracted from SEM images by Vaughan and McCarthy (2010). Wu et al. (2018a) have considered the features illustrated in Fig. 8(a) and have extracted

- The probability density function of fibre radius $\pi_{R_f}(r_f)$;
- The nearest-neighbour net distance probability density function $\pi_{D_{\text{1st}}}(d_{\text{1st}})$; By using the net distance, the effect of fibre's radius on the nearest-neighbour distance can be excluded;
- The probability density function $\pi_{\Theta_{\text{1st}}}(\vartheta_{\text{1st}})$ of the orientation of the un-directed line connecting the centre points of a fibre and of its nearest neighbour, with support $]-\pi,\pi]$;
- The probability density function $\pi_{\Delta D}(\Delta d)$ of the difference between the net distances to the second and to the first nearest-neighbours with $\Delta d = d_{\text{2nd}} - d_{\text{1st}}$; Since $\Delta d \geq 0$ it is easier to generate random variables satisfying $d_{\text{2nd}} \geq d_{\text{1st}}$;
- The probability density function $\pi_{\Delta\Theta}(\Delta\vartheta)$ on $]0, 2\pi]$ of the difference $\Delta\vartheta = \vartheta_{\text{2nd}} - \vartheta_{\text{1st}}$ of the orientations ϑ_{2nd} and ϑ_{1st} of the second and the first nearest-neighbours; This allows localising the second nearest-neighbour with respect to the first nearest-neighbour.

The distributions obtained by Wu et al. (2018a) from the experimental images are illustrated in Fig. 8.

The correlation matrix of the four random variables D_{1st}, Θ_{1st}, ΔD, and $\Delta\Theta$, reads

$$\mathbf{R}_{[D_{\text{1st}}\,\Theta_{\text{1st}}\,\Delta D\,\Delta\Theta]^T} = \begin{array}{c} \\ D_{\text{1st}} \\ \Theta_{\text{1st}} \\ \Delta D \\ \Delta\Theta \end{array} \begin{array}{c} \begin{array}{cccc} D_{\text{1st}} & \Theta_{\text{1st}} & \Delta D & \Delta\Theta \end{array} \\ \begin{pmatrix} 1.0 & 0.014 & 0.205 & 0.022 \\ & 1.0 & 0.002 & 0.020 \\ \text{symmetric} & & 1.0 & -0.005 \\ & & & 1.0 \end{pmatrix} \end{array} . \tag{75}$$

However, since Fig. 8 shows that the distributions of the four spatial parameters d_{1st}, ϑ_{1st}, Δd, and $\Delta\vartheta$ all exhibit non-Gaussianity, the statistical dependence of these random variables is assessed by their distance correlations matrix, whose detailed expressions are given by Székely et al. (2007), which reads in this case

$$\mathbf{dR}_{[D_{\text{1st}}\,\Theta_{\text{1st}}\,\Delta D\,\Delta\Theta]^T} = \begin{array}{c} \\ D_{\text{1st}} \\ \Theta_{\text{1st}} \\ \Delta D \\ \Delta\Theta \end{array} \begin{array}{c} \begin{array}{cccc} D_{\text{1st}} & \Theta_{\text{1st}} & \Delta D & \Delta\Theta \end{array} \\ \begin{pmatrix} 1.0 & 0.040 & 0.273 & 0.075 \\ & 1.0 & 0.048 & 0.046 \\ \text{symmetric} & & 1.0 & 0.064 \\ & & & 1.0 \end{pmatrix} \end{array} . \tag{76}$$

There clearly exists a dependency between the first and second nearest neighbour distances. The other random variables were assumed to be independent.

Reconstruction. Starting from the statistically characterised physical features, Vaughan and McCarthy (2010); Melro et al. (2008); Wu et al. (2018a); Bhuiyan et al. (2020) have developed virtual specimen generators for UD composites and Gupta et al. (2015) for particle reinforced composites.

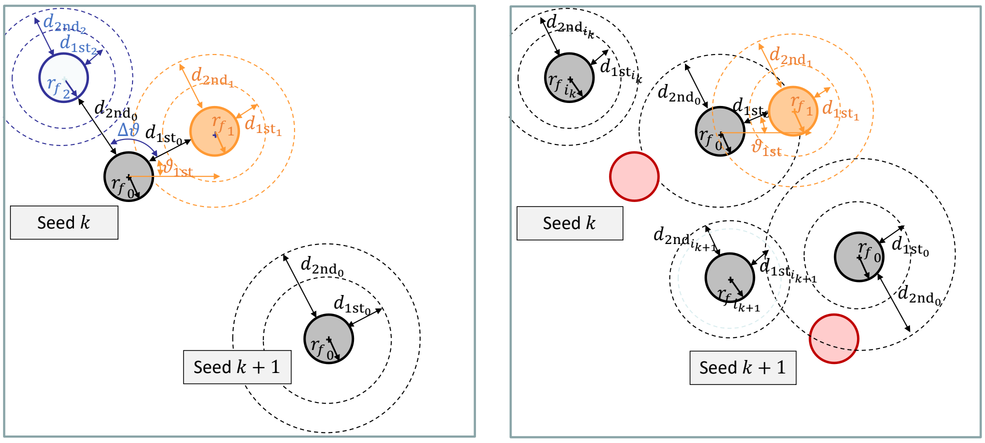

(a) Generator step #1 (b) Generator step #2

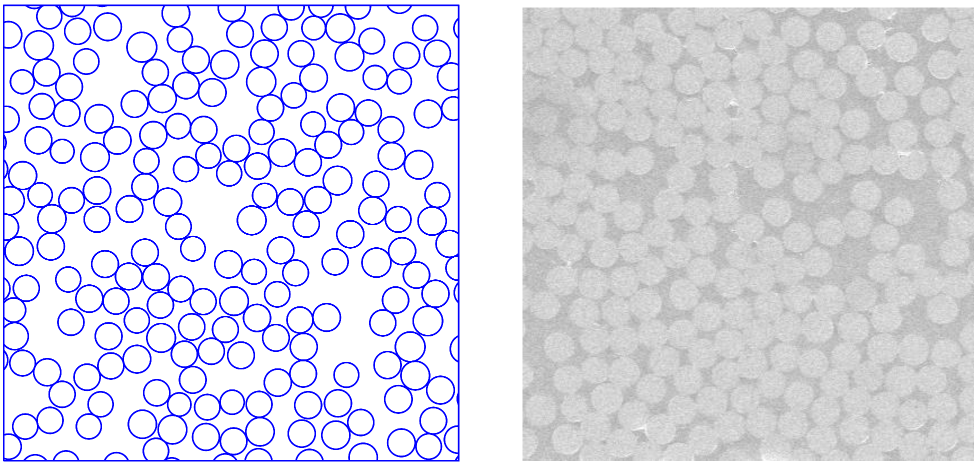

(c) Virtual micro-structure (d) SEM image

Figure 9: Generation of virtual UD micro-structures by Wu et al. (2018a): (a) The two nearest neighbours of seed k are generated with their two closest distances; (b) After having generated the two nearest neighbours of all the seeds, the previously generated neighbours become the new central fibres; (c) A generated micro-structure; and (d) An SEM image; Reprinted from Composite Structures 189, Wu, L., Chung, C.N., Major, Z., Adam, L., Noels, L., From SEM images to elastic responses: A stochastic multiscale analysis of UD fiber reinforced composites, 206-227, Copyright (2018), with permission from Elsevier.

There basically exist two main kinds of random fibres generator:

- The compact process, as developed by Melro et al. (2008), stirs and compacts the existing fibres iteratively in order to reach a target fibre volume fraction; The generated distributions were found to have statistical indicators close to a Poisson distribution;

However for a given micro-structure realisation of limited size, the fibre volume fractions of a real material is not deterministic (Savvas et al., 2016); Moreover, the Poisson distribution is not always representative of the spatial point pattern of fibres;

- The additive process, as developed by Vaughan and McCarthy (2010), positions fibres successively using the statistical spatial descriptors; Wu et al. (2018a) have considered the dependency among these descriptors in order to, on the one hand, allow reaching a high volume fraction and, on the other hand, improve the statistical fidelity.

In the following, we summarise the method developed by Wu et al. (2018a). First, the following method was used to generate realisations of the random (dependent) variables:

- Pseudo-random samples of the independent random variables X, here X stands for either R_f, $\Theta_{1\text{st}}$ or $\Delta\Theta$, are generated using the inverse transform sampling method, see Appendix A.2.1, from their cumulative distribution function $F_X(x)$, which are evaluated by Eq. (8) from their probability density functions illustrated in Fig. 8;
- The pseudo-random samples of the two dependent random variables, here $d_{1\text{st}}$ and Δd, are generated by using their copula constructed from their cumulative distributions $F_{D_{1\text{st}}}(d_{1\text{st}})$ and $F_{\Delta D}(\Delta d)$ following the approach summarised in Appendix A.2.2.

The packing can then proceed as follows:

- Random seeds are located in a window;
- Each seed is considered as a central fibre; a radius r_f, and the net distance functions $d_{1\text{st}}$, Δd, are generated;
- For each central fibre, the first neighbour is generated along with its four random variables, the fibre radius r_f, the orientation $\vartheta_{1\text{st}}$ and the net distances $d_{1\text{st}}$ and $d_{2\text{nd}}$ to be used for locating the upcoming fibres; If the fibre violates some penetration constraints the step is repeated;
- For each central fibre, generate the second neighbour along with its four random variables, the fibre radius r_f, the orientation $\Delta\vartheta$ and the net distances $d_{1\text{st}}$ and $d_{2\text{nd}}$ to be used for locating the upcoming fibres, see Fig. 9(a); If the fibre violates some penetration constraints the step is repeated;
- The process is repeated with as new central fibres the created ones, see Fig. 9(b).

A virtually generated micro-structure is illustrated in Fig. 9(c) and can be compared with an SEM image in Fig. 9(d). Their statistical spatial descriptors are compared in Fig. 8.

The elliptical nature of the fibre cross-section for some material systems was recently taken into account by Bhuiyan et al. (2020).

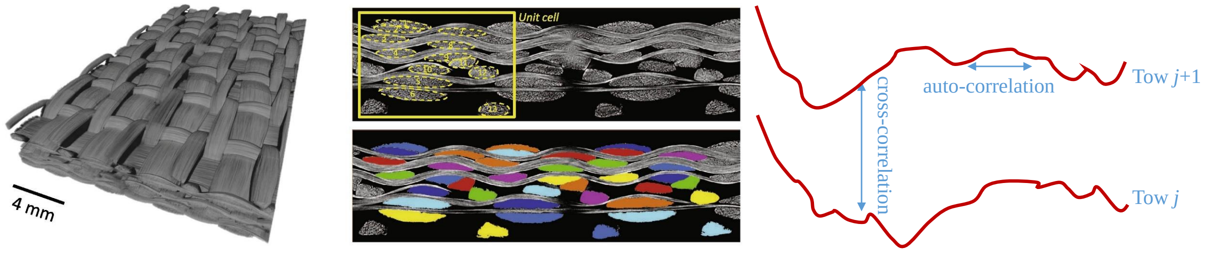

(a) Volume representation (b) Ellipse fitting (c) Auto/Cross correlation

Figure 10: Characterisation of woven composites based on physical descriptors: (a) Volume representation of the sample scanned using micro-Computed Tomography (μ-CT); (b) Image slice in weft direction showing the warp tows in cross-section, with the upper slice showing the warp tows and the fitting ellipses of the tow shapes; and (c) Correlation directions shown on the zero-mean deviations trends of two adjacent tow paths (Vanaerschot et al., 2017); Figure (a) and (b) reprinted from Composite Structures 173, Vanaerschot, A., Panerai, F., Cassell, A., Lomov, S.V., Vandepitte, D., Mansour, N.N Stochastic characterisation methodology for 3-d textiles based on micro-tomography, 44 - 52, Copyright (2017), with permission from Elsevier; and (c) resketched from (Vanaerschot et al., 2017).

3.2.2. Textile composites

Most of the uncertainty quantification work has been conducted on woven composite materials. A volume representation by Vanaerschot et al. (2017) is illustrated in Fig. 10(a). Several length scales are involved in such a material system:

- The torons, weft and warp tows, are usually made of UD composite materials, whose characteristic length is of a few μm, see Section 3.2.1;
- Three-Dimensional (3D) spatial geometrical variability of fibre tows are studied at a scale of a few millimetres (Vanaerschot et al., 2013a; Blacklock et al., 2012) of comparable order to the unit-cell length; A unit cell is defined as the repeated textile pattern and one representation is given in Fig. 2(d) for a 2/2 till woven composite material;
- Finally, tow loci also exhibit deviation at a larger length scale exceeding the unit cell as studied by Rossol et al. (2015), i.e. at the order of several cm.

Most of the characterisation efforts of the literature are related to the scale of the unit-cell. Vanaerschot et al. (2017) noted the importance of the categorisation in tow genuses for a complete and correct statistical description of any textile composite. "Tows belonging to the same genus must share the same trend for all tow characteristics with similar amplitude and period (Vanaerschot et al., 2017)". The six-layer weave depicted in Fig. 10 was represented by 8 warp genuses and 7 weft genuses by Vanaerschot et al. (2017), whilst the 2/2 twill weave depicted in Fig. 2(d) and studied by Vanaerschot et al. (2013a) was represented by 1 warp genus and 1 weft genus.

Data acquisition. In the context of composite materials, X-ray micro-focus Computed Tomography (μ-CT) was used by Vanaerschot et al. (2013a); Blacklock et al. (2012) to characterise the spatial geometrical variability of fibre tows and by Tal and Fish (2016) to characterise the defects at the scale of a few millimetres, see Fig. 10(b). Whereas tow orientations and their variations cannot be clearly identified at the level of one unit-cell, they can be at the level of several ones, requiring μ-CT scanning of the entire sample to be performed by tiling several individual scans as achieved by Vanaerschot et al. (2017), yielding the volume representation of Fig. 10(a). The tow reinforcement was then characterised by extracting two-dimensional slices in the warp and weft directions, as shown in 10(b).

3D Digital Image Correlation (DIC), as a complementary technique, can be used to characterise long-range weave defects in textile composites as achieved by Rossol et al. (2015).

Features. At the level of one meso-scale volume element, the tow reinforcement architecture is essentially characterised by the tow centroïd coordinates and its cross-section shape and size.

One dimensional tow loci were expressed by Blacklock et al. (2012) in terms of the sum of non-stochastic and periodic variations in the coordinates of the tow centroïd, and of stochastic and non-periodic deviations calibrated from the μ-CT images.

Vanaerschot et al. (2013a,b, 2017) have developed a stochastic modelling framework for fabrics, in which tows are represented as a sequence of elliptical cross-sections as identified on Fig. 10(b) from the μ-CT images. The fitted ellipses fully describe the tow path with only a few degrees of freedom: the centroïd coordinates (x, y, z), the tow cross-sectional area a, the tow cross-sectional aspect ratio a_r, and the tow cross-section orientation θ within the slice (i).

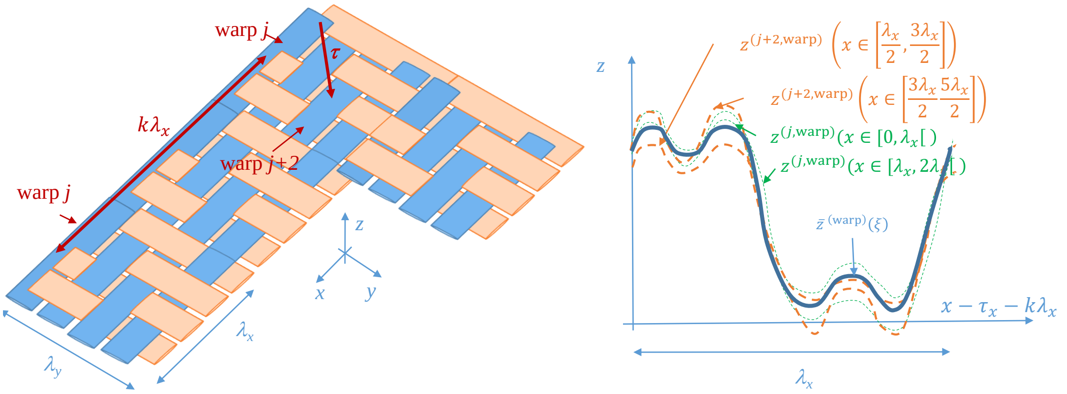

(a) Translation vector $\boldsymbol{\tau}$ (b) Systematic location

Figure 11: Reference period collation method proposed by Bale et al. (2012): (a) A vector $\boldsymbol{\tau}$ translates tow parts of the same genus warp –here all the warp belong the same genus– to the repeated weave of length λ_x; and (b) Definition of the systematic out-of-plane location $\bar{z}^{(\mathrm{warp})}(\xi)$ of the genus warp.

Data are collected for several tows $j = 1..N^{\mathrm{tow}^{(t)}}$ belonging to the same genus t, with different possible genuses $t = 1..N^{\mathrm{genus}}$. In order to account for the weave periodicity, the reference period collation method proposed by Bale et al. (2012), which is illustrated in Fig. 11 for the 2/2 till composite material, is used to define the translation vector $\boldsymbol{\tau}$

in order to bring each tow to a reference point of the repeated weaves, see Fig. 11(a). This allows defining the coordinate along a genus as ξ standing for either $x - \tau_x$ or $y - \tau_y$ for respectively a genus t corresponding to a warp or a weft. Similarly, the cross-section locus of a genus is defined by the coordinate ζ as either $y - \tau_y$ or $x - \tau_x$ for respectively a genus t corresponding to a warp or a weft and by the coordinate z. The tow cross-section is thus characterised by the vector $\boldsymbol{\varepsilon}_{\text{tow}^{(j,\,t)}} = [\zeta\ z\ a_r\ a\ \theta]^T$, defining the random vector $\mathbf{E}_{\text{tow}^{(j,\,t)}} = [\mathrm{Z}\ Z\ A_r\ A\ \Theta]^T : \mathscr{W} \rightarrow \Re^5$ for the tow $j = 1..N^{\text{tow}^{(t)}}$ of the genus $t = 1..N^{\text{genus}}$. The definitions can be completed by a ply index for layered composite materials as done by Vanaerschot et al. (2013a).

Since these random variables are evaluated along the tow direction ξ, one can define the random field $\mathbf{E}(\Xi) = \{\mathbf{E}_{\text{tow}^{(j,\,t)}}(\xi) : \ \xi \in \Xi \subset \Re\}$ as the collection of random vectors $\mathbf{E}_{\text{tow}^{(j,\,t)}}(\xi) : \mathscr{W} \rightarrow \mathscr{S}_{\mathbf{E}}$, where $\mathscr{S}_{\mathbf{E}} = \{\boldsymbol{\varepsilon} \in \Re^5 : \zeta \in \Re,\ z \in \Re,\ a_r \in \Re^+,\ a \in \Re^+,\ \theta \in [0,\ \pi[\}$. The systematic field $\bar{\boldsymbol{\varepsilon}}^{(t)}(\xi)$ of genus t is defined as the average on the number of points $N^{\lambda^{(t)}}$ from the different tows $j = 1..N^{\text{tow}^{(t)}}$ having the same reduced location ξ, i.e.

$$\bar{\boldsymbol{\varepsilon}}^{(t)}(\xi) = \frac{1}{N^{\lambda^{(t)}}} \sum_{j=1}^{N^{\text{tow}^{(t)}}} \sum_{k=1}^{N^{\text{cell}^{(j)}}} \boldsymbol{\varepsilon}^{(j,\,t)}(\xi + k\lambda_\xi)\ , \tag{77}$$

where $N^{\text{cell}^{(j)}}$ is the number of sampled weaves along tow j, and λ_ξ stands for either λ_x or λ_y for respectively a genus t corresponding to a warp or a weft. Application of Eq. (77) on the random field $Z^{(j,\,(warp))}(\Xi)$ is illustrated in Fig. 11(b). The evaluation of $\bar{\boldsymbol{\varepsilon}}^{(t)}(\xi)$ has to be performed for each genus t. Finally, the deviation is defined by

$$\boldsymbol{\varepsilon}'^{(j,\,t)}(\xi + k\lambda_\xi) = \boldsymbol{\varepsilon}^{(j,\,t)}(\xi + k\lambda_\xi) - \bar{\boldsymbol{\varepsilon}}^{(t)}(\xi)\ , \tag{78}$$

defining the deviation random field $\mathbf{E}'_{\text{tow}^{(j,\,t)}}(\Xi) = \{\mathbf{E}'_{\text{tow}^{(j,\,t)}}(\xi) : \xi \in \Xi\}$ as the collection of random vector $\mathbf{E}'_{\text{tow}^{(j,\,t)}}(\xi) : \mathscr{W} \rightarrow \mathscr{S}_{\mathbf{E}'}$, with the support $\mathscr{S}_{\mathbf{E}'} = \{\boldsymbol{\varepsilon}' \in \Re^5 : \zeta' \in \Re,\ z' \in \Re,\ a'_r \in \Re,\ a' \in \Re,\ \theta' \in]-\pi,\ \pi[\}$, and which is a zero-mean random field when considering all the tows j used to define the systematic field.

The micro-structure variability is then characterised by the different correlations, see Section 2.4, assuming homogeneous random fields:

- The standard deviation on a genus t

  $$\sigma_{\mathrm{E}'^{(t)}_r} = \frac{1}{\sum_i N^i - 1} \sqrt{\sum_i \sum_{j,\,k=1}^{N^i} \left[\boldsymbol{\varepsilon}'^{(j,\,t)}(\xi^{(i)} + k\lambda_\xi)\right]^2}\,, \tag{79}$$

  where N^i is the number of sampled data (considering all the tows $j = 1..\text{tow}^{(t)}$ and cells $k = 1..N^{\text{cell}^{(j)}}$) at a same reduced location $\xi^{(i)}$;

- The correlation for pairs of data separated by a distance δ along the tows of the same genus t

  $$R_{\mathbf{E}'_{\text{tow}^{(t)}}{}_{r\,s}}(\Delta\xi = \delta) = \frac{1}{\sigma_{\mathrm{E}'^{(t)}_r}\sigma_{\mathrm{E}'^{(t)}_s}} \mathbb{E}\left[\mathrm{E}'^{(j,\,t)}_r(\xi)\,\mathrm{E}'^{(j,\,t)}_s(\xi + \delta)\right]\ , \tag{80}$$

since the random field $\mathbf{E}'_{\text{tow}^{(j,\,t)}}(\Xi)$ has a zero-mean and where the expectation operator $\mathbb{E}[\bullet_r^{(j,\,t)}(\xi)\bullet_s^{(j,\,t)}(\xi+\delta)]$ here stands for $\frac{1}{\sum_i N^i}\sum_i\sum_{j,\,k=1}^{N^i}\bullet_r^{(j,\,t)}(\xi^{(i)}+k\lambda_\xi)\bullet_s^{(j,\,t)}(\xi^{(i)}+k\lambda_\xi+\delta)$ for N^i sampled data, considering all the tows $j = 1..\text{tow}^{(t)}$ and cells $k = 1..N^{\text{cell}^{(j)}}$ at a same reduced location $\xi^{(i)}$; This case in illustrated as the auto-correlation on Fig. 10(c);

- The correlation for pairs of data taken at the same reduced location ξ but on different tows j and $j+l$ of two genuses t and t' (with possibly $t = t'$) having the same direction

  $$R_{\mathbf{E}'_{\text{tow}^{(t)}},\,\mathbf{E}'_{\text{tow}^{(t')}\,r\,s}}(\Delta j = l) = \frac{1}{\sigma_{\mathrm{E}'^{(t)}_r}\sigma_{\mathrm{E}'^{(t')}_s}}\mathbb{E}\left[\mathrm{E}'^{(j,\,t)}_r(\xi)\,\mathrm{E}'^{(j+l,\,t')}_s(\xi)\right], \tag{81}$$

  where the expectation operator $\mathbb{E}[\bullet_r^{(j,\,t)}(\xi)\,\bullet_s^{(j+l,\,t')}(\xi)]$ here stands for $\frac{1}{\sum_i N^i}\sum_i\sum_{j,\,k=1}^{N^i}$ $\bullet_r^{(j,\,t)}(\xi^{(i)}+k\lambda_\xi)\,\bullet_s^{(j+l,\,t')}(\xi^{(i)}+k\lambda_\xi)$ for N^i sampled data, considering all the tows $j = 1..\text{tow}^{(t)}$ and cells $k = 1..N^{\text{cell}^{(j)}}$ at a same reduced location $\xi^{(i)}$; This case in illustrated as the cross-correlation on Fig. 10(c);

- The correlation between tows of genuses t and t' having different directions evaluated at crossover reduced locations $(x^{(i)} - \tau_x,\, y^{(i')} - \tau_y)$

  $$R_{\mathbf{E}'_{\text{tow}^{(t)}},\,\mathbf{E}'_{\text{tow}^{(t')}\,r\,s}} = \frac{1}{\sigma_{\mathrm{E}'^{(t)}_r}\sigma_{\mathrm{E}'^{(t')}_s}}\mathbb{E}\left[\mathrm{E}'^{(j,\,t)}_r(x-\tau_x)\,\mathrm{E}'^{(j',\,t')}_s(y-\tau_y)\right], \tag{82}$$

  where the expectation operator $\mathbb{E}[\bullet_r^{(j,\,t)}(x)\,\bullet_s^{(j',\,t')}(y)]$ here stands for $\frac{1}{\sum_{(i,\,i')}N^{(i,i')}}\sum_{(i,\,i')}$ $\sum_{j,\,j,\,k,\,k'=1}^{N^{(i,i')}}\bullet_r^{(j,\,t)}(x^{(i)}-\tau_x+k\lambda_x)\,\bullet_s^{(j',\,t')}(y^{(i')}-\tau_y+k'\lambda_y)$ for the $N^{(i,i')}$ sampled data at cross-over locations, considering all the tows $j = 1..\text{tow}^{(t)}$, $j' = 1..\text{tow}^{(t')}$ and cells $k = 1..N^{\text{cell}^{(j)}}$, $k' = 1..N^{\text{cell}^{(j')}}$.

Reconstruction. Vanaerschot et al. (2013a,b, 2017) have developed a stochastic modelling framework for fabrics, in which tows are represented as a sequence of elliptical cross-sections.

A deterministic micro-structure is first generated using WiseTex software (Verpoest and Lomov, 2005), from which the systematic function $\bar{\varepsilon}^{(t)}\left(\xi^{(i)}\right)$ is sampled at different coordinates $\xi^{(i)}$. When the systematic functions appear to be on good agreement with the ones obtained from the experimental measurements, the WiseTex functions are used, whilst when it is not the case, as observed for cross-sectional parameters by Vanaerschot et al. (2013a), the experimental ones are used.

Then, as a second step the deviation random field $\mathbf{E}'_{\text{tow}^{(j,\,t)}}(\Xi)$ has to be generated from the correlations and standard deviations evaluated by Eqs. (80-82). To this end, assuming the deviations can be represented by normal distributions, Vanaerschot et al. (2014) have used the Karhunen-Loève expansion to simulate correlated random fields, see Appendix A.3.3 and Vanaerschot et al. (2013b) have used the Markov chain Monte Carlo (MCMC) algorithm to simulate independent random fields, see Appendix A.5.1. The final random field $\mathbf{E}_{\text{tow}^{(j,\,t)}}(\xi)$ is then obtained by Eq. (78) and sent back to WiseTex to generate a micro-structure.

3.2.3. *Short fibres composites*

Short fibre reinforced composite matrix materials, see Fig. 2(c), are usually characterised by fibres of different lengths and having different orientations. Slender fibres can also exhibit a curvature. The difference in the length can result from the chopping process of the fibre, whilst the fibres orientation result mainly from the composite material process, *e.g.* during injection moulding the fibres take orientations whose randomness depends on the flow. Because of this dependency to the flow, the fibre orientation randomness is not the same at the different locations of the injected sample. As a result, properties distributions are not spatially uniform, affecting the material response.

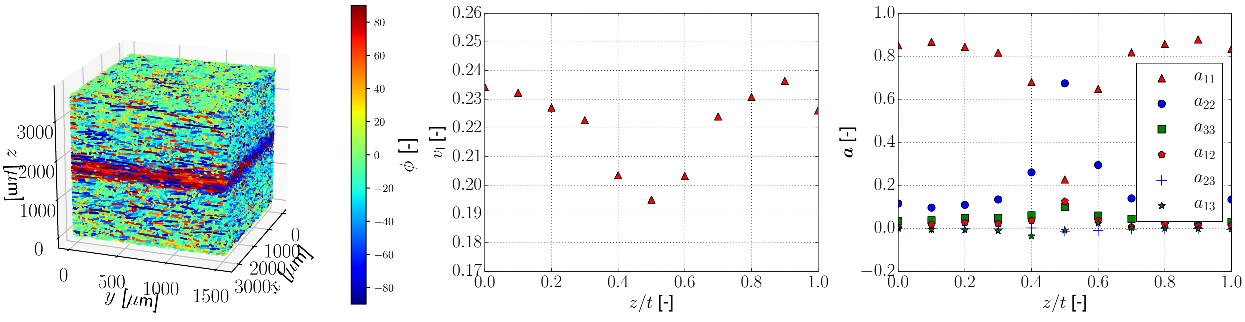

(a) CT-scan (b) $v_\mathrm{I}(z)$ (c) $\boldsymbol{a}(z)$

Figure 12: μ-CT analysis of PA06 reinforced by 40% of weight short E-glass fibres (GF) or PA06-GF40: (a) μ-CT sample; Evolution along the sample thickness of (b) The fibre volume fraction; and of (c) The second-order orientation tensor. Data were obtained by Wu et al. (2020b).

Data acquisition. Fibres are detected using micro-focus Computed Tomography (μ-CT) on mm-long samples, as discussed by Clarke and Eberhardt (2002); Vincent et al. (2005). An example of μ-CT image obtained on a 3.2 mm-thick PA06 reinforced by 40% of weight short E-glass fibres (GF) sample is illustrated in Fig. 12(a). It can be seen that, for such a sample cut from a plate manufactured by injection moulding, the distribution of fibres is not uniform along the cross-section of the plate: whilst at the lower and upper skin the fibres tend to orient themselves with the injection direction, at the core the fibres orientation exhibits more randomness.

Breuer et al. (2021) have extracted the aspect-ratio distribution of the fibres, or more exactly the fibre length distribution and fibre diameter by incinerating a sample of SFRP and measuring the fibres exposed with an optical microscope. The correlation, if any, with the orientation distribution function (ODF) $\pi_{\boldsymbol{P}}(\boldsymbol{p})$ is however lost by the process.

Assuming isotropicity of the micro-structure and ellipsoidal shape of the inclusions, Xu et al. (2014) have developed a 2D to 3D characterisation method allowing using 2D SEM images.

The spatial distribution of fibre orientation and volume fraction can also be predicted by simulating the manufacturing process as achieved by Gupta and Wang (1993); Vincent et al. (2005).

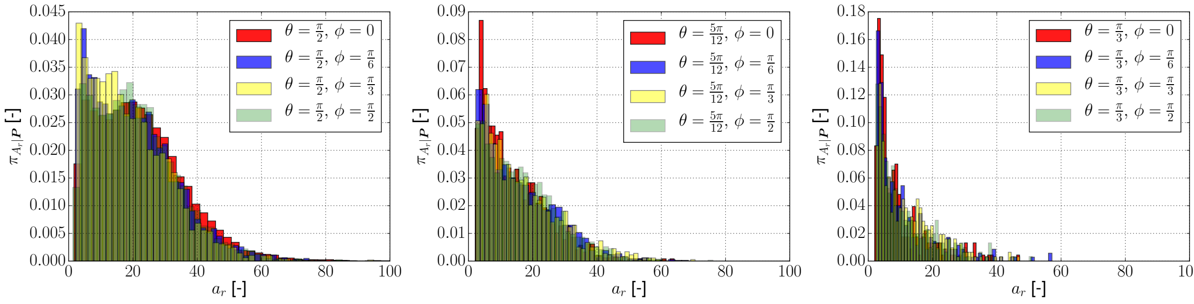

(a) $\pi_{A_r|\boldsymbol{P}}(a_r|\theta = \frac{\pi}{2})$ (b) $\pi_{A_r|\boldsymbol{P}}(a_r|\theta = \frac{5\pi}{12})$ (c) $\pi_{A_r|\boldsymbol{P}}(a_r|\theta = \frac{\pi}{3})$

Figure 13: Conditional distributions $\pi_{A_r|\boldsymbol{P}}$ obtained by injection by Mohamedou et al. (2019) of the fibre aspect ratio a_r of a PA06-GF40 plate for different facet orientations in terms of spherical polar angle θ and azimuthal angle ϕ; Reprinted from Composite Structures 220, Mohamedou, M., Zulueta, K., Chung, C.N., Rappel, H., Beex, L., Adam, L., Arriaga, A., Major, Z., Wu, L., Noels, L., Bayesian identification of mean-field homogenization model parameters and uncertain matrix behavior in non-aligned short fiber composites 64-84, Copyright (2019), with permission from Elsevier.

.

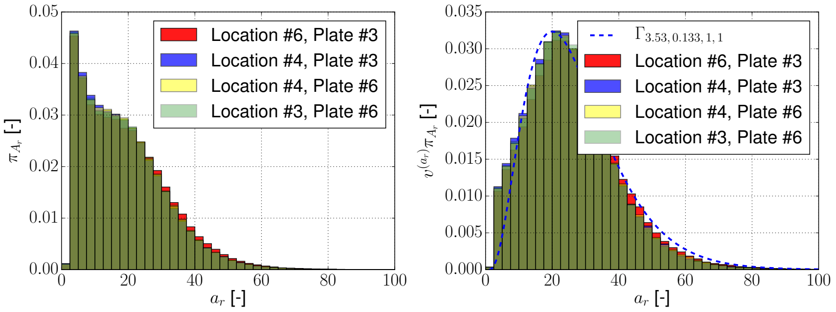

(a) $\pi_{A_r}(a_r)$ (b) $v^{(a_r)}\pi_{A_r}(a_r)$

Figure 14: Thickness averaged fibre aspect ratio distributions for different plate locations and different manufactured PA06-GF40 samples as obtained by Mohamedou et al. (2019): (a) Fibre aspect ratio distribution π_{A_r} in terms of fibres count; and (b) Distribution of volume fraction $v^{(a_r)}\pi_{A_r}$ of inclusions of aspect ratio a_r; Reprinted from Composite Structures 220, Mohamedou, M., Zulueta, K., Chung, C.N., Rappel, H., Beex, L., Adam, L., Arriaga, A., Major, Z., Wu, L., Noels, L., Bayesian identification of mean-field homogenization model parameters and uncertain matrix behavior in non-aligned short fiber composites 64-84, Copyright (2019), with permission from Elsevier.

Features. The main features characterising the short fibres reinforced matrix are:

- The spatial distribution of the fibre volume fraction v_{I}; Fibre volume fraction changes with the studied location, including across the sample thickness, see Fig. 12(b) for PA06 reinforced by 40% of weight short E-glass fibres (GF) or PA06-GF40;
- The fibre orientation distribution, with one fibre orientation characterised by a unit vector $\boldsymbol{p}$ along the fibre axis; The statistical description of orientations $\boldsymbol{P}$ is obtained through a probability density function $\pi_{\boldsymbol{P}}(\boldsymbol{p})$, also called Orientation Distribution

Function (ODF), with $\oint \pi_{\boldsymbol{P}}(\boldsymbol{p})\, \mathrm{d}\boldsymbol{p}{=}1$; For practically reasons, this expression is usually written within the spherical coordinates system, yielding

$$\int_{\theta=0}^{\pi} \oint_{\phi=0}^{2\pi} \pi_{\boldsymbol{P}}\left(\boldsymbol{p}(\theta,\, \phi)\right) \sin(\theta)\, \mathrm{d}\theta\, \mathrm{d}\phi = 1\,, \tag{83}$$

where θ is the polar angle and ϕ is the azimuthal angle; In practice, the ODF $\pi_{\boldsymbol{P}}(\boldsymbol{p})$ is not always directly available, *e.g.* as when considering the process simulation, and it is more common to have access to the ODF-weighted average of $\boldsymbol{p}\otimes\boldsymbol{p}$, where the symbol $\otimes$ designates a tensor or dyadic product, which is called the second-order orientation tensor

$$\mathbf{a} = \oint \boldsymbol{p} \otimes \boldsymbol{p} \pi_{\boldsymbol{P}}(\boldsymbol{p})\, \mathrm{d}\boldsymbol{p}\ ; \tag{84}$$

The ODF $\pi_{\boldsymbol{P}}(\boldsymbol{p})$ can be retrieved from $\mathbf{a}$ by considering some assumptions as in the interpolation method developed in Doghri and Tinel (2005, 2006); The ODF usually spatially varies including with respect to the thickness, see Fig. 12(c);

- The statistical distribution of the aspect ratio $a_r = \frac{l}{d}$, with assuming each fibre of diameters d considered to be straight and of length l; The aspect ratio distribution can spatially vary including with respect to the thickness and the distribution of the aspect ratio also varies with the direction $\boldsymbol{p}$ as illustrated in Fig. 13 for PA06 reinforced by 40% of weight short E-glass fibres (PA06-GF40) plates obtained by Mohamedou et al. (2019); Since the ODF does not differentiate fibres of different aspect ratio values and since the aspect ratio distributions are different along the different directions $\boldsymbol{p}$, Mohamedou et al. (2019) have considered the volume fraction of the fibres of aspect ratio a_r along a direction $\boldsymbol{p}$ as being more representative than the fibres count; Considering the variables v_f, a_r, $\boldsymbol{p}$ as the volume of one fibre v_f, its aspect ratio a_r and its direction $\boldsymbol{p}$ whose probability function reads $\pi_{V_f,\, A_r,\, \boldsymbol{P}}$, the volume fraction $v^{(a_r,\, \boldsymbol{p})} \pi_{A_r,\, \boldsymbol{P}}\left(a_r,\, \boldsymbol{p}\right)$ of fibres having an aspect ratio between a_r and $a_r + \mathrm{d}a_r$ and oriented along a direction between $\boldsymbol{p}$ and $\boldsymbol{p} + \mathrm{d}\boldsymbol{p}$ is defined as

$$v^{(a_r,\, \boldsymbol{p})} = \frac{\int_{\mathbb{R}+} v_f \pi_{V_f | A_r,\, \boldsymbol{P}}\left(v_f | a_r,\, \boldsymbol{p}\right)\, \mathrm{d}v_f}{\oint \int_{\mathbb{R}+} \int_{\mathbb{R}+} v_f \pi_{V_f,\, A_r,\, \boldsymbol{P}}\left(v_f,\, a_r,\, \boldsymbol{p}\right)\, \mathrm{d}v_f\, \mathrm{d}a_r\, \mathrm{d}\boldsymbol{p}}\,, \tag{85}$$

  with $\oint \int_{\mathbb{R}+} v^{(a_r,\boldsymbol{p})} \pi_{A_r,\, \boldsymbol{P}}(a_r,\, \boldsymbol{p})\, \mathrm{d}a_r\, \mathrm{d}\boldsymbol{p}{=}1$; This distribution obtained for PA06-GF40 plates by Mohamedou et al. (2019) is illustrated in Fig. 14;

- The cumulative distribution function of the nearest aggregate/fibre as considered by Xu et al. (2014);

- In some cases, the fibres curvature, in which case the local orientation vector of each fibre should be characterised, see the discussion by Eberhardt and Clarke (2002); The fibres are usually assumed as being ellipsoidal.

Reconstruction. Based on the evaluation of the local orientation vector of the fibres directly from the μ-CT images, Eberhardt and Clarke (2002) have reconstructed a micro-structure, which is however unique for one analysed sample.

Packing algorithms were also developed for different inclusion shapes by Jia and Williams (2001), for sphero-cylinder by Böhm et al. (2002); Williams and Philipse (2003); Tu et al. (2005) and for convex shapes by Stafford and Jackson (2010). An efficient algorithm presented for periodic random packing of ellipsoids based on molecular dynamics (MD) has been extensively described by Budarapu et al. (2019). However the link with the statistical descriptors was not provided. These latter have been considered by Xu et al. (2014) and by Li et al. (2016). In particular, Li et al. (2016) have developed the following packing algorithm:

- The fibres are represented by cylinders with the same diameter, length, and thus by a unique aspect ratio a_r;
- The fibre orientations are sampled from the ODF $\pi_{\boldsymbol{P}}(\boldsymbol{p})$ retrieved from the second-order orientation tensor $\mathbf{a}$;
- Newly generated fibres are located with respect to the existing fibres and the fibre predefined diameter to control the volume fraction, with rejection until no overlap.

In contrast, Breuer et al. (2021) have also used the aspect ratio distribution $\pi_{A_r}(a_r)$ and the ODF $\pi_{\boldsymbol{P}}(\boldsymbol{p})$ (in a uncorrelated way) when generating the micro-structure.

3.2.4. Poly-crystal

Data acquisition. We refer to Section 3.1.5 for a short discussion on data acquisition related to poly-crystalline structures.

Features. The main features considered in the literature are:

- The cell or volume size distribution $\pi_V(v)$; As discussed by Xu and Li (2009), in crystallography, the grain sizes are often shown to follow log-normal distribution, but bi-modal and multi-modal distributions, *i.e.* with more than one local maximum in the probability density function, are also found; When limited information is available, Sankaran and Zabaras (2007) used the Maximum Entropy framework, see Appendix B, with as input the four first statistical moments evaluated from a limited number of phase-field simulations, in order to identify the distribution $\pi_V(v)$, see Fig. 15(a);
- Grains aspect ratio; Saylor et al. (2004) have identified the grains as ellipsoids of semi-axes $(a,\, b,\, c)$ aligned with the sample direction in order to extract the probability density function $\pi_{A,\,B,\,C}(a,\, b,\, c)$ related to the probability to find an ellipsoid of semi-axes between $(a,\, b,\, c)$ and $(a + da,\, b + db,\, c + dc)$ at a given spatial position, which allows deducing the distribution of the aspect ratio and of the grain size;

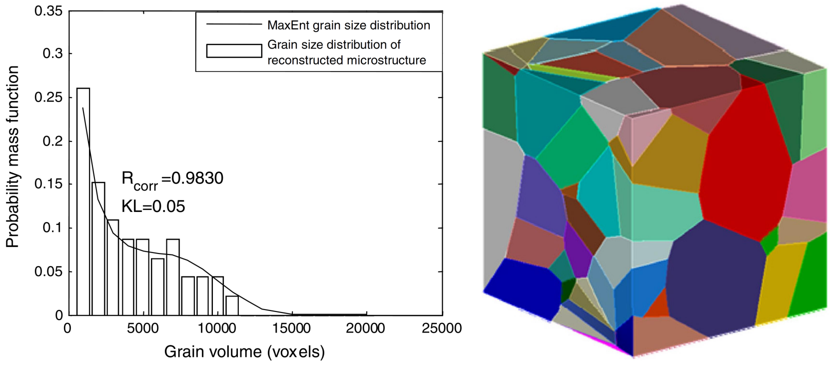

(a) $\pi_V(v)$ (b) Sampled Voronoï

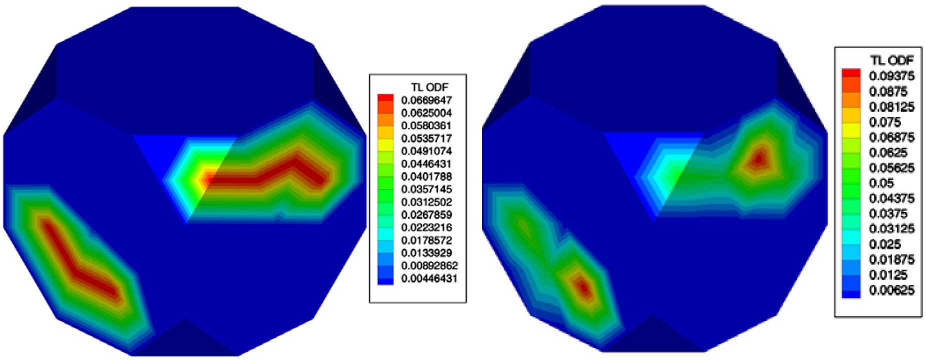

(c) ODF from maximum Entropy (d) ODF of one observation

Figure 15: Reconstruction of poly-crystal by Sankaran and Zabaras (2007): (a) Probability mass function of the grain size constructed using the maximum entropy framework from phase-field simulation results and comparison with the distribution obtained for one poly-crystal realisation (KL is the Kullback-Leibler divergence measure of the two entropies); (b) One Voronoï realisation; (c) Orientation Distribution Function (ODF) illustrated in the Frank-Rodrigues space and constructed using the maximum entropy framework from phase-field simulation results; and (d) Orientation Distribution Function (ODF) of one poly-crystal realisation; Reprinted from Acta Materialia 55, Sankaran, S., Zabaras, N, Computing property variability of polycrystals induced by grain size and orientation uncertainties, 2279-2290, Copyright (2007), with permission from Elsevier.

- Orientation distribution; Saylor et al. (2004) have characterised the orientation, here assumed to be represented by $\boldsymbol{h}_{\text{Euler}}$ following Section 3.1.2, by the probability density function, here denoted, $\pi_{\boldsymbol{H}_{\text{Euler}}}(\boldsymbol{h}_{\text{Euler}})$, related to the probability to find an orientation between $\boldsymbol{h}_{\text{Euler}}$ and $\boldsymbol{h}_{\text{Euler}} + d\boldsymbol{h}_{\text{Euler}}$ at a fixed spatial position; They have also characterised the mis-orientation $\Delta\boldsymbol{h}_{\text{Euler}}$ between two neighbouring grains, by evaluating its probability density function, here denoted, $\pi_{\Delta\boldsymbol{H}_{\text{Euler}}}(\Delta\boldsymbol{h}_{\text{Euler}})$; As done for the grain size distribution, Sankaran and Zabaras (2007) used the Maximum Entropy framework, see Appendix B, in order to obtain the distribution of orientation from a limited number of phase-field simulations; The constraints are then defined as sharp textures corresponding to localisation of intensities, see Fig. 15(c); We note that the possible orientations are not necessary continuous; X-Ray Diffraction (XRD) measurements

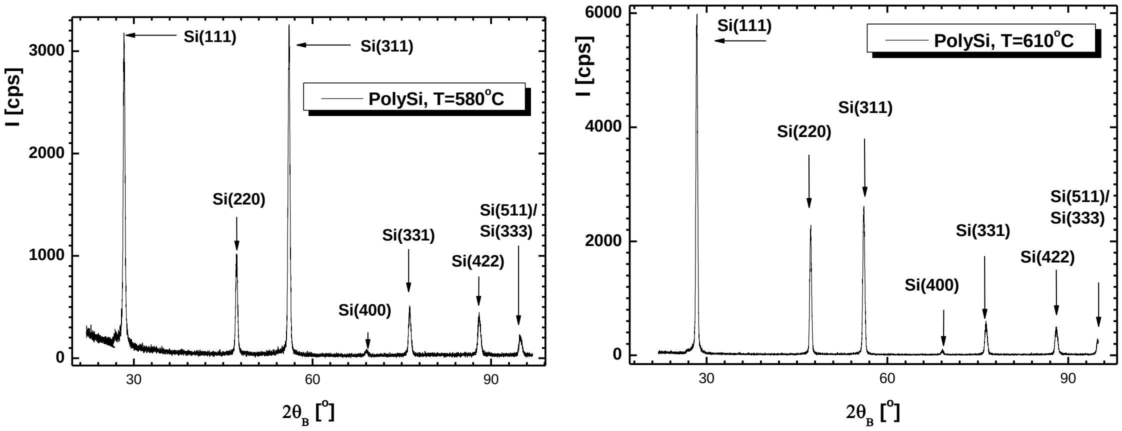

(a) 580^o C

(b) 610^o C

Figure 16: X-Ray Diffraction (XRD) measurements by Lucas et al. (2017) for columnar poly-silicon obtained by Low Pressure Chemical Vapour Deposition (LPCVD) at different temperatures of the fabrication process; The intensity of each peak, associated to one orientation, is given in counts per seconds; Reprinted from International Journal for Numerical Methods in Engineering 111, Lucas, V., Golinval, J.C., Voicu, R.C., Danila, M., Gavrila, R., Müller, R., Dinescu, A., Noels, L., Wu, L, Propagation of material and surface profile uncertainties on mems micro-resonators using a stochastic second-order computational multi-scale approach, 26-68. Copyright (2017), with permission from John Wiley and Sons.

were obtained by Wu et al. (2016); Lucas et al. (2017) on columnar poly-silicon thin sheets obtained by Low Pressure Chemical Vapour Deposition process (LPCVD); As shown by the peaks in Fig. 16, only some orientations are present in the poly-crystal, and the relative intensity of the peaks provides the relative weight fraction for the different orientations.

Reconstruction. The grains geometry are commonly generated from Voronoï tessellation as achieved by Barbe et al. (2001); Saylor et al. (2004); Sankaran and Zabaras (2007); Xu and Li (2009). Among the Voronoï tessellation methods, Poisson-Voronoï uses points as seeds to generate polyhedral shapes from the planes bisecting the bonds connecting each seed and its nearest neighbours. As discussed by Xu and Li (2009), discrepancies with real poly-crystals are found in terms of statistical properties such as average face numbers of cells, grain volume variances etc. A first remedy is the Laguerre tessellation method, which replaces the point seeds by finite size spheres. Another solution is to consider a physically-based growing process such as the Johnson-Mehl-Avrami-Kolmogorov (JMAK) kinetics method developed by Mahin et al. (1980); Ito and Fuller (1993).

In order to recover observed statistical features, such as the grain volume distributions $\pi_V(v)$, including bi-modal ones, Xu and Li (2009, 2010) have added constraints to the Poisson-Voronoï process, leading to an optimisation problem of the seed locations solved using an inverse Monte Carlo process, see Appendix A.5. Saylor et al. (2004) have packed ellipsoids sampled from $\pi_{A,B,C}(a,\ b,\ c)$, the probability density function of their semi-axes, and whose centres became the nucleation site of grains growth simulated using Johnson-

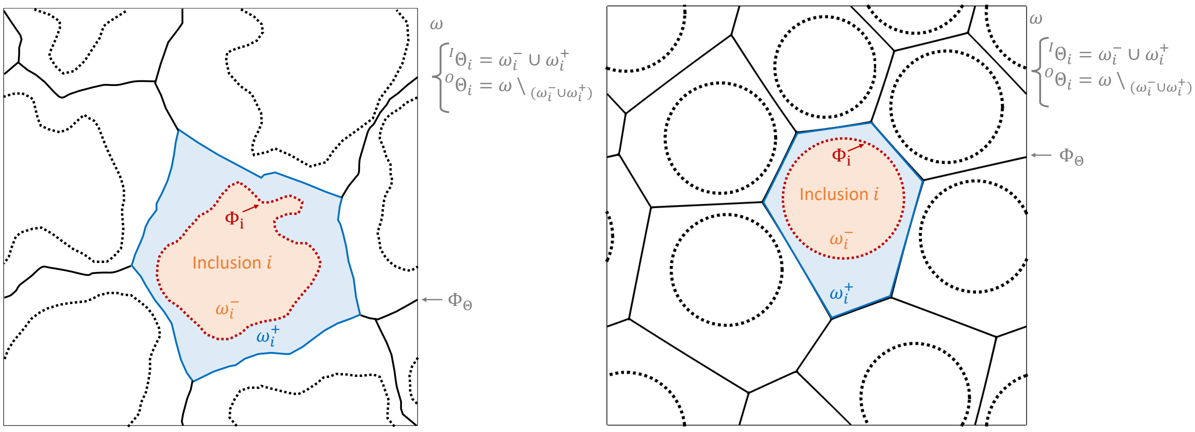

(a) Arbitrary inclusions (b) Spherical inclusions

Figure 17: Domain definitions using the level-set functions, dashed lines denote inclusion boundaries whilst bold lines denote Φ_Θ: (a) Arbitrary-shaped inclusions resketched from the work by Sonon et al. (2015); and (b) Spherical inclusions resketched from the work by Kilingar et al. (2019).

Mehl-Avrami-Kolmogorov (JMAK) kinetics (Ito and Fuller, 1993). Sankaran and Zabaras (2007) have associated to randomly distributed seeds the sizes sampled from $\pi_V(v)$ and developed an iterative process using repulsive forces between overlapping spheres.

Once grains are generated, grain orientation and mis-orientation are then assigned using a Monte Carlo procedure, see Appendix A.5, to recover the probability density function $\pi_{\boldsymbol{H}_{\text{Euler}}}(\boldsymbol{h}_{\text{Euler}})$ and $\pi_{\Delta\boldsymbol{H}_{\text{Euler}}}(\Delta\boldsymbol{h}_{\text{Euler}})$. Saylor et al. (2004) have assigned to each grain an orientation following an iteration process in order to recover the probability density function $\pi_{\boldsymbol{H}_{\text{Euler}}}(\boldsymbol{h}_{\text{Euler}})$ and $\pi_{\Delta\boldsymbol{H}_{\text{Euler}}}(\Delta\boldsymbol{h}_{\text{Euler}})$. Such an orientation assignment was achieved using a Gibbs sampling, see Appendix A.5.4, by Sankaran and Zabaras (2007). We note that these methods do not consider the correlation between the different distributions, of grain sizes and orientation *e.g.*.

Generation using a level-set approach. Although Voronoï tessellation methods (Barbe et al., 2001; Saylor et al., 2004; Sankaran and Zabaras, 2007; Xu and Li, 2009) can be very effective in generating grains assemblies based on a random distribution of points, reaching more complex distribution such as bi-modal distributions of grain sizes leads to complex iterative procedures. Therefore Sonon et al. (2012, 2015) have developed a level-set based approach allowing generating complex micro-structures. In this approach, the level set functions are used as distance indicators. Given a domain ω, see Fig. 17, in which an inclusion i has to be introduced as member of the set $\mathcal{I}$ of all inclusions, ω_i^- and ω_i^+ represent respectively the domains inside and outside the boundary Φ_i of the inclusion. Different definitions are then introduced

- The signed distance field $DS_i(\boldsymbol{x})$ of inclusion i, is the distance from Φ_i, with negative values in ω_i^- and positive in ω_i^+, see Fig. 17;
- The k-th neighbour distance field, $DN_k(\boldsymbol{x})$, denoted as *DN finder*, gives the position

from the k-th nearest Φ_i in the packing and thus, all inclusions in the packing can be represented by using $DN_1(\boldsymbol{x})$ as a level set;

- The k-th neighbour identity map $NN_k(\boldsymbol{x})$, as an integer discontinuous function, gives for each point $\boldsymbol{x}$, the k-th nearest inclusion from $\boldsymbol{x}$ in the set $\mathcal{I}$;
- The "Inner" domain ${}^I\Theta_i$ of inclusion i is the set of points $\boldsymbol{x}$ closer to inclusion i than to any other inclusion, *i.e.* $NN_1(\boldsymbol{x}) = i, \forall\, \boldsymbol{x} \in {}^I\Theta_i$;
- The "Outer" domain ${}^O\Theta_i$ is the set of points closer to another inclusion than inclusion i, *i.e.* $NN_1(\boldsymbol{x}) \neq i$;
- $\Phi_{\Theta i}$ is the boundary of ${}^I\Theta_i$ and Φ_Θ is the union of all $\Phi_{\Theta i}$.

The interest of the distance fields is two-fold. On the one hand it improves the efficiency of the packing algorithm, and on the other hand it can be used to define more complex micro-structures.

When considering a Random Sequential Addition (RSA) algorithm, the rejection rate of a new inclusion i of centre $\boldsymbol{x}_C$ in the micro-structure ω is reduced with an *a priori* knowledge of sub domains where the inclusion will respect all the criteria of the test. The use of the neighbouring distance function fields helps in identifying these regions. For example, for arbitrary shaped inclusions, the smallest enclosing sphere of radius r determines the non-overlap criteria on any inclusion of centre $\boldsymbol{x}_C$ in the micro-structure ω already mapped in $DN_1(\boldsymbol{x})$ when meeting the condition

$$DN_1(\boldsymbol{x}_c) > r\,. \tag{86}$$

In the case of spherical inclusions packing, r is sampled from the radius distribution $\pi_R(r)$ and the regions of ω where (86) is satisfied are readily identified. Besides, closer or more realistic spheres packing can be achieved by a control on the distances from the first, second and third nearest neighbours, denoted by nnl_1, nnl_2 and nnl_3. This can also help producing closer packings, thus enabling higher packing densities. In that case, the possible regions to introduce a new inclusion are identified where meeting the conditions

$$DN_k(\boldsymbol{x}_c) < nnl_k + r \quad \text{with } k = 1..3\,. \tag{87}$$

Thus, the distance field-based RSA algorithm developed by Sonon et al. (2012) reads

1. Construction of the micro-structure domain ω made of a (un)regular grid of points $\boldsymbol{x}_n$ and initialisation of $DN_k(\boldsymbol{x}_n)$ to $+\infty$;
2. Generate trial inclusion i from prescribed size distribution function $\pi_V(v)$;
3. Extract satisfactory locations $\boldsymbol{x}_c$ by applying Eq. (86) to avoid inter-penetration and Eq. (87) to meet neighbour distance criteria; If this set is empty, the RVE is full, terminating the process, if not add the new inclusion i;
4. Update $DN_k(\boldsymbol{x}_n)$ to allow the calculation of $DS_i(\boldsymbol{x}_n)$ of new inclusion i;
5. Follow step 2 until termination criteria is reached or the RVE is full.

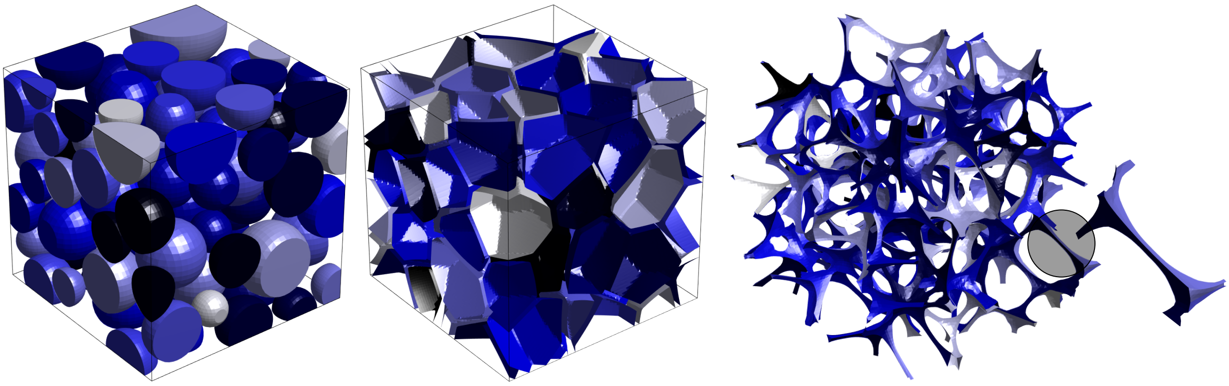

(a) Spheres packing following $\pi_V(v)$ (b) Voronoï tessellation (c) Extracted open-foam micro-structure

Figure 18: Level set-based micro-structure by Kilingar et al. (2019): (a) Spheres packing obtained using the level set-based-RSA following $\pi_V(v)$; (b) Voronoï tesselation obtained using Eq. (88), the image displays a plateau of thickness t resulting from Eq. (89); and (c) Open foam micro-structure with strut-cross section curvature and variation. Reproduced from Kilingar, N.G., Ehab Moustafa Kamel, K., Sonon, B., Massart, T.J., Noels, L., 2019. Computational generation of open-foam representative volume elements with morphological control using distance fields, European Journal of Mechanics - A/Solids 78, 103847. Copyright (c) 2019 Elsevier Masson SAS. All rights reserved.

For a given inclusions packing generated by the level set based-RSA, see Fig. 18(a), a Voronoï tessellation can then be implicitly constructed as the assembly of all ${}^I\Theta_i$ by using the first and the second neighbour distance fields to define the "Voronoï" level set function

$$O_V(\boldsymbol{x}) = DN_2(\boldsymbol{x}) - DN_1(\boldsymbol{x})\,. \tag{88}$$

The value of this function is exactly zero at loci equidistant from two nearest inclusions, see the continuous bold lines in Fig. 17 that correspond to the faces of the tessellations, and is positive everywhere else. Besides, with a view to the generation of more complex structures, a quasi-constant thickness t can be used in combination with O_V to extract a closed cell geometry through the level sets following

$$O_V(\boldsymbol{x}) - t = 0\,. \tag{89}$$

Figure 18(b) illustrates the tessellation with boundaries of thickness t obtained from the packing of Fig. 18(a).

3.2.5. Foamed materials

In this section we restrict ourselves to the open-cell foam case, which forms a class of light-weight cellular materials, see Fig. 2(e). In particular, metallic open-cell foams are usually manufactured either from moulds left after thermal treatment of reticulated polymer foams using investment casting, or by electro-deposition onto a polymeric foam with open cells, which is later removed resulting in hollow struts. The resulting foam morphological characteristics are largely influenced by that of the polymeric foam they are

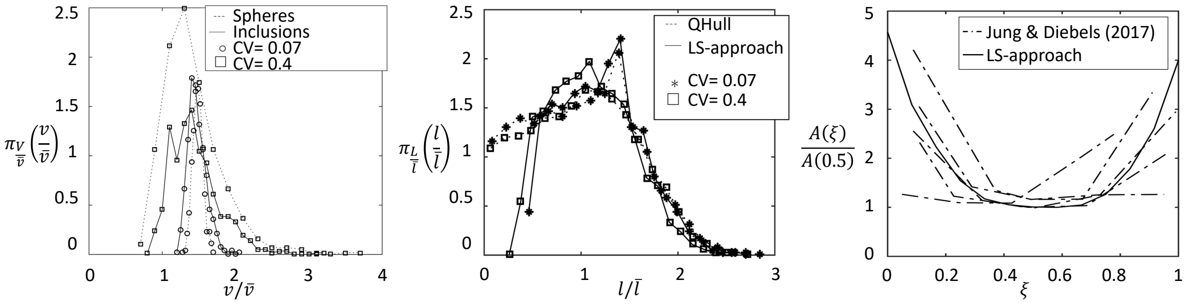

(a) $\pi_V(v)$ (b) $\pi_L(l)$ (c) Struts-cross section variation

Figure 19: Open-foam morphology distribution obtained with the LS-based approach by Kilingar et al. (2019): (a) Probability density function $\pi_V(v)$ of the (normalised) volume distribution for different coefficients of variation $CV = \frac{\sigma_V}{\mathbb{E}(V)}$; (b) Probability density function $\pi_L(l)$ of the (normalised) struts length distribution for different coefficients of variation $CV = \frac{\sigma_V}{\mathbb{E}(V)}$, comparison between the results of QHull (Barber et al., 1996) for a Laguerre Voronoï tessellation and that of the level-set based approach, which is more Gaussian-like; and; (c) Comparison of strut cross-section area with experimental data, dotted lines are resketched from Jung and Diebels (2017) for 20 ppi foams and the bold line depicts the variation of a single strut extracted from the micro-structure generated using the LS-based reconstruction procedure, see Fig. 18(c). Modified from Kilingar, N.G., Ehab Moustafa Kamel, K., Sonon, B., Massart, T.J., Noels, L., 2019. Computational generation of open-foam representative volume elements with morphological control using distance fields, European Journal of Mechanics - A/Solids 78, 103847. Copyright (c) 2019 Elsevier Masson SAS. All rights reserved.

derived from, yielding complex micro-structures consisting of an interconnected network of ligaments forming along the edges of randomly packed cells that evolve during the foaming process of the polymer (Jang et al., 2008).

Data acquisition. Statistical information is usually extracted from 3D reconstruction from micro-Computed Tomography (μ-CT) images. As an example, Liebscher et al. (2012, 2013) have extracted the mean and standard deviation of cell properties such as diameters d, surface area s, volume v, number of facets per cell n_F.

Features. Foamed materials can be characterised at several levels:

- Foams are mainly referred to in terms of their number of pores per (square) inch (ppi), which is strongly related to their porosity: the porosity usually decreases with an increase of the pores per (square) inch (ppi);
- The statistical information that is usually extracted is related to the cells of the foam, and can be found under the form of probability density functions $\pi_D(d)$ of the diameters d, $\pi_S(s)$ of the surface area s, $\pi_V(v)$ of the volume v, see Fig. 19(a), $\pi_{N_F}(n_F^{(i)})$ of the number of facets per cells $n_F^{(i)}$, $\pi_{N_E}(n_E^{(i)})$ of the number of edges per faces $n_E^{(i)}$;
- Finally some information are also extracted related to the struts morphology: some works (Vecchio et al., 2016, *e.g.*) consider the probability density functions $\pi_L(l)$ of the struts length l, see Fig. 19(b), whilst for other features, such as struts cross-section

concavity, and struts cross-section area $A(\xi)$ evolution along the non-dimensional abscissa of the struts ξ, see Fig. 19(c), only a limited amount of measurements, as the ones provided by Jung and Diebels (2017), are available.

Reconstruction. Laguerre tessellation was used by Liebscher et al. (2013) to reconstruct an open-foam micro-structure, in which the initial spheres are obtained by force-biased packing algorithm with radii sampled from a log-normal or gamma distribution $\pi_R(r)$. This distribution $\pi_R(r)$ is parametrised as suggested by Redenbach (2009) in order to recover some statistical foam features (mean and standard deviation of diameters d, surface area s, volume v, number of facets per cells $n_F^{(i)}$). Since this last method only ensures a good fit for a limited set of statistical properties and since it tends to predict struts length distributions with too many short edges, see QHull results in Fig. 19(b), Liebscher (2015) have iterated on the seeds location used in the Laguerre tessellation in order to recover more accurately the observed statistical features.

Another approach used by Kraynik et al. (2003); Vecchio et al. (2016) is to model foam structures based on the computation of the equilibrium micro-structure of soap froth. To this end, the Surface Evolver software developed by Brakke (1992) is initialised with a random packing of spheres and uses the principle of minimisation of surface energy that shapes the “liquid” into Plateau borders. The resulting micro-structure exhibits a Gaussian-like strut length distribution as experimentally observed. However, such a process requires an important computational effort, and the extraction of a finite-element model from the micro-structure remains cumbersome.

Generation using a level-set approach. A practical way to define the morphology of the open-foam, which also allows extracting a finite-element model, is to rely on the level-set method introduced in Section 3.2.4. To this end, Sonon et al. (2015); Kilingar et al. (2019) have considered additional distance fields in order to extract, from the Voronoï tessellation illustrated in Fig. 18(b), the open foam micro-structure illustrated in Fig. 18(c).

Indeed, the open foam micro-structures are defined by the struts morphology, which can in turn be represented by *ad-hoc* level set functions. The first three neighbour distance functions, define the “Plateau” level set function

$$O_P(\boldsymbol{x}) = \frac{(DN_3(\boldsymbol{x}) + DN_2(\boldsymbol{x}))}{2} - DN_1(\boldsymbol{x})\,, \tag{90}$$

which vanishes at the locus where the distance from the three nearest inclusions is the same, and is positive everywhere else. Therefore, the level set of this function consists of triangles with vertex lying on the tessellation cell boundaries, and a plateau border-like geometry of thickness t is represented by

$$O_P(\boldsymbol{x}) - t = 0\,. \tag{91}$$

The struts cross-section area A is also observed to vary along its length following a function $A(\xi)$, where ξ is the non-dimensional abscissa. The variation of the strut cross-section area in the generated morphology is controlled by rewriting Eq. (91) as

$$O_P(\boldsymbol{x}) - t \times O_S(\boldsymbol{x}) = 0\,, \tag{92}$$

where the function $O_S(\boldsymbol{\xi})$ was expressed in terms of level-set functions and of $A(\xi)$ by Kilingar et al. (2019). Figure 18(c) illustrates the morphology of the struts, and a cross-section area evolution is reported in Fig. 19(c).

Beside their area, struts cross-sections are also characterised by their shape, *i.e.* the cross-section curvature. Polyurethane (PU) ligaments usually have a 3-cusp hypocycloid cross-section, whilst most of the metallic foams have a triangular cross-section that tends towards circular with increasing ppi value. To obtain such morphological variations, a non-constant C^2 continuous function is subtracted from the function (92), leading to

$$O_P(\boldsymbol{x}) - t \times O_S(\boldsymbol{x}) - k_c \times O_K(\boldsymbol{x}) = 0, \tag{93}$$

where $0 < k_c < 1$ controls the concavity. Such a C^2 continuous function $O_K(\boldsymbol{x})$ can be defined based on the maintained distance fields as

$$O_K(\boldsymbol{x}) = \min\left(0, \frac{\left(\left(\frac{DN_3(\boldsymbol{x})-DN_2(\boldsymbol{x})}{2}\right)^2 - \left(t \times O_S(\boldsymbol{x})\right)^2\right)}{2t \times O_S(\boldsymbol{x})}\right). \tag{94}$$

Finally, similar operations were defined by Sonon et al. (2015) to introduce coating or again hollow struts.

3.3. Dimension reduction

Like for all stochastic approaches, the number of information can become overwhelming to be treated when the number of random variables characterising the micro-structures increases. This is called the “curse of dimensionality”. Therefore dimension reduction is usually performed in stochastic approaches.

We refer to the work by Bostanabad et al. (2018) for a recent review in the context of micro-structures characterisation and reconstruction, and we here give a short explanation on what is intended by the concept.

3.3.1. Features selection

Since several features are considered simultaneously, one simple approach to conduct dimension reduction is to identify the ones which affect the apparent properties or the ones which are strongly correlated. This approach is naturally applied when describing a micro-stricture using Physical descriptors as done in Section 3.2.

3.3.2. Features extraction

Once the micro-structures have been represented by, *e.g.*, a random vector $\boldsymbol{H}$ valued in $\Re^n$, it is possible to apply an order reduction and to represent the statistical information by another random vector $\mathbf{H}$ valued in $\Re^m$ with $m < n$, *e.g.* using the Principal Component Analysis (PCA) described in Appendix A.3.1, the polynomial chaos expansion (PCE) summarised in Appendix A.4.2, the data-driven probability sampling approach summarised in Appendix A.7, *etc.*.

Similar approaches are also developed for random fields $\boldsymbol{H}(\omega)$, such as the Karhunen-Loève (KL) series expansion summarised in Appendix A.3.2, the PCE of a random field summarised in Appendix A.4.4, *etc.*.

The feature extraction can also be combined with the statistical geometrical characterisation described in Section 3.1. As an example, Yabansu et al. (2017) have extracted the two-point spatial correlation of ternary eutectic alloys before applying a PCA.

3.4. Micro-scale constituents behaviours

When generating micro-structures, beside the geometrical features, material models ought to be associated to the different micro-structure phases and the model parameters also have to be provided. Besides, the existence of spatial variability, defects *etc.* also affects the homogenised material response.

3.4.1. In-situ properties

There are several difficulties related to the definition of the micro-constituent material models and on their identification.

First, the material behaviour of a bulk material within a heterogeneous material phase is not always the same as the one that can be observed in homogeneous macro-samples. Chevalier et al. (2019) have shown that in fibre reinforced epoxy resin, the non-linear matrix behaviour does not follow the model identified from epoxy macro-scale coupons. Although the origin of the discrepancy is not fully identified in this case, Nguyen et al. (2019) have developed a material model for polymers accounting for length-scale effects that allow recovering for a unique set of parameters the response of both composite material and bulk material samples. Another identified source of discrepancy between the material response of heterogeneous material constituents and of a macro-sample of the same material comes from the difference in the manufacturing process. As an example, when considering open metallic foam materials, the standard bulk material properties of the metallic alloy are in general much higher than those identified by reverse engineering from experimental tests performed on foamed materials because of the differences in the grains structure and texture. Heinze et al. (2018) have used an inverse identification of the struts material properties from a compression test performed on a single pore extracted from a foam sample and whose geometry was reproduced using μ-CT. Besides, heterogeneous materials can exhibit residual stresses within the constituents. As an example, the residual stress can originate from the existence of thermal gradient existing during the curing of thermoset-based composite materials. Brauner (2013) has predicted these residual stresses by simulating the manufacturing process with a chained thermal-chemical-mechanical finite element analysis, in which the resin curing kinetics has to be modelled (Karkanas and Partridge, 2000).

A second difficulty results from the possible variations, either between batches or as a spatial variation, of the constituent material properties. This effect of such variations on the homogenised properties was numerically studied by Xu and Graham-Brady (2005) who generated a random (micro-structure) medium of stochastic Young's modulus, by Kamiński and Kleiber (1996); Tootkaboni and Graham-Brady (2010); Kamiśki (2012), who generated unit cell of reinforced composites with stochastic Young's modulii for both phases –a variation with a stochastic fibre embedded in a periodic cell being proposed by Omairey et al. (2019), by Ma et al. (2015) who generated particle refinfored composites with varying hyperelastic properties of both phases following normal distribution, by Savvas and Stefanou (2017) who considered a normal distribution of the matrix Young's modulus in particle reinforced composites. Mehrez et al. (2018) have developed a hierarchical stochastic homogenisation in the context of non-crimp fabric laminates: considering uncertainties in the resin and carbon-fibre properties, they have predicted stochastic apparent properties of a tow and, by considering observations of tow spacing distribution, a new stochastic homogenisation could predict the stochastic apparent properties of the non-crimp fabric. The resin and carbon-fibre properties were assumed to be independent and to have uniform distributions (18) whose supports were defined from mean values and some bounds extrapolated from manufacturer data-sheets. In these works, the properties uncertainties were however not based on a systematic experimental uncertainty quantification.

Relying on the Stochastic Asymptotic Homogenisation-based multi-scale method developed by Fish and Wu (2011) and developed in see Section 4.2.2, Hu et al. (2017) have inferred the probability distribution of material constitutive model parameters, *i.e.* the fibre and matrix strength of their damage model, at the microscale from experimental observations of macroscale quantities of interest by solving a stochastic inverse multi-scale problem. In the same context, Bogdanor et al. (2013, 2015) have inferred rate-dependent damage model parameters of composite material constituents from experimental data using a Bayesian Inference process, see Section 3.4.2. Using the distribution of the constituents damage model parameters, a Gaussian process (GP) was used as a surrogate model for costly finite element analyses.

When it comes to defining material properties as random fields, inverse stochastic identification of single scale constitutive behaviour was considered by Yun and Shang (2016) in the context of elasto-plasticity, by Mehrez et al. (2012b,a) in the context of the homogenised response of composites from vibration tests, as a non-exhaustive list. Using a Bayesian Inference process, see Section 3.4.2, spatially varying elasticity constants, under the form of embedded inclusions, were identified by Koutsourelakis (2012), and Vigliotti et al. (2018) have captured the spatial distribution of material properties from experimental measurements. Nevertheless, identifying material properties as random fields at the micro-structure level with a view to stochastic multi-scale model remains challenging.

3.4.2. Bayesian inference

When building virtual micro-structures, some micro-structural properties can be statistically characterised either from experimental measurements or from the process simulation, *e.g.* following Section 3.1 or Section 3.2. Nevertheless, some micro-structural parameters cannot always be directly (statistically) identified, *e.g.* for the reasons previously recalled. For a multi-scale model to be built, *e.g* following the coming Section 4, in order to conduct virtual (stochastic) testing, these missing properties should be inferred.

One possibility is to evaluate these missing parameters from inverse identification using experimental tests performed on coupons made of the heterogeneous material. However, this identification requires several loading conditions to be performed, and a unique set

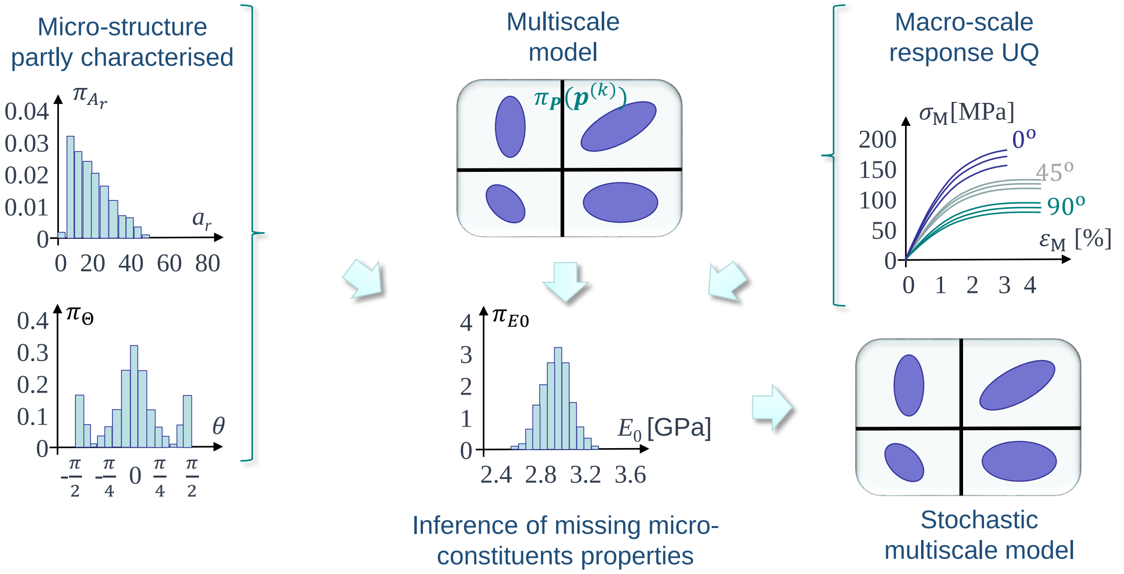

Figure 20: Bayesian inference of multi-scale model parameters: Considering a multi-scale model, some micro-structural properties are statistically characterised and the other ones are inferred under the form of a distribution using different experimental coupon tests performed on the heterogeneous material.

of parameters cannot usually reproduce all the experimental tests because of the model limitations and errors, in particular when considering non-linear responses. Besides, the data are inevitably entailed by experimental errors. These difficulties can be circumvented by considering a Bayesian Inference (BI) (Isenberg, 1979; Beck and Katafygiotis, 1998). In this framework, the uncertainties in the inferred parameters arise from the identification process itself under the form of a so-called posterior probability density function, as illustrated in Fig. 20.

Bayesian inference is structured around Bayes' theorem aiming at evaluating a so-called posterior distribution function $\pi_{\boldsymbol{Q}|\boldsymbol{Y}}(\boldsymbol{q}|\boldsymbol{y})$, also denoted $\pi_{\text{post}}(\boldsymbol{q}|\boldsymbol{y})$, of a random parameters vector $\boldsymbol{Q}$ with values in $\Re^n$, corresponding to the parameters to be inferred, for given observations of another random vector $\boldsymbol{Y}$ with values in $\Re^m$, corresponding to the, *e.g.* experimental, observations. Bayes' theorem states that the posterior distribution is proportional to the prior probability $\pi_{\text{prior}}(\boldsymbol{q})$ multiplied by the likelihood of $\boldsymbol{Y}$ for given observations of $\boldsymbol{Q}$:

$$\pi_{\text{post}}(\boldsymbol{q}|\boldsymbol{y}) \propto \pi_{\boldsymbol{Y}|\boldsymbol{Q}}(\boldsymbol{y}|\boldsymbol{q})\pi_{\text{prior}}(\boldsymbol{q})\,, \tag{95}$$

since $\pi_{\boldsymbol{Y}}(\boldsymbol{y})$ is a constant for given observations. In this equation

- The prior distribution $\pi_{\text{prior}}(\boldsymbol{q})$ reflects the initial belief or knowledge one has on the parameters to be inferred $\boldsymbol{Q}$; In particular physical bounds or previously inferred distributions from other observations can be used to define it;

- The likelihood function is defined by a conditional probability density function $\pi_{\boldsymbol{Y}|\boldsymbol{Q}}(\boldsymbol{y}|\boldsymbol{q})$, which is constructed from the different observation data of $\boldsymbol{Y}$;

- The conditional probability density function $\pi_{\text{post}}(\boldsymbol{q}|\boldsymbol{y})$ is the posterior distribution of the random vector $\boldsymbol{Q}$ that accounts for the observation data of the random vector $\boldsymbol{Y}$.

Many works inferred material model parameters using the Bayesian framework: elasto-perfectly plastic model and cohesive zone parameters were inferred by Most (2010), elasto-plastic material model parameters by Rappel et al. (2019b,a), visco-elasticity constants by Hernandez et al. (2015); Rappel et al. (2018) and a hyperelastic model and its parameters by Madireddy et al. (2015), the list being non-exhaustive. Homogenised elastic constants of composites were also inferred by Lai and Ip (1996); Daghia et al. (2007); Gogu et al. (2013). However in the latter works, the material is considered as homogeneous, which is not appropriate for stochastic virtual testing, motivating the use of Bayes' theorem to infer the parameters of multi-scale models.

Let the multi-scale model $\Phi_{\text{multiscale}}\left(\boldsymbol{Q};\, \boldsymbol{\xi}\right)$ be able to predict observations $\boldsymbol{y}_{\text{multiscale}} = \Phi_{\text{multiscale}}\left(\boldsymbol{q};\, \boldsymbol{\xi}\right)$, such as the macro-scale stress tensor, for a given realisation of the parameters $\boldsymbol{Q}$, and for given conditions $\boldsymbol{\xi}$, such as macro-scale loading conditions (macro-scale strain, loading direction *etc.*). Bayesian inference can be stated by assuming different sources for the errors, such as in the (*e.g.* experimental) observations $\boldsymbol{y}$, the conditions $\boldsymbol{\xi}$ or even the model $\Phi_{\text{multiscale}}$, see the summary by Rappel et al. (2019b). Assuming the main error is in the observations $\boldsymbol{y}$, the relation between the experimental measurements $\boldsymbol{y}$ and the multi-scale model predictions is written as

$$\boldsymbol{Y} = \Phi_{\text{multiscale}}(\boldsymbol{Q};\, \boldsymbol{\xi}) + \Omega_{\boldsymbol{Y}}\,, \tag{96}$$

where $\Omega_{\boldsymbol{Y}}$ is the noise. A Gaussian noise is commonly assumed, as in the work of Koutsourelakis (2012); Most (2010); Gogu et al. (2013); Madireddy et al. (2015); Hernandez et al. (2015); Rappel et al. (2018, 2019b), with $\Omega_{\boldsymbol{Y}} \sim \mathcal{N}_{\boldsymbol{\mu},,\sigma^2}(\boldsymbol{Y})$. Therefore, the conditional distribution or likelihood reads

$$\pi_{\boldsymbol{Y}|\boldsymbol{Q};\boldsymbol{\xi}}(\boldsymbol{y}|\boldsymbol{q};\, \boldsymbol{\xi}) = \mathcal{N}_{0,\,\sigma^2}\left(\boldsymbol{y} - \Phi_{\text{multiscale}}(\boldsymbol{q};\, \boldsymbol{\xi})\right)\,. \tag{97}$$

The evaluation of the posterior distribution in Eq. (95) using this likelihood function can be achieved using a random walking, such as in a Metropolis-Hasting Markov Chain Monte-Carlo algorithm, see Appendix A.5.4 and the details provided by Rappel et al. (2019a).

Mohamedou et al. (2019) have developed a Bayesian inference framework to identify the matrix Young's modulus and the aspect ratio of short fibre reinforced polymer following Eq. (95), in which the multi-scale model is a two-step Mean-Field Homogenization (Camacho et al., 1990; Doghri and Tinel, 2006) model, see also Section 4.2.4.

However, in the context of non-linear multi-scale models, the evaluation of the likelihood function (97) can be costly and has to be repeated several thousands of times because of the Metropolis-Hasting Markov Chain Monte-Carlo algorithm. In the context of the Stochastic Asymptotic Homogenisation-based multi-scale method developed by Fish and Wu (2011) and summarised in see Section 4.2.2, the Bayesian inference was used by Bogdanor et al. (2013, 2015) to calibrate rate-dependent damage models of the composite material constituents from experimental data. Using the distribution of the constituents damage

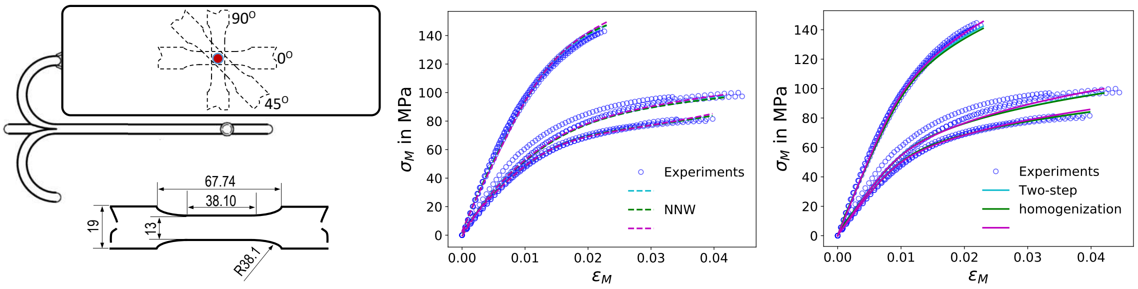

(a) Coupons (b) Exp. *vs.* NNW (c) Exp. *vs.* MFH

Figure 21: Application of Bayesian inference accelerated by a Neural Network surrogate model by Wu et al. (2020b): (a) Locations and geometries (in mm) of tested short fibre reinforced polymer coupons along 0°, 45° and 90° Directions; (b) The comparison of the experimental stress-strain curves to the NNW numerical model $\Phi_{\mathrm{NNW}}(\boldsymbol{q}^k; \boldsymbol{\xi}^i)$ prediction; and (c) The comparison of the experimental stress-strain curves to the two-step homogenization multi-scale model $\Phi_{\mathrm{multiscale}}(\boldsymbol{q}^k; \boldsymbol{\xi}^i)$ for the three parameters observations $\boldsymbol{q}^k$ extracted from Fig. 22; Reprinted from Computer Methods in Applied Mechanics and Engineering 360, Wu, L., Zulueta, K., Major, Z., Arriaga, A., Noels, L., Bayesian inference of non-linear multiscale model parameters accelerated by a deep neural network, 112693. Copyright (2020), with permission from Elsevier.

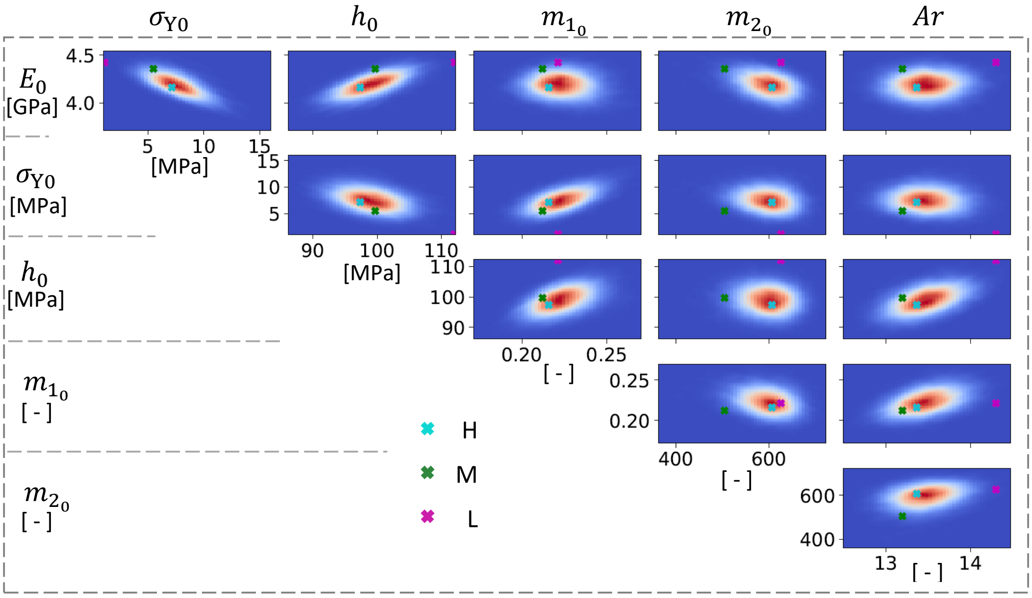

Figure 22: Distributions of the multi-scale model $\Phi_{\mathrm{multiscale}}(\boldsymbol{Q}; \boldsymbol{\xi})$ material properties inferred by Wu et al. (2020b) for short fibre reinforced polymer coupons: E_0 corresponds to the matrix Young's modulus, σ_{Y_0} to the matrix initial yield stress, h_0, m_{1_0} and m_{2_0} to the matrix hardening law $R_0(p_0) = h_0 p_0^{m_{1_0}}(1 - \exp(-m_{2_0} p_0))$ parameters, and A_r to the equivalent inclusion aspect ratio; Three marked points are extracted and correspond to observations of $\boldsymbol{q}^k$ of the Highest, Moderate and Lowest (among the 18000 samples) probabilities; Reprinted from Computer Methods in Applied Mechanics and Engineering 360, Wu, L., Zulueta, K., Major, Z., Arriaga, A., Noels, L., Bayesian inference of non-linear multiscale model parameters accelerated by a deep neural network, 112693. Copyright (2020), with permission from Elsevier.

model parameters, a Gaussian process (GP) is used as a surrogate model for costly finite element analyses. Wu et al. (2020b) have trained an artificial Neural Network (NNW) as a surrogate of a non-linear multi-scale model of short fibre reinforced polymer in order to infer, through a Bayesian process, the polymer non-linear model parameters. Georgios et al. (2021) have developed a PCE model of the homogenised response of a UD unit cell in order to serve as a surrogate model of the composite material stiffness and strength in the Metropolis-Hasting Markov Chain Monte-Carlo algorithm. They have then conducted a Bayesian inference of the fibre volume fraction and matrix damage law from experimental coupon tests. Balokas et al. (2021) have trained neural networks as surrogates of the stiffness and strength of high fibre density UD composites using as data numerical elastic damage simulations of unit cells. These surrogates were further used at the yarn level of braided composites in order to develop a multi-fidelity surrogate of the braided composite failure. To this end numerical damage elastic simulations of a braided unit cell were simulated with fine time steps (high fidelity) and coarse time step (low fidelity). As a result a low fidelity data base and a high fidelity data base were created and were further used to build a multi-fidelity Gaussian Process regression of the braided unit cell strength. In this case the multi-fidelity surrogate was not used to infer the model parameters but to conduct a sensitivity analysis. Paranjape et al. (2021) have trained surrogates of quantities of interest from finite element simulations samples made of superelastic Nickel-Titanium (NiTi) shape memory alloys. The quantities of interest were the global load and local deformation pattern of a loaded diamond-shaped sample, in which case the experimental observations resulted from a digital image correlation analysis. The surrogates (one per quantity of interest) were obtained by training a kernel support vector machine model. They have then conducted a Bayesian inference of the NiTi constitutive model parameters.

In the following, we detail the methodology developed by Wu et al. (2020b) who have trained an artificial Neural Network (NNW) model $\Phi_{\text{NNW}}(\boldsymbol{Q};\,\boldsymbol{\xi})$, using the multi-scale model $\Phi_{\text{multiscale}}(\boldsymbol{Q};\,\boldsymbol{\xi})$ for different material parameters $\boldsymbol{q}^k$ and different loading conditions $\boldsymbol{\xi}^i$ with the aim of conducting a Bayesian inference of the multi-scale model parameters. The multi-scale model was a 2-step homogenisation accounting for the measured fibre ODF, including the skin core effect, of short fibre reinforced polymer materials obtained using an injection moulding process. Uni-axial tension tests were performed on coupons cut along different directions, see Fig. 21(a). The output $\boldsymbol{Y}$ corresponds to the set of macro-scale stress $\sigma_{\text{M}}^{i,j}$ at different strain levels and loading directions $\boldsymbol{\xi}^i$, and for different experimental observations j, see Fig. 21. Using the theory of conditional independence (Bishop, 2006), see the discussion by Wu et al. (2020b), the likelihood (97) thus becomes

$$\pi_{\boldsymbol{Y}|\boldsymbol{Q}}(\boldsymbol{y}|\boldsymbol{q}) = \prod_{i,\,j} n_{0,\,,\sigma^2_{\Sigma^i_{\text{M}}}}\left(\sigma_{\text{M}}^{i,\,j} - \Phi_{\text{NNW}}(\boldsymbol{q};\,\boldsymbol{\xi}^i)\right)\,, \tag{98}$$

which is used in Bayes' theorem (95), with $\sigma^2_{\Sigma^i_{\text{M}}}$ being the variance determined on the stress for loading conditions $\boldsymbol{\xi}^i$. The inferred multi-scale model $\Phi_{\text{multiscale}}(\boldsymbol{Q};\,\boldsymbol{\xi})$ parameters $\boldsymbol{Q}$, here the matrix material behaviour and an equivalent unique fibre aspect ratio, are represented in Fig. 22, in which three realisations $\boldsymbol{q}^k$ of different probabilities are highlighted. The composite material responses obtained for these realisations with the NNW model $\Phi_{\text{NNW}}(\boldsymbol{q}^k;\,\boldsymbol{\xi}^i)$

and with the multi-scale model $\Phi_{\text{multiscale}}(\boldsymbol{q}^k; \boldsymbol{\xi}^i)$ are reported in Fig. 21(b) and Fig. 21(c), respectively. It can be seen that, on the one hand, several combinations of parameters yield similar model responses and that, on the other hand, the NNW and multi-scale models predict similar results (because the loading is proportional and because the NNW was trained for these loading conditions $\boldsymbol{\xi}^i$).

As it can be seen on Fig. 22, Bayesian inference does not provide a unique set of parameters but a joint distribution of the inferred parameters $\boldsymbol{Q}$. Nevertheless, the method cannot represent existing heterogeneities in these parameters because the distributions become narrower when increasing the number of observations, in which case the observation data do not necessarily lie in the predicted values range, as in can be seen in Fig. 21(b) and Fig. 21(c), in which low probability parameters and high probability parameters predict almost similar curves. It is however possible to capture a dispersion in the parameters: properties spatial distributions can be inferred as done byVigliotti et al. (2018), or Bayesian inference can be adapted in order to infer the parameters of an assumed distribution of the material properties instead of the material properties themselves as suggested by Rappel and Beex (2019); Mohamedou et al. (2019).

3.4.3. Defects

Beside the uncertainties in the micro-structure geometrical and material properties, defects can also be present in heterogeneous materials, as a consequence of the manufacturing process. Kamiński and Kleiber (1996); Kamiśki (2012) have studied the effect of defects at the contact interface between fibres and matrix in unidirectional composites, Goldsmith et al. (2015) have introduced porosity voids of non-uniform void size, void shape and void location in the micro-structure of woven ceramic matrix composite. More recently Sokołowski and Kamiíski (2020) have considered spherical elastic inclusions embedded in a hyper-elastic matrix, with as inter-phase a thin layer containing all the particle-matrix interface defects. However a quantitative defect characterisation is still not commonly performed. This quantification could be done either experimentally, or by simulation of the manufacturing process. Bauereiβ et al. (2014) have developed a numerical model to illustrate the formation of defects during powder bed based additive manufacturing; the defects result from the combination of a stochastic powder bed with wetting and capillary forces, which induces significant fluid motion and leads to geometric deviations of the solidified layer.

Tal and Fish (2016) have introduced geometric defects to the micro-scale model of woven composite materials. The defects take the form of discontinuities such as pores, cracks, micro-cracks, voids and micro-voids which are statistically equivalent to the random defects found in real material samples. Equivalent ellipsoids were extracted from 2D cross-sectional micro-graphs as illustrated in Fig. 23(a). Location, radii and orientation of the identified ellipses are statistically studied, including their correlation. Probability density function of the parameters were estimated using a kernel distribution, and a bi-variate normal distribution was used to approximate the joint distribution of the minor and major axes. 3D characteristics of the defects were obtained by assuming that there is a symmetry between the longitudinal and transverse directions. The defects were then introduced in the microstructure by Monte-Carlo simulations so that the statistical content is recovered, see Fig.

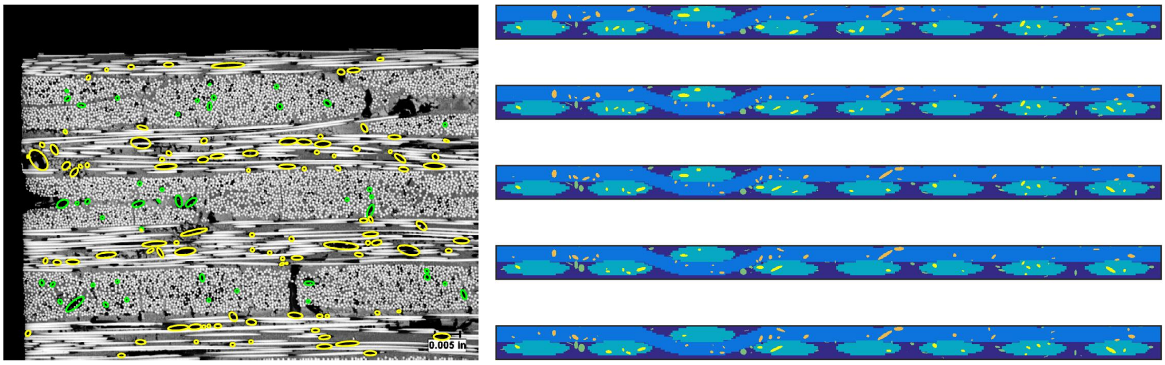

(a) Identification (b) Generation

Figure 23: Generation of defects in woven composite micro-structure by Tal and Fish (2016): (a) Identification of ellipsoidal defect form two-dimensional micro-graphs; and (b) Generated defects in tows and matrix; Reprinted from Composite Structures 153, Tal, D., Fish, J., Generating a statistically equivalent representative volume element with discrete defects, 791 - 803. Copyright (2016), with permission from Elsevier.

23(b).

4. Apparent material properties

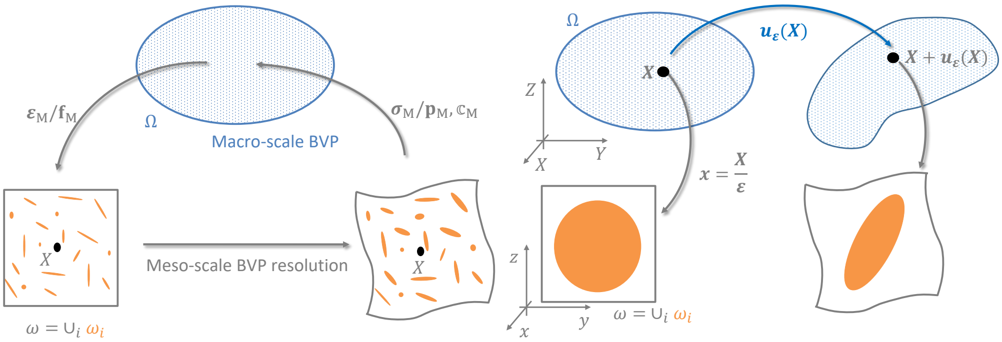

(a) Computational (b) Asymptotic

Figure 24: Homogenisation-based multi-scale method: (a) Schematics of homogenisation principle; and (b) Definition of the asymptotic homogenisation formalism.

We have detailed in the previous chapters how to generate virtual random micro-structure realisations $\omega(w)$, with $w \in \mathcal{W}$. These micro-structure realisations can be exploited to extract the stochastic material response at a higher scale, the so-called meso-scale response. In the context of a homogenisation-based multi-scale method, the homogenised meso-scale material response is estimated from the resolution of a meso-scale boundary value problem

(BVP), see Fig. 24(a). The micro-scale problem is defined on the meso-scale volume element ω of boundary $\partial\omega$, see Fig. 24(a), defined from a virtual micro-structure following Section 3. The meso-scale volume element $\omega(\boldsymbol{X};\, \mathfrak{w})$ is centred on $\boldsymbol{X} \in \Omega$, where Ω is the macro-scale space of interest.

In this section, we first introduce the concepts of Representative and Stochastic Volume Elements, respectively RVEs and SVEs. For the latter, the concept of meso-scale random field of apparent properties is introduced. We then present the most common deterministic homogenisation methods which are developed in the literature, and which can be applied on both RVEs and SVEs. We however restrict our-self to continuum mechanics and homogenisation-based multi-scale approaches. A review detailing multi-scale methods in other contexts such as discrete models was provided by Budarapu et al. (2019). Finally we summarised different intrusive and non-intrusive methods based on the homogenisation theories that can be used to extract the meso-scale random field of apparent properties.

4.1. Statistically representative and stochastic volume elements

When conducting homogenisation, like in Fig. 24(a), the separation of length scales is usually assumed, with

$$l_{\mathrm{M}} >> l_{\mathrm{VE}} >> l_{\mathrm{m}}, \tag{99}$$

in which l_{M} represents a characteristic macro-scale length on which the loading conditions are defined and that is assumed to be much larger than the size l_{VE} of the volume element. This condition is required in order to ensure the accuracy of the homogenisation so that the macro-scale strain can be assumed to be constant over the volume element ω. Beside, the size l_{VE} of the volume element should be large enough as compared to the size of the micro-structure constituents l_{m} in order to be statistically representative of the heterogeneous material behaviour, but also for the response to be independent on the applied admissible boundary condition at the lower scale as it will be discussed in Section 5.3.1.

4.1.1. Statistically Representative Volume Element (RVE)

If this latter condition $l_{\mathrm{VE}} >> l_{\mathrm{m}}$ is fulfilled, the volume element ω is said to be statistically representative and is called Representative Volume Element (RVE).

Assuming the case of statistical representativity of ω, the homogenised material response is deterministic and Huet (1990) has defined, in the context of linear elasticity and under the small displacement assumption, the effective modulus tensor $\mathbb{C}^{\mathrm{eff}}$ and the effective compliance tensor $\mathbb{S}^{\mathrm{eff}}$ through the relationship between the homogenised Cauchy stress tensor $\boldsymbol{\sigma}_{\mathrm{M}}$ and the homogenised small deformation strain tensor $\boldsymbol{\varepsilon}_{\mathrm{M}}$ as

$$\boldsymbol{\sigma}_{\mathrm{M}} = \mathbb{C}^{\mathrm{eff}} : \boldsymbol{\varepsilon}_{\mathrm{M}}\,, \text{ and} \tag{100}$$

$$\boldsymbol{\varepsilon}_{\mathrm{M}} = \mathbb{S}^{\mathrm{eff}} : \boldsymbol{\sigma}_{\mathrm{M}}\,, \tag{101}$$

with the homogenised stress and strain tensors resulting from the volume average operation applied on the volume element

$$\boldsymbol{\sigma}_{\mathrm{M}} = \frac{1}{V(\omega)}\int_{\omega}\boldsymbol{\sigma}_{\mathrm{m}}(\boldsymbol{x})d\boldsymbol{x}\,, \text{ and} \tag{102}$$

$$\boldsymbol{\varepsilon}_{\mathrm{M}} = \frac{1}{V(\omega)}\int_{\omega}\boldsymbol{\varepsilon}_{\mathrm{m}}(\boldsymbol{x})d\boldsymbol{x}\,, \tag{103}$$

where $\boldsymbol{\sigma}_{\mathrm{m}}$ and $\boldsymbol{\varepsilon}_{\mathrm{m}}$ are respectively the local or micro-scale Cauchy stress and strain fields. Since the homogenised material response is deterministic, one has $\mathbb{C}^{\mathrm{eff}} = \mathbb{S}^{\mathrm{eff}^{-1}}$.

At the local or micro-scale level, one has in linear elasticity $\boldsymbol{\sigma}_{\mathrm{m}}(\boldsymbol{x}) = \mathbb{C}^{\mathrm{el}}_{\mathrm{m}}(\boldsymbol{x}) : \boldsymbol{\varepsilon}_{\mathrm{m}}(\boldsymbol{x})$ and $\boldsymbol{\varepsilon}_{\mathrm{m}}(\boldsymbol{x}) = \mathbb{S}^{\mathrm{el}}_{\mathrm{m}}(\boldsymbol{x}) : \boldsymbol{\sigma}_{\mathrm{m}}(\boldsymbol{x})\ \forall \boldsymbol{x} \in \omega$, and the relations (100-101) are rewritten

$$\boldsymbol{\sigma}_{\mathrm{M}} = \frac{1}{V(\omega)}\int_{\omega}\mathbb{C}^{\mathrm{el}}_{\mathrm{m}}(\boldsymbol{x}) : \boldsymbol{\varepsilon}_{\mathrm{m}}(\boldsymbol{x})d\boldsymbol{x} = \mathbb{C}^{\mathrm{eff}} : \boldsymbol{\varepsilon}_{\mathrm{M}}\,, \text{ and} \tag{104}$$

$$\boldsymbol{\varepsilon}_{\mathrm{M}} = \frac{1}{V(\omega)}\int_{\omega}\mathbb{S}^{\mathrm{el}}_{\mathrm{m}}(\boldsymbol{x}) : \boldsymbol{\sigma}_{\mathrm{m}}(\boldsymbol{x})d\boldsymbol{x} = \mathbb{S}^{\mathrm{eff}} : \boldsymbol{\sigma}_{\mathrm{M}}\,, \tag{105}$$

with $\mathbb{S}^{\mathrm{el}}_{\mathrm{m}} = \mathbb{C}^{\mathrm{el}^{-1}}_{\mathrm{m}}$. Let us define the fluctuation fields $\boldsymbol{\sigma}'(\boldsymbol{x})$ and $\boldsymbol{\varepsilon}'(\boldsymbol{x})$ of zero volume average on ω such that

$$\boldsymbol{\sigma}_{\mathrm{m}}(\boldsymbol{x}) = \boldsymbol{\sigma}_{\mathrm{M}} + \boldsymbol{\sigma}'(\boldsymbol{x})\,, \text{ and } \boldsymbol{\varepsilon}_{\mathrm{m}}(\boldsymbol{x}) = \boldsymbol{\varepsilon}_{\mathrm{M}} + \boldsymbol{\varepsilon}'(\boldsymbol{x})\,. \tag{106}$$

As a result, Eqs. (104) and (105) are rewritten as

$$\mathbb{C}^{\mathrm{eff}} : \boldsymbol{\varepsilon}_{\mathrm{M}} = \frac{1}{V(\omega)}\int_{\omega}\mathbb{C}^{\mathrm{el}}_{\mathrm{m}}(\boldsymbol{x})d\boldsymbol{x} : \boldsymbol{\varepsilon}_{\mathrm{M}} + \frac{1}{V(\omega)}\int_{\omega}\mathbb{C}^{\mathrm{el}}_{\mathrm{m}}(\boldsymbol{x}) : \boldsymbol{\varepsilon}'(\boldsymbol{x})d\boldsymbol{x}\,, \text{ and} \tag{107}$$

$$\mathbb{S}^{\mathrm{eff}} : \boldsymbol{\sigma}_{\mathrm{M}} = \frac{1}{V(\omega)}\int_{\omega}\mathbb{S}^{\mathrm{el}}_{\mathrm{m}}(\boldsymbol{x})d\boldsymbol{x} : \boldsymbol{\sigma}_{\mathrm{M}} + \frac{1}{V(\omega)}\int_{\omega}\mathbb{S}^{\mathrm{el}}_{\mathrm{m}}(\boldsymbol{x}) : \boldsymbol{\sigma}'(\boldsymbol{x})d\boldsymbol{x}\,, \tag{108}$$

or again, by defining the perturbation fourth order tensor fields $\mathbb{C}'(\boldsymbol{x})$ and $\mathbb{S}'(\boldsymbol{x})$ of zero volume average on ω such that $\mathbb{C}^{\mathrm{el}}_{\mathrm{m}}(\boldsymbol{x}) = \frac{1}{V(\omega)}\int_{\omega}\mathbb{C}^{\mathrm{el}}_{\mathrm{m}}(\boldsymbol{x})d\boldsymbol{x} + \mathbb{C}'(\boldsymbol{x})$ and $\mathbb{S}^{\mathrm{el}}_{\mathrm{m}}(\boldsymbol{x}) = \frac{1}{V(\omega)}\int_{\omega}\mathbb{S}^{\mathrm{el}}_{\mathrm{m}}(\boldsymbol{x})d\boldsymbol{x} + \mathbb{S}'(\boldsymbol{x})$, as

$$\mathbb{C}^{\mathrm{eff}} : \boldsymbol{\varepsilon}_{\mathrm{M}} = \frac{1}{V(\omega)}\int_{\omega}\mathbb{C}^{\mathrm{el}}_{\mathrm{m}}(\boldsymbol{x})d\boldsymbol{x} : \boldsymbol{\varepsilon}_{\mathrm{M}} + \frac{1}{V(\omega)}\int_{\omega}\mathbb{C}'(\boldsymbol{x}) : \boldsymbol{\varepsilon}'(\boldsymbol{x})d\boldsymbol{x}\,, \text{ and} \tag{109}$$

$$\mathbb{S}^{\mathrm{eff}} : \boldsymbol{\sigma}_{\mathrm{M}} = \frac{1}{V(\omega)}\int_{\omega}\mathbb{S}^{\mathrm{el}}_{\mathrm{m}}(\boldsymbol{x})d\boldsymbol{x} : \boldsymbol{\sigma}_{\mathrm{M}} + \frac{1}{V(\omega)}\int_{\omega}\mathbb{S}'(\boldsymbol{x}) : \boldsymbol{\sigma}'(\boldsymbol{x})d\boldsymbol{x}\,. \tag{110}$$

These equations show that the Hill (1952)-Voigt (1889) tensor $\mathbb{C}^{\mathrm{Voigt}} = \frac{1}{V(\omega)}\int_{\omega}\mathbb{C}^{\mathrm{el}}_{\mathrm{m}}(\boldsymbol{x})d\boldsymbol{x}$ is in general not the effective elasticity tensor $\mathbb{C}^{\mathrm{eff}}$ unless the perturbation strain field vanishes on ω. The tensor $\mathbb{C}^{\mathrm{Voigt}}$ is actually an upper bound of $\mathbb{C}^{\mathrm{eff}}$ whatever the micro-structure of the deterministic RVE ω may be. Similarly, the Hill (1965b)-Reuss (1929) compliance tensor $\mathbb{S}^{\mathrm{Reuss}} = \frac{1}{V(\omega)}\int_{\omega}\mathbb{S}^{\mathrm{el}}_{\mathrm{m}}(\boldsymbol{x})d\boldsymbol{x}$ is in general not the effective compliance tensor $\mathbb{S}^{\mathrm{eff}}$ unless the perturbation stress field vanishes on ω. The tensor $\mathbb{S}^{\mathrm{Reuss}^{-1}}$ is actually a lower bound of $\mathbb{C}^{\mathrm{eff}}$ whatever the micro-structure of the deterministic RVE ω.

A similar study can be conducted by considering the internal energy $\psi(\boldsymbol{\varepsilon}) = \frac{1}{2}\boldsymbol{\varepsilon} : \mathbb{c}^{\mathrm{el}} : \boldsymbol{\varepsilon} = \frac{1}{2}\boldsymbol{\sigma} : \mathbb{s}^{\mathrm{el}} : \boldsymbol{\sigma}$. The deformation energy on the volume element ω thus reads

$$\begin{aligned}\frac{1}{V(\omega)}\int_{\omega}\psi_{\mathrm{m}}(\boldsymbol{\varepsilon})d\boldsymbol{x} &= \frac{1}{2V(\omega)}\int_{\omega}\boldsymbol{\sigma}_{\mathrm{m}} : \boldsymbol{\varepsilon}_{\mathrm{m}}d\boldsymbol{x} = \frac{1}{2}\boldsymbol{\sigma}_{\mathrm{M}} : \boldsymbol{\varepsilon}_{\mathrm{M}} + \frac{1}{2V(\omega)}\int_{\omega}\boldsymbol{\sigma}' : \boldsymbol{\varepsilon}'d\boldsymbol{x}\\ &= \frac{1}{2}\boldsymbol{\varepsilon}_{\mathrm{M}} : \mathbb{c}^{\mathrm{eff}} : \boldsymbol{\varepsilon}_{\mathrm{M}} + \frac{1}{2V(\omega)}\int_{\omega}\boldsymbol{\sigma}' : \boldsymbol{\varepsilon}'d\boldsymbol{x}\\ &= \frac{1}{2}\boldsymbol{\sigma}_{\mathrm{M}} : \mathbb{s}^{\mathrm{eff}} : \boldsymbol{\sigma}_{\mathrm{M}} + \frac{1}{2V(\omega)}\int_{\omega}\boldsymbol{\sigma}' : \boldsymbol{\varepsilon}'d\boldsymbol{x}\,. \end{aligned} \tag{111}$$

The Hill-Mandel condition states that the strain energy should be the same at both scales, *i.e.* $\frac{1}{V(\omega)}\int_{\omega}\psi_{\mathrm{m}}(\boldsymbol{\varepsilon})d\boldsymbol{x} = \frac{1}{2}\boldsymbol{\varepsilon}_{\mathrm{M}} : \mathbb{c}^{\mathrm{eff}} : \boldsymbol{\varepsilon}_{\mathrm{M}} = \frac{1}{2}\boldsymbol{\sigma}_{\mathrm{M}} : \mathbb{s}^{\mathrm{eff}} : \boldsymbol{\sigma}_{\mathrm{M}}$, showing that energy consistency implies

$$\int_{\omega}\boldsymbol{\sigma}' : \boldsymbol{\varepsilon}'d\boldsymbol{x} = 0\,. \tag{112}$$

4.1.2. Stochastic Volume Element (SVE)

When $l_{\mathrm{VE}} \gtrsim l_{\mathrm{m}}$, the volume element $\omega(\boldsymbol{X};\, \mathscr{w})$ depends on the micro-structure realisation $\mathscr{w} \in \mathscr{W}$, and each realisation $\omega(\boldsymbol{X};\, \mathscr{w})$ yields a different homogenised behaviour. We refer to Section 3.1.1 for the notation $\omega(\mathscr{w})$. Following Alzebdeh and Ostoja-Starzewski (1996); Ostoja-Starzewski and Wang (1999), $\omega(\boldsymbol{X};\, \mathscr{w})$ is called a Stochastic Volume Element (SVE), see also the review by Ostoja-Starzewski et al. (2016).

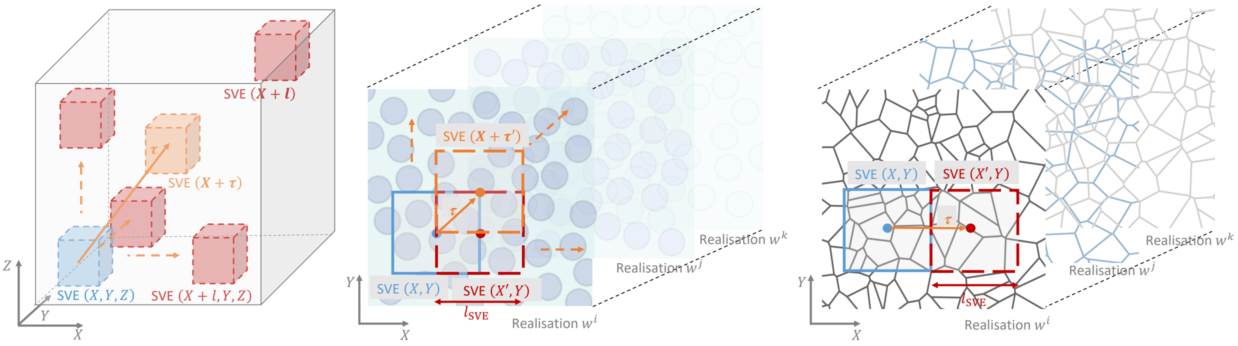

(a) 3D (b) UD (c) Poly-crystal

Figure 25: Schematics of the window technique: (a) Extraction of a series of SVEs $\{\omega(\boldsymbol{X};\, \mathscr{w}) : \boldsymbol{X} \in \Omega,\, \mathscr{w} \in \mathscr{W}\}$ from a random micro-structure $\mathscr{W}$; (b) Illustration in 2D in the case of UD composites, the vector $\boldsymbol{\tau}$ represents the separation between the centres of the SVEs $\omega(\boldsymbol{X};\, \mathscr{w}^i)$ and $\omega(\boldsymbol{X}+\boldsymbol{\tau};\, \mathscr{w}^i)$, with several realisations $\mathscr{w}^i \in \mathscr{W}$ considered; and (c) In the case of poly-crystalline materials, two neighbouring SVEs $\omega(\boldsymbol{X};\, \mathscr{w}^i)$ and $\omega(\boldsymbol{X}';\, \mathscr{w}^i)$ of the same micro-structure realisation $\mathscr{w}^i \in \mathscr{W}$ share common grains all along the shared edge.

Moreover, beside the uncertainty in the homogenised behaviour, the dependency between the homogenised response of two neighbouring macro-scale points $\boldsymbol{X}$ and $\boldsymbol{X}'$, each of them belonging to the macro-scale domain Ω and being the centre of two possibly overlapping

SVEs, respectively $\omega(\boldsymbol{X};\ \mathscr{w})$ and $\omega(\boldsymbol{X}';\ \mathscr{w})$ see Fig. 25(a), needs to be investigated. To this end, we consider several micro-structure realisations $\mathscr{w} \in \mathscr{W}$, see a 2D illustration in Fig. 25(b), allowing to extract the series of SVEs $\{\omega(\boldsymbol{X};\ \mathscr{w}) : \mathscr{w} \in \mathscr{W}\}$ centred on $\boldsymbol{X}$ as well as the series $\{\omega(\boldsymbol{X}+\boldsymbol{\tau};\mathscr{w}) : \mathscr{w} \in \mathscr{W}\}$ centred on $\boldsymbol{X}' = \boldsymbol{X}+\boldsymbol{\tau}$, with the distance vector $\boldsymbol{\tau}$ spanning the different directions.

Still assuming linear elasticity, each SVE realisation $\omega(\boldsymbol{X};\mathscr{w})$ defines apparent elastic properties which are represented under the form of an elastic tensor realisation $\mathbb{C}^{\text{el}}_{\text{M}}(\boldsymbol{X};\mathscr{w})$, also denoted under the matrix form $\mathbf{C}^{\text{el}}_{\text{M}}(\boldsymbol{X};\mathscr{w}) \in \mathbb{M}^{+}_{6}(\Re)$, where $\mathbb{M}^{+}_{n}(\Re)$ refers to all symmetric positive-definite real matrices of size $n \times n$, when using the Voigt notations, or under the vector form of 21-components (in 3D) $\boldsymbol{C}^{\text{el}}_{\text{M}}(\boldsymbol{X};\mathscr{w})$.

Clearly, the set $\{\boldsymbol{C}^{\text{el}}_{\text{M}}(\boldsymbol{X};\mathscr{w}) : \boldsymbol{X} \in \Omega,\ \mathscr{w} \in \mathscr{W}\}$ of random vectors $\boldsymbol{C}^{\text{el}}_{\text{M}}(\boldsymbol{X})$ which map $\mathscr{W} \to \Re^{21}$, defines a random field also denoted by $\{\boldsymbol{C}^{\text{el}}_{\text{M}}(\boldsymbol{X}) : \boldsymbol{X} \in \Omega\}$ or simply $\boldsymbol{C}^{\text{el}}_{\text{M}}(\Omega)$. Assuming strictly positive variances, the spatial correlation can be represented by the correlation matrix $\mathbf{R}_{\boldsymbol{C}^{\text{el}}_{\text{M}}} : \Omega \times \Re^{3} \to \Re^{21\times 21}$, see Section 2.4,

$$R_{\boldsymbol{C}^{\text{el}}_{\text{M}_{r\,s}}}(\boldsymbol{X};\boldsymbol{\tau}) = \frac{\mathbb{E}\left[\left(C^{\text{el}}_{\text{M}_r}(\boldsymbol{X}) - \mathbb{E}\left[C^{\text{el}}_{\text{M}_r}(\boldsymbol{X})\right]\right)\left(C^{\text{el}}_{\text{M}_s}(\boldsymbol{X}+\boldsymbol{\tau}) - \mathbb{E}\left[C^{\text{el}}_{\text{M}_s}(\boldsymbol{X}+\boldsymbol{\tau})\right]\right)\right]}{\sigma_{C^{\text{el}}_{\text{M}_r}}(\boldsymbol{X})\sigma_{C^{\text{el}}_{\text{M}_s}}(\boldsymbol{X}+\boldsymbol{\tau})} \quad \forall\, r,\, s = 1,\, ...,\, 21\,, \tag{113}$$

where $\boldsymbol{\tau}$ is a spatial vector between the centres of two SVEs, see Fig. 25(a). In case of a homogeneous random field $\boldsymbol{C}^{\text{el}}_{\text{M}}(\Omega)$, one has $\mathbf{R}_{\boldsymbol{C}^{\text{el}}_{\text{M}}}(\boldsymbol{X};\boldsymbol{\tau}) = \mathbf{R}_{\boldsymbol{C}^{\text{el}}_{\text{M}}}(\boldsymbol{\tau}) : \Re^{3} \to \Re^{21\times 21}$. Practically, Eq. (113) can be evaluated by assuming ergodicity and homogeneity, in which case the number of micro-structure realisations $\mathscr{w}$ can be limited by considering different initial SVE centres $\boldsymbol{X}$ on the same micro-structure realisation.

Anticipating on Section 5.1, Fig. 26(a) illustrates the component 1 3 of a random field realisation path $\{\mathbb{C}^{\text{el}}_{\text{M}}(\boldsymbol{X};\mathscr{w}) : \boldsymbol{X} \in \Omega\}$ extracted from a poly-silicon micro-structure by Wu et al. (2016) using the window technique sketched on Fig. 25(c). Instead of analysing directly the random field $\{\mathbb{C}^{\text{el}}_{\text{M}}(\boldsymbol{X};\mathscr{w}) : \boldsymbol{X} \in \Omega,\ \mathscr{w} \in \mathscr{W}\}$ of the apparent elasticity tensor, one can take advantage of its semi-definite nature to define through a Cholesky decomposition another random field $\{\boldsymbol{Q}_{\text{M}}(\boldsymbol{X};\mathscr{w}) : \boldsymbol{X} \in \Omega,\ \mathscr{w} \in \mathscr{W}\}$ easier to handle, see details in Section 5.3. Figs. 26(b) and 26(c) illustrate an auto-correlation and a cross-correlation entries of the correlation matrix $\mathbf{R}_{\boldsymbol{Q}_{\text{M}}}(\boldsymbol{\tau})$ extracted from the random fields using Eq. (113). It can be seen that, because of the comparable size of the SVE to the micro-structure size, the auto/cross-correlation only vanishes at distances larger than twice the SVE length, showing that the apparent properties should be considered as a random field $\mathbb{C}_{\text{M}}(\Omega)$ and not as a random tensors.

Wu et al. (2018a) have noted that in the case of UD composites, see Fig. 25(b), the correlation can be neglected for two adjacent SVEs because the amount of shared fibres remains marginal. In that case, if the distributions are close enough from Gaussianity, the homogenised properties of two SVEs are independent and the apparent properties can be considered as random tensors $\{\mathbb{C}^{\text{el}}_{\text{M}}(\mathscr{w}) : \mathscr{w} \in \mathscr{W}\}$ also denoted $\mathbb{C}^{\text{el}}_{\text{M}}$.

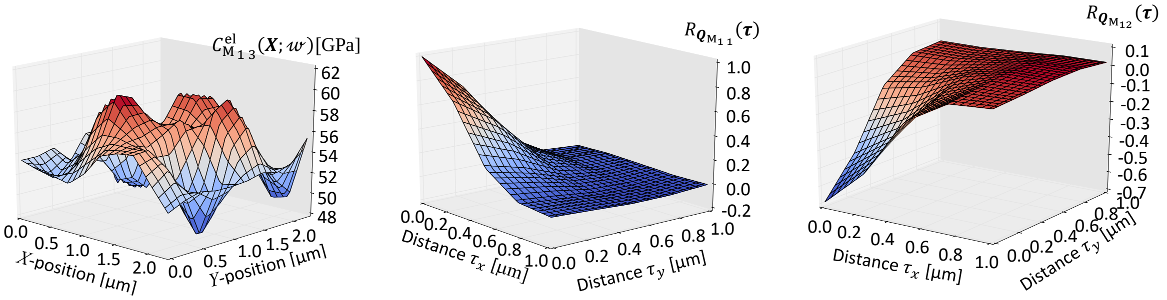

(a) $C^{\mathrm{el}}_{\mathrm{M}_{1\,3}}(\boldsymbol{X}; \omega)$ (b) $R_{\boldsymbol{Q}_{\mathrm{M}_{1\,1}}}(\boldsymbol{\tau})$ (c) $R_{\boldsymbol{Q}_{\mathrm{M}_{1\,2}}}(\boldsymbol{\tau})$

Figure 26: Extraction by Wu et al. (2016) from a columnar poly-silicon micro-structure of average grain size of about $l_{\mathrm{micro}} \simeq 200$ nm and using an SVE size $l_{\mathrm{SVE}} = 0.5\mu$m of (a) The component (1, 3) of a random field realisation path $\{\mathbb{C}^{\mathrm{el}}_{\mathrm{M}}(\boldsymbol{X}; \omega) : \boldsymbol{X} \in \Omega\}$ of the apparent properties; (b) The auto-correlation $R_{\boldsymbol{Q}_{\mathrm{M}_{1\,1}}}(\boldsymbol{\tau})$; and (c) The cross correlation of a random field $\{\boldsymbol{Q}_{\mathrm{M}}(\boldsymbol{X}; \omega) : \boldsymbol{X} \in \Omega,\ \omega \in \mathcal{W}\}$ defined from the Cholesky decomposition of the random field $\{\mathbb{C}^{\mathrm{el}}_{\mathrm{M}}(\boldsymbol{X}; \omega) : \boldsymbol{X} \in \Omega,\ \omega \in \mathcal{W}\}$, see Section 5.3.2 for details; Modified from Computer Methods in Applied Mechanics and Engineering 310, Wu, L., Lucas, V., Nguyen, V.D., Golinval, J.C., Paquay, S., Noels, L., A stochastic multi-scale approach for the modeling of thermo-elastic damping in micro-resonators, 802-839. Copyright (2016)..

4.2. Evaluation of homogenised behaviours

After having defined the effective and apparent properties, in the following we summarise different approaches developed in order to solve the scale transition equations in the more general context of non-linear mechanics. We refer to the reviews by Kanouté et al. (2009); Geers et al. (2010); Noels et al. (2016); Matous et al. (2017); Yvonnet (2019) for more details on multi-scale methods.

4.2.1. Computational homogenisation

One of the most common method used to solve the meso-scale BVP, see Fig. 24(a) is the finite-element method. This method has been widely used in the context of random media in the case of elasticity by Ostoja-Starzewski et al. (2007); Salmi et al. (2012), linear micro-polar continua by Trovalusci et al. (2014, 2015); Reccia et al. (2018), elasto-plasticity by Ostoja-Starzewski et al. (2007), thermo-elasticity by Kanit et al. (2003); Ostoja-Starzewski et al. (2007) or again finite elasticity by Ostoja-Starzewski et al. (2007). In these latter references, the homogenisation was mainly used to define the minimum SVE size allowing statistically representative (and thus unique) homogenised properties to be extracted. We refer to the review by Ostoja-Starzewski et al. (2016) for the details of the homogenisation process for these different cited continua. However stochastic homogenisation was also applied to capture the variation in the homogenised response with a view of up-scaling the resulting uncertainties, in the context of elasticity by Mariani et al. (2011a); Geißendörfer et al. (2014); Lucas et al. (2015); Stefanou et al. (2015); Savvas et al. (2016); Stefanou et al. (2017); Wu et al. (2018a), of thermo-elasticity by Wu et al. (2016), strain-gradient elasticity by Lucas et al. (2017), and non-local damage mechanics by Wu et al. (2019).

In this section, we restrict our-selves to the case of finite-strain mechanics and we define the different kinds of boundary conditions that can be applied on the meso-scale volume element with a particular emphasis on the extraction of the homogenised material response following the multiple-constraint projection method set up by Ainsworth (2001) and detailed by Nguyen et al. (2017).

Definition of the meso-scale BVP. At the micro-scale, we consider the material points $\boldsymbol{x} \in \omega(\boldsymbol{X};\, \varpi)$ with $\varpi \in \mathcal{W}$ and we assume that the classical continuum mechanics equations hold. Besides, we assume that the time for a stress wave to propagate in the meso-scale volume element remains negligible. Therefore, in the absence of dynamical effects the equilibrium equations read

$$\mathbf{P}_{\mathrm{m}}\left(\boldsymbol{x};\, \varpi\right) \cdot \boldsymbol{\nabla}_0 = 0 \qquad \forall \boldsymbol{x} \in \omega(\boldsymbol{X};\, \varpi)\,, \tag{114}$$

$$\mathbf{P}_{\mathrm{m}}\left(\boldsymbol{x};\, \varpi\right) \cdot \boldsymbol{n}_{\mathrm{m}} = \boldsymbol{T}_{\mathrm{m}}\left(\boldsymbol{x};\, \varpi\right) \qquad \forall \boldsymbol{x} \in \partial\omega(\boldsymbol{X};\, \varpi)\,, \tag{115}$$

where the subscript "m" refers to the local value at the micro-scale, $\mathbf{P}_{\mathrm{m}}\left(\boldsymbol{x};\, \varpi\right)$ is the first Piola-Kirchhoff stress tensor, the gradient operator $\boldsymbol{\nabla}_0$ is with respect to the micro-scale reference configuration, and $\boldsymbol{T}_{\mathrm{m}}\left(\boldsymbol{x};\, \varpi\right)$ is the surface traction, per unit reference surface, on the boundary $\partial\omega$ of outward unit normal $\boldsymbol{n}_{\mathrm{m}}$ in the reference configuration.

To complete the micro-scale problem, the local constitutive laws of the different materials at a given time t and material point $\boldsymbol{x}$ are written as

$$\mathbf{P}_{\mathrm{m}}\left(\boldsymbol{x},\, t;\, \varpi\right) = \mathbf{P}_{\mathrm{m}}\left(\mathbf{F}_{\mathrm{m}}\left(\boldsymbol{x},\, t;\, \varpi\right);\boldsymbol{Z}_{\mathrm{m}}\left(\boldsymbol{x},\, \tau;\, \varpi\right),\, \tau \in [0,\, t],\, \varpi\right)\,, \tag{116}$$

where the micro-scale deformation gradient tensor $\mathbf{F}_{\mathrm{m}}(\boldsymbol{x};\, \varpi) = \boldsymbol{U}_{\mathrm{m}}(\boldsymbol{x};\, \varpi) \otimes \boldsymbol{\nabla}_0 + \mathbf{I}$ is evaluated in terms of the micro-scale displacement random field $\boldsymbol{U}_{\mathrm{m}}(\omega)$, and where $\boldsymbol{Z}_{\mathrm{m}}(\omega)$ is a set of internal variables random field allowing history-dependent processes to be accounted for. In all generality, the constitutive equation depends on the micro-structure realisation $\varpi \in \mathcal{W}$ because of the geometrical and material uncertainties.

The volume-elements, SVEs or RVEs, are usually defined as parallelepiped (rectangular in 2D) volumes, with planar boundary faces $\partial\omega^{(i)}$, see Fig. 27. When considering SVEs, the volume element should be as close as possible to a real micro-structure: *e.g.*, Trovalusci et al. (2015) have shown that in the case of particle reinforced matrix, the inclusions should intersect the edges as illustrated in Fig. 27(a) in order to avoid considering artificial bands of matrix, as it would be the case in Fig. 27(b). We note that extracting SVEs using the window technique of Section 4.1.2 from virtual micro-structures naturally leads to the former configuration. Sometimes, a periodic micro-structure is assumed and cell elements as in Fig. 27(c) are considered. In that case different stacking organisations can be considered such as the regular grid with a square volume element or the hexagonal grid with an hexagonal volume element. Circular volume elements were also used by Firooz et al. (2019) to extract isotropic properties of higher volume fraction composites. Based on the cell element containing only one inclusion as illustrated in Fig. 27(c), Pivovarov et al. (2018a) have defined the concept of statistically similar RVE by providing a surrogate model, which possesses some statistical properties of the original model, such as the relation between the inclusion's

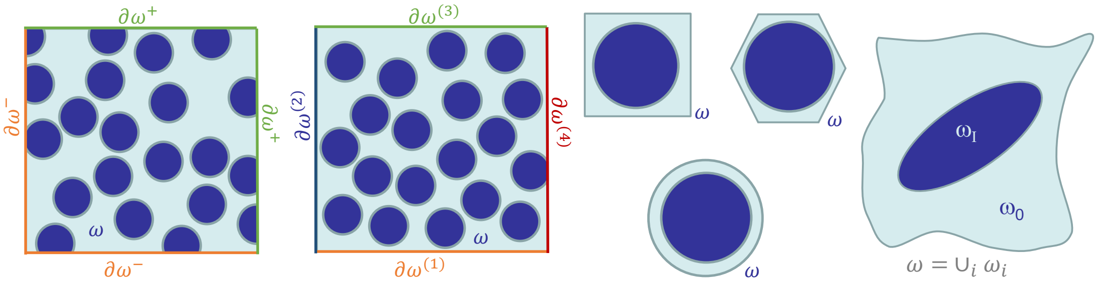

(a) From window technique (b) Without inclusions on edges (c) Cell elements (d) MFH volume element

Figure 27: Definition of the meso-scale volume element ω for computational homogenisation: (a) SVE $\omega(\boldsymbol{X};\, \mathscr{w})$ extracted using the window technique of Section 4.1.2 on particle reinforced matrix, for which the boundary $\partial\omega$ intersects some particles; (b) An SVE with a simplified generation of the particles; (c) Possible shapes of cell elements of a periodic micro-structure; The divisions of the boundary of the parallelepiped volume element into the faces $\partial\omega^{(i)}$ and into positive and negative contours $\partial\omega^-$ and $\partial\omega^+$ are also illustrated; and (d) Definition of the virtual Mean-Field Homogenisation (MFH) volume element ω as an ellipsoidal inclusion embedded in a matrix.

radius and the area around the inclusion. By doing so, assuming ergodicity, they defined an equivalence between a deterministic model, the RVE, with randomly distributed inclusions and a stochastic model, a cell element with statistical properties.

The macro-scale response. At the macro-scale, assuming no dynamical effects, the linear momentum equation reads

$$\mathbf{P}_{\mathrm{M}}(\boldsymbol{X};\, \mathscr{w}) \cdot \boldsymbol{\nabla}_0 + \boldsymbol{b}_{\mathrm{M}} = 0 \quad \forall \boldsymbol{X} \in \Omega,\, \mathscr{w} \in \mathscr{W}\,, \tag{117}$$

where the subscript "M" refers to the values at the macro-scale and $\boldsymbol{b}_{\mathrm{M}}$ is the load per unit reference volume. The boundary conditions read

$$\boldsymbol{U}_{\mathrm{M}}(\boldsymbol{X};\, \mathscr{w}) = \boldsymbol{u}_{\mathrm{D_M}} \qquad \forall \boldsymbol{X} \in \partial_D\Omega\,, \text{ and} \tag{118}$$

$$\mathbf{P}_{\mathrm{M}}(\boldsymbol{X};\, \mathscr{w}) \cdot \boldsymbol{n}_{\mathrm{M}} = \boldsymbol{t}_{\mathrm{M}} \qquad \forall \boldsymbol{X} \in \partial_N\Omega\,, \tag{119}$$

where $\boldsymbol{t}_{\mathrm{M}}$ is the surface traction, per unit reference surface, on the Neumann boundary $\partial_N\Omega$ of outward unit normal $\boldsymbol{n}_{\mathrm{M}}$ in the reference configuration, and $\boldsymbol{u}_{\mathrm{D_M}}$ is the constrained displacement on the Dirichlet boundary $\partial_D\Omega$.

As for the micro-scale problem, the BVP should be completed by a constitutive law

$$\mathbf{P}_{\mathrm{M}}\left(\boldsymbol{X},\, t;\, \mathscr{w}\right) = \mathbf{P}_{\mathrm{M}}\left(\mathbf{F}_{\mathrm{M}}\left(\boldsymbol{X},\, t;\, \mathscr{w}\right); \boldsymbol{Z}_{\mathrm{M}}\left(\boldsymbol{X},\, \tau;\, \mathscr{w}\right),\, \tau \in [0,\, t],\, \mathscr{w}\right)\,, \tag{120}$$

defining the relation in terms of the macro-scale deformation gradient $\mathbf{F}_{\mathrm{M}}\left(\boldsymbol{X},\, t;\, \mathscr{w}\right) = \mathbf{I} + \boldsymbol{U}_{\mathrm{M}}\left(\boldsymbol{X},\, t;\, \mathscr{w}\right) \otimes \boldsymbol{\nabla}_0$, through internal variables $\boldsymbol{Z}_{\mathrm{M}}\left(\boldsymbol{X},\, \tau;\, \mathscr{w}\right)$. However, in the context of homogenisation theories, see Fig. 24(a), this relation is rewritten as a relation between the averages of the respective micro-scale deformation gradient tensor $\mathbf{F}_{\mathrm{m}}(\boldsymbol{x};\, \mathscr{w})$ and stress tensor $\mathbf{P}_{\mathrm{m}}(\boldsymbol{x};\,\varpi)$ over the meso-scale volume element $\omega(\varpi)$, with

$$\begin{aligned}
\mathbf{F}_{\mathrm{M}}\left(\boldsymbol{X};\,\varpi\right) &= \frac{1}{V(\omega)}\int_{\omega(\boldsymbol{X};\,\varpi)}\mathbf{F}_{\mathrm{m}}(\boldsymbol{x};\,\varpi)d\boldsymbol{x}\,,\ \text{and} && (121)\\
\mathbf{P}_{\mathrm{M}}\left(\boldsymbol{X};\,\varpi\right) &= \frac{1}{V(\omega)}\int_{\omega(\boldsymbol{X};\,\varpi)}\mathbf{P}_{\mathrm{m}}(\boldsymbol{x};\,\varpi)d\boldsymbol{x}\,. && (122)
\end{aligned}$$

Since the micro-scale BVP (114-116) depends on the micro-structure realisation $\varpi \in \mathscr{W}$; the homogenised stress tensor (122) has also this dependency, and so does the corresponding homogenised material response (120).

Beside the evaluation of the homogenised stress tensor $\mathbf{P}_{\mathrm{M}}$ for a given deformation gradient $\mathbf{F}_{\mathrm{M}}$, homogenisations also ought to evaluate the algorithmic material tensor

$$\mathbb{C}_{\mathrm{M}}\left(\boldsymbol{X};\,\varpi\right) = \frac{\partial \mathbf{P}_{\mathrm{M}}}{\partial \mathbf{F}_{\mathrm{M}}}\left(\boldsymbol{X};\,\varpi\right)\,. \tag{123}$$

The scale transition. Using the definitions (121-122), the energy consistency between the different scales, which corresponds to the Hill-Mandel condition, is stated as

$$\mathbf{P}_{\mathrm{M}}\left(\boldsymbol{X};\,\varpi\right) : \delta\mathbf{F}_{\mathrm{M}}\left(\boldsymbol{X};\,\varpi\right) = \frac{1}{V(\omega)}\int_{\omega(\boldsymbol{X};\,\varpi)}\mathbf{P}_{\mathrm{m}}\left(\boldsymbol{x};\,\varpi\right) : \delta\mathbf{F}_{\mathrm{m}}\left(\boldsymbol{x};\,\varpi\right)d\boldsymbol{x}\,. \tag{124}$$

A perturbation field $\boldsymbol{U}'(\boldsymbol{x};\,\varpi)$ is introduced in the micro-scale displacement field $\boldsymbol{U}_{\mathrm{m}}(\boldsymbol{x};\,\varpi)$, which is thus rewritten under the form

$$\boldsymbol{U}_{\mathrm{m}}(\boldsymbol{x};\,\varpi) = \left[\mathbf{F}_{\mathrm{M}}\left(\boldsymbol{X};\,\varpi\right) - \mathbf{I}\right]\cdot\left[\boldsymbol{x} - \boldsymbol{X}\right] + \boldsymbol{U}'(\boldsymbol{x};\,\varpi)\,, \tag{125}$$

where $\boldsymbol{X}$ is a reference point of $\omega\left(\boldsymbol{X};\,\varpi\right)$. Considering the definition (121), the perturbation field should satisfy the condition

$$0 = \frac{1}{V(\omega)}\int_{\omega(\boldsymbol{X};\,\varpi)}\boldsymbol{U}'(\boldsymbol{x};\,\varpi)\otimes\boldsymbol{\nabla}_0 d\boldsymbol{x} = \frac{1}{V(\omega)}\int_{\partial\omega(\boldsymbol{X};\,\varpi)}\boldsymbol{U}'(\boldsymbol{x};\,\varpi)\otimes\boldsymbol{n}_{\mathrm{m}}d\boldsymbol{x}\,, \tag{126}$$

where $\boldsymbol{n}_{\mathrm{m}}$ is the outward unit normal to $\partial\omega$ in the reference configuration. The Hill-Mandel condition (124) can be rewritten using Eq. (125) as

$$\begin{aligned}
\mathbf{P}_{\mathrm{M}}\left(\boldsymbol{X};\,\varpi\right) : \delta\mathbf{F}_{\mathrm{M}}\left(\boldsymbol{X};\,\varpi\right) &= \frac{1}{V(\omega)}\int_{\omega(\boldsymbol{X};\,\varpi)}\mathbf{P}_{\mathrm{m}}\left(\boldsymbol{x};\,\varpi\right) : \delta\mathbf{F}_{\mathrm{m}}\left(\boldsymbol{x};\,\varpi\right)d\boldsymbol{x}\\
&= \mathbf{P}_{\mathrm{M}}\left(\boldsymbol{X};\,\varpi\right) : \delta\mathbf{F}_{\mathrm{M}}\left(\boldsymbol{X};\,\varpi\right) +\\
&\quad\ \frac{1}{V(\omega)}\int_{\omega(\boldsymbol{X};\,\varpi)}\mathbf{P}_{\mathrm{m}}\left(\boldsymbol{x};\,\varpi\right) : \left[\delta\boldsymbol{U}'\left(\boldsymbol{x};\,\varpi\right)\otimes\boldsymbol{\nabla}_0\right]d\boldsymbol{x}\,, \quad (127)
\end{aligned}$$

or again after integrating by parts and using the equilibrium Eqs. (114-115), as

$$0 = \int_{\partial\omega(\boldsymbol{X};\,\varpi)}\left(\mathbf{P}_{\mathrm{m}}\left(\boldsymbol{x};\,\varpi\right)\cdot\boldsymbol{n}_{\mathrm{m}}\right)\cdot\delta\boldsymbol{U}'\left(\boldsymbol{x};\,\varpi\right)d\boldsymbol{x} = \int_{\partial\omega(\boldsymbol{X};\,\varpi)}\boldsymbol{T}_{\mathrm{m}}\left(\boldsymbol{x};\,\varpi\right)\cdot\delta\boldsymbol{U}'\left(\boldsymbol{x};\,\varpi\right)d\boldsymbol{x}\,. \tag{128}$$

Definition of the constrained micro-scale finite element problem. For conciseness, in the following, we drop the random micro-structure ϖ, and consider the realisation $\boldsymbol{u}'(\boldsymbol{x}) = \boldsymbol{U}'(\boldsymbol{X};\, \varpi)$, but it is understood that the homogenised response is micro-structure dependent.

With a view to the formulation of the weak form of the micro-scale problem (114-115), Eq. (126) defines the minimum kinematic field $\mathcal{U}^{\min}(\omega)$ of the test and trial functions as

$$\mathcal{U}^{\min}(\omega) = \left\{ \boldsymbol{u}' \in \mathcal{H}(\omega) | \int_{\partial\omega} \boldsymbol{u}' \otimes \boldsymbol{n}_{\mathrm{m}} d\boldsymbol{x} = 0 \right\} , \tag{129}$$

where $\mathcal{H}(\omega)$ is the Hilbert space. Then, the weak form of the micro-scale Eqs. (114-115) reads finding $\boldsymbol{u}' \in \mathcal{U}(\omega) \subset \mathcal{U}^{\min}(\omega)$ such that

$$\int_{\omega} \mathbf{p}_{\mathrm{m}}(\boldsymbol{u}') : (\delta\boldsymbol{u}' \otimes \boldsymbol{\nabla}_0)\, d\boldsymbol{x} = 0\,, \quad \forall \delta\boldsymbol{u}' \in \mathcal{U}(\omega) \subset \mathcal{U}^{\min}(\omega)\,, \tag{130}$$

where $\delta\boldsymbol{u}' \in \mathcal{U}(\omega)$ is a test function belonging to an admissible kinematic vector field $\mathcal{U}(\omega)$ subset of the minimum kinematic field $\mathcal{U}^{\min}$ and where $\mathbf{p}_{\mathrm{m}}$ stands for a realisation $\mathbf{P}_{\mathrm{m}}(\varpi)$. The resolution of this weak form with $\delta\boldsymbol{u}' \in \mathcal{U}(\omega) \subset \mathcal{U}^{\min}(\omega)$ makes the second term of the right hand side of Eq. (127) to vanish, so that the Hill-Mandel condition (124) is always satisfied.

This variational statement (130) of the Hill-Mandel condition was introduced by Peric et al. (2010); Schröder et al. (2016). Its implementation was detailed by Nguyen et al. (2017) and is carried out by defining specific boundary conditions on the meso-scale volume element whose constraint is to satisfy Eq. (126).

The commonly applied boundary conditions on the meso-scale volume elements ω are:

- The Kinematic Uniform Boundary Conditions (KUBCs), for which the admissible kinematic vector field $\mathcal{U}(\omega)$ is defined by

  $$\mathcal{U}^{\mathrm{KUBC}}(\omega) \quad = \quad \{ \boldsymbol{u}' \in \mathcal{H}(\omega) | \boldsymbol{u}' = 0 \quad \forall \boldsymbol{x} \in \partial\omega \} \subset \mathcal{U}^{\min}(\omega)\,, \tag{131}$$

  i.e. there is no fluctuation on the boundary $\partial\omega$;

- The Periodic Boundary Conditions (PBCs), for which the admissible kinematic vector field $\mathcal{U}$ is defined by

  $$\begin{aligned} \mathcal{U}^{\mathrm{PBC}}(\omega) \quad = \quad & \{ \boldsymbol{u}' \in \mathcal{H}(\omega) | \boldsymbol{u}_{\mathrm{m}}(\boldsymbol{x}^+) - \boldsymbol{u}_{\mathrm{m}}(\boldsymbol{x}^-) = [\mathbf{F}_{\mathrm{M}} - \mathbf{I}] \cdot (\boldsymbol{x}^+ - \boldsymbol{x}^-)\,, \\ & \forall \boldsymbol{x}^+ \in \partial\omega^+ \text{ and corresponding } \boldsymbol{x}^- \in \partial\omega^- \} \subset \mathcal{U}^{\min}(\omega)\,, \end{aligned} \tag{132}$$

  where the parallelepiped SVE faces have been separated in opposite surfaces $\partial\omega^-$ and $\partial\omega^+$; In a kinematically-based finite-element formulation, the variational statement does not require constraints on the symmetry of the surface traction in order to satisfy the Hill-Mandel condition: this symmetry is a consequence of the micro-scale problem resolution as shown by considering arbitrary $\delta\boldsymbol{u}' \in \mathcal{U}^{\mathrm{PBC}}(\omega)$ in Eq. (128);

- The Zero Average Fluctuation Boundary Conditions (ZAFBCs) for which the admissible kinematic vector field $\mathcal{U}$ is defined by

$$\mathcal{U}^{\text{ZAFBC}}(\omega) \quad = \quad \left\{ \boldsymbol{u}' \in \mathcal{H}(\omega) | \int_{\partial\omega^{(l)}} \boldsymbol{u}' d\boldsymbol{x} = 0 \quad \forall \text{ face } \partial\omega^{(l)} \in \partial\omega \right\} , \tag{133}$$

  where the parallelepiped SVE boundary $\partial\omega$ has been decomposed in opposite faces $\partial\omega = \cup_{i=1}^{6} \partial\omega^{(i)}$ in which case $\mathcal{U}^{\text{ZAFC}}(\omega) \subset \mathcal{U}^{\text{min}}(\omega)$;

- The Static Uniform Boundary Conditions (SUBCs), which are formally written as $\boldsymbol{t}_m = \mathbf{P}_{\text{M}} \left(\boldsymbol{X};\, \mathfrak{w} \right) \cdot \boldsymbol{n}_{\text{m}} \quad \forall \boldsymbol{x} \in \partial\omega$; This BC requires adding constraints in a kinematically-based finite element formulation and is sometimes mimicked by considering ZAFBC. Indeed, introducing Eq. (133) in Eq. (128) leads to an equation which is always satisfied by considering arbitrary $\delta\boldsymbol{u}' \in \mathcal{U}^{\text{ZAFBC}}(\omega)$.

- The Orthogonal Uniform Mixed Boundary Conditions (OUMBCs), which is a combination of KUBCs along direction i and ZAFBCs along the two other directions $j \neq i$, and which is defined by

$$\begin{aligned} \mathcal{U}^{\text{OUMBC}}(\omega) \quad = \quad & \{ \boldsymbol{u}' \in \mathcal{H}(\omega) | u'_i = 0 \quad \forall \boldsymbol{x} \in \partial\omega,\ i = 1,\ 2,\ \text{ or } 3 \text{ and} \\ & \left. \int_{\partial\omega^{(l)}} u'_j d\boldsymbol{x} = 0 \quad \forall \text{ face } \partial\omega^{(l)} \in \partial\omega,\ j \neq i \right\} . \end{aligned} \tag{134}$$

  This type of boundary condition is usually used when PBCs cannot be easily implemented, like on non-periodic micro-structures.

We note that the Voigt assumption, *i.e.* $\mathcal{U}^{\text{Voigt}}(\omega) = \{ \boldsymbol{u}' \in \mathcal{H}(\omega) | \boldsymbol{u}' = 0 \quad \forall \boldsymbol{x} \in \omega \} \subset \mathcal{U}^{\text{min}}(\omega)$ for which there is no fluctuation on the volume ω, usually violates the balance of linear momentum, leading to an unreachable upper-bound of the material operator (Firooz et al., 2019). A similar observation can be drawn for the Reuss assumption.

The effect of the BC choice has been extensively studied in the literature. Recently Firooz et al. (2019) have studied this effect on periodic and random 15% volume ratio particle-reinforced matrix. For the random composite material, a single realisation of a random micro-structure with a volume element ω of increasing relative size, see Fig. 28, is considered. For a periodic micro-structure, see Fig. 28(a), KUBCs and SUBCs respectively overestimate and underestimate the effective response predicted by the PBCs. For a non-periodic micro-structure, see Fig. 28(b), the same trend can be observed although some oscillations appear. In particular one can see that the PBCs converge faster to the effective properties, even for a few inclusions, and that this effective property is not the same as for the periodic micro-structure.

Using the reconstruction technique described in Section 3.2.1 and illustrated in Fig. 9 to generate virtual micro-structures, Wu et al. (2018a) have studied random 52% volume ratio particle-reinforced matrix using the window technique for two SVE lengths: $l_{\text{SVE}} = 10\mu$m and $l_{\text{SVE}} = 25\mu$m. The extracted apparent Young's modulus distributions for different kinds of boundary conditions are illustrated in Figs. 29(a) and 29(b), respectively. On average,

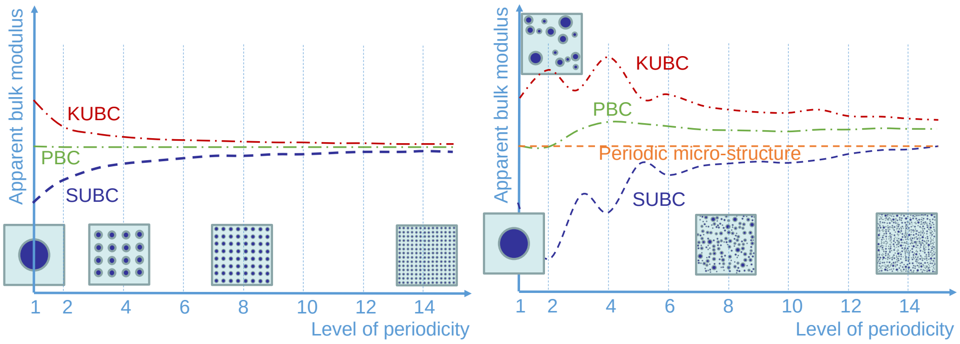

(a) Periodic (b) Random

Figure 28: Effect of the micro-structure periodicity, boundary conditions and volume element size on the apparent properties as studied by Firooz et al. (2019); Images resketched from (Firooz et al., 2019); The problem consists of a 15% volume fraction 10 times stiffer inclusion reinforced matrix and with (a) A periodic micro-structure; and (b) A single realisation of a random micro-structure.

the apparent Young's modulii are lower for the SUBCs than for the PBCs, and for the latter than for the KUBCs. As noted by Wu et al. (2018a) when considering the response of an SVE of reduced size, the *in-situ* apparent properties of the SVE will not be equal to those obtained for any of the three boundary condition kinds. Instead,

- If the surrounding material is stiffer than that of the SVE, *e.g.* when the SVE has a lower content of stiffer fibre, strong constraints are *in situ* applied on this SVE and its response will be close to the results obtained under KUBCs;
- If the surrounding material is more compliant than that of the SVE, *e.g.* when the SVE has a higher content of stiffer fibre, weak constraints are *in-situ* applied on this SVE and its response will be close to the results obtained under SUBCs;
- Finally, if the stiffness of the surrounding material is comparable to that of the SVE, its response will be close to the results obtained under PBCs.

Nevertheless, the relevance of the PBCs in linear elasticity was asserted by Wu et al. (2018a) by solving 100 so-called "Big SVEs" (BSVEs) of size $100 \times 100\,\mu\text{m}^2$ in two ways:

- By direct computation homogenisation using PBC as presented here above;
- By performing first a computational homogenisation on windows of size $25 \times 25\,\mu\text{m}^2$, so called "Small SVEs" (SSVEs) using the different kinds of boundary condition, and using those apparent properties during a second-step homogenisation .

Figure 29(c) shows that the use of PBCs on the SSVEs yields results in good agreement with the direct computational homogenisation. For these reasons, PBCs are commonly used during stochastic homogenisation. We also refer to the discussion by Pivovarov et al. (2019).

An alternative developed by Cottereau (2013) in the spirit of the Arlequin method is to weakly couple a stochastic spatial region (SVE-like) within a deterministic homogenised

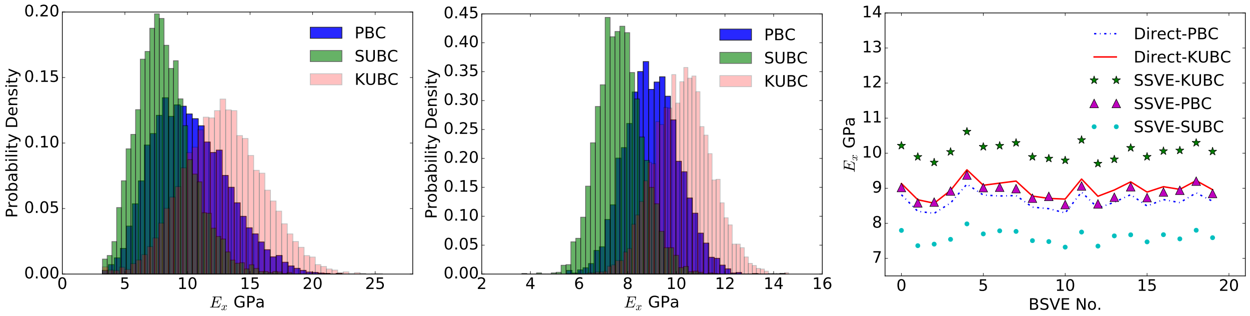

(a) $l_{\mathrm{SVE}} = 10\mu$m (b) $l_{\mathrm{SVE}} = 25\mu$m (c) 2-step

Figure 29: Effect of the boundary conditions and volume element size on the apparent properties as studied by Wu et al. (2018a); The problem consists of a 52% volume fraction inclusion reinforced matrix with (a) 8100 realisations and an SVE size of $l_{\mathrm{SVE}} = 10\mu$m; and (b) 4900 realisations and an SVE size of $l_{\mathrm{SVE}} = 25\mu$m; (c) The effect of the boundary condition is also studied by considering a 2-step computational homogenisation performed on several Big SVE (BSVE) realisations; Reprinted from Composite Structures 189, Wu, L., Chung, C.N., Major, Z., Adam, L., Noels, L., From SEM images to elastic responses: A stochastic multiscale analysis of UD fiber reinforced composites, 206-227, Copyright (2018), with permission from Elsevier.

domain, whose elastic parameters are iteratively updated. It was shown that this methodology alleviates the biases introduced by applying SUBC or KUBC on the SVE since a self-consistent homogenisation is actually performed, whilst the weak coupling ensures the absence of stress/strain concentrations.

Resolution of the constrained micro-scale finite element problem. The numerical resolution of the meso-scale BVP relies on the spatial Galerkin finite elements discretization of the meso-scale volume element $\omega = \omega\left(\boldsymbol{X};\, \mathfrak{w}\right)$ into finite elements ω^e. The micro-displacement field $\boldsymbol{u}_{\mathrm{m}}$ and the test function $\delta\boldsymbol{u}'$ are then written as

$$\boldsymbol{u}_{\mathrm{m}} = \sum_a \varphi^{(a)}\boldsymbol{u}^{(a)} \in \mathscr{H}(\omega) \text{ and } \delta\boldsymbol{u}' = \sum_a \varphi^{(a)}\delta\boldsymbol{u}'^{(a)} \in \mathscr{H}(\omega)\,, \tag{135}$$

where $\varphi^{(a)}$ are the nodal shape functions and $\boldsymbol{u}^{(a)}$ are the nodal degrees of freedom. We note that Eq. (125) allows relating the fluctuation $\boldsymbol{u}'(\boldsymbol{x})$ to the displacement $\boldsymbol{u}(\boldsymbol{x})$ and thus to the degrees of freedom $\boldsymbol{u}^{(a)}$, see Appendix C.1.1. Applying the constraints such as the boundary conditions (131-134) on the finite element discretization of Eq. (130) leads to a set of coupled equations

$$\begin{cases} \boldsymbol{f}_{\mathrm{int}}\left(\boldsymbol{d}_{\mathrm{m}}\right) - \mathbf{c}^T\boldsymbol{\lambda} = 0\,, \text{ and} \\ \mathbf{c}\boldsymbol{d}_{\mathrm{m}} - \mathbf{s}\boldsymbol{f}_{\mathrm{M}}^{\mathrm{k}} = 0\,, \end{cases} \tag{136}$$

where $\boldsymbol{f}_{\mathrm{int}}$ is the vector of internal forces associated to the weak form (130) of the unconstrained meso-scale volume element, $\boldsymbol{d}_{\mathrm{m}}$ is the vector gathering all the nodal displacements $\boldsymbol{u}^{(a)}$ –as well as the degrees of freedom used to define periodic boundary conditions as explained below, $\boldsymbol{\lambda}$ is the vector of the Lagrange multipliers enforcing the constraints, $\boldsymbol{f}_{\mathrm{M}}^{\mathrm{k}}$ represents the macro-scale kinematic variable realisation $\mathbf{f}_{\mathrm{M}} - \mathbf{I} = \mathbf{F}_{\mathrm{M}}(\mathfrak{w}) - \mathbf{I} = \boldsymbol{u}_{\mathrm{M}} \otimes \nabla_{\mathrm{M}}$

written under a vector form, and where $\mathbf{c}$ and $\mathbf{s}$ are the so-called constraints matrix and kinematic matrix, respectively, built from the different constraints. The explicit expression of the vector of internal forces is given by

$$\boldsymbol{f}_{\text{int}} \;=\; \bigwedge_{\omega^e} \int_{\omega^e} \left(\mathbf{b}^e\right)^T \boldsymbol{p}_{\mathrm{m}} d\boldsymbol{x}\,, \tag{137}$$

where $\mathbf{b}^e$ is the elementary matrix of the shape functions gradient associated to the displacement vector field, $\boldsymbol{p}_{\mathrm{m}}$ is the first Piola-Kirchhoff stress tensor realisation $\mathbf{p}_{\mathrm{m}} = \mathbf{P}_{\mathrm{m}}(\omega)$ written in the vector form, and where $\bigwedge_{\omega^e}$ is used to symbolise the assembly process. The stiffness matrix $\mathbf{k}_{\mathrm{m}}$ of the unconstrained meso-scale volume element reads

$$\mathbf{k}_{\mathrm{m}} \;=\; \bigwedge_{\omega^e} \int_{\omega^e} \left(\mathbf{b}^e\right)^T \mathbf{c}_{\mathrm{m}} \mathbf{b}^e d\boldsymbol{x}\,, \tag{138}$$

where $\mathbf{c}_{\mathrm{m}} = \frac{\partial \boldsymbol{p}_{\mathrm{m}}}{\partial \boldsymbol{f}_{\mathrm{m}}}$ is the matrix notation of the micro-scale fourth-order material tensor $\mathbb{c}_{\mathrm{m}} = \frac{\partial \mathbf{p}_{\mathrm{m}}}{\partial \mathbf{f}_{\mathrm{m}}}$, with $\boldsymbol{f}_{\mathrm{m}}$ the deformation gradient $\mathbf{f}_{\mathrm{m}}$ written in the vector form.

Since we have shown that PBCs (132) are commonly used for non-periodic microstructures, we consider this particular case. Since the mesh is not periodic on the opposite faces, the polynomial interpolation method suggested by Nguyen et al. (2012) is introduced to enforce approximately the set of Eqs. (132). Considering the pairs $i = 1,\, 2,\, 3$ of opposite faces $(\partial\omega^{(i-)},\, \partial\omega^{(i+)})$, the interpolation form of degree n is defined as

$$\boldsymbol{\varphi}^{(i)}\left(\boldsymbol{x}\right) = \sum_{k=1}^{n+1} \varphi_{(k)}^{(i)}\left(\boldsymbol{x}\right) \boldsymbol{a}_{(k)}^{(i)} \;(\text{no sum on } i)\,, \tag{139}$$

where $\varphi_{(k)}^{(i)}$ with $k = 1, ..., n+1$ are the interpolation shape functions, and $\boldsymbol{a}_{(k)}^{(i)}$ with $k = 1, ..., n+1$ are first-order tensors of new degrees of freedom corresponding to the interpolation form $\boldsymbol{\varphi}^{(i)}$. These new degrees of freedom $\boldsymbol{a}_{(j)}^{(i)}$ with $j = 1, ..., n+1$ govern the fluctuation field on the boundary $\boldsymbol{x} \in \partial\omega^{(i-)}$ and are thus evaluated as to satisfy the PBCs (132) through

$$\begin{cases} \boldsymbol{u}'\left(\boldsymbol{x}^+;\, \boldsymbol{a}_{(1)}^{(i)}, \ldots, \boldsymbol{a}_{(n+1)}^{(i)}\right) & = \boldsymbol{\varphi}^{(i)}\left(\boldsymbol{x}^-;\, \boldsymbol{a}_{(1)}^{(i)}, \ldots, \boldsymbol{a}_{(n+1)}^{(i)}\right) \; \forall \boldsymbol{x}^+ \in \partial\omega^{(i+)}\,, \text{ and} \\ \boldsymbol{u}'\left(\boldsymbol{x}^-;\, \boldsymbol{a}_{(1)}^{(i)}, \ldots, \boldsymbol{a}_{(n+1)}^{(i)}\right) & = \boldsymbol{\varphi}^{(i)}\left(\boldsymbol{x}^-;\, \boldsymbol{a}_{(1)}^{(i)}, \ldots, \boldsymbol{a}_{(n+1)}^{(i)}\right) \; \forall \boldsymbol{x}^- \in \partial\omega^{(i-)}\,. \end{cases} \tag{140}$$

The functions $\varphi_{(k)}^{(i)}$ depend on the interpolation method: *e.g.* a bi-linear patch Coons formulation was derived by Nguyen et al. (2012). Finally, the constraints and kinematic matrices involved in the set of Eqs. (136) were deduced from these functions by Nguyen et al. (2017), see details in Appendix C.1.1 –we refer to the work by Nguyen et al. (2017) for other BC cases.

The set of Eqs. (136) is solved by the multiple-constraint projection method set up by Ainsworth (2001) and summarised in Appendix C.1.2.

Extraction of the meso-scale response. During the resolution of the set of Eqs. (136), for a given $\mathbf{f}_{\mathrm{M}}$, two quantities are directly extracted:

- The homogenised first Piola-Kirchhoff stress tensor $\mathbf{p}_{\mathrm{M}} = \frac{1}{V(\omega)} \sum_e \int_{\omega^e} \mathbf{p}_{\mathrm{m}} d\boldsymbol{x}$; and
- The fourth order macro-scale material tensor $\mathbb{c}_{\mathrm{M}} = \frac{\partial \mathbf{p}_{\mathrm{M}}}{\partial \mathbf{f}_{\mathrm{M}}}$, which is required during the Newton-Raphson iterations of a multi-scale analysis, or which is the sought apparent material tensor in the case of a linear behaviour.

The latter fourth order macro-scale material tensor is extracted in the matrix form $\mathbf{c}_{\mathrm{M}}$ at no additional cost since the matrix inverse which is required is the same as during the finite-element resolution of the system (136), see the details in Appendix C.1.3.

We note that given stress states of the meso-scale volume element, *e.g.* plane stress state, can easily be enforced by limiting the size of the constraints term $\mathbf{s}\boldsymbol{f}^{\mathrm{k}}_{\mathrm{M}}$ of the set of Eqs. (136), and by performing Newton-Raphson iterations in order to reach the sought components of the first Piola-Kirchhoff stress tensor $\mathbf{p}_{\mathrm{M}}$ using the tensor $\mathbb{c}_{\mathrm{M}}$. *E.g.*, simple uni-axial tension is obtained by limiting the constraints term $\mathbf{s}\boldsymbol{f}^{\mathrm{k}}_{\mathrm{M}}$ of the set of Eqs. (136) to $\mathbf{s}\nabla_{0_x} u_{\mathrm{M}_x}$, and enforcing $p_{\mathrm{M}_{ij}} = 0$ for i or $j \neq x$.

Failure analysis. In the case of failure analyses, the extraction of the apparent stress-strain curves holds up to strain softening onset only, since the stress-stain curve looses objectivity beyond that point. However, the objectivity with the dimensions of the microscopic problems can be recovered, *e.g.* in terms of a homogenised Traction Separation Law (TSL) Nguyen et al. (2010); Verhoosel et al. (2010); Wu et al. (2013c).

In the context of micro-structures with geometrical uncertainties, Nguyen et al. (2019) have studied carbon fibre reinforced high-cross-linked RTM6 epoxy resin in which the matrix failure is modelled by a multi-mechanism damage model. They have then extracted objective quantities such as the critical strength and energy release rates from SVE direct simulations. Bhuiyan et al. (2020) have studied the statistical strength envelope of UD composites for several loading conditions. A random field of apparent paper fibre network strength and failure strain was extracted by Mansour et al. (2019). Mulay et al. (2015) have extracted probabilistic meso-scale cohesive laws for poly-silicon thin film by considering random orientation of the grains and inter-granular and intra-granular micro-scale cohesive laws, the later being identified in terms of the crystal orientation. Shabir et al. (2019) has studied the possibility to apply a scaling law, *i.e.* the application of simple linear elastic fracture mechanics scaling relations to extract load-displacement curves for specimens with the same microstructure and for various cohesive law parameters from a master load-displacement curve, on the SVE failure response of poly-crystals.

4.2.2. Asymptotic homogenisation

The Asymptotic Homogenisation (AH) framework was initially developed assuming a periodic micro-structure that can be represented by a cell volume element as illustrated in Fig. 27(c). The formalism of AH is illustrated in Fig. 24(b), in which a magnification by a ratio $\frac{1}{\varepsilon}$ of the macro-scale structure Ω yields a representation of the periodic micro-structure

$\omega(\boldsymbol{X};\,\mathscr{w})$. For conciseness, in the following volume integrals, we note the volume element realization $\omega = \omega(\boldsymbol{X};\,\mathscr{w})$, in which we omit the reference to $\mathscr{w}$, but it is understood that the homogenized response is micro-structure dependent.

We first present the AH formalism in finite strains as developed by Pruchnicki (1998) so that it can be compared to the computational homogenisation case. Then the formalism resolution is detailed for linear elasticity and for stochastic small strain elasto-plasticity using a reduced order model as developed by Fish and Wu (2011).

The multi-scale problem. The multi-scale problem, assuming no dynamical effect, is framed by the linear momentum equation expressed as

$$\mathbf{P}_\varepsilon(\boldsymbol{X};\,\mathscr{w})\cdot\boldsymbol{\nabla}_0 + \boldsymbol{b}(\boldsymbol{X}) = 0 \quad \forall \boldsymbol{X}\in\Omega,\, \mathscr{w}\in\mathscr{W}\,, \tag{141}$$

where the subscript "ε" refers to the stochastic multi-scale problem, $\mathbf{P}_\varepsilon(\boldsymbol{X};\,\mathscr{w})$ is the first Piola-Kirchhoff stress tensor, $\boldsymbol{\nabla}_0$ refers to derivatives with respect to the material position in the reference configuration of the volume Ω and $\boldsymbol{b}$ is the load per unit reference volume. The boundary conditions read

$$\boldsymbol{U}_\varepsilon(\boldsymbol{X};\,\mathscr{w}) = \boldsymbol{u}_{\mathrm{D}}(\boldsymbol{X}) \qquad \forall \boldsymbol{X}\in\partial_D\Omega,\, \mathscr{w}\in\mathscr{W}\,, \text{ and} \tag{142}$$

$$\mathbf{P}_\varepsilon(\boldsymbol{X};\,\mathscr{w})\cdot\boldsymbol{n}_{\mathrm{M}} = \boldsymbol{t}(\boldsymbol{X}) \qquad \forall \boldsymbol{X}\in\partial_N\Omega,\, \mathscr{w}\in\mathscr{W}\,, \tag{143}$$

where $\boldsymbol{U}_\varepsilon(\boldsymbol{X};\,\mathscr{w})$ is the displacement field, $\boldsymbol{t}$ is the surface traction, per unit reference surface, on the Neumann boundary $\partial_N\Omega$ of outward unit normal $\boldsymbol{n}_{\mathrm{M}}$ in the reference configuration, and $\boldsymbol{u}_{\mathrm{D}}$ is the constrained displacement on the Dirichlet boundary $\partial_D\Omega$. The deformation gradient field $\mathbf{F}_\varepsilon(\Omega)$ is computed from the displacement field $\boldsymbol{U}_\varepsilon(\Omega)$ as

$$\mathbf{F}_\varepsilon(\boldsymbol{X};\,\mathscr{w}) = \mathbf{I} + \boldsymbol{U}_\varepsilon(\boldsymbol{X};\,\mathscr{w})\otimes\boldsymbol{\nabla}_0 \quad \forall \boldsymbol{X}\in\Omega,\, \mathscr{w}\in\mathscr{W}\,. \tag{144}$$

The multi-scale problem is completed by a constitutive relationship

$$\mathbf{P}_\varepsilon\left(\boldsymbol{X},\,t;\,\mathscr{w}\right) = \mathbf{P}\left(\mathbf{F}_\varepsilon\left(\boldsymbol{X},\,t;\,\mathscr{w}\right);\boldsymbol{Z}_\varepsilon\left(\boldsymbol{X},\,\tau;\,\mathscr{w}\right),\,\tau\in[0,\,t],\,\mathscr{w}\right)\,, \tag{145}$$

defining the relationship of the stress tensor $\mathbf{P}_\varepsilon(\boldsymbol{X};\,\mathscr{w})$ with the deformation gradient $\mathbf{F}_\varepsilon(\boldsymbol{X};\,\mathscr{w})$ through internal variables $\boldsymbol{Z}_\varepsilon(\boldsymbol{X},\,\tau;\,\mathscr{w})$. Assuming the existence of an energy potential ψ in hyper-elasticity, Pruchnicki (1998) has considered the form

$$\mathbf{P}_\varepsilon\left(\boldsymbol{X};\,\mathscr{w}\right) = \frac{\partial\Psi\left(\mathbf{F}_\varepsilon;\,\mathscr{w}\right)}{\partial\mathbf{F}_\varepsilon}\left(\boldsymbol{X};\,\mathscr{w}\right)\,. \tag{146}$$

Asymptotic expansion. The basis of AH is to develop the displacement field $\boldsymbol{U}_\varepsilon(\boldsymbol{X};\,\mathscr{w})$ into contributions $\boldsymbol{U}_i$ at different scales $i = 0,\,1,\,\ldots$ as[5]

$$\boldsymbol{U}_\varepsilon(\boldsymbol{X};\;\mathscr{w}) = \boldsymbol{U}_0(\boldsymbol{X};\;\mathscr{w}) + \sum_{i=1,\,2\ldots}\varepsilon^i\boldsymbol{U}_i\left(\boldsymbol{X},\,\boldsymbol{x};\,\mathscr{w}\right)\,, \tag{147}$$

---

[5] One could consider $\boldsymbol{U}_0(\boldsymbol{X},\,\boldsymbol{x};\,\mathscr{w})$ in the development, but Fish et al. (1997) showed that when identifying terms of different orders this would lead to $\boldsymbol{\nabla}_{\boldsymbol{x}}\boldsymbol{U}_0(\boldsymbol{X},\,\boldsymbol{x};\,\mathscr{w}) = 0$, allowing to remove the dependency on $\boldsymbol{x}$.

where $\boldsymbol{U}_i$ for $i = 1, \ldots$ is expressed explicitly in terms of the fine grid $\boldsymbol{x} = \frac{\boldsymbol{X}}{\varepsilon}$ with $\varepsilon \to 0$. Similarly, the material derivatives with respect to the reference configuration $\boldsymbol{\nabla}_0$ are expressed in terms of the partial derivatives with respect to $\boldsymbol{X}$ and to $\boldsymbol{x}$ respectively at the coarse and fine scales, with the operator $(\boldsymbol{\nabla}_0)$ becoming

$$(\boldsymbol{\nabla}_0) = \left(\boldsymbol{\nabla}_{\boldsymbol{X}} + \frac{1}{\varepsilon}\boldsymbol{\nabla}_{\boldsymbol{x}}\right) . \tag{148}$$

Using Eq. (148) to express the deformation gradient $\mathbf{F}_\varepsilon$ from the displacement series (147) yields

$$\begin{aligned}\mathbf{F}_\varepsilon(\boldsymbol{X};\, \omega) \quad = \quad & \underbrace{\mathbf{I} + \boldsymbol{U}_0(\boldsymbol{X};\, \omega) \otimes \boldsymbol{\nabla}_{\boldsymbol{X}} + \boldsymbol{U}_1(\boldsymbol{X},\, \boldsymbol{x};\, \omega) \otimes \boldsymbol{\nabla}_{\boldsymbol{x}}}_{\mathbf{F}_0(\boldsymbol{X},\boldsymbol{x};\,\omega)} + \\ & \varepsilon \underbrace{\left[\boldsymbol{U}_1(\boldsymbol{X},\, \boldsymbol{x};\, \omega) \otimes \boldsymbol{\nabla}_{\boldsymbol{X}} + \boldsymbol{U}_2(\boldsymbol{X},\, \boldsymbol{x};\, \omega) \otimes \boldsymbol{\nabla}_{\boldsymbol{x}}\right]}_{\mathbf{F}_1(\boldsymbol{X},\boldsymbol{x};\,\omega)} + \ldots \\ & \varepsilon^i \underbrace{\left[\boldsymbol{U}_i(\boldsymbol{X},\, \boldsymbol{x};\, \omega) \otimes \boldsymbol{\nabla}_{\boldsymbol{X}} + \boldsymbol{U}_{i+1}(\boldsymbol{X},\, \boldsymbol{x};\, \omega) \otimes \boldsymbol{\nabla}_{\boldsymbol{x}}\right]}_{\mathbf{F}_i(\boldsymbol{X},\boldsymbol{x};\,\omega)} + \ldots\end{aligned} \tag{149}$$

The Piola-Kirchhoff stress tensor (145) can be asymptotically expanded using Eq. (149) into a series of contributions $\mathbf{P}_i$ at different scales $i = 0, 1, \ldots$ following

$$\mathbf{P}_\varepsilon\left(\boldsymbol{X};\, \omega\right) = \mathbf{P}_0\left(\boldsymbol{X},\, \boldsymbol{x};\, \omega\right) + \sum_{i=1,\,2\ldots} \varepsilon^i \mathbf{P}_i\left(\boldsymbol{X},\, \boldsymbol{x};\, \omega\right) , \tag{150}$$

where

$$\mathbf{P}_0\left(\boldsymbol{X},\, \boldsymbol{x},\, t;\, \omega\right) = \mathbf{P}\left(\mathbf{F}_0\left(\boldsymbol{X},\, \boldsymbol{x},\, t;\, \omega\right); \boldsymbol{Z}\left(\boldsymbol{X},\, \boldsymbol{x}\,, \tau;\, \omega\right),\, \tau \in [0,\, t],\, \omega\right) . \tag{151}$$

In the particular case for which Eq. (146) holds, one has

$$\mathbf{P}_0\left(\boldsymbol{X},\, \boldsymbol{x};\, \omega\right) = \frac{\partial \Psi\left(\mathbf{F}_0;\, \omega\right)}{\partial \mathbf{F}_0}(\boldsymbol{X},\, \boldsymbol{x};\, \omega) . \tag{152}$$

The other terms $\mathbf{P}_i$ at the different scales $i = 1, \ldots$ represent the i^{th}-order terms of the asymptotic expansion of $\frac{\partial \Psi(\mathbf{F}_\varepsilon;\, \omega)}{\partial \mathbf{F}_\varepsilon}$.

Finally, using the operator (148), the linear momentum balance equations (141) is expanded as

$$\begin{aligned} 0 \quad = \quad & \frac{1}{\varepsilon}\mathbf{P}_0(\boldsymbol{X},\, \boldsymbol{x};\, \omega) \cdot \boldsymbol{\nabla}_{\boldsymbol{x}} + \left[\mathbf{P}_0(\boldsymbol{X},\, \boldsymbol{x};\, \omega) \cdot \boldsymbol{\nabla}_{\boldsymbol{X}} + \mathbf{P}_1(\boldsymbol{X},\, \boldsymbol{x};\, \omega) \cdot \boldsymbol{\nabla}_{\boldsymbol{x}} + \boldsymbol{b}\right] + \\ & \quad \varepsilon\left[\mathbf{P}_1(\boldsymbol{X},\, \boldsymbol{x};\, \omega) \cdot \boldsymbol{\nabla}_{\boldsymbol{X}} + \mathbf{P}_2(\boldsymbol{X},\, \boldsymbol{x};\, \omega) \cdot \boldsymbol{\nabla}_{\boldsymbol{x}}\right] + \ldots + \\ & \qquad \varepsilon^i\left[\mathbf{P}_i(\boldsymbol{X},\, \boldsymbol{x};\, \omega) \cdot \boldsymbol{\nabla}_{\boldsymbol{X}} + \mathbf{P}_{i+1}(\boldsymbol{X},\, \boldsymbol{x};\, \omega) \cdot \boldsymbol{\nabla}_{\boldsymbol{x}}\right] \ldots \end{aligned} \tag{153}$$

Identifying the terms of same power in ε yields to the system of equations at the different scales

$$\begin{aligned}
\text{Order -1:}\quad 0 =&\quad \mathbf{P}_0(\boldsymbol{X},\,\boldsymbol{x};\,\mathscr{w})\cdot\boldsymbol{\nabla}_{\boldsymbol{x}}\quad \forall\boldsymbol{X}\times\boldsymbol{x}\in\Omega\times\omega(\boldsymbol{X};\,\mathscr{w}),\ \mathscr{w}\in\mathscr{W}\,, && (154)\\
\text{Order 0:}\quad 0 =&\quad \mathbf{P}_0(\boldsymbol{X},\,\boldsymbol{x};\,\mathscr{w})\cdot\boldsymbol{\nabla}_{\boldsymbol{X}}+\mathbf{P}_1(\boldsymbol{X},\,\boldsymbol{x};\,\mathscr{w})\cdot\boldsymbol{\nabla}_{\boldsymbol{x}}+\boldsymbol{b}(\boldsymbol{X})\\
&\qquad\qquad\qquad \forall\boldsymbol{X}\times\boldsymbol{x}\in\Omega\times\omega(\boldsymbol{X};\,\mathscr{w}),\ \mathscr{w}\in\mathscr{W}\,, && (155)\\
\text{Order } i\geq 1:\quad 0 =&\quad \mathbf{P}_i(\boldsymbol{X},\,\boldsymbol{x};\,\mathscr{w})\cdot\boldsymbol{\nabla}_{\boldsymbol{X}}+\mathbf{P}_{i+1}(\boldsymbol{X},\,\boldsymbol{x};\,\mathscr{w})\cdot\boldsymbol{\nabla}_{\boldsymbol{x}}\\
&\qquad\qquad\qquad \forall\boldsymbol{X}\times\boldsymbol{x}\in\Omega\times\omega(\boldsymbol{X};\,\mathscr{w}),\ \mathscr{w}\in\mathscr{W}\,. && (156)
\end{aligned}$$

Meso-scale problem. For each fixed $\boldsymbol{X}\in\Omega$, the micro-scale deformation gradient

$$\mathbf{F}_0\,(\boldsymbol{X},\,\boldsymbol{x};\,\mathscr{w})=\mathbf{I}+\boldsymbol{U}_0(\boldsymbol{X};\,\mathscr{w})\otimes\boldsymbol{\nabla}_{\boldsymbol{X}}+\boldsymbol{U}_1(\boldsymbol{X},\,\boldsymbol{x};\,\mathscr{w})\otimes\boldsymbol{\nabla}_{\boldsymbol{x}}\,, \tag{157}$$

describes the evolution of the deformation gradient in ω. When comparing this equation with the gradient of the local displacement field (125) of the meso-scale problem in the computational homogenisation framework, it can be seen that $\boldsymbol{U}_0(\boldsymbol{X};\,\mathscr{w})\otimes\boldsymbol{\nabla}_{\boldsymbol{X}}$ plays the role of $\mathbf{F}_{\mathrm{M}}$ and $\boldsymbol{U}_1(\boldsymbol{X},\,\boldsymbol{x};\,\mathscr{w})$ the role of the perturbation field $\boldsymbol{U}'(\boldsymbol{x};\,\mathscr{w})$. As for the perturbation field, and in order to avoid indetermination of the meso-scale problem, this field should have a zero-average on ω, with

$$\frac{1}{V(\omega)}\int_{\omega}\boldsymbol{U}_1(\boldsymbol{X},\,\boldsymbol{x};\,\mathscr{w})d\boldsymbol{x}=0\quad\forall\boldsymbol{X}\in\Omega,\ \mathscr{w}\in\mathscr{W}\,. \tag{158}$$

The micro-scale stress tensor $\mathbf{P}_0\,(\boldsymbol{X},\,\boldsymbol{x};\,\mathscr{w})$ follows from either Eq. (151) or Eq. (152). Finally, the governing equation corresponds to Eq. (154). When comparing this set of equations with the meso-scale problem (114-116) in the computational homogenisation framework, it can be seen that they are equivalent for a given $\boldsymbol{X}\in\Omega$, which plays the role of a parameter into the meso-scale problem of the asymptotic homogenisation framework.

The resolution of the set of Eqs. (154) for a given $\boldsymbol{U}_0(\boldsymbol{X};\,\mathscr{w})\otimes\boldsymbol{\nabla}_{\boldsymbol{X}}$ under the constraint (158) yields the description of the fields $\boldsymbol{U}_1(\boldsymbol{X},\,\boldsymbol{x};\,\mathscr{w})$ and $\mathbf{P}_0(\boldsymbol{X},\,\boldsymbol{x};\,\mathscr{w})$ in $\Omega\times\omega(\boldsymbol{X};\,\mathscr{w})$, $\mathscr{w}\in\mathscr{W}$, and is called the localisation step.

Macro-scale problem. The macro-scale problem is defined through the averaging over the periodic micro-structure ω of Eq. (155), yielding

$$\begin{aligned}
&\frac{1}{V(\omega)}\int_{\omega}\mathbf{P}_0(\boldsymbol{X},\,\boldsymbol{x};\,\mathscr{w})\cdot\boldsymbol{\nabla}_{\boldsymbol{X}}d\boldsymbol{x}+\frac{1}{V(\omega)}\int_{\omega}\mathbf{P}_1(\boldsymbol{X},\,\boldsymbol{x};\,\mathscr{w})\cdot\boldsymbol{\nabla}_{\boldsymbol{x}}d\boldsymbol{x}+\frac{1}{V(\omega)}\int_{\omega}\boldsymbol{b}(\boldsymbol{X})d\boldsymbol{x}\\
&=\frac{1}{V(\omega)}\int_{\omega}\mathbf{P}_0(\boldsymbol{X},\,\boldsymbol{x};\,\mathscr{w})d\boldsymbol{x}\cdot\boldsymbol{\nabla}_{\boldsymbol{X}}+\frac{1}{V(\omega)}\int_{\partial\omega}\mathbf{P}_1(\boldsymbol{X},\,\boldsymbol{x};\,\mathscr{w})\cdot\boldsymbol{n}_{\mathrm{m}}d\boldsymbol{x}+\boldsymbol{b}(\boldsymbol{X})\\
&=0\quad\forall\boldsymbol{X}\in\Omega\,, && (159)
\end{aligned}$$

where $\boldsymbol{n}_{\mathrm{m}}$ is the outward unit normal to ω in the reference configuration. By analogy with Eq. (122), we define

$$\mathbf{P}_{\mathrm{M}}\,(\boldsymbol{X};\,\mathscr{w})\quad=\quad\frac{1}{V(\omega)}\int_{\omega}\mathbf{P}_0(\boldsymbol{X},\,\boldsymbol{x};\,\mathscr{w})d\boldsymbol{x}\,. \tag{160}$$

Besides, since ω is periodic, so is $\mathbf{P}_1(\boldsymbol{X},\, \boldsymbol{x};\, \mathscr{w})$ and one has $\mathbf{P}_1(\boldsymbol{X},\, \boldsymbol{x}^-;\, \mathscr{w}) \cdot \boldsymbol{n}_{\mathrm{m}}(\boldsymbol{x}^-) = -\mathbf{P}_1(\boldsymbol{X},\, \boldsymbol{x}^+;\, \mathscr{w}) \cdot \boldsymbol{n}_{\mathrm{m}}(\boldsymbol{x}^+)$ for any pair $(\boldsymbol{x}^-,\, \boldsymbol{x}^+)$ of opposite points $\boldsymbol{x}^- \in \partial\omega^-$ and $\boldsymbol{x}^+ \in \partial\omega^+$, see the notations of Fig. 27. Therefore, the system (159) reduces to

$$0 \;=\; \mathbf{P}_M(\boldsymbol{X};\, \mathscr{w}) \cdot \boldsymbol{\nabla}_{\boldsymbol{X}} + \boldsymbol{b}(\boldsymbol{X}) \quad \forall \boldsymbol{X} \in \Omega,\, \mathscr{w} \in \mathscr{W}\,. \tag{161}$$

By analogy with Eq. (121) and using Eq. (157), we define

$$\begin{aligned}
\mathbf{F}_{\mathrm{M}}(\boldsymbol{X};\, \mathscr{w}) &= \frac{1}{V(\omega)} \int_\omega \mathbf{F}_0(\boldsymbol{X},\, \boldsymbol{x};\, \mathscr{w}) d\boldsymbol{x} \\
&= \mathbf{I} + \boldsymbol{U}_0(\boldsymbol{X};\, \mathscr{w}) \otimes \boldsymbol{\nabla}_{\boldsymbol{X}} + \frac{1}{V(\omega)} \int_\omega \boldsymbol{U}_1(\boldsymbol{X},\, \boldsymbol{x};\, \mathscr{w}) \otimes \boldsymbol{\nabla}_{\boldsymbol{x}} d\boldsymbol{x} \\
&= \mathbf{I} + \boldsymbol{U}_0(\boldsymbol{X};\, \mathscr{w}) \otimes \boldsymbol{\nabla}_{\boldsymbol{X}},
\end{aligned} \tag{162}$$

because of the periodicity of $\boldsymbol{U}_1(\boldsymbol{X},\, \boldsymbol{x};\, \mathscr{w})$.

Finally, the Hill-Mandel condition results from Eq. (152) written in the incremental form integrated over ω, with

$$\begin{aligned}
\frac{1}{V(\omega)} \delta \int_\omega \Psi\left(\mathbf{F}_0(\boldsymbol{X},\, \boldsymbol{x};\, \mathscr{w});\, \mathscr{w}\right) d\boldsymbol{x} &= \\
\frac{1}{V(\omega)} \int_\omega \mathbf{P}_0\left(\boldsymbol{X},\, \boldsymbol{x};\, \mathscr{w}\right) : \delta\mathbf{F}_0\left(\boldsymbol{X},\, \boldsymbol{x};\, \mathscr{w}\right) d\boldsymbol{x} &= \\
\frac{1}{V(\omega)} \int_\omega \mathbf{P}_0\left(\boldsymbol{X},\, \boldsymbol{x};\, \mathscr{w}\right) d\boldsymbol{x} : \left(\delta\boldsymbol{U}_0(\boldsymbol{X};\, \mathscr{w}) \otimes \boldsymbol{\nabla}_{\boldsymbol{X}}\right) &+ \\
\frac{1}{V(\omega)} \int_\omega \mathbf{P}_0\left(\boldsymbol{X},\, \boldsymbol{x};\, \mathscr{w}\right) : \left(\delta\boldsymbol{U}_1(\boldsymbol{X},\, \boldsymbol{x};\, \mathscr{w}) \otimes \boldsymbol{\nabla}_{\boldsymbol{x}}\right) d\boldsymbol{x}&\,.
\end{aligned} \tag{163}$$

The last term on the right hand side vanishes since

$$\begin{aligned}
\int_\omega \mathbf{P}_0\left(\boldsymbol{X},\, \boldsymbol{x};\, \mathscr{w}\right) : \left(\delta\boldsymbol{U}_1(\boldsymbol{X},\, \boldsymbol{x};\, \mathscr{w}) \otimes \boldsymbol{\nabla}_{\boldsymbol{x}}\right) d\boldsymbol{x} &= \\
\int_{\partial\omega} \delta\boldsymbol{U}_1(\boldsymbol{X},\, \boldsymbol{x};\, \mathscr{w}) \cdot \mathbf{P}_0\left(\boldsymbol{X},\, \boldsymbol{x};\, \mathscr{w}\right) \cdot \boldsymbol{n}_{\mathrm{m}} d\partial\omega &- \\
\int_\omega \left(\mathbf{P}_0\left(\boldsymbol{X},\, \boldsymbol{x};\, \mathscr{w}\right) \cdot \boldsymbol{\nabla}_{\boldsymbol{x}}\right) \cdot \delta\boldsymbol{U}_1(\boldsymbol{X},\, \boldsymbol{x};\, \mathscr{w}) d\boldsymbol{x} &= 0\,,
\end{aligned} \tag{164}$$

where we have used Eq. (154) and the periodicity of ω which implies $\mathbf{P}_0(\boldsymbol{X},\, \boldsymbol{x}^-;\, \mathscr{w}) \cdot \boldsymbol{n}_{\mathrm{m}}(\boldsymbol{x}^-) = -\mathbf{P}_0(\boldsymbol{X},\, \boldsymbol{x}^+;\, \mathscr{w}) \cdot \boldsymbol{n}_{\mathrm{m}}(\boldsymbol{x}^+)$ and $\boldsymbol{U}_1(\boldsymbol{X},\, \boldsymbol{x}^-;\, \mathscr{w}) = \boldsymbol{U}_1(\boldsymbol{X},\, \boldsymbol{x}^+;\, \mathscr{w})$ for any pair $(\boldsymbol{x}^-,\, \boldsymbol{x}^+)$ of opposite points $\boldsymbol{x}^- \in \partial\omega^-$ and $\boldsymbol{x}^+ \in \partial\omega^+$. Therefore, using Eq. (160) and (162), Eq. (163) is rewritten

$$\frac{1}{V(\omega)} \delta \int_\omega \Psi\left(\mathbf{F}_0(\boldsymbol{X},\, \boldsymbol{x};\, \mathscr{w});\, \mathscr{w}\right) d\boldsymbol{x} = \mathbf{P}_{\mathrm{M}}\left(\boldsymbol{X};\, \mathscr{w}\right) : \delta\mathbf{F}_{\mathrm{M}}\left(\boldsymbol{X}\right)\,, \tag{165}$$

which satisfies the Hill-Mandel condition. We also note that when the stress indeed derives from the energy potential, this last equation implies that

$$\mathbf{P}_{\mathrm{M}}\left(\boldsymbol{X};\, \mathcal{w}\right) = \frac{1}{V(\omega)} \frac{\partial \int_{\omega} \Psi\left(\mathbf{F}_0(\boldsymbol{X},\, \boldsymbol{x});\, \mathcal{w}\right) d\boldsymbol{x}}{\partial \mathbf{F}_{\mathrm{M}}}\,. \tag{166}$$

Finally, the problem should be completed by the constraints on the Dirichlet and Neumann boundaries obtained by considering only the 0-order terms of the expansions and performing a volume average, *i.e*

$$\boldsymbol{U}_0(\boldsymbol{X};\, \mathcal{w}) = \boldsymbol{u}_{\mathrm{D}}(\boldsymbol{X}) \qquad \forall \boldsymbol{X} \in \partial_D\Omega\,, \text{ and} \tag{167}$$

$$\mathbf{P}_{\mathrm{M}}(\boldsymbol{X};\, \mathcal{w}) \cdot \boldsymbol{n}_{\mathrm{M}} = \boldsymbol{t}(\boldsymbol{X}) \qquad \forall \boldsymbol{X} \in \partial_N\Omega\,. \tag{168}$$

We note that close to the boundary, the periodicity assumption of the global solution might lead to unrealistic constraints. We refer to the discussion by Kanouté et al. (2009).

Resolution in the case of linear elasticity. In the case of linear elasticity, the multi-scale problem (141-146) is rewritten by approximating the Piola-Kirchhoff stress tensor by the Cauchy stress tensor $\boldsymbol{\Sigma}_\varepsilon(\boldsymbol{X};\, \mathcal{w})$, leading to the conservation of linear momentum

$$\boldsymbol{\Sigma}_\varepsilon(\boldsymbol{X};\, \mathcal{w}) \cdot \boldsymbol{\nabla}_0 + \boldsymbol{b}(\boldsymbol{X}) = 0 \quad \forall \boldsymbol{X} \in \Omega,\, \mathcal{w} \in \mathcal{W}\,, \tag{169}$$

by considering the Cauchy strain tensor $\mathbf{E}_\varepsilon(\boldsymbol{X};\, \mathcal{w})$

$$\mathbf{E}_\varepsilon(\boldsymbol{U}_\varepsilon(\boldsymbol{X};\, \mathcal{w})) = \frac{1}{2}\left(\boldsymbol{U}_\varepsilon(\boldsymbol{X};\, \mathcal{w}) \otimes \boldsymbol{\nabla}_0 + \boldsymbol{\nabla}_0 \otimes \boldsymbol{U}_\varepsilon(\boldsymbol{X};\, \mathcal{w})\right) \quad \forall \boldsymbol{X} \in \Omega,\, \mathcal{w} \in \mathcal{W}\,, \tag{170}$$

and by using the potential $\Psi\left(\mathbf{E}(\boldsymbol{X};\, \mathcal{w});\, \mathcal{w}\right) = \frac{1}{2}\mathbf{E}(\boldsymbol{X};\, \mathcal{w}) : \mathbb{C}^{\mathrm{el}}(\boldsymbol{X};\, \mathcal{w}) : \mathbf{E}(\boldsymbol{X};\, \mathcal{w})$ in the constitutive law

$$\boldsymbol{\Sigma}_\varepsilon\left(\boldsymbol{X};\, \mathcal{w}\right) = \frac{\partial \psi\left(\mathbf{E}_\varepsilon;\, \mathcal{w}\right)}{\partial \mathbf{E}_\varepsilon}(\boldsymbol{X};\, \mathcal{w}) = \mathbb{C}^{\mathrm{el}}_\varepsilon(\boldsymbol{X};\, \mathcal{w}) : \mathbf{E}_\varepsilon(\boldsymbol{X};\, \mathcal{w})\,, \tag{171}$$

where $\mathbb{C}^{\mathrm{el}}_\varepsilon(\boldsymbol{X};\, \mathcal{w})$ is the elastic material tensor of the multi-scale problem.

Considering the expansion (147) allows writing the strain tensor (170) as

$$\begin{aligned}\mathbf{E}_\varepsilon(\boldsymbol{X};\, \mathcal{w}) \quad = \quad & \underbrace{\boldsymbol{\varepsilon}_{\boldsymbol{X}}\left(\boldsymbol{U}_0(\boldsymbol{X};\, \mathcal{w})\right) + \boldsymbol{\varepsilon}_{\boldsymbol{x}}\left(\boldsymbol{U}_1(\boldsymbol{X},\, \boldsymbol{x};\, \mathcal{w})\right)}_{\mathbf{E}_0(\boldsymbol{X},\, \boldsymbol{x};\, \mathcal{w})} + \\ & \varepsilon \underbrace{\left[\boldsymbol{\varepsilon}_{\boldsymbol{X}}\left(\boldsymbol{U}_1(\boldsymbol{X},\, \boldsymbol{x};\, \mathcal{w})\right) + \boldsymbol{\varepsilon}_{\boldsymbol{x}}\left(\boldsymbol{U}_2(\boldsymbol{X},\, \boldsymbol{x};\, \mathcal{w})\right)\right]}_{\mathbf{E}_1(\boldsymbol{X},\, \boldsymbol{x};\, \mathcal{w})} + \ldots\end{aligned} \tag{172}$$

with $\boldsymbol{\varepsilon}_{\boldsymbol{X}}\left(\bullet\right) = \frac{1}{2}\left(\boldsymbol{\nabla}_{\boldsymbol{X}} \otimes \bullet + \bullet \otimes \boldsymbol{\nabla}_{\boldsymbol{X}}\right)$ and $\boldsymbol{\varepsilon}_{\boldsymbol{x}}\left(\bullet\right) = \frac{1}{2}\left(\boldsymbol{\nabla}_{\boldsymbol{x}} \otimes \bullet + \bullet \otimes \boldsymbol{\nabla}_{\boldsymbol{x}}\right)$. Similarly to Eq. (150), the Cauchy stress tensor is expended into a series of contributions $\boldsymbol{\Sigma}_i$ at different scales $i = 0,\, 1,\, \ldots$ following

$$\boldsymbol{\Sigma}_\varepsilon\left(\boldsymbol{X};\, \mathcal{w}\right) = \boldsymbol{\Sigma}_0\left(\boldsymbol{X},\, \boldsymbol{x};\, \mathcal{w}\right) + \sum_{i=1,\,2\ldots} \varepsilon^i \boldsymbol{\Sigma}_i\left(\boldsymbol{X},\, \boldsymbol{x};\, \mathcal{w}\right)\,, \tag{173}$$

where we have

$$\boldsymbol{\Sigma}_i\left(\boldsymbol{X},\,\boldsymbol{x};\,\mathscr{w}\right)=\mathbb{C}^{\mathrm{el}}_{\mathrm{m}}(\boldsymbol{X},\,\boldsymbol{x};\,\mathscr{w}):\mathbf{E}_i\left(\boldsymbol{X},\,\boldsymbol{x};\,\mathscr{w}\right)\,,\quad i=0,\,1\ldots \tag{174}$$

the latter equation being obtained as a local rewriting of Eq. (171).

Finally, as done to derive Eqs. (154-156) by applying the operator (148) on Eq. (169), one has

$$\begin{aligned}
\text{Order -1:}\quad 0=\;& \boldsymbol{\Sigma}_0(\boldsymbol{X},\,\boldsymbol{x};\,\mathscr{w})\cdot\boldsymbol{\nabla}_{\boldsymbol{x}}\quad \forall\boldsymbol{X}\times\boldsymbol{x}\in\Omega\times\omega(\boldsymbol{X};\,\mathscr{w}),\,\mathscr{w}\in\mathscr{W}\,, && (175)\\
\text{Order 0:}\quad 0=\;& \boldsymbol{\Sigma}_0(\boldsymbol{X},\,\boldsymbol{x};\,\mathscr{w})\cdot\boldsymbol{\nabla}_{\boldsymbol{X}}+\boldsymbol{\Sigma}_1(\boldsymbol{X},\,\boldsymbol{x};\,\mathscr{w})\cdot\boldsymbol{\nabla}_{\boldsymbol{x}}+\boldsymbol{b}(\boldsymbol{X})\\
& \qquad\qquad\forall\boldsymbol{X}\times\boldsymbol{x}\in\Omega\times\omega(\boldsymbol{X};\,\mathscr{w}),\,\mathscr{w}\in\mathscr{W}\,, && (176)\\
\text{Order } i\geq 1\text{:}\quad 0=\;& \boldsymbol{\Sigma}_i(\boldsymbol{X},\,\boldsymbol{x};\mathscr{w})\cdot\boldsymbol{\nabla}_{\boldsymbol{X}}+\boldsymbol{\Sigma}_{i+1}(\boldsymbol{X},\,\boldsymbol{x};\,\mathscr{w})\cdot\boldsymbol{\nabla}_{\boldsymbol{x}}\\
& \qquad\qquad\forall\boldsymbol{X}\times\boldsymbol{x}\in\Omega\times\omega(\boldsymbol{X};\,\mathscr{w}),\,\mathscr{w}\in\mathscr{W}\,. && (177)
\end{aligned}$$

Following the same argumentation as to derive Eqs. (160-161), Eq. (176) results into

$$0\;=\;\boldsymbol{\Sigma}_M(\boldsymbol{X};\,\mathscr{w})\cdot\boldsymbol{\nabla}_{\boldsymbol{X}}+\boldsymbol{b}(\boldsymbol{X})\quad\forall\boldsymbol{X}\in\Omega\,, \tag{178}$$

with the homogenised stress tensor

$$\boldsymbol{\Sigma}_{\mathrm{M}}\left(\boldsymbol{X};\,\mathscr{w}\right)\;=\;\frac{1}{V(\omega)}\int_{\omega}\boldsymbol{\Sigma}_0(\boldsymbol{X},\,\boldsymbol{x};\,\mathscr{w})d\boldsymbol{x}\,. \tag{179}$$

The apparent response $\boldsymbol{\Sigma}_{\mathrm{M}}$ is obtained by multiplying Eq. (175) by a periodic test function $\delta\boldsymbol{v}\in\mathcal{U}^{\mathrm{PBC}}(\omega)$ and integrating by part on ω, yielding

$$\int_{\omega}\boldsymbol{\varepsilon}_{\boldsymbol{x}}\left(\delta\boldsymbol{v}\right):\mathbb{C}^{\mathrm{el}}_{\mathrm{m}}(\boldsymbol{X},\,\boldsymbol{x};\,\mathscr{w}):\left[\boldsymbol{\varepsilon}_{\boldsymbol{X}}\left(\boldsymbol{U}_0(\boldsymbol{X};\,\mathscr{w})\right)+\boldsymbol{\varepsilon}_{\boldsymbol{x}}\left(\boldsymbol{U}_1(\boldsymbol{X},\,\boldsymbol{x};\,\mathscr{w})\right]d\boldsymbol{x}=0\,\forall\delta\boldsymbol{v}\in\mathcal{U}^{\mathrm{PBC}}(\omega)\,, \tag{180}$$

where we have used Eqs. (172) and (174) and the periodicity of ω which implies $\boldsymbol{\Sigma}_0(\boldsymbol{X},\,\boldsymbol{x}^-;\,\mathscr{w})\cdot\boldsymbol{n}_{\mathrm{m}}(\boldsymbol{x}^-)=-\boldsymbol{\Sigma}_0(\boldsymbol{X},\,\boldsymbol{x}^+;\,\mathscr{w})\cdot\boldsymbol{n}_{\mathrm{m}}(\boldsymbol{x}^+)$ for any pair $(\boldsymbol{x}^-,\,\boldsymbol{x}^+)$ of opposite points $\boldsymbol{x}^-\in\partial\omega^-$ and $\boldsymbol{x}^+\in\partial\omega^+$, see the notations of Fig. 27. As discussed by Kanouté et al. (2009); Fish et al. (1997), the problem (180) is solved by introducing a separation of variables through a third-order tensor $\overset{3}{\mathbb{H}}(\boldsymbol{X},\,\boldsymbol{x};\,\mathscr{w})$ –periodic on ω– such that

$$\boldsymbol{U}_1(\boldsymbol{x},\,\boldsymbol{X};\,\mathscr{w})=\overset{3}{\mathbb{H}}(\boldsymbol{X},\,\boldsymbol{x};\,\mathscr{w}):\boldsymbol{\varepsilon}_{\boldsymbol{X}}\left(\boldsymbol{U}_0(\boldsymbol{X};\,\mathscr{w})\right)\in\mathcal{U}^{\mathrm{PBC}}(\omega)\,, \tag{181}$$

with the constraint (158). Defining the fourth-order tensor $\mathbb{H}(\boldsymbol{X},\,\boldsymbol{x};\,\mathscr{w})$ such that $H_{ijkl}=\frac{1}{2}\frac{\partial}{\partial x_j}\overset{3}{H}_{ikl}+\frac{1}{2}\frac{\partial}{\partial x_i}\overset{3}{H}_{jkl}$, the problem (180) is stated as finding the periodic $\overset{3}{\mathbb{H}}(\boldsymbol{X},\,\boldsymbol{x};\,\mathscr{w})$ such that

$$\int_{\omega}\boldsymbol{\varepsilon}_{\boldsymbol{x}}\left(\delta\boldsymbol{v}\right):\mathbb{C}^{\mathrm{el}}_{\mathrm{m}}(\boldsymbol{X},\,\boldsymbol{x};\,\mathscr{w}):\left[\mathbb{I}+\mathbb{H}(\boldsymbol{X},\,\boldsymbol{x};\,\mathscr{w})\right]d\boldsymbol{x}=0\quad\forall\delta\boldsymbol{v}\in\mathcal{U}^{\mathrm{PBC}}(\omega)\,, \tag{182}$$

where $\mathbb{I}$ is the fourth-order identity tensor with $I_{ijkl}=\frac{1}{2}\delta_{ik}\delta_{jl}+\frac{1}{2}\delta_{il}\delta_{jk}$. We note that $\mathbb{H}$ (and thus $\mathbb{I}+\mathbb{H}$) possesses minor symmetry properties, *i.e.* $H_{ijkl}=H_{jilk}=H_{jikl}=H_{ijlk}$, but not necessarily major symmetry properties. The tensor $\mathbb{I}+\mathbb{H}$ is also called elastic strain concentration tensor. Assuming the solution $\overset{3}{\mathbb{H}}(\boldsymbol{X},\, \boldsymbol{x};\, \mathcal{w})$ of the problem (182) is known, Eq. (179) is rewritten as

$$\mathbf{\Sigma}_{\mathrm{M}}\left(\boldsymbol{X};\, \mathcal{w}\right) \;=\; \mathbb{C}^{\mathrm{el}}_{\mathrm{M}}(\boldsymbol{X};\, \mathcal{w}) : \boldsymbol{\varepsilon}_{\boldsymbol{X}}\left(\boldsymbol{U}_0(\boldsymbol{X};\, \mathcal{w})\right)\,, \tag{183}$$

with the apparent elastic properties

$$\mathbb{C}^{\mathrm{el}}_{\mathrm{M}}(\boldsymbol{X};\, \mathcal{w}) = \frac{1}{V(\omega)} \int_{\omega} \mathbb{C}^{\mathrm{el}}_{\mathrm{m}}(\boldsymbol{X},\, \boldsymbol{x};\, \mathcal{w}) : \left[\mathbb{I} + \mathbb{H}(\boldsymbol{X},\, \boldsymbol{x};\, \mathcal{w})\right] d\boldsymbol{x}\,. \tag{184}$$

Following Fish et al. (1994), multiplying (175) by the periodic $\overset{3}{\mathbb{H}}(\boldsymbol{X},\, \boldsymbol{x};\, \mathcal{w})$, integrating by parts on ω and making use of the periodicity on ω, yields

$$\int_{\omega} \mathbb{H}^{T}\left(\boldsymbol{X},\, \boldsymbol{x};\, \mathcal{w}\right) : \mathbb{C}^{\mathrm{el}}_{\mathrm{m}}(\boldsymbol{X},\, \boldsymbol{x};\, \mathcal{w}) : \left[\mathbb{I} + \mathbb{H}(\boldsymbol{X},\, \boldsymbol{x};\, \mathcal{w})\right] d\boldsymbol{x} = 0\,, \tag{185}$$

where $(H^T)_{ijkl} = H_{klij}$. Therefore, the apparent elastic properties (184) can then also be written

$$\mathbb{C}^{\mathrm{el}}_{\mathrm{M}}(\boldsymbol{X},\, \mathcal{w}) = \frac{1}{V(\omega)} \int_{\omega} \left[\mathbb{I} + \mathbb{H}(\boldsymbol{X},\, \boldsymbol{x};\, \mathcal{w})\right]^{T} : \mathbb{C}^{\mathrm{el}}_{\mathrm{m}}(\boldsymbol{X},\, \boldsymbol{x};\, \mathcal{w}) : \left[\mathbb{I} + \mathbb{H}(\boldsymbol{X},\, \boldsymbol{x};\, \mathcal{w})\right] d\boldsymbol{x}\,. \tag{186}$$

Finally, the system (182) is usually solved using a finite-element discretisation of the cell volume element as detailed in Appendix C.2.1.

Elasto-plasticity and damage. Fish et al. (1997) have extended the method in the case of elasto-plasticity. In elasto-plasticity, the constitutive law (171) of the multi-scale problem reads

$$\mathbf{\Sigma}_{\varepsilon}\left(\boldsymbol{X};\, \mathcal{w}\right) = \mathbb{C}^{\mathrm{el}}_{\varepsilon}(\boldsymbol{X};\, \mathcal{w}) : \left[\mathbf{E}_{\varepsilon}(\boldsymbol{X};\, \mathcal{w}) - \mathbf{M}_{\varepsilon}(\boldsymbol{X};\, \mathcal{w})\right]\,, \tag{187}$$

where $\mathbf{M}_{\varepsilon}(\boldsymbol{X};\, \mathcal{w})$ is the eigen-strain second-order tensor that characterises irreversible deformations, such as plastic strains. Therefore, a new expansion is considered

$$\mathbf{M}_{\varepsilon}(\boldsymbol{X};\, \mathcal{w}) = \sum_{i=0,\,1\ldots} \varepsilon^{i} \mathbf{M}_{i}\left(\boldsymbol{X},\, \boldsymbol{x};\, \mathcal{w}\right)\,, \tag{188}$$

where $\mathbf{M}_i$ for $i = 0$, ... is expressed explicitly in terms of the fine grid $\boldsymbol{x} = \frac{\boldsymbol{X}}{\varepsilon}$.

Therefore, the expansion (173) still holds, but the stress tensors (174) at the different scales are rewritten

$$\mathbf{\Sigma}_{i}\left(\boldsymbol{X},\, \boldsymbol{x};\, \mathcal{w}\right) = \mathbb{C}^{\mathrm{el}}_{\mathrm{m}}(\boldsymbol{X},\, \boldsymbol{x};\, \mathcal{w}) : \left[\mathbf{E}_{i}\left(\boldsymbol{X},\, \boldsymbol{x};\, \mathcal{w}\right) - \mathbf{M}_{i}\left(\boldsymbol{X},\, \boldsymbol{x};\, \mathcal{w}\right)\right]\,, \tag{189}$$

the latter equation being obtained as a local rewriting of Eq. (187), with $\mathbf{E}_i\left(\boldsymbol{X},\, \boldsymbol{x};\, \mathcal{w}\right)$ given by Eq. (172).

Following the details provided in Appendix C.2.2, the homogenised stress tensor (179) then follows as

$$\boldsymbol{\Sigma}_{\mathrm{M}}\left(\boldsymbol{X};\, \mathscr{w}\right) \;=\; \mathbb{C}^{\mathrm{el}}_{\mathrm{M}}(\boldsymbol{X},\, \mathscr{w}) : \left[\boldsymbol{\varepsilon}_{\boldsymbol{X}}\left(\boldsymbol{U}_0(\boldsymbol{X};\, \mathscr{w})\right) - \mathbf{M}_{\mathrm{M}}(\boldsymbol{X};\, \mathscr{w})\right] \,, \tag{190}$$

where $\boldsymbol{\varepsilon}_{\boldsymbol{X}}\left(\boldsymbol{U}_0(\boldsymbol{X};\, \mathscr{w})\right) = \boldsymbol{\varepsilon}_{\mathrm{M}}(\boldsymbol{X};\, \mathscr{w})$, and where the overall eigen-strain $\mathbf{M}_{\mathrm{M}}(\boldsymbol{X};\, \mathscr{w})$ reads

$$\begin{aligned}&\mathbf{M}_{\mathrm{M}}(\boldsymbol{X};\, \mathscr{w}) = \\ &{\mathbb{C}^{\mathrm{el}}_{\mathrm{M}}}^{-1}(\boldsymbol{X};\, \mathscr{w}) : \frac{1}{V(\omega)}\int_{\omega}\left[\mathbb{H}^{T}(\boldsymbol{X},\, \boldsymbol{x};\, \mathscr{w}) + \mathbb{I}\right] : \mathbb{C}^{\mathrm{el}}_{\mathrm{m}}(\boldsymbol{X},\, \boldsymbol{x};\, \mathscr{w}) : \mathbf{M}_0(\boldsymbol{X},\, \boldsymbol{x};\, \mathscr{w}) d\boldsymbol{x} \,.\end{aligned} \tag{191}$$

In this case, the method involves a model order reduction which bears similarity with the Transform Field Analysis: the eigen-strains $\mathbf{M}_0\left(\boldsymbol{X},\, \boldsymbol{x};\, \mathscr{w}\right)$ are approximated using the separation of variables

$$\mathbf{M}_0\left(\boldsymbol{X},\, \boldsymbol{x};\, \mathscr{w}\right) = \sum_{k} h^{(k)}(\boldsymbol{x})\mathbf{M}^{(k)}(\boldsymbol{X};\, \mathscr{w}) \,, \tag{192}$$

where $\{h^{(k)}(\boldsymbol{x})\}$ is a set of C^{-1} continuous functions. In practice, piece-wise continuous functions on some elements or clusters of elements $\delta\omega^{(k)}$ in the cell volume element ω can be considered, in which case the functions $h^{(k)}$ are the spatial indicators (60). For these particular functions, as detailed in Appendix C.2.3, the macro-stress tensor reads

$$\boldsymbol{\Sigma}_{\mathrm{M}}\left(\boldsymbol{X};\, \mathscr{w}\right) = \mathbb{C}^{\mathrm{el}}_{\mathrm{M}}(\boldsymbol{X};\, \mathscr{w}) : \boldsymbol{\varepsilon}_{\boldsymbol{X}}\left(\boldsymbol{U}_0(\boldsymbol{X};\, \mathscr{w})\right) + \sum_{k} \mathbb{S}^{\delta\omega^{(k)}}_{\mathrm{M}}(\boldsymbol{X};\, \mathscr{w}) : \mathbf{M}^{\delta\omega^{(k)}}\left(\boldsymbol{X};\, \mathscr{w}\right) \,. \tag{193}$$

In this equation, the apparent elastic tensor $\mathbb{C}^{\mathrm{el}}_{\mathrm{M}}(\boldsymbol{X};\, \mathscr{w})$ results from Eq. (184), whilst the inelastic influence tensors from

$$\mathbb{S}^{\delta\omega^{(k)}}_{\mathrm{M}}(\boldsymbol{X};\, \mathscr{w}) = \frac{1}{V(\omega)}\int_{\omega}\mathbb{C}^{\mathrm{el}}_{\mathrm{m}}(\boldsymbol{X},\, \boldsymbol{x};\, \mathscr{w}) : \left[\mathbb{D}^{\delta\omega^{(k)}}(\boldsymbol{X},\, \boldsymbol{x};\, \mathscr{w}) - \mathbb{I}_{\delta\omega^{(k)}}(\boldsymbol{x})\right] d\boldsymbol{x} \,, \tag{194}$$

with the eigen-strain influence functions

$$\begin{aligned}\mathbb{D}^{\delta\omega^{(k)}}(\boldsymbol{X},\, \boldsymbol{x};\, \mathscr{w}) \;=\;& \frac{V\left(\delta\omega^{(k)}\right)}{V(\omega)}\mathbb{H}(\boldsymbol{X},\, \boldsymbol{x};\, \mathscr{w}) : \left[\mathbb{C}^{\mathrm{Voigt}}(\boldsymbol{X};\, \mathscr{w}) - \mathbb{C}^{\mathrm{el}}_{\mathrm{M}}(\boldsymbol{X};\, \mathscr{w})\right]^{-1} : \\ & \frac{1}{V\left(\delta\omega^{(k)}\right)}\int_{\delta\omega^{(k)}}\mathbb{H}^{T}(\boldsymbol{x};\, \mathscr{w}) : \mathbb{C}^{\mathrm{el}}_{\mathrm{m}}(\boldsymbol{X},\, \boldsymbol{x};\, \mathscr{w}) d\boldsymbol{x} \,,\end{aligned} \tag{195}$$

and the indicator tensors

$$\mathbb{I}_{\delta\omega^{(k)}}(\boldsymbol{x}) = \begin{cases}\mathbb{I} & \text{if } \boldsymbol{x} \in \delta\omega^{(k)} \,, \\ 0 & \text{if } \boldsymbol{x} \notin \delta\omega^{(k)} \,.\end{cases} \tag{196}$$

In this formulation, both $\mathbb{C}^{\mathrm{el}}_{\mathrm{M}}(\boldsymbol{X};\, \mathscr{w})$ and $\mathbb{S}^{\delta\omega^{(k)}}_{\mathrm{M}}(\boldsymbol{X};\, \mathscr{w})$ can be computed off-line, whilst the tensors $\boldsymbol{\mu}^{\delta\omega^{(k)}}\left(\boldsymbol{X}\right) = \mathbf{M}^{\delta\omega^{(k)}}\left(\boldsymbol{X};\, \mathscr{w}\right)$ are the average inelastic strains on the clusters $\delta\omega^{(k)}$ and are locally solved in-line at the micro-scale using the constitutive material law

$$\boldsymbol{\sigma}^{\delta\omega^{(k)}}_{\mathrm{m}} = \boldsymbol{\sigma}^{\delta\omega^{(k)}}_{\mathrm{m}}\left(\boldsymbol{\varepsilon}^{\delta\omega^{(k)}}_{0}\left(\boldsymbol{X}\right);\, \boldsymbol{\mu}^{\delta\omega^{(k)}}\left(\boldsymbol{X};\, \tau \in [0,\, t]\right),\, \mathscr{w}\right) \,, \tag{197}$$

and the expression of average strain tensors $\boldsymbol{\varepsilon}_0^{\delta\omega^{(k)}}(\boldsymbol{X}) = \mathbf{E}_0^{\delta\omega^{(l)}}(\boldsymbol{X};\,\mathfrak{w})$ on the clusters $\delta\omega^{(k)}$, which involves the different $\boldsymbol{\mu}^{\delta\omega^{(l)}}(\boldsymbol{X})$ following next equations, see Appendix C.2.3 for details. The average strain on cluster $\delta\omega^{(l)}$ results from

$$\mathbf{E}_0^{\delta\omega^{(l)}}(\boldsymbol{X};\,\mathfrak{w}) \;=\; \mathbb{A}^{\delta\omega^{(l)}}(\boldsymbol{X};\,\mathfrak{w}) : \boldsymbol{\varepsilon}_{\boldsymbol{X}}\left(\boldsymbol{U}_0(\boldsymbol{X};\,\mathfrak{w})\right) + \sum_k \mathbb{D}^{\delta\omega^{(l)}\,\delta\omega^{(k)}}(\boldsymbol{X};\,\mathfrak{w}) : \mathbf{M}^{\delta\omega^{(k)}}(\boldsymbol{X};\,\mathfrak{w})\;, \tag{198}$$

with

$$\mathbb{A}^{\delta\omega^{(l)}}(\boldsymbol{X};\,\mathfrak{w}) \;=\; \frac{1}{V\left(\delta\omega^{(l)}\right)}\int_{\delta\omega^{(l)}} \left[\mathbb{I} + \mathbb{H}(\boldsymbol{X},\,\boldsymbol{x};\,\mathfrak{w})\right] d\boldsymbol{x}\,, \text{ and} \tag{199}$$

$$\mathbb{D}^{\delta\omega^{(l)}\,\delta\omega^{(k)}}(\boldsymbol{X};\,\mathfrak{w}) \;=\; \frac{1}{V\left(\delta\omega^{(l)}\right)}\int_{\delta\omega^{(l)}} \mathbb{D}^{\delta\omega^{(k)}}(\boldsymbol{X},\,\boldsymbol{x};\,\mathfrak{w})d\boldsymbol{x}\,. \tag{200}$$

The formulation has been extended to finite strains by Fish and Shek (1999), Fish et al. (1999) have then considered damage-enhanced elasticity, Oskay and Fish (2007) have also included interface separation between the clusters, and Yuan and Fish (2009) have considered a hierarchical formulation involving multiple scales.

Stochastic AH. Fish and Wu (2011) have used this formalism to account for uncertainties (i) in the elastic constitutive parameters $\mathbb{C}_{\mathrm{m}}^{\mathrm{el}}(\boldsymbol{X},\,\boldsymbol{x};\,\mathfrak{w})$, (ii) in the inelastic parameters of the constitutive law (197), or (iii) in the geometrical parameters, such as volume fraction, of the unit cell $\omega(\boldsymbol{X};\,\mathfrak{w})$. On the one hand, when the elastic constitutive parameters $\mathbb{C}_{\mathrm{m}}^{\mathrm{el}}(\boldsymbol{X},\,\boldsymbol{x};\,\mathfrak{w})$ or the geometrical description are considered as uncertain, the influence functions $\mathbb{C}_{\mathrm{M}}^{\mathrm{el}}(\boldsymbol{X};\,\mathfrak{w})$, $\mathbb{S}_{\mathrm{M}}^{\delta\omega^{(k)}}(\boldsymbol{X};\,\mathfrak{w})$, $\mathbb{A}^{\delta\omega^{(l)}}(\boldsymbol{X};\,\mathfrak{w})$, and $\mathbb{D}^{\delta\omega^{(l)}\,\delta\omega^{(k)}}(\boldsymbol{X};\,\mathfrak{w})$ have to be recomputed for each realisation $\mathfrak{w}$. On the other hand, when only the inelastic properties of the constitutive law (197) change, the influence functions are constant. Besides, two cases were considered by Fish and Wu (2011): on the one hand, in the case of a random field, the properties can vary from one unit cell $\omega(\boldsymbol{X};\,\mathfrak{w})$ to the other, and on the other hand, in the case of random variables, the properties are uniform on Ω.

In this context of stochastic asymptotic homogenisation in which the fine-scale and coarse scale resolutions are concurrent, Fish and Wu (2011) generated the random fields corresponding to fine-scale constitutive inelastic parameters of the constitutive law (197) using KL expansion, see Appendix A.3.2. Elastic and micro-structural properties were considered as random variables.

4.2.3. Reduced order models (ROMs) & Neural Networks (NNWs) as surrogates

Because when considering computational homogenisation, the response of the SVEs have to be obtained by full-field analyses, the computation cost can become high in the non-linear range. This important computational cost is however alleviated when the SVE analyses can be conducted pre-off-line in order to define the meso-scale random fields, as it will be seen in Section 5.1, allowing for a highly scalable parallelisation of the process. Nevertheless, the cost can remain too high for complex 3D micro-structures.

Therefore, research has been carried on in the context of model order reduction, data-driven analyses and surrogate models.

Reduced Order Models. A Reduced Order Model (ROM) aims at providing an efficient homogenisation process with a reduced version of the full-field analysis. This usually trades space for time by relying on pre-off-line computations. The purpose of this section is to provide a brief review of the existing methods, and is by no means exhaustive.

Reduced versions of models can be created by projection of the governing equations into suitably selected sub-spaces based on the acquired information from pre-off-line computations performed on a finite-element discretisation of the meso-scale volume. In the case of computational homogenisation, the reduced number of unknown variables is defined by means of proper orthogonal decomposition (POD) of the displacement field (135) –or of its fluctuation part– as suggested by Yvonnet and He (2007). In this context, the equilibrium equations (136) of the meso-scale volume are projected in a basis of reduced size, which speeds up the resolution process of the meso-scale volume equilibrium. The basis can also be defined from the discrete strain energy of the system by modifying the POD norm definition as proposed by Goury et al. (2016). A further order reduction, see the work by Hernández et al. (2014); Soldner et al. (2017); Caicedo et al. (2019), is called hyper-reduction and aims at reducing the computations of the internal forces (137) and tangent matrix (138) evaluations. The idea behaind this hyper-reduction is to evaluate the constitutive laws at a reduced set of points or elements within the meso-scale material domain. Soldner et al. (2017) have compared the different projection-based ROMs in computational homogenisation.

In the context of POD-based ROM, a basis is defined from pre-off-line sampling of the meso-scale volume element responses obtained for different paths of the macro-scale kinematic variable $\mathbf{f}_{\mathrm{M}}$. This defines the so-called snapshots that are used to conduct the POD. The difficulty is to select the loading paths so that the snapshots are varied enough for the built reduced basis to represent with a controlled error a wide variety of solutions corresponding to arbitrary loading conditions. Goury et al. (2016) have suggested to define random walks as loading paths with a given norm of the strain increment. Snapshots can be enriched by considering new loading paths, for which the evaluation of the direct solution is required, if the error of the ROM on test data is not found to be low enough. In order to increase the efficiency of the loading paths sampling, as an alternative to this “brute force” method, Goury et al. (2016) have defined a sequence of random loading paths spaces starting from monotonic loading of random direction (lower degree space) and subsequently increasing the number of changes of direction in a loading path realisation (space of degree 1 has one change of direction per path *etc.*). This sequence of random loading spaces makes it possible to infer which level of refinement is necessary in order to build a ROM with a required accuracy; *i.e.* when a ROM constructed from snapshots of the space of degree n can represent a solution in the space of degree $n + 1$. In order to select the snapshots, for which the evaluation of the direct solution is required, in the space of a given degree n that will be used to construct the ROM, a Gaussian process regression of an error indicator is built, and used to infer the loading path which maximises the error indicator through a Bayesian optimisation. This new loading path thus enriches the loading path sampling space of degree n by a new snapshot located in a region of potential error of the model and thus allows constructing a ROM of a given error from a limited number of evaluations of the direct solution.

ROMs can also be based on micro-mechanics models involving much less variables. The computation of the influence function in the asymptotic homogenisation method presented in Section 4.2.2 in combination to the reduction (192), which derives from the Uniform Transform Field Analysis (TFA) developed by Dvorak (1992); Dvorak et al. (1994), belongs to this category. Order reduction was achieved by Michel and Suquet (2009) in the nonuniform transformation field analysis (NTFA) by using the pre-defined internal variables modes obtained from pre-off-line full-field analyses. Michel and Suquet (2016) have then applied a tangent second-order (TSO) expansion of the dissipation potential, which corresponds to a reduction of the evolution equations related to the reduced internal variables. Fritzen and Leuschner (2013) have developed an alternative to the TSO-expansion by extending the NTFA in terms of a potential-based Reduced Basis Model Order Reduction (pRBMOR), which provides the evolution law for the reduced degrees of freedom from a mixed incremental variational principle. Fritzen and Hodapp (2016) have then combined this approach with a GPU acceleration.

ROMs can also be obtained by dividing the volume element phases into clusters of similar strains obtained through full-field analyses. Wulfinghoff et al. (2018); Cavaliere et al. (2020) have used a Hashin-Shtrikman analysis of the clusters but the method is limited to non-linear reversible behaviours and requires the definition of a homogeneous reference stiffness. Liu et al. (2016, 2018) have defined the clusters from linear analyses and applied a self-consistent homogenisation of the non-linear clusters response with constant internal variables per cluster. In this so-called Self-Clustering Analysis (SCA), during the on-line stage, the Lippmann-Schwinger equation is used as coupling equation between the clusters. The interaction between the clusters is defined by influence functions expressed by the Green's function of a selected homogeneous material corresponding, either to a reference material, or to the continuously updated self-consistent homogeneous and isotropic stiffness. Huang et al. (2021) have used the SCA to study the impact of fibre volume fraction and waviness variations on UD laminate compression response.

Data-driven methods and deep material networks. Liu et al. (2019); Liu and Wu (2019) have developed the so-called deep material network (DMN) approach as a homogenisation method based on analytical micro-mechanics models, such as laminate theory, defining mechanistic building blocks, the latter being organised in a binary hierarchical topological structure. During the training process defined from homogenised elasticity tensors of a fixed microstructure with different elastic properties, the DMN "learns" the weight ratio and interactions of the building blocks. Once trained, the DMN is able to predict non-linear responses through a forward homogenisation process and a backward de-homogenisation process of the linearisation of the stress-strain behaviour. Accurate results were obtained in the non-linear range although only linear elastic data were used during the offline training. The reason of this good handling of extrapolation was theoretically explained by Gajek et al. (2020). Nguyen and Noels (2022) have provided an efficient implementation of the forward homogenisation process and a backward de-homogenisation process for arbitrary tree structures and Nguyen and Noels (2021) have removed the laminate assumption in order to account for evolving micro-structures like in porous materials. More complex micro-mechanical models such as mean-field homogenisation can also be used in the mechanistic building blocks as proposed by Wu et al. (2021) for woven composite materials, which allowed reducing the needed number of blocks to a few couples.

Data-driven methods and surrogate models. Recently, data-driven approaches have seen an increasing popularity, in which the data are numerically obtained from the resolution of the meso-scale volume elements.

Conducting off-line non-linear simulations in order to extract homogenised stress-strain responses through computational homogenisation, see Section 4.2.1, is also a way of building a synthetic data-base that can be used to construct surrogate models of the inelastic response of the meso-scale volume elements. This synthetic data-base was used by Xu et al. (2020) to conduct data-driven and model-free analyses (Kirchdoerfer and Ortiz, 2016; Eggersmann et al., 2019).

This synthetic data-base can alternatively be used to build surrogate models, which basically consist into mapping functions. Surrogate models can be of different natures. Wirtz et al. (2015) have built such a surrogate using kernel methods, Perrin et al. (2012) have used the polynomial chaos expansion *etc.* Omairey et al. (2019) have considered a polynomial regression fit to represent the relationship between uncertainties and their effect on apparent elastic properties of UD composites using data points obtained by computational homogenisation. Recently the use of neural-networks as surrogates has seen a fast growing interest. In that context, the synthetic data-base is used to train the NNWs, which serve as surrogate either of the homogenised strain energy surface from which the stress-strain can be derived as proposed by Le et al. (2015); Bessa et al. (2017), of directly the stress-strain response as in the works by Fritzen et al. (2019); Yang et al. (2019), or of a function of both the current stress and the plastic dissipation density as suggested by Zhang and Mohr (2020).

In the context of reversible behaviours, *i.e.* linear elasticity or nonlinear elasticity, feed-forward NNWs, for which the information moves only along the forward direction, are usually used. However, in the case of history-dependent behaviours, *e.g.* plasticity, there is an extra-difficulty with feed-forward NNW, in both the ANN architecture and offline training, since the information moves only along one direction, which cannot account for complex loading conditions, *e.g.* unloading, reloading. Although Huang et al. (2020) have enriched feed-forward NNWs by variables corresponding to the strain paths, *e.g.* length of strain paths, in order to introduce the history-dependency, the alternative of Recurrent Neural Network (RNN) was shown by Mozaffar et al. (2019); Gorji et al. (2020); Ghavamian and Simone (2019); Wu et al. (2020a); Logarzo et al. (2021) to be efficient and accurate in approximating the history-dependent homogenised stress-strain relationships, because of their ability to account for the information about what has been computed so far. Indeed, RNNs make use of sequential information: they are called recurrent because they perform the same task on every step input of a sequence, with the output being dependent on the previous evaluations. They thus exhibit a “memory”, which captures information about what has been calculated so far. Nevertheless, their training requires a synthetic data-base which covers enough possible loading history paths. The generation of this data-base thus requires to introduce some stochasticity in the loading paths, either under the form of Gaussian process as suggested by Mozaffar et al. (2019), cubic-spline interpolations as conducted by Gorji et al. (2020), or more generally under the form of a random walk as developed by Wu et al. (2020a). We refer to the recent review by Rocha et al. (2020) for a critical comparison in the context of composite materials. Wu and Noels (2022) have combined recurrent neural networks with dimensionality reduction for high dimensional mechanical problems. In this context, beside the macro-stressmacro-strain response of the meso-scale boundary value problem, the state field distribution at the micro-structure level could also be recovered for complex loading scenarios.

Stochastic surrogate models. ROM and NNW-based mappings offer the opportunity to build stochastic surrogate models that can be used to propagate uncertainties. In the context of stochastic finite elasticity, a ROM was built by Clément et al. (2012); Yvonnet et al. (2013) from the resolution of SVEs, which are called composite material elementary cells, by defining a meso-scale potential capturing the uncertainties related to the fibres geometry/distribution in composites. Rao and Liu (2020) have trained a three-dimensional deep convolution neural network (3D-CNN) using a data-set consisting of spherical inclusion micro-structure images and of the predicted homogenised elasticity tensors obtained by computational homogenisation. It was shown that the 3D-CNN is able to predict the anisotropic effective material properties of micro-structures with random inclusions. In the context of non-linear electrical conduction, Lu et al. (2021) have developed a hybrid neural-networkinterpolation. Assuming deterministic effective properties at the microscopic scale with respect to the microstructure for a given volume fraction, the hybrid neural-network-interpolation was build by interpolating data-set obtained at given volume fractions. At the macro-scale, uncertainties related to non-homogeneous distributions of volume fractions could then be accounted for in non-linear analysis by using the hybrid neural-networkinterpolation as a stochastic meso-scale surrogate.

Clearly, the use of NNW as surrogate is a promising way of achieving stochastic multi-scale methods, providing they can be trained with a rich enough synthetic data-base. This creation of a data base requires a large number of direct numerical simulations of the meso-scale volume elements (or a large number of experiments), which can be overwhelming. One solution is to rely on interpolation in the parameter range as with the hybrid neural-network-interpolation method, or to use ROMs to construct the off-line simulation data-base needed for data-driven macro-scale analyses Bessa et al. (2017).

4.2.4. Mean-Field Homogenisation (MFH)

The MFH approach is a computationally efficient semi-analytical framework for the homogenisation of 2-phase composites developed using different extensions of the Eshelby (1957) single inclusion solution to account for the multiple-inclusion interactions. The most popular extensions are the Mori-Tanaka (Mori and Tanaka, 1973; Benveniste, 1987) and the self-consistent (Kröner, 1958; Hill, 1965b) schemes.

By opposition to the computational homogenisation framework described in Section 4.2.1, the microstructure is not explicitly represented but defined from the phases material properties, the phases volume fractions and either from the inclusions geometrical shape, see Fig. 27(d), or from their spatial correlation (Ponte Castañeda and Willis, 1995). The homogenisation framework is then formulated by a series of equations, completed by the knowledge of phases properties, that can be solved iteratively.

Although it can provide accurate prediction of the homogenised behaviour in some cases, MFH relies on some assumptions and is thus not as general as computational homogenisation. Nevertheless, it provides a computationally affordable solution, which can also be seen as a ROM, and that will be further used in a multi-fidelity approach in Section 5.4.

Generalities on the MFH for two-phase composites. Considering a realisation $\mathcal{w} \in \mathcal{W}$ of the micro-structure $\omega(\boldsymbol{X};\, \mathcal{w})$ and a two-phase composite material with the respective volume fractions $V_0(\mathcal{w}) + V_{\mathrm{I}}(\mathcal{w}) = 1$ (subscript 0 refers to the matrix and I to the inclusions), the volume average over the volume element $\omega(\boldsymbol{X};\, \mathcal{w})$ is explicitly expressed in terms of the volume averages over the two phases $\omega_0(\boldsymbol{X};\, \mathcal{w})$ and $\omega_{\mathrm{I}}(\boldsymbol{X};\, \mathcal{w})$, with

$$\mathbf{E}_{\mathrm{M}}(\mathcal{w}) = V_0(\mathcal{w})\frac{1}{V(\omega_0)}\int_{\omega_0} \mathbf{E}_{\mathrm{m}}(\boldsymbol{x};\, \mathcal{w})d\boldsymbol{x} + V_{\mathrm{I}}(\mathcal{w})\frac{1}{V(\omega_{\mathrm{I}})}\int_{\omega_{\mathrm{I}}} \mathbf{E}_{\mathrm{m}}(\boldsymbol{x};\, \mathcal{w})d\boldsymbol{x}\,, \text{ and} \tag{201}$$

$$\boldsymbol{\Sigma}_{\mathrm{M}}(\mathcal{w}) = V_0(\mathcal{w})\frac{1}{V(\omega_0)}\int_{\omega_0} \boldsymbol{\Sigma}_{\mathrm{m}}(\boldsymbol{x};\, \mathcal{w})d\boldsymbol{x} + V_{\mathrm{I}}(\mathcal{w})\frac{1}{V(\omega_{\mathrm{I}})}\int_{\omega_{\mathrm{I}}} \boldsymbol{\Sigma}_{\mathrm{m}}(\boldsymbol{x};\, \mathcal{w})d\boldsymbol{x}\,. \tag{202}$$

For conciseness, in the following volume integrals, we note the volume element realization $\omega = \omega(\boldsymbol{X};\, \mathcal{w})$, in which we omit the reference to $\mathcal{w}$, but it is understood that the homogenized response is micro-structure dependent. The key-point of the MFH method is to define the relation between the strain averages in the different phases, using a strain concentration tensor $\mathbb{B}^{\epsilon}(\mathcal{w})$. For linear material systems, this implies

$$\bar{\mathbf{E}}_{\mathrm{I}}(\mathcal{w}) = \mathbb{B}^{\epsilon}(\mathrm{I}(\mathcal{w}), \mathbb{C}_0^{\mathrm{el}}(\mathcal{w}),\, \mathbb{C}_{\mathrm{I}}^{\mathrm{el}}(\mathcal{w})) : \bar{\mathbf{E}}_0(\mathcal{w})\,, \tag{203}$$

where $\mathrm{I}(\mathcal{w})$ represents the equivalent inclusion realisation in terms of geometry, $\mathbb{C}_i^{\mathrm{el}}(\mathcal{w})$ is the elastic stiffness tensor in phase $\omega_i(\mathcal{w})$, and where we have used $\bar{\bullet}_i$ to represent the volume average over the phase $\omega_i(\mathcal{w})$, *i.e.* $\frac{1}{V(\omega_i)}\int_{\omega_i} \bullet_{\mathrm{m}}(\boldsymbol{x};\, \mathcal{w})d\boldsymbol{x}$, for conciseness. Note that $\bar{\bullet}_i$ represents the first statistical value estimate of the field $\bullet$. A popular approach to define the strain concentration tensor $\mathbb{B}^{\epsilon}(\mathcal{w})$ is to extend the single inclusion solution of Eshelby (1957) to multiple inclusions interacting in an average way. Common homogenisation schemes are

- The Voigt model assumes the same average strain in the two phases. This hypothesis leads to the following strain concentration tensor:

$$\mathbb{B}^{\epsilon}(\mathcal{w}) = \mathbb{I}\,; \tag{204}$$

- The Reuss model considers that the average stress is the same in the two phases. Consequently, the following expression arises:

$$\mathbb{B}^{\epsilon}(\mathcal{w}) = \left(\mathbb{C}_{\mathrm{I}}^{\mathrm{el}}(\mathcal{w})\right)^{-1} : \mathbb{C}_0^{\mathrm{el}}(\mathcal{w})\,; \tag{205}$$

- The Mori and Tanaka (1973) method (M-T), in which the average strain in the matrix phase of the multiple-inclusion composite material corresponds to the strain at infinity of the single inclusion problem, results in

$$\mathbb{B}^{\epsilon}(\mathrm{I}(\omega), \mathbb{C}_0^{\mathrm{el}}(\omega),\, \mathbb{C}_{\mathrm{I}}^{\mathrm{el}}(\omega)) = \{\mathbb{I} + \mathbb{Y}(\omega) : [(\mathbb{C}_0^{\mathrm{el}})^{-1}(\omega) : \mathbb{C}_{\mathrm{I}}^{\mathrm{el}}(\omega) - \mathbb{I}]\}^{-1}\,, \tag{206}$$

  where the Eshelby (1957) tensor $\mathbb{Y}(\mathrm{I}(\omega),\, \mathbb{C}_0^{\mathrm{el}}(\omega))$ depends on the geometry of the inclusion $\mathrm{I}(\omega)$ and on the elastic tensor of the matrix phase $\mathbb{C}_0^{\mathrm{el}}(\omega)$.

Non-linear MFH. Being computationally efficient, MFH methods were extensively developed to account for non-linear material behaviours. In such cases, the linear equations are applied on a so-called linear comparison composite (LCC) Talbot and Willis (1985, 1987); Ponte Castañeda (1991, 1992); Talbot and Willis (1992); Doghri and Ouaar (2003); Molinari et al. (2004); Doghri et al. (2010); Wu et al. (2013a). This LCC is defined as a virtual composite material whose constituents linear behaviours behave similarly to the linearised behaviours of the real constituents at given stress-strain states.

For non-linear material systems, Eqs. (201-202) are rewritten

$$\begin{aligned} \Delta\mathbf{E}_{\mathrm{M}}(\omega) &= V_0(\omega)\Delta\bar{\mathbf{E}}_0(\omega) + V_{\mathrm{I}}(\omega)\Delta\bar{\mathbf{E}}_{\mathrm{I}}(\omega)\,, \text{ and} && (207)\\ \mathbf{\Sigma}_{\mathrm{M}}(\omega) &= V_0(\omega)\bar{\mathbf{\Sigma}}_0(\omega) + V_{\mathrm{I}}(\omega)\bar{\mathbf{\Sigma}}_{\mathrm{I}}(\omega)\,, && (208)\end{aligned}$$

and the strain concentration tensor is constructed using a linear comparison composite (LCC), yet to be defined, which represents the linearized behaviour of the composite material phases through their virtual elastic operators, *i.e.* $\hat{\mathbb{C}}_0^{\mathrm{LCC}}(\omega)$ for the matrix phase and $\hat{\mathbb{C}}_{\mathrm{I}}^{\mathrm{LCC}}(\omega)$ for the inclusions phase. Equation (203) is thus rewritten

$$\Delta\bar{\mathbf{E}}_{\mathrm{I}}(\omega) = \mathbb{B}^{\epsilon}\left(\mathrm{I}(\omega), \hat{\mathbb{C}}_0^{\mathrm{LCC}}(\omega),\, \hat{\mathbb{C}}_{\mathrm{I}}^{\mathrm{LCC}}(\omega)\right) : \Delta\bar{\mathbf{E}}_0(\omega)\,. \tag{209}$$

Depending on the assumptions behind the definition of the LCC, the tensors $\hat{\mathbb{C}}_0^{\mathrm{LCC}}(\omega)$ and $\hat{\mathbb{C}}_{\mathrm{I}}^{\mathrm{LCC}}(\omega)$ are constructed in different ways. However, they are constructed in such a way that they are uniform over each phase, hence the $\hat{\bullet}_i$ notation. In the secant method developed by Berveiller and Zaoui (1978) the material is linearized as $\bar{\mathbf{\Sigma}}_i(\omega) = \hat{\mathbb{C}}_i^{\mathrm{sec}}(\omega) : \bar{\mathbf{E}}_i(\omega)$, in which case only monotonic loading conditions can be considered. In the incremental-tangent formulation pioneered by Hill (1965a) and developed by Pettermann et al. (1999); Doghri and Ouaar (2003), the non-linear material is linearized as $d\bar{\mathbf{\Sigma}}_i(\omega) = \hat{\mathbb{C}}_i^{\mathrm{tan}}(\omega) : d\bar{\mathbf{E}}_i(\omega)$, where $\hat{\mathbb{C}}_i^{\mathrm{tan}}(\omega)$ is an elasto-plastic tangent operator, allowing considering unloading. In the affine method, which was first proposed by Molinari et al. (1987, 2004) for visco-plastic materials, see also the work by Pierard and Doghri (2006); Doghri et al. (2010), the material is linearized using a polarisation stress $\mathbf{M}_i(\omega)$ as $\bar{\mathbf{\Sigma}}_i(\omega) = \hat{\mathbb{C}}_i(\omega) : \bar{\mathbf{E}}_i(\omega) + \mathbf{M}_i(\omega)$, where $\hat{\mathbb{C}}_i(\omega)$ can be different from the tangent moduli. Wu et al. (2013a,b) have also developed the incremental-secant formulation, which contrarily to the secant method allows considering cyclic loading, by defining the LCC and the operators $\hat{\mathbb{C}}_i^{\mathrm{LCC}}(\omega)$ from a virtually unloaded state of the composite material. This last definition of the LCC has several advantages as compared to other formulations. First, the isotropization step required by the affine and incremental-tangent methods as discussed by Chaboche et al. (2005) is avoided because the secant operators are naturally isotropic. Second, the method has a better accuracy in the case of non-proportional loading as shown by Wu et al. (2013a) and in the case of damage-enhanced elasto-plasticity since the virtual unloading step allows capturing a phase elastic unloading during softening of another one as illustrated by Wu et al. (2013b).

With the first statistical moments formula, the equivalent von Mises stresses and equivalent increment strains, corresponding to the averaged stress and strain tensors in the phases ω_{i}, are evaluated as

$$\hat{\Sigma}_i^{\mathrm{eq}}(w) = \sqrt{\frac{3}{2}\frac{1}{V(\omega_i)}\int_{\omega_i}\boldsymbol{\Sigma}(\boldsymbol{x};\, w)d\boldsymbol{x} : \mathbb{I}^{\mathrm{dev}} : \frac{1}{V(\omega_i)}\int_{\omega_i}\boldsymbol{\Sigma}(\boldsymbol{x};\, w)d\boldsymbol{x}} \tag{210}$$

$$\text{and}\quad \Delta\hat{E}_i^{\mathrm{eq}}(w) = \sqrt{\frac{2}{3}\frac{1}{V(\omega_i)}\int_{\omega_i}\Delta\mathbf{E}(\boldsymbol{x};\, w)d\boldsymbol{x} : \mathbb{I}^{\mathrm{dev}} : \frac{1}{V(\omega_i)}\int_{\omega_i}\Delta\mathbf{E}(\boldsymbol{x};\, w)d\boldsymbol{x}}\,, \tag{211}$$

where $\mathbb{I}^{\mathrm{dev}}$ is the deviatoric fourth-order tensor. However, when considering the first statistical moment values in the different phases when predicting their plastic flow, the plastic yield is not always accurately captured in some material systems such as short fibres composite materials, as discussed by Moulinec and Suquet (2003). In order to improve the predictions, MFH was enriched by accounting for the second statistical moment estimates $\frac{1}{V(\omega_i)}\int_{\omega_i}\bullet\otimes\bullet d\boldsymbol{x}$ of field $\bullet$. The second statistical moment estimate of the equivalent strain increment in phase ω_i reads

$$\Delta\hat{\hat{E}}_i^{\mathrm{eq}}(w) = \sqrt{\frac{2}{3}\mathbb{I}^{\mathrm{dev}} :: \frac{1}{V(\omega_i)}\int_{\omega_i}\Delta\mathbf{E}_{\mathrm{m}}(\boldsymbol{x};\, w)\otimes\Delta\mathbf{E}_{\mathrm{m}}(\boldsymbol{x};\, w)d\boldsymbol{x}}\,, \tag{212}$$

and the second statistical moment estimate of the equivalent stress increment in the phase ω_i reads

$$\Delta\hat{\hat{\Sigma}}_i^{\mathrm{eq}}(w) = \sqrt{\frac{3}{2}\mathbb{I}^{\mathrm{dev}} :: \frac{1}{V(\omega_i)}\int_{\omega_i}\Delta\boldsymbol{\Sigma}_{\mathrm{m}}(\boldsymbol{x};\, w)\otimes\Delta\boldsymbol{\Sigma}_{\mathrm{m}}(\boldsymbol{x};\, w)d\boldsymbol{x}}\,. \tag{213}$$

In particular, the second statistical moment estimate of the incremental strain field in the phase ω_i can be computed by

$$\frac{1}{V(\omega_i)}\int_{\omega_i}\Delta\mathbf{E}_{\mathrm{m}}(\boldsymbol{x};\, w)\otimes\Delta\mathbf{E}_{\mathrm{m}}(\boldsymbol{x};\, w)d\boldsymbol{x} = \frac{1}{v_i}\Delta\mathbf{E}_{\mathrm{M}}(w) : \frac{\partial\hat{\mathbb{C}}^{\mathrm{LCC}}(w)}{\partial\hat{\mathbb{C}}_i^{\mathrm{LCC}}}(w) : \Delta\mathbf{E}_{\mathrm{M}}(w)\,, \tag{214}$$

as detailed by Bobeth and Diener (1987); Buryachenko (2001), where $\hat{\mathbb{C}}^{\mathrm{LCC}}(w)$ is the effective elastic tensor of the LCC, corresponding to the given phase virtual elastic operators $\hat{\mathbb{C}}_0^{\mathrm{LCC}}(w)$ and $\hat{\mathbb{C}}_{\mathrm{I}}^{\mathrm{LCC}}(w)$. Second statistical moment values were accounted for by Suquet (1995) while using the so-called modified-secant approach, by Ponte Castañeda (1996); Doghri et al. (2011) while using the incremental tangent method, and by Wu et al. (2017) while using the incremental-secant method. In order to capture with more accuracy the field fluctuations, Ponte Castañeda (2002a,b) have considered "generalised secant moduli" incorporating both first and second statistical moment information and have applied the method to visco-plastic composite materials.

Second statistical moments values are also accounted for when developing MFH methods based on variational principles as pioneered by Ponte Castañeda (1992) and further developed by Lahellec and Suquet (2007a,b) in the context of in-elasticity, by Lahellec et al. (2011) in the context of thermo-elasticity, and by Brassart et al. (2011, 2012); Lahellec and Suquet (2013); Boudet et al. (2016) in the context of elasto-(visco-)plasticity.

4.3. Extraction of stochastic homogenised behaviours

For a given stochastic micro-structure $\mathscr{w} \in \mathscr{W}$, the apparent properties observation, *e.g.* the homogenised material tensor $\mathbb{C}_{\mathrm{M}}(\boldsymbol{X};\, \mathscr{w})$, can be extracted using the approaches developed in Section 4.2. In order to extract the random field $\{\mathbb{C}_{\mathrm{M}}(\boldsymbol{X};\, \mathscr{w}) : \boldsymbol{X} \in \Omega,\, \mathscr{w} \in \mathscr{W}\}$, the sample space $\mathscr{W}$ has to be spanned, and different methods can be considered. For conciseness, in the following volume integrals, we note the volume element realization $\omega = \omega(\boldsymbol{X};\, \mathscr{w})$, in which we omit the reference to $\mathscr{w}$, but it is understood that the homogenized response is micro-structure dependent.

These methods are developed here in the particular case of stochastic micro-structure homogenisation, but they can also be used when propagating uncertainties to the structural scale as discussed in Section 5.5, where we further discuss their variations, advantages and drawbacks.

4.3.1. Monte-Carlo simulations

The Monte-Carlo (MC) simulation method is the simplest resolution method. It involves sampling several micro-structures $\mathscr{w} \in \mathscr{W}$, from which the apparent properties, *e.g.* the homogenised material tensor $\mathbb{C}_{\mathrm{M}}(\boldsymbol{X};\, \mathscr{w})$, can be extracted using the approaches developed in Section 4.2. For enough samples, the set of solutions corresponds to an accurate estimation of the sought stochastic response. MC is a robust method that has widely been used in stochastic homogenisation by Cottereau (2013); Lucas et al. (2015); Stefanou et al. (2015); Wu et al. (2016); Lucas et al. (2017); Stefanou et al. (2017), *e.g.*

As examples, the correlation of the homogenised random field $\{\mathbb{C}_{\mathrm{M}}(\boldsymbol{X};\, \mathscr{w}) : \boldsymbol{X} \in \Omega,\, \mathscr{w} \in \mathscr{W}\}$ of apparent poly-crystal properties sudied in Fig. 26 and the apparent UD composite property distributions illustrated in Fig. 29 have been obtained by combining MC simulations with the computational homogenisation framework presented in Section 4.2.1.

4.3.2. Perturbation stochastic finite elements

We consider the probability space $(\mathscr{W},\, \mathcal{F},\, \mathbb{P})$ and as (continuous) random field $\boldsymbol{U}'(\omega) = \{\boldsymbol{U}'(\boldsymbol{x}) : \boldsymbol{x} \in \omega\}$ the perturbation field (125) defined in the computational homogenisation framework, with $\boldsymbol{U}'(\boldsymbol{x};\, \mathscr{w}) \in \mathcal{U}(\omega)$ where $\mathcal{U}(\omega)$ is an admissible kinematic vector field subset of the minimum kinematic field $\mathcal{U}^{\min}$ (129) defined depending on the boundary conditions applied on the SVE.. It is assumed that the uncertainties can be expressed in terms of $\boldsymbol{\Xi} = [\Xi_1 \ldots \Xi_i \ldots \Xi_n]^T$ a vector of n random variables $\Xi_i : \mathscr{W} \rightarrow \Re$. The stochastic strong form of the micro-scale problem reads

$$\left[\mathbf{P}_\mathrm{m}\left(\boldsymbol{U}'(\boldsymbol{x};\,\boldsymbol{\xi});\,\boldsymbol{\xi}\right)\right]\cdot\boldsymbol{\nabla}_0 = 0\,, \tag{215}$$

with $\boldsymbol{\xi} = \Xi(\omega)$.

We follow the summary given by Nouy (1999) of the perturbation stochastic framework and adapt it to linear elasticity. The stochastic strong form of the micro-scale problem (215) thus becomes

$$\left[\boldsymbol{\Sigma}_\mathrm{m}\left(\boldsymbol{U}'(\boldsymbol{x};\,\boldsymbol{\xi});\,\boldsymbol{\xi}\right)\right]\cdot\boldsymbol{\nabla}_0 = 0\,, \tag{216}$$

with $\boldsymbol{\xi} = \Xi(\omega)$ and $\boldsymbol{\Sigma}_\mathrm{m}\left(\bullet;\,\boldsymbol{\xi}\right)$ the Cauchy stress tensor, which is here seen as an operator. This operator is then developed around its value evaluated for $\mathbb{E}[\boldsymbol{\Xi}]$ as

$$\begin{aligned}\boldsymbol{\Sigma}_\mathrm{m}\left(\boldsymbol{U}';\,\boldsymbol{\xi}\right) \;=\;& \underbrace{\boldsymbol{\Sigma}_\mathrm{m}\left(\boldsymbol{U}';\,\mathbb{E}\left[\boldsymbol{\Xi}\right]\right)}_{\boldsymbol{\Sigma}_0(\boldsymbol{U}')} + \underbrace{\sum_k \frac{\partial}{\partial \Xi_k}\boldsymbol{\Sigma}_\mathrm{m}\left(\boldsymbol{U}';\,\mathbb{E}\left[\boldsymbol{\Xi}\right]\right)}_{\boldsymbol{\Sigma}_{,k}(\boldsymbol{U}')}\left(\xi_k - \mathbb{E}[\Xi_k]\right) + \\ & \frac{1}{2}\sum_k\sum_l \underbrace{\frac{\partial^2}{\partial \Xi_k \partial \Xi_l}\boldsymbol{\Sigma}_\mathrm{m}\left(\boldsymbol{U}';\,\mathbb{E}\left[\boldsymbol{\Xi}\right]\right)}_{\boldsymbol{\Sigma}_{,kl}(\boldsymbol{U}')}\left(\xi_k - \mathbb{E}[\Xi_k]\right)\left(\xi_l - \mathbb{E}[\Xi_l]\right) + \ldots\end{aligned} \tag{217}$$

The random field of unknowns is developed around its value evaluated for $\mathbb{E}(\boldsymbol{\Xi})$ in a similar way

$$\begin{aligned}\boldsymbol{U}'(\boldsymbol{x};\,\boldsymbol{\xi}) \;=\;& \underbrace{\boldsymbol{U}'\left(\boldsymbol{x};\,\mathbb{E}[\boldsymbol{\Xi}]\right)}_{\boldsymbol{u}'_0(\boldsymbol{x})} + \sum_i \underbrace{\frac{\partial}{\partial \Xi_i}\boldsymbol{U}'\left(\boldsymbol{x};\,\mathbb{E}[\boldsymbol{\Xi}]\right)}_{\boldsymbol{u}'_{,i}(\boldsymbol{x})}\left(\xi_i - \mathbb{E}[\Xi_i]\right) + \\ & \frac{1}{2}\sum_i\sum_j \underbrace{\frac{\partial^2}{\partial \Xi_i \partial \Xi_j}\boldsymbol{U}'\left(\boldsymbol{x};\,\mathbb{E}[\boldsymbol{\Xi}]\right)}_{\boldsymbol{u}'_{,ij}(\boldsymbol{x})}\left(\xi_i - \mathbb{E}[\Xi_i]\right)\left(\xi_j - \mathbb{E}[\Xi_j]\right) + \ldots\end{aligned} \tag{218}$$

Using the two developments (217) and (218), and assuming the operator is linear with the unknown field, *i.e.* assuming linear elasticity in the present context, the strong form

(216) reads

$$\begin{aligned}
0 \;=\; & \left[\boldsymbol{\Sigma}_0\left(\boldsymbol{u}'_0\right)\right]\cdot\boldsymbol{\nabla}_0 + \sum_i \left[\boldsymbol{\Sigma}_0\left(\boldsymbol{u}'_{,i}\right)\right]\cdot\boldsymbol{\nabla}_0\left(\xi_i - \mathbb{E}[\Xi_i]\right) + \\
& \frac{1}{2}\sum_i\sum_j \left[\boldsymbol{\Sigma}_0\left(\boldsymbol{u}'_{,ij}\right)\right]\cdot\boldsymbol{\nabla}_0\left(\xi_i - \mathbb{E}[\Xi_i]\right)\left(\xi_j - \mathbb{E}[\Xi_j]\right) + \ldots + \\
& \sum_k \left[\boldsymbol{\Sigma}_{,k}\left(\boldsymbol{u}'_0\right)\right]\cdot\boldsymbol{\nabla}_0\left(\xi_k - \mathbb{E}[\Xi_k]\right) + \sum_k\sum_i \left[\boldsymbol{\Sigma}_{,k}\left(\boldsymbol{u}'_{,i}\right)\right]\cdot\boldsymbol{\nabla}_0\left(\xi_k - \mathbb{E}[\Xi_k]\right)\left(\xi_i - \mathbb{E}[\Xi_i]\right) + \\
& \frac{1}{2}\sum_k\sum_i\sum_j \left[\boldsymbol{\Sigma}_{,k}\left(\boldsymbol{u}'_{,ij}\right)\right]\cdot\boldsymbol{\nabla}_0\left(\xi_k - \mathbb{E}[\Xi_k]\right)\left(\xi_i - \mathbb{E}[\Xi_i]\right)\left(\xi_j - \mathbb{E}[\Xi_j]\right) + \ldots + \\
& \frac{1}{2}\sum_k\sum_l \left[\boldsymbol{\Sigma}_{,kl}\left(\boldsymbol{u}'_0\right)\right]\cdot\boldsymbol{\nabla}_0\left(\xi_k - \mathbb{E}[\Xi_k]\right)\left(\xi_l - \mathbb{E}[\Xi_l]\right) + \\
& \frac{1}{2}\sum_k\sum_l\sum_i \left[\boldsymbol{\Sigma}_{,kl}\left(\boldsymbol{u}'_{,i}\right)\right]\cdot\boldsymbol{\nabla}_0\left(\xi_k - \mathbb{E}[\Xi_k]\right)\left(\xi_l - \mathbb{E}[\Xi_l]\right)\left(\xi_i - \mathbb{E}[\Xi_i]\right) + \\
& \frac{1}{4}\sum_k\sum_l\sum_i\sum_j \left[\boldsymbol{\Sigma}_{,kl}\left(\boldsymbol{u}'_{,ij}\right)\right]\cdot\boldsymbol{\nabla}_0\left(\xi_k - \mathbb{E}[\Xi_k]\right)\left(\xi_l - \mathbb{E}[\Xi_l]\right)\left(\xi_i - \mathbb{E}[\Xi_i]\right)\left(\xi_j - \mathbb{E}[\Xi_j]\right) + \ldots
\end{aligned} \tag{219}$$

This set of equations can be rewritten as a set of recursive deterministic problems

$$\text{Order 0:}\quad 0 = \left[\boldsymbol{\Sigma}_0\left(\boldsymbol{u}'_0\right)\right]\cdot\boldsymbol{\nabla}_0\,, \tag{220}$$

$$\text{Order 1:}\quad 0 = \left[\boldsymbol{\Sigma}_0\left(\boldsymbol{u}'_{,i}\right)\right]\cdot\boldsymbol{\nabla}_0 + \left[\boldsymbol{\Sigma}_{,i}\left(\boldsymbol{u}'_0\right)\right]\cdot\boldsymbol{\nabla}_0\;\forall i = 1..n\,, \tag{221}$$

$$\begin{aligned}\text{Order 2:}\quad 0 = \; & \left[\boldsymbol{\Sigma}_0\left(\boldsymbol{u}'_{,ij}\right)\right]\cdot\boldsymbol{\nabla}_0 + \left[\boldsymbol{\Sigma}_{,i}\left(\boldsymbol{u}'_{,j}\right)\right]\cdot\boldsymbol{\nabla}_0 + \left[\boldsymbol{\Sigma}_{,j}\left(\boldsymbol{u}'_{,i}\right)\right]\cdot\boldsymbol{\nabla}_0 + \\ & \left[\boldsymbol{\Sigma}_{,ij}\left(\boldsymbol{u}'_0\right)\right]\cdot\boldsymbol{\nabla}_0\;\forall i,\,j = 1..n\,,\end{aligned} \tag{222}$$

$$\ldots \quad \ldots \quad \ldots$$

of unknowns $\boldsymbol{u}'_0$, $\boldsymbol{u}'_{,i}$, $\boldsymbol{u}'_{,ij}$ ... The definition of these deterministic problems involves the computation of the operator derivatives $\boldsymbol{\Sigma}_{,i}\left(\boldsymbol{U}'\right)$ with respect of the random variables Ξ_i. Since the method is developed for linear elasticity, considering the stochastic elasticity tensor $\boldsymbol{C}^{\text{el}}_{\text{m}}\left(\boldsymbol{x};\,\boldsymbol{\Xi}(\omega)\right)$ these derivatives read

$$\text{Order 0:}\quad \boldsymbol{\Sigma}_0\left(\boldsymbol{x};\,\boldsymbol{U}'\right) = \boldsymbol{C}^{\text{el}}_{\text{m}}\left(\boldsymbol{x};\,\mathbb{E}[\boldsymbol{\Xi}]\right) : \boldsymbol{\varepsilon}_{\boldsymbol{x}}(\boldsymbol{U}')\,, \tag{223}$$

$$\text{Order 1:}\quad \boldsymbol{\Sigma}_{,i}\left(\boldsymbol{x};\,\boldsymbol{U}'\right) = \frac{\partial \boldsymbol{C}^{\text{el}}_{\text{m}}}{\partial \Xi_i}\left(\boldsymbol{x};\,\mathbb{E}[\boldsymbol{\Xi}]\right) : \boldsymbol{\varepsilon}_{\boldsymbol{x}}(\boldsymbol{U}')\,, \tag{224}$$

$$\ldots \qquad \ldots \qquad \ldots$$

Once the recursive set of deterministic problems (220-222) solved, *e.g.* using a finite-element discretisation, the stochastic field solution results from Eq. (218). Moments of the solution can readily be evaluated

$$\mathbb{E}\left[\boldsymbol{U}'\right] \;=\; \boldsymbol{u}'_0 + \frac{1}{2}\sum_i\sum_j \tilde{R}_{\boldsymbol{\Xi}_{(i\,j)}}\boldsymbol{u}'_{,ij} + \ldots\,, \tag{225}$$

$$\mathbb{E}\left[\left(\boldsymbol{U}' - \mathbb{E}[\boldsymbol{U}']\right)\otimes\left(\boldsymbol{U}' - \mathbb{E}[\boldsymbol{U}']\right)\right] \;=\; \sum_i\sum_j \tilde{R}_{\boldsymbol{\Xi}_{(i\,j)}}\boldsymbol{u}'_{,i}\otimes\boldsymbol{u}'_{,j} + \ldots\,, \tag{226}$$

with the covariance matrix $\tilde{\mathbf{R}}_{\boldsymbol{\Xi}}$ of the random vector $\boldsymbol{\Xi}$ defined by Eq. (46).

As an example, Sakata and Ashida (2011) have extracted the homogenised properties of elastic fibre reinforced composites in which either the matrix properties of the volume fraction of inclusions follows a given distribution. In that case, the theory of equivalent inclusions, see also Section 4.2.4, was used. Lepage et al. (2011) formulated the homogenisation problem using the asymptotic method described in Section 4.2.2, and have applied the development in the uncertainties on the tensor (184) solving the problem using the finite element discretisation of a poly-crystalline volume element. The perturbation stochastic method was then applied to evaluate the mean and variance of the homogenised elastic properties as a function of the grains property uncertainty of the poly-crystal.

4.3.3. Galerkin stochastic finite elements

The theory was pioneered by Ghanem and Spanos (1991) and further developed by Ghanem and Kruger (1996); Ghanem (1999) who have set the bases of the Spectral Stochastic Finite Element Method (SSFEM). The Galerkin stochastic finite element method is an intrusive techniques avoiding the extensive sampling and deterministic simulations of the MC methods and allowing treating more general cases than the perturbation method. More details can also be found in the works by Nouy (1999) and Ernst and Ullmann (2010).

Finite approximation of the expansion of a random field. Let us consider the continuous random field $\boldsymbol{U}'(\omega) = \{\boldsymbol{U}'(\boldsymbol{x}) : \boldsymbol{x} \in \omega\}$, of random vectors $\boldsymbol{U}'$ that take values in $\Re^m$, for $\omega \subset \Re^d$ a space of material points $\boldsymbol{x}$, with $d \in \mathbb{N}$. Its expectation (26) is denoted by $\bar{\boldsymbol{u}}'(\boldsymbol{x}) = \mathbb{E}[\boldsymbol{U}'(\boldsymbol{x})] : \omega \to \Re^m$. When considering a purely mechanical problem, the size m is equal to the dimension d.

Let $\boldsymbol{\Xi} = [\Xi_1 \ldots \Xi_i \ldots \Xi_n]^T$ be a vector of n independent, zero-mean, and unit variance random variables $\Xi_i : \mathscr{W} \to \Re$ of finite second order moment and of support $\mathscr{S}_{\Xi_i}$. The support of $\boldsymbol{\Xi}$ is denoted by $\mathscr{S}_{\boldsymbol{\Xi}} = \mathscr{S}_{\Xi_1} \times \ldots \times \mathscr{S}_{\Xi_i} \times \ldots \times \mathscr{S}_{\Xi_n}$. Similarly as set in Appendix A.4.4, and in particular Eq. (A.75), the stochastic field $\boldsymbol{U}'(\omega) = \{\boldsymbol{U}'(\boldsymbol{x}) : \boldsymbol{x} \in \omega\}$ is represented by the finite separated expansion through the random vector $\boldsymbol{\Xi}$, for which a realisation $\mathscr{w} \in \mathscr{W}$ reads

$$\boldsymbol{u}'(\boldsymbol{x}) = \boldsymbol{U}'(\boldsymbol{x};\, \boldsymbol{\Xi}(\mathscr{w})) \simeq \bar{\boldsymbol{u}}'(\boldsymbol{x}) + \sum_{l=1}^{n_p^{\mathrm{C}}} \boldsymbol{u}_{\boldsymbol{k}^{(l)}}(\boldsymbol{x})\, \psi_{\boldsymbol{k}^{(l)}}(\boldsymbol{\Xi}(\mathscr{w}))\ , \tag{227}$$

with the multi-index $\boldsymbol{k}^{(l)} = \{k_1^{(l)},\, \ldots,\, k_n^{(l)}\} \in \mathbb{N}_0^n$ defined in

$$\mathscr{K}_p^{\mathrm{C}} = \{\boldsymbol{k}^{(l)} \in \mathbb{N}_0^n : k_1^{(l)} + \ldots + k_i^{(l)} + \ldots k_n^{(l)} \leq p\,, l = 0..n_p^{\mathrm{C}}\}\,, \tag{228}$$

of total degree at most p and elements $\boldsymbol{k}^{(0)} = \{0,\, \ldots,\, 0\}$, $\boldsymbol{k}^{(1)}$, …, $\boldsymbol{k}^{(n_p^{\mathrm{C}})}$, with $n_p^{\mathrm{C}} = \frac{(n+p)!}{n!p!} - 1$.

In Eq. (227), $\{\psi_{\boldsymbol{k}^{(l)}}(\boldsymbol{\xi}) = \psi^{(1)}_{k_1^{(l)}}(\xi_1) \times \ldots \times \psi^{(i)}_{k_i^{(l)}}(\xi_i) \times \ldots \times \psi^{(n)}_{k_n^{(l)}}(\xi_n) : \boldsymbol{k}^{(l)} \in \mathscr{K}_p^{\mathrm{C}};\, \boldsymbol{\xi} = \boldsymbol{\Xi}(\mathscr{w})\}$ is an orthonormal polynomial family belonging to the Hilbert space $\mathscr{H}(\mathscr{W})$, and the coefficients

$\boldsymbol{u}_{\boldsymbol{k}^{(l)}}(\boldsymbol{x})$ valued in $\Re^m$ are evaluated by

$$\begin{aligned}\boldsymbol{u}_{\boldsymbol{k}^{(l)}}(\boldsymbol{x}) &= \mathbb{E}\left[\left(\boldsymbol{U}'(\boldsymbol{x}) - \bar{\boldsymbol{u}}'(\boldsymbol{x})\right)\psi_{\boldsymbol{k}^{(l)}}(\boldsymbol{\Xi})\right] \\ &= \int_{\Re^n}\left(\boldsymbol{U}'(\boldsymbol{x};\,\boldsymbol{\xi}) - \bar{\boldsymbol{u}}'(\boldsymbol{x})\right)\psi_{\boldsymbol{k}^{(l)}}(\boldsymbol{\xi})\pi_{\boldsymbol{\Xi}}(\boldsymbol{\xi})\mathrm{d}\boldsymbol{\xi}\,, \quad l = 1..n_p^{\mathrm{C}}\,. \end{aligned} \tag{229}$$

Defining $\boldsymbol{u}_{\boldsymbol{k}^{(0)}}(\boldsymbol{x}) = \bar{\boldsymbol{u}}'(\boldsymbol{x})$ and considering $\psi_{\boldsymbol{k}^{(0)}}(\boldsymbol{\xi}) = 1$, Eq. (227) becomes

$$\boldsymbol{u}'(\boldsymbol{x}) = \boldsymbol{U}'\left(\boldsymbol{x};\,\boldsymbol{\Xi}(\mathscr{w})\right) \simeq \sum_{l=0}^{n_p^{\mathrm{C}}} \boldsymbol{u}_{\boldsymbol{k}^{(l)}}\left(\boldsymbol{x}\right)\psi_{\boldsymbol{k}^{(l)}}\left(\boldsymbol{\Xi}(\mathscr{w})\right)\,. \tag{230}$$

A common choice for the orthonormal polynomials family $\{\psi_l^{(i)} : l \in \mathbb{N}_0,\, i = 1..n\}$ is based on the Hermite polynomials $H_l(\xi)$, see Eq. (A.52), with $\psi_l^{(i)}(\xi_i) = H_l(\xi_i)$.

Stochastic Galerkin finite element. We now consider the probability space $(\mathscr{W},\, \mathscr{F},\, \mathbb{P})$ and as (continuous) random field $\boldsymbol{U}'(\omega) = \{\boldsymbol{U}'(\boldsymbol{x}) : \boldsymbol{x} \in \omega\}$ the perturbation field (125) defined in the computational homogenisation framework.

It is assumed that, through a non-linear mapping, see Appendix A.1, the uncertainties can be expressed in terms of $\boldsymbol{\Xi} = [\Xi_1 \ldots \Xi_i \ldots \Xi_n]^T$ a vector of n independent, zero-mean, and unit variance random variables $\Xi_i : \mathscr{W} \rightarrow \Re$ of finite second order moment and of support $\mathcal{S}_{\Xi_i}$.

Therefore the strong form of the micro-scale problem reads

$$\left[\mathbf{P}_{\mathrm{m}}\left(\boldsymbol{U}'(\boldsymbol{x};\,\boldsymbol{\xi});\,\boldsymbol{\xi}\right)\right] \cdot \boldsymbol{\nabla}_0 = 0\,, \tag{231}$$

with $\boldsymbol{\xi} = \boldsymbol{\Xi}(\mathscr{w})$.

Following Pivovarov and Steinmann (2016), we now multiply Eq. (231) by a stochastic test function $\delta\boldsymbol{U}'(\boldsymbol{x};\,\boldsymbol{\xi}) \in \mathcal{U}(\omega) \times \mathcal{H}(\mathscr{W})$, where $\mathcal{U}(\omega)$ is an admissible kinematic vector field subset of the minimum kinematic field $\mathcal{U}^{\min}$ (129) defined depending on the boundary conditions applied on the SVE. Integrating on the probabilistic space and on the spatial domain yields

$$\int_\omega \int_{\mathcal{S}_{\boldsymbol{\Xi}}} \delta\boldsymbol{U}'(\boldsymbol{x};\,\boldsymbol{\xi}) \cdot \left[\left[\mathbf{P}_{\mathrm{m}}\left(\boldsymbol{U}'(\boldsymbol{x};\,\boldsymbol{\xi});\,\boldsymbol{\xi}\right)\right] \cdot \boldsymbol{\nabla}_0\right] \pi_{\boldsymbol{\Xi}}(\boldsymbol{\xi})\mathrm{d}\boldsymbol{\xi}d\boldsymbol{x} = 0 \quad \forall \delta\boldsymbol{U}' \in \mathcal{U}(\omega) \times \mathcal{H}(\mathscr{W})\,. \tag{232}$$

Integrating by parts in the spatial domain, the weak form (130) is then restated on the product between the physical and probabilistic spaces as finding $\boldsymbol{U}' \in \mathcal{U}(\omega) \times \mathcal{H}(\mathscr{W})$ such that

$$\int_\omega \int_{\mathcal{S}_{\boldsymbol{\Xi}}} \mathbf{P}_{\mathrm{m}}\left(\boldsymbol{U}'(\boldsymbol{x};\,\boldsymbol{\xi});\,\boldsymbol{\xi}\right) : \left(\delta\boldsymbol{U}'(\boldsymbol{x};\,\boldsymbol{\xi}) \otimes \boldsymbol{\nabla}_0\right) \pi_{\boldsymbol{\Xi}}(\boldsymbol{\xi})\mathrm{d}\boldsymbol{\xi}d\boldsymbol{x} = 0\,, \quad \forall \delta\boldsymbol{U}' \in \mathcal{U}(\omega) \times \mathcal{H}(\mathscr{W})\,. \tag{233}$$

The finite element discretisation of Eq. (233) is based on the separation of variables with the use of the finite element discretisation (135) and of the expansion (230), yielding

$$\begin{cases} \boldsymbol{U}(\boldsymbol{x};\,\boldsymbol{\xi}) &= \sum_a \sum_{l=0}^{n_p^{\mathrm{C}}} \varphi^{(a)}(\boldsymbol{x})\psi_{\boldsymbol{k}^{(l)}}\left(\boldsymbol{\Xi}(\mathscr{w})\right)\boldsymbol{u}_{\boldsymbol{k}^{(l)}}^{(a)}\,;\ \text{and} \\ \delta\boldsymbol{U}'(\boldsymbol{x};\,\boldsymbol{\xi}) &= \sum_a \sum_{l=0}^{n_p^{\mathrm{C}}} \varphi^{(a)}(\boldsymbol{x})\psi_{\boldsymbol{k}^{(l)}}\left(\boldsymbol{\Xi}(\mathscr{w})\right)\delta\boldsymbol{u}_{\boldsymbol{k}^{(l)}}^{(a)}\,. \end{cases} \tag{234}$$

We note that Eq. (125) allows relating the fluctuation $\boldsymbol{U}'(\boldsymbol{x};\,\boldsymbol{\xi})$ to the displacement $\boldsymbol{U}(\boldsymbol{x};\,\boldsymbol{\xi})$ and thus to the degrees of freedom. The degrees of freedom $\boldsymbol{u}^{(a)}_{\boldsymbol{k}^{(l)}}$ represent $n_p^{\mathrm{C}}+1$ nodal displacement vectors resulting from the expansion (230), and are collected in the vector $\boldsymbol{d}_{\mathrm{m}}$, which has now a size of $d \times (n_p^{\mathrm{C}}+1) \times n^{\mathrm{node}}$, for n^{node} nodes and a physical space of dimension d. It is seen that the system is similar to the traditional finite elements, with however more degrees of freedom whose number increases dramatically with the size of the stochastic process.

The vector $\boldsymbol{f}_{\mathrm{int}}$ of the internal forces associated to the weak forms (233) reads

$$\boldsymbol{f}_{\mathrm{int}} \;=\; \bigwedge_{\omega^e} \int_{\omega^e} \int_{\mathcal{S}_{\Xi}} \left(\mathbf{b}'^e\right)^T \boldsymbol{P}_{\mathrm{m}}(\boldsymbol{x};\,\boldsymbol{\xi}) \pi_{\Xi}(\boldsymbol{\xi}) \mathrm{d}\boldsymbol{\xi} d\boldsymbol{x}\,, \tag{235}$$

where $\mathbf{b}'^e$ is the elementary matrix of the shape functions gradient associated to the stochastic displacement vector field, *i.e.* built from $\boldsymbol{\nabla}\varphi^{(a)}(\boldsymbol{x})\psi_{\boldsymbol{k}^{(l)}}\left(\Xi(\mathscr{w})\right)$, $\boldsymbol{P}_{\mathrm{m}}$ is the first Piola-Kirchhoff stress tensor $\mathbf{P}_{\mathrm{m}}$ written in the vector form, and where $\bigwedge_{\omega^e}$ is used to symbolise the assembly process.

The stiffness matrix $\mathbf{k}_{\mathrm{m}}$ of the unconstrained meso-scale volume element reads

$$\mathbf{k}_{\mathrm{m}} \;=\; \frac{\partial \boldsymbol{f}_{\mathrm{int}}}{\partial \boldsymbol{d}_{\mathrm{m}}} = \bigwedge_{\omega^e} \int_{\omega^e} \int_{\mathcal{S}_{\Xi}} \left(\mathbf{b}'^e\right)^T \mathbf{C}_{\mathrm{m}}(\boldsymbol{x};\,\boldsymbol{\xi}) \mathbf{b}'^e \pi_{\Xi}(\boldsymbol{\xi}) \mathrm{d}\boldsymbol{\xi} d\boldsymbol{x}\,, \tag{236}$$

where $\boldsymbol{d}_{\mathrm{m}}$ is the vector gathering all the micro-scale degrees of freedom, *i.e.* the nodal displacements $\boldsymbol{u}^{(a)}_{\boldsymbol{k}^{(l)}}$, $\mathbf{C}_{\mathrm{m}} = \frac{\partial \boldsymbol{P}_{\mathrm{m}}}{\partial \boldsymbol{F}_{\mathrm{m}}}$ is the matrix notation of the micro-scale fourth-order material tensor $\mathbb{C}_{\mathrm{m}} = \frac{\partial \mathbf{P}_{\mathrm{m}}}{\partial \mathbf{F}_{\mathrm{m}}}$, with $\boldsymbol{F}_{\mathrm{m}}$ the deformation gradient $\mathbf{F}_{\mathrm{m}}$ written in the vector form.

Spectral Stochastic Finite Element Method (SSFEM). In the context of linear elasticity, the Galerkin stochastic finite element method simplifies as shown by Ghanem and Kruger (1996); Ghanem and Brzakala (1996); Ghanem (1999), see also the review by Nouy (1999).

Assuming linear elasticity, the stress tensor reads

$$\mathbf{\Sigma}_{\mathrm{m}}(\boldsymbol{x};\,\mathscr{w}) = \mathbb{C}^{\mathrm{el}}_{\mathrm{m}}(\boldsymbol{x};\,\mathscr{w}) : \mathbf{E}_{\mathrm{m}}(\boldsymbol{x};\,\mathscr{w})\,, \tag{237}$$

where the local elasticity tensor $\mathbb{C}^{\mathrm{el}}_{\mathrm{m}}(\boldsymbol{x};\,\mathscr{w})$ is a realisation of the random field $\{\mathbb{C}^{\mathrm{el}}_{\mathrm{m}}(\boldsymbol{x};\,\mathscr{w}) : \boldsymbol{x} \in \omega,\, \mathscr{w} \in \mathscr{W}\}$ assumed to be characterised through the covariance matrix $\tilde{\mathbf{R}}_{\boldsymbol{C}^{\mathrm{el}}_{\mathrm{m}}}(\boldsymbol{x};\,\boldsymbol{\tau})$, in which we have considered the elasticity properties written under the 21-component vector form $\boldsymbol{C}^{\mathrm{el}}_{\mathrm{m}}$ and a vector $\boldsymbol{\tau}$ separating two points of ω.

Following Appendix A.3.2, a Karhunen Loève expansion allows representing the random field $\boldsymbol{C}^{\mathrm{el}}_{\mathrm{m}}(\omega)$ by the collection of

$$\boldsymbol{C}^{\mathrm{el}}_{\mathrm{m}}(\boldsymbol{x};\,\mathscr{w}) \simeq \bar{\boldsymbol{c}}^{\mathrm{el}}_{\mathrm{m}}(\boldsymbol{x}) + \sum_{i=1}^{n} \sqrt{\lambda^{(i)}_{\boldsymbol{C}^{\mathrm{el}}_{\mathrm{m}}}} \mathrm{H}_i(\mathscr{w}) \boldsymbol{u}^{(i)}_{\boldsymbol{C}^{\mathrm{el}}_{\mathrm{m}}}(\boldsymbol{x}) = \sum_{i=0}^{n} \sqrt{\lambda^{(i)}_{\boldsymbol{C}^{\mathrm{el}}_{\mathrm{m}}}} \mathrm{H}_i(\mathscr{w}) \boldsymbol{u}^{(i)}_{\boldsymbol{C}^{\mathrm{el}}_{\mathrm{m}}}(\boldsymbol{x})\,, \tag{238}$$

where $\mathbf{H}$ is a new random vector of zero-mean, unit variance and uncorrelated (but possibly dependent) components H_i, $\lambda^{(i)}_{\boldsymbol{C}^{\mathrm{el}}_{\mathrm{m}}}$ and $\boldsymbol{u}^{(i)}_{\boldsymbol{C}^{\mathrm{el}}_{\mathrm{m}}}(\boldsymbol{x})$ for $i > 0$ are the ordered eigen-values and orthonormal eigen-basis of the covariance matrix $\tilde{\mathbf{R}}_{\boldsymbol{C}^{\mathrm{el}}_{\mathrm{m}}}(\boldsymbol{x};\, \boldsymbol{\tau})$, n is the order of the expansion, and where we have defined $\mathrm{H}_0(\mathcal{w}) = \lambda^{(0)}_{\boldsymbol{C}^{\mathrm{el}}_{\mathrm{m}}} = 1$ and $\boldsymbol{u}^{(0)}_{\boldsymbol{C}^{\mathrm{el}}_{\mathrm{m}}}(\boldsymbol{x})$ as the expectation $\bar{\boldsymbol{c}}^{\mathrm{el}}_{\mathrm{m}}(\boldsymbol{x})$.

In particular, if the random process $\{\boldsymbol{C}^{\mathrm{el}}_{\mathrm{m}}(\boldsymbol{x};\, \omega);\, \boldsymbol{x} \in \omega,\, \mathcal{w} \in \mathcal{W}\}$ is Gaussian[6], the random variables $\{\mathrm{H}_i\}$ are not only zero-mean and of unit variance, but they are also independent, as discussed in Appendix A.3.2. It is thus assumed that the finite separation expansion (230) of the displacement field is built on the same random variables, and Eq. (238) is rewritten for convenience as

$$\boldsymbol{C}^{\mathrm{el}}_{\mathrm{m}}(\boldsymbol{x};\, \mathcal{w}) \simeq \bar{\boldsymbol{c}}^{\mathrm{el}}_{\mathrm{m}}(\boldsymbol{x}) + \sum_{i=1}^{n} \sqrt{\lambda^{(i)}_{\boldsymbol{C}^{\mathrm{el}}_{\mathrm{m}}}}\xi_i \boldsymbol{u}^{(i)}_{\boldsymbol{C}^{\mathrm{el}}_{\mathrm{m}}}(\boldsymbol{x}) = \sum_{i=0}^{n} \sqrt{\lambda^{(i)}_{\boldsymbol{C}^{\mathrm{el}}_{\mathrm{m}}}}\Xi_i(\mathcal{w})\boldsymbol{u}^{(i)}_{\boldsymbol{C}^{\mathrm{el}}_{\mathrm{m}}}(\boldsymbol{x})\,, \tag{239}$$

where $\boldsymbol{\Xi} = [\Xi_1 \dots \Xi_i \dots \Xi_n]^T$ is a vector of n independent, zero-mean, and unit variance Gaussian random variables $\Xi_i : \mathcal{W} \to \Re$ of finite second order moment and of support $\mathcal{S}_{\Xi_i} = \Re$. Therefore, starting from the stochastic weak form (233) and considering the small strain approximation with Eqs. (237) and (238) yields finding $\boldsymbol{U}(\boldsymbol{x};\, \boldsymbol{\xi})$[7] such that

$$\begin{aligned}&\int_{\omega}\int_{\mathcal{S}_{\boldsymbol{\Xi}}} \sum_{i=0}^{n}\left[\sqrt{\lambda^{(i)}_{\boldsymbol{C}^{\mathrm{el}}_{\mathrm{m}}}}\xi_i \mathbf{u}^{(i)}_{\mathbf{C}^{\mathrm{el}}_{\mathrm{m}}}(\boldsymbol{x}) : (\boldsymbol{U}(\boldsymbol{x};\, \boldsymbol{\xi}) \otimes \boldsymbol{\nabla}_0)\right] : [\delta \boldsymbol{U}'(\boldsymbol{x};\, \boldsymbol{\xi}) \otimes \boldsymbol{\nabla}_0]\, \pi_{\boldsymbol{\Xi}}(\boldsymbol{\xi})\mathrm{d}\boldsymbol{\xi} d\boldsymbol{x} = 0\,,\\ &\forall \delta \boldsymbol{U}' \in \mathcal{U}(\omega) \times \mathcal{H}(\mathcal{W})\,,\end{aligned} \tag{240}$$

where $\mathbf{u}^{(i)}_{\mathbf{C}^{\mathrm{el}}_{\mathrm{m}}}$ is the symmetric matrix notation of $\boldsymbol{u}^{(i)}_{\boldsymbol{C}^{\mathrm{el}}_{\mathrm{m}}}$. Introducing the discretization (234), this last equation becomes

$$\begin{aligned}&\sum_{i=0}^{n}\sum_{p=0}^{n^{\mathrm{C}}_p}\sum_{q=0}^{n^{\mathrm{C}}_p} \delta \boldsymbol{d}^T_{\boldsymbol{k}^{(q)}} \bigwedge_{\omega^e} \int_{\omega^e}\int_{\mathcal{S}_{\boldsymbol{\Xi}}} \quad \left[\sqrt{\lambda^{(i)}_{\boldsymbol{C}^{\mathrm{el}}_{\mathrm{m}}}}\xi_i \psi_{\boldsymbol{k}^{(p)}}\left(\boldsymbol{\xi}\right) \psi_{\boldsymbol{k}^{(q)}}\left(\boldsymbol{\xi}\right)\right]\\ &\qquad\qquad (\mathbf{b}^e)^T\, \mathbf{u}^{(i)}_{\mathbf{C}^{\mathrm{el}}_{\mathrm{m}}}(\boldsymbol{x})\mathbf{b}^e \pi_{\boldsymbol{\Xi}}(\boldsymbol{\xi})\mathrm{d}\boldsymbol{\xi} d\boldsymbol{x} \quad \boldsymbol{d}_{\boldsymbol{k}^{(p)}} = 0\,, \quad \forall \delta \boldsymbol{d}_{\boldsymbol{k}^{(q)}}\,,\end{aligned} \tag{241}$$

where $\boldsymbol{d}_{\boldsymbol{k}^{(p)}}$ is the vector of $\boldsymbol{u}^{(a)}_{\boldsymbol{k}^{(p)}}$, part of $\boldsymbol{d}_{\mathrm{m}}$, or again

$$\begin{aligned}&\sum_{p=0}^{n^{\mathrm{C}}_p}\sum_{i=0}^{n} \underbrace{\bigwedge_{\omega^e} \int_{\omega^e} (\mathbf{b}^e)^T\, \mathbf{u}^{(i)}_{\mathbf{C}^{\mathrm{el}}_{\mathrm{m}}}(\boldsymbol{x})\mathbf{b}^e d\boldsymbol{x}}_{\mathbf{k}^{(i)}_{\mathrm{m}}} \underbrace{\int_{\mathcal{S}_{\boldsymbol{\Xi}}} \left[\sqrt{\lambda^{(i)}_{\boldsymbol{C}^{\mathrm{el}}_{\mathrm{m}}}}\xi_i \psi_{\boldsymbol{k}^{(p)}}\left(\boldsymbol{\xi}\right) \psi_{\boldsymbol{k}^{(q)}}\left(\boldsymbol{\xi}\right)\right] \pi_{\boldsymbol{\Xi}}(\boldsymbol{\xi})\mathrm{d}\boldsymbol{\xi}}_{c^{(i,\,p,\,q)}}\, \boldsymbol{d}_{\boldsymbol{k}^{(p)}} = 0\,,\\ &\qquad\qquad\qquad\qquad\qquad\qquad \forall q = 0..n^{\mathrm{C}}_p\,,\end{aligned} \tag{242}$$

The stiffness matrix $\mathbf{k}_{\mathrm{m}}$ (236) is thus made of the blocks $\mathbf{k}^{(p,\,q)}_{\mathrm{m}} = \sum_{i=0}^{n} c^{(i,\,p,\,q)}\mathbf{k}^{(i)}_{\mathrm{m}}$, $\forall\, p,\, q = 0..n^{\mathrm{C}}_p$. Ghanem and Kruger (1996) have used this formalism to study the loading of a sample

---

[6] which is an approximation since the material tensor is actually definite positive.

[7] We recall that Eq. (125) allows relating the fluctuation $\boldsymbol{U}'(\boldsymbol{x};\, \boldsymbol{\xi})$ to the displacement $\boldsymbol{U}(\boldsymbol{x};\, \boldsymbol{\xi})$.

with spatially varying Young's modulus taking advantage of the structure of the stiffness matrix.

In the case for which the material stochasticity process is not Gaussian, Ghanem and Brzakala (1996); Ghanem (1999) have assumed that $\boldsymbol{C}_{\mathrm{m}}^{\mathrm{el}}(\boldsymbol{x};\, \varpi)$ depends in a non-linear manner on a Gaussian process. For example Ghanem and Brzakala (1996) have considered an interface between two media defined by the height

$$h(\boldsymbol{x};\, \varpi) = h(\boldsymbol{x};\, \boldsymbol{\Xi}(\varpi)) \simeq \bar{h}(\boldsymbol{x}) + \sum_{i=1}^{n} \sqrt{\lambda_H^{(i)}} \Xi_i(\varpi) u_H^{(i)}(\boldsymbol{x}) = \sum_{i=0}^{n} \sqrt{\lambda_H^{(i)}} \Xi_i(\varpi) u_H^{(i)}(\boldsymbol{x})\,, \tag{243}$$

where the random variables $\{\Xi_i\}$ form a Gaussian vector of zero-mean and unit-covariance matrix, $\lambda_H^{(i)}$ and $\boldsymbol{u}_H^{(i)}(\boldsymbol{x})$ for $i > 0$ are the ordered eigen-values and orthonormal eigen-basis of the correlation $R_H(\boldsymbol{x};\, \boldsymbol{\tau})$, n is the order of the expansion, and where we have defined $\mathrm{H}_0(\varpi) = \lambda_H^{(0)} = 1$ and $u_H^{(0)}(\boldsymbol{x})$ as the expectation $\bar{h}(\boldsymbol{x})$. As to obtain (230), the polynomial chaos is then applied on the material operator $\boldsymbol{C}_{\mathrm{m}}^{\mathrm{el}}(\boldsymbol{x};\, \varpi)$ written in the vector form as

$$\boldsymbol{C}_{\mathrm{m}}^{\mathrm{el}}(\boldsymbol{x};\, \varpi) = \boldsymbol{C}_{\mathrm{m}}^{\mathrm{el}}(\boldsymbol{x};\, h(\boldsymbol{x};\, \varpi)) \simeq \boldsymbol{C}_{\mathrm{m}}^{\mathrm{el}}\left(\boldsymbol{x};\, h(\boldsymbol{x};\, \boldsymbol{\Xi}(\varpi))\right) = \sum_{l=0}^{n_p^{\mathrm{C}}} \boldsymbol{u}_{\boldsymbol{k}^{(l)}}\left(\boldsymbol{X}\right) \psi_{\boldsymbol{k}^{(l)}}\left(\boldsymbol{\Xi}(\varpi)\right)\,, \tag{244}$$

with the coefficients $\boldsymbol{u}_{\boldsymbol{k}^{(l)}}(\boldsymbol{x})$ evaluated by

$$\begin{aligned} \boldsymbol{u}_{\boldsymbol{k}^{(l)}}(\boldsymbol{x}) &= \mathbb{E}\left[\left(\boldsymbol{C}_{\mathrm{m}}^{\mathrm{el}}(\boldsymbol{x}; \mathcal{W}) - \bar{\boldsymbol{c}}_{\mathrm{m}}^{\mathrm{el}}(\boldsymbol{x})\right) \psi_{\boldsymbol{k}^{(l)}}(\boldsymbol{\Xi})\right] \\ &= \int_{\Re^n} \left(\boldsymbol{C}_{\mathrm{m}}^{\mathrm{el}}(\boldsymbol{x};\, h(\boldsymbol{x};\, \boldsymbol{\xi})) - \bar{\boldsymbol{c}}_{\mathrm{m}}^{\mathrm{el}}(\boldsymbol{x})\right) \psi_{\boldsymbol{k}^{(l)}}(\boldsymbol{\xi}) \pi_{\boldsymbol{\Xi}}(\boldsymbol{\xi}) \mathrm{d}\boldsymbol{\xi}\,, \quad l = 1..n_p^{\mathrm{C}}\,, \end{aligned} \tag{245}$$

and $\boldsymbol{u}_{\boldsymbol{k}^{(0)}}(\boldsymbol{x}) = \bar{\boldsymbol{c}}_{\mathrm{m}}^{\mathrm{el}}(\boldsymbol{x})$. The terms $\boldsymbol{u}_{\boldsymbol{k}^{(l)}}(\boldsymbol{x})$ of Eq. (245) can be evaluated from the non-linear dependency of $\boldsymbol{C}_{\mathrm{m}}^{\mathrm{el}}(\boldsymbol{x};\, \varpi)$ with the Gaussian random field $\{H(\boldsymbol{x};\, \varpi);\, \boldsymbol{x} \in \omega,\, \varpi \in \mathcal{W}\}$ developed under the Karhunen-Loève expansion (243). Proceeding as before, Eq. (241) becomes

$$\begin{aligned} \sum_{i=0}^{n_p^{\mathrm{C}}} \sum_{p=0}^{n_p^{\mathrm{C}}} \sum_{q=0}^{n_p^{\mathrm{C}}} \delta \boldsymbol{d}_{\boldsymbol{k}^{(q)}}^{T} \bigwedge_{\omega^e} \int_{\omega^e} \int_{\mathcal{S}_{\boldsymbol{\Xi}}} \quad & \left[\psi_{\boldsymbol{k}^{(i)}}\left(\boldsymbol{\xi}\right) \psi_{\boldsymbol{k}^{(p)}}\left(\boldsymbol{\xi}\right) \psi_{\boldsymbol{k}^{(q)}}\left(\boldsymbol{\xi}\right)\right] \\ & \left(\mathbf{b}^e\right)^T \mathbf{u}_{\boldsymbol{k}^{(i)}}(\boldsymbol{x}) \mathbf{b}^e \pi_{\boldsymbol{\Xi}}(\boldsymbol{\xi}) \mathrm{d}\boldsymbol{\xi} d\boldsymbol{x} \quad \boldsymbol{d}_{\boldsymbol{k}^{(p)}} = 0\,, \quad \forall \delta \boldsymbol{d}_{\boldsymbol{k}^{(q)}}\,, \end{aligned} \tag{246}$$

where $\mathbf{u}_{\boldsymbol{k}^{(i)}}(\boldsymbol{x})$ is the symmetric matrix notation of $\boldsymbol{u}_{\boldsymbol{k}^{(l)}}$, or again

$$\sum_{p=0}^{n_p^{\mathrm{C}}} \sum_{i=0}^{n_p^{\mathrm{C}}} \underbrace{\bigwedge_{\omega^e} \int_{\omega^e} \left(\mathbf{b}^e\right)^T \mathbf{u}_{\boldsymbol{k}^{(i)}}(\boldsymbol{x}) \mathbf{b}^e d\boldsymbol{x}}_{\mathbf{k}_{\mathrm{m}}^{(i)}} \underbrace{\int_{\mathcal{S}_{\boldsymbol{\Xi}}} \left[\psi_{\boldsymbol{k}^{(i)}}\left(\boldsymbol{\xi}\right) \psi_{\boldsymbol{k}^{(p)}}\left(\boldsymbol{\xi}\right) \psi_{\boldsymbol{k}^{(q)}}\left(\boldsymbol{\xi}\right)\right] \pi_{\boldsymbol{\Xi}}(\boldsymbol{\xi}) \mathrm{d}\boldsymbol{\xi}}_{c^{(i,\, p,\, q)}} \quad \boldsymbol{d}_{\boldsymbol{k}^{(p)}} = 0\,, \quad \forall q = 1..n_p^{\mathrm{C}}\,, \tag{247}$$

In Tootkaboni and Graham-Brady (2010), a spectral stochastic computational scheme was proposed that links the global properties of multiphase periodic composites to the random material properties of their microstructural components. In particular, they have considered the case for which material properties of the two phases of the composite material are uncorrelated and the case of perforated two-phase composites with correlated elastic properties. Xu and Graham-Brady (2005) have analysed the elastic behaviour of random media by considering varying elasticity constants, for the two cases of Gaussian and non-Gaussian processes.

Finally, the case of perfect plasticity with varying elasticity constants and yield stress was studied by Rosi and Matthies (2008).

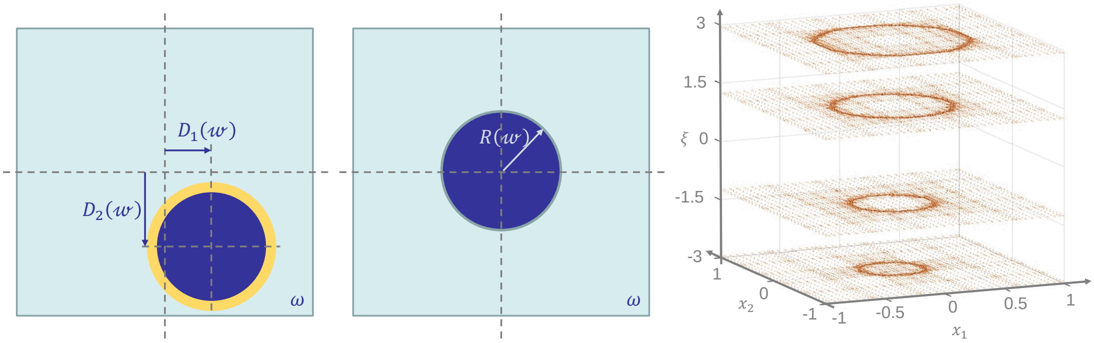

(a) Random inclusion location (b) Random inclusion radius (c) Integration points of the random inclusion radius

Figure 30: Schematics of the random unit cells studied: (a) by Pivovarov and Steinmann (2016) in which the centre location (d_1, d_2) of the particle is defined by a couple of random variables (D_1, D_2); (b) by Pivovarov et al. (2018b) in which the inclusion radius r is defined by a random variable R; and (c) in which a global stochastic finite element method is considered with the displayed integration points, resketched from (Pivovarov et al., 2018b).

Local & global Galerkin finite elements. The difficulty with the Galerkin stochastic finite element method is to define the boundary of phases in heterogeneous structures since the latter are varying with the realisation $w \in \mathcal{W}$. Another difficulty with the Galerkin stochastic finite element method is the definition of the integration process both in the physical domain ω and in the stochastic support $\mathcal{S}_{\boldsymbol{\Xi}}$.

In the context of non-linear elasticity, Pivovarov and Steinmann (2016) have considered an inclusion embedded in a matrix, see Fig. 30(a), and whose centre (d_1, d_2) is defined by a couple of random variables $D_1 \sim \mathcal{N}^{\text{trunc}}_{\bar{d}_1, \sigma_1^2}$ and $D_2 \sim \mathcal{N}^{\text{trunc}}_{\bar{d}_2, \sigma_2^2}$, where $\mathcal{N}^{\text{trunc}}$ is the truncated normal distribution $\mathcal{N}$ (17). These random variables can be defined from two independent, zero-mean, and unit variance random variables $\Xi_1, \Xi_2 : \mathcal{W} \to \Re$ with $\Xi_1, \Xi_2 \sim \mathcal{N}^{\text{trunc}}_{0,1}$ and

$$D_1(w) = \bar{d}_1 + \sigma_1 \Xi_1(w); \quad D_2(w) = \bar{d}_2 + \sigma_1 \Xi_2(w) \,. \tag{248}$$

The boundary of the inclusion of deterministic radius r is implicitly defined though a level-set function

$$z(\boldsymbol{x},\, \omega) = r\left[\sqrt{\frac{[x_1 - D_1(\omega)]^2}{r^2} + \frac{[x_2 - D_2(\omega)]^2}{r^2}} - 1\right]\,, \tag{249}$$

defined as being negative within the inclusion and positive within the matrix. The material properties, such as the shear modulus μ, are then described by a hyperbolic tangent of the level set function

$$\mu(\boldsymbol{x},\, \omega) = \mu_0 + \frac{1}{2}\left[\mu_{\mathrm{I}} - \mu_0\right]\left[1 - \tanh\left(kz(\boldsymbol{x},\, \omega)\right)\right]\,, \tag{250}$$

where the subscripts I and 0 refer to the inclusion and matrix respectively, avoiding the use of a Karhunen-Loève expansion to define the random field. A regular spatial mesh was then used in the stochastic finite element discretisation. Since the material properties have large variations in a reduced space, this requires an increase of the basis $\{\psi_l^{(i)} : l \in \mathbb{N}_0,\, i = 1..2\}$ and thus of the order of the Hermite polynomials, yielding oscillations due to numerical errors when performing the integration process in the stochastic support $\mathcal{S}_{\boldsymbol{\Xi}}$. This required a special treatment and a new quadrature rule, in particular in the case of truncated Gaussian distributions (Pivovarov and Steinmann, 2016). In this stochastic-local finite element method, Pivovarov and Steinmann (2016) have also considered usual Lagrangian shape functions $\varphi^{(a)}(\boldsymbol{x})$ in the physical domain, and sequences of trigonometric functions to define the shape function $\psi_{\boldsymbol{k}^{(l)}}\left(\boldsymbol{\Xi}(\omega)\right)$ in the stochastic domain.

A stochastic-global finite element method was developed by Pivovarov et al. (2018b) in which the inclusion radius r is defined by a random variable R which follows a log-normal distribution, see Fig. 30(b). Trigonometric shape functions are considered for both the physical domain and the stochastic domain, resulting in a global discretisation and integration rule as illustrated in Fig. 30(c). For the physical domain, the functions are enriched by discontinuous functions defined by the level-set (249), and a rectangular splitting was performed to get a local refinement. Compared to local stochastic finite elements, the stiffness matrix is of reduced size, but its sparsity is lower. Accuracy is also generally lower (Pivovarov et al., 2018b).

These approaches are in-line with the concept of statistically similar RVE proposed by Pivovarov et al. (2018a) and shortly presented in Section 4.2.1 since in the latter a stochastic model of a cell element with statistical properties has to be solved.

5. Stochastic macro-scale simulations

In the general context of non-linear and history dependent material behaviours at the micro-structure scale, following Eq. (116), the macro-scale response of a body Ω ought to capture this history-dependency and the meso-scale constitutive law (120) at a given time t and material point $\boldsymbol{X} \in \Omega$ is written as

$$\mathbf{P}_{\mathrm{M}}\left(\boldsymbol{X},\, t;\, \omega\right) = \mathbf{P}_{\mathrm{M}}\left(\mathbf{F}_{\mathrm{M}}\left(\boldsymbol{X},\, t;\, \omega\right);\boldsymbol{Z}_{\mathrm{M}}\left(\boldsymbol{X},\, \tau;\, \omega\right),\, \tau \in [0,\, t],\, \omega\right)\,, \tag{251}$$

where the macro-scale deformation gradient tensor $\mathbf{F}_{\mathrm{M}}(\boldsymbol{X};\,\omega) = \mathbf{I} + \boldsymbol{U}_{\mathrm{M}}(\boldsymbol{X};\,\omega) \otimes \boldsymbol{\nabla}_0$ is evaluated in terms of the macro-scale displacement $\boldsymbol{U}_{\mathrm{M}}(\boldsymbol{X};\,\omega)$ and constitutes the average deformation gradient at the micro-scale following Eq. (121), and where $\boldsymbol{Z}_{\mathrm{M}}(\boldsymbol{X};\,\omega)$ is a set of internal variables allowing history-dependent processes to be accounted for. In all generalities, the constitutive equation depends on the micro-structure realisation $\omega \in \mathcal{W}$ because of the geometrical and material uncertainties. In a classical multi-scale simulation the macro-scale first Piola-Kirchhoff stress tensor $\mathbf{P}_{\mathrm{M}}(\boldsymbol{X},\,t;\,\omega)$ follows from the volume averaging of the micro-scale following Eq. (122) which thus substitutes to the constitutive law (251). However conducting concurrent deterministic non-linear multi-scale analyses is already computationally demanding, so that concurrent stochastic non-linear multi-scale analyses is usually unreachable, although in some particular cases it is possible to solve the stochastic multi-scale problem in a fully coupled way. For example, in the context of stochastic asymptotic homogenisation in which the fine-scale and coarse scale resolutions are concurrent, see Section 4.2.2, Fish and Wu (2011) generated the material fields, corresponding to fine-scale constitutive inelastic parameters of the constitutive law (197), using KL expansion. However, this method can be expensive, and one alternative is to extract apparent properties during an off-line stage, and to generate random fields at the meso-scale level that can then be used for stochastic macro-scale simulations. In that case, the stochastic meso-scale law (251) should be substituted by a surrogate model defined from these meso-scale random fields.

In what follows, we first introduce general concepts on the discretisation of a random-field when considering macro-scale stochastic finite elements. Particular attention is paid on the requirements allowing the stochastic macro-scale simulation to capture the statistical content of the random field. The different methods developed to represent a random field, but also to generate pseudo-samples of the random field, are then introduced in a general context. Some of these methods are particularised, first, in the context of random tensor fields for stochastic linear analyses and then in the context of stochastic non-linear analyses for which some multi-fidelity examples are given. Some stochastic finite element methods used at the macro-scale are then briefly summarised since they closely follow the methods developed at the micro-scale in Section 4.3.

5.1. Random fields and stochastic finite-element discretisation

5.1.1. Random field description

As discussed in Section 4.1.2, the window technique illustrated in Fig. 25 allows a meso-scale random field $\{\boldsymbol{Q}_{\mathrm{M}}(\boldsymbol{X},\,\omega) :\ \boldsymbol{X} \in \Omega,\, \omega \in \mathcal{W}\}$, with the random vectors $\boldsymbol{Q}_{\mathrm{M}}(\boldsymbol{X})$ valued in $\Re^n$, to be extracted on the macro-scale domain Ω. This random field is characterised by a correlation matrix $\mathbf{R}_{\boldsymbol{Q}_{\mathrm{M}}}(\boldsymbol{X};\,\boldsymbol{\tau}) :\ \Omega \times \Re^3 \rightarrow \Re^{n\times n}$ defined by Eq. (47), where $\boldsymbol{\tau}$ is the separation vector between two points of Ω. Assuming an homogeneous random field, the correlation matrix simplifies into $\mathbf{R}_{\boldsymbol{Q}_{\mathrm{M}}}(\boldsymbol{X};\,\boldsymbol{\tau}) = \mathbf{R}_{\boldsymbol{Q}_{\mathrm{M}}}(\boldsymbol{\tau})$, and is characterised by the correlation lengths

$$l_{R_{\boldsymbol{Q}_{\mathrm{M}\,r\,s}}} = \frac{\int_{-\infty}^{\infty} R_{\boldsymbol{Q}_{\mathrm{M}\,r\,s}}(\tau)d\tau}{R_{\boldsymbol{Q}_{\mathrm{M}\,r\,s}}(0)}\,. \tag{252}$$

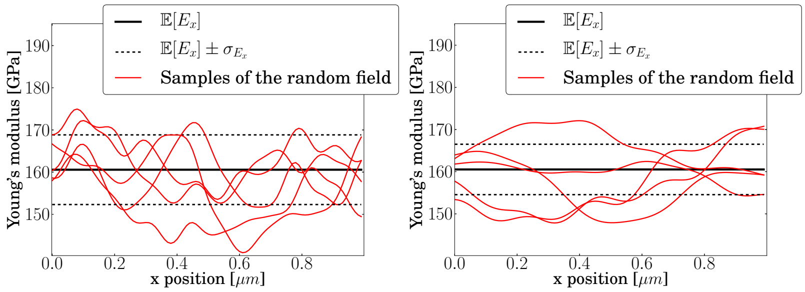

(a) $l_{\mathrm{SVE}} = 0.1\mu\mathrm{m}$ (b) $l_{\mathrm{SVE}} = 0.4\mu\mathrm{m}$

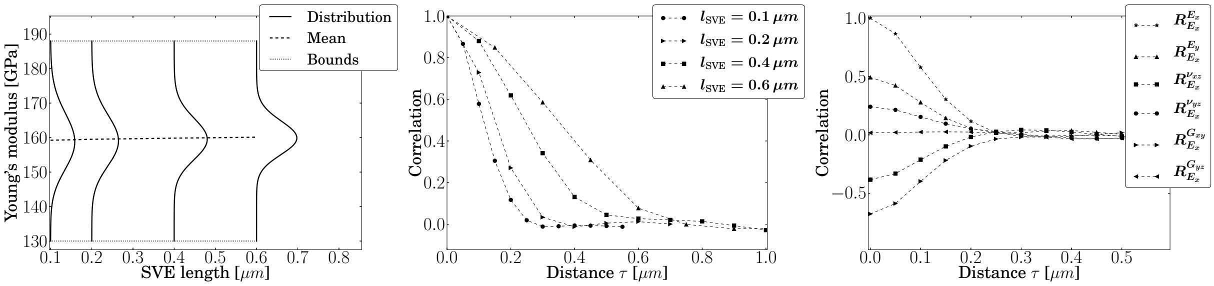

(c) π_{E_x} (d) $R_{E_x}(\tau)$ (e) $\mathbf{R}(\tau)$; $l_{\mathrm{SVE}} = 0.1\mu\mathrm{m}$

Figure 31: Extraction by Lucas et al. (2015) of different random field realisations $E_x(X, \omega^i)$, with $\omega^i \in \mathcal{W}$ and $i = 1..5$, of the apparent Young's modulus E_x of a columnar poly-silicon micro-structure of average grain size of about $l_{\mathrm{micro}} \simeq 200$ nm for: (a) An SVE length $l_{\mathrm{SVE}} = 0.1\mu$m and; (b) An SVE length $l_{\mathrm{SVE}} = 0.4\mu$m; and extraction of (c) The probability density function π_{E_x} of the apparent Young's modulus E_x for different SVE sizes l_{SVE}; (d) The corresponding apparent Young's modulus auto-correlation $R_{E_x}(\tau)$ for different SVE sizes l_{SVE}; and (e) Different entries (auto and cross) of the correlation matrix $\mathbf{R}(\tau)$ for $l_{\mathrm{SVE}} = 0.1\mu$m; Reprinted from Computer Methods in Applied Mechanics and Engineering 294, Lucas, V., Golinval, J.C., Paquay, S., Nguyen, V.D., Noels, L., A stochastic computational multiscale approach; application to mems resonators, 141-167. Copyright (2015), with permission from Elsevier.

As an example, Fig. 31 illustrates apparent properties extracted for different SVE length l_{SVE} values by Lucas et al. (2015) on poly-silicon micro-structures, see Fig. 25(c), of average grain size of about $l_{\mathrm{micro}} \simeq 200$ nm. Figures 31(a) and 31(b) illustrate five random field realisations $E_x(X, \omega^i)$ of the Young's modulus obtained with the window technique, see Section 4.1.2, for two different SVE length sizes of respectively $l_{\mathrm{SVE}} = 0.1\mu$m and $l_{\mathrm{SVE}} = 0.4\mu$m. Clearly, when increasing the SVE length, the "randomness" of the field decreases since less spatial variations are observed and since the standard deviation σ_{E_x} decreases. This is confirmed by Fig. 31(c), which reports the probability density function π_{E_x} of the apparent Young's modulus for different sizes l_{SVE} of the SVEs. It can be seen than when l_{SVE} increases, the coefficient of variation of the distribution decreases, and that the apparent properties tend toward the effective properties of a RVE. Beside its entries distribution, the random field $\boldsymbol{Q}_{\mathrm{M}}(\Omega)$ defined from the apparent elasticity properties of the anisotropic homogenised material –different Young's moduli, Poisson ratios and shear moduli– is characterised by its correlation matrix $\mathbf{R}_{\boldsymbol{Q}_{\mathrm{M}}}(\boldsymbol{X};\, \boldsymbol{\tau}) : \Omega \times \Re^3 \rightarrow \Re^{n \times n}$. The auto-correlation of the apparent Young's modulus is illustrated in Fig. 31(d) for different SVE length l_{SVE} values. As shown in Fig. 25(c), since two SVEs share common grains even if they are not intersecting, a correlation is observed at distances beyond the SVE length, although the correlation at a distance equal or larger than the SVE size tends to vanish when the SVE length increases. Finally, some components of the correlation matrix $\mathbf{R}_{\boldsymbol{Q}_{\mathrm{M}}}(\boldsymbol{\tau})$, see Eq. (113), of the homogeneous random field are reported in Fig. 31(e) for a given SVE length $l_{\mathrm{SVE}} = 0.1\mu\mathrm{m}$ of the SVEs. It can be seen that the different auto- and cross-correlations are characterised by a similar correlation length (252).

Several questions have then to be addressed when it comes to consider these random fields as material input for stochastic macro-scale simulations, such as how to discretise the random field with respect to the finite elements, but also, since the random field depends on the choice of the SVE size, what are the conditions ensuring converge of the distribution of the macro-scale response.

5.1.2. Discretisation of the random field

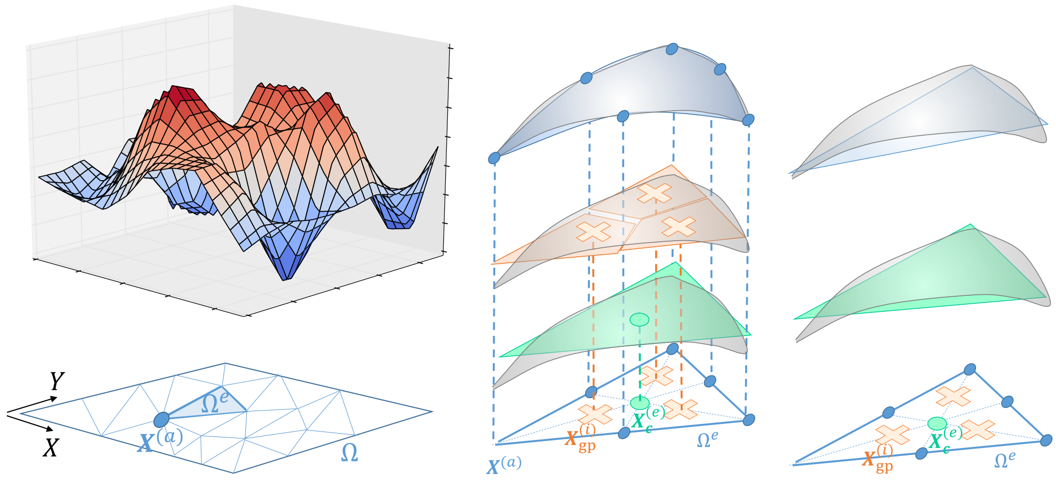

(a) FE mesh (b) Point-discretisation (c) Average-discretisation

Figure 32: Random field discretisation: (a) Illustration of a uni-variate random field realisation path $\{Q_{\mathrm{M}}(\boldsymbol{X},\ \omega) :\ \boldsymbol{X} \in \Omega\}$ and of a finite element mesh discretization $\Omega \simeq \cup_e \Omega^e$ into finite element Ω^e; (b) Illustration of different point discretisation methods of the random field sketched in grey with the mid-point method in green, Gauss-point method in orange and shape function method in blue; and (c) Illustration of different average discretisation methods of the random field sketched in grey with the spatial-average method in green and the weighed integral method in blue.

Assuming the random field $\{\boldsymbol{Q}_{\mathrm{M}}(\boldsymbol{X},\ \omega) :\ \boldsymbol{X} \in \Omega,\ \omega \in \mathcal{W}\}$ description is available –this point will be discussed in the random-field generation Section 5.2– for any point $\boldsymbol{X}$ in the finite element discretisation $\cup_e^{n^e} \Omega^e$ of the macro-structure Ω, the n stochastic material properties at the n^{gp} integration points $\boldsymbol{X}_{\mathrm{gp}}^{(i)}$ of the n^e finite elements Ω^e can be extracted from a discretization of the random field, see Fig. 32(a). During this discretization the approximated random field is defined from a finite set of N random vectors $\boldsymbol{U}^{(i)}$ valued in $\Re^n$ grouped in the form of a global random vector $\boldsymbol{U}_{\mathrm{g}} = \left[\boldsymbol{U}^{(1)^T}\,\boldsymbol{U}^{(2)^T} \ldots \boldsymbol{U}^{(N)^T}\right]^T$ valued in

$\Re^{n \cdot N}$. In order to define this random field approximation, including the value of N and the expression of the random vectors $\boldsymbol{U}^{(i)}$, different methods have been developed and their accuracy has been compared by Der Kiureghian and Ke (1988); Matthies et al. (1997). We here below give the main lines of some popular methods and refer to the review by Sudret and Der Kiureghian (2000) for more details

Point discretisation method. For the point discretisation method, the N random vectors $\boldsymbol{U}^{(i)}$ correspond to the evaluation $\boldsymbol{Q}_{\mathrm{M}}(\boldsymbol{X}_{\mathrm{p}}^{(i)})$ of the random field at N locations $\boldsymbol{X}_{\mathrm{p}}^{(i)} \in \boldsymbol{X}$, $i = 1..N$. The number N of points and their locations $\boldsymbol{X}_{\mathrm{p}}^{(i)}$ depend on the method, see Fig. 32(b):

- The mid-point method considers the $N = n^e$ finite element centroïds location $\boldsymbol{X}_p^{(e)} = \boldsymbol{X}_{\mathrm{c}}^{(e)}$, see the green sketch of Fig. 32(b); The random field approximation is then defined by the random vector $\boldsymbol{U}_{\mathrm{g}} = \left[\boldsymbol{Q}_{\mathrm{M}}^T(\boldsymbol{X}_{\mathrm{c}}^{(1)})\, \boldsymbol{Q}_{\mathrm{M}}^T(\boldsymbol{X}_{\mathrm{c}}^{(2)}) \ldots \boldsymbol{Q}_{\mathrm{M}}^T(\boldsymbol{X}_{\mathrm{c}}^{(n^e)})\right]^T$ valued in $\Re^{n \cdot n^e}$, and the random field at the Gauss integration point $\boldsymbol{X}_{\mathrm{gp}}^{(i)} \in \Omega^e$ is approximated by $\boldsymbol{Q}_{\mathrm{M}}\left(\boldsymbol{X}_{\mathrm{gp}}^{(i)}\right) \simeq \boldsymbol{Q}_{\mathrm{M}}\left(\boldsymbol{X}_{\mathrm{c}}^{(e)}\right)$; The mid-point method tends to over-represent the variability of the random field as shown by Der Kiureghian and Ke (1988);

- The integration point method is a similar approach in which the random field is directly evaluated at the $N = n^{\mathrm{gp}}$ Gauss points at location $\boldsymbol{X}_{\mathrm{p}}^{(i)} = \boldsymbol{X}_{\mathrm{gp}}^{(i)}$, see the orange sketch of Fig. 32(b); The random vector $\boldsymbol{U}_{\mathrm{g}} = \left[\boldsymbol{Q}_{\mathrm{M}}^T\left(\boldsymbol{X}_{\mathrm{gp}}^{(1)}\right) \boldsymbol{Q}_{\mathrm{M}}^T\left(\boldsymbol{X}_{\mathrm{gp}}^{(2)}\right) \ldots \boldsymbol{Q}_{\mathrm{M}}^T\left(\boldsymbol{X}_{\mathrm{gp}}^{(n^{\mathrm{gp}})}\right)\right]^T$ valued in $\Re^{n \cdot n^{\mathrm{gp}}}$ then defines the random field approximation, and the random field at Gauss integration point $\boldsymbol{X}_{\mathrm{gp}}^{(i)}$ is approximated by $\boldsymbol{Q}_{\mathrm{M}}\left(\boldsymbol{X}_{\mathrm{gp}}^{(i)}\right)$; This improves the accuracy as compared to the mid-point method and we will discuss further on the accuracy of this approach in the context of stochastic multi-scale method in Section 5.1.3;

- With the shape function method, the random field is evaluated at the $N = n^{\mathrm{node}}$ finite element nodes of locations $\boldsymbol{X}_{\mathrm{p}}^{(a)} = \boldsymbol{X}^{(a)}$, see the blue sketch of Fig. 32(b), and the random vector $\boldsymbol{U}_{\mathrm{g}} = \left[\boldsymbol{Q}_{\mathrm{M}}^T\left(\boldsymbol{X}^{(1)}\right) \boldsymbol{Q}_{\mathrm{M}}^T\left(\boldsymbol{X}^{(2)}\right) \ldots \boldsymbol{Q}_{\mathrm{M}}^T\left(\boldsymbol{X}^{(n^{\mathrm{node}})}\right)\right]^T$ valued in $\Re^{n \cdot n^{\mathrm{node}}}$ defines the random field approximation; The random field at Gauss integration point $\boldsymbol{X}_{\mathrm{gp}}^{(i)}$ is then approximated using the finite element discretization (135) by $\boldsymbol{Q}_{\mathrm{M}}\left(\boldsymbol{X}_{\mathrm{gp}}^{(i)}\right) \simeq \sum_{(a)} \varphi^{(a)}\left(\boldsymbol{X}_{\mathrm{gp}}^{(i)}\right) \boldsymbol{Q}_{\mathrm{M}}\left(\boldsymbol{X}^{(a)}\right)$, where $\varphi^{(a)}(\boldsymbol{X})$ are the nodal shape functions;

- The optimal linear estimation method builds an approximated field under the form $\boldsymbol{Q}_{\mathrm{M}}(\boldsymbol{X}) \simeq \boldsymbol{a}(\boldsymbol{X}) + \mathbf{b}(\boldsymbol{X})\boldsymbol{U}_{\mathrm{g}}$, with $\boldsymbol{U}_{\mathrm{g}}$ the random vector constructed from N random vectors $\boldsymbol{U}^{(i)}$ corresponding to the evaluation $\boldsymbol{Q}_{\mathrm{M}}(\boldsymbol{X}_{\mathrm{p}}^{(i)})$ of the random field at N locations $\boldsymbol{X}_{\mathrm{p}}^{(i)} \in \Omega$, $i = 1..N$; The coefficients functions $\boldsymbol{a}(\boldsymbol{X})$ and $\mathbf{b}(\boldsymbol{X})$ are evaluated in order to minimise at each point $\boldsymbol{X} \in \Omega$ the variance of the error whilst keeping the mean unbiased, see the details given by Sudret and Der Kiureghian (2000); In order to minimise the variance error, one wants

$$
\begin{aligned}
b_{pq}(\boldsymbol{X}) \quad &= \arg\,\min_{b'_{pq}(\boldsymbol{X})} \quad \Bigg(\mathbb{E}\Bigg[\Bigg(Q_{\mathrm{M}_i}(\boldsymbol{X}) - \bar{q}_{\mathrm{M}_i}(\boldsymbol{X}) - \sum_k^{n\cdot N} b'_{ik}(\boldsymbol{X})(U_{\mathrm{g}_k} - \bar{u}_{\mathrm{g}_k})\Bigg) \\
&\qquad \Bigg(Q_{\mathrm{M}_j}(\boldsymbol{X}) - \bar{q}_{\mathrm{M}_j}(\boldsymbol{X}) - \sum_k^{n\cdot N} b'_{jk}(\boldsymbol{X})(U_{\mathrm{g}_k} - \bar{u}_{\mathrm{g}_k})\Bigg)\Bigg]\Bigg) \\
&\qquad \forall i,\, j,\, p = 1..n,\, q = 1..n\cdot N\,; \qquad (253)
\end{aligned}
$$

The solution is obtained by evaluating the stationary point in terms of $b_{pq}(\boldsymbol{X})$ –*i.e.* evaluating the root of the derivative, yielding

$$
\mathbf{b}(\boldsymbol{X}) = \tilde{\mathbf{R}}^{-1}_{\boldsymbol{U}_\mathrm{g}} \tilde{\mathbf{R}}_{\boldsymbol{U}_\mathrm{g},\, \boldsymbol{Q}_\mathrm{M}(\boldsymbol{X})}\,; \qquad (254)
$$

Minimisation of the expectation error implies

$$
a_p(\boldsymbol{X}) \quad = \arg\,\min_{a'_p(\boldsymbol{X})} \quad \Bigg(\bar{q}_{\mathrm{M}_i}(\boldsymbol{X}) - a_i(\boldsymbol{X}) - \sum_k^{n\cdot N} b'_{ik}(\boldsymbol{X})\bar{u}_{\mathrm{g}_k}\Bigg) \ \forall i,\, p = 1..n\,; \qquad (255)
$$

which is obtained directly by

$$
\boldsymbol{a}(\boldsymbol{X}) \quad = \quad \bar{\boldsymbol{q}}_\mathrm{M}(\boldsymbol{X}) - \mathbf{b}(\boldsymbol{X})\bar{\boldsymbol{u}}_\mathrm{g}\,; \qquad (256)
$$

This method always under-estimates the variance of the original random field.

Average discretisation methods. For the average discretisation method, the $N = n^e$ random vectors $\boldsymbol{U}^{(e)}$ correspond to the weighted averages of the random field over the finite element Ω^e with $\boldsymbol{U}^{(e)} = \int_{\Omega^e} \boldsymbol{Q}_\mathrm{M}(\boldsymbol{X}) w(\boldsymbol{X}) d\Omega^e$, with the weight function $w(\boldsymbol{X})$ and $e = 1..n^e$, n^e being the number of finite elements.

- In the spatial average method, the weight function is simply taken as $w(\boldsymbol{X}) = \frac{1}{V(\Omega^e)}$ to evaluate the random vectors $\boldsymbol{U}^{(e)}$, see the green sketch in Fig. 32(c), with $\boldsymbol{U}_\mathrm{g}$ the random vector valued in $\Re^{n\cdot n^e}$ constructed from the n^e random vectors $\boldsymbol{U}^{(e)}$; The random field at the Gauss integration point $\boldsymbol{X}^{(i)}_{\mathrm{gp}} \in \Omega^e$ is approximated by $\boldsymbol{U}^{(e)}$; The spatial-average method tends to under-represent the variability of the random field as shown by Der Kiureghian and Ke (1988); Besides, Matthies et al. (1997) have pointed out difficulties in the case of non-rectangular elements, such as the possibility to obtain a non-positive-definite covariance matrix.

- The weighted integral method performs the integration directly on the stiffness matrix $\mathbf{K}_\mathrm{M} = \bigwedge_{\Omega^e} \int_{\Omega^e} (\mathbf{b}^e)^T \, \mathbf{C}^{\mathrm{el}}_\mathrm{M} \mathbf{b}^e d\boldsymbol{X}$; Assuming linear elasticity, and assuming that the elasticity tensor $\mathbb{C}^{\mathrm{el}}_\mathrm{M}$ can be written under the matrix form $\mathbf{C}^{\mathrm{el}}_\mathrm{M} = \bar{\mathbf{c}}^{\mathrm{el}}_\mathrm{M}\left[1 + Q_\mathrm{M}(\boldsymbol{X})\right]$

with the zero-mean uni-variate random field $Q_{\mathrm{M}}(\boldsymbol{X})$, the elementary stiffness matrix is rewritten

$$\mathbf{K}_{\mathrm{M}}^{(e)} = \underbrace{\int_{\Omega^e} \left(\mathbf{b}^e\right)^T \bar{\mathbf{c}}_{\mathrm{M}}^{\mathrm{el}} \mathbf{b}^e \mathrm{d}\omega^e}_{\mathbf{K}_{\mathrm{M}}^{e(0)}} + \sum_{l=1}^{n^{\mathrm{monomials}}} \mathbf{a}^{(l)} \underbrace{\int_{\Omega^e} X^{\alpha^{(l)}} Y^{\beta^{(l)}} Z^{\alpha^{(l)}} Q_{\mathrm{M}}(\boldsymbol{X})}_{U_{(l)}^{(e)}}, \tag{257}$$

where $n^{\mathrm{monomials}}$ is the number of monomials $X^{\alpha^{(l)}} Y^{\beta^{(l)}} Z^{\alpha^{(l)}}$ resulting from the gradient of the shape function $\mathbf{b}^e$ and possibly from the tensor $\bar{\mathbf{c}}_{\mathrm{M}}^{\mathrm{el}}$, and where $\mathbf{a}^{(l)}$ is their coefficients; One thus has the $n^e \cdot n^{\mathrm{monomials}}$ random variables $U_{(l)}^{(e)}$ with $\boldsymbol{U}_{\mathrm{g}}$ the random vector valued in $\Re^{n^e \cdot n^{\mathrm{monomials}}}$ constructed from the $n^e \cdot n^{\mathrm{monomials}}$ random variables $U_{(l)}^{(e)}$; The interpretation of the method is sketched in blue in Fig. 32(c); This method bears similarities with the shape function point discretization method, but considering as polynomial approximation the one defined from the gradient of the shape function $\mathbf{b}^e$ and possibly from the tensor $\mathbb{C}_{\mathrm{M}}^{\mathrm{el}}$.

5.1.3. *Convergence analysis*

In order to study the effect of the SVE size and of the finite-element size on the distribution of the macro-scale response, Lucas et al. (2015) have studied the eigen-frequencies of a poly-crystalline MEMS (standing for MicroElectroMechanical Systems) beam. The micro-structure corresponds to columnar poly-silicon grains of average size of about $l_{\mathrm{micro}} \simeq 200$ nm, which is not several order of magnitude lower than the characteristic MEMS beam length of a few μm.

As a reference case, direct Monte Carlo simulations were conducted on the fully discretised beam as illustrated in Fig. 33(a). A random field $\{E_X(\boldsymbol{X},\ \omega) : \ \boldsymbol{X} \in \Omega,\ \omega \in \mathcal{W}\}$ of the homogenised Young's modulus E_x was then extracted using the window technique described in Section 4.1.2, for different SVE lengths as illustrated in Fig. 31. For each SVE, the stochastic computational homogenisation was performed using the framework described in Section 4.2.1. A stochastic multi-scale method could then be performed by considering beam finite elements whose material properties were defined by discretising the random field $E_X(\boldsymbol{X})$ using the integration point method (one Gauss integration point by beam element). Several random fields $\{E_X(\boldsymbol{X},\ \omega) : \ \boldsymbol{X} \in \Omega\}$ trajectories, with $\omega \in \mathcal{W}$, obtained for different SVE lengths l_{SVE}, and thus characterised by different corresponding correlation lengths $l_{R_{E_X}}$, were considered for different mesh sizes l_{mesh}, defining the ratio $\alpha = \frac{l_{R_{E_X}}}{l_{\mathrm{mesh}}}$, see Fig. 33(b). A large value of α corresponds *in fine* to overlapping SVE larger than the finite element, and on the contrary a small value of α corresponds to smaller SVE than the finite elements.

Fig. 33(c) shows than when the value of α becomes larger than one, *i.e.* when the mesh size is smaller than the correlation length, the coefficient of variation of the structural quantity of interest distribution, *i.e.* the first eigen-frequency of the beam, predicted by the stochastic multi-scale method is converging to the one observed by the direct Monte Carlo simulations conducted on the fully discretised poly-crystalline beam. This observation holds

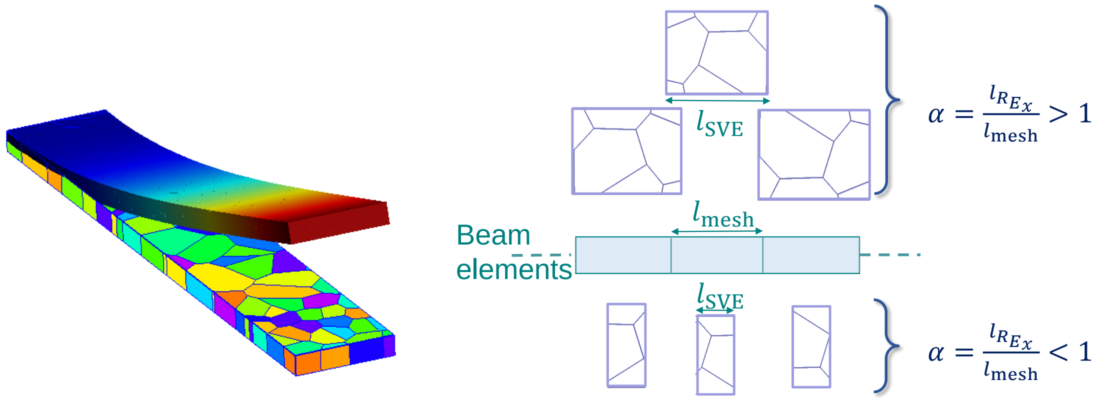

(a) Direct realisation ω (b) Stochastic multi-scale

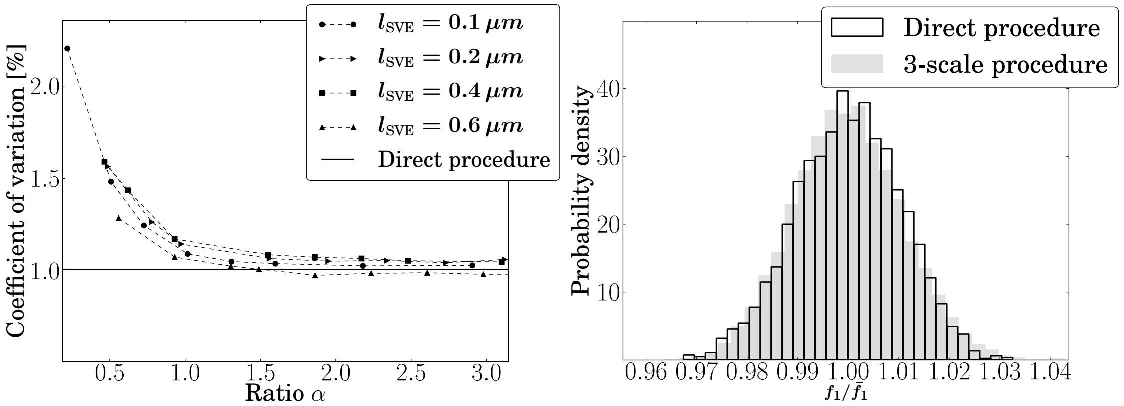

(c) Coefficient of variation (d) Distribution at given α

Figure 33: Convergence analysis conducted by Lucas et al. (2015) of the stochastic multi-scale method on the vibration analysis of a poly-silicon MEMS beam: (a) One realisation of a direct simulation in which all the grains of the micro-structure realisation ω are meshed; (b) Stochastic multi-scale simulation for different values of the ratio $\alpha = \frac{l_{R_{E_x}}}{l_{\text{mesh}}}$, the ratio between the correlation length of the Youngs modulus, $l_{R_{E_x}}$, and the mesh size, l_{mesh}, of the beam elements; (c) Comparison of the coefficient of variation $\left(\frac{\sigma_{F_1}}{\mathbb{E}[F_1]}\right)$ of the first resonance frequency f_1 obtained with the direct stochastic method with the ones predicted by the stochastic multi-scale method for different values of the ratio $\alpha = \frac{l_{E_{E_x}}}{l_{\text{mesh}}}$ and of the SVE length l_{SVE}; and (d) Comparison of the first resonance frequency histogram obtained with the direct stochastic method with the one obtained with the stochastic multi-scale simulation for an SVE length $l_{SVE} = 0.4$ μm and a beam mesh size $l_{SVE} = 0.27$ μm; Reprinted from Computer Methods in Applied Mechanics and Engineering 294, 189, Lucas, V., Golinval, J.C., Paquay, S., Nguyen, V.D., Noels, L., A stochastic computational multiscale approach; application to mems resonators, 141-167. Copyright (2015), with permission from Elsevier.

for the different sizes of the SVE. Besides, the distributions were also found to be in good agreement for $\alpha > 1$ as shown in Fig. 33(d). The requirement to use $\alpha > 1$ can be physically understood from Fig. 33(b). Indeed, if the mesh size is larger then the SVE size used to evaluate the random field, *i.e.* for the cases $\alpha < 1$, the random vector of properties associated to the elements over-represents the scatter, see also Fig. 31(c). On the contrary, in the cases in which the SVEs overlap each other, *i.e.* for the cases $\alpha > 1$, although the random vector of properties in a given finite element under-estimates the scatter, this effect is corrected by using a random field which naturally involves a spatial correlation. A similar analysis holds in the case of several Gauss integration points per elements by using the length associated to a Gauss integration point instead of the Finite Element length in the definition of α.

This example illustrates several important points:

- Because of the existing spatial correlation between the homogenised properties from the SVEs, the meso-scale properties should be defined under the form of a random-field and not considered as random vectors;
- The SVE length modifies the characteristics of the meso-scale random field of homogenised properties; However, as long as its correlation length remains small compared to the structure size, it is possible to conduct stochastic multi-scale analyses;
- At the structural scale, the finite element length, or the length associated to a Gauss point subdomain in the case of the integration point method, should remain smaller than the meso-sale correlation length, which depends on the SVE length: considering smaller SVE results in decreasing the size of the finite elements at the structural scale.

5.1.4. Case of spatially uncorrelated meso-scale properties

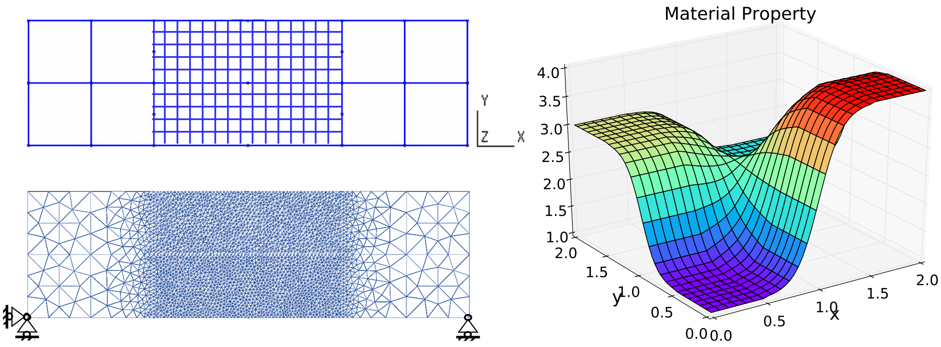

(a) Discretisations

(b) Interpolation

Figure 34: Stochastic multi-scale simulation of elastic UD composites conducted by Wu et al. (2018a): (a) discretisation of the random field (top) into cells having the size of the SVEs and of the structure (bottom) into finite elements of size smaller than the RF discretisation; and (b) properties interpolation smoothed at the SVEs boundaries; Reprinted from Composite Structures 189, Wu, L., Chung, C.N., Major, Z., Adam, L., Noels, L., From SEM images to elastic responses: A stochastic multiscale analysis of UD fiber reinforced composites, 206-227, Copyright (2018), with permission from Elsevier.

In some cases, as in the homogenisation of elastic UD composites conducted by Wu et al. (2018a) and illustrated in Figs. 25(b) and 29(b), the correlation can be neglected for two adjacent SVEs because the amount of shared fibres remain marginal. In that case, if the distributions are close enough from Gaussianity, which was the case for large enough SVEs, see Fig. 29(b), the homogenised properties of two adjacent SVEs are independent and the apparent properties can be considered as random tensors $\{\mathbb{C}^{\mathrm{el}}_{\mathrm{M}}(\omega) :\ \omega \in \mathcal{W}\}$ or simply $\mathbb{C}^{\mathrm{el}}_{\mathrm{M}}$.

Stochastic multi-scale simulations were then conducted by considering the discretisation of the random field and of the finite elements illustrated in Fig. 34(a). The random field at the two ends of the sample was discretised into domains of size $125 \times 125\mu\mathrm{m}^2$ whilst the random field of material properties was discretized into squares of $25 \times 25\mu\mathrm{m}^2$ in the central part in which higher strain gradients were expected because of the loading condition. The random material properties were generated under the form of random tensors $\{\mathbb{C}^{\mathrm{el}}_{\mathrm{M}}(\omega) :\ \omega \in \mathcal{W}\}$ based on the homogenisation of SVEs of sizes matching the cell size of the random-field discretization, *i.e.* either $125 \times 125\mu\mathrm{m}^2$ or $25 \times 25\mu\mathrm{m}^2$. As a result, the transition of the material properties in the random vector field discretization follows a step function, leading to a strong contrast of material properties at the boundaries of the random field discretization. In order to avoid an artificial stress concentration which could arise in the finite element resolution at the boundaries of the random field discretization, smooth-step functions, see Fig. 34(b), were used to describe the transition of material properties at the internal boundaries of the random field discretization. The finite element discretization was then conducted so that the finite elements remain smaller that the grid of the random vector field discretisation in order to account for the correct amount of properties scatter.

Alternatively, one can still consider random fields $\{\mathbb{C}_{\mathrm{M}}(\boldsymbol{X},\ \omega) :\ \boldsymbol{X} \in \Omega,\ \omega \in \mathcal{W}\}$ as in Section 5.1.3, thus avoiding the need for the smooth-step functions.

5.2. *Representation and Generation of random vectors and fields*

During the stochastic resolution of the structural problem using *e.g.* MC simulations, see Section 5.5, several random fields of the apparent properties need to be considered: one for each structural scale resolution. Besides, if the structural-scale domain geometry changes, the random fields need to be defined on a different spatial discretisation. It is thus not possible to define the random field realisations directly from the stochastic homogenisation described in Section 4. Similarly, when considering Spectral Stochastic Finite Element, the random field of the apparent meso-scale properties needs to be adequately represented.

It is thus necessary to represent the random field from the apparent properties extracted during the stochastic homogenisation and, if needed, to be able to generate pseudo-samples of it, with an arbitrary number and on an arbitrary spatial domain.

We here below summarise some methods that are commonly considered in the literature and which are more detailed in Appendix A.

5.2.1. *Expansion method*

Considering the random vector field $\boldsymbol{Q}_{\mathrm{M}}(\Omega) = \{\boldsymbol{Q}_{\mathrm{M}}(\boldsymbol{X},\ \omega) :\ \boldsymbol{X} \in \Omega,\ \omega \in \mathcal{W}\}$, with the random vector $\boldsymbol{Q}_{\mathrm{M}}$ valued in $\Re^n$. The expectation is denoted by $\bar{\boldsymbol{q}}_{\mathrm{M}}(\boldsymbol{X}) = \mathbb{E}\left[\boldsymbol{Q}_{\mathrm{M}}(\boldsymbol{X})\right] : \Omega \rightarrow \Re^n$ and the covariance matrix by $\tilde{\mathbf{R}}_{\boldsymbol{Q}_{\mathrm{M}}}(\boldsymbol{X};\ \boldsymbol{\tau})$, see Eq. (50).

Representation.

- As already introduced in Section 4.3.3, following Appendix A.3.2, a Karhunen Loève (KL) expansion allows representing the random field $\boldsymbol{Q}_{\mathrm{M}}(\Omega)$ by the collection of

$$\boldsymbol{Q}_{\mathrm{M}}(\boldsymbol{X};\, \mathscr{w}) \simeq \bar{\boldsymbol{q}}_{\mathrm{M}}(\boldsymbol{X}) + \sum_{i=1}^{m} \sqrt{\lambda_{\boldsymbol{Q}}^{(i)}}\mathrm{H}_i(\mathscr{w})\boldsymbol{u}_{\boldsymbol{Q}_{\mathrm{M}}}^{(i)}(\boldsymbol{X}) = \sum_{i=0}^{m} \sqrt{\lambda_{\boldsymbol{Q}_{\mathrm{M}}}^{(i)}}\mathrm{H}_i(\mathscr{w})\boldsymbol{u}_{\boldsymbol{Q}_{\mathrm{M}}}^{(i)}(\boldsymbol{X})\,, \quad (258)$$

  where $\mathbf{H}$ is a new random vector of uncorrelated (but possibly dependent) components H_i, $\lambda_{\boldsymbol{Q}_{\mathrm{M}}}^{(i)}$ and $\boldsymbol{u}_{\boldsymbol{Q}_{\mathrm{M}}}^{(i)}(\boldsymbol{X})$ for $i > 0$ are the ordered eigen-values and orthonormal eigen-basis of the covariance matrix $\tilde{\mathbf{R}}_{\boldsymbol{Q}_{\mathrm{M}}}(\boldsymbol{X};\, \boldsymbol{\tau})$, m is the order of the expansion, and where we have defined $\mathrm{H}_0(\mathscr{w}) = \lambda_{\boldsymbol{Q}_{\mathrm{M}}}^{(0)} = 1$ and $\boldsymbol{u}_{\boldsymbol{Q}_{\mathrm{M}}}^{(0)}(\boldsymbol{X})$ as the expectation $\bar{\boldsymbol{q}}_{\mathrm{M}}$. The method is largely used for Gaussian processes $\{\boldsymbol{Q}_{\mathrm{M}}\,(\boldsymbol{X};\, \mathscr{w}) \,:\, \boldsymbol{X} \in \Omega,\, \mathscr{w} \in \mathscr{W})$ in which case $\mathrm{H} = [\mathrm{H}_1 \ldots \mathrm{H}_i \ldots \mathrm{H}_m]^T$ is a vector of m independent, zero-mean, and unit variance Gaussian random variables $\mathrm{H}_i : \mathscr{W} \to \Re$ of finite second order moment and of support $\mathscr{S}_{\mathrm{H}_i} = \Re$. The difficulty with the KL approach is to solve the eigen-value problem as explained in Appendix A.3.2. One solution consists in defining a Galerkin-type procedure as suggested by Ghanem and Spanos (1991). Recently, in order to ease the implementation in the case of physical domain of given complexity, the use of isogeometric basis functions in the Galerkin-type procedure was developed by Li et al. (2018). Another approach is to sample the random field as the collection $\{\boldsymbol{Q}_{\mathrm{M}}(\boldsymbol{X}^{(1)}),\, \ldots,\, \boldsymbol{Q}_{\mathrm{M}}(\boldsymbol{X}^{(N)})\}$, following Section 5.1.2, in order to define a new random vector $\boldsymbol{Y}$ valued in $\Re^{N\cdot n}$ and to build a covariance matrix whose eigen-values and vectors can be extracted using the PCA as summarised in Appendix A.3.2.

- In the context of non-Gaussian random field, following Appendix A.4.4, the random vector field $\boldsymbol{Q}_{\mathrm{M}}(\Omega) = \{\boldsymbol{Q}_{\mathrm{M}}(\boldsymbol{X},\, \mathscr{w}) \,:\, \boldsymbol{X} \in \Omega,\, \mathscr{w} \in \mathscr{W}\}$, with the random vector $\boldsymbol{Q}_{\mathrm{M}}$ valued in $\Re^n$ can then be considered as a deterministic non-linear mapping of the random germ Ξ valued in $\Re^{n^g}$ following the Polynomial Chaos Expansion (PCE)

$$\boldsymbol{Q}_{\mathrm{M}}(\boldsymbol{X};\, \mathscr{w}) \simeq \bar{\boldsymbol{q}}_{\mathrm{M}}(\boldsymbol{X}) + \sum_{l=1}^{n_p^{\mathrm{C}}} \boldsymbol{u}_{\boldsymbol{k}^{(l)}}(\boldsymbol{X})\psi_{\boldsymbol{k}^{(l)}}(\Xi(\mathscr{w}))\,, \quad (259)$$

  with the complete multi-index set of total degree at most p defined by Eq. (228) and composed of the elements $\boldsymbol{k}^{(0)} = \{0,\, \ldots,\, 0\}$, $\boldsymbol{k}^{(1)}$, ..., $\boldsymbol{k}^{(n_p^{\mathrm{C}})}$, with $n_p^{\mathrm{C}} = \frac{(n^g+p)!}{n^g!p!} - 1$, and with the multi-variate polynomial chaos $\psi_{\boldsymbol{k}^{(l)}}(\Xi)$ taken from a polynomial orthonormal family $\{\psi_{\boldsymbol{k}^{(l)}}(\Xi)\}$ of the Hilbert space $\mathscr{H}(\mathscr{W})$. The coefficients $\boldsymbol{u}_{\boldsymbol{k}^{(l)}}(\boldsymbol{X})$ are defined as

$$\begin{aligned}\boldsymbol{u}_{\boldsymbol{k}^{(l)}}(\boldsymbol{X}) &= \mathbb{E}\left[\left(\boldsymbol{Q}_{\mathrm{M}}(\boldsymbol{x}) - \bar{\boldsymbol{q}}_{\mathrm{M}}(\boldsymbol{X})\right)\psi_{\boldsymbol{k}^{(l)}}(\Xi)\right] \\ &= \int_{\Re^{n^g}} \left(\boldsymbol{Q}_{\mathrm{M}}(\boldsymbol{X}) - \bar{\boldsymbol{q}}_{\mathrm{M}}(\boldsymbol{X})\right)\psi_{\boldsymbol{k}^{(l)}}(\boldsymbol{\xi})\pi_{\Xi}(\boldsymbol{\xi})d\boldsymbol{\xi}\,, \quad l = 1..n_p^{\mathrm{C}}\,. \quad (260)\end{aligned}$$

- In order to define the polynomials chaos $\psi_{\boldsymbol{k}^{(l)}}(\Xi)$ and to identify the coefficients $\boldsymbol{u}_{\boldsymbol{k}^{(l)}}(\boldsymbol{X})$, the PCE can be applied on the random vector $\mathbf{H}$ valued in $\Re^m$ of uncorrelated (but dependent in the non-Gaussian case) components H_i defined in the KL expansion

(258), with $\mathbf{H} = \boldsymbol{f}(\boldsymbol{\Xi}) \simeq \sum_{l=0}^{n_p^{\mathrm{C}}} \boldsymbol{c}_{\boldsymbol{k}^{(l)}} \psi_{\boldsymbol{k}^{(l)}}(\boldsymbol{\Xi})$, see the details in Appendix A.4.4. This consists in a deterministic non-linear mapping of the random germ $\boldsymbol{\Xi}$, *e.g.*, considering the random germ as $n^g = m$ independent and uniformly distributed random variables Ξ_i. As an example, one can consider the inverse of the Rosenblatt transform with $\boldsymbol{\Xi} = \boldsymbol{f}^{\mathcal{R}\,\mathcal{U}}(\mathbf{H})$ following Appendix A.1.3, in combination with the shifted Legendre polynomial for $\psi_{\boldsymbol{k}^{(l)}}(\boldsymbol{\Xi})$, see the details provided in Appendix A.4.3. The coefficients valued in $\Re^m$ are then evaluated by

$$\boldsymbol{c}_{\boldsymbol{k}^{(l)}} = \mathbb{E}\left[\mathbf{H}\psi_{\boldsymbol{k}^{(l)}}(\boldsymbol{\Xi})\right] = \int_{\Re^m} \boldsymbol{f}(\boldsymbol{\xi})\psi_{\boldsymbol{k}^{(l)}}(\boldsymbol{\xi})\pi_{\boldsymbol{\Xi}}(\boldsymbol{\xi})d\boldsymbol{\xi}\,, \tag{261}$$

and $\boldsymbol{u}_{\boldsymbol{k}^{(l)}}(\boldsymbol{X})$ of Eq. (260) corresponds to $\boldsymbol{u}_{\boldsymbol{k}^{(l)}}(\boldsymbol{X}) = \sum_{i=1}^{m} \sqrt{\lambda_{\boldsymbol{Q}_{\mathrm{M}}}^{(i)}} c_{\boldsymbol{k}^{(l)}i} \boldsymbol{u}_{\boldsymbol{Q}_{\mathrm{M}}}^{(i)}(\boldsymbol{X})$. As for the KL expansion, in order to evaluate $\lambda_{\boldsymbol{Q}_{\mathrm{M}}}^{(i)}$ and $\boldsymbol{u}_{\boldsymbol{Q}_{\mathrm{M}}}^{(i)}(\boldsymbol{X})$, the approach can be applied on the random vector $\boldsymbol{Y} = \left[\boldsymbol{Q}_{\mathrm{M}}^{T}(\boldsymbol{X}^{(1)}) \ldots \boldsymbol{Q}_{\mathrm{M}}^{T}(\boldsymbol{X}^{(N)})\right]^{T}$ taking values in $\Re^{n\cdot N}$ and built as the collection defined by $\{\boldsymbol{Q}_{\mathrm{M}}(\boldsymbol{X}^{(1)}), \ldots, \boldsymbol{Q}_{\mathrm{M}}(\boldsymbol{X}^{(N)})\}$ of random vectors sampled for $\mathbf{X} = (\boldsymbol{X}^{(1)}, \ldots, \boldsymbol{X}^{(N)})$. This last approach however suffers from the curse of dimensionality when the size of the expansion $m \leq n \cdot N$ increases.

Generation.

- For Gaussian random fields, starting from the KL expansion (258), pseudo-samples can be generated as

$$\boldsymbol{q}_{\mathrm{M}}^{p}(\boldsymbol{X}) \simeq \bar{\boldsymbol{q}}_{\mathrm{M}}(\boldsymbol{X}) + \sum_{i=1}^{m} \sqrt{\lambda_{\boldsymbol{Q}_{\mathrm{M}}}^{(i)}} \eta_i^p \boldsymbol{u}_{\boldsymbol{Q}_{\mathrm{M}}}^{(i)}(\boldsymbol{X})\,, \tag{262}$$

  from pseudo-samples $\boldsymbol{\eta}^p$. Assuming Gaussianity, the pseudo-samples $\boldsymbol{\eta}^p$ are generated as m independent Gaussian variables η_i^p using either Monte Carlo sampling (MC) or Latin Hyper-cube Sampling (LHS). In the case in which the random field was sampled as the collection $\{\boldsymbol{Q}_{\mathrm{M}}(\boldsymbol{X}^{(1)}), \ldots, \boldsymbol{Q}_{\mathrm{M}}(\boldsymbol{X}^{(N)})\}$ in order to build a larger random vector $\boldsymbol{Y}$ on which PCA was applied, the formula is still used to generate pseudo samples $\boldsymbol{y}^p$ of the random vector $\boldsymbol{Y}$ and the random field pseudo-samples $\{\boldsymbol{q}_{\mathrm{M}}^{p}(\boldsymbol{X}^{(1)}), \ldots, \boldsymbol{q}_{\mathrm{M}}^{p}(\boldsymbol{X}^{(N)})\}$ are obtained by extraction of their components as summarised in Appendix A.3.3. If other locations $\boldsymbol{X}$ than at the initial sampling points $\boldsymbol{X}^{(k)}$, $k = 1..N$ are sought, an optimal linear estimation, see details in Section 5.1.2, can be used. A non-Gaussian transformation, see Appendix A.1, can also be applied in order to simulate non-Gaussian random fields, with the details reported by Vořechovský (2008). The method has however some limitations as studied by Vořechovský (2008). An iterative procedure combined to a non-linear transformation can also be applied on the pseudo-samples $\boldsymbol{\eta}^p$ in order to generate non-Gaussian random fields as summarised in Appendix A.3.4.

- For non-Gaussian random fields, considering the PCE (259), and assuming that the coefficients $\boldsymbol{u}_{\boldsymbol{k}^{(l)}}(\boldsymbol{X})$ of the polynomials chaos $\psi_{\boldsymbol{k}^{(l)}}(\boldsymbol{\Xi})$ have been identified, pseudo-samples can be generated as

$$\boldsymbol{q}^p_{\mathrm{M}}(\boldsymbol{X}) \simeq \bar{\boldsymbol{q}}_{\mathrm{M}}(\boldsymbol{X}) + \sum_{l=1}^{n_p^{\mathrm{C}}} \boldsymbol{u}_{\boldsymbol{k}^{(l)}}(\boldsymbol{X})\psi_{\boldsymbol{k}^{(l)}}(\boldsymbol{\xi}^p)\,, \tag{263}$$

from pseudo-samples $\boldsymbol{\xi}^p$ of the random germ.

- After having applied the PCE on the KL expansion, see Eq. (261), and assuming the coefficient $\boldsymbol{c}_{\boldsymbol{k}^{(l)}}$ have been identified for a given germ $\boldsymbol{\Xi}$ and a family $\{\psi_{\boldsymbol{k}^{(l)}}(\boldsymbol{\Xi})\}$ of the Hilbert space, pseudo-samples of the random field follow from Eq. (262), for given pseudo-samples $\boldsymbol{\eta}^p$. The latter follow from pseudo-samples $\boldsymbol{\xi}^p$ of the random germ following $\boldsymbol{\eta}^p = \boldsymbol{f}(\boldsymbol{\xi}^p) \simeq \sum_{l=0}^{n_p^{\mathrm{C}}} \boldsymbol{c}_{\boldsymbol{k}^{(l)}}\psi_{\boldsymbol{k}^{(l)}}(\boldsymbol{\xi}^p)$. The generation of the pseudo samples $\boldsymbol{\xi}^p$ is straightforward if the transform $\mathbf{H} = \boldsymbol{f}(\boldsymbol{\Xi})$ was designed such that the random germ $\boldsymbol{\Xi}$ can be considered as m independent random variables Ξ_i, see Appendix A.4.3.

5.2.2. Spectral methods

Considering the random vector field $\boldsymbol{Q}_{\mathrm{M}}(\Omega) = \{\boldsymbol{Q}_{\mathrm{M}}(\boldsymbol{X},\, \omega) : \boldsymbol{X} \in \Omega,\, \omega \in \mathcal{W}\}$, with the random vector $\boldsymbol{Q}_{\mathrm{M}}$ valued in $\Re^n$. The expectation is denoted by $\bar{\boldsymbol{q}}_{\mathrm{M}}(\boldsymbol{X}) = \mathbb{E}\left[\boldsymbol{Q}_{\mathrm{M}}(\boldsymbol{X})\right] : \Omega \to \Re^n$ and the covariance matrix by $\tilde{\mathbf{R}}_{\boldsymbol{Q}_{\mathrm{M}}}(\boldsymbol{X};\, \boldsymbol{\tau})$, see Eq. (50). We assume that the random field is homogeneous with the covariance matrix $\tilde{\mathbf{R}}_{\boldsymbol{Q}_{\mathrm{M}}}(\boldsymbol{\tau}) : \Re^d \to \Re^{n\times n}$, with d the space dimension.

Representation. Following Shinozuka and Jan (1972), a spectral representation can be constructed from the random field evaluation at a set of discrete positions $\boldsymbol{\tau} = \{\boldsymbol{\tau}^{(n_x\, n_y\, n_z)}\}$ defined by the vector components $\boldsymbol{\tau}^{(n_x\, n_y\, n_z)} = [n_x\Delta\tau_x \;\; n_y\Delta\tau_y \;\; n_z\Delta\tau_z]^T$, where $\Delta\tau_i$, for $i = x,\, y,\, z$, is the spatial increment in each dimension i and where $n_i = 0,\, 1,\, 2,\, ...,\, N_i - 1$, for $i = x,\, y,\, z$, with N_i the total number of discrete points in each dimension i. This allows redefining the covariance $\tilde{\mathbf{R}}[\boldsymbol{\tau}]$ as the set

$$\tilde{R}_{r\,s}[\boldsymbol{\tau}] = \left\{R_{\boldsymbol{Q}_{\mathrm{M}_{r\,s}}}\left(\boldsymbol{\tau}^{(n_x\, n_y\, n_z)}\right)\right\}, \tag{264}$$

from which the set of spectral density matrix $\mathbf{S}[\boldsymbol{\kappa}]$ can be computed using the Discrete Fourier Transform (DFT) method, see details in Appendix A.6, with the set $\boldsymbol{\kappa} = \{\boldsymbol{\kappa}^{(m_x\, m_y\, m_z)}\}$ of regularly spaced sampling points in the frequency domain of vector components $\boldsymbol{\kappa}^{(m_x\, m_y\, m_z)} = \left[\kappa_x^{(m_x)} \;\; \kappa_y^{(m_y)} \;\; \kappa_z^{(m_z)}\right]^T$ with $m_i = 0,\, 1,\, ...$ for $i = x,\, y,\, z$.

Generation. The set of spectral density matrix $\mathbf{S}[\boldsymbol{\kappa}]$ represents the random field in the frequency domain and serves as a basis to generate pseudo-random fields

- Considering first the case of a Gaussian Random field, since $\mathbf{S}\left(\boldsymbol{\kappa}^{(m_x\, m_y\, m_z)}\right)$ is an Hermitian matrix, one has $\mathbf{S}\left(\boldsymbol{\kappa}^{(m_x\, m_y\, m_z)}\right) = \mathbf{H}\left(\boldsymbol{\kappa}^{(m_x\, m_y\, m_z)}\right)\mathbf{H}^*\left(\boldsymbol{\kappa}^{(m_x\, m_y\, m_z)}\right)$, with $\mathbf{H}^*$ the conjugate transpose of $\mathbf{H}$. A pseudo-sample realisation of random field $\boldsymbol{Q}_{\mathrm{M}}(\Omega)$

is generated as a set of random vector realisations $\boldsymbol{q}^p_{\mathrm{M}}(\boldsymbol{X}^{(i)})$ at different locations $\boldsymbol{X}^{(i)} \in \Omega$, with for entry r of a realisation

$$q^p_{\mathrm{M}_r}(\boldsymbol{X}^{(i)}) = \bar{q}_{\mathrm{M}_r} + \sqrt{2\Delta}\Re\left\{\sum_{s=1}^{n}\sum_{m_x}\sum_{m_y}\sum_{m_z} H_{r\,s}\left(\boldsymbol{\kappa}^{(m_x\,m_y\,m_z)}\right)\right.$$
$$\left.\eta^{(s\,m_x\,m_y\,m_z)}e^{2\pi i\left(\boldsymbol{X}^{(i)}\cdot\boldsymbol{\kappa}^{(m_x\,m_y\,m_z)}+\theta^{(s\,m_x\,m_y\,m_z)}\right)}\right\}\,, \tag{265}$$

where $\Delta = \Delta\kappa_x\,\Delta\kappa_y\,\Delta\kappa_z$, where $\theta^{(s\,m_x\,m_y\,m_z)}$ is an independent random variable (for each s, m_x, m_y, m_z) sampled from $\Theta \sim \mathcal{U}_{0,1}$, and where $\eta^{(s\,m_x\,m_y\,m_z)}$ is sampled from a logarithmic transformation of a uniform distribution, see details in Appendix A.6.1.

- Following Deodatis and Micaletti (2001), it is possible to map the Gaussian field generated by Eq. (265) to a non-Gaussian field. To this end, an intermediate spectral representation $\mathbf{S}^n\left[\boldsymbol{\kappa}\right]$ to be used in the generator of the Gaussian random fields (265) is iteratively built so that the generated random field, after mapping, has the correct spectral representation $\mathbf{S}^{\mathrm{Target}}\left[\boldsymbol{\kappa}\right]$, see details in Appendix A.6.2.

5.2.3. Maximum entropy

Considering the random vector $\boldsymbol{Q}_{\mathrm{M}}$ valued in $\Re^n$, the maximum entropy principle allows constructing a probability mass or density function when only a limited amount of information is available, see Appendix B, without making assumptions on what is unknown.

Representation. In order to construct the probability density function, assuming a continuous random vector, the Shannon entropy $s\left(\pi_{\boldsymbol{Q}_{\mathrm{M}}}\right) \in \Re$ of the probability density function $\pi_{\boldsymbol{Q}_{\mathrm{M}}}$, which represents the measure of the uncertainties of the random vector $\boldsymbol{Q}_{\mathrm{M}}$, with

$$s\left(\pi_{\boldsymbol{Q}_{\mathrm{M}}}\right) = -\int_{\Re^n} \pi_{\boldsymbol{Q}_{\mathrm{M}}}(\boldsymbol{q}_{\mathrm{M}})\log\left(\pi_{\boldsymbol{Q}_{\mathrm{M}}}(\boldsymbol{q}_{\mathrm{M}})\right)d\boldsymbol{q}_{\mathrm{M}}\,, \tag{266}$$

is maximised under some known constraints. The constraints can correspond to the known statistical information such as the support $\mathcal{S}_{\boldsymbol{Q}_{\mathrm{M}}} \subset \Re^n$ of the distribution or some statistical properties written under the form

$$\int_{\Re^n} \boldsymbol{g}(\boldsymbol{q}_{\mathrm{M}})\pi_{\boldsymbol{Q}_{\mathrm{M}}}(\boldsymbol{q}_{\mathrm{M}})d\boldsymbol{q}_{\mathrm{M}} = \boldsymbol{b} \in \Re^m\,, \tag{267}$$

with the mapping $\boldsymbol{g}(\boldsymbol{q}_{\mathrm{M}}) : \Re^n \to \Re^m$. As an example, statistical moments can be used to define the constraints. The maximum entropy principle is then stated as

$$\pi_{\boldsymbol{Q}_{\mathrm{M}}} = \arg\max_{\pi\in\mathscr{P}} s(\pi)\,, \quad \text{with}$$
$$\mathscr{P} = \left\{\pi \text{ of support } \mathcal{S}_{\boldsymbol{Q}_{\mathrm{M}}} : \int_{\Re^n}\pi(\boldsymbol{q}_{\mathrm{M}})d\boldsymbol{q}_{\mathrm{M}} = 1\,,\ \text{and}\ \int_{\Re^n}\boldsymbol{g}(\boldsymbol{q}_{\mathrm{M}})\pi(\boldsymbol{q}_{\mathrm{M}})d\boldsymbol{q}_{\mathrm{M}} = \boldsymbol{b}\right\}\,, \tag{268}$$

where the second constraint is a normalisation. The constrained problem resolution consists in introducing Lagrange multipliers $(\lambda_0,\, \boldsymbol{\lambda}) \in \Re^{+} \times \Re^{m}$ with $\int_{\Re^n} \exp\left(-\boldsymbol{\lambda}^T \boldsymbol{g}(\boldsymbol{q}_{\mathrm{M}})\right) d\boldsymbol{q}_{\mathrm{M}} < \infty$, yielding the Lagrangian

$$\mathscr{L}(\pi;\, \lambda_0,\, \boldsymbol{\lambda}) = s(\pi) - (\lambda_0 - 1)\left(\int_{\Re^n} \pi(\boldsymbol{q}_{\mathrm{M}}) d\boldsymbol{q}_{\mathrm{M}} - 1\right) - \boldsymbol{\lambda}^T \left(\int_{\Re^n} \boldsymbol{g}(\boldsymbol{q}_{\mathrm{M}}) \pi(\boldsymbol{q}_{\mathrm{M}}) d\boldsymbol{q}_{\mathrm{M}} - \boldsymbol{b}\right) . \tag{269}$$

The problem (268) is then substituted by finding the stationary point of $\mathscr{L}(\pi;\, \lambda_0,\, \boldsymbol{\lambda})$ at $\boldsymbol{\pi}_{\boldsymbol{Q}_{\mathrm{M}}}$ for $(\lambda_0,\, \boldsymbol{\lambda}) = (\lambda_0^{\mathrm{sol}},\, \boldsymbol{\lambda}^{\mathrm{sol}})$, with

$$\pi_{\boldsymbol{Q}_{\mathrm{M}}}(\boldsymbol{q}_{\mathrm{M}}) = \begin{cases} \frac{\exp\left(-\boldsymbol{\lambda}^{\mathrm{sol}\,T} \boldsymbol{g}(\boldsymbol{q}_{\mathrm{M}})\right)}{\exp\left(\lambda_0^{\mathrm{sol}}\right)} & \text{if } \boldsymbol{q}_{\mathrm{M}} \in \mathscr{S}_{\boldsymbol{Q}_{\mathrm{M}}} ; \\ 0 & \text{if } \boldsymbol{q}_{\mathrm{M}} \notin \mathscr{S}_{\boldsymbol{Q}_{\mathrm{M}}} . \end{cases} \tag{270}$$

- A numerical method can be develop to solve the optimisation problem and is summarised in Appendix B.3.

- In some cases a closed form expression of $\pi_{\boldsymbol{Q}_{\mathrm{M}}}$ can be derived. For example, in the case in which the support $\mathscr{S}_{\boldsymbol{Q}_{\mathrm{M}}} = \Re^n$, the expectation denoted by $\bar{\boldsymbol{q}}_{\mathrm{M}} = \mathbb{E}\left[\boldsymbol{Q}_{\mathrm{M}}\right] \in \Re^n$ is known and in which the covariance matrix denoted by $\tilde{\mathbf{R}}_{\boldsymbol{Q}_{\mathrm{M}}}$, see Eq. (50), is also known, the maximum entropy principle yields, as shown by Soize (2017),

  $$\pi_{\boldsymbol{Q}_{\mathrm{M}}}(\boldsymbol{q}_{\mathrm{M}}) = \frac{1}{(2\pi)^{\frac{n}{2}} \sqrt{\det\left(\tilde{\mathbf{R}}_{\boldsymbol{Q}_{\mathrm{M}}}\right)}} \exp\left(-\frac{1}{2}\left(\boldsymbol{q}_{\mathrm{M}} - \bar{\boldsymbol{q}}_{\mathrm{M}}\right)^T \tilde{\mathbf{R}}_{\boldsymbol{Q}_{\mathrm{M}}}^{-1} \left(\boldsymbol{q}_{\mathrm{M}} - \bar{\boldsymbol{q}}_{\mathrm{M}}\right)\right) , \tag{271}$$

  resulting in a multi-variate Gaussian distribution. In all generalities, the random variables Q_{M_r} are dependent. Other examples including cases of bounded support and/or in which only the first moment is given are detailed by Soize (2017).

- We now consider the random vector field $\boldsymbol{Q}_{\mathrm{M}}(\Omega) = \{\boldsymbol{Q}_{\mathrm{M}}(\boldsymbol{X},\, \omega) : \boldsymbol{X} \in \Omega,\, \omega \in \mathscr{W}\}$, with the random vector $\boldsymbol{Q}_{\mathrm{M}}$ valued in $\Re^n$ and of support $\mathscr{S}_{\boldsymbol{Q}_{\mathrm{M}}} = \Re^n$. For simplicity, we also assume that the random field is homogeneous, but this is not mandatory. We still consider that both the expectation, denoted by $\bar{\boldsymbol{q}}_{\mathrm{M}} = \bar{\boldsymbol{q}}_{\mathrm{M}}\left(\boldsymbol{X}\right) = \mathbb{E}\left[\boldsymbol{Q}_{\mathrm{M}}\left(\boldsymbol{X}\right)\right] : \Omega \to \Re^n$ and the covariance matrix denoted by $\tilde{\mathbf{R}}_{\boldsymbol{Q}_{\mathrm{M}}}\left(\boldsymbol{\tau}\right) = \tilde{\mathbf{R}}_{\boldsymbol{Q}_{\mathrm{M}}}\left(\boldsymbol{X};\, \boldsymbol{\tau}\right)$, are known and have to be constrained. Since the maximum entropy principle yields in this case a multi-variate Gaussian distribution (271), one can define the homogeneous germ $\boldsymbol{\Xi}(\boldsymbol{X})$ valued in $\Re^n$ of independent and zero-mean random fields $\Xi_r(\Omega)$, $r = 1..n$, *i.e.* with the covariance matrix $\tilde{\mathbf{R}}_{\boldsymbol{\Xi}}(\boldsymbol{\tau})$ such that $\tilde{\mathbf{R}}_{\boldsymbol{\Xi}}(\mathbf{0}) = \mathbf{I}_n$. This germ is obtained from the non-linear transformation $\boldsymbol{\Xi}(\boldsymbol{X}) = \boldsymbol{f}^n(\boldsymbol{Q}_{\mathrm{M}}(\boldsymbol{X}))$ with

  $$\boldsymbol{\Xi}(\boldsymbol{X}) = \boldsymbol{f}^n(\boldsymbol{Q}_{\mathrm{M}}(\boldsymbol{X})) = \mathbf{L}_{\boldsymbol{Q}_{\mathrm{M}}}^{-1}\left(\boldsymbol{Q}_{\mathrm{M}}(\boldsymbol{X}) - \bar{\boldsymbol{q}}_{\mathrm{M}}\right) , \tag{272}$$

  where the matrix $\mathbf{L}_{\boldsymbol{Q}_{\mathrm{M}}}$ has been obtained by the Cholesky decomposition of $\tilde{\mathbf{R}}_{\boldsymbol{Q}_{\mathrm{M}}}(\mathbf{0})$, *i.e.* $\tilde{\mathbf{R}}_{\boldsymbol{Q}_{\mathrm{M}}}(\mathbf{0}) = \mathbf{L}_{\boldsymbol{Q}_{\mathrm{M}}} \mathbf{L}_{\boldsymbol{Q}_{\mathrm{M}}}^T$, see Appendix A.1.1. In that case, the $d \times n$, with d the spatial dimension, correlation lengths $\{\boldsymbol{l}_{R_{\Xi_{i\,i}}}\}_k$, with $k = 1..d$ and $i = 1..n$, define the correlation of the random field.

Generation.

- In all generalities Markov chain Monte Carlo (MCMC) simulations, see Appendix A.5.4, are used to generate pseudo-samples $\boldsymbol{q}_{\mathrm{M}}^{p}$. Let us consider a stationary random process $\boldsymbol{Z}(\mathcal{T}) = \{\boldsymbol{Z}(t^{(i)}) : t^{(i)} \in \mathcal{T} \subset \Re_0^+\}$ in the discrete set $\mathcal{T} = (t^{(1)}, ..., t^{(k)}, ...)$, with $t^{(k)} - t^{(k-1)} = \Delta t$ and $\boldsymbol{Z}(t^{(i)})$ valued in $\Re^n$. Having a pseudo-sample $\boldsymbol{z}\left(t^{(p)}\right) = \boldsymbol{z}^p$, the pseudo-sample $\boldsymbol{z}\left(t^{(p+1)}\right)$ can be constructed in order to simulate the random vector $\boldsymbol{Q}_{\mathrm{M}}$ taking values in $\Re^n$ and having as stationary distribution $\pi_{\boldsymbol{Z}(t)}(\boldsymbol{z})$ of the Markov chain, the distribution density function $\pi_{\boldsymbol{Q}_{\mathrm{M}}}(\boldsymbol{q}_{\mathrm{M}})$ (270), see details in Appendix A.5.4.

- In the case of a Gaussian like distribution as in Eq. (271), Monte Carlo (MC) simulations can be used after having defined the germ $\boldsymbol{\Xi}$ valued in $\Re^n$ as a zero-mean with unit covariance matrix, *i.e.* $\tilde{\mathbf{R}}_{\boldsymbol{\Xi}} = \mathbf{I}_n$, Gaussian distribution, from the non-linear transformation (272).

- In the case of a random field which can be expressed in terms of a germ $\boldsymbol{\Xi}(\boldsymbol{X})$ valued in $\Re^n$ as a zero-mean with unit covariance matrix, *i.e.* $\tilde{\mathbf{R}}_{\boldsymbol{\Xi}}(\mathbf{0}) = \mathbf{I}_n$, Gaussian distribution with the correlation structure $\{\boldsymbol{l}_{R_{\boldsymbol{\Xi}_{i\,i}}}\}_k$ with $k = 1..d$, $i = 1..n$ known, a Gaussian generation process such as the one developed by Shinozuka (1971), see Section 5.2.2, can generate pseudo samples $\xi_i^p(\boldsymbol{X}^{(q)})$, $i = 1..n$ at different locations $\boldsymbol{X}^{(q)}$ from which the pseudo-samples $\boldsymbol{q}_{\mathrm{m}}^{p}(\boldsymbol{X}^{(q)}) = \boldsymbol{f}^{n-1}\left(\boldsymbol{\xi}^p(\boldsymbol{X}^{(q)})\right)$ arise, *e.g.* by inverting Eq. (272) in the case in which the maximum entropy yields the multi-variate distribution (271).

5.2.4. Data-driven probability sampling

We here present the data-driven sampling method that has recently been developed by Soize and Ghanem (2016) and that is detailed in Appendix A.7.

Representation. Considering the random vector $\boldsymbol{Q}_{\mathrm{M}}$ valued in $\Re^n$, and with support $\mathcal{S}_{\boldsymbol{Q}_{\mathrm{M}}} \subset \Re^n$, it is assumed that the available information consists in a given set of N statistically independent realisations $\boldsymbol{q}_{\mathrm{M}}^{k} = \boldsymbol{Q}_{\mathrm{M}}(\mathscr{w}^k)$, with $\mathscr{w}^k \in \mathscr{W}$, $k = 1..N$. It is further assumed that the local structure of the given data-set is preserved via a random matrix $\mathbf{Q}_{\mathrm{M}} = [\boldsymbol{Q}_{\mathrm{M}}^{1} \ldots \boldsymbol{Q}_{\mathrm{M}}^{k} \ldots \boldsymbol{Q}_{\mathrm{M}}^{N}]$, which is defined on $(\mathscr{W}, \mathcal{F}, \mathbb{P})$, with value in $\Re^{n\times N}$ and in which each column $\boldsymbol{Q}_{\mathrm{M}}^{k}$, $k = 1..N$, is an independent copy of the random vector $\boldsymbol{Q}_{\mathrm{M}}$. Therefore, the matrix $\mathbf{q}_{\mathrm{M}} = [\boldsymbol{q}_{\mathrm{M}}^{1} \ldots \boldsymbol{q}_{\mathrm{M}}^{k} \ldots \boldsymbol{q}_{\mathrm{M}}^{N}]$ is a realisation of $\mathbf{Q}_{\mathrm{M}}$.

The observation data-set $\mathbf{q}_{\mathrm{M}}$ is then used to

- Define a random matrix realisation $\boldsymbol{\eta} = [\boldsymbol{\eta}^1 \ldots \boldsymbol{\eta}^k \ldots \boldsymbol{\eta}^N]$ of size $n \times N$ defined from the realisations of the random vector $\mathbf{H}$ of zero-mean and unit variance obtained through a PCA, see Appendix A.3.1, with

$$\{\boldsymbol{\eta}^k\}_i = \frac{1}{\sqrt{\lambda_{\boldsymbol{Q}_{\mathrm{M}}}^{(i)}}} (\boldsymbol{q}_{\mathrm{M}}^{k} - \bar{\boldsymbol{q}}_{\mathrm{M}})^T \boldsymbol{u}_{\boldsymbol{Q}_{\mathrm{M}}}^{(i)}, \qquad k = 1..N\,, \tag{273}$$

  with the ordered eigen-values $\lambda_{\boldsymbol{Q}_{\mathrm{M}}}^{(i)} > 0$, and the normalised eigen-vectors $\boldsymbol{u}_{\boldsymbol{Q}_{\mathrm{M}}}^{(i)}$ of the covariance matrix $\tilde{\mathbf{R}}_{\boldsymbol{Q}_{\mathrm{M}}}$, and with the mean $\bar{\boldsymbol{q}}_{\mathrm{M}}$.

- Construct a kernel-density estimation of the probability distribution of the random vector $\mathbf{H}$;
- Construct a diffusion-map basis $\boldsymbol{\phi} \in \Re^{N\times N}$ from the observation data-set $\boldsymbol{\eta}$ for discovering and characterising the geometry and the structure of the data-set; A reduced-order representation of the diffusion map $\boldsymbol{\phi}_\mathrm{r} \in \Re^{N\times m}$ then follows;

These three steps are detailed in Appendix A.7.

Generation. A MCMC process is then used to generate extra data samples based on the matrix $\mathbf{q}_\mathrm{M}$ through the following steps:

- Since the given data-set $\boldsymbol{\eta}$ serves as N realisations of the random vector $\mathbf{H}$, it is also a realisation of the random matrix $\mathbf{V} = [\mathbf{H}^1 \,...\, \mathbf{H}^k \,...\, \mathbf{H}^N]$ with value in $\Re^{n\times N}$. This random matrix $\mathbf{V}$ is then represented using the reduced diffusion map basis $\boldsymbol{\phi}_\mathrm{r}$ as
$$\mathbf{V} = \mathbf{Z}\boldsymbol{\phi}_\mathrm{r}^\mathrm{T}\,, \tag{274}$$
in which
$$\mathbf{Z} = \mathbf{V}\mathbf{a},\ \text{with}\ \mathbf{a} = \boldsymbol{\phi}_\mathrm{r}\left(\boldsymbol{\phi}_\mathrm{r}^\mathrm{T}\boldsymbol{\phi}_\mathrm{r}\right)^{-1} \in \Re^{N\times m}\,. \tag{275}$$
In particular, using the realisation $\boldsymbol{\eta}$ of the stochastic matrix $\mathbf{V}$ yields the realisation $\mathbf{z} = \boldsymbol{\eta}\mathbf{a} \in \Re^{n\times m}$.
- Additional realisations $\boldsymbol{\eta}^p$ of the random matrix $\mathbf{V}$ are computed through Eq. (274) from additional realisations $\mathbf{z}^p$ of $\mathbf{Z}$ obtained using a MCMC algorithm, see Appendix A.7.
- The generated random data-set $\boldsymbol{\eta}^p = [\boldsymbol{\eta}^{1^p} \,...\, \boldsymbol{\eta}^{N^p}]$ is transferred back to recover the scale and mean of the original data-set by inverting Eq. (273), yielding N new pseudo-samples
$$\boldsymbol{q}_\mathrm{M}^{i^p} = \bar{\boldsymbol{q}}_\mathrm{M} + \sum_{j=1}^{n}\sqrt{\lambda_{\boldsymbol{Q}_\mathrm{M}}^{(j)}}\boldsymbol{u}_{\boldsymbol{Q}_\mathrm{M}}^{(j)}\eta_j^{i^p}\,, \quad \forall i = 1..N\,, \tag{276}$$
providing N pseudo-samples for each value of p.

5.3. Linear cases & Tensor random fields

In the context of linear problems, random fields of dependent material properties can be generated using the expansions methods. Liebscher et al. (2013) have considered a particular spatial correlation structure as an exponential function multiplied by sine- and cosine-functions and an iterative KL expansion to generate non-Gaussian random-fields as summarised in Appendix A.3.4. Mehrez et al. (2018) have considered hierarchical stochastic homogenisation in the context of non-crimp fabric laminates: considering uncertainties in the resin and carbon-fibre properties, stochastic apparent properties of a tow could be described using the Polynomial Chaos Expansion as described in Section 5.2.1; apparent properties of non-crimp fabric could then be predicted from observations of tow spacing distribution and represented using the Polynomial Chaos Expansion and so on...

However, because the partial differential equations of a boundary value problem can be stated in terms of positive-definite matrices, there is an interest in being able to represent and generate random matrices or random matrix fields. For example, in the context of linear mechanics, the meso-scale stochastic constitutive law (251) simplifies as

$$\boldsymbol{\Sigma}_{\mathrm{M}}(\boldsymbol{X};\, \omega) = \mathbb{C}_{\mathrm{M}}^{\mathrm{el}}(\boldsymbol{X},\, \omega) : \boldsymbol{\varepsilon}_{\boldsymbol{X}}(\boldsymbol{U}_{\mathrm{M}}(\boldsymbol{X};\, \omega))\,, \tag{277}$$

with the Cauchy stress tensor $\boldsymbol{\Sigma}_{\mathrm{M}}(\boldsymbol{X};\, \omega)$ and the small deformation tensor operator $\boldsymbol{\varepsilon}_{\boldsymbol{X}}\,(\boldsymbol{U})$ standing for the small strain tensor $\frac{1}{2}\left(\boldsymbol{\nabla}_0 \otimes \boldsymbol{U} + \boldsymbol{U} \otimes \boldsymbol{\nabla}_0\right)$. The constitutive behaviour is thus defined by the random field $\{\mathbb{C}_{\mathrm{M}}^{\mathrm{el}}(\boldsymbol{X},\, \omega) :\, \boldsymbol{X} \in \Omega,\, \omega \in \mathcal{W}\}$ of the meso-scale apparent properties expressed as a random fourth-order tensor field, the latter being also expressed as a 6×6 positive definite random matrix field $\{\mathbf{C}_{\mathrm{M}}^{\mathrm{el}}(\boldsymbol{X},\, \omega) :\, \boldsymbol{X} \in \Omega,\, \omega \in \mathcal{W}\}$ using the Voigt notations.

Without loss of generality, we here consider the random field $\{\mathbf{C}_{\mathrm{M}}^{\mathrm{el}}(\boldsymbol{X},\, \omega) :\, \boldsymbol{X} \in \Omega,\, \omega \in \mathcal{W}\}$, with $\mathbf{C}_{\mathrm{M}}^{\mathrm{el}} : \mathcal{W} \rightarrow \mathbb{M}_n^+(\Re)$, where $\mathbb{M}_n^+(\Re)$ refers to all symmetric positive-definite real matrices of size $n \times n$. A realisation $\omega \in \mathcal{W}$ is denoted by $\mathbf{c}_{\mathrm{M}}^{\mathrm{el}}(\boldsymbol{X}) = \mathbf{C}_{\mathrm{M}}^{\mathrm{el}}(\boldsymbol{X},\, \omega) \in \mathbb{M}_n^+(\Re)$, $\forall \boldsymbol{X} \in \Omega$.

We here introduce some concepts for a $n \times n$ symmetric matrix $\mathbf{b} \in \mathbb{M}_n(\Re)$:

- The norm of the matrix

$$\|\mathbf{b}\| = \sup_{\|\boldsymbol{z}\| \leq 1,\, \boldsymbol{z} \in \Re^n} \left(\|\mathbf{b}\boldsymbol{z}\|\right) = |\lambda_{\mathbf{b}}^{\max}|\,, \tag{278}$$

  with $\lambda_{\mathbf{b}}^{\max}$ the eigen-value of largest absolute value of the matrix $\mathbf{b}$;

- The Frobenius norm

$$\|\mathbf{b}\|_F^2 = \mathrm{tr}\left(\mathbf{b}^T\mathbf{b}\right) = \sum_{i=1}^{n}\sum_{j=1}^{n} \mathbf{b}_{ij}^2 \tag{279}$$

  with the properties

$$\|\mathbf{b}\| \leq \|\mathbf{b}\|_F \leq \sqrt{n}\|\mathbf{b}\|\,; \tag{280}$$

- The Loewner ordering definition

$$\begin{cases} \mathbf{a} < \mathbf{b} & \text{if } \mathbf{b} - \mathbf{a} \in \mathbb{M}_n^+(\Re)\,; \\ \mathbf{a} \leq \mathbf{b} & \text{if } \mathbf{b} - \mathbf{a} \in \mathbb{M}_{0_n}^+(\Re)\,. \end{cases} \tag{281}$$

In order to represent, and afterwards to generate, random fields, several physical constraints have to be satisfied, *e.g.* a material tensor should remain symmetric and some terms have to be strictly positive. Besides, as emphasised by Soize (2006), in order to be able to conduct macro-scale stochastic analyses, an important property for the random matrix field is its invertibility, which is stated as

$$\mathbb{E}\left[\|\left(\mathbf{C}_{\mathrm{M}}^{\mathrm{el}}(\boldsymbol{X})\right)^{-1}\|^2\right] \leq c^2 < +\infty \quad \forall \boldsymbol{X} \in \Omega\,. \tag{282}$$

As pointed out by Soize (2006), if $\mathbf{c}_{\mathrm{M}}^{\mathrm{el}}(\boldsymbol{X})$ belongs almost surely[8] to $\mathbb{M}_n^+(\Re)$, then $\left(\mathbf{c}_{\mathrm{M}}^{\mathrm{el}}(\boldsymbol{X})\right)^{-1}$ exists almost surely, but this does not imply the mean-square convergence and Eq. (282) cannot simply be deduced.

In this section we present several approach for generating pseudo-samples $\mathbf{c}_{\mathrm{M}}^{\mathrm{el}^p}(\boldsymbol{X})$ of the random field $\{\mathbf{C}_{\mathrm{M}}^{\mathrm{el}}(\boldsymbol{X},\, w) :\, \boldsymbol{X} \in \Omega,\, w \in \mathcal{W}\}$ whilst ensuring invertibility.

5.3.1. Partition theorem

Remembering the definition of a statistically Representative Volume Element (RVE), here denoted $\omega_{\mathrm{RVE}}(w)$, of size l_{VE} large enough as compared to the size of the micro-structure constituents l_{m}, see Section 4.1.1, following Huet (1990) there exists in the context of linear elasticity and under the small displacement assumption, an effective modulus tensor $\mathbb{c}^{\mathrm{eff}}$, which is independent on the micro-structure realisation $w \in \mathcal{W}$ and on the boundary conditions.

Considering now Stochastic Volume Elements (SVE) realisations $\omega_{l_{\mathrm{SVE}}}(w)$ of a given size l_{SVE} and with $w \in \mathcal{W}$, in the context of linear elasticity the apparent homogenised elasticity tensor $\mathbb{C}_{l_{\mathrm{SVE}}}^{\mathrm{app}}(w)$ can be extracted following the approach described in Section 4.2.1 for a given realisation of a given SVE length l_{SVE}. In particular the problem can be solved either using constrained boundary displacement (131), with the so-called KUBCs, or constrained surface traction, with the so-called SUBCs, yielding respectively $\mathbb{C}_{l_{\mathrm{SVE}}}^{\mathrm{app\,KUBC}}(w)$ and $\mathbb{C}_{l_{\mathrm{SVE}}}^{\mathrm{app\,SUBC}}(w)$, with $\mathbb{S}_{l_{\mathrm{SVE}}}^{\mathrm{app\,KUBC}}(w)$ and $\mathbb{S}_{l_{\mathrm{SVE}}}^{\mathrm{app\,SUBC}}(w)$ their respective inverse, *i.e.* the compliance tensors.

Huet (1990); Ostoja-Starzewski (1993)[9] have formulated the so-called partition theorem from energetic considerations:

$$\mathbf{s}^{\mathrm{Reuss}\,-1} \leq \left(\mathbb{E}\left[\mathbf{S}_{l'_{\mathrm{SVE}}}^{\mathrm{app\,SUBC}}\right]\right)^{-1} \leq \left(\mathbb{E}\left[\mathbf{S}_{l_{\mathrm{SVE}}}^{\mathrm{app\,SUBC}}\right]\right)^{-1} \leq \left(\mathbf{s}^{\mathrm{eff}}\right)^{-1} = \\ \mathbf{c}^{\mathrm{eff}} \leq \mathbb{E}\left[\mathbf{C}_{l_{\mathrm{SVE}}}^{\mathrm{app\,KUBC}}\right] \leq \mathbb{E}\left[\mathbf{C}_{l'_{\mathrm{SVE}}}^{\mathrm{app\,KUBC}}\right] \leq \mathbf{c}^{\mathrm{Voigt}}\,, \tag{283}$$

for $l'_{\mathrm{SVE}} \leq l_{\mathrm{SVE}}$, and where we have used the Voigt notations and Loewner ordering.

5.3.2. High number of parameters approach

We here assume that the random field $\{\mathbf{C}_{\mathrm{M}}^{\mathrm{el}}(\boldsymbol{X},\, w) \,:\, \boldsymbol{X} \in \Omega,\, w \in \mathcal{W}\}$, with $\mathbf{C}_{\mathrm{M}}^{\mathrm{el}} : \mathcal{W} \to \mathbb{M}_n^+(\Re)$ could be extracted in an accurate way, *e.g.* following the window technique illustrated in Fig. 25 and discussed in Section 4.1.2, by evaluating enough realisations $\mathbf{c}_{\mathrm{M}}^{i}(\boldsymbol{X}) = \mathbf{C}_{\mathrm{M}}^{\mathrm{el}}(\boldsymbol{X},\, w) \in \mathbb{M}_n^+(\Re)$, for $w \in \mathcal{W}$.

Introduction of a lower bound and of a Cholesky decomposition. In order to ensure the invertibility (282), a deterministic symmetric positive definite lower bound $\mathbf{c}_{\mathrm{L}}$ is introduced such that

$$0 \leq \mathbf{s}_{\mathrm{L}} - \mathbf{S}_{\mathrm{M}}^{\mathrm{el}}(\boldsymbol{X},\, w) \quad \forall \boldsymbol{X} \in \Omega,\, w \in \mathcal{W}\,, \tag{284}$$

---

[8] A condition is almost surely satisfied if there is a subset of probability 0 where it is not respected

[9] Huet (1990) has actually established a formulation in which the SVEs are subsets of the RVE

where we have defined the inverse of the lower bound $\mathbf{s}_{\mathrm{L}} = \mathbf{c}_{\mathrm{L}}^{-1}$, which exists and is also positive definite, the random matrix $\mathbf{S}_{\mathrm{M}}^{\mathrm{el}}(\boldsymbol{X},\, w) = \left(\mathbf{C}_{\mathrm{M}}^{\mathrm{el}}(\boldsymbol{X},\, w)\right)^{-1}$, and where we have used the Loewner ordering definition (281). We note that we have $\mathbf{C}_{\mathrm{M}}^{\mathrm{el}}(\boldsymbol{X},\, w) - \mathbf{c}_{\mathrm{L}} \geq 0$.[10] From the definition of a positive semi-definite matrix, one has:

$$\boldsymbol{z}^T \mathbf{s}_{\mathrm{L}} \boldsymbol{z} - \boldsymbol{z}^T \mathbf{S}_{\mathrm{M}}^{\mathrm{el}}(\boldsymbol{X},\, w) \boldsymbol{z} \geq 0 \quad \forall \boldsymbol{z} \in \Re^n \,. \tag{288}$$

In particular, considering as vector $\boldsymbol{z}$ the normalised eigen-vector $\boldsymbol{u}_{\mathbf{S}}^{\max}(\boldsymbol{X})$ corresponding to $\lambda_{\mathbf{S}}^{\max}(\boldsymbol{X})$, the maximum eigen-value of the positive definite matrix $\mathbf{S}_{\mathrm{M}}^{\mathrm{el}}(\boldsymbol{X}, w)$, this last relation becomes

$$\left(\boldsymbol{u}_{\mathbf{S}}^{\max}(\boldsymbol{X})\right)^T \mathbf{s}_{\mathrm{L}} \boldsymbol{u}_{\mathbf{S}}^{\max}(\boldsymbol{X}) - \left(\boldsymbol{u}_{\mathbf{S}}^{\max}(\boldsymbol{X})\right)^T \mathbf{S}_{\mathrm{M}}^{\mathrm{el}}(\boldsymbol{X},\, w) \boldsymbol{u}_{\mathbf{S}}^{\max}(\boldsymbol{X}) \geq 0 \,, \tag{289}$$

or, using the properties of eigen-values and normalised eigen-vectors,

$$\left(\boldsymbol{u}_{\mathbf{S}}^{\max}(\boldsymbol{X})\right)^T \mathbf{s}_{\mathrm{L}} \boldsymbol{u}_{\mathbf{S}}^{\max}(\boldsymbol{X}) \geq \lambda_{\mathbf{S}}^{\max}(\boldsymbol{X}) \,. \tag{290}$$

Since $\mathbf{s}_{\mathrm{L}} = \mathbf{c}_{\mathrm{L}}^{-1}$ is positive definite, one always has

$$\boldsymbol{z}^T \mathbf{s}_{\mathrm{L}} \boldsymbol{z} \leq \lambda_{\mathbf{s}_{\mathrm{L}}}^{\max} \boldsymbol{z}^T \boldsymbol{z} \quad \forall \boldsymbol{z} \in \Re^n \,, \tag{291}$$

with $\lambda_{\mathbf{s}_{\mathrm{L}}}^{\max}$ the maximum eigen-value of the positive definite matrix $\mathbf{s}_{\mathrm{L}}$. Considering for $\boldsymbol{z}$ the particular case of the normalised eigen-vector $\boldsymbol{u}_{\mathbf{S}}^{\max}(\boldsymbol{X})$ in the last equation, Eq. (290) is rewritten as

$$\lambda_{\mathbf{s}_{\mathrm{L}}}^{\max} \geq \lambda_{\mathbf{S}}^{\max}(\boldsymbol{X}) \,, \tag{292}$$

which demonstrates the property (282).

The lower bound introduced in Eq. (284) allows defining the random field $\{\Delta\mathbf{C}_{\mathrm{M}}^{\mathrm{el}}(\boldsymbol{X},\, w) : \boldsymbol{X} \in \Omega,\, w \in \mathcal{W}\}$, with $\Delta\mathbf{C}_{\mathrm{M}}^{\mathrm{el}} : \mathcal{W} \rightarrow \mathbb{M}_{0n}^{+}(\Re)$ as

$$\Delta\mathbf{C}_{\mathrm{M}}^{\mathrm{el}}(\boldsymbol{X},\, w) = \mathbf{C}_{\mathrm{M}}^{\mathrm{el}}(\boldsymbol{X},\, w) - \mathbf{c}_{\mathrm{L}} \,. \tag{293}$$

---

[10] We remark that if $\mathbf{s}_{\mathrm{L}} \geq \mathbf{s}_{\mathrm{M}}$, and considering $\mathbf{u}_{\mathbf{c}_{\mathrm{L}}}$ and $\mathbf{u}_{\mathbf{c}_{\mathrm{M}}}$ as the respective square root matrices of $\mathbf{c}_{\mathrm{L}}$ and $\mathbf{c}_{\mathrm{M}}$ –which exist because they are symmetric positive definite– one has starting from Eq. (288) with $\boldsymbol{z} = \mathbf{u}_{\mathbf{c}_{\mathrm{M}}} \boldsymbol{y}$:

$$\boldsymbol{y}^T \mathbf{u}_{\mathbf{c}_{\mathrm{M}}}^T \mathbf{s}_{\mathrm{L}} \mathbf{u}_{\mathbf{c}_{\mathrm{M}}} \boldsymbol{y} \geq \boldsymbol{y}^T \mathbf{u}_{\mathbf{c}_{\mathrm{M}}}^T \mathbf{s}_{\mathrm{M}} \mathbf{u}_{\mathbf{c}_{\mathrm{M}}} \boldsymbol{y} = \boldsymbol{y}^T \mathbf{I} \boldsymbol{y} \,, \forall \boldsymbol{y} \in \Re^n |\, \boldsymbol{y} \neq \mathbf{0} \,. \tag{285}$$

This shows that $\mathbf{g} = \mathbf{u}_{\mathbf{c}_{\mathrm{M}}}^T \mathbf{s}_{\mathrm{L}} \mathbf{u}_{\mathbf{c}_{\mathrm{M}}} \geq \mathbf{I}$, with $\mathbf{g}$ a symmetric definite positive matrix and $\mathbf{g} = \boldsymbol{u}_{\mathbf{g}} \boldsymbol{u}_{\mathbf{g}}$. Therefore, considering $\boldsymbol{y} = \boldsymbol{u}_{\mathbf{g}}^{-1} \boldsymbol{z}$ for any $\boldsymbol{z} \in \Re^n | \boldsymbol{z} \neq \mathbf{0}$ in this last equation results in

$$\boldsymbol{z}^T \mathbf{I} \boldsymbol{z} = \boldsymbol{z}^T \mathbf{u}_{\mathbf{g}}^{-1} \mathbf{g} \mathbf{u}_{\mathbf{g}}^{-1} \boldsymbol{z} \geq \boldsymbol{z}^T \mathbf{g}^{-1} \boldsymbol{z} = \boldsymbol{z}^T \mathbf{u}_{\mathbf{c}_{\mathrm{M}}}^{-1} \mathbf{c}_{\mathrm{L}} \mathbf{u}_{\mathbf{c}_{\mathrm{M}}}^{-1} \boldsymbol{z} \,, \forall \boldsymbol{z} \in \Re^n |\, \boldsymbol{z} \neq \mathbf{0} \,. \tag{286}$$

Considering this time $\boldsymbol{z} = \mathbf{u}_{\mathbf{c}_{\mathrm{M}}} \boldsymbol{p}$ for any $\boldsymbol{p} \in \Re^n | \boldsymbol{p} \neq \mathbf{0}$ in this last result yields

$$\boldsymbol{p}^T \mathbf{c}_{\mathrm{M}} \boldsymbol{p} = \boldsymbol{p}^T \mathbf{u}_{\mathbf{c}_{\mathrm{M}}} \mathbf{u}_{\mathbf{c}_{\mathrm{M}}} \boldsymbol{p} \geq \boldsymbol{p}^T \mathbf{c}_{\mathrm{L}} \boldsymbol{p} \,, \forall \boldsymbol{p} \in \Re^n |\, \boldsymbol{p} \neq \mathbf{0} \,, \tag{287}$$

showing that $\mathbf{c}_{\mathrm{M}} \geq \mathbf{c}_{\mathrm{L}}$.

Besides, the Cholesky decomposition allows defining the random field $\{\mathbf{L}_{\Delta\mathbf{C}_{\mathrm{M}}^{\mathrm{el}}}(\boldsymbol{X},\,\omega),\ \boldsymbol{X}\in\Omega,\,\omega\in\mathcal{W}\}$, with the realisation $\mathbf{L}_{\Delta\mathbf{C}_{\mathrm{M}}^{\mathrm{el}}}(\boldsymbol{X},\,\omega)$ a lower triangular matrix in $\Re^{n\times n}$ with

$$\Delta\mathbf{C}_{\mathrm{M}}^{\mathrm{el}}(\boldsymbol{X},\,\omega)=\mathbf{L}_{\Delta\mathbf{C}_{\mathrm{M}}^{\mathrm{el}}}(\boldsymbol{X},\,\omega)\left(\mathbf{L}_{\Delta\mathbf{C}_{\mathrm{M}}^{\mathrm{el}}}(\boldsymbol{X},\,\omega)\right)^{T}\,. \tag{294}$$

The matrix $\mathbf{L}_{\Delta\mathbf{C}_{\mathrm{M}}^{\mathrm{el}}}(\boldsymbol{X},\,\omega)$ has $n(n+1)/2$ non-zero entries, which form the $n(n+1)/2$ dependent entries of a new random vector field $\boldsymbol{Q}_{\mathrm{M}}(\Omega)=\{\boldsymbol{Q}_{\mathrm{M}}(\boldsymbol{X},\,\omega):\ \boldsymbol{X}\in\Omega,\,\omega\in\mathcal{W}\}$, with the random vector $\boldsymbol{Q}_{\mathrm{M}}$ valued in $\Re^{\frac{n(n+1)}{2}}$. No conditions are required on the elements of the random vector field $\boldsymbol{Q}_{\mathrm{M}}(\Omega)$ since Eq. (293) ensures the invertibility (282).

Definition of the random vector field. The random vector field $\boldsymbol{Q}_{\mathrm{M}}(\Omega)=\{\boldsymbol{Q}_{\mathrm{M}}(\boldsymbol{X},\,\omega):\ \boldsymbol{X}\in\Omega,\,\omega\in\mathcal{W}\}$, with the random vector $\boldsymbol{Q}_{\mathrm{M}}$ valued in $\Re^{m}$ and of support $\mathcal{S}_{\boldsymbol{Q}_{\mathrm{M}}}=\Re^{m}$ can be defined from the entries of the triangular matrices of the Cholesky decomposition (294), possibly applied on different dependent random fields*e.g.* when considering a multi-physics problem characterised by several tensorial properties. Considering a random field defined by n^{tensor} dependent random matrix fields $\{\mathbf{C}_{\mathrm{M}}^{(i)}(\boldsymbol{X},\,\omega):\ \boldsymbol{X}\in\Omega,\,\omega\in\mathcal{W}\}$, $i=1..n^{\mathrm{tensor}}$, with $\mathbf{C}_{\mathrm{M}}^{(i)}(\boldsymbol{X},\,\omega)$ valued in $\Re^{n^{(i)}\times n^{(i)}}$, each random matrix field yields the triangular matrix field $\{\mathbf{L}_{\Delta\mathbf{C}_{\mathrm{M}}^{(i)}}(\boldsymbol{X},\,\omega),\ \boldsymbol{X}\in\Omega,\,\omega\in\mathcal{W}\}$ of $\frac{n^{(i)}(n^{(i)}+1)}{2}$ dependent entries valued in $\Re$. The random vector field $\boldsymbol{Q}_{\mathrm{M}}(\Omega)=\{\boldsymbol{Q}_{\mathrm{M}}(\boldsymbol{X},\,\omega):\ \boldsymbol{X}\in\Omega,\,\omega\in\mathcal{W}\}$ is then defined from the random vector $\boldsymbol{Q}_{\mathrm{M}}$ valued in $\Re^{m}$ and of support $\mathcal{S}_{\boldsymbol{Q}_{\mathrm{M}}}=\Re^{m}$ with $m=\sum_{i=1}^{n^{\mathrm{tensor}}}\frac{n^{(i)}(n^{(i)}+1)}{2}$ and with

$$\boldsymbol{Q}_{\mathrm{M}}=\left[L_{\Delta\mathbf{C}_{\mathrm{M}}^{(1)}{}_{11}}\ L_{\Delta\mathbf{C}_{\mathrm{M}}^{(1)}{}_{21}}\ L_{\Delta\mathbf{C}_{\mathrm{M}}^{(1)}{}_{22}}\ \ldots L_{\Delta\mathbf{C}_{\mathrm{M}}^{(1)}{}_{n^{(1)}\,n^{(1)}}}\ \ldots L_{\Delta\mathbf{C}_{\mathrm{M}}^{(n^{\mathrm{tensor}})}{}_{n^{(n^{\mathrm{tensor}})}\,n^{(n^{\mathrm{tensor}})}}}\right]^{T}\,. \tag{295}$$

It is mandatory to define a single random field in the case in which different apparent properties are obtained from the stochastic homogenisation process in order to take into account their dependency.

Lucas et al. (2015) have used this approach in order to define a vector random field $\boldsymbol{Q}_{\mathrm{M}}$ valued in $\Re^{21}$ from the random field $\{\mathbb{C}_{\mathrm{M}}^{\mathrm{el}}(\boldsymbol{X},\,\omega):\ \boldsymbol{X}\in\Omega,\,\omega\in\mathcal{W}\}$ of the meso-scale apparent properties of a columnar poly-crystalline material. After applying the Cholesky decomposition (294) on the matrix random field $\Delta\mathbf{C}_{\mathrm{M}}^{\mathrm{el}}(\Omega)$ obtained from Eq. (293), the 21 entries of the random triangular matrix field $\mathbf{L}_{\Delta\mathbf{C}_{\mathrm{M}}^{\mathrm{el}}}(\Omega)$ were used to define the vector random field $\boldsymbol{Q}_{\mathrm{M}}(\Omega)$.

When extending to thermo-mechanical damping, Wu et al. (2016) have also applied the Cholesky decomposition (294) on the apparent thermal conductivity random tensor field $\{\mathbf{K}_{\mathrm{M}}(\boldsymbol{X},\,\omega):\ \boldsymbol{X}\in\Omega,\,\omega\in\mathcal{W}\}$, yielding the 6 entries of the random triangular matrix field $\mathbf{L}_{\Delta\mathbf{K}_{\mathrm{M}}}(\Omega)$. The 21st entries of the random vector field $\boldsymbol{Q}_{\mathrm{M}}(\Omega)=\{\boldsymbol{Q}_{\mathrm{M}}(\boldsymbol{X},\,\omega):\ \boldsymbol{X}\in\Omega,\,\omega\in\mathcal{W}\}$, with $\boldsymbol{Q}_{\mathrm{M}}(\boldsymbol{X},\,\omega)\in\Re^{33}$, were then obtained from $\mathbf{L}_{\Delta\mathbf{C}_{\mathrm{M}}^{\mathrm{el}}}(\Omega)$, the Cholesky decomposition of the elasticity tensor increment, and the entries 22 to 27 from $\mathbf{L}_{\Delta\mathbf{K}_{\mathrm{M}}}(\Omega)$ the Cholesky decomposition of the conductivity tensor. Entries 28 to 33 were obtained from the dilation coefficient random matrix field $\{\mathbf{A}_{\mathrm{M}}(\boldsymbol{X},\,\omega):\ \boldsymbol{X}\in\Omega,\,\omega\in\mathcal{W}\}$, which does not require a Cholesky decomposition because there is no restriction on its definite positive nature.

Lucas et al. (2017) have considered stochastic higher order homogenisation of 3D micro-structures for plate structural simulations, yielding the random matrix field $\{\mathbf{U}_{\mathrm{M}}(\boldsymbol{X},\, w) : \boldsymbol{X} \in \Omega,\, w \in \mathscr{W}\}$ valued in $\Re^6 \times \Re^6$ of the so-called A-B-D matrix of thin structures. Because of the characteristic of the micro-structure (rough surface in that case), the apparent density per unit surface was also defining a random value field $\{\mathrm{P}_{\mathrm{M}}(\boldsymbol{X},\, w) : \boldsymbol{X} \in \Omega,\, w \in \mathscr{W}\}$, with a lower bound ρ_{L}. The 21st entries of the random vector field $\boldsymbol{Q}_{\mathrm{M}}(\Omega) = \{\boldsymbol{Q}_{\mathrm{M}}(\boldsymbol{X},\, w) : \boldsymbol{X} \in \Omega,\, w \in \mathscr{W}\}$, with $\boldsymbol{Q}_{\mathrm{M}}(\boldsymbol{X},\, w) \in \Re^{22}$, were then obtained from $\mathbf{L}_{\Delta\mathbf{U}_{\mathrm{M}}}(\Omega)$ the Cholesky decomposition of the A-B-D matrix increment, and the 22nd entry was obtained by considering the random value field resulting from the transformation $\log(\mathrm{P}_{\mathrm{M}}(\boldsymbol{X},\, w) - \rho_{\mathrm{L}})$ in order to ensure the positive nature of the density ρ_{M}.

Evaluation of the lower bound. The definition of the lower bound $\mathbf{s}_{\mathrm{L}}$ depends on the material system under consideration. For a multi-phase material $\omega = \cup_i \omega_i$ of known and fixed volume fractions v_i, the Reuss bound $\mathbb{s}^{\mathrm{Reuss}} = \frac{1}{V(\omega)} \int_\omega \mathbb{s}_{\mathrm{m}}(\boldsymbol{x}) d\omega = \sum_i v_i \mathbb{s}_i$ can be evaluated from the phases material compliance tensor $\mathbb{s}_i$ and can be used to define the lower bound $\mathbf{c}_{\mathrm{L}}$. However, when evaluating the random field from SVE simulations, *e.g.* following the window technique illustrated in Fig. 25, the volume fraction is not constant from one SVE to the others and the Reuss bound cannot be used.

In the context of the homogenisation of the mechanical properties of a poly-crystal, Lucas et al. (2015) have considered as lower bound $\mathbf{c}_{\mathrm{L}}$ an isotropic elasticity tensor $\mathbf{c}_{\mathrm{iso}}(E_{\mathrm{iso}},\, \nu_{\mathrm{iso}})$ whose Young's modulus E_{iso} and Poisson ratio ν_{iso} result from an optimisation problem

$$\begin{aligned} & E_{\mathrm{iso}},\, \nu_{\mathrm{iso}} = \arg\min_{(E'_{\mathrm{iso}},\, \nu'_{\mathrm{iso}}) \in \mathcal{C}} \left\| \mathbf{c}_{\mathrm{iso}}(E'_{\mathrm{iso}},\, \nu'_{\mathrm{iso}}) - \mathbf{c}_{\mathrm{crystal}} \right\| \\ & \text{with } \mathcal{C} = \left\{ E'_{\mathrm{iso}},\, \nu'_{\mathrm{iso}} \in \Re^+ : \mathbf{c}_{\mathrm{iso}}(E'_{\mathrm{iso}},\, \nu'_{\mathrm{iso}}) \leq \mathbf{c}_{\mathrm{crystal}} \right\}\,, \end{aligned} \tag{296}$$

with $\mathbf{c}_{\mathrm{crystal}}$ the elasticity tensor of a single-crystal.

Wu et al. (2016) have considered thermo-mechanical damping problem and have considered $\mathbf{c}_{\mathrm{iso}}(E_{\mathrm{iso}},\, \nu_{\mathrm{iso}})$ with Eq. (296) as a bound $\mathbf{c}_{\mathrm{L}}$ for the elasticity tensor random field $\{\mathbb{C}^{\mathrm{el}}_{\mathrm{M}}(\boldsymbol{X},\, w) : \boldsymbol{X} \in \Omega,\, w \in \mathscr{W}\}$. An empirical monotonic relation in terms of the grain size was used to define the lower scale conductivity tensor $\boldsymbol{\kappa}_{\mathrm{m}}(\boldsymbol{x})$ during the application of the window technique. Knowing the minimum grain size of the SVE realisations w, the same relation was used in order to evaluate the bound $\boldsymbol{\kappa}_{\mathrm{L}}$ of the homogenised thermal conductivity tensor field $\{\mathbf{K}_{\mathrm{M}}(\boldsymbol{X},\, w) : \boldsymbol{X} \in \Omega,\, w \in \mathscr{W}\}$.

In the case of a higher order homogenisation of 3D micro-structures for plate structural simulations, Lucas et al. (2017) have used the available realisations extracted following the window technique in order to evaluate a bound $\mathbb{u}_{\mathrm{L}}$ of the random field $\{\mathbf{U}_{\mathrm{M}}(\boldsymbol{X},\, w) : \boldsymbol{X} \in \Omega,\, w \in \mathscr{W}\}$ valued in $\Re^{6\times 6}$ of the so-called A-B-D matrix of thin structures. To this end, they set

$$\mathbb{u}_{\mathrm{L}} = \epsilon \lambda_{\min} \mathbb{I}_6\,, \tag{297}$$

where $\lambda_{\min}$ is the smallest of the eigen-values of the evaluated realisations $\mathbf{U}_{\mathrm{M}}(\boldsymbol{X},\, w)$ and $0 < \epsilon < 1$. A similar approach was used to evaluate the apparent density bound.

Generation. The method able to generate pseudo-samples $\mathbf{c}_{\mathrm{M}}^{(i)^{p}}(\boldsymbol{X})$ of the n^{tensor} dependent random matrix fields $\{\mathbf{C}_{\mathrm{M}}^{(i)}(\boldsymbol{X},\,\omega):\ \boldsymbol{X}\in\Omega,\,\omega\in\mathcal{W}\}$, $i=1..n^{\text{tensor}}$, with $\mathbf{C}_{\mathrm{M}}^{(i)}(\boldsymbol{X},\,\omega)$ valued in $\Re^{n^{(i)}\times n^{(i)}}$ is then summarised as

- Evaluate a number of observations $\mathbf{C}_{\mathrm{M}}^{(i)}(\boldsymbol{X},\,\omega^{l})$, $\omega^{l}\in\mathcal{W}$ with $l=1..n^{\text{observation}}$, *e.g.* from SVE simulations following the window technique illustrated in Fig. 25 and discussed in Section 4.1.2;

- When required, *i.e.* when $\mathbf{c}_{\mathrm{M}}^{(i)}(\boldsymbol{X})\in\mathbb{M}_{n^{(i)}}^{+}(\Re)$, evaluate a lower bound and apply the Cholesky decomposition (294) to evaluate the observations $\mathbf{L}_{\Delta\mathbf{C}_{\mathrm{M}}^{(i)}}(\boldsymbol{X},\,\omega^{l})$ of the triangular random matrix field $\{\mathbf{L}_{\Delta\mathbf{C}_{\mathrm{M}}^{(i)}}(\boldsymbol{X},\,\omega):\ \boldsymbol{X}\in\Omega,\,\omega\in\mathcal{W}\}$ of $\frac{n^{(i)}(n^{(i)}+1)}{2}$ dependent entries valued in $\Re$;

- Build the realisations $\boldsymbol{Q}_{\mathrm{M}}(\boldsymbol{X},\,\omega^{l})$ of the random vector field $\boldsymbol{Q}_{\mathrm{M}}(\Omega)=\{\boldsymbol{Q}_{\mathrm{M}}(\boldsymbol{X},\,\omega):\ \boldsymbol{X}\in\Omega,\,\omega\in\mathcal{W}\}$ valued in $\Re^{m}$ and of support $\mathcal{S}_{\boldsymbol{Q}_{\mathrm{M}}}=\Re^{m}$ with $m=\sum_{i=1}^{n^{\text{tensor}}}\frac{n^{(i)}(n^{(i)}+1)}{2}$ following Eq. (295);

- Use the realisations $\boldsymbol{Q}_{\mathrm{M}}(\boldsymbol{X},\,\omega^{l})$ to build a random vector field representation and generator following Section 5.2; In particular, assuming that enough realisations could be extracted in order to represent the fields in an accurate way, an expansion method or a spectral method followed by a non-Gaussian mapping can be considered;

- Generate pseudo-samples $\boldsymbol{q}_{\mathrm{M}}^{p}(\boldsymbol{X})$;

- Deduce the pseudo-samples $\mathbf{l}^{p}_{\Delta\mathbf{C}_{\mathrm{M}}^{(i)}}(\boldsymbol{X})$ from Eq. (295); and deduce the pseudo samples $\mathbf{c}_{\mathrm{M}}^{(i)^{p}}(\boldsymbol{X})$ from Eq. (294).

This methodology was used in combination with a spectral generator in the context of poly-silicon elasticity by Lucas et al. (2015), thermo-elastic damping by Wu et al. (2016), and plate bending by Lucas et al. (2017), and in the context of two-phase composite materials by Stefanou et al. (2017). It was used in combination with a copula method, see Appendix A.2.2, by Wu et al. (2018a) in the context of two-phase composite materials. Liebscher et al. (2012) have considered both the KL expansion and the spectral generator in the context of open foams. Finally, Sena et al. (2013) have used the window technique to extract the spatial correlation structure of a two-phase material.

As an illustration example, the described methodology using a spectral generator combined to a non-Gaussian mapping, see Section 5.2.2, was applied by Wu et al. (2016) to generate pseudo-samples of the apparent thermo-mechanical properties of a poly-silicon microstructure. Figure 35 compares, for some entries, the distributions and cross-correlation evaluated from the observations $\mathbf{C}_{\mathrm{M}}^{(i)}(\boldsymbol{X},\,\omega^{l})$, $\omega^{l}\in\mathcal{W}$ with $l=1..n^{\text{observation}}$ extracted from SVE simulations, *e.g.* following the window technique illustrated in Fig. 25, with the distributions and cross-correlation arising from the generated pseudo-samples $\mathbf{c}_{\mathrm{M}}^{(i)^{p}}(\boldsymbol{X})$, $p=1,\,2,\,\ldots$ This example shows that the method can represent non-Gaussian distributions, see Figs. 35(a) and 35(b), whilst preserving the cross-correlation, see Figs. 35(c) and 35(d). However, Wu et al. (2016) showed that although non-Gaussian distributions of the random vector field $\boldsymbol{Q}_{\mathrm{M}}(\Omega) = \{\boldsymbol{Q}_{\mathrm{M}}(\boldsymbol{X},\, \varpi) \,:\, \boldsymbol{X} \in \Omega,\, \varpi \in \mathscr{W}\}$ valued in $\Re^m$ are always accurately captured by the intermediate pseudo-samples $\boldsymbol{q}_{\mathrm{M}}^{p}(\boldsymbol{X})$, when combining their entries to evaluate the pseudo samples $\mathbf{c}_{\mathrm{M}}^{(i)^p}(\boldsymbol{X})$ to represent the random fields $\{\mathbf{C}_{\mathrm{M}}^{(i)}(\boldsymbol{X},\, \varpi) \,:\, \boldsymbol{X} \in \Omega,\, \varpi \in \mathscr{W}\}$, $i = 1..n^{\text{tensor}}$, with $\mathbf{C}_{\mathrm{M}}^{(i)}(\boldsymbol{X},\, \varpi)$ valued in $\Re^{n^{(i)} \times n^{(i)}}$, some components loose accuracy when they result from several dependent component of $\boldsymbol{q}_{\mathrm{M}}^{p}(\boldsymbol{X})$. Illustrations of a random field realisation directly deduced from the window technique and as generated are also given in respectively Fig. 35(e) and 35(f) showing that the "randomness" of the random field is preserved by the generator.

5.3.3. Covariance structure and spectral representation of elasticity tensors

Malyarenko and Ostoja-Starzewski (2016b,c, 2017) have developed models of second-order random fields, taking values in some sets of tensors, for each of the eight different elasticity symmetry classes of crystal. For these models, the one-point, *i.e.* mean $\bar{\mathbb{C}}_{\mathrm{M}}^{\mathrm{el}}$, and two-point covariance, *i.e.* $\tilde{\mathbb{R}}_{\mathbb{C}_{\mathrm{M}}^{\mathrm{el}}}(\boldsymbol{\tau})$ where $\tilde{\mathbb{R}}$ is a 8th-order tensor and $\boldsymbol{\tau}$ is the vector between two material points, functions need to be explicitly specified, under the assumption of statistical homogeneity and wide sense isotropy[11] The two-point correlation is needed to account for the dependency in the orientation of neighbouring crystals.

In particular Malyarenko and Ostoja-Starzewski (2017) derived the general form of the two-point covariance tensor $\tilde{\mathbb{R}}_{\mathbb{C}_{\mathrm{M}}^{\mathrm{el}}}(\tau)$ under the form (Karimi et al., 2020)

$$\tilde{R}_{\mathbb{C}^{\mathrm{el}}_{\mathrm{M}_{i\,j\,k\,l\,p\,r\,s\,t}}}(\boldsymbol{\tau}) = \sum_{n=1}^{29} L^{(n)}_{i\,j\,k\,l\,p\,r\,s\,t}(\boldsymbol{\tau}) K^{(n)}(\tau)\,, \tag{298}$$

where the 8th-order tensors $\mathbb{L}^{(n)}$ depend on the symmetry class and are given by Malyarenko and Ostoja-Starzewski (2016a), and where the scalar functions $K^{(n)}(\tau)$ can be obtained by micro-mechanics considerations: *e.g.* using the window techniques in combination with MC simulations, as described in Section 5.3.2, see also the work by Sena et al. (2013). Finally, using this structure, Malyarenko and Ostoja-Starzewski (2017) have also derived the general expression of the spectral expansion of the random field $\mathbb{C}_{\mathrm{M}}^{\mathrm{el}}$.

Extending this approach to account for the SVE size has been studied by Karimi et al. (2020), using as a basis the partition theorem, see Section 5.3.1.

5.3.4. Bayesian inference of meso-scale random fields

More recently, assuming that realisations $\mathbf{c}_{\mathrm{M}}^{i}(\boldsymbol{X}) = \mathbf{C}_{\mathrm{M}}^{\mathrm{el}}(\boldsymbol{X},\, \varpi^i) \in \mathbb{M}_n^+(\Re)$, for $\varpi^i \in \mathscr{W}$, could be extracted following the window technique illustrated in Fig. 25 and discussed in Section 4.1.2, the random field of an apparent uni-variate elastic property, and in particular its correlation structure, was inferred using the Bayesian approach, see Section 3.4.2.

---

[11] Here homogeneity and wide sense isotropy are related to the random field and not the material property, *i.e.* $\tilde{\mathbb{R}}_{\mathbb{C}_{\mathrm{M}}^{\mathrm{el}}}(k\boldsymbol{\tau}) = r(k)\tilde{\mathbb{R}}_{\mathbb{C}_{\mathrm{M}}^{\mathrm{el}}}(\boldsymbol{\tau})r^{-1}(k)$ for k belonging to the group of rotation and reflection in $\Re^3$ and $r(k)$ an orthogonal representation of that group.

Rappel et al. (2019c) have inferred the Young's modulus random field of poly-crystalline beams by constructing a random field characterised by non-Gaussian uni-variate marginal distributions (at different material points $\boldsymbol{X}^{(q)} \in \Omega$) that are joined in a single distribution using Gaussian copulas. They used a beta distributions for the uni-variate marginal distributions of the Young's modulus in order to ensure its positiveness. The parameters of the correlation matrix, characterising the spatial correlation, and of the uni-variate distribution were inferred from the SVE realisations using the Bayesian approach. Using Bayesian learning, Savvas et al. (2020) have identified the most appropriate correlation kernels and marginal distributions of uni-variate random field corresponding to different entries of the apparent elasticity tensor field $\{\mathbf{C}^{\mathrm{el}}_{\mathrm{M}}(\boldsymbol{X},\, \omega) : \boldsymbol{X} \in \Omega,\, \omega \in \mathcal{W}\}$ of two-phase composite materials. The method should be extended to multi-variate random fields to account for the cross-correlation function between the entries.

5.3.5. Limited amount of information is available

Soize (2005, 2006); Guilleminot et al. (2011); Noshadravan et al. (2013) have applied the maximum entropy principle, see the summary in Section 5.2.3, in order to represent random matrices when the available information is limited. The available information is typically the positive definite nature of the matrix, some statistical moments, or again some known bounds on the matrix. The maximum entropy principle was also applied by Mignolet and Soize (2008) to enforce the variance of a set of eigenvalues in stochastic dynamics problems.

Case in which the expectation is known. This case was developed by Soize (2005) who considered the random matrix field $\{\mathbf{C}^{\mathrm{el}}_{\mathrm{M}}(\boldsymbol{X},\, \omega) : \boldsymbol{X} \in \Omega,\, \omega \in \mathcal{W}\}$, with $\mathbf{C}^{\mathrm{el}}_{\mathrm{M}} : \mathcal{W} \to \mathbb{M}^{+}_{n}(\Re)$, with the expectation $\bar{\mathbf{c}}^{\mathrm{el}}_{\mathrm{M}}(\boldsymbol{X}) = \mathbb{E}\left[\mathbf{C}^{\mathrm{el}}_{\mathrm{M}}(\boldsymbol{X})\right] \in \mathbb{M}^{+}_{n}(\Re)$ known. Because of the positive definite nature of the expectation, the Cholesky decomposition allows defining the lower triangular matrix $\mathbf{l}_{\bar{\mathbf{c}}^{\mathrm{el}}_{\mathrm{M}}}(\boldsymbol{X})$

$$\bar{\mathbf{c}}^{\mathrm{el}}_{\mathrm{M}}(\boldsymbol{X}) = \mathbf{l}_{\bar{\mathbf{c}}^{\mathrm{el}}_{\mathrm{M}}}(\boldsymbol{X}) \left(\mathbf{l}_{\bar{\mathbf{c}}^{\mathrm{el}}_{\mathrm{M}}}(\boldsymbol{X})\right)^{T} . \tag{299}$$

This, in turns, allows defining the symmetric random matrix field $\{\mathbf{G}(\boldsymbol{X},\, \omega) : \boldsymbol{X} \in \Omega,\, \omega \in \mathcal{W}\}$, with $\mathbf{G} : \mathcal{W} \to \mathbb{M}^{+}_{n}(\Re)$ and with identity as mean value, following

$$\mathbf{C}^{\mathrm{el}}_{\mathrm{M}}(\boldsymbol{X}) = \mathbf{l}_{\bar{\mathbf{c}}^{\mathrm{el}}_{\mathrm{M}}}(\boldsymbol{X}) \mathbf{G}(\boldsymbol{X}) \left(\mathbf{l}_{\bar{\mathbf{c}}^{\mathrm{el}}_{\mathrm{M}}}(\boldsymbol{X})\right)^{T} , \tag{300}$$

with $\mathbb{E}\left[\mathbf{G}(\boldsymbol{X})\right] = \mathbf{I}_{n}$.

Considering the random matrix $\mathbf{G} : \mathcal{W} \to \mathbb{M}^{+}_{n}(\Re)$, the associated Shannon entropy (266) is written as

$$s\left(\pi_{\mathbf{G}}\right) = -\int_{\mathbb{M}^{+}_{n}(\Re)} \pi_{\mathbf{G}}(\mathbf{g}) \log\left(\pi_{\mathbf{G}}(\mathbf{g})\right) d\mathbf{g} \,, \tag{301}$$

whose constrained maximisation defines the probability density function $\pi_{\mathbf{G}}$. The maximum entropy principle (268) then becomes

$$\pi_{\mathbf{G}} = \arg\max_{\pi \in \mathscr{P}} s(\pi)\,, \qquad \text{with}$$
$$\mathscr{P} = \left\{ \pi \text{ of support } \mathbb{M}_n^+(\Re) : \int_{\mathbb{M}_n^+(\Re)} \pi(\mathbf{g}) d\mathbf{g} = 1\,, \int_{\mathbb{M}_n^+(\Re)} \mathbf{g}\pi(\mathbf{g}) d\mathbf{g} = \mathbf{I}_n\,, \right.$$
$$\left. \text{and} \int_{\mathbb{M}_n^+(\Re)} \log\left(\det(\mathbf{g})\right) \pi(\mathbf{g}) d\mathbf{g} = c_{\mathbf{g}}\,,\ |c_{\mathbf{g}}| < +\infty \right\}. \tag{302}$$

The first constraint defining the manifold $\mathscr{P}$ enforces the positive-definiteness of $\mathbf{G}$, the second constraint enforces the normalisation of the probability density function, and the third constraint the matrix expectation. The last constraint of the manifold $\mathscr{P}$ was introduced by Soize (2005) in order to ensure the invertibility relation (282).

The solution of the constrained optimisation problem can be expressed in terms of the Lagrange multipliers following Eq. (270), and in turns in terms of $c_{\mathbf{g}}$ used as a constraint in Eq. (302). Following Soize (2000), expressing the distribution in terms of the latter parameter is not necessarily useful since its purpose is to ensure the invertibility. Instead, the probability density function can be written as

$$\pi_{\mathbf{G}}\left(\mathbf{g}\right) = \begin{cases} c_0 \left(\det(\mathbf{g})\right)^{\frac{(n+1)(1-\delta_{\mathbf{G}}^2)}{2\delta_{\mathbf{G}}^2}} \exp\left(-\frac{n+1}{2\delta_{\mathbf{G}}^2} \operatorname{tr}\left(\mathbf{g}\right)\right) & \text{if } \mathbf{g} \in \mathbb{M}_n^+(\Re)\,; \\ 0 & \text{if } \mathbf{g} \notin \mathbb{M}_n^+(\Re)\,; \end{cases} \tag{303}$$

in which c_0 is the normalisation constant and $\delta_{\mathbf{G}}$ is the dispersion parameter controlling the fluctuation of the random matrix and defined as:

$$\delta_{\mathbf{G}}^2 = \frac{\mathbb{E}\left[||\mathbf{G} - \mathbf{I}_n||_F^2\right]}{n}\,, \tag{304}$$

where $0 < \delta_{\mathbf{G}} < \sqrt{\frac{n+1}{n+5}}$ is required to hold in order to ensure $\mathbb{E}\left[\|\left(\mathbf{C}_{\mathrm{M}}^{\mathrm{el}}(\boldsymbol{X})\right)^{-1}\|_F^2\right] \leq c^2 < +\infty$ (Soize, 2005) and thus, because of Eq. (280), the invertibility (282). This last condition substitutes to the last constraint of the optimisation problem defined by Eq. (302).

Case in which bounds are known. Assuming a deterministic symmetric positive definite lower bound $\mathbf{c}_{\mathrm{L}}$ is known such that $\mathbf{C}_{\mathrm{M}}^{\mathrm{el}}(\boldsymbol{X},\, w) > \mathbf{c}_{\mathrm{L}}(\boldsymbol{X})$ is satisfied, then the random field $\{\Delta\mathbf{C}_{\mathrm{M}}^{\mathrm{el}}(\boldsymbol{X},\, w) : \boldsymbol{X} \in \Omega,\, w \in \mathscr{W}\}$, where $\Delta\mathbf{C}_{\mathrm{M}}^{\mathrm{el}} : \mathscr{W} \to \mathbb{M}_n^+(\Re)$ can be defined from Eq. (293) and the approach developed in the previous paragraph can be applied on the latter.

Guilleminot et al. (2011); Noshadravan et al. (2013) have developed two methods in order to introduce both a deterministic symmetric positive definite lower bound $\mathbf{c}_{\mathrm{L}}$ and a deterministic symmetric positive definite upper bound $\mathbf{c}_{\mathrm{U}}$ such that

$$0 < \mathbf{c}_{\mathrm{L}}(\boldsymbol{X}) < \mathbf{C}_{\mathrm{M}}^{\mathrm{el}}(\boldsymbol{X},\, w) < \mathbf{c}_{\mathrm{U}}(\boldsymbol{X}) \quad \forall \boldsymbol{X} \in \Omega,\, w \in \mathscr{W}\,, \tag{305}$$

allowing the following non-linear transformation

$$\mathbf{N}(\boldsymbol{X},\, w) = \left(\mathbf{C}_{\mathrm{M}}^{\mathrm{el}}(\boldsymbol{X},\, w) - \mathbf{c}_{\mathrm{L}}(\boldsymbol{X})\right)^{-1} - \left(\mathbf{c}_{\mathrm{U}}(\boldsymbol{X}) - \mathbf{c}_{\mathrm{L}}(\boldsymbol{X})\right)^{-1}. \tag{306}$$

It is also considered that the expectation $\bar{\mathbf{n}}(\boldsymbol{X}) = \mathbb{E}\left[\mathbf{N}(\boldsymbol{X})\right] \in \mathbb{M}_n^+(\Re)$ is known. The approach developed in the previous paragraph can then be applied on the random tensor field $\{\mathbf{N}(\boldsymbol{X},\, \omega) \,:\, \boldsymbol{X} \in \Omega,\, \omega \in \mathcal{W}\}$, with $\mathbf{N} \,:\, \mathcal{W} \to \mathbb{M}_n^+(\Re)$. We note that, because of the non-linear mapping, this method does not constrain the expectation of $\mathbf{C}_{\mathrm{M}}^{\mathrm{el}}(\boldsymbol{X})$, so that generated samples based on this formalism will not have the same expectation.

Another approach proposed by Guilleminot et al. (2011) is to introduce the bounds when writing the constrained optimisation problem (302), which now becomes

$$
\begin{aligned}
\pi_{\mathbf{C}_{\mathrm{M}}^{\mathrm{el}}} &= \arg\max\nolimits_{\pi\in\mathcal{P}} s(\pi)\,, \qquad \text{with}\\
\mathcal{P} = \Bigg\{ \pi \text{ of support } \mathcal{S}_{\mathbf{C}_{\mathrm{M}}^{\mathrm{el}}} \text{ with } \mathcal{S}_{\mathbf{C}_{\mathrm{M}}^{\mathrm{el}}} &= \{\mathbf{c}_{\mathrm{M}}^{\mathrm{el}} \in \mathbb{M}_n^+(\Re) \,:\, \mathbf{c}_{\mathrm{L}} < \mathbf{c}_{\mathrm{M}}^{\mathrm{el}} < \mathbf{c}_{\mathrm{U}}\} \,:\\
\int_{\mathcal{S}_{\mathbf{C}_{\mathrm{M}}^{\mathrm{el}}}} \pi(\mathbf{c}_{\mathrm{M}}^{\mathrm{el}}) d\mathbf{c}_{\mathrm{M}}^{\mathrm{el}} = 1\,, & \int_{\mathcal{S}_{\mathbf{C}_{\mathrm{M}}^{\mathrm{el}}}} \mathbf{c}_{\mathrm{M}}^{\mathrm{el}} \pi(\mathbf{c}_{\mathrm{M}}^{\mathrm{el}}) d\mathbf{c}_{\mathrm{M}}^{\mathrm{el}} = \bar{\mathbf{c}}_{\mathrm{M}}^{\mathrm{el}}\,,\\
\int_{\mathcal{S}_{\mathbf{C}_{\mathrm{M}}^{\mathrm{el}}}} \log\left(\det(\mathbf{c}_{\mathrm{M}}^{\mathrm{el}} - \mathbf{c}_{\mathrm{L}})\right) \pi(\mathbf{c}_{\mathrm{M}}^{\mathrm{el}}) d\mathbf{c}_{\mathrm{M}}^{\mathrm{el}} &= c_{\mathrm{L}}\,,\ |c_{\mathrm{L}}| < +\infty\\
\text{and } \int_{\mathcal{S}_{\mathbf{C}_{\mathrm{M}}^{\mathrm{el}}}} \log\left(\det(\mathbf{c}_{\mathrm{U}} - \mathbf{c}_{\mathrm{M}}^{\mathrm{el}})\right) \pi(\mathbf{c}_{\mathrm{M}}^{\mathrm{el}}) d\mathbf{c}_{\mathrm{M}}^{\mathrm{el}} &= c_{\mathrm{U}}\,,\ |c_{\mathrm{U}}| < +\infty \Bigg\}\,.
\end{aligned}
\tag{307}
$$

The first constraint defines the support, the second constraint enforces the normalisation of the probability density function, and the third constraint the matrix expectation. The last two constraints were introduced by Das and Ghanem (2009) to control the behaviour near the bounds.

The lower and upper bounds were evaluated by Guilleminot et al. (2011); Noshadravan et al. (2013) from micro-structure realisations using the partition theorem, see Section 5.3.1, in the context of poly-crystalline materials.

Generation of random matrix field. The resolution of the constrained optimisation problem (307) yields a distribution in terms of the Lagrange multipliers following Eq. (270), and in turns in terms of c_{L} and c_{U}. The generation of pseudo-samples $\mathbf{c}_{\mathrm{M}}^{p}$ can be achieved using a Markov Chain Monte Carlo method, see Appendix A.5.3.

The other cases result in the probability density function (303) of the random matrix field $\{\mathbf{G}(\boldsymbol{X},\, \omega) \,:\, \boldsymbol{X} \in \Omega,\, \omega \in \mathcal{W}\}$, with $\mathbf{G} \,:\, \mathcal{W} \to \mathbb{M}_n^+(\Re)$ with identity as mean value. The probability density function is controlled by the dispersion parameter $\delta_{\mathbf{G}}$ (304). Following Soize (2005); Guilleminot et al. (2011), one can define the $\frac{n(n+1)}{2}$ homogeneous germs $\Xi_{i\,j}(\boldsymbol{X})$ valued in $\Re$ of independent and zero-mean random fields, *i.e.* with the covariance[12] $\tilde{R}_{\Xi_{i\,j}}(\boldsymbol{\tau})$ such that $\tilde{R}_{\Xi_{i\,j}}(\mathbf{0}) = 1$, $1 \leq i \leq j \leq n$. This germ is obtained from a non-linear transformation of the lower triangular random matrix field $\{\mathbf{L}_{\mathbf{G}}(\boldsymbol{X},\, \omega) \,:\, \boldsymbol{X} \in \Omega,\, \omega \in \mathcal{W}\}$ of the new Cholesky decomposition

$$
\mathbf{G}(\boldsymbol{X},\, \omega) = \mathbf{L}_{\mathbf{G}}(\boldsymbol{X},\, \omega)\left(\mathbf{L}_{\mathbf{G}}(\boldsymbol{X},\, \omega)\right)^{T}\,. \tag{308}
$$

---

[12] In this section, the symbol $\tilde{R}_{\Xi_{i\,j}}(\boldsymbol{\tau})$ is not the component $i\,j$ of the matrix $\tilde{\boldsymbol{R}}_{\Xi}(\boldsymbol{\tau})$ but the covariance of the random variable field $\Xi_{i\,j}$.

The non-linear transformation reads

$$\begin{cases} L_{\mathbf{G}_{i\,i}}(\boldsymbol{X}) = \frac{\delta_{\mathbf{G}}}{\sqrt{n+1}}\sqrt{2h_{a_i}\left(\Xi_{i\,i}(\boldsymbol{X})\right)} & \text{and;} \\ L_{\mathbf{G}_{i\,j}}(\boldsymbol{X}) = \frac{\delta_{\mathbf{G}}}{\sqrt{n+1}}\Xi_{i\,j}(\boldsymbol{X}) & \text{if } j > i\,; \end{cases} \tag{309}$$

with the parameter $a_i = \frac{(n+1)}{(2\delta_{\boldsymbol{G}}^2)} + \frac{(1-i)}{2}$ and where h_{a_i} defines a non-linear mapping from a Gaussian random variable towards a Gamma random variable of shape parameter a_i and rate parameter 1, *i.e.*

$$\Gamma = h_{a_i}(\Xi) = {F^{\Gamma}_{a_i,\,1,\,0,\,1}}^{-1}\left(F^{\mathcal{N}}_{0,1}(\Xi)\right) \qquad \sim \Gamma_{a_i,\,1,\,0,\,1}\,, \tag{310}$$

where $F^{\mathcal{N}}_{0,1}$ is the zero-mean and unit variance Gaussian cumulative distribution, and where $F^{\Gamma}_{a_i,\,1,\,0,\,1}$ is the cumulative distribution of the Gamma distribution $\Gamma_{a_i,\,1,\,0,\,1}$ defined by Eq. (20). Since the $\frac{n(n+1)}{2}$ homogeneous germs $\Xi_{i\,j}(\boldsymbol{X})$, $1 \leq i \leq j \leq n$, valued in $\Re$ are independent with the covariance $\tilde{R}_{\Xi_{i\,j}}(\boldsymbol{\tau})$ such that $\tilde{R}_{\Xi_{i\,j}}(\mathbf{0}) = 1$, the $d \times \frac{n(n+1)}{2}$, with d the spatial dimension, correlation lengths $\{\boldsymbol{l}_{R_{\Xi_{i\,j}}}\}_k$ with $k = 1..d$, $1 \leq i \leq j \leq n$, define the correlation of the random field.

In this case, the generation of pseudo-samples $\mathbf{c}_{\mathrm{M}}^{\mathrm{el}^p}$ follows

- Evaluate a number of realisations $\mathbf{C}_{\mathrm{M}}^{\mathrm{el}}(\boldsymbol{X},\,\omega^i)$, *e.g.* from SVE simulations;
- If required evaluate a lower bound $\mathbf{c}_{\mathrm{L}}(\boldsymbol{X})$ and an upper bound $\mathbf{c}_{\mathrm{U}}(\boldsymbol{X})$, *e.g.* using partition theorem (283) as suggested by Guilleminot et al. (2011); Noshadravan et al. (2013), in order to define the observations $\Delta\mathbf{C}_{\mathrm{M}}^{\mathrm{el}}(\boldsymbol{X},\,\omega^i)$, with $\boldsymbol{X} \in \Omega$, $\omega^i \in \mathcal{W}$, through Eq. (293) or the observation $\mathbf{N}(\boldsymbol{X},\,\omega^i)$, with $\boldsymbol{X} \in \Omega$, $\omega^i \in \mathcal{W}$, through Eq. (306); These observations then substitutes to $\mathbf{C}_{\mathrm{M}}^{\mathrm{el}}(\boldsymbol{X},\,\omega^i)$ in the following;
- Perform the different non-linear mappings, *i.e.* through (300), from either the observations $\mathbf{C}_{\mathrm{M}}^{\mathrm{el}}(\boldsymbol{X},\,\omega^i)$, $\Delta\mathbf{C}_{\mathrm{M}}^{\mathrm{el}}(\boldsymbol{X},\,\omega^i)$ or $\mathbf{N}(\boldsymbol{X},\,\omega^i)$, with $\boldsymbol{X} \in \Omega$, $\omega^i \in \mathcal{W}$, in order to evaluate the observations $\mathbf{G}(\boldsymbol{X},\,\omega^i)$ and the dispersion parameter $\delta_{\mathbf{G}}$ from Eq. (304);
- Evaluate the $d \times \frac{n(n+1)}{2}$ correlation lengths $\{\boldsymbol{l}_{R_{\Xi_{i\,j}}}\}_k$ with $k = 1..d$, $1 \leq i \leq j \leq n$, *e.g.* from the non-linear mappings (308-310);
- Use a Gaussian generation process such as the one developed by Shinozuka (1971), see Appendix A.6.1, to generate pseudo samples $\xi^p_{i\,j}(\boldsymbol{X}^{(q)})$, $1 \leq i \leq j \leq n$, at different locations $\boldsymbol{X}^{(q)}$, with $\Xi_{i\,j}$ the independent and normalised Gaussian variables of correlation lengths $\{\boldsymbol{l}_{R_{\Xi_{i\,j}}}\}_k$ with $k = 1..d$.
- From the pseudo-samples $\xi^p_{i\,j}(\boldsymbol{X}^{(k)})$ evaluate the pseudo samples $\mathbf{g}^p(\boldsymbol{X}^{(q)})$ through the mappings (308-310);
- Perform the different non-linear mappings, *i.e.* through Eq. (300), from the pseudo samples $\mathbf{g}^p(\boldsymbol{X}^{(q)})$ to obtain the pseudo-samples of either $\mathbf{c}_{\mathrm{M}}^{\mathrm{el}^p}(\boldsymbol{X}^{(q)})$, $\Delta\mathbf{c}_{\mathrm{M}}^{\mathrm{el}^p}(\boldsymbol{X}^{(q)})$ or $\mathbf{n}^p(\boldsymbol{X}^{(q)})$, and in the last cases finally evaluate the pseudo-samples of $\mathbf{c}_{\mathrm{M}}^{\mathrm{el}^p}(\boldsymbol{X}^{(q)})$ through either Eq. (293) or Eq. (306).

5.4. Non-linear cases: multi-fidelity approach

In the linear case, the meso-scale stochastic constitutive law (251) simplifies in the evaluation of tensor random fields, as detailed in Section 5.3, since the macro-scale behaviours is fully characterised by the latter. However, in the context of non-linear and history dependent material behaviours at the micro-structure scale, following Eq. (116), a surrogate of Eq. (251) has to be provided, which bears some difficulties since it should remain accurate for different loading conditions but also for the full range of micro-structure realisations.

Because of the prohibitive cost of direct computational homogenisation and of the possible loss of accuracy of reduced order models, it is possible to conduct multi-fidelity analyses in which a high fidelity model (HFM) is first calibrated and then used to train a low fidelity model as suggested by Fish et al. (2018).

In particular, Fish et al. (2018) have used such a multi-fidelity model to develop a computational certification framework of woven composites under limited experimental data, in which the high fidelity model is a first-order computational homogenization model, which resolves microstructural details including the structure of defects, as illustrated in Fig. 23, and in which the low fidelity model is a reduced-order homogenization in the spirit of the unit cells used in Section 4.2.2.

This multi-fidelity approach is a pragmatic approach for stochastic multi-scale simulation in the non-linear range since it allows the definition of a "fast" stochastic model and since stochastic computational homogenisation is unreachable.

5.4.1. Meso-scopic constitutive behaviours

One solution is to use an existing constitutive model whose parameters are defined as random fields. Yin et al. (2008) have conducted simulations on porous SVEs in order to obtain the stochastic properties of the parameters of a porous steel alloy constitutive material model, and Yin et al. (2009) used the Karhunen-Loève expansion method to generate these stochastic parameters.

Hun et al. (2019) have homogenised 2D particle-reinforced matrix using a circular moving window technique to extract the random-field $\{[K(\boldsymbol{X};\, \omega)\, G((\boldsymbol{X};\, \omega))]^T;\, \boldsymbol{X} \in \Omega,\, \omega \in \mathcal{W}\}$ of an assumed isotropic elastic behaviour characterised by apparent bulk k and shear g moduli. They have extracted a homogenised critical energy release rate, which was approximated as being deterministic. Hun et al. (2019) have generated random field realisations $\{[k^p(\boldsymbol{X})\, g^p(\boldsymbol{X})]^T \,:\, \boldsymbol{X} \in \Omega\}$, though a non-linear transformation from a bi-variate Gaussian field. They have thus built a stochastic meso-scale elasticity-phase-field formulation using the homogenised critical energy release rate extracted from lower scale simulation and approximated as being deterministic.

In the context of MicroElectroMechanical Systems (MEMS), adhesive surface forces, such as van der Waals (vdW) forces and capillary forces, are of comparable order of magnitude as the repulsive surface forces described by a Hertz model. As a result, the contact forces $f_{\mathrm{M}}(d_{\mathrm{M}};\, \boldsymbol{X})$ exhibit an attractive and a repulsive parts in terms of the contact distance d_{M} as sketched in Fig. 36(a). Because the surface roughness is of random nature, the apparent force evolution at the meso-scale exhibits uncertainties. Hoang et al. (2017, 2018) have generated random surfaces, standing for micro-scale realisations $\omega^k \in \mathcal{W}$, from which the apparent contact force evolution $F_{\mathrm{M}}(d_{\mathrm{M}}; \boldsymbol{X}, \mathfrak{w}^k)$ could be predicted from a micro-mechanics model standing as high-fidelity model. Clearly the evolution is non-linear with the separation distance d_{M}, and, in order to perform stochastic analyses of the MEMS behaviour, a stochastic low fidelity model of the adhesive contact force was developed. Since the adhesive contact curve has a shape similar to a Morse potential, it was described by

$$f_{\mathrm{M}}(d_{\mathrm{M}}) = \begin{cases} f_{\max}(\mathrm{e}^{-2a_{\mathrm{right}}(d_{\mathrm{M}}-d_{\max})} - 2\mathrm{e}^{-a_{\mathrm{right}}(d_{\mathrm{M}}-d_{\max})}) & \text{for} \quad d_{\mathrm{M}} \geq d_{\max}; \\ f_{\max}(\mathrm{e}^{-2a_{\mathrm{left}}(d_{\mathrm{M}}-d_{\max})} - 2\mathrm{e}^{-a_{\mathrm{left}}(d_{\mathrm{M}}-d_{\max})}) & \text{for} \quad d_{\mathrm{M}} < d_{\max}. \end{cases} \tag{311}$$

which reaches the maximum adhesive force $f_{\max}$ at a distance $d_{\max}$, and involves the adhesive energy $e_{\mathrm{M}} = a_{\mathrm{right}} + a_{\mathrm{left}}$. A fourth parameter is defined as the distance d_{lim} at which the compressive force reaches a given value, *e.g.* 2 MPa.

Performing Monte-Carlo (MC) simulations of the micro-mechanics model allowed extracting the observations $f^k_{\max}$, $d^k_{\max}$, e^k_{M}, and d^k_{lim} for each micro-mechanics model realisation $\mathfrak{w}^k \in \mathfrak{W}$, see the observation curves in Fig. 36(b). The observation vectors were then constructed as

$$\boldsymbol{q}^k_{\mathrm{M}} = \left[\frac{\log(e^k_{\mathrm{M}})}{\sigma_{\log(E_{\mathrm{M}})}} \; \frac{\log(f^k_{\max})}{\sigma_{\log(F_{\max})}} \; \frac{d^k_{\max}}{\sigma_{D_{\max}}} \; \frac{\log(d^k_{\max} - d^k_{\mathrm{lim}})}{\sigma_{\log(D_{\max}-D_{\mathrm{lim}})}} \right]^T , \tag{312}$$

in which the log operators are used to enforce the physical constraints, *i.e.* the positive nature, during the generation process. The vectors $\boldsymbol{q}^k_{\mathrm{M}}$ correspond to observations of the random vector $\boldsymbol{Q}_{\mathrm{M}} : \mathfrak{W} \rightarrow \Re^4$. Hoang et al. (2017, 2018) have shown that two neighbouring SVEs $\omega(\boldsymbol{X}; \mathfrak{w}^k)$ and $\omega(\boldsymbol{X}'; \mathfrak{w}^k)$ yield spatially uncorrelated apparent properties $\boldsymbol{Q}_{\mathrm{M}}$. Following the discussion in Section 5.1.4, the apparent properties were thus considered as random vectors and not random vector fields.

A polynomial chaos expansion of the random vector $\boldsymbol{Q}_{\mathrm{M}} : \mathfrak{W} \rightarrow \Re^4$ was then considered and a generator was constructed following the polynomial chaos expansion (PCE) methodology summarised in Section 5.2.1 and detailed in Appendix A.4.3. Pseudo-samples $\boldsymbol{q}^p_{\mathrm{M}}$ could then be obtained from which the pseudo-samples $f^p_{\max}$, $d^p_{\max}$, e^p_{M}, and d^p_{lim} are deduced from Eq. (312) and the pseudo-samples of the adhesive contact curves $f^p_{\mathrm{M}}(d_{\mathrm{M}})$ from Eq. (311), see some examples in Fig. 36(c).

5.4.2. Stochastic MFH model

In the following we detail a process developed by Wu et al. (2018b, 2019) for particle-reinforced composites using Mean-Field Homogenisation (MFH) as a stochastic low fidelity model. In the context of MFH, the volume element ω is not discretised and is defined by an equivalent ellipsoid embedded in a matrix material, see Fig. 27(d), on which a micro-mechanics based model is applied to extract the homogenised response, see Section 4.2.4. Wu et al. (2018b, 2019) have identified the equivalent MFH model from computational homogenisation performed on different SVE realisations as sketched in Fig. 37, leading to a stochastic MFH meso-scale model. MFH was also considered by Hoang et al. (2016) as a low fidelity model in order to determine the size of RVE. Equivalent MFH models of nano-composites have also been identified by Yang et al. (2013) from the overall mechanical behaviour given by molecular dynamics simulations.

Inverse identification of the stochastic MFH model. Wu et al. (2018b, 2019) have considered as high-fidelity model the computational homogenisation described in Section 4.2.1 and applied on SVE of random 52% volume ratio particle-reinforced matrix constructed using the technique described in Section 3.2.1 and illustrated in Fig. 9. The SVE length considered was $l_{\mathrm{SVE}} = 25\mu$m and the extracted apparent Young's modulus distributions are illustrated in Fig. 29(b). The low fidelity model considered was the MFH model described in Section 4.2.4.

In the context of linear elasticity, Wu et al. (2018b) have extracted the fibre volume fraction v_{I}, the equivalent inclusions of equivalent semi-axes $\tilde{a}$ and $\tilde{b}$, equivalent orientation $\tilde{\theta}$ and the equivalent matrix elastic properties as illustrated in Fig. 38(a) for each SVE realisation $\omega(\boldsymbol{X};\, \mathfrak{w}^k)$ whose homogenised elasticity tensor was extracted in Section 4.2.1. The resulting equivalent values are reported in Fig. 39 in the first three and in the last columns, where the dependency between the parameters can be observed.

Wu et al. (2019) have extended this methodology in the context of elastic inclusions embedded in an elasto-plastic matrix as illustrated in Fig. 38(b). In that case, the incremental-secant MFH is used as low fidelity model and, beside the equivalent inclusions and elastic matrix properties being evaluated in the elastic regime, an equivalent matrix yield stress $\tilde{\sigma}_{Y0}$ and hardening law $\tilde{r}_0(\tilde{p}_0) = \tilde{k}_{1_0}\tilde{p}_0 + \tilde{k}_{2_0}\left(1 - e^{-\tilde{m}_0\tilde{p}_0}\right)$ of the non-linear incremental secant MFH model, see Fig. 38(b), was extracted from each SVE realisation $\omega(\boldsymbol{X};\, \mathfrak{w}^k)$ by computational homogenisation. The extracted effective parameters for the different SVE realisations $\omega(\boldsymbol{X};\, \mathfrak{w}^k)$ with $\mathfrak{w}^k \in \mathcal{W}$ are reported in Fig. 39, and the study of the correlation distance matrix by Wu et al. (2019) showed a dependency between most of the parameters.

Taking advantage of the incremental-secant MFH scheme which can account for Lemaitre-Chaboche damage-enhanced materials through a virtual unloading, the inverse identification was then applied by Wu et al. (2019) to the case of elastic-inclusions embedded in a damage-enhanced elasto-plastic matrix following the methodology illustrated in Figs. 38(c)-38(d). For a given SVE, once the equivalent inclusion and matrix elastic properties are identified from the elastic behaviour, see Fig. 38(a), the equivalent damage evolution law $\tilde{d}_0(\tilde{p}_0)$ is identified from the virtual unloading step of the incremental-secant formulation through the change in the elastic response, see Fig. 38(c). The equivalent matrix hardening law $\tilde{r}_0(\tilde{p}_0) = \tilde{k}_{1_0}\tilde{p}_0 + \tilde{k}_{2_0}\left(1 - e^{-\tilde{m}_0\tilde{p}_0}\right)$ can then be extracted from the effective (or undamaged) stress $\frac{\tilde{\sigma}_0}{1-\tilde{d}_0}$ evolution evaluated during the reloading process, see Fig. 38(d). The extracted effective elasto-plastic parameters are also reported in Fig. 39 for the different SVE realisations $\omega(\boldsymbol{X};\, \mathfrak{w}^k)$, with $\mathfrak{w}^k \in \mathcal{W}$. The application to the damage-enhanced elasto-plasticity holds up to strain softening onset only since the stress-stain curve looses objectivity beyond that point. The method can still be applied during strain softening by considering other objective quantities such as an equivalent fracture critical energy release rate. Critical strength and energy release rates were extracted from SVE direct simulations by Nguyen et al. (2019) for carbon fibre reinforced high-cross-linked RTM6 epoxy resin and exploited in the MFH inverse identification process by Calleja et al. (In Preparation).

One important note is that, apart in the elastic-regime for which the homogenisation is not assuming a loading case, the equivalent properties extracted with the methodology can depend on the loading case, in which case the micro-model should be enriched.

Random field generation process. This low fidelity model of an SVE $\omega(\boldsymbol{X};\, \mathscr{w}^k)$ is defined by its fibre volume fraction v_{I}, by the equivalent semi-axes $\tilde{a}$ and $\tilde{b}$ of the equivalent inclusion of equivalent orientation $\tilde{\theta}$, by the equivalent matrix Young's modulus $\tilde{E}_0$ and Poisson ratio $\tilde{\nu}_0$, by an equivalent matrix yield stress $\tilde{\sigma}_{Y0}$ and by an equivalent matrix hardening law $\tilde{r}_0(\tilde{p}_0) = \tilde{k}_{1_0}\tilde{p}_0 + \tilde{k}_{2_0}\left(1 - e^{-\tilde{m}_0\tilde{p}_0}\right)$.

Since each SVE realisation $\omega\left(\mathscr{w}^k\right)$, $\mathscr{w}^k \in \mathscr{W}$, yields new effective values, Wu et al. (2019) have defined the observation vector $\boldsymbol{q}_{\mathrm{M}}^k = [v_{\mathrm{I}}^k\, \frac{\tilde{a}^k}{\tilde{b}^k}\, \tilde{\theta}^k\, \tilde{E}_0^k\, \tilde{\nu}_0^k\, \tilde{\sigma}_0^k\, \tilde{k}_{1_0}^k\, \tilde{k}_{2_0}^k\, \tilde{m}_0^k]^T$, where the superscript k refers to the SVE realisation $\omega\left(\mathscr{w}^k\right)$. These vectors $\boldsymbol{q}_{\mathrm{M}}^k$ correspond to observations of the random vector $\boldsymbol{Q}_{\mathrm{M}} : \mathscr{W} \rightarrow \Re^9$ of meso-scale effective properties. Following the discussion in Section 5.1.4, two neighbouring SVEs $\omega(\boldsymbol{X};\, \mathscr{w}^k)$ and $\omega(\boldsymbol{X}';\, \mathscr{w}^k)$ of particle-reinforced composites yield spatially uncorrelated apparent properties $\boldsymbol{Q}_{\mathrm{M}}$ and the apparent properties are thus considered as random vectors and not random vector fields.

Considering $n^{\mathrm{SVE}} = 1900$ independent realisations allowed Wu et al. (2019) to define the observation data-set $\mathbf{q}_{\mathrm{M}} = [\boldsymbol{q}_{\mathrm{M}}^1 \dots \boldsymbol{q}_{\mathrm{M}}^k \dots \boldsymbol{q}_{\mathrm{M}}^{n^{\mathrm{SVE}}}]$ as a realisation of the random matrix $\mathbf{Q}_{\mathrm{M}}$. The data-driven sampling method developed by Soize and Ghanem (2016) and summarised in Section 5.2.4, was then applied in order to generate 18,000 additional samples. 300 random observations and 300 pseudo-samples are illustrated in Fig. 40 showing that the pseudo-samples respect the statistical content, including dependency, of the observations.

5.5. Macro-scale realisations

In the absence of dynamical effects the equilibrium of the body Ω was formulated by Eq. (117) repeated here for clarity as

$$\mathbf{P}_{\mathrm{M}}\left(\boldsymbol{X};\, \mathscr{w}\right) \cdot \boldsymbol{\nabla}_0 + \boldsymbol{b}(\boldsymbol{X}) = 0 \qquad \forall \boldsymbol{X} \in \Omega\,, \quad \forall \mathscr{w} \in \mathscr{W}\,, \tag{313}$$

where the subscript "M" refers to the local value at the macro-scale, $\mathbf{P}_{\mathrm{M}}$ is the first Piola-Kirchhoff stress tensor, and the gradient operator $\boldsymbol{\nabla}_0$ refers to the macro-scale reference configuration. The linear momentum equation is completed by the boundary conditions (118-119), also repeated for clarity as

$$\boldsymbol{U}_{\mathrm{M}}(\boldsymbol{X};\, \mathscr{w}) = \boldsymbol{u}_{\mathrm{D_M}} \qquad \forall \boldsymbol{X} \in \partial_D\Omega\,, \quad \forall \mathscr{w} \in \mathscr{W}\,, \text{ and} \tag{314}$$

$$\mathbf{P}_{\mathrm{M}}(\boldsymbol{X};\, \mathscr{w}) \cdot \boldsymbol{n}_{\mathrm{M}} = \boldsymbol{t}_{\mathrm{M}} \qquad \forall \boldsymbol{X} \in \partial_N\Omega\,, \quad \forall \mathscr{w} \in \mathscr{W}\,, \tag{315}$$

where $\boldsymbol{t}_{\mathrm{M}}$ is the surface traction, per unit reference surface, on the Neumann boundary $\partial_N\Omega$ of outward unit normal $\boldsymbol{n}_{\mathrm{M}}$ in the reference configuration, and $\bar{\boldsymbol{u}}_{\mathrm{D_M}}$ is the constrained displacement on the Dirichlet boundary $\partial_D\Omega$. In these equations we assume that the uncertainties result from the micro-scale information only.

The uncertainties of the material properties can then be propagated to the macro-scale structural response through a stochastic finite element discretisation $\Omega \sim \cup_e\Omega^e$ of the boundary value problem problem (313) as suggested by Alzebdeh and Ostoja-Starzewski (1996); Ostoja-Starzewski and Wang (1999); Ghanem and Spanos (1991); Le Maitre and Knio (2010). To this end, the problem is completed by the stochastic constitutive behaviour

(251) which is formulated under the form of a random field, see Section 5.3 in the linear range and Section 5.4 in the non-linear range. The random field is discretised following the methods developed in Section 5.1.

The different stochastic finite element methods detailed in Section 4.3 can then be used to evaluate the stochastic structural behaviour. These methods are here summarised in the context of handling the meso-scale random field $\{\boldsymbol{Q}_{\mathrm{M}}(\boldsymbol{X},\ \omega) :\ \boldsymbol{X} \in \Omega,\ \omega \in \mathcal{W}\}$ of apparent meso-scale properties and their technical aspects are discussed. A recent discussion on their practical applications was given by Arregui-Mena et al. (2016). Finally, an alternative to the stochastic multi-scale approach is to consider a multi-scale adaptive model, which locally resolves the heterogeneity and their randomness in sub-domains where they affect the separation of scales, whilst considering an homogenous deterministic continuum elsewhere. This will be briefly summarised in Section 5.5.4.

5.5.1. Monte-Carlo simulations

The Monte-Carlo simulation strategy, see also Section 4.3.1, involves considering n^{MC} realisations $\boldsymbol{Q}_{\mathrm{M}}(\boldsymbol{X},\ \omega^i)$, with $\omega^i \in \mathcal{W}$, of the random field $\boldsymbol{Q}_{\mathrm{M}}(\Omega)$. In practice pseudo-samples $\{\boldsymbol{q}^p_{\mathrm{M}}(\boldsymbol{X}^{(q)}) :\ \boldsymbol{X}^{(q)} \in \Omega\}$ are generated by any of the different methods summarised in Section 5.2 and a deterministic simulation is conducted for each realisation. As an example, Fig. 33(c) was obtained using the MC simulation approach.

Assuming the standard deviation of the structural response F_{M} is $\sigma_{F_{\mathrm{M}}}$, the error on the expectation of F_{M} is a random variable E following a Gaussian distribution (Nouy, 1999)

$$E = \mathbb{E}[F_{\mathrm{M}}] - \frac{1}{n^{\mathrm{MC}}}\sum_{i}^{n^{\mathrm{MC}}} F_{\mathrm{M}}(\omega^i) \sim \frac{\sigma_{F_{\mathrm{M}}}}{\sqrt{n^{\mathrm{MC}}}}\mathcal{N}_{0,\,1}\,, \tag{316}$$

with the normal distribution (17), showing that the error decreases with the square-root of the number of pseudo-samples but does not depend on the dimension of the random field.

The Monte-Carlo simulations method has several advantages

- Any of the different random-field representation and generation methods, see Section 5.2, can be considered;
- Both linear and non-linear problems can be handled;
- Modifications to an existing finite-element code are limited to the discretisation of the random field, see Section 5.1;
- It can capture rare events, but this requires a high number of realisations n^{MC} in order to have enough samples in the regions of rare events;
- It can handle systems that have large variability and involve complex models that include several dependent random variables since Eq. (316) shows that the error does not depend on the size of the random field;

- Parallelisation is straightforward since it consists in sending the different uncoupled deterministic resolutions on different processors.

The main disadvantage of the MC simulation method is that it can require a high number of realisations in order to be accurate, as shown by the error (316) of order $\mathcal{O}({n^{\mathrm{MC}}}^{-1/2})$, which decreases with the square root of the number of samples. Accuracy has to be assessed during the iterations by asserting the convergence of the structural responses distribution. Several strategies have thus been developed to reduce the number of samplings, which are detailed by Caflisch (1998); Nouy (1999); Stefanou (2009), among which two commonly used methods are

- Variance-reduction techniques in which the generation of pseudo-samples is controlled in order to improve the efficiency, *e.g.* in the importance sampling technique the generation of samples is controlled by a sampling distribution concentrated in the regions of rare events; this is, however, only efficient for a limited number of random variables; in the stratified sampling technique, the sampling region is first divided, *e.g.* with a regular grid with uniform density;

- Quasi-Monte Carlo method: Whilst Monte Carlo methods use independent pseudo-samples (following pseudo-random sequences), with the Quasi-Monte Carlo method, the pseudo-samples are correlated (following a quasi-random or low discrepancy sequence) to make them more uniform; Convergence is faster, order $\mathcal{O}\left({n^{\mathrm{MC}}}^{-1}\log^k(n^{\mathrm{MC}})\right)$ instead of $\mathcal{O}({n^{\mathrm{MC}}}^{-1/2})$; The method is however rather used for integration than simulation and behaves like Monte Carlo in high dimension (Caflisch, 1998); However, it can provide faster convergence when studying structural failure as shown by Pitz and Pochiraju (2019).

5.5.2. Stochastic Galerkin finite element method

The displacement field solution of (313) is written as a continuous random field $\boldsymbol{U}(\Omega) = \{\boldsymbol{U}(\boldsymbol{X}) : \boldsymbol{X} \in \Omega\}$, which takes values in $\Re^d$, for $\Omega \subset \Re^d$ a space of material points $\boldsymbol{X}$, with $d \in \mathbb{N}$. Its expectation (26) is denoted by $\bar{\boldsymbol{u}}(\boldsymbol{X}) = \mathbb{E}[\boldsymbol{U}(\boldsymbol{X})] : \Omega \to \Re^d$. Let $\boldsymbol{\Xi} = [\Xi_1 \dots \Xi_i \dots \Xi_n]^T$ be a vector of n independent, zero-mean, and unit variance random variables $\Xi_i : \mathcal{W} \to \Re$ of finite second order moment and of support $\mathcal{S}_{\Xi_i}$. The support of $\boldsymbol{\Xi}$ is denoted by $\mathcal{S}_{\boldsymbol{\Xi}} = \mathcal{S}_{\Xi_1} \times \dots \times \mathcal{S}_{\Xi_1} \times \dots \times \mathcal{S}_{\Xi_n}$. Similarly as set in Appendix A.4.4, and in particular Eq. (A.75), the stochastic field $\boldsymbol{U}(\Omega) = \{\boldsymbol{U}(\boldsymbol{X}) : \boldsymbol{X} \in \omega\}$ is represented by the finite separated expansion through the random vector $\boldsymbol{\Xi}$, with for a realisation $w \in \mathcal{W}$

$$\boldsymbol{u}(\boldsymbol{X}) = \boldsymbol{U}\left(\boldsymbol{X}; \boldsymbol{\Xi}(w)\right) \simeq \sum_{l=0}^{n_p^{\mathrm{C}}} \boldsymbol{u}_{\boldsymbol{k}^{(l)}}\left(\boldsymbol{X}\right) \psi_{\boldsymbol{k}^{(l)}}\left(\boldsymbol{\Xi}(w)\right) , \tag{317}$$

with the multi-index $\boldsymbol{k}^{(l)} = \{k_1^{(l)}, \dots, k_n^{(l)}\} \in \mathbb{N}_0^n$ defined by Eq. (228) and of total degree at most p and with $n_p^{\mathrm{C}} = \frac{(n+p)!}{n!p!} - 1$, with $\{\psi_{\boldsymbol{k}^{(l)}}(\boldsymbol{\xi}) = \psi^{(1)}_{k_1^{(l)}}(\xi_1) \times \dots \times \psi^{(i)}_{k_i^{(l)}}(\xi_i) \times \dots \times \psi^{(n)}_{k_n^{(l)}}(\xi_n) :$

$\boldsymbol{k}^{(l)} \in \mathcal{K}_p^{\mathrm{C}};\, \boldsymbol{\xi} = \boldsymbol{\Xi}(\boldsymbol{w})\}$ an orthonormal polynomial family belonging to the Hilbert space $\mathcal{H}(\mathcal{W})$, and with the coefficients $\boldsymbol{u}_{\boldsymbol{k}^{(l)}}(\boldsymbol{X})$ valued in $\Re^d$ and evaluated for $\boldsymbol{\xi} = \boldsymbol{\Xi}(\boldsymbol{w})$ by

$$\boldsymbol{u}_{\boldsymbol{k}^{(l)}}(\boldsymbol{X}) = \int_{\Re^n} \left(\boldsymbol{U}(\boldsymbol{X};\, \boldsymbol{\xi}) - \bar{\boldsymbol{u}}(\boldsymbol{X})\right) \psi_{\boldsymbol{k}^{(l)}}(\boldsymbol{\xi}) \pi_{\boldsymbol{\Xi}}(\boldsymbol{\xi}) \mathrm{d}\boldsymbol{\xi}\,, \quad l = 1..n_p^{\mathrm{C}}\,, \tag{318}$$

and by $\boldsymbol{u}_{\boldsymbol{k}^{(0)}}(\boldsymbol{X}) = \bar{\boldsymbol{u}}(\boldsymbol{X})$. In the Stochastic Galerkin finite element approach, the stochastic problem (313) is solved simultaneously in the spatial and stochastic domains by considering stochastic test functions $\delta\boldsymbol{U}(\boldsymbol{X};\, \boldsymbol{\xi}) \in \mathcal{U}(\Omega) \times \mathcal{H}(\mathcal{W})$, where $\mathcal{U}(\Omega)$ is an admissible kinematic vector field subset of $\mathcal{H}(\Omega)$. The weak form associated to Eq. (313) is then restated on the product between the physical and probabilistic spaces as finding $\boldsymbol{U} \in \mathcal{H}(\Omega) \times \mathcal{H}(\mathcal{W})$ such that, assuming no external forces for conciseness,

$$\int_{\omega} \int_{\mathcal{S}_{\boldsymbol{\Xi}}} \mathbf{P}_{\mathrm{M}} \left(\boldsymbol{U}(\boldsymbol{X};\, \boldsymbol{\xi})\right) : \left(\delta\boldsymbol{U}(\boldsymbol{X};\, \boldsymbol{\xi}) \otimes \boldsymbol{\nabla}_0\right) \pi_{\boldsymbol{\Xi}}(\boldsymbol{\xi}) \mathrm{d}\boldsymbol{\xi} \mathrm{d}\omega = 0\,, \quad \forall \delta\boldsymbol{U} \in \mathcal{U}(\Omega) \times \mathcal{H}(\mathcal{W})\,, \tag{319}$$

see details in Section 4.3.3. The finite element discretisation of the latter is based on the separation of variables with the use of the finite element discretisation

$$\boldsymbol{u} = \sum_a \varphi^{(a)}(\boldsymbol{X}) \boldsymbol{u}^{(a)} \in \mathcal{H}(\Omega) \text{ and } \delta\boldsymbol{u} = \sum_a \varphi^{(a)}(\boldsymbol{X}) \delta\boldsymbol{u}^{(a)} \in \mathcal{H}(\Omega)\,, \tag{320}$$

where $\varphi^{(a)}(\boldsymbol{X})$ are the nodal shape functions and $\boldsymbol{u}^{(a)}$ are the nodal degrees of freedom, and of the expansion (317), yielding

$$\begin{cases} \boldsymbol{U}(\boldsymbol{X};\, \boldsymbol{\xi}) & = \sum_a \sum_{l=0}^{n_p^{\mathrm{C}}} \varphi^{(a)}(\boldsymbol{X}) \psi_{\boldsymbol{k}^{(l)}} \left(\boldsymbol{\Xi}(\boldsymbol{w})\right) \boldsymbol{u}^{(a)}_{\boldsymbol{k}^{(l)}}\ ; \text{ and} \\ \delta\boldsymbol{U}(\boldsymbol{X};\, \boldsymbol{\xi}) & = \sum_a \sum_{l=0}^{n_p^{\mathrm{C}}} \varphi^{(a)}(\boldsymbol{X}) \psi_{\boldsymbol{k}^{(l)}} \left(\boldsymbol{\Xi}(\boldsymbol{w})\right) \delta\boldsymbol{u}^{(a)}_{\boldsymbol{k}^{(l)}}\,. \end{cases} \tag{321}$$

The degrees of freedom $\boldsymbol{u}^{(a)}_{\boldsymbol{k}^{(l)}}$ represent $n_p^{\mathrm{C}} + 1$ nodal displacements resulting from the expansion (317), and are collected in the vector $\boldsymbol{d}_{\mathrm{M}}$, which has now a size of $d \times (n_p^{\mathrm{C}} + 1) \times n^{\mathrm{node}}$, for n^{node} nodes and a physical space of dimension d. The stochastic Galerkin finite element form thus yields, see details in Section 4.3.3, the vector $\boldsymbol{f}_{\mathrm{M}}$ of the internal forces and the stiffness matrix $\mathbf{k}_{\mathrm{M}}$

$$\boldsymbol{f}_{\mathrm{M}} = \bigwedge_{\Omega^e} \int_{\Omega^e} \int_{\mathcal{S}_{\boldsymbol{\Xi}}} \left(\mathbf{b}'^e\right)^T \boldsymbol{P}_{\mathrm{M}}(\boldsymbol{X};\, \boldsymbol{\xi}) \pi_{\boldsymbol{\Xi}}(\boldsymbol{\xi}) \mathrm{d}\boldsymbol{\xi} \mathrm{d}\boldsymbol{X}\,, \tag{322}$$

$$\mathbf{k}_{\mathrm{M}} = \bigwedge_{\Omega^e} \int_{\Omega^e} \int_{\mathcal{S}_{\boldsymbol{\Xi}}} \left(\mathbf{b}'^e\right)^T \mathbf{C}_{\mathrm{M}}(\boldsymbol{X};\, \boldsymbol{\xi}) \mathbf{b}'^e \pi_{\boldsymbol{\Xi}}(\boldsymbol{\xi}) \mathrm{d}\boldsymbol{\xi} \mathrm{d}\boldsymbol{X}\,, \tag{323}$$

where $\mathbf{b}'^e$ is the elementary matrix of the shape functions gradient associated to the stochastic displacement vector field, *i.e.* built from $\boldsymbol{\nabla}\varphi^{(a)} \psi_{\boldsymbol{k}^{(l)}} \left(\boldsymbol{\Xi}(\boldsymbol{w})\right)$, $\mathbf{C}_{\mathrm{M}}$ is the matrix notation of the fourth-order material tensor $\mathbb{C}_{\mathrm{M}} = \frac{\partial \mathbf{P}_{\mathrm{M}}}{\partial \mathbf{F}_{\mathrm{M}}}$, and where $\bigwedge_{\Omega^e}$ is used to symbolise the assembly process.

Some remarks on the method

- It is seen that the system is similar to the traditional finite elements, with however more degrees of freedom whose number increases dramatically with the size n of the stochastic process.

- Assuming linear elasticity and the random field $\{\mathbf{C}_{\mathrm{M}}^{\mathrm{el}}(\boldsymbol{X}, w) : \boldsymbol{X} \in \Omega, w \in \mathcal{W}\}$ of the elastic properties, in the Spectral Stochastic Finite Element approach, Ghanem and Kruger (1996); Ghanem and Brzakala (1996); Ghanem (1999), see also the review by Nouy (1999), have considered an expansion of $\mathbf{C}_{\mathrm{M}}^{\mathrm{el}}(\Omega)$, either a KL expansion or a PCE for respectively Gaussian and non-Gaussian processes, with the stochastic germ $\boldsymbol{\Xi} = [\Xi_1 \ldots \Xi_i \ldots \Xi_n]^T$, of n independent, zero-mean, and unit variance random variables $\Xi_i : \mathcal{W} \to \Re$, consisting of the same random vector as the one used for the displacement separation of variables, Eq. (317). This allows evaluating the stochastic stiffness matrix (323) as detailed in Section 4.3.3. Recently, still in the context of linear elasticity, in order to ease the implementation in the case of physical domains of given complexity, Li et al. (2018) have used isogeometric basis functions in the KL expansion of the random field, see Section Appendix A.3.2, and a PCE for the displacement separation of variables, Eq. (317). Liu et al. (2021) used the same discretisation of the random field but have represented the structural response in the basis vectors of the Krylov subspace to reduce the dimensions.

- Although the consideration of linear elasticity with an expansion of the random field is the most common approach, it is possible to also express meso-scale material properties directly in terms of independent, zero-mean, and unit variance random variables and to perform non-linear analyses, see the work by Pivovarov and Steinmann (2016); Pivovarov et al. (2018b) summarised in Section 4.3.3.

5.5.3. Perturbation stochastic finite element method

In the perturbation method, the displacement field solution of Eq. (313) is written as a random field $\boldsymbol{U}(\Omega) = \{\boldsymbol{U}(\boldsymbol{X}) : \boldsymbol{X} \in \Omega\}$ and is expressed in terms of the random vector $\boldsymbol{\Xi} = [\Xi_1 \ldots \Xi_i \ldots \Xi_n]^T$ of n random variables $\Xi_i : \mathcal{W} \to \Re$. The random field $\boldsymbol{U}(\Omega)$ is then developed around its value evaluated for $\mathbb{E}[\boldsymbol{\Xi}]$, yielding,

$$\begin{aligned} \boldsymbol{U}(\boldsymbol{X}; \boldsymbol{\Xi}) &= \boldsymbol{u}_0(\boldsymbol{X}) + \sum_i \boldsymbol{u}_{,i}(\boldsymbol{X}) \left(\Xi_i - \mathbb{E}[\Xi_i]\right) + \\ &\quad \frac{1}{2} \sum_i \sum_j \boldsymbol{u}_{,ij}(\boldsymbol{X}) \left(\Xi_i - \mathbb{E}[\Xi_i]\right) \left(\Xi_j - \mathbb{E}[\Xi_j]\right) + \ldots , \end{aligned} \tag{324}$$

where the operator $\bullet_{,i}$ means derivative with respect to the random variable Ξ_i, see Section 4.3.2 for details. Assuming a linear response and no external forces for conciseness, after having applied a similar development on the Cauchy stress tensor, this yields a system of deterministic problems to be solved, see Section 4.3.2 for details,

$$\begin{aligned}
\text{Order 0:}\quad 0 = &\ \left[\boldsymbol{C}^{\text{el}}_{\text{M}}\left(\boldsymbol{X};\,\mathbb{E}[\Xi]\right) : \boldsymbol{\varepsilon}_{\boldsymbol{X}}(\boldsymbol{u}_0)\right]\cdot\boldsymbol{\nabla}_0\,, && (325)\\
\text{Order 1:}\quad 0 = &\ \left[\boldsymbol{C}^{\text{el}}_{\text{M}}\left(\boldsymbol{X};\,\mathbb{E}[\Xi]\right) : \boldsymbol{\varepsilon}_{\boldsymbol{X}}\left(\boldsymbol{u}_{,i}\right)\right]\cdot\boldsymbol{\nabla}_0 + \\
&\ \left[\frac{\partial\boldsymbol{C}^{\text{el}}_{\text{M}}}{\partial\Xi_i}\left(\boldsymbol{X};\,\mathbb{E}[\Xi]\right) : \boldsymbol{\varepsilon}_{\boldsymbol{X}}\left(\boldsymbol{u}_0\right)\right]\cdot\boldsymbol{\nabla}_0\,\forall i = 1..n\,, && (326)\\
\cdots\quad\cdots &\quad \cdots\,,
\end{aligned}$$

where the operator $\boldsymbol{\varepsilon}_{\boldsymbol{X}}\left(\boldsymbol{u}\right)$ stands for the small strain tensor $\frac{1}{2}\left(\boldsymbol{\nabla}_0\otimes\boldsymbol{u}+\boldsymbol{u}\otimes\boldsymbol{\nabla}_0\right)$.

The method has some practical limitations

- As pointed out by Nouy (1999), although theoretically the method can be used for a complete representation of the solution, the perturbation method is practically limited to second order and can thus be applied only when the coefficient of variation remains limited.
- Although non-linear extensions have been considered by Liu et al. (1986), the method is mainly applied to linear systems.

5.5.4. Adaptive multi-scale model

This model initially aims at reducing the error arising when considering a deterministic homogeneous model at the macro-scale by locally accounting explicitly for heterogeneous and random structures. In that context, the body Ω is initially divided into sub-domains Ω_k with $\Omega = \cup_k\Omega_k$. Considering at first that the solution is deterministic and can be obtained, in the linear range, by considering the meso-scale effective elastic properties $\mathbb{c}^{\text{eff}}_{\text{M}}$ on each $\Omega_k\subset\Omega$, the governing Eq. (313) is rewritten

$$\boldsymbol{\nabla}_0\cdot\left[\mathbb{c}^{\text{eff}}_{\text{M}} : \boldsymbol{\varepsilon}_{\boldsymbol{X}}\left(\boldsymbol{u}^h_{\text{M}}(\boldsymbol{X})\right)\right]+\boldsymbol{b}(\boldsymbol{X}) = 0 \qquad \forall\boldsymbol{X}\in\Omega\,, \tag{327}$$

where $\boldsymbol{u}^h_{\text{M}}(\boldsymbol{X})$ is the homogeneous solution obtained by a deterministic multi-scale process. A dual problem is then defined from the definition of a quantity of interest, *e.g.* a quantity defined from statistical properties of $\boldsymbol{U}_{\text{M}}(\boldsymbol{X};\,\omega)$ on some $\Omega_l\subset\Omega$. If the quantity of interest only involves statistical properties of $\boldsymbol{U}_{\text{M}}(\boldsymbol{X};\,\omega)$, the solution $\boldsymbol{w}^h_{\text{M}}(\boldsymbol{X})$ of the dual problem considered with the meso-scale effective elastic properties $\mathbf{c}^{\text{eff}}_{\text{M}}$ on each $\Omega_k\subset\Omega$ is also deterministic (Albert et al., 2006). Using these two solutions, lower and upper bounds of the homogenisation error can be computed from the random field $\{\mathbb{C}^{\text{el}}_{\text{M}}(\boldsymbol{X},\,\omega) :\ \boldsymbol{X}\in\Omega,\,\omega\in\mathcal{W}\}$, *e.g.* using Monte-Carlo simulations. From the error bounds, some sub-domains $\Omega_k\subset\Omega$ can be solved locally using stochastic finite elements stated. The governing equations in these sub-domains read

$$\boldsymbol{\nabla}_0\cdot\left[\mathbb{C}^{\text{el}}_{\text{m}}(\boldsymbol{x},\,\omega) : \boldsymbol{\varepsilon}_{\boldsymbol{x}}\left(\boldsymbol{U}^l_{\text{m}}(\boldsymbol{x},\,\omega)\right)\right]+\boldsymbol{b}(\boldsymbol{x}) = 0 \qquad \forall\boldsymbol{x}\in\Omega_k\,,\quad\forall\omega\in\mathcal{W}\,, \tag{328}$$

where the heterogeneities of the sub-domain Ω_k have to be explicitly represented, hence the use of the subscript "m" referring to the local value at the micro-scale, and where $\{\boldsymbol{U}^l_{\text{m}}(\boldsymbol{x},\,\omega) :\ \boldsymbol{x}\in\Omega_k,\,\omega\in\mathcal{W}\}$ is the local random field. This problem is completed by applying Dirichlet boundary conditions arising from the homogeneous solution obtained by the deterministic multi-scale process, *i.e.* $\boldsymbol{u}^h_{\mathrm{M}}(\boldsymbol{X})$ the homogeneous solution obtained by the deterministic multi-scale process, yielding

$$\boldsymbol{U}^l_{\mathrm{m}}(\boldsymbol{x},\, \omega) = \boldsymbol{u}^h_{\mathrm{M}}(\boldsymbol{X}) \qquad \forall \boldsymbol{x} = \boldsymbol{X} \in \partial\Omega_k \backslash \partial_N \Omega\,, \quad \forall \omega \in \mathcal{W}\,. \tag{329}$$

Finally, using the indicator function $\chi_{\Omega_k}(\boldsymbol{X})$ the random field on the full domain Ω reads $\{\boldsymbol{U}_{\mathrm{M}}(\boldsymbol{x},\, \omega) = \boldsymbol{u}^h_{\mathrm{M}}(\boldsymbol{X}) + \chi_{\Omega_k}(\boldsymbol{X}) \left[\boldsymbol{U}^l_{\mathrm{m}}(\boldsymbol{x},\, \omega) - \boldsymbol{u}^h_{\mathrm{M}}(\boldsymbol{X})\right] :\, \boldsymbol{x} \in \Omega,\, \omega \in \mathcal{W}\}$.

Some remarks on the method

- As discussed in Section 4.2.1, enforcing Dirichlet boundary conditions might result in stress/strain concentrations, motivating the use of Arlekin methods as the alternative developed by Cottereau (2013).

- Bonilla-Villalba et al. (2020) have developed error estimates based on Huet's partition theorem (283), which prevents the need of performing the integration in the small scale features.

- The different stochastic finite element methods detailed in Section 4.3 can be readily used to solve the problem (328-329).

6. Conclusions

In this work we have reviewed different methods aiming at conducting stochastic virtual testing. There remain however several problems motivating future research.

In order to build accurate virtual micro-structures, which represent the variability of real micro-structure geometry and local material responses, it is necessary to account for environment and process parameters of the manufacturing technique. In particular, whilst most of the current research has focused on the geometrical uncertainty characterisation, identifying material properties as random field at the micro-structure level remains challenging. Similarly, a quantitative defects characterisation is still not commonly performed, although they strongly affect the failure behaviour. These quantifications require a combination of *in-situ* experimental measurements and accurate models of the manufacturing process, which should allow for building data-base of micro-structures by relying on data-driven concepts and tools developed for uncertainty quantification, statistical analysis, dimension reduction, machine learning, and data mining methods. This approach has recently led to the so-called material data sciences (Kalidindi et al., 2016).

Coupling stochastic micro-scale behaviour to stochastic macro-scale response remains challenging in the non-linear range since the stochastic apparent properties of the Stochastic Volume Elements cannot be decoupled from the macro-scale stochastic finite element analyses. One more time, data-driven approaches relying on data obtained from numerical realisations of the virtual random micro-structures (Clément et al., 2012; Yvonnet et al., 2013; Bessa et al., 2017) offer a possibility to couple micro-scale and structural scale analysis at affordable cost in the context of uncertainty quantification for non-linear systems.

In this context the use of Neural Networks as surrogate appears to be a promising tool as illustrated by the first results (Rao and Liu, 2020; Lu et al., 2021), but which is yet to be deepened.

The problem of failure is only partly addressed in the literature because of the loss of objectivity of the stress-strain curves during homogenisation. Stochastic multi-scale methods are currently only addressing strength envelope and in some cases the brittle failure response.

With these tools in hand, it would be possible to develop a so-called process-(micro)structure-(structural)properties (PSP) linkage (Gupta et al., 2015; Yang et al., 2018, *e.g.*), which, from the simulation of the manufacturing, via the prediction of micro-scale properties and geometry, including their uncertainties, could provide a relationship between manufacturing conditions and the statistical structural response. This, in turn, would allow optimising process and design in order to achieve some targeted performance within a given confidence interval.

Acknowledgement

This project has received funding from the European Unions Horizon 2020 research and innovation programme under grant agreement No 862015 for the project “Multi-scale Optimisation for Additive Manufacturing of fatigue resistant shock-absorbing MetaMaterials (MOAMMM) of the H2020-EU.1.2.1. - FET Open Programme.

Appendix A. Generation tools

The purpose of this appendix is not to provide complete formalisms, but to give a quick overview of the different methods used in the literature. These methods are discussed further in the provided references. Before presenting the main methods, we recall some common probabilistic transformations.

Appendix A.1. Probabilistic transformations

Let us consider the n-dimension random vector $\boldsymbol{Q} : \mathcal{Q} \rightarrow \Re^n$. Its expectation (26) is denoted by $\bar{\boldsymbol{q}} = \mathbb{E}[\boldsymbol{Q}]$, and its covariance matrix (46) by $\tilde{\mathbf{R}}_{\boldsymbol{Q}} \in \mathbb{M}_n^+(\Re)$. We note that we assume the positive definite nature of $\tilde{\mathbf{R}}_{\boldsymbol{Q}}$[13], and the existence of the probability density function $\pi_{\boldsymbol{Q}} : \Re^n \rightarrow [0, \infty[$ following Eq. (24).

In this section, we apply a transformation $\boldsymbol{\Xi} = \boldsymbol{f}(\boldsymbol{Q})$ in order to obtain some sought particular properties of the random vector $\boldsymbol{\Xi}$ valued in $\Re^n$, of covariance matrix $\tilde{\mathbf{R}}_{\boldsymbol{\Xi}} \in \mathbb{M}_n^+(\Re)$, and of probability density function $\pi_{\boldsymbol{\Xi}} : \Re^n \rightarrow [0, \infty[$.

---

[13] We assume in this section that the standard deviations σ_{Q_r} of the random variables Q_r are all strictly positive

Appendix A.1.1. Transformation of a Gaussian random vector

Assuming $\boldsymbol{Q}$ follows a Gaussian distribution with expectation $\bar{\boldsymbol{q}} = \mathbb{E}\left[\boldsymbol{Q}\right]$ and covariance matrix $\tilde{\mathbf{R}}_{\boldsymbol{Q}} \in \mathbb{M}_n^+(\Re)$ and assuming we want $\boldsymbol{\Xi}$ to follow a zero-mean with unit covariance matrix, *i.e.* $\tilde{\mathbf{R}}_{\boldsymbol{\Xi}} = \mathbf{I}_n$ with $\mathbf{I}_n$ the unit matrix of size n, Gaussian distribution, we consider the non-linear transformation $\boldsymbol{\Xi} = \boldsymbol{f}^{\mathcal{N}}(\boldsymbol{Q})$ which reads

$$\boldsymbol{\Xi} = \boldsymbol{f}^{\mathcal{N}}(\boldsymbol{Q}) = \mathbf{L}_{\boldsymbol{Q}}^{-1}\left(\boldsymbol{Q} - \bar{\boldsymbol{q}}\right) , \tag{A.1}$$

with the lower triangular matrix $\mathbf{L}_{\boldsymbol{Q}}$ obtained by the Cholesky decomposition of $\tilde{\mathbf{R}}_{\boldsymbol{Q}}$, *i.e.* $\tilde{\mathbf{R}}_{\boldsymbol{Q}} = \mathbf{L}_{\boldsymbol{Q}}\mathbf{L}_{\boldsymbol{Q}}^T$.

Appendix A.1.2. Nataf transformation of a non-Gaussian random vector

In this section, we consider the random vector $\boldsymbol{Q}$ with the n dependent components Q_i and with the correlation matrix $\mathbf{R}_{\boldsymbol{Q}}$ given by Eq. (47). Each random variable has a marginal cumulative distribution function $F_{Q_i}(q_i) : \Re \to [0,\, 1]$ assumed to be continuous and of support $\mathcal{S}_{Q_i}$. We assume we want $\boldsymbol{\Xi}$ to follow a zero-mean with unit covariance matrix, *i.e.* $\tilde{\mathbf{R}}_{\boldsymbol{\Xi}} = \mathbf{R}_{\boldsymbol{\Xi}} = \mathbf{I}_n$, Gaussian distribution through the non-linear Nataf transformation $\boldsymbol{\Xi} = \boldsymbol{f}^{\mathcal{T}}(\boldsymbol{Q})$.

First a Gaussian random vector $\boldsymbol{Z}$ is constructed from

$$z_i = F_{0,1}^{\mathcal{N}^{-1}}\left(F_{Q_i}(q_i)\right) , \tag{A.2}$$

where $F_{0,1}^{\mathcal{N}}$ is the zero-mean and unit variance Gaussian cumulative distribution. It is then assumed that the joint probability density function reads

$$\pi_{\boldsymbol{Z}}(\boldsymbol{z}) = \frac{1}{(2\pi)^{n/2}\sqrt{\det(\mathbf{R}_{\boldsymbol{Z}})}}\exp\left(-\frac{1}{2}\boldsymbol{z}^T\mathbf{R}_{\boldsymbol{Z}}^{-1}\boldsymbol{z}\right) , \tag{A.3}$$

with the correlation matrix $\mathbf{R}_{\boldsymbol{Z}}$ that has to be evaluated so that the joint probability density function of $\boldsymbol{Q}$ can be written as

$$\pi_{\boldsymbol{Q}}(\boldsymbol{q}) = \pi_{Q_1}(q_1)\ldots\pi_{Q_n}(q_n)\frac{\pi_{\boldsymbol{Z}}(\boldsymbol{z})}{\mathcal{N}_{0,1}(z_1)\ldots\mathcal{N}_{0,1}(z_n)} \tag{A.4}$$

with the probability density function (A.3) and the normal probability density function $\mathcal{N}_{0,1}$ given by Eq. (17). The correlation matrix $\mathbf{R}_{\boldsymbol{Z}}$ is now computed so that the correlation of two components Q_i and Q_j arising from Eq. (A.4) matches the prescribed correlation $R_{\boldsymbol{Q}_{i\,j}}$, yielding, see the details by Der Kiureghian and Ke (1988), the following implicit equation in the unknown correlation $R_{\boldsymbol{Z}_{i\,j}}$ to be solved

$$R_{\boldsymbol{Q}_{i\,j}} = \int_{-\infty}^{\infty}\int_{-\infty}^{\infty}\left(\frac{q_i - \bar{q}_i}{\sigma_{Q_i}}\right)\left(\frac{q_j - \bar{q}_j}{\sigma_{Q_j}}\right)\pi_{[Z_i\,Z_j]^T}([z_i\,z_j]^T)dz_idz_j , \tag{A.5}$$

with $\pi_{[Z_i\,Z_j]^T}([z_i\,z_j]^T) = \frac{1}{(2\pi)\sqrt{\det(\mathbf{R}_{[z_i\,z_j]^T})}}\exp\left(-\frac{1}{2}[z_i\,z_j]\mathbf{R}_{[Z_i\,Z_j]^T}^{-1}[z_i\,z_j]^T\right)$ the standard bi-variate Gaussian density function of zero-mean, unit variance and correlation $R_{\boldsymbol{Z}_{i\,j}}$ (we note that the diagonal terms of $\mathbf{R}_{[Z_i\,Z_j]^T}$ are 1 and the out of diagonal terms $R_{\boldsymbol{Z}_{i\,j}}$).

Assuming $\boldsymbol{Q}$ has a Nataf joint probability density function, then $\boldsymbol{Z}$ is a Gaussian random vector of zero-mean and covariance matrix $\tilde{\mathbf{R}}_{\boldsymbol{Z}} = \mathbf{R}_{\boldsymbol{Z}} = \mathbf{L}_{\boldsymbol{Z}}\mathbf{L}_{\boldsymbol{Z}}^T$. The transformation (A.1) can then be applied

$$\boldsymbol{\Xi} = \mathbf{L}_{\boldsymbol{Z}}^{-1}\boldsymbol{Z}\,, \tag{A.6}$$

yielding $\boldsymbol{\Xi}$ a random vector of zero-mean with unit covariance matrix, *i.e.* $\tilde{\mathbf{R}}_{\boldsymbol{\Xi}} = \mathbf{I}_n$, following a Gaussian distribution.

We note that this transformation has required some assumptions on the joint probability distribution of $\boldsymbol{Q}$.

Appendix A.1.3. Rosenblatt Transformation of a non-Gaussian random vector

Contrarily to the other transformations, the conditional probability density functions have first to be evaluated from

$$\pi_{Q_k|Q_{k-1},\dots,Q_1}(q_k|q_{k-1},\,\dots,\,q_1) = \frac{\pi_{Q_k,\,Q_{k-1},\dots,Q_1}(q_k,\,q_{k-1},\,\dots q_1)}{\int_{\Re}\pi_{Q_k,\,Q_{k-1},\dots,Q_1}(q_k,\,q_{k-1},\,\dots q_1)dq_k}\,,\; k = 1..n\,, \tag{A.7}$$

and the conditional cumulative distribution follows from

$$F_{Q_k|Q_{k-1},\dots,Q_1}(q_k|q_{k-1},\,\dots,\,q_1) = \int_{-\infty}^{q_k}\pi_{Q_k|Q_{k-1},\dots,Q_1}(q_k'|q_{k-1},\,\dots,\,q_1)dq_k'\,,\; k = 1..n\,. \tag{A.8}$$

To hyper-cube distribution. We first consider the case in which we want $\boldsymbol{\Xi}$ to be defined as n independent and uniformly distributed random variables Ξ_i in the support $\mathcal{S}_{\boldsymbol{\Xi}} = [0,\,1]^n$, *i.e.*

$$\pi_{\boldsymbol{\Xi}}(\boldsymbol{\xi}) = \mathcal{U}_{0,\,1}\times\dots\times\mathcal{U}_{0,\,1}\,, \tag{A.9}$$

with $\mathcal{U}_{0,\,1}$ defined by Eq. (18).

The non-linear transformation $\boldsymbol{\Xi} = \boldsymbol{f}^{\mathscr{R}\,\mathcal{U}}(\boldsymbol{Q})$ thus reads

$$\xi_1 = F_{Q_1}(q_1),\; \xi_2 = F_{Q_2|Q_1}(q_2|q_1),\;\dots,\; \xi_n = F_{Q_n|Q_{n-1},\dots,Q_1}(q_n|q_{n-1},\,\dots,\,q_1)\,, \tag{A.10}$$

with the conditional cumulative distribution following from Eq. (A.8).

To Gaussian distribution. In the case in which we want $\boldsymbol{\Xi}$ to follow a zero-mean with unit covariance matrix, *i.e.* $\tilde{\mathbf{R}}_{\boldsymbol{\Xi}} = \mathbf{I}_n$, Gaussian distribution, we consider the non-linear transformation $\boldsymbol{\Xi} = \boldsymbol{f}^{\mathscr{R}\,\mathcal{N}}(\boldsymbol{Q})$ which reads

$$\begin{aligned}\xi_1 = F_{0,\,1}^{\mathcal{N}^{-1}}\left(F_{Q_1}(q_1)\right),\; \xi_2 = F_{0,\,1}^{\mathcal{N}^{-1}}\left(F_{Q_2|Q_1}(q_2|q_1)\right),\;\dots,\\ \xi_n = F_{0,\,1}^{\mathcal{N}^{-1}}\left(F_{Q_n|Q_{n-1},\dots,Q_1}(q_n|q_{n-1},\,\dots,\,q_1)\right)\,,\end{aligned} \tag{A.11}$$

where $F_{0,\,1}^{\mathcal{N}}$ is the zero-mean and unit variance Gaussian cumulative distribution and where the conditional cumulative distribution follows from Eq. (A.8).

Appendix A.2. Generation from cumulative distribution functions

Appendix A.2.1. Inverse transform sampling

Pseudo-random samples of a random variable Q can be generated by constructing the inverse $F_Q^{-1} : [0,\, 1] \rightarrow \mathcal{S}_Q$ of the cumulative distribution function, assumed to be continuous, of support $\mathcal{S}_Q$. Therefore, considering a random variable $U \sim \mathcal{U}_{0,1}$ following a uniform distribution, see Eq. (18), one has the inverse function

$$Q = F_Q^{-1}(U)\,. \tag{A.12}$$

By generating pseudo-random samples u^p of the random variable $U \sim \mathcal{U}_{0,1}$, pseudo random samples of the random variable Q are obtained as $\{q^p : q^p = F_Q^{-1}(u^p)\}$ using Eq. (A.12).

Appendix A.2.2. Copula method

Let us consider the random vector $\boldsymbol{Q} = [Q_1 \, ... \, Q_n]^T$ of dependent random variables Q_i. Each random variable has a marginal cumulative distribution function $F_{Q_i}(q_i) : \Re \rightarrow [0,\, 1]$ assumed to be continuous and of support $\mathcal{S}_{Q_i}$. A random vector $\boldsymbol{U} = [U_1 \, ... \, U_n]^T$ whose components marginal probability density functions π_{U_i} are uniform, *i.e.* $U_i \sim \mathcal{U}_{0,1}$, see Eq. (18), is then defined as

$$[U_1 \, ... \, U_2]^T = [F_{Q_1}(Q_1) \, ... \, F_{Q_n}(Q_n)]^T\,. \tag{A.13}$$

The copula of $\boldsymbol{Q}$ is defined as the joint cumulative distribution function $F_{\boldsymbol{U}} : [0,\, 1]^n \rightarrow [0,\, 1]$ of the random vector $\boldsymbol{U}$, see Eq. (21), and is denoted

$$C(u_1,\, ...,\, u_n) = \mathbb{P}\left(U_1 \leq u_1,\, ...,\, U_n \leq u_n\right)\,, \tag{A.14}$$

or using Eq. (A.13),

$$C(u_1,\, ...,\, u_n) = \mathbb{P}\left(Q_1 \leq F_{Q_1}^{-1}(u_1),\, ...,\, Q_n \leq F_{Q_n}^{-1}(u_n)\right)\,. \tag{A.15}$$

Therefore, considering a random variable $\boldsymbol{U}$ whose joint cumulative distribution function $F_{\boldsymbol{U}}$ follows the copula (A.14), one has the inverse function

$$[Q_1 \, ... \, Q_n]^T = [F_{Q_1}^{-1}(U_1) \, ... \, F_{Q_n}^{-1}(U_n)]^T\,. \tag{A.16}$$

Pseudo-random samples $\boldsymbol{u}^p$ of $\boldsymbol{U}$ are generated from the copula distribution $F_{\boldsymbol{U}}(\boldsymbol{u}) = C(u_1,\, ...,\, u_n)$ using the process described here below and the pseudo-random samples of the random vector $\boldsymbol{Q}$ are obtained as $\{\boldsymbol{q}^p : \boldsymbol{q}^p = [F_{Q_1}^{-1}(u_1^p) \, ... \, F_{Q_n}^{-1}(u_n^p)]^T\}$ using Eq. (A.16).

In order to generate a pseudo-sample $\boldsymbol{u}^p$ of $\boldsymbol{U}$ following the copula joint cumulative distribution $C(u_1,\, ...,\, u_n) = F_{\boldsymbol{U}}(\boldsymbol{u})$, one follows the chain rule

- Draw a pseudo sample u_n^p from $\mathcal{U}_{0,1}$;

- Evaluate the conditional probability density $\pi_{U_{n-1}|U_n}\left(u_{n-1}|u_n^p\right)$ from

$$\pi_{U_{n-1}|U_n}\left(u_{n-1}|u_n^p\right) = \frac{1}{\mathcal{U}_{0,1}(u_n^p)}\frac{\partial^2}{\partial u_{n-1}\partial u_n}F_{U_{n-1},U_n}\left(u_{n-1},\, u_n^p\right)\,; \tag{A.17}$$

  Draw a pseudo sample u_{n-1}^p from the conditional probability density $\pi_{U_{n-1}|U_n}\left(u_{n-1}|u_n^p\right)$, using the inverse transform sampling of Appendix A.2.1;

- ...

- Evaluate the conditional probability density $\pi_{U_{n-i-1}|U_{n-i},\ldots,U_n}\left(u_{n-i-1}|u_{n-i}^p,\, \ldots,\, u_n^p\right)$ from

$$\pi_{U_{n-i-1}|U_{n-i},\ldots,U_n}\left(u_{n-i-1}|u_{n-i}^p,\, \ldots,\, u_n^p\right) = \frac{1}{\left[\pi_{U_{n-i}|U_{n-i+1},\ldots,U_n}(u_{n-i}^p|u_{n-i+1}^p,\, \ldots,\, u_n^p) \times \ldots \times \pi_{U_{n-1}|U_n}(u_{n-1}^p|u_n^p) \times \mathcal{U}_{0,1}(u_n^p)\right]} \frac{\partial^{i+2}}{\partial u_{n-i-1}\ldots\partial u_n}F_{U_{n-i-1},\ldots,U_n}\left(u_{n-i-1},\, u_{n-i}^p,\, \ldots,\, u_n^p\right)\,; \tag{A.18}$$

  Draw a pseudo sample u_{n-i-1}^p from the conditional probability density $\pi_{U_{n-i-1}|U_{n-i},\ldots,U_n}$ $\left(u_{n-i-1}|u_{n-i}^p,\, \ldots,\, u_n^p\right)$, using the inverse transform sampling of Appendix A.2.1;

- ...

- Evaluate the conditional probability density $\pi_{U_1|U_2,\ldots,U_n}\left(u_1|u_2^p,\, \ldots,\, u_n^p\right)$ from

$$\pi_{U_1|U_2,\ldots,U_n}\left(u_1|u_2^p,\, \ldots,\, u_n^p\right) = \frac{1}{\left[\pi_{U_2|U_3,\ldots,U_n}(u_2^p|u_3^p,\, \ldots,\, u_n^p) \times \ldots \times \pi_{U_{n-1}|U_n}(u_{n-1}^p|u_n^p) \times \mathcal{U}_{0,1}(u_n^p)\right]} \frac{\partial^{n}}{\partial u_1\ldots\partial u_n}F_{U_1,\ldots,U_n}\left(u_1,\, u_2^p,\, \ldots,\, u_n^p\right)\,; \tag{A.19}$$

  Draw a pseudo sample u_1^p from $\pi_{U_1|U_2,\ldots,U_n}\left(u_1|u_2^p,\, \ldots,\, u_n^p\right)$, using the inverse transform sampling of Appendix A.2.1.

In this method, the derivatives $\frac{\partial^{i+2}}{\partial u_{n-i-1}\ldots\partial u_n}F_{U_{n-i-1},\ldots,U_n}\left(u_{n-i-1},\, u_{n-1}^p,\, \ldots,\, u_n^p\right)$ are evaluated numerically using a hash-table of the observations $\boldsymbol{u}^k$ obtained from Eq. (A.13) for the observations $\boldsymbol{q}^k = \boldsymbol{Q}(q^k)$, with $q^k \in \mathcal{Q}$.

More details are provided by Strelen and Nassaj (2007).

Appendix A.3. Principal Components Analysis & Karhunen-Loève (KL) series expansion

Appendix A.3.1. Principal Components Analysis (PCA)

Let us consider the n-dimension random vector $\boldsymbol{Q} : \mathcal{Q} \rightarrow \Re^n$. Its expectation (26) is denoted by $\bar{\boldsymbol{q}} = \mathbb{E}\left[\boldsymbol{Q}\right]$, and its covariance matrix (46) by $\tilde{\mathbf{R}}_{\boldsymbol{Q}} \in \mathbb{M}_n^+(\Re)$. We note that we assume the positive definite nature of $\tilde{\mathbf{R}}_{\boldsymbol{Q}}$.

One can extract the n eigen-vectors $\boldsymbol{u}_{\boldsymbol{Q}}^{(i)}$ and the n eigen-values $\lambda_{\boldsymbol{Q}}^{(i)}$ of the matrix $\tilde{\mathbf{R}}_{\boldsymbol{Q}}$, with

$$\tilde{\mathbf{R}}_{\boldsymbol{Q}}\, \boldsymbol{u}_{\boldsymbol{Q}}^{(i)} = \lambda_{\boldsymbol{Q}}^{(i)} \boldsymbol{u}_{\boldsymbol{Q}}^{(i)} \quad \forall i = 1..n\,, \tag{A.20}$$

with no sum on (i) intended. The eigen-values are ordered as $\lambda_{\boldsymbol{Q}}^{(n)} \geq \lambda_{\boldsymbol{Q}}^{(n-1)} \geq ... \geq \lambda_{\boldsymbol{Q}}^{(1)} > 0$, and the eigen-vectors are normalised so that $\left(\boldsymbol{u}_{\boldsymbol{Q}}^{(i)}\right)^T \boldsymbol{u}_{\boldsymbol{Q}}^{(j)} = \delta_{ij}$.

A new random vector $\mathbf{H}$ with values in $\Re^n$ is then defined, with its realisation $\boldsymbol{\eta} \in \Re^n$ such that

$$\eta_i = \frac{1}{\sqrt{\lambda_{\boldsymbol{Q}}^{(i)}}} \left(\boldsymbol{q} - \bar{\boldsymbol{q}}\right)^T \boldsymbol{u}_{\boldsymbol{Q}}^{(i)} \quad \forall i = 1..n\,. \tag{A.21}$$

The random vector $\mathbf{H}$ is characterised by the following properties

$$\mathbb{E}[\mathbf{H}] = \mathbf{0}_n \quad \text{and } \tilde{\mathbf{R}}_{\mathbf{H}} = \mathbf{I}_n\,, \tag{A.22}$$

with $\mathbf{0}_n$ a zero vector of size n and $\mathbf{I}_n$ the unit matrix of size n. We note that the components of $\mathbf{H}$ are uncorrelated, but can be dependent. For Gaussian distributions, they are also independent since uncorrelated.

Using the orthogonality property of the eigen-modes, inverting Eq. (A.21) allows expressing a realisation $\boldsymbol{q}$ of the random vector $\boldsymbol{Q}$ from the relation

$$\boldsymbol{q} \simeq \bar{\boldsymbol{q}} + \sum_{i=1}^{m \leq n} \sqrt{\lambda_{\boldsymbol{Q}}^{(i)}} \eta_i \boldsymbol{u}_{\boldsymbol{Q}}^{(i)}\,. \tag{A.23}$$

In the case $m = n$, Eq. (A.23) is exact whilst in the case $m < n$ one has performed an order reduction.

Appendix A.3.2. Karhunen-Loève (KL) series expansion

Let us consider the continuous random vector field $\boldsymbol{Q}(\Omega) = \{\boldsymbol{Q}(\boldsymbol{x}) : \boldsymbol{x} \in \Omega\}$ for $\Omega \subset \Re^d$ a space of material points $\boldsymbol{x}$, with $d \in \mathbb{N}$. Its expectation (26) is denoted by $\bar{\boldsymbol{q}}\left(\boldsymbol{x}\right) = \mathbb{E}\left[\boldsymbol{Q}\left(\boldsymbol{x}\right)\right] : \Omega \rightarrow \Re^n$, and its covariance matrix by $\tilde{\mathbf{R}}_{\boldsymbol{Q}}\left(\boldsymbol{x};\, \boldsymbol{\tau}\right)$, see Eq. (50). In this section, using $\boldsymbol{x'} = \boldsymbol{x} + \boldsymbol{\tau}$, we use the notation $\tilde{\mathbf{R}}_{\boldsymbol{Q}}\left(\boldsymbol{x},\, \boldsymbol{x'}\right) : \Omega \times \Omega \rightarrow \Re^{n\times n}$.

Eigen-vectors $\boldsymbol{u}_{\boldsymbol{Q}}^{(i)}(\boldsymbol{x})$ and eigen-values $\lambda_{\boldsymbol{Q}}^{(i)}$ have to be extracted from the Fredholm integral equation of the second kind

$$\int_{\Omega} \tilde{\mathbf{R}}_{\boldsymbol{Q}}\left(\boldsymbol{x},\ \boldsymbol{x'}\right) \boldsymbol{u}_{\boldsymbol{Q}}^{(i)}(\boldsymbol{x'}) d\boldsymbol{x'} = \lambda_{\boldsymbol{Q}}^{(i)} \boldsymbol{u}_{\boldsymbol{Q}}^{(i)}(\boldsymbol{x})\,, \quad \forall i \in \mathbb{N}\,, \tag{A.24}$$

with the ordered eigen-values $\lambda_{\boldsymbol{Q}}^{(1)} \geq \lambda_{\boldsymbol{Q}}^{(2)} \geq ... \rightarrow 0$, and with the orthonormal eigen basis such that $\int_{\Omega} \left(\boldsymbol{u}_{\boldsymbol{Q}}^{(i)}(\boldsymbol{x})\right)^T \boldsymbol{u}_{\boldsymbol{Q}}^{(j)}(\boldsymbol{x}) d\boldsymbol{x} = \delta_{ij}$.

A new random vector $\mathbf{H}$ is then defined, with its realisation $\boldsymbol{\eta}$ such that

$$\eta_i = \frac{1}{\sqrt{\lambda_{\boldsymbol{Q}}^{(i)}}} \int_{\Omega} \left(\boldsymbol{q}(\boldsymbol{x}) - \bar{\boldsymbol{q}}(\boldsymbol{x})\right)^T \boldsymbol{u}_{\boldsymbol{Q}}^{(i)}(\boldsymbol{x}) d\boldsymbol{x} \quad \forall i \in \mathbb{N}\,. \tag{A.25}$$

The random vector $\mathbf{H}$ is characterised by the following properties

$$\mathbb{E}[\mathrm{H}_r] = 0 \quad \text{and } \tilde{R}_{\mathbf{H}_{r,\,s}} = \delta_{rs} \quad \forall r,\, s \in \mathbb{N}\,. \tag{A.26}$$

We note that the components of $\mathbf{H}$ are uncorrelated, but can be dependent. For Gaussian fields, they are also independent since uncorrelated.

The random field $\boldsymbol{Q}(\Omega)$ can then be represented by the collection of realisations

$$\boldsymbol{q}(\boldsymbol{x}) \simeq \bar{\boldsymbol{q}}\,(\boldsymbol{x}) + \sum_{i=1}^{m} \sqrt{\lambda_{\boldsymbol{Q}}^{(i)}}\eta_i \boldsymbol{u}_{\boldsymbol{Q}}^{(i)}(\boldsymbol{x})\,, \tag{A.27}$$

where the relation is exact for $m \to \infty$.

Since the resolution of Eq. (A.24) cannot always be pursued, it is possible to consider the collection $\{\boldsymbol{Q}(\boldsymbol{x}^{(1)}),\, ...,\, \boldsymbol{Q}(\boldsymbol{x}^{(N)})\}$ of random vectors sampled for $\mathbf{x} = (\boldsymbol{x}^{(1)},\, ...,\, \boldsymbol{x}^{(N)})$, *i.e.* N members of Ω, defining the random vector $\boldsymbol{Y} = \left[\boldsymbol{Q}^T(\boldsymbol{x}^{(1)}) \ldots \boldsymbol{Q}^T(\boldsymbol{x}^{(N)})\right]^T$ taking values in $\Re^{n\cdot N}$, see details in Section 5.1.2. From its expectation $\bar{\boldsymbol{y}}$ and its covariance matrix $\tilde{\mathbf{R}}_{\boldsymbol{Y}}$ the PCA described in Appendix A.3.1 is applied in order to construct a statistical reduction similar to Eq. (A.23), *i.e.*

$$\boldsymbol{y} \simeq \bar{\boldsymbol{y}} + \sum_{i=1}^{m\leq n\cdot N} \sqrt{\lambda_{\boldsymbol{Y}}^{(i)}}\eta_i' \boldsymbol{u}_{\boldsymbol{Y}}^{(i)}\,, \tag{A.28}$$

with the $n \cdot N$ eigen-vectors $\boldsymbol{u}_{\boldsymbol{Y}}^{(i)}$ and the $n \cdot N$ ordered eigen-values $\lambda_{\boldsymbol{Y}}^{(i)}$ of the matrix $\tilde{\mathbf{R}}_{\boldsymbol{Y}}$, and realisations of the random variable $\mathbf{H}'$ obtained as

$$\eta_i' = \frac{1}{\sqrt{\lambda_{\boldsymbol{Y}}^{(i)}}} \left(\boldsymbol{y} - \bar{\boldsymbol{y}}\right)^T \boldsymbol{u}_{\boldsymbol{Y}}^{(i)} \quad \forall i = 1..n \cdot N\,. \tag{A.29}$$

An approximation of $\{\boldsymbol{Q}(\boldsymbol{x}^{(1)}),\, ...,\, \boldsymbol{Q}(\boldsymbol{x}^{(N)})\}$ is deduced directly from Eq. (A.28) by reordering the components of $\boldsymbol{Y}$, or if other locations $\boldsymbol{x}$ than at the initial sampling points $\boldsymbol{x}^{(k)}$, $k = 1..N$, are sought by using an optimal linear estimation, see details in Section 5.1.2.

Another solution to solve the system of Eqs. (A.24) consists in defining a Galerkin-type procedure as suggested for uni-variate random fields by Ghanem and Spanos (1991) and summarised by Sudret and Der Kiureghian (2000). Recently, Li et al. (2018) have used isogeometric basis functions in this Galerkin-type procedure.

Appendix A.3.3. Generation of Gaussian random fields using the Karhunen-Loève (KL) expansion

We here consider as random field the collection $\{\boldsymbol{Q}(\boldsymbol{x}^{(1)}),\, ...,\, \boldsymbol{Q}(\boldsymbol{x}^{(N)})\}$ of N random vectors valued in $\Re^n$ and extracted for $\mathbf{x} = (\boldsymbol{x}^{(1)},\, ...,\, \boldsymbol{x}^{(N)})$, with $\boldsymbol{x}^{(j)} \in \Omega$, $j = 1..N$, see details in Section 5.1.2. An approximation of a Gaussian random field can be sampled following

- The definition of the random vector $\boldsymbol{Y} = \left[\boldsymbol{Q}^T(\boldsymbol{x}^{(1)}) \ldots \boldsymbol{Q}^T(\boldsymbol{x}^{(N)})\right]^T$ taking values in $\Re^{n\cdot N}$;

- The pseudo-sampling of the random field using Eq. (A.28) as

$$\boldsymbol{y}^p \simeq \bar{\boldsymbol{y}} + \sum_{i=1}^{m \leq n \cdot N} \sqrt{\lambda_{\boldsymbol{Y}}^{(i)}} \eta_i'^p \boldsymbol{u}_{\boldsymbol{Y}}^{(i)} \,, \tag{A.30}$$

  from pseudo-samples η'^p. Assuming Gaussianity, the pseudo-samples η'^p are generated as m independent Gaussian variables $\eta_i'^p$ using either Monte Carlo sampling (MC) or Latin Hyper-cube Sampling (LHS);

- The extraction of a pseudo-sample of $\{\boldsymbol{q}^p(\boldsymbol{x}^{(1)}), \, ..., \, \boldsymbol{q}^p(\boldsymbol{x}^{(N)})\}$ from Eq. (A.30) by reordering the components of $\boldsymbol{y}^p$, or through an optimal linear estimation, see details in Section 5.1.2, if other locations $\boldsymbol{x}$ than at the initial sampling points $\boldsymbol{x}^{(k)}$, $k = 1..N$, are sought.

However, the size $m \leq n \cdot N$ of the covariance matrix can be overwhelming when N or n increases. Therefore, Vořechovský (2008) has developed a method to simulate cross correlated Gaussian homogeneous random fields by using the KL series expansion method, which reduces the size of the correlation matrix to be considered. It is assumed that the random field is homogeneous, yielding $\bar{\boldsymbol{q}}\left(\boldsymbol{x}\right) = \bar{\boldsymbol{q}}$ and a covariance matrix $\tilde{\mathbf{R}}_{\boldsymbol{Q}} \in \mathbb{M}_n^+(\Re)$. Besides, it is assumed that all the components Q_i of the random vector $\boldsymbol{Q}$ share the same spatial correlation function on Ω.

First, for a fixed $\boldsymbol{x}^{(j)}$, $j = 1..N$, the eigen-values and vectors of $\tilde{\mathbf{R}}_{\boldsymbol{Q}}$ are extracted, see Appendix A.3.1, yielding the n eigen values $\lambda_{\boldsymbol{Q}}^{(i)}$ and orthonormal eigen-vectors $\boldsymbol{u}_{\boldsymbol{Q}}^{(i)}$. Then the uni-variate random field $U(\Omega)$ valued in $\Re$ can be defined from any random field $Q_i(\Omega)$ and yields the correlation $R_U(\boldsymbol{x}, \, \boldsymbol{x}')$. Since it is assumed that all the components share the same spatial correlation, any value $i = 1..n$ can be chosen providing the correlation is used instead of the covariance since the variance might change between components. The eigen-values and vectors of $R_U(\boldsymbol{x}, \, \boldsymbol{x}')$ are extracted, and N eigen values $\lambda_U^{(j)}$ and orthonormal eigen-vectors $u_U^{(j)}(\boldsymbol{x})$ related to the unit standard deviation are retained. This extraction can result from the sampling at the N locations $\boldsymbol{x}^{(j)}$ using $\boldsymbol{U} = [Q_i(\boldsymbol{x}^{(1)}) \ldots Q_i(\boldsymbol{x}^{(N)})]^T$ as described in Appendix A.3.2 and following the methods described in Section 5.1.2, yielding the N eigen values $\lambda_{\boldsymbol{U}}^{(j)}$ and orthonormal eigen-vectors $\boldsymbol{u}_{\boldsymbol{U}}^{(j)}$ related to a unit standard deviation.

Second, a random vector $\boldsymbol{\Xi}$ with values in $\Re^{N \cdot n}$ is defined. The idea suggested by Vořechovský (2008) is that the components $\Xi_{(j-1)\cdot N+1}$ to $\Xi_{j \cdot N}$, for $j = 1..n$ represent a Gaussian random vector with N independent random variables, whilst the components $\Xi_{(j-1)\cdot N+1}$ to $\Xi_{j \cdot N}$ are correlated to $\Xi_{(k-1)\cdot N+1}$ to $\Xi_{k \cdot N}$, for $k = 1..n$. We use the notation

$$\boldsymbol{\Xi} = \begin{array}{c} Q_1 \\ \ldots \\ Q_j \\ \ldots \\ Q_n \end{array} \left(\begin{array}{c} [\Xi_1 \ldots \Xi_N]^T \\ \ldots \\ [\Xi_{(j-1)\cdot N+1} \ldots \Xi_{j \cdot N}]^T \\ \ldots \\ [\Xi_{(n-1)\cdot N+1} \ldots \Xi_{n \cdot N}]^T \end{array} \right) . \tag{A.31}$$

Its covariance matrix $\tilde{\mathbf{R}}_{\boldsymbol{\Xi}} \in \mathbb{M}^+_{n \cdot N}(\Re)$ is built from the covariance matrix $\tilde{\mathbf{R}}_{\boldsymbol{Q}} \in \mathbb{M}^+_{n}(\Re)$ as follows

$$\tilde{\mathbf{R}}_{\boldsymbol{\Xi}} = \begin{array}{c} \\ Q_1 \\ \dots \\ Q_j \\ \dots \\ Q_n \end{array} \begin{array}{c} \begin{array}{ccccc} Q_1 & \dots & Q_i & \dots & Q_n \end{array} \\ \begin{pmatrix} \tilde{R}_{\boldsymbol{Q}_{1\,1}}\mathbf{I}_N & \dots & \tilde{R}_{\boldsymbol{Q}_{1\,i}}\mathbf{I}_N & \dots & \tilde{R}_{\boldsymbol{Q}_{1\,n}}\mathbf{I}_N \\ \dots & \dots & \dots & \dots & \dots \\ \tilde{R}_{\boldsymbol{Q}_{j\,1}}\mathbf{I}_N & \dots & \tilde{R}_{\boldsymbol{Q}_{j\,i}}\mathbf{I}_N & \dots & \tilde{R}_{\boldsymbol{Q}_{j\,n}}\mathbf{I}_N \\ \dots & \dots & \dots & \dots & \dots \\ \tilde{R}_{\boldsymbol{Q}_{n\,1}}\mathbf{I}_N & \dots & \tilde{R}_{\boldsymbol{Q}_{n\,i}}\mathbf{I}_N & \dots & \tilde{R}_{\boldsymbol{Q}_{n \cdot n}}\mathbf{I}_N \end{pmatrix} \end{array}, \tag{A.32}$$

where $\mathbf{I}_N$ is the $N \times N$ identity matrix. The matrix $\tilde{\mathbf{R}}_{\boldsymbol{\Xi}}$ has the ordered eigen-values $\lambda^{(i)}_{\boldsymbol{\Xi}}$, which are N repeated times the eigen values $\lambda^{(i)}_{\boldsymbol{Q}}$, and the orthonormal eigen-vectors $\boldsymbol{u}^{(i)}_{\boldsymbol{\Xi}}$, which are constructed from $\boldsymbol{u}^{(i)}_{\boldsymbol{Q}}$ (avoiding the resolution of the eigen-value problem).

Similarly to Eq. (A.23), the random vector $\boldsymbol{\Xi}$ has realisations $\boldsymbol{\xi} \in \Re^{N \cdot n}$

$$\boldsymbol{\xi} = \sum_{i=1}^{n \cdot N} \sqrt{\lambda^{(i)}_{\boldsymbol{\Xi}}}\, \boldsymbol{u}^{(i)}_{\boldsymbol{\Xi}} \zeta_i \quad \forall i = 1..n \cdot N\,, \tag{A.33}$$

with the random vector $\mathbf{Z}$ –of realisations $\boldsymbol{\zeta}$– having independent Gaussian random variables as components:

$$\mathbb{E}[\mathrm{Z}_r] = 0 \quad \text{and } \tilde{R}_{\mathbf{Z}_{r\,s}} = \delta_{rs} \quad \forall r,\, s = 1..n \cdot N\,. \tag{A.34}$$

Finally, pseudo-samples $\boldsymbol{\xi}^p$ are obtained from Eq. (A.33) by generating $n \cdot m$ independent Gaussian variables $\zeta_i'^p$ using either Monte Carlo sampling (MC) or Latin Hyper-cube Sampling (LHS). One can then express pseudo-sampling $\boldsymbol{q}^p$ of the Gaussian random vector $\boldsymbol{Q}$ from the relation

$$q^p_j(\boldsymbol{x}) \sim \bar{q}_j + \sigma_{Q_j} \sum_{i=1}^{N} \sqrt{\lambda^{(i)}_U}\, \xi^p_{(j-1) \cdot N + i}\, u^{(i)}_U(\boldsymbol{x})\,, \quad \forall j = 1..n\,, \tag{A.35}$$

where we note the use of the eigen-vectors and eigen-values resulting from the uni-variate random field $U(\Omega)$. In the case in which the PCA was achieved from the sampling at the N locations $\boldsymbol{x}^{(j)}$ using $\boldsymbol{U} = [Q_i(\boldsymbol{x}^{(1)}) \dots Q_i(\boldsymbol{x}^{(N)})]^T$, pseudo-samples of the Gaussian random vector at locations $\boldsymbol{x}^{(k)}$, $k = 1..N$, arise from

$$q^p_j(\boldsymbol{x}^{(k)}) \sim \bar{q}_j + \sigma_{Q_j} \sum_{i=1}^{N} \sqrt{\lambda^{(i)}_{\boldsymbol{U}}}\, \xi^p_{(j-1) \cdot N + i}\, u^{(i)}_{\boldsymbol{U}_k}\,, \quad \forall j = 1..n \quad \forall k = 1..N\,, \tag{A.36}$$

where we note the use of the eigen-vectors and eigen-values resulting from the spatial sampling. If other locations $\boldsymbol{x}$ than at the initial sampling points $\boldsymbol{x}^{(k)}$, $k = 1..N$, are sought, an optimal linear estimation, see details in Section 5.1.2, can be used.

Besides, it is possible to apply order reduction in both equation (A.33) and (A.35).

Appendix A.3.4. Generation of non-Gaussian random fields using the Karhunen-Loève (KL) expansion

Following Eq. (A.27), the random field $\boldsymbol{Q}(\Omega)$, with $\boldsymbol{Q}$ valued in $\Re^n$, can be represented by the collection

$$\boldsymbol{q}(\boldsymbol{x}) \simeq \bar{\boldsymbol{q}}\left(\boldsymbol{x}\right) + \sum_{i=1}^{m} \sqrt{\lambda_{\boldsymbol{Q}}^{(i)}} \eta_i \boldsymbol{u}_{\boldsymbol{Q}}^{(i)}\left(\boldsymbol{x}\right), \tag{A.37}$$

where the relation is exact for $m \to \infty$. As previously described, for Gaussian random fields, starting from the KL expansion (A.37), pseudo-samples can be generated as

$$\boldsymbol{q}^p(\boldsymbol{x}) \simeq \bar{\boldsymbol{q}}(\boldsymbol{x}) + \sum_{i=1}^{m} \sqrt{\lambda_{\boldsymbol{Q}}^{(i)}} \eta_i^p \boldsymbol{u}_{\boldsymbol{Q}}^{(i)}\left(\boldsymbol{x}\right), \tag{A.38}$$

from pseudo-samples $\boldsymbol{\eta}^p$ generated as m independent Gaussian variables η_i^p using either Monte Carlo sampling (MC) or Latin Hyper-cube Sampling (LHS).

If one wants to generate pseudo-samples following the targeted marginal cumulative distributions F_{Q_r} of the random variables Q_r, Phoon et al. (2005) have proposed the following iterative process:

- Construct the inverse $F_{Q_r}^{-1} : [0,\, 1] \to \mathcal{S}_{Q_r}$ of the marginal cumulative distribution functions, assumed to be continuous, of support $\mathcal{S}_{Q_r}$ of the component r of the random vector $\boldsymbol{Q}$;

- Initialise the pseudo-samples $\eta_i^{p^{(0)}}$, see the discussion for the univariate case given by Phoon et al. (2005), as m independent variables drawn from a zero-mean and unit variance distribution;

- Repeat until convergence
  1. At iteration (k), generate several pseudo-samples

     $$\tilde{\boldsymbol{q}}^{p^{(k)}}(\boldsymbol{x}) \simeq \bar{\boldsymbol{q}}\left(\boldsymbol{x}\right) + \sum_{i=1}^{m} \sqrt{\lambda_{\boldsymbol{Q}}^{(i)}} \eta_i^{p^{(k)}} \boldsymbol{u}_{\boldsymbol{Q}}^{(i)}\left(\boldsymbol{x}\right), \tag{A.39}$$

     from the pseudo-samples $\eta_i^{p^{(k)}}$;
  2. Estimate the marginal cumulative distributions $F_{\tilde{Q}_r^{(k)}}$ from the pseudo-samples (A.39);
  3. Transform each pseudo-sample to have the target marginal distribution following

     $$q_r^{p^{(k)}}(\boldsymbol{x}) = F_{Q_r}^{-1}\left(F_{\tilde{Q}_r^{(k)}}(\tilde{q}_r^{p^{(k)}}(\boldsymbol{x}))\right), \quad r = 1..n\,; \tag{A.40}$$

  4. Estimate the new pseudo-samples $\eta_i^{p^{(k+1)}}$ from

     $$\eta_i^{p^{(k+1)}} = \frac{1}{\sqrt{\lambda_{\boldsymbol{Q}}^{(i)}}} \int_{\Omega} \left(\boldsymbol{q}^{p^{(k)}}(\boldsymbol{x}) - \bar{\boldsymbol{q}}^{p^{(k)}}(\boldsymbol{x})\right)^T \boldsymbol{u}_{\boldsymbol{Q}}^{(i)}(\boldsymbol{x}) d\boldsymbol{x}, \quad i = 1..m\,, \tag{A.41}$$

     followed by a standardisation to give unit variance to $\eta_i^{p^{(k+1)}}$;

5. Ensure that the updated $\eta_i^{p^{(k+1)}}$ random variables are approximately uncorrelated by product-moment orthogonalisation technique, see the developments by Phoon et al. (2005);
6. Go back to step #1 until convergence.

We note that the method was developed by Phoon et al. (2005) in the uni-variate case, *i.e.* assuming $n = 1$, but has been used by Liebscher et al. (2012) when considering correlated random variables Q_r.

The method described in Appendix A.3.3 was also extended to non-Gaussian random-fields by considering a non-linear transformation, see Appendix A.1, before applying the KL expansion. In particular, Vořechovský (2008) has applied the Nataf transformation, see Appendix A.1.2, and adapted the block-generation process described in Appendix A.3.3. The following difficulty was however pointed out: "We remark also that not every combination of the auto-correlation structure with the non-Gaussian marginal distribution can be admissible for the mapping via underlying Gaussian random field. There are two possible incompatibilities. The first one arises when the auto-correlation functions of the non-Gaussian fields do not have a corresponding admissible correlations in the Gaussian space (this happens often in cases of high negative correlations combined with strongly non-Gaussian marginals). The second incompatibility arises when the auto-correlation function (or matrix) in the Gaussian space becomes non-positive definite and, therefore, not admissible."

Appendix A.4. Polynomial Chaos Expansion (PCE)

Appendix A.4.1. Definitions

Let $\boldsymbol{\Xi} = [\Xi_1 \ldots \Xi_i \ldots \Xi_n]^T$ be a vector of n random variables $\Xi_i : \mathcal{Q} \to \Re$ with the joint probability density function $\pi_{\boldsymbol{\Xi}} : \Re^n \to [0, \infty[$ and which is p^{th}-order, see Eq. (27), $\forall p \in \mathbb{N}$. The support of $\boldsymbol{\Xi}$ is denoted by $\mathcal{S}_{\boldsymbol{\Xi}}$. Following Soize (2017), the random vector $\boldsymbol{\Xi}$ is called a random germ. We thus have the realisation $\boldsymbol{\Xi}(q) \in \mathcal{S}_{\boldsymbol{\Xi}}$ for all $q \in \mathcal{Q}$.

Let us consider the second-order random vector $\boldsymbol{X} = \boldsymbol{f}(\boldsymbol{\Xi})$ valued in $\Re^m$ as the deterministic non-linear mapping of the random germ $\boldsymbol{\Xi}$ such that $\boldsymbol{x} = \boldsymbol{f}(\boldsymbol{\xi}) : \Re^n \to \Re^m$.

The algebraic form of the polynomial chaos expansion of $\boldsymbol{X} = \boldsymbol{f}(\boldsymbol{\Xi})$ reads

$$\boldsymbol{X} = \sum_{k=0}^{\infty} \boldsymbol{c}^{(k)} \psi_{\alpha^{(k)}}(\boldsymbol{\Xi}) \,, \tag{A.42}$$

where $\{\psi_{\alpha^{(k)}}(\boldsymbol{\Xi}) : k \in \mathbb{N}_0\}$ are the multi-variate polynomial chaos and where $\{\boldsymbol{c}^{(k)} : \boldsymbol{c}^{(k)} \in \Re^m,\ k \in \mathbb{N}_0\}$ are the vector valued coefficients.

Finally, we define the Hilbert space $\mathcal{H}(\mathcal{Q})$ of $\Re$-valued functions square integrable on $\Re^n$ with respect to the probability density function $\pi_{\boldsymbol{\Xi}}(\boldsymbol{\xi})$ so that for two functions $f(\boldsymbol{\Xi})$ and $g(\boldsymbol{\Xi})$ in $\mathcal{H}(\mathcal{Q})$, the inner product is defined by

$$\mathbb{E}\left[f(\boldsymbol{\Xi})g(\boldsymbol{\Xi})\right] = \int_{\Re^n} f(\boldsymbol{\xi})g(\boldsymbol{\xi})\pi_{\boldsymbol{\Xi}}(\boldsymbol{\xi})d\boldsymbol{\xi} \,. \tag{A.43}$$

Appendix A.4.2. Polynomial Chaos Expansion of a random vector

Let $\boldsymbol{k}^{(l)} = \{k_1^{(l)}, \ldots, k_n^{(l)}\} \in \mathcal{K} = \mathbb{N}_0^n$ be the multi-index, with $|\boldsymbol{k}^{(l)}| = k_1^{(l)} + \ldots + k_n^{(l)}$. We then consider the Hilbert basis $\{\psi_{\boldsymbol{k}^{(l)}} : \boldsymbol{k}^{(l)} \in \mathcal{K}, \, l \in \mathbb{N}_0\}$, as an orthonormal family of $\mathcal{H}(\mathcal{Q})$, *i.e.*:

$$\mathbb{E}\left[\psi_{\boldsymbol{k}^{(l)}} \psi_{\boldsymbol{k}^{(l')}}\right] = \delta_{\boldsymbol{k}^{(l)}\boldsymbol{k}^{(l')}} \quad \forall \boldsymbol{k}^{(l)}, \, \boldsymbol{k}^{(l')} \in \mathcal{K} \, , \tag{A.44}$$

and as a total family, *i.e.* if $\mathbb{E}\left[\psi_{\boldsymbol{k}^{(l)}} g\right] = 0$ for all $\boldsymbol{k}^{(l)} \in \mathcal{K}$ then $g = 0$.

The expansion of the random vector $\boldsymbol{X} = \boldsymbol{f}(\Xi)$ valued in $\Re^m$ thus reads

$$\boldsymbol{X} = \boldsymbol{f}(\Xi) = \sum_{\boldsymbol{k}^{(l)} \in \mathcal{K}} \boldsymbol{c}_{\boldsymbol{k}^{(l)}} \psi_{\boldsymbol{k}^{(l)}}(\Xi) \, , \tag{A.45}$$

with the coefficients $\boldsymbol{c}_{\boldsymbol{k}^{(l)}}$ valued in $\Re^m$ given by

$$\boldsymbol{c}_{\boldsymbol{k}^{(l)}} = \mathbb{E}\left[\boldsymbol{X} \psi_{\boldsymbol{k}^{(l)}}(\Xi)\right] = \int_{\Re^n} \boldsymbol{f}(\boldsymbol{\xi}) \psi_{\boldsymbol{k}^{(l)}}(\boldsymbol{\xi}) \pi_{\boldsymbol{\Xi}}(\boldsymbol{\xi}) d\boldsymbol{\xi} \, . \tag{A.46}$$

Finite approximation of the expansion. The complete multi-index set of total degree at most p is defined as

$$\mathcal{K}_p^{\mathrm{C}} = \{\boldsymbol{k}^{(l)} \in \mathbb{N}_0^n : k_1^{(l)} + \ldots + k_i^{(l)} + \ldots k_n^{(l)} \leq p, \, l = 0..n_p^{\mathrm{C}}\} \subset \mathcal{K} \, , \tag{A.47}$$

and has the elements $\boldsymbol{k}^{(0)} = \{0, \ldots, 0\}$, $\boldsymbol{k}^{(1)}, \ldots, \boldsymbol{k}^{(n_p^{\mathrm{C}})}$, with $n_p^{\mathrm{C}} = \frac{(n+p)!}{n!p!} - 1$.

The approximation of the expansion (A.46) of the random vector $\boldsymbol{X} = \boldsymbol{f}(\Xi)$ valued in $\Re^m$ thus reads

$$\boldsymbol{X} = \boldsymbol{f}(\Xi) \simeq \sum_{\boldsymbol{k}^{(l)} \in \mathcal{K}_p^{\mathrm{C}}} \boldsymbol{c}_{\boldsymbol{k}^{(l)}} \psi_{\boldsymbol{k}^{(l)}}(\Xi) = \sum_{l=0}^{n_p^{\mathrm{C}}} \boldsymbol{c}_{\boldsymbol{k}^{(l)}} \psi_{\boldsymbol{k}^{(l)}}(\Xi) \, , \tag{A.48}$$

with the coefficients valued in $\Re^m$ evaluated by

$$\boldsymbol{c}_{\boldsymbol{k}^{(l)}} = \mathbb{E}\left[\boldsymbol{X} \psi_{\boldsymbol{k}^{(l)}}(\Xi)\right] = \int_{\Re^n} \boldsymbol{f}(\boldsymbol{\xi}) \psi_{\boldsymbol{k}^{(l)}}(\boldsymbol{\xi}) \pi_{\boldsymbol{\Xi}}(\boldsymbol{\xi}) d\boldsymbol{\xi} \, . \tag{A.49}$$

Particular case of independent Ξ_i*.* Let $\boldsymbol{\Xi} = [\Xi_1 \ldots \Xi_i \ldots \Xi_n]^T$ be defined from n independent random variables $\Xi_i : \mathcal{Q} \to \Re$. Therefore, the joint probability density function $\pi_{\boldsymbol{\Xi}} : \Re^n \to [0, \infty[$ reads $\pi_{\boldsymbol{\Xi}}(\boldsymbol{\xi}) = \pi_{\Xi_1}(\xi_1) \times \ldots \times \pi_{\Xi_i}(\xi_i) \times \ldots \times \pi_{\Xi_n}(\xi_n)$, with the probability density function $\pi_{\Xi_i} : \Re \to [0, \infty[$ of the random variable Ξ_i. Besides, the support of $\boldsymbol{\Xi}$ reads $\mathcal{S}_{\boldsymbol{\Xi}} = \mathcal{S}_{\Xi_1} \times \ldots \times \mathcal{S}_{\Xi_i} \times \ldots \times \mathcal{S}_{\Xi_n}$, with $\mathcal{S}_{\Xi_i}$ the support of Ξ_i.

Let $\{\psi_l^{(i)} : l \in \mathbb{N}_0, \, i = 1..n\}$ be the family of orthonormal polynomials such that

$$\int_{\mathcal{S}_{\Xi_i}} \psi_l^{(i)} \psi_o^{(i)} \pi_{\Xi_i}(\xi_i) d\xi_i = \delta_{lo} \, , \tag{A.50}$$

then the Hilbert basis $\{\psi_{\boldsymbol{k}^{(l)}} : \boldsymbol{k}^{(l)} \in \mathcal{K}\}$ can be defined from the multi-variate polynomials

$$\psi_{\boldsymbol{k}^{(l)}}(\boldsymbol{\xi}) = \psi_{k_1^{(l)}}^{(1)}(\xi_1) \times \ldots \times \psi_{k_i^{(l)}}^{(i)}(\xi_i) \times \ldots \times \psi_{k_n^{(l)}}^{(n)}(\xi_n) \, , \tag{A.51}$$

since Eq. (A.44) is satisfied.

Gaussian polynomial chaos expansion. Considering the particular case for which $\boldsymbol{\Xi} = [\Xi_1 \ldots \Xi_i \ldots \Xi_n]^T$ is defined from n independent random variables $\Xi_i : \mathcal{Q} \to \Re$ whose distributions follow a Gaussian density probability function, $\Xi_i \sim \mathcal{N}_{0,1}$, of zero-mean and unit variance, see Eq. (17), a common choice for the orthonormal polynomials family $\{\psi_l^{(i)} : l \in \mathbb{N}_0,\, i = 1..n\}$ is based on the Hermite polynomials

$$\psi_{l+1}^{(i)}(\xi_i) = H_{l+1}(\xi_i) = \frac{1}{\sqrt{l+1}} \left(\xi_i H_l(\xi_i) - \frac{dH_l(\xi_i)}{d\xi_i} \right) \quad \forall i = 1..n\,,\ l \in \mathbb{N}_0\,, \tag{A.52}$$

with $H_0(\xi_i) = 1$, $H_1(\xi_i) = \xi_i$, $H_2(\xi_i) = \frac{\xi_i^2 - 1}{\sqrt{2}}$ etc.

The approximation of the Gaussian polynomial expansion of the random vector $\boldsymbol{X} = \boldsymbol{f}(\boldsymbol{\Xi})$ valued in $\Re^m$ is then defined by Eqs. (A.48-A.49) with the multi-variate polynomials (A.51) defined using the Hermite polynomials (A.52). We finally note that, because of the shape of $H_0(\xi_i)$, Eq. (A.48) can alternatively be rewritten when considering a realisation $\boldsymbol{x}$ for $q \in \mathcal{Q}$ as

$$\boldsymbol{x} = \boldsymbol{f}(\boldsymbol{\Xi}(q)) \simeq \sum_{l=0}^{n_p^{\mathrm{C}}} \boldsymbol{c}_{\boldsymbol{k}^{(l)}} \psi_{\boldsymbol{k}^{(l)}}(\boldsymbol{\Xi}(q)) = \bar{\boldsymbol{x}} + \sum_{l=1}^{n_p^{\mathrm{C}}} \boldsymbol{c}_{\boldsymbol{k}^{(l)}} \psi_{\boldsymbol{k}^{(l)}}(\boldsymbol{\Xi}(q))\,, \tag{A.53}$$

with

$$\begin{aligned} \psi_{\boldsymbol{k}^{(l)}}(\boldsymbol{\xi}) &= \psi^{(1)}_{k_1^{(l)}}(\xi_1) \times \ldots \times \psi^{(i)}_{k_i^{(l)}}(\xi_i) \times \ldots \times \psi^{(n)}_{k_n^{(l)}}(\xi_n) \\ &= H_{k_1^{(l)}}(\xi_1) \times \ldots \times H_{k_i^{(l)}}(\xi_i) \times \ldots \times H_{k_n^{(l)}}(\xi_n)\,. \end{aligned} \tag{A.54}$$

Appendix A.4.3. Generation of non-Gaussian random vectors

Let us consider the n-dimension random vector $\boldsymbol{Q} : \mathcal{Q} \to \Re^n$. Its expectation (26) is denoted by $\bar{\boldsymbol{q}} = \mathbb{E}[\boldsymbol{Q}]$, and its covariance matrix (46) by $\tilde{\mathbf{R}}_{\boldsymbol{Q}} \in \mathbb{M}_n^+(\Re)$. We note that we assume the positive definite nature of $\tilde{\mathbf{R}}_{\boldsymbol{Q}}$. Following Appendix A.3.1, a principal component analysis can be conducted up to order $m \leq n$ to approximate the random vector realisations by

$$\boldsymbol{Q}(q) \simeq \bar{\boldsymbol{q}} + \sum_{i=1}^{m \leq n} \sqrt{\lambda_{\boldsymbol{Q}}^{(i)}} \mathrm{H}_i(q) \boldsymbol{u}_{\boldsymbol{Q}}^{(i)} = \sum_{i=0}^{m} \sqrt{\lambda_{\boldsymbol{Q}}^{(i)}} \mathrm{H}_i(q) \boldsymbol{u}_{\boldsymbol{Q}}^{(i)}\,, \tag{A.55}$$

where $\mathbf{H}$ is a new random vector of uncorrelated (but possibly dependent) components H_i, $\lambda_{\boldsymbol{Q}}^{(i)}$ and $\boldsymbol{u}_{\boldsymbol{Q}}^{(i)}$ for $i > 0$ are the ordered eigen-values and orthonormal eigen-basis of the covariance matrix $\tilde{\mathbf{R}}_{\boldsymbol{Q}}$, m is the order of the expansion, and where we have defined $\mathrm{H}_0(q) = \lambda_{\boldsymbol{Q}}^{(0)} = 1$ and $\boldsymbol{u}_{\boldsymbol{Q}}^{(0)}$ as the expectation $\bar{\boldsymbol{q}}$. We note that the components of $\mathbf{H}$ are uncorrelated, but can be dependent; however, for Gaussian distributions they are also independent since uncorrelated. Besides, the random vector $\mathbf{H}$ is characterised by the following properties

$$\mathbb{E}[\mathbf{H}] = \mathbf{0}_m \quad \text{and } \tilde{\mathbf{R}}_{\mathbf{H}} = \mathbf{I}_m\,. \tag{A.56}$$

A finite PCE on the random vector $\mathbf{H}$ valued in $\Re^m$ can then be considered as a deterministic non-linear mapping of the random germ $\boldsymbol{\Xi}$ valued in $\Re^m$. Following Appendix A.4.2, it comes

$$\mathbf{H} = \boldsymbol{f}(\boldsymbol{\Xi}) \simeq \sum_{\boldsymbol{k}^{(l)} \in \mathcal{K}_p^{\mathrm{C}}} \boldsymbol{c}_{\boldsymbol{k}^{(l)}} \psi_{\boldsymbol{k}^{(l)}}(\boldsymbol{\Xi}) = \sum_{l=0}^{n_p^{\mathrm{C}}} \boldsymbol{c}_{\boldsymbol{k}^{(l)}} \psi_{\boldsymbol{k}^{(l)}}(\boldsymbol{\Xi}) \,, \tag{A.57}$$

with the coefficients valued in $\Re^m$ evaluated by

$$\boldsymbol{c}_{\boldsymbol{k}^{(l)}} = \mathbb{E}\left[\mathbf{H} \psi_{\boldsymbol{k}^{(l)}}(\boldsymbol{\Xi})\right] = \int_{\Re^m} \boldsymbol{f}(\boldsymbol{\xi}) \psi_{\boldsymbol{k}^{(l)}}(\boldsymbol{\xi}) \pi_{\boldsymbol{\Xi}}(\boldsymbol{\xi}) d\boldsymbol{\xi} \,, \tag{A.58}$$

and with the complete multi-index set of total degree at most p defined by Eq. (A.47) and composed of the elements $\boldsymbol{k}^{(0)} = \{0, \ldots, 0\}$, $\boldsymbol{k}^{(1)}$, ..., $\boldsymbol{k}^{(n_p^{\mathrm{C}})}$, with $n_p^{\mathrm{C}} = \frac{(m+p)!}{m!p!} - 1$. Because of the properties (A.56), Eq. (A.57) implies that the following properties must be satisfied

$$\boldsymbol{c}_{\boldsymbol{k}^{(0)}} = 0 \quad \text{and} \quad \sum_{l=1}^{n_p^{\mathrm{C}}} \boldsymbol{c}_{\boldsymbol{k}^{(l)}} \boldsymbol{c}_{\boldsymbol{k}^{(l)}}^T = \mathbf{I}_m \,, \tag{A.59}$$

with $\mathbf{I}_m$ the identity matrix of size m.

Starting from Eq. (A.57), the question is to identify the coefficient $\boldsymbol{c}_{\boldsymbol{k}^{(l)}}$ and the appropriate germ $\boldsymbol{\Xi}$ valued in $\Re^m$ in order to build a suitable generator. We here follow the method summarised by Hoang et al. (2017).

Multivariate kernel density estimation. The random vector $\mathbf{H}$ with values in $\Re^m$ can be sampled from n^η realisations $\boldsymbol{q}^s$ following

$$\eta_i^s = \frac{1}{\sqrt{\lambda_{\boldsymbol{Q}}^{(i)}}} \left(\boldsymbol{q}^s - \bar{\boldsymbol{q}}\right)^T \boldsymbol{u}_{\boldsymbol{Q}}^{(i)} \quad \forall i = 1..m \,, \tag{A.60}$$

allowing defining an approximation of the probability density $\pi_{\mathbf{H}}(\boldsymbol{\eta})$, for example using as bandwidth matrix the thumb-up rule proposed by Scott (2015) with

$$\pi_{\mathbf{H}}(\boldsymbol{\eta}) \simeq \frac{1}{n^\eta} \sum_{s=1}^{n^\eta} \frac{1}{(2\pi)^{m/2} \left(n^\eta\right)^{-m/(m+4)}} \exp\left(-\frac{\left\|\boldsymbol{\eta} - \boldsymbol{\eta}^s\right\|^2}{2\left(n^\eta\right)^{-2/(m+4)}}\right) . \tag{A.61}$$

The conditional probability density functions thus arise from

$$\pi_{\mathrm{H}_k|\mathrm{H}_{k-1}, \ldots, \mathrm{H}_1}(\eta_k | \eta_{k-1}, \ldots, \eta_1) = \frac{\pi_{\mathrm{H}_k, \mathrm{H}_{k-1}, \ldots, \mathrm{H}_1}(\eta_k, \eta_{k-1}, \ldots \eta_1)}{\int_{\Re} \pi_{\mathrm{H}_k, \mathrm{H}_{k-1}, \ldots, \mathrm{H}_1}(\eta_k, \eta_{k-1}, \ldots \eta_1) d\eta_k} \,, \ k = 1..m \,, \tag{A.62}$$

and the conditional cumulative distribution follows from

$$F_{\mathrm{H}_k|\mathrm{H}_{k-1}, \ldots, \mathrm{H}_1}(\eta_k | \eta_{k-1}, \ldots, \eta_1) = \int_{-\infty}^{\eta_k} \pi_{\mathrm{H}_k|\mathrm{H}_{k-1}, \ldots, \mathrm{H}_1}(\eta_k' | \eta_{k-1}, \ldots, \eta_1) d\eta_k' \,, \ k = 1..m \,. \tag{A.63}$$

Rosenblatt transformation. In order to obtain a germ $\boldsymbol{\Xi}$ defined as m independent and uniformly distributed random variables Ξ_i with the support $\mathcal{S}_{\boldsymbol{\Xi}} = [0,\,1]^m$, *i.e.*

$$\pi_{\boldsymbol{\Xi}}(\boldsymbol{\xi}) = \mathcal{U}_{0,\,1} \times \dots \times \mathcal{U}_{0,\,1}\,, \tag{A.64}$$

with $\mathcal{U}_{0,\,1}$ defined by Eq. (18), we apply the Rosenblatt transformation $\boldsymbol{\Xi} = \boldsymbol{f}^{\mathscr{R}\,\mathcal{U}}(\mathbf{H})$ following Appendix A.1.3, with Eq. (A.10) evaluated from the conditional cumulative distribution following from Eq. (A.63) as

$$\xi_1 = F_{\mathrm{H}_1}(\eta_1),\; \xi_2 = F_{\mathrm{H}_2|\mathrm{H}_1}(\eta_2|\eta_1),\; \dots,\; \xi_m = F_{\mathrm{H}_m|\mathrm{H}_{m-1},\dots,\mathrm{H}_1}(\eta_m|\eta_{m-1},\,\dots,\,\eta_1)\,. \tag{A.65}$$

Legendre polynomials. Since the random variables Ξ_i, $i = 1..m$, are independent, the Hilbert basis can be defined by the multi-variate polynomials (A.51), with the family of orthonormal polynomials $\{\psi_p^{(i)} \,:\, p \in \mathbb{N}_0,\, i = 1..m\}$. A practical choice for the polynomials $\psi_p^{(i)}$ is to consider the Legendre polynomials shifted in the domain $[0,\,1]$, with

$$\psi_p^{(i)}(\xi_i) = P_p(2\xi_i - 1)\sqrt{2p+1}\,, \tag{A.66}$$

where P_p is the Legendre polynomial of order p with $P_0(x) = 1$, $P_1(x) = x$, ..., $P_{p+1}(x) = \frac{2p+1}{p+1}xP_p(x) - \frac{p}{p+1}P_{p-1}(x)$, for $x \in [-1,\,1]$. Finally, one has

$$\psi_{\boldsymbol{k}^{(l)}}(\boldsymbol{\xi}) \;=\; \psi^{(1)}_{k_1^{(l)}}(\xi_1) \times \dots \times \psi^{(i)}_{k_i^{(l)}}(\xi_i) \times \dots \times \psi^{(m)}_{k_m^{(l)}}(\xi_m)\,. \tag{A.67}$$

Identification of the PCE coefficients. Considering the multi-variate polynomial chaos $\{\psi_{\boldsymbol{k}^{(l)}}(\boldsymbol{\Xi}) : l = 1..n_p^{\mathrm{C}}\}$ built using the Legendre polynomials (A.66), and using Eq. (A.64), the coefficients (A.58) are obtained from the inverse Rosenblatt transformation following

$$\boldsymbol{c}_{\boldsymbol{k}^{(l)}} = \mathbb{E}\left[\mathbf{H}\psi_{\boldsymbol{k}^{(l)}}(\boldsymbol{\Xi})\right] = \int_{\Re^m} \boldsymbol{f}(\boldsymbol{\xi})\psi_{\boldsymbol{k}^{(l)}}(\boldsymbol{\xi})\pi_{\boldsymbol{\Xi}}(\boldsymbol{\xi})d\boldsymbol{\xi} = \int_{\mathcal{S}_{\boldsymbol{\Xi}}} \boldsymbol{f}^{\mathscr{R}\,\mathcal{U}^{-1}}(\boldsymbol{\xi})\psi_{\boldsymbol{k}^{(l)}}d\boldsymbol{\xi}\,, \tag{A.68}$$

which is detailed components by components as

$$\begin{aligned}
c_{\boldsymbol{k}^{(l)}1} &= \int_{[0\,1]} F^{-1}_{\mathrm{H}_1}(\xi_1)\psi_{\boldsymbol{k}^{(l)}}(\xi_1)d\xi_1\,,\\
c_{\boldsymbol{k}^{(l)}2} &= \int_{[0\,1]^2} F^{-1}_{\mathrm{H}_2|\mathrm{H}_1}(\xi_2|\xi_1)\psi_{\boldsymbol{k}^{(l)}}(\xi_1,\,\xi_2)d\xi_1 d\xi_2\,, \dots,\\
c_{\boldsymbol{k}^{(l)}m} &= \int_{[0\,1]^m} F^{-1}_{\mathrm{H}_m|\mathrm{H}_{m-1}\dots\mathrm{H}_1}(\xi_m|\xi_{m-1}\dots\xi_1)\psi_{\boldsymbol{k}^{(l)}}(\xi_1,\,\xi_2,\,\dots,\,\xi_m)d\xi_1 d\xi_2\dots d\xi_m\,,
\end{aligned} \tag{A.69}$$

with $\psi_{\boldsymbol{k}^{(l)}}(\xi_1,\,\xi_2,\,\dots,\,\xi_i) = \int_{[0,\,1]^{m-i}} \psi_{\boldsymbol{k}^{(l)}}(\boldsymbol{\xi})d\xi_{i+1}d\xi_{i+2}\dots d\xi_m$.

Sampling of non-Gaussian random vectors. Once the coefficient $\boldsymbol{c}_{\boldsymbol{k}^{(l)}}$ are identified, pseudo-samples $\boldsymbol{q}^p$ of the random vector $\boldsymbol{Q}$ can be generated as follows:

- Pseudo-samples $\boldsymbol{\xi}^p$ can be readily generated from $\Xi_i \sim \mathcal{U}_{0,\,1}$;
- Transform them into pseudo-samples $\boldsymbol{\eta}^p$ using Eq. (A.57);
- Transform the latter into pseudo-samples $\boldsymbol{q}^p$ using Eq. (A.55).

Appendix A.4.4. PCE of a random field

Let us consider the continuous random vector field $\boldsymbol{Q}(\Omega) = \{\boldsymbol{Q}(\boldsymbol{x}) : \boldsymbol{x} \in \Omega\}$ for $\Omega \subset \Re^d$ a space of material points $\boldsymbol{x}$, with $d \in \mathbb{N}$. Its expectation (26) is denoted by $\bar{\boldsymbol{q}}(\boldsymbol{x}) = \mathbb{E}[\boldsymbol{Q}(\boldsymbol{x})] : \Omega \to \Re^n$, and its covariance matrix by $\tilde{\mathbf{R}}_{\boldsymbol{Q}}(\boldsymbol{x};\, \boldsymbol{\tau})$, see Eq. (50). In this section, using $\boldsymbol{x'} = \boldsymbol{x} + \boldsymbol{\tau}$, we use the notation $\tilde{\mathbf{R}}_{\boldsymbol{Q}}(\boldsymbol{x},\, \boldsymbol{x}') : \Omega \times \Omega \to \Re^{n\times n}$.

Following Appendix A.3.2, a finite Karhunen Loève expansion up to order m allows approximating the random field $\boldsymbol{Q}(\Omega)$ by the collection of

$$\boldsymbol{Q}(\boldsymbol{x};\, q) \simeq \bar{\boldsymbol{q}}(\boldsymbol{x}) + \sum_{i=1}^{m} \sqrt{\lambda_{\boldsymbol{Q}}^{(i)}}\mathrm{H}_i(q)\boldsymbol{u}_{\boldsymbol{Q}}^{(i)}(\boldsymbol{x}) = \sum_{i=0}^{m} \sqrt{\lambda_{\boldsymbol{Q}}^{(i)}}\mathrm{H}_i(q)\boldsymbol{u}_{\boldsymbol{Q}}^{(i)}(\boldsymbol{x}), \tag{A.70}$$

where $\mathbf{H}$ is a new random vector of uncorrelated (but possibly dependent) components H_i, $\lambda_{\boldsymbol{Q}}^{(i)}$ and $\boldsymbol{u}_{\boldsymbol{Q}}^{(i)}(\boldsymbol{x})$ for $i > 0$ are the ordered eigen-values and orthonormal eigen-vectors of the covariance matrix $\tilde{\mathbf{R}}_{\boldsymbol{Q}}(\boldsymbol{x},\, \boldsymbol{x}')$, m is the order of the expansion, and where we have defined $\mathrm{H}_0(q) = \lambda_{\boldsymbol{Q}}^{(0)} = 1$ and $\boldsymbol{u}_{\boldsymbol{Q}}^{(0)}(\boldsymbol{x})$ as the expectation $\bar{\boldsymbol{q}}(\boldsymbol{x})$. Besides, the random vector $\mathbf{H}$ is characterised by the following properties

$$\mathbb{E}[\mathbf{H}] = \mathbf{0}_m \quad \text{and } \tilde{\mathbf{R}}_{\mathbf{H}} = \mathbf{I}_m\,. \tag{A.71}$$

A PCE of the random field consists in performing a finite PCE on the random vector $\mathbf{H}$ valued in $\Re^m$ and considered as the deterministic non-linear mapping of the random germ $\boldsymbol{\Xi}$ valued in $\Re^{n^g}$. Following Appendix A.4.2, it comes

$$\mathbf{H} = \boldsymbol{f}(\boldsymbol{\Xi}) \simeq \sum_{\boldsymbol{k}^{(l)} \in \mathcal{K}_p^{\mathrm{C}}} \boldsymbol{c}_{\boldsymbol{k}^{(l)}}\psi_{\boldsymbol{k}^{(l)}}(\boldsymbol{\Xi}) = \sum_{l=0}^{n_p^{\mathrm{C}}} \boldsymbol{c}_{\boldsymbol{k}^{(l)}}\psi_{\boldsymbol{k}^{(l)}}(\boldsymbol{\Xi}), \tag{A.72}$$

with the coefficients valued in $\Re^m$ evaluated by

$$\boldsymbol{c}_{\boldsymbol{k}^{(l)}} = \mathbb{E}\left[\mathbf{H}\psi_{\boldsymbol{k}^{(l)}}(\boldsymbol{\Xi})\right] = \int_{\Re^{n^g}} \boldsymbol{f}(\boldsymbol{\xi})\psi_{\boldsymbol{k}^{(l)}}(\boldsymbol{\xi})\pi_{\boldsymbol{\Xi}}(\boldsymbol{\xi})d\boldsymbol{\xi}\,, \tag{A.73}$$

and with the complete multi-index set of total degree at most p defined by Eq. (A.47) and of elements $\boldsymbol{k}^{(0)} = \{0,\, ...,\, 0\}$, $\boldsymbol{k}^{(1)}$, ..., $\boldsymbol{k}^{(n_p^{\mathrm{C}})}$, with $n_p^{\mathrm{C}} = \frac{(n^g+p)!}{n^g!p!} - 1$. Because of the properties (A.71), Eq. (A.72) implies that the following conditions must be satisfied

$$\boldsymbol{c}_{\boldsymbol{k}^{(0)}} = 0 \quad \text{and} \quad \sum_{l=1}^{n_p^{\mathrm{C}}} \boldsymbol{c}_{\boldsymbol{k}^{(l)}}\boldsymbol{c}_{\boldsymbol{k}^{(l)}}^T = \mathbf{I}_m\,, \tag{A.74}$$

with $\mathbf{I}_m$ the identity matrix of size m.

Defining $\boldsymbol{u}_{\boldsymbol{k}^{(l)}}(\boldsymbol{x}) = \sum_{i=1}^{m} \sqrt{\lambda_{\boldsymbol{Q}}^{(i)}} c_{\boldsymbol{k}^{(l)}i}\boldsymbol{u}_{\boldsymbol{Q}}^{(i)}(\boldsymbol{x})$, Eq. (A.70) is then rewritten

$$\boldsymbol{Q}(\boldsymbol{x};\, q) \simeq \bar{\boldsymbol{q}}(\boldsymbol{x}) + \sum_{l=1}^{n_p^{\mathrm{C}}} \boldsymbol{u}_{\boldsymbol{k}^{(l)}}(\boldsymbol{x})\psi_{\boldsymbol{k}^{(l)}}(\boldsymbol{\Xi}(q))\,, \tag{A.75}$$

with, using Eq. (A.74) and the orthonormal properties of $\boldsymbol{u}_{\boldsymbol{Q}}^{(i)}(\boldsymbol{x})$,

$$\boldsymbol{u}_{\boldsymbol{k}^{(0)}} = 0 \quad \text{and} \quad \int_{\Omega} \boldsymbol{u}_{\boldsymbol{k}^{(l)}}(\boldsymbol{x})^T \boldsymbol{u}_{\boldsymbol{k}^{(l')}}(\boldsymbol{x}) d\boldsymbol{x} = \sum_{i=1}^{m} \lambda^{(i)} c_{\boldsymbol{k}^{(l)}i} c_{\boldsymbol{k}^{(l')}i} \quad l,\, l' = 1..n_p^{\mathrm{C}}\,, \tag{A.76}$$

and with

$$\begin{aligned} \boldsymbol{u}_{\boldsymbol{k}^{(l)}}(\boldsymbol{x}) &= \mathbb{E}\left[\left(\boldsymbol{Q}(\boldsymbol{x}) - \bar{\boldsymbol{q}}\left(\boldsymbol{x}\right)\right) \psi_{\boldsymbol{k}^{(l)}}(\boldsymbol{\Xi})\right] \\ &= \int_{\Re^{n^g}} \left(\boldsymbol{Q}(\boldsymbol{x}) - \bar{\boldsymbol{q}}\left(\boldsymbol{x}\right)\right) \psi_{\boldsymbol{k}^{(l)}}(\boldsymbol{\xi}) \pi_{\boldsymbol{\Xi}}(\boldsymbol{\xi}) d\boldsymbol{\xi} \quad l = 1..n_p^{\mathrm{C}}\,. \end{aligned} \tag{A.77}$$

Appendix A.5. Markov chain Monte Carlo

Appendix A.5.1. Markov Chain of discrete random vectors

Definition. Let us consider a random process $\boldsymbol{Q}(\mathcal{T}) = \{\boldsymbol{Q}(t^{(i)}) \;:\; t^{(i)} \in \mathcal{T} \subset \Re_0^+\}$, the collection of random vectors in the discrete set $\mathcal{T} = (t^{(1)}, ..., t^{(k)}, ...)$, with $0 \leq t^{(1)} < t^{(2)} < ... < t^{(k-1)} < t^{(k)}$. Besides it is assumed that $\boldsymbol{Q}(t^{(i)})$ takes values in a countable support $\mathcal{S}_{\boldsymbol{Q}} \subset \Re^n$ with N possible states $\boldsymbol{q}^{(j)} \in \mathcal{S}_{\boldsymbol{Q}}$, $j = 1..N$.

The random process is a Markov chain if the probability of an event at $t^{(k)}$ only depends on the event at $t^{(k-1)}$, *i.e.*

$$\begin{aligned} &\mathbb{P}\left(\boldsymbol{Q}(t^{(k)}) = \boldsymbol{q}^{(j)} | \boldsymbol{Q}(t^{(k-1)}) = \boldsymbol{q}^{k-1},\right. \\ &\qquad \left.\boldsymbol{Q}(t^{(k-2)}) = \boldsymbol{q}^{k-2},\, ...,\, \boldsymbol{Q}(t^{(2)}) = \boldsymbol{q}^{2},\, \boldsymbol{Q}(t^{(1)}) = \boldsymbol{q}^{1}\right) = \\ &\qquad\qquad \mathbb{P}\left(\boldsymbol{Q}(t^{(k)}) = \boldsymbol{q}^{(j)} | \boldsymbol{Q}(t^{(k-1)}) = \boldsymbol{q}^{k-1}\right) = \,...\,, \end{aligned} \tag{A.78}$$

where $\boldsymbol{q}^{p-1} \in \mathcal{S}_{\boldsymbol{Q}}$ denotes the state taken by $\boldsymbol{Q}(t^{(p-1)})$.

Transition matrix & homogeneous Markov chain. For an homogeneous Markov chain process indexed in the discrete set $\mathcal{T} = (t^{(1)}, ..., t^{(k)}, ...)$, with $0 \leq t^{(1)} < t^{(2)} < ... < t^{(k-1)} < t^{(k)}$, and assuming $t^{(k)} - t^{(k-1)} = t^{(k-1)} - t^{(k-2)} = ... = \Delta t$, one has a transition probability that depends only on $\Delta t = t^{(i)} - t^{(i-1)}$ with,

$$\begin{aligned} p_{\boldsymbol{Q}}\left(\boldsymbol{q}^{(i)};\, \boldsymbol{q}^{(j)},\, \Delta t\right) &= \mathbb{P}\left(\boldsymbol{Q}(t^{(k)}) = \boldsymbol{q}^{(j)} | \boldsymbol{Q}(t^{(k-1)}) = \boldsymbol{q}^{(i)}\right) \\ &= \mathbb{P}\left(\boldsymbol{Q}(t^{(k-1)}) = \boldsymbol{q}^{(j)} | \boldsymbol{Q}(t^{(k-2)}) = \boldsymbol{q}^{(i)}\right)\,, \end{aligned} \tag{A.79}$$

where $p_{\boldsymbol{Q}}\left(\boldsymbol{q}^{(i)};\, \boldsymbol{q}^{(j)},\, \Delta t\right)$ is the transition probability of the homogeneous process, which corresponds to a conditional probability mass function, and which defines the transition matrix

$$\mathbf{P}_{\boldsymbol{Q}}\left(\Delta t\right) = \begin{pmatrix} p_{\boldsymbol{Q}}\left(\boldsymbol{q}^{(1)};\, \boldsymbol{q}^{(1)},\, \Delta t\right) & ... & p_{\boldsymbol{Q}}\left(\boldsymbol{q}^{(1)};\, \boldsymbol{q}^{(m)},\, \Delta t\right) & ... & p_{\boldsymbol{Q}}\left(\boldsymbol{q}^{(1)};\, \boldsymbol{q}^{(N)},\, \Delta t\right) \\ ... & ... & ... & ... & ... \\ p_{\boldsymbol{Q}}\left(\boldsymbol{q}^{(n)};\, \boldsymbol{q}^{(1)},\, \Delta t\right) & ... & p_{\boldsymbol{Q}}\left(\boldsymbol{q}^{(n)};\, \boldsymbol{q}^{(n)},\, \Delta t\right) & ... & p_{\boldsymbol{Q}}\left(\boldsymbol{q}^{(n)};\, \boldsymbol{q}^{(N)},\, \Delta t\right) \\ ... & ... & ... & ... & ... \\ p_{\boldsymbol{Q}}\left(\boldsymbol{q}^{(N)};\, \boldsymbol{q}^{(1)},\, \Delta t\right) & ... & p_{\boldsymbol{Q}}\left(\boldsymbol{q}^{(N)};\, \boldsymbol{q}^{(m)},\, \Delta t\right) & ... & p_{\boldsymbol{Q}}\left(\boldsymbol{q}^{(N)};\, \boldsymbol{q}^{(N)},\, \Delta t\right) \end{pmatrix}. \tag{A.80}$$

The transition matrix is a stochastic matrix, *i.e.* of non-negative entries $p_{\boldsymbol{Q}}\left(\boldsymbol{q}^{(i)};\, \boldsymbol{q}^{(j)},\, \Delta t\right) \geq 0$ and whose rows have a unit sum $\sum_{j=1}^{N} p_{\boldsymbol{Q}}\left(\boldsymbol{q}^{(i)};\, \boldsymbol{q}^{(j)},\, \Delta t\right) = 1$, and its entries are denoted $P_{\boldsymbol{Q}_{rs}}\left(\Delta t\right) = p_{\boldsymbol{Q}}\left(\boldsymbol{q}^{(r)};\, \boldsymbol{q}^{(s)},\, \Delta t\right)$.

Stationary distribution. Considering the Markov chain process indexed in the discrete set $\mathcal{T} = (t^{(1)}, \ldots, t^{(k)}, \ldots)$, with $0 \leq t^{(1)} < t^{(2)} < \ldots < t^{(k-1)} < t^{(k)}$ and assuming $t^{(k)} - t^{(k-1)} = t^{(k-1)} - t^{(k-2)} = \ldots = \Delta t$, the distribution at sampling point $t^{(j)}$ is represented by the vector

$$\boldsymbol{\pi}_{\boldsymbol{Q}}\left(t^{(j)}\right) = \left[\mathbb{P}\left(\boldsymbol{Q}(t^{(j)}) = \boldsymbol{q}^{(1)}\right) \quad \ldots \quad \mathbb{P}\left(\boldsymbol{Q}(t^{(j)}) = \boldsymbol{q}^{(N)}\right)\right]^T , \tag{A.81}$$

with its entry $\{\boldsymbol{\pi}_{\boldsymbol{Q}}\left(t^{(j)}\right)\}_r = \pi_{\boldsymbol{Q}}\left(\boldsymbol{q}^{(r)};\, t^{(j)}\right) \in [0,\, 1]$ and $\sum_{i=1}^{N} \pi_{\boldsymbol{Q}}\left(\boldsymbol{q}^{(i)};\, t^{(j)}\right) = 1$. Assuming a homogeneous chain, one has $\boldsymbol{\pi}_{\boldsymbol{Q}}^T\left(t^{(j+1)}\right) = \boldsymbol{\pi}_{\boldsymbol{Q}}^T\left(t^{(j)}\right)\mathbf{P}_{\boldsymbol{Q}}(\Delta t)$.

The distribution $\boldsymbol{\pi}_{\boldsymbol{Q}}$ is a stationary distribution of the homogeneous chain if

$$\boldsymbol{\pi}_{\boldsymbol{Q}}^T = \boldsymbol{\pi}_{\boldsymbol{Q}}^T\mathbf{P}_{\boldsymbol{Q}}(\Delta t) = \boldsymbol{\pi}_{\boldsymbol{Q}}^T\mathbf{P}_{\boldsymbol{Q}}^m(\Delta t) \quad \forall m \in \mathbb{N}_0 \,. \tag{A.82}$$

Reversibility. If $\boldsymbol{Q}(\mathcal{T}) = \{\boldsymbol{Q}(t^{(i)}) :\ t^{(i)} \in \mathcal{T}\}$, with $\mathcal{T} = (t^{(1)}, \ldots, t^{(k)})$ and assuming $t^{(k)} - t^{(k-1)} = t^{(k-1)} - t^{(k-2)} = \ldots = \Delta t$, is an irreducible non-null persistent Markov chain with transition matrix $\mathbf{P}_{\boldsymbol{Q}}\left(\Delta t\right)$ and stationary distribution $\boldsymbol{\pi}_{\boldsymbol{Q}}$, the sequence $\boldsymbol{Y}(\mathcal{T}) = \{\boldsymbol{Y}\left(t^{(i)}\right) = \boldsymbol{Q}\left(t^{(k-i+1)}\right) :\ t^{(i)} \in \mathcal{T},\ 1 \leq i \leq k\}$ is also a Markov chain with

$$\mathbb{P}\left(\boldsymbol{Y}(t^{(k)}) = \boldsymbol{q}^{(j)} | \boldsymbol{Y}(t^{(k-1)}) = \boldsymbol{q}^{(i)}\right) = \frac{\pi_{\boldsymbol{Q}}\left(\boldsymbol{q}^{(j)}\right)}{\pi_{\boldsymbol{Q}}\left(\boldsymbol{q}^{(i)}\right)} p_{\boldsymbol{Q}}\left(\boldsymbol{q}^{(j)};\, \boldsymbol{q}^{(i)},\, \Delta t\right) , \tag{A.83}$$

with no sum intended.

The Markov chain $\boldsymbol{Q}(\mathcal{T}) = \{\boldsymbol{Q}(t^{(i)}) :\ t^{(i)} \in \mathcal{T}\}$ is said to be reversible if its transition matrix is the same as the one of $\boldsymbol{Y}(\mathcal{T}) = \{\boldsymbol{Y}\left(t^{(i)}\right) = \boldsymbol{Q}\left(t^{(k-i+1)}\right) :\ t^{(i)} \in \mathcal{T},\ 1 \leq i \leq k\}$, *i.e.*

$$p_{\boldsymbol{Q}}\left(\boldsymbol{q}^{(i)};\, \boldsymbol{q}^{(j)},\, \Delta t\right) = \frac{\pi_{\boldsymbol{Q}}\left(\boldsymbol{q}^{(j)}\right)}{\pi_{\boldsymbol{Q}}\left(\boldsymbol{q}^{(i)}\right)} p_{\boldsymbol{Q}}\left(\boldsymbol{q}^{(j)};\, \boldsymbol{q}^{(i)},\, \Delta t\right) , \tag{A.84}$$

with no sum intended.

Appendix A.5.2. Markov chain Monte Carlo simulation of a discrete random vector

Let us consider a stationary random process $\boldsymbol{Q}(\mathcal{T}) = \{\boldsymbol{Q}(t^{(i)}) :\ t^{(i)} \in \mathcal{T} \subset \Re_0^+\}$ in the discrete set $\mathcal{T} = (t^{(1)}, \ldots, t^{(k)})$, with $t^{(j+1)} - t^{(j)} = \Delta t$ and $\boldsymbol{Q}(t^{(i)})$ taking values in a countable support $\mathcal{S}_{\boldsymbol{Q}} \subset \Re^n$, with N possible states $\boldsymbol{q}^{(j)} \in \mathcal{S}_{\boldsymbol{Q}}$, $j = 1..N$. Besides, it is assumed that the chain is reversible, so that the transition probability satisfies Eq. (A.84).

Having a pseudo-sample $\boldsymbol{q}\left(t^{(p)}\right) = \boldsymbol{q}^{(i)}$, the pseudo-sample $\boldsymbol{q}\left(t^{(p+1)}\right)$ can be constructed to simulate a random vector $\boldsymbol{Z}$ taking values in a countable support $\mathcal{S}_{\boldsymbol{Q}} \subset \Re^n$ and having as probability mass function $\pi_{\boldsymbol{Z}}\left(\boldsymbol{z}\right)$ the stationary distribution $\boldsymbol{\pi}_{\boldsymbol{Q}}$ of the Markov chain.

Principles. The general lines of the algorithm are

- The so-called proposal stochastic matrix $\mathbf{H}$ of size $N \times N$ is first constructed; Its entries are denoted $H_{i\,j}$, with $H_{i\,j} > 0$ and $\sum_{i=1}^{N} H_{i\,j} = 1$;
- The realisation $\boldsymbol{y}$ of the random vector $\boldsymbol{Y}$ is picked so that $\mathbb{P}\left(\boldsymbol{Y} = \boldsymbol{q}^{(j)} | \boldsymbol{q}\left(t^{(p)}\right) = \boldsymbol{q}^{(i)}\right) = H_{i\,j}$;

- The so-called acceptance matrix $\mathbf{A}$, with entries $0 \leq A_{i\,j} = a\left(\boldsymbol{q}^{(i)};\, \boldsymbol{q}^{(j)}\right) \leq 1$ and of size $N \times N$ is then constructed;
- Knowing $\boldsymbol{Y} = \boldsymbol{q}^{(j)}$, the pseudo-sample $\boldsymbol{q}\left(t^{(p+1)}\right)$ is constructed as follows

$$\boldsymbol{q}\left(t^{(p+1)}\right) = \begin{cases} \boldsymbol{q}^{(j)} & \text{with probability } A_{i\,j}; \\ \boldsymbol{q}\left(t^{(p)}\right) & \text{with probability } 1 - A_{i\,j}\,. \end{cases} \tag{A.85}$$

In order to define $\mathbf{H}$ and $\mathbf{A}$, following Grimmett and Stirzaker (2001), the transition probability of Eq. (A.85) reads

$$p_{\boldsymbol{Q}}\left(\boldsymbol{q}^{(i)};\, \boldsymbol{q}^{(j)},\, \Delta t\right) = \begin{cases} H_{i\,j} A_{i\,j} & \text{if } i \neq j; \\ 1 - \sum_{j':\, j' \neq i} H_{i\,j'} A_{i\,j'} & \text{if } i = j\,; \end{cases} \tag{A.86}$$

and Eq. (A.84) is satisfied by the Hasting algorithm

$$A_{i\,j} = a\left(\boldsymbol{q}^{(i)};\, \boldsymbol{q}^{(j)}\right) = \begin{cases} \frac{\pi_{\boldsymbol{Z}}\left(\boldsymbol{q}^{(j)}\right) H_{j\,i}}{\pi_{\boldsymbol{Z}}\left(\boldsymbol{q}^{(i)}\right) H_{i\,j}} & \text{if } \frac{\pi_{\boldsymbol{Z}}\left(\boldsymbol{q}^{(j)}\right) H_{j\,i}}{\pi_{\boldsymbol{Z}}\left(\boldsymbol{q}^{(i)}\right) H_{i\,j}} < 1; \\ 1 & \text{if not}\,. \end{cases} \tag{A.87}$$

A particular case is studied here below.

Markov chain Monte Carlo simulation of a uni-variate random process/field. We here summarise the methodology developed by Blacklock et al. (2012) to generate pseudo-samples $q\left(t^{(p)}\right)$ satisfying the statistical properties of the random variable field $Q(\mathcal{T})$ (or random vector, of independent components, fields).

Considering a random process $Q(\mathcal{T}) = \{Q(t^{(i)})\,:\; t^{(i)} \in \mathcal{T} \subset \Re_0^+\}$ in the discrete set $\mathcal{T} = (t^{(1)},\, ...,\, t^{(k)},\, ...)$, with $t^{(k+1)} - t^{(k)} = \Delta t$ and $Q(t^{(i)})$ taking values in an uncountable support $\mathcal{S}_Q$, the random variable $Q\left(t^{(j)}\right)$ is then discretized on a $N = 2N^m + 1$-grid with values $q^{(m)} - \bar{q} = (m - N^m - 1)\Delta q$, with $m = 1..2N^m + 1$. This corresponds to the creation of a discrete random variable, so that the algorithms of Appendix A.5.1 can be applied. The distribution (A.81) of $Q\left(t^{(j)}\right)$ at sampling point $t^{(j)}$ is thus represented by the vector $\boldsymbol{\pi}_Q\left(t^{(j)}\right)$ of size $N = 2N^m + 1$.

We also define the associated cumulative distribution function

$$F_Q(q;\, t^{(j)}) = \begin{cases} 0 & \text{if } q < q^{(1)}\,; \\ \sum_{k:\, q^{(k)} < q} \mathbb{P}\left(Q(t^{(j)}) = q^{(k)}\right) & \text{if } q^{(1)} \leq q < q^{(2N_M+1)}\,; \\ 1 & \text{if } q^{(2N^m+1)} \leq q\,. \end{cases} \tag{A.88}$$

Assuming an homogeneous Markov chain process, one has

$$\boldsymbol{\pi}_Q^T\left(t^{(j+1)}\right) = \boldsymbol{\pi}_Q^T\left(t^{(j)}\right) \mathbf{P}_Q\left(\Delta t\right)\,, \tag{A.89}$$

with the probability transition matrix $\mathbf{P}_Q\left(\Delta t\right)$.

Assuming a stationary process of distribution $\boldsymbol{\pi}_Q$, the matrix $\mathbf{P}_Q$ has to be calibrated so that, in the asymptotic regime, the distribution $\boldsymbol{\pi}_Q\left(t^{(j)}\right)$, but also the correlation between $\boldsymbol{\pi}_Q(t^{(j)})$ and $\boldsymbol{\pi}_Q\left(t^{(j-1)}\right)$, are good approximations of the random field $Q(\mathcal{T})$ to be simulated.

Once the matrix $\mathbf{P}_Q$ has been calibrated, one can generate pseudo-samples following the argumentation by Blacklock et al. (2012).

- Generate a pseudo-sample u^1 from the random variable $U \sim \mathcal{U}_{0,1}$;
- Initialise the function $F_Q(q;\, t^{(1)})$ from the stationary distribution $\boldsymbol{\pi}_Q$ in order to avoid a transient stage;
- Compare u^1 with the function $F_Q(q;\, t^{(1)})$ to generate $q\left(t^{(1)}\right) = q^{(i)}$ with $F_Q(q^{(i)};\, t^{(1)}) \leq u^1 < F_Q(q^{(i+1)};\, t^{(1)})$, giving the first point of the pseudo-sample of the random process to be simulated;
- Repeat the iterative process
  1. Given the generated pseudo-sample $q\left(t^{(p)}\right) = q^{(i)}$ create the distribution vector $\boldsymbol{\pi}_Q(t^{(p)}) = [0 \ldots 1 \ldots 0]^T$ with the only non-zero entry at location i;
  2. Evaluate the distribution vector $\boldsymbol{\pi}_Q^T\left(t^{(p+1)}\right) = \boldsymbol{\pi}_Q^T\left(t^{(p)}\right)\mathbf{P}_Q$;
  3. Generate a pseudo-sample u^{p+1} from the random variable $U \sim \mathcal{U}_{0,1}$;
  4. Compare u^{p+1} with the function $F_Q\left(q;\, t^{(p+1)}\right)$ to generate $q\left(t^{(p+1)}\right) = q^{(j)}$ with $F_Q\left(q^{(j)};\, t^{(p+1)}\right) \leq u^{p+1} < F_Q\left(q^{(j+1)};\, t^{(p+1)}\right)$;
  5. Increment p and go back to step #1.

Appendix A.5.3. Markov Chain of continuous random vectors

We refer to the book by Soize (2017) for a complete description and give here the main concepts in order to build a Metropolis-Hasting Markov Chain Monte-Carlo algorithm.

Definition. Let us consider a random process $\boldsymbol{Q}(\mathcal{T}) = \{\boldsymbol{Q}(t^{(i)}) \,:\, t^{(i)} \in \mathcal{T} \subset \Re_0^+\}$ the collection of random vectors in the, here assumed discrete, set $\mathcal{T} = (t^{(1)},\, ...,\, t^{(k)},\, ...)$, with $0 \leq t^{(1)} < t^{(2)} < ... < t^{(k-1)} < t^{(k)}$. Besides, it is assumed that $\boldsymbol{Q}(t^{(i)})$ takes values in an uncountable support $\mathcal{S}_{\boldsymbol{Q}} \subset \Re^n$.

The random process is a Markov chain if the probability of an event at $t^{(k)}$ only depends on the event at $t^{(k-1)}$, *i.e.*

$$\begin{aligned}\mathbb{P}\left(\boldsymbol{Q}(t^{(k)}) \in \mathcal{A} | \boldsymbol{Q}(t^{(k-1)}) = \boldsymbol{q}^{k-1},\right.&\\ \left.\boldsymbol{Q}(t^{(k-2)}) = \boldsymbol{q}^{k-2},\, ...,\, \boldsymbol{Q}(t^{(2)}) = \boldsymbol{q}^2,\, \boldsymbol{Q}(t^{(1)}) = \boldsymbol{q}^1\right) &=\\ \mathbb{P}\left(\boldsymbol{Q}(t^{(k)}) \in \mathcal{A} | \boldsymbol{Q}(t^{(k-1)}) = \boldsymbol{q}^{k-1}\right)&\,, \end{aligned} \tag{A.90}$$

where $\boldsymbol{q}^p \in \mathcal{S}_{\boldsymbol{Q}}$ denotes the state taken by $\boldsymbol{Q}(t^{(p-1)})$.

Similarly, the random process $\boldsymbol{Q}(\Re_0^+) = \{\boldsymbol{Q}(t) \,:\, t \in \Re_0^+\}$, defined as the collection of random vectors indexed by continuous time and taking values in an uncountable support

$\mathscr{S}_{\boldsymbol{Q}} \subset \Re^n$, has a Markov property if the state at time $t + dt$ depends on the state at time t only, *i.e.* if

$$\begin{aligned}&\mathbb{P}\left(\boldsymbol{Q}(t) \in \mathscr{A} | \boldsymbol{Q}(s) = \boldsymbol{q},\right.\\ &\quad\left.\boldsymbol{Q}(t^k) = \boldsymbol{q}^k,\, ...,\, \boldsymbol{Q}(t^2) = \boldsymbol{q}^2,\, \boldsymbol{Q}(t^1) = \boldsymbol{q}^1\right) =\\ &\qquad\mathbb{P}\left(\boldsymbol{Q}(t) \in \mathscr{A} | \boldsymbol{Q}(s) = \boldsymbol{q}\right) ,\end{aligned} \tag{A.91}$$

where $0 \leq t^1 < ... < t^k < s < t$ and where $\boldsymbol{q}^p \in \mathscr{S}_{\boldsymbol{Q}}$ denotes the state taken by $\boldsymbol{Q}(t^p)$.

Transition probability (density) distribution. For an homogeneous Markov chain process indexed in the discrete set $\mathscr{T} = (t^{(1)}, ..., t^{(k)}, ...)$, with $0 \leq t^{(1)} < t^{(2)} < ... < t^{(k-1)} < t^{(k)}$, one has a transition probability that depends only on $\Delta t^k = t^{(k)} - t^{(k-1)}$ and neither on $t^{(k)}$ nor on $t^{(k-1)}$ with,

$$p_{\boldsymbol{Q}}\left(\boldsymbol{q};\, \mathscr{A},\, \Delta t^k\right) \;=\; \mathbb{P}\left(\boldsymbol{Q}(t^{(k)}) \in \mathscr{A} | \boldsymbol{Q}(t^{(k-1)}) = \boldsymbol{q}\right) = \int_{\mathscr{A}} \rho_{\boldsymbol{Q}}\left(\boldsymbol{q};\, \boldsymbol{q}',\, \Delta t^k\right) d\boldsymbol{q}' \,, \tag{A.92}$$

where $p_{\boldsymbol{Q}}\left(\boldsymbol{q};\, \mathscr{A},\, \Delta t^k\right)$ is a transition probability with $\int_{\boldsymbol{q}' \in \Re^n} p_{\boldsymbol{Q}}\left(\boldsymbol{q};\, d\boldsymbol{q}',\, \Delta t^k\right) = \int_{\boldsymbol{q}' \in \Re^n} \rho_{\boldsymbol{Q}}\left(\boldsymbol{q};\, \boldsymbol{q}',\, \Delta t^k\right) d\boldsymbol{q}'$ 1, and where $\rho_{\boldsymbol{Q}}\left(\boldsymbol{q};\, \boldsymbol{q}',\, \Delta t^k\right)$ is the transition probability density function of the homogeneous process. Therefore, for an homogeneous process, one can write

$$\begin{aligned}&\mathbb{P}\left(\boldsymbol{Q}(t^{(k)}) \in \mathscr{A}_k,\, ...,\, \boldsymbol{Q}(t^{(1)}) \in \mathscr{A}_1\right) =\\ &\int_{\mathscr{A}_k} ... \int_{\mathscr{A}_1} \pi_{\boldsymbol{Q}(t^{(1)}), ..., \boldsymbol{Q}(t^{(k)})}\left(\boldsymbol{q}^1,\, ...,\, \boldsymbol{q}^k;\, t^{(1)},\, ...,\, t^{(k)}\right) d\boldsymbol{q}^1 ... d\boldsymbol{q}^k =\\ &\int_{\mathscr{A}_k} ... \int_{\mathscr{A}_1} \pi_{\boldsymbol{Q}(t^{(1)})}\left(\boldsymbol{q}^1;\, t^{(1)}\right) \rho_{\boldsymbol{Q}}\left(\boldsymbol{q}^1;\, \boldsymbol{q}^2,\, \Delta t^2\right) ... \rho_{\boldsymbol{Q}}\left(\boldsymbol{q}^{k-1};\, \boldsymbol{q}^k,\, \Delta t^k\right) d\boldsymbol{q}^1 d\boldsymbol{q}^2 ... d\boldsymbol{q}^k \,,\end{aligned} \tag{A.93}$$

where we have used the transition probability density functions and where $\pi_{\boldsymbol{Q}(t^{(1)})}\left(\boldsymbol{q};\, t^{(1)}\right)$ is the probability density function of $\boldsymbol{Q}(t^{(1)})$.

Similarly, for an homogeneous Markov chain process indexed by a continuous time in $\Re_0^+$, with $0 \leq s < t$, one has a transition probability dependent on the difference $t - s$ and not on the time indices t and s with

$$p_{\boldsymbol{Q}}\left(\boldsymbol{q};\, \mathscr{A},\, t-s\right) \;=\; \mathbb{P}\left(\boldsymbol{Q}(t) \in \mathscr{A} | \boldsymbol{Q}(s) = \boldsymbol{q}\right) = \int_{\mathscr{A}} \rho_{\boldsymbol{Q}}\left(\boldsymbol{q};\, \boldsymbol{q}',\, t-s\right) d\boldsymbol{q}' \,, \tag{A.94}$$

where $p_{\boldsymbol{Q}}\left(\boldsymbol{q};\, \mathscr{A},\, t-s\right)$ is a transition probability, *i.e.* $p_{\boldsymbol{Q}}\left(\boldsymbol{q};\, \mathscr{A},\, \Delta t\right) : \Re^n \to [0,\, 1]$ and $\int_{\boldsymbol{q}' \in \Re^n} p_{\boldsymbol{Q}}\left(\boldsymbol{q};\, d\boldsymbol{q}',\, t-s\right) = \int_{\boldsymbol{q}' \in \Re^n} \rho_{\boldsymbol{Q}}\left(\boldsymbol{q};\, \boldsymbol{q}',\, t-s\right) d\boldsymbol{q}' = 1$, and where $\rho_{\boldsymbol{Q}}\left(\boldsymbol{q};\, \boldsymbol{q}',\, t-s\right)$ is the transition probability density function of the homogeneous process. Also, for an homogeneous process one can write

$$\begin{aligned}&\mathbb{P}\left(\boldsymbol{Q}(t^k) \in \mathscr{A}_k,\, ...,\, \boldsymbol{Q}(t^1) \in \mathscr{A}_1\right) =\\ &\int_{\mathscr{A}_k} ... \int_{\mathscr{A}_1} \pi_{\boldsymbol{Q}(t^1), ..., \boldsymbol{Q}(t^k)}\left(\boldsymbol{q}^1,\, ...,\, \boldsymbol{q}^k;\, t^1,\, ...,\, t^k\right) d\boldsymbol{q}^1 ... d\boldsymbol{q}^k =\\ &\int_{\mathscr{A}_k} ... \int_{\mathscr{A}_1} \pi_{\boldsymbol{Q}(t^1)}\left(\boldsymbol{q}^1;\, t^1\right) \rho_{\boldsymbol{Q}}\left(\boldsymbol{q}^1;\, \boldsymbol{q}^2,\, \Delta t^2\right) ... \rho_{\boldsymbol{Q}}\left(\boldsymbol{q}^{k-1};\, \boldsymbol{q}^k,\, \Delta t^k\right) d\boldsymbol{q}^1 d\boldsymbol{q}^2 ... d\boldsymbol{q}^k \,,\end{aligned} \tag{A.95}$$

where we have used the transition probability density functions and where $\pi_{\boldsymbol{Q}(t^1)}\left(\boldsymbol{q};\, t^1\right)$ is the probability density function of $\boldsymbol{Q}(t^1)$.

Stationary distribution. Considering the stochastic process indexed in the discrete set $\mathcal{T} = (t^{(1)},\, ...,\, t^{(k)},\, ...)$, with $0 \leq t^{(1)} < t^{(2)} < ... < t^{(k-1)} < t^{(k)}$ and $\Delta t^i = t^{(i)} - t^{(i-1)}$, it is said to be stationary if, for a shift $u \geq 0$, one has

$$\mathbb{P}\left(\boldsymbol{Q}(t^{(k)} + u) \in \mathcal{A}_k,\, ...,\, \boldsymbol{Q}(t^{(1)} + u) \in \mathcal{A}_1\right) = \mathbb{P}\left(\boldsymbol{Q}(t^{(k)}) \in \mathcal{A}_k,\, ...,\, \boldsymbol{Q}(t^{(1)}) \in \mathcal{A}_1\right) . \tag{A.96}$$

A necessary and sufficient condition for a process to be stationary is to be homogeneous and to have $\pi_{\boldsymbol{Q}(t^{(i)})}\left(\boldsymbol{q};\, t^{(i)}\right) = \pi_{\boldsymbol{Q}}(\boldsymbol{q})$ the probability density function of $\boldsymbol{Q}(t^{(i)})$ independent on $t^{(i)}$. Since for a stationary process $\pi_{\boldsymbol{Q}(t^{(1)})}\left(\boldsymbol{q};\, t^{(1)}\right)$ is independent on $t^{(1)}$, Eq. (A.93) becomes

$$\mathbb{P}\left(\boldsymbol{Q}(t^{(k)}) \in \mathcal{A}_k,\, ...,\, \boldsymbol{Q}(t^{(1)}) \in \mathcal{A}_1\right) = \int_{\mathcal{A}_k} ... \int_{\mathcal{A}_1} \pi_{\boldsymbol{Q}}\left(\boldsymbol{q}_1\right) \rho_{\boldsymbol{Q}}\left(\boldsymbol{q}^1;\, \boldsymbol{q}^2,\, \Delta t^2\right) ... \rho_{\boldsymbol{Q}}\left(\boldsymbol{q}^{k-1};\, \boldsymbol{q}^k,\, \Delta t^k\right) d\boldsymbol{q}^1 d\boldsymbol{q}^2 ... d\boldsymbol{q}^k . \tag{A.97}$$

Similarly, considering the stochastic process indexed by a continuous time t in $\Re_0^+$ with $0 \leq t^1 < t^2 < ... < t^k$, with $\Delta t^i = t^i - t^{i-1}$, it is said to be stationary if, for a shift $u \geq 0$, one has

$$\mathbb{P}\left(\boldsymbol{Q}(t^k + u) \in \mathcal{A}_k,\, ...,\, \boldsymbol{Q}(t^1 + u) \in \mathcal{A}_1\right) = \mathbb{P}\left(\boldsymbol{Q}(t^k) \in \mathcal{A}_k,\, ...,\, \boldsymbol{Q}(t^1) \in \mathcal{A}_1\right) . \tag{A.98}$$

A necessary and sufficient condition for a process to be stationary is to be homogeneous and to have $\pi_{\boldsymbol{Q}(t^i)}\left(\boldsymbol{q};\, t^i\right) = \pi_{\boldsymbol{Q}}(\boldsymbol{q})$ the probability density function of $\boldsymbol{Q}(t^i)$ independent on t^i. Therefore, Eq. (A.95) is rewritten

$$\mathbb{P}\left(\boldsymbol{Q}(t^k) \in \mathcal{A}_k,\, ...,\, \boldsymbol{Q}(t^1) \in \mathcal{A}_1\right) = \int_{\mathcal{A}_k} ... \int_{\mathcal{A}_1} \pi_{\boldsymbol{Q}}\left(\boldsymbol{q}^1\right) \rho_{\boldsymbol{Q}}\left(\boldsymbol{q}^1;\, \boldsymbol{q}^2,\, \Delta t^2\right) ... \rho_{\boldsymbol{Q}}\left(\boldsymbol{q}^{k-1};\, \boldsymbol{q}^k,\, \Delta t^k\right) d\boldsymbol{q}^1 d\boldsymbol{q}^2 ... d\boldsymbol{q}^k . \tag{A.99}$$

Wiener process. A process $\boldsymbol{W}(\Re_0^+) = \{\boldsymbol{W}(t) :\, t \in \Re_0^+\}$ defined as the collection of random vectors valued in $\Re^n$ and indexed by a continuous time is said to be a normalised Wiener process if i) the $\Re$-valued processes W_i, $i = 1..n$, are mutually independent; ii) $\boldsymbol{W}(0) = \boldsymbol{0}_n$; iii) $\{\boldsymbol{W}(t) :\ t \in \mathcal{T} \subset \Re_0^+\}$ is a process with random increments; and (iv) $\Delta\boldsymbol{W}^{st} = \boldsymbol{W}(t) - \boldsymbol{W}(s)$, $0 \leq s < t$, in an $\Re^n$ valued second order zero-mean Gaussian random vector of covariance matrix $\tilde{\mathbf{R}}_{\boldsymbol{W}^{st}} = (t - s)\mathbf{I}_n \in \mathbb{M}_n^+(\Re)$, for $t > s$.

The normalised Wiener stochastic process $\boldsymbol{W}(\Re_0^+)$ is a homogeneous Markov process with the transition probability density function written for $t > s$,

$$\rho_{\boldsymbol{W}}\left(\boldsymbol{w};\, \boldsymbol{w}',\, t - s\right) = \frac{1}{\left(2\pi(t-s)\right)^{\frac{n}{2}}} \exp\left(-\frac{1}{2}\frac{(\boldsymbol{w}' - \boldsymbol{w})^T(\boldsymbol{w}' - \boldsymbol{w})}{t - s}\right) . \tag{A.100}$$

The probability density function of $\boldsymbol{W}(t)$ reads for $t > 0$

$$\pi_{\boldsymbol{W}(t)}\left(\boldsymbol{w};\, t\right) = \frac{1}{(2\pi t)^{\frac{n}{2}}} \exp\left(-\frac{1}{2}\frac{\boldsymbol{w}^T\boldsymbol{w}}{t}\right) , \tag{A.101}$$

which depends on t showing that the Wiener process is not stationary.

Appendix A.5.4. Markov chain Monte Carlo simulation of a continuous random vector

Let us consider a stationary random process $\boldsymbol{Q}(\mathscr{T}) = \{\boldsymbol{Q}(t^{(i)}) : t^{(i)} \in \mathscr{T} \subset \Re_0^+\}$ in the discrete set $\mathscr{T} = (t^{(1)}, ..., t^{(k)}, ...)$, with $t^{(k)} - t^{(k-1)} = \Delta t$ and $\boldsymbol{Q}(t^{(i)})$ taking values in an uncountable support $\mathscr{S}_{\boldsymbol{Q}} \subset \Re^n$.

Having a pseudo-sample $\boldsymbol{q}\left(t^{(p)}\right) = \boldsymbol{q}^p$, the pseudo-sample $\boldsymbol{q}\left(t^{(p+1)}\right)$ can be constructed in order to simulate a random vector $\boldsymbol{Z}$ taking values in $\Re^n$ and having as distribution density function $\pi_{\boldsymbol{Z}}\left(\boldsymbol{z}\right)$ the stationary distribution $\boldsymbol{\pi}_{\boldsymbol{Q}\left(t^{(i)}\right)}\left(\boldsymbol{q};\, t^{(i)}\right) = \boldsymbol{\pi}_{\boldsymbol{Q}}\left(\boldsymbol{q}\right)$ of the Markov chain.

Principles. The general lines of the algorithm are

- The so-called proposal distribution density $\rho\left(\boldsymbol{q};\, \boldsymbol{y}\right)$ is constructed with $\rho\left(\boldsymbol{q};\, \boldsymbol{y}\right) > 0$ and $\int_{\Re^n} \rho\left(\boldsymbol{q};\, \boldsymbol{y}\right) d\boldsymbol{y} = 1$;
- The realisation $\boldsymbol{y}$ of the random vector $\boldsymbol{Y}$ is picked from the probability distribution $\pi_{\boldsymbol{Y}|\boldsymbol{Q}(t^{(p)})}\left(\boldsymbol{y}|\boldsymbol{q}\left(t^{(p)}\right)\right) d\boldsymbol{y} = \rho\left(\boldsymbol{q}^p;\, \boldsymbol{y}\right) d\boldsymbol{y}$;
- Construct an acceptance ratio $a\left(\boldsymbol{q}^p;\, \boldsymbol{q}\right)$ with $0 \leq a\left(\boldsymbol{q}^p;\, \boldsymbol{q}\right) \leq 1$;
- Knowing $\boldsymbol{y}$, the pseudo-sample $\boldsymbol{q}\left(t^{(p+1)}\right)$ is constructed as follows

$$\boldsymbol{q}\left(t^{(p+1)}\right) = \begin{cases} \boldsymbol{y} & \text{with probability } a\left(\boldsymbol{q}^p;\, \boldsymbol{y}\right); \\ \boldsymbol{q}\left(t^{(p)}\right) = \boldsymbol{q}^p & \text{with probability } 1 - a\left(\boldsymbol{q}^p;\, \boldsymbol{y}\right). \end{cases} \tag{A.102}$$

The equivalent of the Hasting acceptance (A.87) reads

$$a\left(\boldsymbol{q}^p;\, \boldsymbol{q}\right) = \begin{cases} \frac{\pi_{\boldsymbol{Z}}(\boldsymbol{q})\rho(\boldsymbol{q};\, \boldsymbol{q}^p)}{\pi_{\boldsymbol{Z}}(\boldsymbol{q}^p)\rho(\boldsymbol{q}^p;\, \boldsymbol{q})} & \text{if } \frac{\pi_{\boldsymbol{Z}}(\boldsymbol{q})\rho(\boldsymbol{q};\, \boldsymbol{q}^p)}{\pi_{\boldsymbol{Z}}(\boldsymbol{q}^p)\rho(\boldsymbol{q}^p;\, \boldsymbol{q})} < 1; \\ 1 & \text{if not}. \end{cases} \tag{A.103}$$

Common particular choices for the proposal distribution density and acceptance ratio are described here below.

Metropolis Hastings algorithm. The proposal matrix has to be chosen, and there is no general form. Here we consider a normal distribution (17) centred on the previous realisation with a covariance matrix regularly adapted as proposed by Haario et al. (1999), *i.e.*

$$\rho\left(\boldsymbol{q};\, \boldsymbol{y}\right) = \mathcal{N}_{\boldsymbol{q},\, \frac{2.38^2}{n}\tilde{\mathbf{R}}_{\boldsymbol{Q}}}\left(\boldsymbol{y}\right), \tag{A.104}$$

where $\tilde{\mathbf{R}}_{\boldsymbol{Q}} \in \mathbb{M}_n^+(\Re)$ is the covariance matrix updated from the last N_k sampling.

The algorithm is as follows

- Initialise $\tilde{\mathbf{R}}_{\boldsymbol{Q}}$ to the $n \times n$ identity matrix $\mathbf{I}_n$;
- Take an initial pseudo-sample $\boldsymbol{q}\left(t^{(1)}\right) \in \Re^n$;
- Repeat the iterative process

1. Given the pseudo-sample $\boldsymbol{q}(t^{(p)}) = \boldsymbol{q}^p$, generate a pseudo-sample $\boldsymbol{y}^{p+1}$ from $\boldsymbol{Y} \sim \mathcal{N}_{\boldsymbol{q}(t^{(p)}),\, \frac{2.38^2}{n}\tilde{\mathbf{R}}_{\boldsymbol{Q}}}$;
2. Evaluate the Hasting acceptance (A.103), which simplifies because the proposal matrix is symmetric into
$$a\left(\boldsymbol{q}(t^{(p)});\, \boldsymbol{y}^{p+1}\right) = \begin{cases} \frac{\pi_{\boldsymbol{Z}}\left(\boldsymbol{y}^{p+1}\right)}{\pi_{\boldsymbol{Z}}\left(\boldsymbol{q}(t^{(p)})\right)} & \text{if } \frac{\pi_{\boldsymbol{Z}}\left(\boldsymbol{y}^{p+1}\right)}{\pi_{\boldsymbol{Z}}\left(\boldsymbol{q}(t^{(p)})\right)} < 1; \\ 1 & \text{if not}\,. \end{cases} \tag{A.105}$$
3. Generate a pseudo-sample u^{p+1} from the random variable $U \sim \mathcal{U}_{0,1}$;
4. If $a\left(\boldsymbol{q}(t^{(p)});\, \boldsymbol{y}^{p+1}\right) \geq u^{p+1}$ then $\boldsymbol{q}(t^{(p+1)}) = \boldsymbol{y}^{p+1}$; If $a\left(\boldsymbol{q}(t^{(p)});\, \boldsymbol{y}^{p+1}\right) < u^{p+1}$ reject the pseudo-sample and go back to step #1;
5. For steps $p+1 = x \cdot N_k$, $x \in \mathbb{N}$ reevaluate the covariance matrix, *i.e.*
$$\tilde{\mathbf{R}}_{\boldsymbol{Q}} = \frac{1}{N_k - 1}\sum_{k=1}^{N_k}\left(\boldsymbol{q}(t^{(p-N_k+1+k)}) - \mathbb{E}[\boldsymbol{Q}]\right)\left(\boldsymbol{q}(t^{(p-N_k+1+k)}) - \mathbb{E}[\boldsymbol{Q}]\right)^T ; \tag{A.106}$$
6. Increment p and go back to step #1.

- Do not consider the first thousands of pseudo-samples in order to have a stationary process.

Gibbs sampling. Each step of the Gibbs sampling process corresponds in replacing the value of the component i of the sampled vector by a value drawn from the conditional distribution of that variable knowing the remaining components. The proposal matrix thus reads

$$\rho\left(\boldsymbol{q};\, \boldsymbol{y}\right) = \pi_{Z_i|Z_1,\ldots,Z_{i-1},Z_{i+1},\ldots,Z_n}\left(y_i|q_1,\, \ldots,\, q_{i-1},\, q_{i+1},\, \ldots,\, q_n\right)\,. \tag{A.107}$$

This method thus requires the possibility to build the conditional distributions, contrarily to the Metropolis Hastings algorithm. However, because of the definition of the proposal (A.107), the Hasting acceptance (A.103) simplifies into

$$a\left(\boldsymbol{q}^p;\, \boldsymbol{q}\right) = 1\,, \tag{A.108}$$

since

$$\begin{aligned}\frac{\pi_{\boldsymbol{Z}}\left(\boldsymbol{q}\right)\rho\left(\boldsymbol{q};\, \boldsymbol{q}^p\right)}{\pi_{\boldsymbol{Z}}\left(\boldsymbol{q}^p\right)\rho\left(\boldsymbol{q}^p;\, \boldsymbol{q}\right)} &= \frac{\pi_{\boldsymbol{Z}}\left(\boldsymbol{q}\right)\pi_{Z_i|Z_1,\ldots,Z_{i-1},Z_{i+1},\ldots,Z_n}\left(q_i^p|q_1,\, \ldots,\, q_{i-1},\, q_{i+1},\, \ldots,\, q_n\right)}{\pi_{\boldsymbol{Z}}\left(\boldsymbol{q}^p\right)\pi_{Z_i|Z_1,\ldots,Z_{i-1},Z_{i+1},\ldots,Z_n}\left(q_i|q_1^p,\, \ldots,\, q_{i-1}^p,\, q_{i+1}^p,\, \ldots,\, q_n^p\right)} \\ &= \frac{\pi_{\boldsymbol{Z}}\left(\boldsymbol{q}\right)\pi_{Z_i|\boldsymbol{Z}_{-i}}\left(q_i^p|\boldsymbol{q}_{-i}\right)}{\pi_{\boldsymbol{Z}}\left(\boldsymbol{q}^p\right)\pi_{Z_i|\boldsymbol{Z}_{-i}}\left(q_i|\boldsymbol{q}_{-i}^p\right)} = \frac{\pi_{Z_i|\boldsymbol{Z}_{-i}}\left(q_i|\boldsymbol{q}_{-i}\right)\pi_{\boldsymbol{Z}_{-i}}\left(\boldsymbol{q}_{-i}\right)\pi_{Z_i|\boldsymbol{Z}_{-i}}\left(q_i^p|\boldsymbol{q}_{-i}\right)}{\pi_{Z_i|\boldsymbol{Z}_{-i}}\left(q_i^p|\boldsymbol{q}_{-i}^p\right)\pi_{\boldsymbol{Z}_{-i}}\left(\boldsymbol{q}_{-i}^p\right)\pi_{Z_i|\boldsymbol{Z}_{-i}}\left(q_i|\boldsymbol{q}_{-i}^p\right)} \\ &= \frac{\pi_{Z_i|\boldsymbol{Z}_{-i}}\left(q_i|\boldsymbol{q}_{-i}^p\right)\pi_{\boldsymbol{Z}_{-i}}\left(\boldsymbol{q}_{-i}^p\right)\pi_{Z_i|\boldsymbol{Z}_{-i}}\left(q_i^p|\boldsymbol{q}_{-i}^p\right)}{\pi_{Z_i|\boldsymbol{Z}_{-i}}\left(q_i^p|\boldsymbol{q}_{-i}^p\right)\pi_{\boldsymbol{Z}_{-i}}\left(\boldsymbol{q}_{-i}^p\right)\pi_{Z_i|\boldsymbol{Z}_{-i}}\left(q_i|\boldsymbol{q}_{-i}^p\right)} = 1\,,\end{aligned} \tag{A.109}$$

where $\boldsymbol{Z}_{-i} = [Z_1 \ldots Z_{i-1}\, Z_{i+1} \ldots Z_n]^T$ is the random vector with realisations $\boldsymbol{z}_{-i}$ in $\Re^{n-1}$, and where we have used the fact that $\boldsymbol{q}_{-i} = \boldsymbol{q}_{-i}^p$.

The algorithm is as follows

- Take an initial pseudo-sample $\boldsymbol{q}\left(t^{(1)}\right) \in \Re^n$;
- Repeat the iterative process
    1. Given the pseudo-sample $\boldsymbol{q}(t^{(p)}) = \boldsymbol{q}^p$, select the component $i \in [1,\, n]$ either from a uniform distribution or following a given order;
    2. Generate a pseudo-sample y^{p+1} from Y defined using the conditional distribution $Y \sim \pi_{Z_i|Z_1,\dots,Z_{i-1},Z_{i+1},\dots,Z_n}\left(y|q_1^p,\, \dots,\, q_{i-1}^p,\, q_{i+1}^p,\, \dots,\, q_n^p\right)$;
    3. The new pseudo-sample is constructed as $\boldsymbol{q}^{p+1} = [q_1^p \dots q_{i-1}^p\; y^{p+1}\; q_{i+1}^p \dots q_n^p]^T$;
    4. The Hasting acceptance (A.103) simplifies into $a\left(\boldsymbol{q}(t^{(p)});\, \boldsymbol{q}^{p+1}\right) = 1$, so that pseudo-sample $\boldsymbol{q}(t^{(p+1)}) = \boldsymbol{q}^{p+1}$ is accepted;
    5. Increment p and go back to step #1.
- Do not consider the first thousands of pseudo-samples in order to have a stationary process.

Itô Stochastic Differential Equations (ISDEs). Considering the random vector $\boldsymbol{Z}$ with a probability density function $\pi_{\boldsymbol{Z}}(\boldsymbol{z})$, we assume the support $\mathcal{S}_{\boldsymbol{Z}} = \Re^n$, the cases of bounded supports being detailed by Soize (2017). There is thus a potential function $\phi(\boldsymbol{z})$, assumed to be continuous, and a normalisation constant c such that

$$\pi_{\boldsymbol{Z}}(\boldsymbol{z}) = c\exp\left(-\phi(\boldsymbol{z})\right) . \tag{A.110}$$

The ISDEs are defined as a Markov stochastic process $\left\{(\boldsymbol{Q}(t),\, \boldsymbol{Y}(t)) : t \in \Re_0^+\right\}$ on the probability space $(\mathcal{Q}, \mathcal{F}, \mathbb{P})$, with value in $\Re^n \times \Re^n$, indexed on $\Re_0^+$. The ISDEs are defined for $t > 0$ as

$$\mathrm{d}\boldsymbol{Q}(t) = \boldsymbol{Y}(t)\mathrm{d}t\,, \tag{A.111}$$

$$\mathrm{d}\boldsymbol{Y}(t) = -\nabla_{\boldsymbol{q}}\phi\left(\boldsymbol{Q}(t)\right)dt - \frac{1}{2}f_0\boldsymbol{Y}(t)\mathrm{d}t + \sqrt{f_0}\mathrm{d}\boldsymbol{W}(t)\,, \tag{A.112}$$

with the initial conditions

$$\boldsymbol{Q}(0) = \boldsymbol{z}_0 \in \Re^n\,, \quad \boldsymbol{Y}(0) = \boldsymbol{y}_0 \in \Re^n\,, \quad \boldsymbol{W}(0) = \boldsymbol{0}_n\,, \tag{A.113}$$

where $\boldsymbol{W}(t)$ consists in a normalised Wiener process valued in $\Re^n$, see Appendix A.5.3, and $f_0 > 0$ is an algorithmic parameter. In general the initial boundary conditions are taken as $\boldsymbol{z}_0 = \boldsymbol{0}$ and y_{0_r} sampled from $Y_{0_r} \sim \mathcal{N}_{0,1}$.

There is a unique asymptotic stationary solution, which is a Markov process with

$$\lim_{t\to\infty}\pi_{\boldsymbol{Q}(t),\boldsymbol{Y}(t)}(\boldsymbol{q},\, \boldsymbol{y};\, t,\, t)d\boldsymbol{q}d\boldsymbol{y} = \rho_s(\boldsymbol{q};\, \boldsymbol{y})d\boldsymbol{q}d\boldsymbol{y} \tag{A.114}$$

with

$$\rho_s(\boldsymbol{q};\, \boldsymbol{y}) = c_2\exp\left(-\frac{1}{2}\boldsymbol{y}^T\boldsymbol{y} - \phi(\boldsymbol{q})\right)\,, \tag{A.115}$$

where c_2 is a normalisation constant. As a result, using the definition (A.110), one has

$$\lim_{t\to\infty}\pi_{\boldsymbol{Q}(t)}(\boldsymbol{q};\, t) = \pi_{\boldsymbol{Z}}(\boldsymbol{q})\,, \tag{A.116}$$

showing that the stationary state of the Markov chain process $\boldsymbol{Q}(\Re_0^+)$ can simulate the random vector $\boldsymbol{Z}$ taking values in $\Re^n$ and having as distribution density function $\pi_{\boldsymbol{Z}}\left(\boldsymbol{z}\right)$ since it corresponds to the stationary distribution $\pi_{\boldsymbol{Q}}\left(\boldsymbol{q}\right)$ of the Markov chain process $\boldsymbol{Q}(\Re_0^+)$.

The ISDEs presented in Eqs. (A.111-A.112) are discretised and integrated using the Störmer-Verlet scheme. The continuous index parameter t is discretized into $t^{(0)}$, $t^{(1)}$, ..., $t^{(l)}$, ... with the constant sampling step Δt and $t^{(l)} = l\Delta t$. Using the following notations $\boldsymbol{Q}^l = \boldsymbol{Q}(t^{(l)})$, $\boldsymbol{Y}^l = \boldsymbol{Y}(t^{(l)})$ and $\boldsymbol{W}^l = \boldsymbol{W}(t^{(l)})$, the Störmer-Verlet scheme yields

$$\begin{aligned}
\boldsymbol{Q}^{l+\frac{1}{2}} &= \boldsymbol{Q}^l + \frac{\Delta t}{2}\boldsymbol{Y}^l\,,\\
\boldsymbol{Y}^{l+1} &= \frac{1-\alpha}{1+\alpha}\boldsymbol{Y}^l + \frac{\Delta t}{1+\alpha}\boldsymbol{L}^{l+\frac{1}{2}} + \frac{\sqrt{f_0}}{1+\alpha}\Delta\boldsymbol{W}^{l+1}\,,\\
\boldsymbol{Q}^{l+1} &= \boldsymbol{Q}^{l+\frac{1}{2}} + \frac{\Delta t}{2}\boldsymbol{Y}^{l+1}\,,
\end{aligned} \tag{A.117}$$

where $\boldsymbol{L}^{l+\frac{1}{2}} = \boldsymbol{L}\left(\boldsymbol{Q}^{l+\frac{1}{2}}\right)$, with $\boldsymbol{L}\left(\boldsymbol{q}\right) = -\boldsymbol{\nabla}_{\boldsymbol{q}}\phi(\boldsymbol{q})$, and $\alpha = f_0\Delta t/4$.

The generation algorithm consists in evaluating the stationary state of the realisation path $\left\{(\boldsymbol{Q}(t;\, q),\, \boldsymbol{Y}(t;\, q)) :\, t\in\Re_0^+\right\}$, *i.e.* for given $q\in\mathfrak{Q}$ of the stochastic process, as follows

- Take initial conditions $\boldsymbol{Q}(0;\, q) = \boldsymbol{0}$ and $\boldsymbol{Y}(0;\, q)$ drawn from n zero-mean normalised Gaussian distributions;
- Consider a time integration with $t^{(l)} = l\Delta t$, and generate a Wiener process realisation $\boldsymbol{W}(\Re^+,\, q) = \{\boldsymbol{W}(t;\, q) :\, t\in\Re^+\}$ from which the increments $\Delta\boldsymbol{W}^l(q)$ arise;
- Integrate the differential equations using the Störmer-Verlet scheme (A.117) yielding one realisation path $\left\{(\boldsymbol{Q}(t;\, q),\, \boldsymbol{Y}(t;\, q)) :\, t\in\Re_0^+\right\}$ of the stationary diffusion process;
- Extract the pseudo-samples $\boldsymbol{q}^p = \boldsymbol{Q}\left(pM_0\Delta t;\, q\right)$, where M_0 is a positive integer sampling parameter.

Appendix A.6. Spectral Generator

Let us consider the continuous random vector field $\boldsymbol{Q}(\Omega) = \{\boldsymbol{Q}(\boldsymbol{x}) :\, \boldsymbol{x}\in\Omega\}$ for $\Omega\subset\Re^d$ a space of material points $\boldsymbol{x}$, with $d = 3$ in this section. Its expectation (26) is denoted by $\bar{\boldsymbol{q}}\left(\boldsymbol{x}\right) = \mathbb{E}\left[\boldsymbol{Q}\left(\boldsymbol{x}\right)\right] :\, \Omega\to\Re^n$, and its covariance matrix by $\tilde{\mathbf{R}}_{\boldsymbol{Q}}\left(\boldsymbol{x};\, \boldsymbol{\tau}\right)$, see Eq. (50). We assume that the random field is homogeneous, *i.e.* we consider the covariance matrix $\tilde{\mathbf{R}}_{\boldsymbol{Q}}\left(\boldsymbol{\tau}\right) :\, \Re^d\to\Re^{n\times n}$.

Appendix A.6.1. Gaussian random field generator

In this section we detail the spectral representation method (Shinozuka and Jan, 1972), which is applied to generate the required Gaussian random field $\boldsymbol{Q}(\Omega) = \{\boldsymbol{Q}(\boldsymbol{x}) : \boldsymbol{x} \in \Omega\}$.

The covariance entries are denoted $\tilde{R}_{\boldsymbol{Q}_{r\,s}}(\boldsymbol{\tau})\,,\ r,\, s = 1..n$. In order to use the Discrete Fourier Transform (DFT), we first define the covariance matrices set $\tilde{\mathbf{R}}[\boldsymbol{\tau}]$ as

$$\tilde{R}_{r\,s}[\boldsymbol{\tau}] = \left\{R_{\boldsymbol{Q}_{r\,s}}\left(\boldsymbol{\tau}^{(n_x\,n_y\,n_z)}\right)\right\}, \tag{A.118}$$

where the set of discrete positions $\boldsymbol{\tau} = \left\{\boldsymbol{\tau}^{(n_x\,n_y\,n_z)}\right\}$ is defined by its vector components $\boldsymbol{\tau}^{(n_x\,n_y\,n_z)} = [n_x\Delta\tau_x\ \ n_y\Delta\tau_y\ \ n_z\Delta\tau_z]^T$, where $\Delta\tau_i$, for $i = x,\, y,\, z$, is the spatial increment in each dimension i and where $n_i = 0,\, 1,\, 2,\, ...,\, N_i - 1$, for $i = x,\, y,\, z$, with N_i the total number of discrete points in each dimension i. Depending on the spatial size, $[l_x\, l_y\, l_z]^T$, of the random field to be generated, it is required that $N_i\Delta\tau_i \geq l_i$ (with no sum on i intended). This is achieved through a zero-padding once $\tilde{\mathbf{R}}(\boldsymbol{\tau})$ reaches zero, allowing the number of points N_i to be increased as required. The set of covariance matrix $\tilde{\mathbf{R}}[\boldsymbol{\tau}]$ is now periodised by adding extra discrete points at its end in order to satisfy

$$\begin{aligned}\tilde{\mathbf{R}}\left([(N_x - 1 + j)\Delta\tau_x\ (N_y - 1 + k)\Delta\tau_y\ (N_z - 1 + p)\Delta\tau_z]^T\right) &= \\ \tilde{\mathbf{R}}\left([(N_x - j)\Delta\tau_x\ (N_y - k)\Delta\tau_y\ (N_z - p)\Delta\tau_z]^T\right)& \\ \text{for}\quad j = 1..N_x - 1;\ k = 1..N_y - 1;\ p = 1..N_z - 1\,,&\end{aligned} \tag{A.119}$$

and to have $2N_i - 1$ discrete points along each dimension.

The indices set $\mathbf{m}$ is defined by the vector components $\boldsymbol{m}^{(m_x\,m_y\,m_z)} = [m_x\ m_y\ m_z]^T$ with $m_i = 0,\, 1,\, ...,\, 2N_i - 2$ for $i = x,\, y,\, z$. The increments in the frequency domain are defined in each direction as

$$\Delta\kappa_i = \frac{1}{(2N_i - 1)\Delta\tau_i}, \quad i = x,\, y,\, z\,, \tag{A.120}$$

allowing defining the set $\boldsymbol{\kappa} = \left\{\boldsymbol{\kappa}^{(m_x\,m_y\,m_z)}\right\}$ of sampling points in the frequency domain from the vector components $\boldsymbol{\kappa}^{(m_x\,m_y\,m_z)} = \left[\kappa_x^{(m_x)}\ \kappa_y^{(m_y)}\ \kappa_z^{(m_z)}\right]^T$ defined as (no sum on $i = x,\, y,\, z$)

$$\kappa_i^{(m_i)} = \begin{cases} m_i\Delta\kappa_i & \text{if}\quad m_i < (2N_i - 1)/2; \\ [m_i - (2N_i - 1)]\Delta\kappa_i & \text{if}\quad m_i > (2N_i - 1)/2; \end{cases} \tag{A.121}$$

where the second case is consider in order to avoid the failure of power and logarithm identities during the inverse DFT of the coming random field generation.

The spectral density matrix $\mathbf{S}[\boldsymbol{\kappa}]$ of the covariance matrices set $\tilde{\mathbf{R}}[\boldsymbol{\tau}]$ is computed using the DFT method following

$$\begin{aligned} & S_{r\,s}\left(\boldsymbol{\kappa}^{(m_x\,m_y\,m_z)}\right) \\ = \quad & \Delta\tau_x\Delta\tau_y\Delta\tau_z \sum_{n_x=0}^{2N_x-2}\sum_{n_y=0}^{2N_y-2}\sum_{n_z=0}^{2N_z-2} \tilde{R}_{r\,s}\left(\boldsymbol{\tau}^{(n_x\,n_y\,n_z)}\right) e^{-2\pi i \boldsymbol{\kappa}^{(m_x\,m_y\,m_z)}.\boldsymbol{\tau}^{(n_x\,n_y\,n_z)}} \\ = \quad & \Delta\tau_x\Delta\tau_y\Delta\tau_z \sum_{n_x=0}^{2N_x-2}\sum_{n_y=0}^{2N_y-2}\sum_{n_z=0}^{2N_z-2} \tilde{R}_{r\,s}\left(\boldsymbol{\tau}^{(n_x\,n_y\,n_z)}\right) e^{-2\pi i\left(\frac{m_x n_x}{2N_x-1}+\frac{m_y n_y}{2N_y-1}+\frac{m_z n_z}{2N_z-1}\right)}\,, \end{aligned} \tag{A.122}$$

for $m_i < (2N_i - 1)/2$. We note that the matrix $S_{r\,s}\left(\boldsymbol{\kappa}^{(m_x\,m_y\,m_z)}\right)$ actually depends on $\boldsymbol{m}^{(m_x\,m_y\,m_z)}$ and not $\boldsymbol{\kappa}^{(m_x\,m_y\,m_z)}$. The matrix $\mathbf{S}\left(\boldsymbol{\kappa}^{(m_x\,m_y\,m_z)}\right)$ is an Hermitian matrix, which can be expressed as

$$\mathbf{S}\left(\boldsymbol{\kappa}^{(m_x m_y m_z)}\right) = \mathbf{H}\left(\boldsymbol{\kappa}^{(m_x\,m_y\,m_z)}\right)\mathbf{H}^*\left(\boldsymbol{\kappa}^{(m_x\,m_y\,m_z)}\right)\,, \tag{A.123}$$

with $\mathbf{H}^*\left(\boldsymbol{\kappa}^{(m_x\,m_y\,m_z)}\right)$ the conjugate transpose of the matrix $\mathbf{H}\left(\boldsymbol{\kappa}^{(m_x\,m_y\,m_z)}\right)$.

Eventually, a pseudo-sample realisation of random field $\boldsymbol{Q}(\Omega)$ is generated as a set of random vector realisations $\boldsymbol{q}^p(\boldsymbol{x})$ at different locations $\boldsymbol{x}^{(i)} \in \Omega$, with for entry r of a realisation

$$\begin{aligned} q_r^p(\boldsymbol{x}^{(i)}) = \bar{q}_r + \sqrt{2\Delta}\Re\Bigg\{ & \sum_{s=1}^{n}\sum_{m_x=0}^{2N_x-2}\sum_{m_y=0}^{2N_y-2}\sum_{m_z=0}^{2N_z-2} H_{r\,s}\left(\boldsymbol{\kappa}^{(m_x\,m_y\,m_z)}\right) \\ & \eta^{(s\,m_x\,m_y\,m_z)} e^{2\pi i\left(\boldsymbol{x}^{(i)}\cdot\boldsymbol{\kappa}^{(m_x\,m_y\,m_z)}+\theta^{(s\,m_x\,m_y\,m_z)}\right)}\Bigg\}\,, \end{aligned} \tag{A.124}$$

where $\Delta = \Delta\kappa_x\Delta\kappa_y\;\Delta\kappa_z$, where $\theta^{(s\,m_x\,m_y\,m_z)}$ is an independent random variable (for each s, m_x, m_y, m_z) sampled from $\Theta \sim \mathcal{U}_{0,1}$, and where $\eta^{(s\,m_x\,m_y\,m_z)}$ can be defined in the two following ways

$$\eta^{(s\,m_x\,m_y\,m_z)} = \begin{cases} 1 & \text{yields a Gaussian field only when} \\ & N_x,\ N_y,\ N_z \rightarrow \infty; \\ \sqrt{-\log\varphi^{(s\,m_x\,m_y\,m_z)}} & \text{yields a Gaussian field when} \\ & \varphi^{(s\,m_x\,m_y\,m_z)} \text{ is sampled from } \Phi \sim \mathcal{U}_{0,1}. \end{cases} \tag{A.125}$$

Appendix A.6.2. Non-Gaussian random field generator

In order to generate a non-Gaussian random field, the described method of Appendix A.6.1 is first applied to generate an intermediate Gaussian random field. Afterwards, this Gaussian stochastic vector field is transformed into a non-Gaussian random field using proper mapping techniques, see for example the work by Popescu et al. (1998).

The Discrete Fourier Transform (DFT), Eq. (A.122), was computed on evenly spaced discrete points using the periodised covariance matrices set $\tilde{R}_{r\,s}[\boldsymbol{\tau}]$, with the set of discrete positions $\boldsymbol{\tau} = \{\boldsymbol{\tau}^{(n_x\,n_y\,n_z)}\}$. This defines the target spectrum $S_{r\,s}^{\text{cont Target}}(\boldsymbol{\kappa}) = (\Delta\tau_x\Delta\tau_y\Delta\tau_z)S_{r\,s}^{\text{Target}}(\boldsymbol{\kappa})$

evaluated in the frequency range at $\boldsymbol{\kappa}$ as

$$\begin{aligned} S^{\text{cont Target}}_{r\,s}(\boldsymbol{\kappa}) &= (\Delta\tau_x\Delta\tau_y\Delta\tau_z) S^{\text{Target}}_{r\,s}(\boldsymbol{\kappa}) \\ &= (\Delta\tau_x\Delta\tau_y\Delta\tau_z) \sum_{n_x=0}^{2N_x-2} \sum_{n_y=0}^{2N_y-2} \sum_{n_z=0}^{2N_z-2} \tilde{R}_{r\,s}\left(\boldsymbol{\tau}^{(n_x\,n_y\,n_z)}\right) e^{-2\pi i \boldsymbol{\tau}^{(n_x\,n_y\,n_z)}\cdot\boldsymbol{\kappa}}\,, \end{aligned} \tag{A.126}$$

where $\mathbf{S}^{\text{cont Target}}(\boldsymbol{\kappa})$ is the continuous form of the spectrum $\mathbf{S}^{\text{Target}}(\boldsymbol{\kappa})$, $\boldsymbol{\tau}^{(n_x\,n_y\,n_z)}$ are the spatial points coordinates, $[\Delta\tau_x\ \Delta\tau_y\ \Delta\tau_z]^T$ the coordinates increments and $\tilde{\mathbf{R}}(\boldsymbol{\tau})$ the periodised covariance matrix following Eq. (A.119).

A pseudo-sample of the non-Gaussian vector field is obtained following the steps:

- Construct the inverse $F^{-1}_{Q_r} : [0, 1] \to \mathscr{S}_{Q_r}$ of the marginal cumulative distribution functions, assumed to be continuous and of support $\mathscr{S}_{Q_r}$, of the components r of the random vector $\boldsymbol{Q}$;

- Initialise the spectrum of the Gaussian spectral representation $\mathbf{S}^{\text{cont}\,n^{(0)}}(\boldsymbol{\kappa}) = \mathbf{S}^{\text{cont Target}}(\boldsymbol{\kappa})$; and iteration index at $(k) = 0$;

- Repeat until convergence
  1. Generate the Gaussian pseudo-samples $\{\boldsymbol{q}^{n^p}(\boldsymbol{x}^{(i)})\}$ of the Gaussian field $\boldsymbol{Q}^{n}(\Omega)$ from Eq. (A.124) using as spectrum $\mathbf{S}^{\text{cont}\,n^{(k)}}(\boldsymbol{\kappa})$ (in the continuous form);
  2. Evaluate the expectation $\bar{q}_r$ and the standard deviation $\sigma_{Q^n_r}$ from the pseudo-samples $\boldsymbol{q}^{n^p}$;
  3. Following Deodatis and Micaletti (2001), map the Gaussian field to a non-Gaussian field by
  $$q^{\text{NG}^p}_r(\boldsymbol{x}^{(i)}) = F^{-1}_{Q_r}\left[F^{n}_{\bar{q}_r,\sigma^2_{Q^n_r}}\left(q^{n^p}_r(\boldsymbol{x}^{(i)})\right)\right]\,, \tag{A.127}$$
  where $F^{n}_{\bar{q}_r,\sigma^2_{Q^n_r}}(\bullet)$ is the marginal cumulative Gaussian distribution function, and $F^{-1}_{Q_r}$ is the inverse of the (targeted) marginal cumulative distribution function of the random variable Q_r;
  4. Compute the continuum spectrum $\mathbf{S}^{\text{cont NG}}(\boldsymbol{\kappa})$ of the non-Gaussian random field $\boldsymbol{Q}^{\text{NG}}(\Omega)$ obtained from Eq. (A.127) using the Fourier transform $\hat{\boldsymbol{Q}}^{\text{NG}}(\boldsymbol{\kappa})$ with
  $$\hat{\boldsymbol{Q}}^{\text{NG}}(\boldsymbol{\kappa}) = \sum_{\boldsymbol{x}^{(i)}=\boldsymbol{0}}^{\boldsymbol{l}} \left(\boldsymbol{q}^{\text{NG}^p}\left(\boldsymbol{x}^{(i)}\right) - \bar{\boldsymbol{q}}\right) e^{-2\pi i \boldsymbol{x}^{(i)}\cdot\boldsymbol{\kappa}}\,; \tag{A.128}$$
  and
  $$\mathbf{S}^{\text{cont NG}}(\boldsymbol{\kappa}) = \frac{\Delta\tau_x\Delta\tau_y\Delta\tau_z}{N^{\boldsymbol{x}}} \bar{\hat{\boldsymbol{Q}}}^{\text{NG}}(\boldsymbol{\kappa}) \left(\hat{\boldsymbol{Q}}^{\text{NG}}(\boldsymbol{\kappa})\right)^T\,, \tag{A.129}$$
  where $N^{\boldsymbol{x}}$ is the total number of discrete points of the generated field, and $\bar{\hat{\boldsymbol{Q}}}^{\text{NG}}(\boldsymbol{\kappa})$ is the conjugate of $\hat{\boldsymbol{Q}}^{\text{NG}}(\boldsymbol{\kappa})$; Because sample points of each random field are not

enough to calculate the converged spectrum $\mathbf{S}^{\text{cont NG}}(\boldsymbol{\kappa})$, thousands of pseudo-samples $\{\boldsymbol{q}^{\eta^p}(\boldsymbol{x}^{(i)})\}$ of the random fields are generated at once in step #1 to calculate the converged spectrum $\boldsymbol{S}^{\text{cont NG}}(\boldsymbol{\kappa})$ in this step;

5. Compare $\mathbf{S}^{\text{cont NG}}(\boldsymbol{\kappa})$ to $\mathbf{S}^{\text{cont Target}}(\boldsymbol{\kappa})$, the error being calculated by (Popescu et al., 1998)
$$e = \frac{\int_{\boldsymbol{\kappa}} \sum_r |S_{r\,r}^{\text{cont NG}}(\boldsymbol{\kappa}) - S_{r\,r}^{\text{cont Target}}(\boldsymbol{\kappa})| d\boldsymbol{\kappa}}{\int_{\boldsymbol{\kappa}} \sum_r |S_{r\,r}^{\text{cont Target}}(\boldsymbol{\kappa})| d\boldsymbol{\kappa}} \; ; \tag{A.130}$$
6. If $e < Tol$, then the pseudo-samples $\boldsymbol{q}^{\text{NG}^p}(\Omega)$ computed from Eq. (A.127) correspond to pseudo-samples of the random field $\boldsymbol{Q}(\Omega)$; Else, if $e > Tol$, update the spectrum $\mathbf{S}^{\text{cont}\,\eta^{(k)}}(\boldsymbol{\kappa})$ of the Gaussian spectral representation following Wu et al. (2016)
$$S_{r\,r}^{\text{cont}\,\eta^{(k+1)}}(\boldsymbol{\kappa}) = S_{r\,r}^{\text{cont}\,\eta^{(k)}}(\boldsymbol{\kappa}) \frac{S_{r\,r}^{\text{cont Target}}(\boldsymbol{\kappa})}{S_{r\,r}^{\text{cont NG}}(\boldsymbol{\kappa})} \, , \tag{A.131}$$
$$S_{r\,s}^{\text{cont}\,\eta^{(k+1)}}(\boldsymbol{\kappa}) = S_{r\,s}^{\text{cont}\,\eta^{(k)}}(\boldsymbol{\kappa}) \left(\frac{S_{r\,r}^{\text{cont Target}}(\boldsymbol{\kappa}) S_{s\,s}^{\text{cont Target}}(\boldsymbol{\kappa})}{S_{r\,r}^{\text{cont NG}}(\boldsymbol{\kappa}) S_{s\,s}^{\text{cont NG}}(\boldsymbol{\kappa})} \right)^{\frac{1}{2}} \; ; \tag{A.132}$$
Set $(k) = (k+1)$; and go back to step #1.

Appendix A.7. Data-driven probability sampling

The data-driven sampling method has been developed by Soize and Ghanem (2016).

Let us consider the probability space $(\mathcal{Q}, \mathcal{F}, \mathbb{P})$ and the random vector $\boldsymbol{Q} = [Q_1 \dots Q_n]^T : \mathcal{Q} \to \Re^n$ of dependent random variables Q_i and of support $\mathcal{S}_{\boldsymbol{Q}} \subset \Re^n$. The available information consists of a given set of N statistically independent realisations $\boldsymbol{q}^k = \boldsymbol{Q}(q^k)$, with $q^k \in \mathcal{Q}$, $k = 1..N$. It is further assumed that the local structure of the given data-set is preserved via a random matrix $\mathbf{Q} = [\boldsymbol{Q}^1 \dots \boldsymbol{Q}^k \dots \boldsymbol{Q}^N]$, which is defined on $(\mathcal{Q}, \mathcal{F}, \mathbb{P})$, with values in $\Re^{n \times N}$ and in which each column $\boldsymbol{Q}^k$, $k = 1..N$, is an independent copy of the random vector $\boldsymbol{Q}$. Therefore, the matrix $\mathbf{q} = [\boldsymbol{q}^1 \dots \boldsymbol{q}^k \dots \boldsymbol{q}^N]$ is a realisation of $\mathbf{Q}$.

A MCMC process is then used to generate extra data samples based on the matrix $\mathbf{q}$ following the detailed three sequential sub-processes:

- The original data-set $\boldsymbol{q}^k$, $k = 1..N$ is first normalised by removing the mean and scaling it to the unit variance using the PCA, see Appendix A.3.1, from the covariance matrix
$$\tilde{\mathbf{R}}_{\boldsymbol{Q}} = \frac{1}{N-1} \sum_{k=1}^{N} \left(\boldsymbol{q}^k - \bar{\boldsymbol{q}}\right) \left(\boldsymbol{q}^k - \bar{\boldsymbol{q}}\right)^{\mathrm{T}} \, , \tag{A.133}$$
with the mean $\bar{\boldsymbol{q}} = \frac{1}{N} \sum_{k=1}^{N} \boldsymbol{q}^k$; The normalised data-set is then computed from Eq. (A.21) by
$$\{\boldsymbol{\eta}^k\}_i = \frac{1}{\sqrt{\lambda_{\boldsymbol{Q}}^{(i)}}} (\boldsymbol{q}^k - \bar{\boldsymbol{q}})^T \boldsymbol{u}_{\boldsymbol{Q}}^{(i)} , \qquad k = 1..N, \qquad i = 1..n \, , \tag{A.134}$$

with the ordered eigen-values $\lambda_{\boldsymbol{Q}}^{(i)} > 0$, and the normalised eigen-vectors $\boldsymbol{u}_{\boldsymbol{Q}}^{(i)}$ of $\tilde{\mathbf{R}}_{\boldsymbol{Q}}$; The original data-set $\mathbf{q}$ of size $n \times N$ is thus transferred to $\boldsymbol{\eta} = [\boldsymbol{\eta}^1 \, ... \, \boldsymbol{\eta}^k \, ... \, \boldsymbol{\eta}^N]$ of size $n \times N$;

- The random data generating process is built through the following steps:
  1. The given data-set $\{\boldsymbol{\eta}^k : \; k = 1..N\}$ serves as N realisations of the random vector $\mathbf{H} : \mathcal{Q} \rightarrow \Re^n$ defined so that $\mathbb{E}[\mathbf{H}] = \mathbf{0}_n$ and $\tilde{\mathbf{R}}_{\mathbf{H}} = \mathbf{I}_n$ because of the PCA; The non-parametric estimate of the probability density function $\pi_{\mathbf{H}}$ is obtained using the Gaussian kernel-density estimation method, with

$$\pi_{\mathbf{H}}(\boldsymbol{\eta}) = \frac{1}{N} \sum_{i=1}^{N} \frac{1}{(\sqrt{2\pi}\hat{s}_n)^n} \exp\left(-\frac{1}{2\hat{s}_n^2} \| \frac{\hat{s}_n}{s_n} \boldsymbol{\eta}^i - \boldsymbol{\eta} \|^2 \right) , \tag{A.135}$$

     where $\|\boldsymbol{\eta}\|^2 = \eta_1^2 + ... + \eta_n^2$, and where the multidimensional optimal Silverman bandwidth s_n and parameter $\hat{s}_n$ read

$$s_n = \left[\frac{4}{N(2+n)} \right]^{1/(4+n)} , \quad \hat{s}_n = \frac{s_n}{\sqrt{s_n^2 + \frac{N-1}{N}}} ; \tag{A.136}$$

  2. Based on the observation data-set $\boldsymbol{\eta}$, a diffusion-map basis $\boldsymbol{\phi} \in \Re^{N \times N}$ is constructed as follows
     (a) Considering the Gaussian kernel defined on $\Re^n \times \Re^n$

$$k_\epsilon(\boldsymbol{\eta}^i, \boldsymbol{\eta}^j) = \exp\left(-\frac{1}{4\epsilon} \|\boldsymbol{\eta}^i - \boldsymbol{\eta}^j\|^2 \right) , \qquad i, j = 1..N , \tag{A.137}$$

     the symmetric matrix $\mathbf{K}$ is defined in $\mathbb{M}_N(\Re)$ with entries $K_{ij} = k_\epsilon(\boldsymbol{\eta}^i, \boldsymbol{\eta}^j)$;
     (b) A diagonal real matrix $\boldsymbol{\rho} = \mathrm{diag}(\rho^1, ..., \rho^N)$ is constructed in $\mathbb{M}_N$ with

$$\rho^i = \sum_{j=1}^{N} K_{ij}, \qquad i, j = 1..N ; \tag{A.138}$$

     (c) A symmetric matrix $\mathbf{P}_{\mathrm{s}}$ is then defined as

$$\mathbf{P}_{\mathrm{s}} = \boldsymbol{\rho}^{-1/2} \mathbf{K} \boldsymbol{\rho}^{-1/2} , \tag{A.139}$$

     with its eigen-values $\lambda_{\mathbf{P}_{\mathrm{s}}}^{(i)}$ and eigen-vectors $\boldsymbol{u}_{\mathbf{P}_{\mathrm{s}}}^{(i)}$, with $i = 1..N$. The definition of $\mathbf{P}_{\mathrm{s}}$, Eq. (A.139), and multiplying by $\boldsymbol{\rho}^{-1/2}$ its corresponding eigen-value problem, lead to

$$\boldsymbol{\rho}^{-1} \mathbf{K} \boldsymbol{\rho}^{-1/2} \boldsymbol{u}_{\mathbf{P}_{\mathrm{s}}}^{(i)} \;=\; \lambda_{\mathbf{P}_{\mathrm{s}}}^{(i)} \boldsymbol{\rho}^{-1/2} \boldsymbol{u}_{\mathbf{P}_{\mathrm{s}}}^{(i)} , \tag{A.140}$$

     which corresponds to the new eigen-value problem,

$$\mathbf{P} \boldsymbol{u}_{\mathbf{P}}^{(i)} \;=\; \lambda_{\mathbf{P}}^{(i)} \boldsymbol{u}_{\mathbf{P}}^{(i)} , \qquad i = 1..N , \tag{A.141}$$

with the matrix $\mathbf{P} = \boldsymbol{\rho}^{-1}\mathbf{K}$ and its eigen-values $\lambda_{\mathbf{P}}^{(i)} = \lambda_{\mathbf{P}_\mathrm{s}}^{(i)}$ and eigen-vectors $\boldsymbol{u}_{\mathbf{P}}^{(i)} = \boldsymbol{\rho}^{-1/2}\boldsymbol{u}_{\mathbf{P}_\mathrm{s}}^{(i)}$; Because of the definition of the diagonal matrix $\boldsymbol{\rho}$, Eq. (A.138), one has $\sum_{j=1}^{N} \mathbf{P}_{ij} = 1$, $\forall i = 1..N$; Therefore, $\mathbf{P}$ is a transition matrix, obtained in one step, of a Markov chain, see Appendix A.5.1;

(d) The diffusion map basis is defined by $\boldsymbol{\phi} = [\boldsymbol{\phi}^1 \,...\, \boldsymbol{\phi}^k \,...\, \boldsymbol{\phi}^N] \in \Re^{N\times N}$, such that

$$\boldsymbol{\phi}^k = \lambda_{\mathbf{P}}^{(k)}\boldsymbol{u}_{\mathbf{P}}^{(k)} \in \Re^N, \qquad k = 1..N\,; \tag{A.142}$$

Assuming the eigen-values of $\mathbf{P}$ are ordered in a descending order, it can be proved that

$$1 = \lambda_{\mathbf{P}}^{(1)} \geq \lambda_{\mathbf{P}}^{(2)} \geq ... \geq \lambda_{\mathbf{P}}^{(N)}\,; \tag{A.143}$$

A dimension reduction can be achieved by discarding the basis vectors corresponding to the eigen-values which are lower than a threshold value τ, such that

$$\tau \geq \lambda_{\mathbf{P}}^{(m+1)} \geq \lambda_{\mathbf{P}}^{(m+2)} \geq ... \geq \lambda_{\mathbf{P}}^{(N)}\,, \tag{A.144}$$

leading to the reduced basis $\boldsymbol{\phi}_\mathrm{r} = [\boldsymbol{\phi}^1 \,...\, \boldsymbol{\phi}^m] \in \Re^{N\times m}$.

Remembering that the given data-set $\boldsymbol{\eta}$ serves as N realisations of the random vector $\mathbf{H}$, it can also be seen as a realisation of the random matrix $\mathbf{V} = [\mathbf{H}^1 \,...\, \mathbf{H}^k \,...\, \mathbf{H}^N]$, which is defined on the probability space $(\mathcal{Q}, \mathcal{F}, \mathbb{P})$, with value in $\Re^{n\times N}$; This random matrix $\mathbf{V}$ is then represented using the reduced diffusion map basis $\boldsymbol{\phi}_\mathrm{r}$ as

$$\mathbf{V} = \mathbf{Z}\boldsymbol{\phi}_\mathrm{r}^\mathrm{T}\,, \tag{A.145}$$

in which

$$\mathbf{Z} = \mathbf{V}\mathbf{a}, \text{ with } \mathbf{a} = \boldsymbol{\phi}_\mathrm{r}\left(\boldsymbol{\phi}_\mathrm{r}^\mathrm{T}\boldsymbol{\phi}_\mathrm{r}\right)^{-1} \in \Re^{N\times m}\,; \tag{A.146}$$

In particular, using the realisation $\boldsymbol{\eta}$ of the stochastic matrix $\mathbf{V}$ yields the realisation

$$\mathbf{z} = \boldsymbol{\eta}\mathbf{a} \in \Re^{n\times m}\,; \tag{A.147}$$

Remark: In the absence of order reduction in the random vector generating process, the step of diffusion map basis construction is not necessary anymore and one has $\mathbf{a} = \mathbf{I}_{N\times N}$, $m = N$ and $\boldsymbol{\phi}_\mathrm{r} = \boldsymbol{\phi} = \mathbf{I}_N$;

3. Additional realisations of the random matrix $\mathbf{V}$ are computed through Eq. (A.145) with additional realisations of $\mathbf{Z}$, which are generated by solving the Itô stochastic differential equations (ISDEs), see Appendix A.5.4; Considering stochastic matrices, the ISDEs are defined as a Markov stochastic process $\left\{(\mathcal{Z}(r), \mathcal{Y}(r)) : r \in \Re_0^+\right\}$ on the probability space $(\mathcal{Q}, \mathcal{F}, \mathbb{P})$, with values in $\Re^{n\times m} \times \Re^{n\times m}$, indexed on $\Re_0^+$; The ISDEs for $r > 0$ are defined as

$$\mathrm{d}\mathcal{Z}(r) = \mathcal{Y}(r)\mathrm{d}r\,, \tag{A.148}$$

$$\mathrm{d}\mathcal{Y}(r) = \mathcal{L}(\mathcal{Z}(r))\mathrm{d}r - \frac{1}{2}f_0\mathcal{Y}(r)\mathrm{d}r + \sqrt{f_0}\mathrm{d}\mathcal{W}(r)\,, \tag{A.149}$$

with the initial conditions

$$\mathcal{Z}^0 = \mathbf{z} = \boldsymbol{\upeta}\mathbf{a}\,, \quad \mathcal{Y}^0 = \mathcal{N}\mathbf{a}\,, \quad \mathcal{W}^0 = \mathbf{0}_{n\times m}\,, \tag{A.150}$$

where $\mathcal{N}$ represents the random matrix whose entries are $n \times N$ independent random variables with normalised Gaussian distribution, and $\mathrm{d}\mathcal{W}(r) = \mathrm{d}\boldsymbol{W}(r)\mathbf{a}$ with $\mathrm{d}\mathbf{W}(r)$ consisting of a $n \times N$ independent normalised Wiener process; The term $\mathcal{L}\left(\mathcal{Z}(r)\right)$ of size $n \times m$ in Eq. (A.149) is expressed as

$$\mathcal{L}\left(\mathcal{Z}(r)\right) = \mathbf{L}\left(\mathcal{Z}(r)\boldsymbol{\upphi}_{\mathrm{r}}^{\mathrm{T}}\right)\mathbf{a}\,; \tag{A.151}$$

The columns of the matrix $\mathbf{L}\left(\mathbf{y}\right)$ read

$$\{\mathbf{L}\left(\mathbf{y}\right)\}_{:,i} = -\frac{\partial \mathcal{V}(\boldsymbol{g})}{\partial \boldsymbol{g}}|_{\boldsymbol{g}=\{\mathcal{Z}(r)\boldsymbol{\upphi}_{\mathrm{r}}^{\mathrm{T}}\}_{:\,i}}\,, \quad \forall i = 1..N\,, \tag{A.152}$$

where the potential $\mathcal{V}(\boldsymbol{g})$ is evaluated using column i of $\mathcal{Z}(r)\boldsymbol{\upphi}_{\mathrm{r}}^{\mathrm{T}}$ and is defined on $\Re^n$ from the probability density function (A.135), with values in $\Re^+$, *i.e.*

$$\mathcal{V}(\boldsymbol{g}) = -\log\left[\frac{1}{N}\sum_{j=1}^{N}\exp\left(-\frac{1}{2\hat{s}_n^2}\|\frac{\hat{s}_n}{s_n}\boldsymbol{\eta}^j - \boldsymbol{g}\|^2\right)\right]\,; \tag{A.153}$$

In this last equation, $\boldsymbol{\eta}^j$, $\forall j = 1..N$ are column vectors of the given data-set $\boldsymbol{\upeta}$, and the parameters $\hat{s}_n$ and s_n are defined in Eq. (A.136);

4. The ISDEs presented in Eqs. (A.148-A.149) is then solved with the Störmer-Verlet scheme (A.117); The continuous index parameter r is discretized into $r^{(0)}$, $r^{(1)}$, ..., $r^{(l)}$, ... with the constant sampling step Δr and $r^{(l)} = l\Delta r$; Performing the integration for one realisation $q \in \mathcal{Q}$ of the stochastic process yields the stationary state of the realisation path $\left\{(\mathcal{Z}(r;\,q),\, \mathcal{Y}(r;\,q)) : r \in \Re_0^+\right\}$; The additional realisations of $\mathbf{Z}$ are sampled after every M_0 steps of the realisation path $\left\{\mathcal{Z}(r;\,q) : r \in \Re_0^+\right\}$; Let $\mathbf{z}^p$ denote the additional samples of $\mathbf{Z}$, which take the value of $\mathcal{Z}(r^{(l)};\,q)$ at $l = pM_0$ with $p = 1..N^{\mathrm{MC}}$, where N^{MC} is the number of the required additional realisations and M_0 is a positive integer sampling parameter, hence, the additional realisations of the random matrix $\mathbf{V}$ are obtained by rewriting Eq. (A.145) as

$$\boldsymbol{\upeta}^p = \mathbf{z}^p\boldsymbol{\upphi}_{\mathrm{r}}^{\mathrm{T}} \in \Re^{n\times N}\,, \quad \forall p = 1..N^{\mathrm{MC}}\,. \tag{A.154}$$

- Generated data are finally expressed according to the original data-set using Eq. (A.134); The generated random data-set $\boldsymbol{\upeta}^p = [\boldsymbol{\eta}^{1^p}\ \ldots\ \boldsymbol{\eta}^{N^p}]$, with $p = 1..N^{\mathrm{MC}}$, is transferred back to recover the scale and mean of the original data-set by

$$\boldsymbol{q}^{i^p} = \bar{\boldsymbol{q}} + \sum_{j=1}^{n}\sqrt{\lambda_{\boldsymbol{Q}}^{(j)}}\boldsymbol{u}_{\boldsymbol{Q}}^{(j)}\eta_j^{i^p}\,, \quad \forall i = 1..N\,, \tag{A.155}$$

providing N additional pseudo-samples of $\boldsymbol{Q}$ for each $p = 1..N^{\mathrm{MC}}$.

Appendix B. Maximum Entropy framework

Let us consider the probability space $(\mathcal{Q},\, \mathcal{F},\, \mathbb{P})$ and the random vector $\boldsymbol{Q} = [Q_1 \,...\, Q_n]^T : \mathcal{Q} \to \Re^n$ of dependent random variables Q_i and of support $\mathcal{S}_{\boldsymbol{Q}} \subset \Re^n$.

Appendix B.1. Shannon entropy

The Shannon entropy $s\left(\pi_{\boldsymbol{Q}}\right) \in \Re$ ($\Re^+$ for discrete random variables) of the probability mass or density function $\pi_{\boldsymbol{Q}}$ represents the measure of the uncertainties of the random vector $\boldsymbol{Q}$, with

$$s\left(\pi_{\boldsymbol{Q}}\right) = - \sum_{\boldsymbol{q}^{(i)} \in \mathcal{S}_{\boldsymbol{Q}}} \pi_{\boldsymbol{Q}}(\boldsymbol{q}^{(i)}) \log\left(\pi_{\boldsymbol{Q}}(\boldsymbol{q}^{(i)})\right)\,, \tag{B.1}$$

and

$$s\left(\pi_{\boldsymbol{Q}}\right) = - \int_{\Re^n} \pi_{\boldsymbol{Q}}(\boldsymbol{q}) \log\left(\pi_{\boldsymbol{Q}}(\boldsymbol{q})\right) d\boldsymbol{q}\,, \tag{B.2}$$

for respectively discrete and continuous random vectors.

Appendix B.2. Maximum entropy principle

The maximum entropy principle allows constructing a probability mass or density function when only a limited amount of information is available. In this section we assume a continuous random vector.

Following Jaynes (2003), "Amongst the probability distributions that satisfy our incomplete information about the system, the probability distribution that maximises entropy is the least-biased estimate that can be made. It agrees with everything that is known but carefully avoids anything that is unknown."

In particular what is known are the support $\mathcal{S}_{\boldsymbol{Q}} \subset \Re^n$ of the distribution and some statistical properties written under the form

$$\int_{\Re^n} \boldsymbol{g}(\boldsymbol{q}) \pi_{\boldsymbol{Q}}(\boldsymbol{q}) d\boldsymbol{q} = \boldsymbol{b} \in \Re^m\,, \tag{B.3}$$

with the mapping $\boldsymbol{g}(\boldsymbol{q}) : \Re^n \to \Re^m$. As an example, statistical moments can be used to define the constraints.

The maximum entropy principle is then stated as

$$\begin{gathered}\pi_{\boldsymbol{Q}} = \arg\max_{\pi \in \mathcal{P}} s(\pi)\,, \qquad \text{with} \\ \mathcal{P} = \left\{ \pi \text{ of support } \mathcal{S}_{\boldsymbol{Q}} : \int_{\Re^n} \pi(\boldsymbol{q}) d\boldsymbol{q} = 1\,,\ \text{and} \int_{\Re^n} \boldsymbol{g}(\boldsymbol{q}) \pi(\boldsymbol{q}) d\boldsymbol{q} = \boldsymbol{b} \right\}\,.\end{gathered} \tag{B.4}$$

Appendix B.3. Constrained problem resolution

Following Agmon et al. (1979); Soize (2017), the optimisation problem (B.4) is solved by introducing Lagrange multipliers $(\lambda_0,\, \boldsymbol{\lambda}) \in \Re^+ \times \Re^m$ with $\int_{\Re^n} \exp\left(-\boldsymbol{\lambda}^T \boldsymbol{g}(\boldsymbol{q})\right) d\boldsymbol{q} < \infty$, yielding the Lagrangian

$$\mathcal{L}(\pi;\, \lambda_0,\, \boldsymbol{\lambda}) = s(\pi) - (\lambda_0 - 1) \left(\int_{\Re^n} \pi(\boldsymbol{q}) d\boldsymbol{q} - 1 \right) - \boldsymbol{\lambda}^T \left(\int_{\Re^n} \boldsymbol{g}(\boldsymbol{q}) \pi(\boldsymbol{q}) d\boldsymbol{q} - \boldsymbol{b} \right)\,. \tag{B.5}$$

The problem (B.4) is then substituted by finding the stationary point of $\mathscr{L}(\pi;\, \lambda_0,\, \boldsymbol{\lambda})$ at $\pi_{\boldsymbol{Q}}$ for $(\lambda_0,\, \boldsymbol{\lambda}) = (\lambda_0^{\text{sol}},\, \boldsymbol{\lambda}^{\text{sol}})$, with

$$\pi_{\boldsymbol{Q}}\left(\boldsymbol{q}\right) = \begin{cases} \frac{\exp\left(-\boldsymbol{\lambda}^{\text{sol}^T}\boldsymbol{g}(\boldsymbol{q})\right)}{\exp\left(\lambda_0^{\text{sol}}\right)} & \text{if } \boldsymbol{q} \in \mathscr{S}_{\boldsymbol{Q}} \;; \\ 0 & \text{if } \boldsymbol{q} \notin \mathscr{S}_{\boldsymbol{Q}} \;. \end{cases} \tag{B.6}$$

Finding the solution $(\lambda_0^{\text{sol}},\, \boldsymbol{\lambda}^{\text{sol}})$ usually requires a numerical method. First, the solution (B.6) is rewritten as

$$\pi_{\boldsymbol{Q}}\left(\boldsymbol{q}\right) = \begin{cases} \frac{\exp\left(-\boldsymbol{\lambda}^{\text{sol}^T}\boldsymbol{g}(\boldsymbol{q})\right)}{\int_{\mathscr{S}_{\boldsymbol{Q}}}\exp\left(-\boldsymbol{\lambda}^{\text{sol}^T}\boldsymbol{g}(\boldsymbol{q}')\right)d\boldsymbol{q}'} & \text{if } \boldsymbol{q} \in \mathscr{S}_{\boldsymbol{Q}} \;; \\ 0 & \text{if } \boldsymbol{q} \notin \mathscr{S}_{\boldsymbol{Q}} \;. \end{cases} \tag{B.7}$$

The constraints equation (B.3) then becomes

$$\frac{1}{\int_{\mathscr{S}_{\boldsymbol{Q}}} \exp\left(-\boldsymbol{\lambda}^{\text{sol}^T}\boldsymbol{g}(\boldsymbol{q}')\right)d\boldsymbol{q}'} \int_{\mathscr{S}_{\boldsymbol{Q}}} \boldsymbol{g}(\boldsymbol{q})\exp\left(-\boldsymbol{\lambda}^{\text{sol}^T}\boldsymbol{g}(\boldsymbol{q})\right)d\boldsymbol{q} = \boldsymbol{b}\,. \tag{B.8}$$

The dual optimisation problem of (B.4) is restated as finding $\boldsymbol{\lambda}^{\text{sol}} \in \Re^m$ such that

$$\boldsymbol{\lambda}^{\text{sol}} = \arg\min_{\boldsymbol{\lambda}}\Gamma(\boldsymbol{\lambda}) \text{ with } \Gamma(\boldsymbol{\lambda}) = \boldsymbol{\lambda}^T\boldsymbol{b} + \log\left(\int_{\mathscr{S}_{\boldsymbol{Q}}} \exp\left(-\boldsymbol{\lambda}^T\boldsymbol{g}(\boldsymbol{q}')\right)d\boldsymbol{q}'\right)\,, \tag{B.9}$$

since the gradient reads

$$\boldsymbol{\nabla}_{\boldsymbol{\lambda}}\Gamma(\boldsymbol{\lambda}) = \boldsymbol{b} - \frac{\int_{\mathscr{S}_{\boldsymbol{Q}}} \boldsymbol{g}(\boldsymbol{q}')\exp\left(-\boldsymbol{\lambda}^T\boldsymbol{g}(\boldsymbol{q}')\right)d\boldsymbol{q}'}{\int_{\mathscr{S}_{\boldsymbol{Q}}} \exp\left(-\boldsymbol{\lambda}^T\boldsymbol{g}(\boldsymbol{q}')\right)d\boldsymbol{q}'}\,, \tag{B.10}$$

showing that the constraints equation (B.8) is the solution of $\boldsymbol{\nabla}_{\boldsymbol{\lambda}}\Gamma(\boldsymbol{\lambda}) = 0$, justifying the optimisation problem (B.9). The problem (B.9), *i.e.* $\boldsymbol{\nabla}_{\boldsymbol{\lambda}}\Gamma(\boldsymbol{\lambda}) = 0$, is solved using a Newton Raphson method, with the Hessian

$$\begin{aligned} \boldsymbol{\nabla}_{\boldsymbol{\lambda}}\left(\boldsymbol{\nabla}_{\boldsymbol{\lambda}}\Gamma(\boldsymbol{\lambda})\right) \quad = \quad & \frac{\int_{\mathscr{S}_{\boldsymbol{Q}}} \left(\boldsymbol{g}(\boldsymbol{q}')\right)\left(\boldsymbol{g}(\boldsymbol{q}')\right)^T \exp\left(-\boldsymbol{\lambda}^T\boldsymbol{g}(\boldsymbol{q}')\right)d\boldsymbol{q}'}{\int_{\mathscr{S}_{\boldsymbol{Q}}} \exp\left(-\boldsymbol{\lambda}^T\boldsymbol{g}(\boldsymbol{q}')\right)d\boldsymbol{q}'} - \\ & \frac{\left(\int_{\mathscr{S}_{\boldsymbol{Q}}} \boldsymbol{g}(\boldsymbol{q}')\exp\left(-\boldsymbol{\lambda}^T\boldsymbol{g}(\boldsymbol{q}')\right)d\boldsymbol{q}'\right)\left(\int_{\mathscr{S}_{\boldsymbol{Q}}} \boldsymbol{g}(\boldsymbol{q}')\exp\left(-\boldsymbol{\lambda}^T\boldsymbol{g}(\boldsymbol{q}')\right)d\boldsymbol{q}'\right)^T}{\left(\int_{\mathscr{S}_{\boldsymbol{Q}}} \exp\left(-\boldsymbol{\lambda}^T\boldsymbol{g}(\boldsymbol{q}')\right)d\boldsymbol{q}'\right)^2}\,. \end{aligned} \tag{B.11}$$

Appendix C. Finite element resolution of the homogenisation problems

Appendix C.1. Resolution of the constrained micro-scale finite element problem

Appendix C.1.1. Constraint and kinematic matrices for PBCs

Using Eq. (125) allows relating the fluctuation $\boldsymbol{u}'$ to the nodal unknowns $\boldsymbol{u}^{(a)}$ on the boundary gathered in the nodal vector $\boldsymbol{d}_{\mathrm{m}}^{\pm}$, where the superscript "±" refers to all the boundary nodes, and Eq. (140) becomes

$$\boldsymbol{d}_{\mathrm{m}}^{\pm} - \mathbf{s}\boldsymbol{f}_{\mathrm{M}}^{\mathrm{k}} - \mathbf{a}\boldsymbol{d}_{\mathrm{m}}^{a} = 0\,, \tag{C.1}$$

where $\mathbf{a}$ is the constraint coefficients matrix constructed from the values of the interpolation bases $\varphi_{(k)}^{(i)}(\boldsymbol{x}^{-})$, where $\boldsymbol{a}_{(k)}^{(i)}$ with $k = 1, ..., n+1$ are gathered under the nodal vector $\boldsymbol{d}_{\mathrm{m}}^{a}$ of size $9(n+1)$ (3 surfaces $\partial\omega^{(i)}$ and three degrees of freedom per term $\boldsymbol{a}_{(k)}^{(i)}$), and where $\mathbf{s}$ is the assembly matrix of boundary nodal positions $\boldsymbol{x}^{\pm}$ from $\boldsymbol{X}$

$$\mathbf{s}_{3n^b\times 9} = \begin{bmatrix} \boldsymbol{x}_x^{\pm T} & 0_{1\times n^b} & 0_{1\times n^b} \\ \boldsymbol{x}_y^{\pm T} & 0_{1\times n^b} & 0_{1\times n^b} \\ \boldsymbol{x}_z^{\pm T} & 0_{1\times n^b} & 0_{1\times n^b} \\ 0_{1\times n^b} & \boldsymbol{x}_x^{\pm T} & 0_{1\times n^b} \\ 0_{1\times n^b} & \boldsymbol{x}_y^{\pm T} & 0_{1\times n^b} \\ 0_{1\times n^b} & \boldsymbol{x}_z^{\pm T} & 0_{1\times n^b} \\ 0_{1\times n^b} & 0_{1\times n^b} & \boldsymbol{x}_x^{\pm T} \\ 0_{1\times n^b} & 0_{1\times n^b} & \boldsymbol{x}_y^{\pm T} \\ 0_{1\times n^b} & 0_{1\times n^b} & \boldsymbol{x}_z^{\pm T} \end{bmatrix}^T , \tag{C.2}$$

where n^b is the number of boundary nodes.

The set of Eqs. (136) is then rewritten by considering as degrees of freedom $\boldsymbol{d}_m = [\boldsymbol{d}_{\mathrm{m}}^{IT} \;\; \boldsymbol{d}_{\mathrm{m}}^{\pm T} \;\; \boldsymbol{d}_{\mathrm{m}}^{aT}]^T$, where $\boldsymbol{d}_{\mathrm{m}}^{I}$ are the nodal degrees of freedom $\boldsymbol{u}^{(a)}$ of the n^I nodes not lying on the boundary $\partial\omega$.

The missing matrices read

$$\mathbf{c} = \begin{bmatrix} 0_{3n^b\times 3n^I} & \mathbf{I}_{3n^b\times 3n^b} & -\mathbf{a}_{3n^b\times 9(n+1)} \end{bmatrix} , \tag{C.3}$$

and

$$\mathbf{k}_{\mathrm{m}} = \begin{bmatrix} \mathbf{k}_m^{II} & \mathbf{k}_m^{I\pm} & 0_{3n^I\times 9(n+1)} \\ \mathbf{k}_m^{\pm I} & \mathbf{k}_m^{\pm\pm} & 0_{3n^b\times 9(n+1)} \\ 0_{9(n+1)\times 3n^I} & 0_{9(n+1)\times 3n^b} & 0_{9(n+1)\times 9(n+1)} \end{bmatrix} , \tag{C.4}$$

where the micro-scale BVP stiffness matrix (138) has been redefined in terms of the internal and boudary displacement degrees of freedom and completed to match the system size. More details about the implementation are given by Nguyen et al. (2017).

Appendix C.1.2. Resolution of the constrained meso-scale BVP

The set of Eqs. (136) is solved by the multiplier elimination method pioneered by Ainsworth (2001) and detailed by Nguyen et al. (2017). The first set of equations of the system (136) yields $\boldsymbol{\lambda} = \left(\mathbf{c}\mathbf{c}^T\right)^{-1} \mathbf{c}\boldsymbol{f}_{\mathrm{int}}$, allowing the system (136) to be rewritten under the residual form

$$\begin{cases} \boldsymbol{r}_{\mathrm{m}} = \boldsymbol{f}_{\mathrm{int}} - \mathbf{c}^T\boldsymbol{\lambda} = \mathbf{q}^T\boldsymbol{f}_{\mathrm{int}} = 0\,, \text{ and} \\ \boldsymbol{r}_{\mathrm{c}} = \mathbf{c}\boldsymbol{d}_{\mathrm{m}} - \mathbf{s}\boldsymbol{f}^{\mathrm{k}}_{\mathrm{M}} = 0\,, \end{cases} \tag{C.5}$$

with $\mathbf{q} = \mathbf{I} - \mathbf{c}^T \left(\mathbf{c}\mathbf{c}^T\right)^{-1} \mathbf{c}$. Linearizing the system (C.5) with respect to both the micro-scale unknown fields $\boldsymbol{d}_{\mathrm{m}}$ and the macro-scale kinematic field $\boldsymbol{f}^{\mathrm{k}}_{\mathrm{M}}$ leads to

$$\begin{cases} \boldsymbol{r}_{\mathrm{m}} + \mathbf{q}^T\mathbf{k}_{\mathrm{m}}\mathbf{q}\delta\boldsymbol{d}_{\mathrm{m}} - \mathbf{q}^T\mathbf{k}_{\mathrm{m}}\mathbf{c}^T\left(\mathbf{c}\mathbf{c}^T\right)^{-1}\left[\boldsymbol{r}_{\mathrm{c}} - \mathbf{s}\delta\boldsymbol{f}^{\mathrm{k}}_{\mathrm{M}}\right] = 0\,, \text{ and} \\ \boldsymbol{r}_{\mathrm{c}} + \mathbf{c}\delta\boldsymbol{d}_{\mathrm{m}} - \mathbf{s}\delta\boldsymbol{f}^{\mathrm{k}}_{\mathrm{M}} = 0\,, \end{cases} \tag{C.6}$$

where the stiffness matrix $\mathbf{k}_{\mathrm{m}}$ is given in Appendix C.1.1.

The solution of the meso-scale BVP is obtained by considering $\delta\boldsymbol{f}^{\mathrm{k}}_{\mathrm{M}} = 0$ in Eq. (C.6) and the solution reads

$$\delta\boldsymbol{d}_{\mathrm{m}} = -\tilde{\mathbf{k}}_{\mathrm{m}}^{-1}\tilde{\boldsymbol{r}}_{\mathrm{m}}\,, \tag{C.7}$$

with

$$\begin{cases} \tilde{\mathbf{k}}_{\mathrm{m}} = \mathbf{c}^T\mathbf{c} + \mathbf{q}^T\mathbf{k}_{\mathrm{m}}\mathbf{q}\,, \text{ and} \\ \tilde{\boldsymbol{r}}_{\mathrm{m}} = \boldsymbol{r}_{\mathrm{m}} + \left(\mathbf{c}^T - \mathbf{q}^T\mathbf{k}_{\mathrm{m}}\mathbf{c}^T\left(\mathbf{c}\mathbf{c}^T\right)^{-1}\right)\boldsymbol{r}_{\mathrm{c}}\,. \end{cases} \tag{C.8}$$

Appendix C.1.3. Extraction of homogenised material tensors

Following the Lagrange multiplier elimination approach detailed by Nguyen et al. (2017) and summarised in Appendix C.1.2, the fourth order macro-scale material tensors $\mathbb{c}_{\mathrm{M}}$ can be extracted in the matrix form $\mathbf{c}_{\mathrm{M}}$ as

$$\mathbf{c}_{\mathrm{M}} = \frac{\partial\boldsymbol{p}_{\mathrm{M}}}{\partial\boldsymbol{f}_{\mathrm{M}}} = \frac{\partial}{\partial\boldsymbol{d}_{\mathrm{m}}}\left(\frac{1}{V(\omega)}\int_{\omega}\boldsymbol{p}_{\mathrm{m}}d\boldsymbol{x}\right)\frac{\partial\boldsymbol{d}_{\mathrm{m}}}{\partial\boldsymbol{f}^{\mathrm{k}}_{\mathrm{M}}} = \mathbf{d}\frac{\partial\boldsymbol{d}_{\mathrm{m}}}{\partial\boldsymbol{f}^{\mathrm{k}}_{\mathrm{M}}}\,. \tag{C.9}$$

The last term on the right hand side is obtained by considering zero-residual in the system of Eqs. (C.6), yielding

$$\mathbf{c}_{\mathrm{M}} = \mathbf{d}\tilde{\mathbf{k}}_{\mathrm{m}}^{-1}\left(\mathbf{c}^T - \mathbf{q}^T\mathbf{k}_{\mathrm{m}}\mathbf{c}^T\left(\mathbf{c}\mathbf{c}^T\right)^{-1}\right)\mathbf{s}\,, \tag{C.10}$$

where the last term $\mathbf{d} = \frac{\partial}{\partial\boldsymbol{d}_{\mathrm{m}}}\left(\frac{1}{V(\omega)}\int_{\omega}\boldsymbol{p}_{\mathrm{m}}d\boldsymbol{x}\right)$ reads

$$\mathbf{d} = \frac{1}{V(\omega)}\bigwedge_{\omega^e}\int_{\omega^e}\mathbf{c}_{\mathrm{m}}\mathbf{b}^e d\boldsymbol{x}\,. \tag{C.11}$$

The extraction of the meso-scale material tensor (C.10) is obtained at no additional cost since the required matrix inverse $\tilde{\mathbf{k}}_{\mathrm{m}}^{-1}$ is the same as during the finite-element resolution (C.7).

Appendix C.2. Resolution of AH

For conciseness, in the following, we drop the reference to the random micro-structure ϖ symbol, and consider the realisation $\boldsymbol{u} = \boldsymbol{U}(\varpi)$, $\boldsymbol{\sigma} = \boldsymbol{\Sigma}(\varpi)$, $\boldsymbol{\varepsilon} = \mathbf{E}(\varpi)$, $\boldsymbol{\mu} = \mathbf{M}(\varpi)$, and the different material tensor realisations $\mathbb{c}^{\text{el}} = \mathbb{C}^{\text{el}}(\varpi)$ and $\mathbb{h} = \mathbb{H}(\varpi)$.

Appendix C.2.1. Resolution of the AH finite element problem

Omitting the reference to the macro-scale material point $\boldsymbol{X}$, each meso-scale problem is stated as finding the periodic $\overset{3}{\mathbb{h}}(\boldsymbol{x})$ with the periodicity constraint (158) such that

$$\int_{\omega} \boldsymbol{\varepsilon}_{\boldsymbol{x}}(\delta \boldsymbol{v}) : \mathbb{c}^{\text{el}}_{\text{m}}(\boldsymbol{x}) : [\mathbb{I} + \mathbb{h}(\boldsymbol{x})]\, d\boldsymbol{x} = 0 \quad \forall \delta \boldsymbol{v} \in \mathcal{U}^{\text{PBC}}(\omega)\,, \tag{C.12}$$

where $\mathbb{I}$ is the fourth-order identity tensor with $I_{ijkl} = \frac{1}{2}\delta_{ik}\delta_{jl} + \frac{1}{2}\delta_{il}\delta_{jk}$, and the fourth-order tensor $\mathbb{h}(\boldsymbol{x})$ is defined as $h_{ijkl} = \frac{1}{2}\frac{\partial}{\partial x_j}\overset{3}{h}_{ikl} + \frac{1}{2}\frac{\partial}{\partial x_i}\overset{3}{h}_{jkl}$.

Each component $\overset{3}{h}_{ijk}(\boldsymbol{x})$ is written under the form $\overset{3}{h}_{ijk}(\boldsymbol{x}) = \varphi^{(a)}(\boldsymbol{x})\overset{3}{h}{}^{(a)}_{ijk}$, where $\varphi^{(a)}(\boldsymbol{x})$ is the shape function related to the node $a = 1..n^{\text{node}}$ and $\overset{3}{h}{}^{(a)}_{ijk}$ is the nodal unknowns, with n^{node} the number of nodes. As a result $h_{ijkl}(\boldsymbol{x}) = \frac{1}{2}\frac{\partial}{\partial x_j}\overset{3}{h}_{ikl}(\boldsymbol{x}) + \frac{1}{2}\frac{\partial}{\partial x_i}\overset{3}{h}_{jkl}(\boldsymbol{x}) = \frac{1}{2}b_j^{(a)}(\boldsymbol{x})\overset{3}{h}{}^{(a)}_{ikl} + \frac{1}{2}b_i^{(a)}(\boldsymbol{x})\overset{3}{h}{}^{(a)}_{jkl}$, where $\boldsymbol{b}^{(a)}(\boldsymbol{x})$ is the gradient of the shape function at node $a = 1..n^{\text{node}}$.

Because $\overset{3}{h}{}^{(a)}_{ikl} = \overset{3}{h}{}^{(a)}_{ilk}$, the unknowns can be sorted in the matrix $\mathbf{d}_{\text{m}}$ with

$$\mathbf{d}_{\text{m}_{3n^{\text{node}}\times 6}} = \begin{bmatrix} \overset{3}{h}{}^{(1)}_{111} & \overset{3}{h}{}^{(1)}_{112} & \dots & \overset{3}{h}{}^{(1)}_{133} \\ \dots & \dots & \dots & \\ \overset{3}{h}{}^{(n^{\text{node}})}_{111} & \overset{3}{h}{}^{(n^{\text{node}})}_{112} & \dots & \overset{3}{h}{}^{(n^{\text{node}})}_{133} \\ \overset{3}{h}{}^{(1)}_{211} & \overset{3}{h}{}^{(1)}_{212} & \dots & \overset{3}{h}{}^{(1)}_{233} \\ \dots & \dots & \dots & \\ \overset{3}{h}{}^{(n^{\text{node}})}_{211} & \overset{3}{h}{}^{(n^{\text{node}})}_{212} & \dots & \overset{3}{h}{}^{(n^{\text{node}})}_{233} \\ \overset{3}{h}{}^{(1)}_{311} & \overset{3}{h}{}^{(1)}_{312} & \dots & \overset{3}{h}{}^{(1)}_{333} \\ \dots & \dots & \dots & \\ \overset{3}{h}{}^{(n^{\text{node}})}_{311} & \overset{3}{h}{}^{(n^{\text{node}})}_{312} & \dots & \overset{3}{h}{}^{(n^{\text{node}})}_{333} \end{bmatrix}. \tag{C.13}$$

The system of Eqs. (C.12) is thus rewritten as

$$\bigwedge_{\omega^e}\int_{\omega^e} (\mathbf{b}^e)^T \mathbf{c}^{\text{el}}_{\text{m}}(\boldsymbol{x}) d\boldsymbol{x} + \bigwedge_{\omega^e}\int_{\omega^e} (\mathbf{b}^e)^T \mathbf{c}^{\text{el}}_{\text{m}}(\boldsymbol{x}) \mathbf{b}^e d\boldsymbol{x}\, \mathbf{d}_{\text{m}_{3n^{\text{node}}\times 6}} = 0\,, \tag{C.14}$$

where $\mathbf{b}^e$ is the elementary matrix of the shape functions gradient of size $6 \times 3n^{\text{node}}$ and $\mathbf{c}_{\text{m}}^{\text{el}}$ of size 6×6 is the matrix notation of the material tensor $\mathbb{c}_{\text{m}}^{\text{el}}$. The set of Eq. (C.14) actually consists into 6 problems that can be successively solved under the constraints of periodic boundary condition and of zero-average on ω.

Appendix C.2.2. Extension of the AH to elasto-plasticity

Using (189), the governing equation (175) at order ε^{-1} is thus rewritten

$$0 = \left\{\mathbb{c}_{\text{m}}^{\text{el}}(\boldsymbol{X},\, \boldsymbol{x}) : \left[\boldsymbol{\varepsilon}_{\boldsymbol{X}}\left(\boldsymbol{u}_0(\boldsymbol{X})\right) + \boldsymbol{\varepsilon}_{\boldsymbol{x}}\left(\boldsymbol{u}_1(\boldsymbol{X},\, \boldsymbol{x})\right) - \boldsymbol{\mu}_0\left(\boldsymbol{X},\, \boldsymbol{x}\right)\right]\right\} \cdot \boldsymbol{\nabla}_{\boldsymbol{x}} \qquad \forall \boldsymbol{X} \times \boldsymbol{x} \in \Omega \times \omega\,. \tag{C.15}$$

This problem is solved by introducing the separation of variables similarly to Eq. (181) but accounting for the eigen-strain through the tensor $\boldsymbol{d}_\mu(\boldsymbol{X})$, which is the macroscopic portion of the solution resulting from the eigen-strains (Fish et al., 1997), with $\boldsymbol{d}_\mu(\boldsymbol{X}) = 0$ when $\boldsymbol{\mu}_0\left(\boldsymbol{X},\, \boldsymbol{x}\right) = 0$. One thus has, with the third-order tensor $\overset{3}{\mathbb{h}}\left(\boldsymbol{X},\, \boldsymbol{x}\right)$ periodic on ω,

$$\boldsymbol{u}_1(\boldsymbol{x},\, \boldsymbol{X}) = \overset{3}{\mathbb{h}}\left(\boldsymbol{X},\, \boldsymbol{x}\right) : \left[\boldsymbol{\varepsilon}_{\boldsymbol{X}}\left(\boldsymbol{u}_0(\boldsymbol{X})\right) + \boldsymbol{d}_\mu(\boldsymbol{X})\right] \in \mathcal{U}^{\text{PBC}}(\omega)\,. \tag{C.16}$$

Equation (C.15) thus becomes

$$\begin{aligned} 0 \;=\; & \left\{\mathbb{c}_{\text{m}}^{\text{el}}\left(\boldsymbol{X},\, \boldsymbol{x}\right) : \left[\mathbb{I} + \mathbb{h}\left(\boldsymbol{X},\, \boldsymbol{x}\right)\right] : \boldsymbol{\varepsilon}_{\boldsymbol{X}}\left(\boldsymbol{u}_0(\boldsymbol{X})\right) + \right. \\ & \left. \mathbb{c}_{\text{m}}^{\text{el}}\left(\boldsymbol{X},\, \boldsymbol{x}\right) : \mathbb{h}\left(\boldsymbol{X},\, \boldsymbol{x}\right) : \boldsymbol{d}_\mu(\boldsymbol{X}) - \mathbb{c}_{\text{m}}^{\text{el}}\left(\boldsymbol{X},\, \boldsymbol{x}\right) : \boldsymbol{\mu}_0\left(\boldsymbol{X},\, \boldsymbol{x}\right)\right\} \cdot \boldsymbol{\nabla}_{\boldsymbol{x}} \\ & \quad \forall \boldsymbol{X} \times \boldsymbol{x} \in \Omega \times \omega\,, \end{aligned} \tag{C.17}$$

with the fourth-order tensor $\mathbb{h}\left(\boldsymbol{X},\, \boldsymbol{x}\right)$ such that $h_{ijkl} = \frac{1}{2}\frac{\partial}{\partial x_j}\overset{3}{h}_{ikl} + \frac{1}{2}\frac{\partial}{\partial x_i}\overset{3}{h}_{jkl}$. Since this equation should be satisfied for arbitrary elastic responses, this equation can be split into

$$0 = \boldsymbol{\nabla}_{\boldsymbol{x}} \cdot^2 \left\{\mathbb{c}_{\text{m}}^{\text{el}}(\boldsymbol{X},\, \boldsymbol{x}) : \left[\mathbb{I} + \mathbb{h}(\boldsymbol{X},\, \boldsymbol{x})\right]\right\} : \boldsymbol{\varepsilon}_{\boldsymbol{X}}\left(\boldsymbol{u}_0(\boldsymbol{X})\right) \;\forall \boldsymbol{X} \times \boldsymbol{x} \in \Omega \times \omega\,; \tag{C.18}$$

$$0 = \boldsymbol{\nabla}_{\boldsymbol{x}} \cdot^2 \left\{\mathbb{c}_{\text{m}}^{\text{el}}(\boldsymbol{X},\, \boldsymbol{x}) : \mathbb{h}(\boldsymbol{X},\, \boldsymbol{x})\right\} : \boldsymbol{d}_\mu(\boldsymbol{X}) - \boldsymbol{\nabla}_{\boldsymbol{x}} \cdot^2 \left\{\mathbb{c}_{\text{m}}^{\text{el}}(\boldsymbol{X},\, \boldsymbol{x}) : \boldsymbol{\mu}_0\left(\boldsymbol{X},\, \boldsymbol{x}\right)\right\} \quad \forall \boldsymbol{X} \times \boldsymbol{x} \in \Omega \times \omega\,, \tag{C.19}$$

where $\cdot^2$ means a contraction on the second index of the right hand side.

Equation (C.18) is the same as in the linear case and, after multiplying by a test function, integrating by parts and accounting for periodicity, yields Eq. (182). The resolution of this system in terms of $\overset{3}{\mathbb{h}}\left(\boldsymbol{X},\, \boldsymbol{x}\right)$ is detailed in Appendix C.2.1. This results in the apparent elastic properties $\mathbb{c}_{\text{M}}^{\text{el}}(\boldsymbol{X})$ defined by either Eq. (184) or Eq. (186).

From the knowledge of $\overset{3}{\mathbb{h}}\left(\boldsymbol{X},\, \boldsymbol{x}\right)$, Eq. (C.19) can now be solved. To this end, Eq. (C.19) is multiplied by $\overset{3}{\mathbb{h}}\left(\boldsymbol{X},\, \boldsymbol{x}\right)$, integrated by parts over ω, which, because of the periodicity of $\overset{3}{\mathbb{h}}\left(\boldsymbol{x}\right)$, results in

$$\begin{aligned} & \frac{1}{V(\omega)}\int_\omega \mathbb{h}^T(\boldsymbol{X},\, \boldsymbol{x}) : \mathbb{c}_{\text{m}}^{\text{el}}(\boldsymbol{X},\, \boldsymbol{x}) : \mathbb{h}(\boldsymbol{X},\, \boldsymbol{x}) d\boldsymbol{x} : \boldsymbol{d}_\mu(\boldsymbol{X}) = \\ & \qquad \frac{1}{V(\omega)}\int_\omega \mathbb{h}^T(\boldsymbol{x}) : \mathbb{c}_{\text{m}}^{\text{el}}(\boldsymbol{X},\, \boldsymbol{x}) : \boldsymbol{\mu}_0\left(\boldsymbol{X},\, \boldsymbol{x}\right) d\boldsymbol{x}\,, \end{aligned} \tag{C.20}$$

where $(h^T)_{ijkl} = h_{klij}$. Substituting $\mathbbm{h}(\boldsymbol{X},\, \boldsymbol{x})$ by $\mathbbm{I} + \mathbbm{h}(\boldsymbol{X},\, \boldsymbol{x}) - \mathbbm{I}$ in the left hand side, and using both Eq. (184) and Eq. (186) result in

$$\boldsymbol{d}_{\mu}(\boldsymbol{X}) = \frac{1}{V(\omega)} \left[\mathbbm{c}^{\text{Voigt}}(\boldsymbol{X}) - \mathbbm{c}^{\text{el}}_{\text{M}}(\boldsymbol{X})\right]^{-1} : \int_{\omega} \mathbbm{h}^T(\boldsymbol{X},\, \boldsymbol{x}) : \mathbbm{c}^{\text{el}}_{\text{m}}(\boldsymbol{X},\, \boldsymbol{x}) : \boldsymbol{\mu}_0\left(\boldsymbol{X},\, \boldsymbol{x}\right) d\boldsymbol{x}\,. \tag{C.21}$$

This system can be solved using a ROM, see Appendix C.2.3.

Using this expression, the strain at zero order $\boldsymbol{\varepsilon}_0\left(\boldsymbol{X},\, \boldsymbol{x}\right)$ is evaluated using Eq. (C.16) as

$$\boldsymbol{\varepsilon}_0\left(\boldsymbol{X},\, \boldsymbol{x}\right) = \boldsymbol{\varepsilon}_{\boldsymbol{X}}\left(\boldsymbol{u}_0(\boldsymbol{X})\right) + \boldsymbol{\varepsilon}_{\boldsymbol{x}}\left(\boldsymbol{u}_1(\boldsymbol{X},\, \boldsymbol{x})\right) = \left[\mathbbm{I} + \mathbbm{h}(\boldsymbol{X},\, \boldsymbol{x})\right] : \boldsymbol{\varepsilon}_{\boldsymbol{X}}\left(\boldsymbol{u}_0(\boldsymbol{X})\right) + \mathbbm{h}(\boldsymbol{X},\, \boldsymbol{x}) : \boldsymbol{d}_{\mu}(\boldsymbol{X})\,. \tag{C.22}$$

The homogenised stress tensor (179) then follows as

$$\begin{aligned}
\boldsymbol{\sigma}_{\text{M}}\left(\boldsymbol{X}\right) &= \frac{1}{V(\omega)} \int_{\omega} \boldsymbol{\sigma}_0(\boldsymbol{X},\, \boldsymbol{x}) d\boldsymbol{x} = \frac{1}{V(\omega)} \int_{\omega} \mathbbm{c}^{\text{el}}_{\text{m}}(\boldsymbol{X},\, \boldsymbol{x}) : \left[\boldsymbol{\varepsilon}_0\left(\boldsymbol{X},\, \boldsymbol{x}\right) - \boldsymbol{\mu}_0(\boldsymbol{X},\, \boldsymbol{x})\right] d\boldsymbol{x} \\
&= \frac{1}{V(\omega)} \int_{\omega} \mathbbm{c}^{\text{el}}_{\text{m}}(\boldsymbol{X},\, \boldsymbol{x}) : \left[\mathbbm{I} + \mathbbm{h}(\boldsymbol{X},\, \boldsymbol{x})\right] d\boldsymbol{x} : \boldsymbol{\varepsilon}_{\boldsymbol{X}}\left(\boldsymbol{u}_0(\boldsymbol{X})\right) + \\
&\quad \frac{1}{V(\omega)} \int_{\omega} \mathbbm{c}^{\text{el}}_{\text{m}}(\boldsymbol{X},\, \boldsymbol{x}) : \mathbbm{h}(\boldsymbol{X},\, \boldsymbol{x}) d\boldsymbol{x} : \boldsymbol{d}_{\mu}(\boldsymbol{X}) - \frac{1}{V(\omega)} \int_{\omega} \mathbbm{c}^{\text{el}}_{\text{m}}(\boldsymbol{X},\, \boldsymbol{x}) : \boldsymbol{\mu}_0(\boldsymbol{X},\, \boldsymbol{x}) d\boldsymbol{x}\,.
\end{aligned} \tag{C.23}$$

The overall eigen-strain tensor $\boldsymbol{\mu}_{\text{M}}(\boldsymbol{X})$ is defined such that

$$\begin{aligned}
-\mathbbm{c}^{\text{el}}_{\text{M}}(\boldsymbol{X}) : \boldsymbol{\mu}_{\text{M}}(\boldsymbol{X}) &= \frac{1}{V(\omega)} \int_{\omega} \mathbbm{c}^{\text{el}}_{\text{m}}(\boldsymbol{X},\, \boldsymbol{x}) : \mathbbm{h}(\boldsymbol{X},\, \boldsymbol{x}) d\boldsymbol{x} : \boldsymbol{d}_{\mu}(\boldsymbol{X}) - \\
&\quad \frac{1}{V(\omega)} \int_{\omega} \mathbbm{c}^{\text{el}}_{\text{m}}(\boldsymbol{X},\, \boldsymbol{x}) : \boldsymbol{\mu}_0(\boldsymbol{X},\, \boldsymbol{x}) d\boldsymbol{x} \\
&= \frac{1}{V(\omega)} \int_{\omega} \mathbbm{c}^{\text{el}}_{\text{m}}(\boldsymbol{X},\, \boldsymbol{x}) : \left[\mathbbm{h}(\boldsymbol{X},\, \boldsymbol{x}) + \mathbbm{I}\right] d\boldsymbol{x} : \boldsymbol{d}_{\mu}(\boldsymbol{X}) - \\
&\quad \frac{1}{V(\omega)} \int_{\omega} \mathbbm{c}^{\text{el}}_{\text{m}}(\boldsymbol{X},\, \boldsymbol{x}) d\boldsymbol{x} : \boldsymbol{d}_{\mu}(\boldsymbol{X}) - \\
&\quad \frac{1}{V(\omega)} \int_{\omega} \mathbbm{c}^{\text{el}}_{\text{m}}(\boldsymbol{X},\, \boldsymbol{x}) : \boldsymbol{\mu}_0(\boldsymbol{X},\, \boldsymbol{x}) d\boldsymbol{x} \\
&= \left[\mathbbm{c}^{\text{el}}_{\text{M}}(\boldsymbol{X}) - \mathbbm{c}^{\text{Voigt}}(\boldsymbol{X})\right] : \boldsymbol{d}_{\mu}(\boldsymbol{X}) - \frac{1}{V(\omega)} \int_{\omega} \mathbbm{c}^{\text{el}}_{\text{m}}(\boldsymbol{X},\, \boldsymbol{x}) : \boldsymbol{\mu}_0(\boldsymbol{X},\, \boldsymbol{x}) d\boldsymbol{x}\,,
\end{aligned} \tag{C.24}$$

where we have used Eq. (184). Using Eq. (C.21), this last result reads

$$\boldsymbol{\mu}_{\text{M}}(\boldsymbol{X}) = {\mathbbm{c}^{\text{el}}_{\text{M}}}^{-1}(\boldsymbol{X}) : \frac{1}{V(\omega)} \int_{\omega} \left[\mathbbm{h}^T(\boldsymbol{X},\, \boldsymbol{x}) + \mathbbm{I}\right] : \mathbbm{c}^{\text{el}}_{\text{m}}(\boldsymbol{X},\, \boldsymbol{x}) : \boldsymbol{\mu}_0(\boldsymbol{X},\, \boldsymbol{x}) d\boldsymbol{x}\,, \tag{C.25}$$

and the homogenised stress tensor (C.23) reads

$$\boldsymbol{\sigma}_{\text{M}}\left(\boldsymbol{X}\right) = \mathbbm{c}^{\text{el}}_{\text{M}}(\boldsymbol{X}) : \left[\boldsymbol{\varepsilon}_{\boldsymbol{X}}\left(\boldsymbol{u}_0(\boldsymbol{X})\right) - \boldsymbol{\mu}_{\text{M}}(\boldsymbol{X})\right]\,, \tag{C.26}$$

with $\boldsymbol{\varepsilon}_{\boldsymbol{X}}\left(\boldsymbol{u}_0(\boldsymbol{X})\right) = \boldsymbol{\varepsilon}_{\text{M}}(\boldsymbol{X})$.

Appendix C.2.3. Reduced Order Modelling within AH

The eigen-strains $\boldsymbol{\mu}_0\left(\boldsymbol{X},\,\boldsymbol{x}\right)$ are approximated using the separation of variables (192). Equation (C.21) thus becomes

$$\mathbb{h}(\boldsymbol{X},\,\boldsymbol{x}):\boldsymbol{d}_\mu(\boldsymbol{X})=\sum_k \mathbb{d}^{(k)}(\boldsymbol{X},\,\boldsymbol{x}):\boldsymbol{\mu}^{(k)}\left(\boldsymbol{X}\right)\,. \tag{C.27}$$

with

$$\begin{aligned}\mathbb{d}^{(k)}(\boldsymbol{X},\,\boldsymbol{x}) &= \frac{1}{V(\omega)}\mathbb{h}(\boldsymbol{X},\,\boldsymbol{x}):\left[\mathbb{c}^{\text{Voigt}}(\boldsymbol{X})-\mathbb{c}^{\text{el}}_{\text{M}}(\boldsymbol{X})\right]^{-1}:\\ &\int_\omega \mathbb{h}^T(\boldsymbol{X},\,\boldsymbol{x}):\mathbb{c}^{\text{el}}_{\text{m}}(\boldsymbol{X},\,\boldsymbol{x})h^{(k)}(\boldsymbol{x})d\boldsymbol{x}\,.\end{aligned} \tag{C.28}$$

Assuming piece-wise constant functions for $h^{(k)}(\boldsymbol{x})$ on the partition $\delta\omega^{(k)}$ of ω, the functions $h^{(k)}(\boldsymbol{x})$ correspond to the spatial indicators (60), repeated here below

$$h^{(k)}(\boldsymbol{x})=\chi_{\delta\omega^{(k)}}\left(\boldsymbol{x}\right)=\begin{cases}1 & \text{if } \boldsymbol{x}\in\delta\omega^{(k)}\,;\\ 0 & \text{if not}\,;\end{cases} \tag{C.29}$$

with $\frac{1}{V\left(\delta\omega^{(j)}\right)}\int_\omega \chi_{\delta\omega^{(j)}}\left(\boldsymbol{x}\right)\chi_{\delta\omega^{(k)}}\left(\boldsymbol{x}\right)d\boldsymbol{x}=\delta_{jk}$. In that case, in order to unify the notations, the separation of variables (192) is rewritten

$$\boldsymbol{\mu}_0\left(\boldsymbol{X},\,\boldsymbol{x}\right)=\sum_k \chi_{\delta\omega^{(k)}}\left(\boldsymbol{x}\right)\boldsymbol{\mu}^{\delta\omega^{(k)}}(\boldsymbol{X})\,, \tag{C.30}$$

with

$$\boldsymbol{\mu}^{\delta\omega^{(k)}}(\boldsymbol{X})=\frac{1}{V\left(\delta\omega^{(k)}\right)}\int_{\delta\omega^{(k)}}\boldsymbol{\mu}_0\left(\boldsymbol{X},\,\boldsymbol{x}\right)d\boldsymbol{x}=\frac{1}{V\left(\delta\omega^{(k)}\right)}\int_\omega \boldsymbol{\mu}_0\left(\boldsymbol{X},\,\boldsymbol{x}\right)\chi_{\delta\omega^{(k)}}\left(\boldsymbol{x}\right)d\boldsymbol{x}\,, \tag{C.31}$$

and Eq. (C.27) is rewritten

$$\mathbb{h}(\boldsymbol{X},\,\boldsymbol{x}):\boldsymbol{d}_\mu(\boldsymbol{X})=\sum_k \mathbb{d}^{\delta\omega^{(k)}}(\boldsymbol{X},\,\boldsymbol{x}):\boldsymbol{\mu}^{\delta\omega^{(k)}}\left(\boldsymbol{X}\right)\,, \tag{C.32}$$

with

$$\begin{aligned}\mathbb{d}^{\delta\omega^{(k)}}(\boldsymbol{X},\,\boldsymbol{x}) &= \frac{V\left(\delta\omega^{(k)}\right)}{V(\omega)}\mathbb{h}(\boldsymbol{X},\,\boldsymbol{x}):\left[\mathbb{c}^{\text{Voigt}}(\boldsymbol{X})-\mathbb{c}^{\text{el}}_{\text{M}}(\boldsymbol{X})\right]^{-1}:\\ &\frac{1}{V\left(\delta\omega^{(k)}\right)}\int_{\delta\omega^{(k)}}\mathbb{h}^T(\boldsymbol{X},\,\boldsymbol{x}):\mathbb{c}^{\text{el}}_{\text{m}}(\boldsymbol{X},\,\boldsymbol{x})d\boldsymbol{x}\,.\end{aligned} \tag{C.33}$$

Equation (C.17) is then used to deduce the micro-scale stress tensor, which, using Eq. (C.30) and Eq. (C.32), reads

$$\boldsymbol{\sigma}_0\left(\boldsymbol{X},\,\boldsymbol{x}\right)=\mathbb{c}^{\text{el}}_{\text{m}}:\left\{\left[\mathbb{I}+\mathbb{h}(\boldsymbol{X},\,\boldsymbol{x})\right]:\boldsymbol{\varepsilon}_{\boldsymbol{X}}\left(\boldsymbol{u}_0(\boldsymbol{X})\right)+\sum_k \mathbb{s}^{\delta\omega^{(k)}}(\boldsymbol{X},\,\boldsymbol{x}):\boldsymbol{\mu}^{\delta\omega^{(k)}}\left(\boldsymbol{X}\right)\right\}\,, \tag{C.34}$$

with the fourth-order tensors

$$\mathbb{s}^{\delta\omega^{(k)}}(\boldsymbol{X},\,\boldsymbol{x}) = \mathbb{d}^{\delta\omega^{(k)}}(\boldsymbol{X},\,\boldsymbol{x}) - \mathbb{I}_{\delta\omega^{(k)}}(\boldsymbol{x}) \text{ and } \mathbb{I}_{\delta\omega^{(k)}}(\boldsymbol{x}) = \begin{cases} \mathbb{I} & \text{if } \boldsymbol{x} \in \delta\omega^{(k)} \\ 0 & \text{if } \boldsymbol{x} \notin \delta\omega^{(k)} \end{cases} . \tag{C.35}$$

Similarly, the strain at zero order $\boldsymbol{\varepsilon}_0\,(\boldsymbol{X},\,\boldsymbol{x})$ (C.22) is rewritten as

$$\boldsymbol{\varepsilon}_0\,(\boldsymbol{X},\,\boldsymbol{x}) = [\mathbb{I} + \mathbb{h}(\boldsymbol{X},\,\boldsymbol{x})] : \boldsymbol{\varepsilon}_{\boldsymbol{X}}\,(\boldsymbol{u}_0(\boldsymbol{X})) + \sum_k \mathbb{d}^{\delta\omega^{(k)}}(\boldsymbol{X},\,\boldsymbol{x}) : \boldsymbol{\mu}^{\delta\omega^{(k)}}\,(\boldsymbol{X})\,. \tag{C.36}$$

The average strain on cluster $\delta\omega^{(l)}$ results from the volume averaging of Eq. (C.36), yielding

$$\begin{aligned} \boldsymbol{\varepsilon}_0^{\delta\omega^{(l)}}\,(\boldsymbol{X}) &= \frac{1}{V\left(\delta\omega^{(l)}\right)} \int_{\delta\omega^{(l)}} \boldsymbol{\varepsilon}_0\,(\boldsymbol{X},\,\boldsymbol{x})\,d\boldsymbol{x} \\ &= \mathbb{a}^{\delta\omega^{(l)}}\,(\boldsymbol{X}) : \boldsymbol{\varepsilon}_{\boldsymbol{X}}\,(\boldsymbol{u}_0(\boldsymbol{X})) + \sum_k \mathbb{d}^{\delta\omega^{(l)}\,\delta\omega^{(k)}}\,(\boldsymbol{X}) : \boldsymbol{\mu}^{\delta\omega^{(k)}}\,(\boldsymbol{X})\,. \end{aligned} \tag{C.37}$$

with

$$\begin{aligned} \mathbb{a}^{\delta\omega^{(l)}}\,(\boldsymbol{X}) &= \frac{1}{V\left(\delta\omega^{(l)}\right)} \int_{\delta\omega^{(l)}} [\mathbb{I} + \mathbb{h}(\boldsymbol{X},\,\boldsymbol{x})]\,d\boldsymbol{x} \\ &= \frac{1}{V\left(\delta\omega^{(l)}\right)} \int_{\omega} [\mathbb{I} + \mathbb{h}(\boldsymbol{X},\,\boldsymbol{x})]\,\chi_{\delta\omega^{(l)}}\,(\boldsymbol{x})\,d\boldsymbol{x}\,, \text{ and} \end{aligned} \tag{C.38}$$

$$\begin{aligned} \mathbb{d}^{\delta\omega^{(l)}\,\delta\omega^{(k)}}\,(\boldsymbol{X}) &= \frac{1}{V\left(\delta\omega^{(l)}\right)} \int_{\delta\omega^{(l)}} \mathbb{d}^{\delta\omega^{(k)}}(\boldsymbol{X},\,\boldsymbol{x})d\boldsymbol{x} \\ &= \frac{1}{V\left(\delta\omega^{(l)}\right)} \int_{\omega} \mathbb{d}^{\delta\omega^{(k)}}(\boldsymbol{X},\,\boldsymbol{x})\chi_{\delta\omega^{(l)}}\,(\boldsymbol{x})\,d\boldsymbol{x}\,. \end{aligned} \tag{C.39}$$

Considering the constitutive law (116) written for each cluster $\delta\omega^{(l)}$, with the internal variables $\boldsymbol{\mu}^{\delta\omega^{(l)}}\,(\boldsymbol{X})$, *i.e.*

$$\boldsymbol{\sigma}_{\mathrm{m}}^{\delta\omega^{(l)}} = \boldsymbol{\sigma}_{\mathrm{m}}^{\delta\omega^{(l)}}\left(\boldsymbol{\varepsilon}_0^{\delta\omega^{(l)}}\,(\boldsymbol{X});\; \boldsymbol{\mu}^{\delta\omega^{(l)}}\,(\boldsymbol{X};\,\tau \in [0,\,t])\right)\,, \tag{C.40}$$

in combination with Eq. (C.37) constitutes a set of $6 \times N^{\delta\omega}$ equations in $\boldsymbol{\varepsilon}_0^{\delta\omega^{(l)}}\,(\boldsymbol{X})$, with $N^{\delta\omega}$ the number of clusters $\delta\omega^{(k)}$.

The homogenised stress tensor (179) then follows from Eq. (C.23) using Eqs. (C.32) and (C.30) as

$$\begin{aligned} \boldsymbol{\sigma}_{\mathrm{M}}\,(\boldsymbol{X}) &= \frac{1}{V(\omega)} \int_{\omega} \mathbb{c}_{\mathrm{m}}^{\mathrm{el}}(\boldsymbol{X},\,\boldsymbol{x}) : [\mathbb{I} + \mathbb{h}(\boldsymbol{X},\,\boldsymbol{x})]\,d\boldsymbol{x} : \boldsymbol{\varepsilon}_{\boldsymbol{X}}\,(\boldsymbol{u}_0(\boldsymbol{X})) + \\ &\quad \frac{1}{V(\omega)} \int_{\omega} \mathbb{c}_{\mathrm{m}}^{\mathrm{el}}(\boldsymbol{X},\,\boldsymbol{x}) : \mathbb{h}(\boldsymbol{X},\,\boldsymbol{x})d\boldsymbol{x} : \boldsymbol{d}_{\mu}(\boldsymbol{X}) - \frac{1}{V(\omega)} \int_{\omega} \mathbb{c}_{\mathrm{m}}^{\mathrm{el}}(\boldsymbol{X},\,\boldsymbol{x}) : \boldsymbol{\mu}_0(\boldsymbol{X},\,\boldsymbol{x})d\boldsymbol{x} \\ &= \mathbb{c}_{\mathrm{M}}^{\mathrm{el}}\,(\boldsymbol{X}) : \boldsymbol{\varepsilon}_{\boldsymbol{X}}\,(\boldsymbol{u}_0(\boldsymbol{X})) + \sum_k \frac{1}{V(\omega)} \int_{\omega} \mathbb{c}_{\mathrm{m}}^{\mathrm{el}}(\boldsymbol{X},\,\boldsymbol{x}) : \mathbb{d}^{\delta\omega^{(k)}}(\boldsymbol{X},\,\boldsymbol{x})d\boldsymbol{x} : \boldsymbol{\mu}^{\delta\omega^{(k)}}\,(\boldsymbol{X}) - \\ &\quad \sum_k \frac{1}{V(\omega)} \int_{\omega} \mathbb{c}_{\mathrm{m}}^{\mathrm{el}}(\boldsymbol{X},\,\boldsymbol{x}) : \mathbb{I}_{\delta\omega^{(k)}}\,(\boldsymbol{X},\,\boldsymbol{x})\,d\boldsymbol{x} : \boldsymbol{\mu}^{\delta\omega^{(k)}}(\boldsymbol{X})\,, \end{aligned} \tag{C.41}$$

or using Eq. (C.35) as

$$\boldsymbol{\sigma}_{\mathrm{M}}\left(\boldsymbol{X}\right) \;=\; \mathbb{c}^{\mathrm{el}}_{\mathrm{M}}\left(\boldsymbol{X}\right) : \boldsymbol{\varepsilon}_{\boldsymbol{X}}\left(\boldsymbol{u}_0(\boldsymbol{X})\right) + \sum_k \mathbb{s}^{\delta\omega^{(k)}}_{\mathrm{M}}\left(\boldsymbol{X}\right) : \boldsymbol{\mu}^{\delta\omega^{(k)}}\left(\boldsymbol{X}\right) . \tag{C.42}$$

with $\mathbb{s}^{\delta\omega^{(k)}}_{\mathrm{M}}\left(\boldsymbol{X}\right) = \frac{1}{V(\omega)}\int_\omega \mathbb{c}^{\mathrm{el}}_{\mathrm{m}}(\boldsymbol{X},\, \boldsymbol{x}) : \mathbb{s}^{\delta\omega^{(k)}}(\boldsymbol{X},\, \boldsymbol{x}) d\boldsymbol{x}$.

Adams, B.L., Gao, X.C., Kalidindi, S.R., 2005. Finite approximations to the second-order properties closure in single phase polycrystals. Acta Materialia 53, 3563 – 3577. doi:10.1016/j.actamat.2005.03.052.

Agmon, N., Alhassid, Y., Levine, R., 1979. An algorithm for finding the distribution of maximal entropy. Journal of Computational Physics 30, 250 – 258. doi:10.1016/0021-9991(79)90102-5.

Ainsworth, M., 2001. Essential boundary conditions and multi-point constraints in finite element analysis. Computer Methods in Applied Mechanics and Engineering 190, 6323 – 6339. doi:10.1016/S0045-7825(01)00236-5.

Albert, R., Oden, J.T., Vemaganti, K., 2006. Multi-scale goal-oriented adaptive modeling of random heterogeneous materials. Mechanics of Materials 38, 859–872. URL: https://www.sciencedirect.com/science/article/pii/S0167663605001675, doi:https://doi.org/10.1016/j.mechmat.2005.06.028. advances in Disordered Materials.

Alzebdeh, K., Ostoja-Starzewski, M., 1996. Micromechanically based stochastic finite elements: length scales and anisotropy. Probabilistic Engineering Mechanics 11, 205 – 214. doi:10.1016/0266-8920(96)00015-X. third International Stochastic Structural Dynamics Conference.

Anderson, D.F., Seppäläinen, T., Valkó, B., 2017. Introduction to probability, in: Dietterich, T.G., Becker, S., Ghahramani, Z. (Eds.), Cambridge Mathematical Textbooks. Cambridge University Press.

Arregui-Mena, J.D., Margetts, L., Mummery, P.M., 2016. Practical application of the stochastic finite element method. Archives of Computational Methods in Engineering 23, 171–190. doi:10.1007/s11831-014-9139-3.

Bale, H., Blacklock, M., Begley, M.R., Marshall, D.B., Cox, B.N., Ritchie, R.O., 2012. Characterizing three-dimensional textile ceramic composites using synchrotron x-ray micro-computed-tomography. Journal of the American Ceramic Society 95, 392–402. doi:10.1111/j.1551-2916.2011.04802.x.

Balokas, G., Kriegesmann, B., Czichon, S., Rolfes, R., 2021. A variable-fidelity hybrid surrogate approach for quantifying uncertainties in the nonlinear response of braided composites. Computer Methods in Applied Mechanics and Engineering 381, 113851. URL: https://www.sciencedirect.com/science/article/pii/S0045782521001882, doi:https://doi.org/10.1016/j.cma.2021.113851.

Barbe, F., Decker, L., Jeulin, D., Cailletaud, G., 2001. Intergranular and intragranular behavior of polycrystalline aggregates. part 1: F.e. model. International Journal of Plasticity 17, 513 – 536. doi:10.1016/S0749-6419(00)00061-9.

Barber, C.B., Dobkin, D.P., Huhdanpaa, H., 1996. The quickhull algorithm for convex hulls. ACM Transactions on Mathematical Software 22, 469–483. doi:10.1145/235815.235821.

Bauereiβ, A., Scharowsky, T., Körner, C., 2014. Defect generation and propagation mechanism during additive manufacturing by selective beam melting. Journal of Materials Processing Technology 214, 2522 – 2528. doi:10.1016/j.jmatprotec.2014.05.002.

Beck, J.L., Katafygiotis, L.S., 1998. Updating models and their uncertainties. I: Bayesian statistical framework. Journal of Engineering Mechanics 124, 455–461.

Benveniste, Y., 1987. A new approach to the application of Mori-Tanaka's theory in composite materials. Mechanics of Materials 6, 147 – 157. doi:DOI:10.1016/0167-6636(87)90005-6.

Berveiller, M., Zaoui, A., 1978. An extension of the self-consistent scheme to plastically-flowing polycrystals. Journal of the Mechanics and Physics of Solids 26, 325 – 344. doi:DOI:10.1016/0022-5096(78)90003-0.

Bessa, M., Bostanabad, R., Liu, Z., Hu, A., Apley, D.W., Brinson, C., Chen, W., Liu, W.K., 2017. A framework for data-driven analysis of materials under uncertainty: Countering the curse of dimensionality. Computer Methods in Applied Mechanics and Engineering 320, 633 – 667. doi:10.1016/j.cma.2017.03.037.

Bhuiyan, F.H., Sanei, S.H.R., Fertif III, R.S., 2020. Predicting variability in transverse effective elastic moduli and failure initiation strengths in ud composite microstructures due to randomness in fiber location and morphology. Composite Structures 237, 111887. doi:10.1016/j.compstruct.2020.111887.

Bishop, C.M., 2006. Information science and statistics, in: Pattern Recognition and Machine Learning. Springer-Verlag, New York, USA.

Blacklock, M., Bale, H., Begley, M., Cox, B., 2012. Generating virtual textile composite specimens using statistical data from micro-computed tomography: 1d tow representations for the binary model. Journal of the Mechanics and Physics of Solids 60, 451 – 470. doi:10.1016/j.jmps.2011.11.010.

Bobeth, M., Diener, G., 1987. Static elastic and thermoelastic field fluctuations in multiphase composites. Journal of the Mechanics and Physics of Solids 35, 137 – 149. doi:10.1016/0022-5096(87)90033-0.

Bogdanor, M.J., Mahadevan, S., Oskay, C., 2013. Uncertainty quantification in damage modeling of heterogeneous materials. International Journal for Multiscale Computational Engineering 11, 289–307. doi:10.1615/IntJMultCompEng.2013005821.

Bogdanor, M.J., Oskay, C., Clay, S.B., 2015. Multiscale modeling of failure in composites under model parameter uncertainty. Computational Mechanics 56, 389–404. doi:10.1007/s00466-015-1177-7.

Böhm, H., Eckschlager, A., Han, W., 2002. Multi-inclusion unit cell models for metal matrix composites with randomly oriented discontinuous reinforcements. Computational Materials Science 25, 42 – 53. doi:10.1016/S0927-0256(02)00248-3.

Bonilla-Villalba, P., Claus, S., Kundu, A., Kerfriden, P., 2020. Goal-oriented model adaptivity in stochastic elastodynamics: simultaneous control of discretisation, surrogate model and sampling errors. International Journal for Uncertainty Quantification 10, 195–223.

Bostanabad, R., Zhang, Y., Li, X., Kearny, T., Brinson, L.C., Apley, D.W., Liu, W.K., Chen, W., 2018. Computational microstructure characterization and reconstruction: Review of the state-of-the-art techniques. Progress in Materials Science 95, 1 – 41. doi:10.1016/j.pmatsci.2018.01.005.

Boudet, J., Auslender, F., Bornert, M., Lapusta, Y., 2016. An incremental variational formulation for the prediction of the effective work-hardening behavior and field statistics of elasto-(visco)plastic composites. International Journal of Solids and Structures 83, 90 – 113. doi:10.1016/j.ijsolstr.2016.01.003.

Brakke, K.A., 1992. Minimal surfaces, corners, and wires. Journal of Geometric Analysis 2, 11–36. doi:10.1007/BF02921333.

Brassart, L., Stainier, L., Doghri, I., Delannay, L., 2011. A variational formulation for the incremental homogenization of elasto-plastic composites. Journal of the Mechanics and Physics of Solids 59, 2455 – 2475. doi:10.1016/j.jmps.2011.09.004.

Brassart, L., Stainier, L., Doghri, I., Delannay, L., 2012. Homogenization of elasto-(visco) plastic composites based on an incremental variational principle. International Journal of Plasticity 36, 86 – 112. doi:10.1016/j.ijplas.2012.03.010.

Brauner, C., 2013. Analysis of process-induced distortions and residual stresses of composite structures, in: Herrmann, A.S. (Ed.), Science-Report aus dem Faserinstitut Bremen. Logos Verlag.

Breuer, K., Spickenheuer, A., Stommel, M., 2021. Statistical analysis of mechanical stressing in short fiber reinforced composites by means of statistical and representative volume elements. Fibers 9. URL: https://www.mdpi.com/2079-6439/9/5/32, doi:10.3390/fib9050032.

Budarapu, P.R., Zhuang, X., Rabczuk, T., Bordas, S.P., 2019. Chapter one - multiscale modeling of material failure: Theory and computational methods, in: Hussein, M.I. (Ed.), Advances in Crystals and Elastic Metamaterials, Part 2. Elsevier. volume 52 of *Advances in Applied Mechanics*, pp. 1–103. URL: https://www.sciencedirect.com/science/article/pii/S006521561930002X, doi:https://doi.org/10.1016/bs.aams.2019.04.002.

Buryachenko, V.A., 2001. Multiparticle Effective Field and Related Methods in Micromechanics of Composite Materials. Applied Mechanics Reviews 54, 1. doi:10.1115/1.3097287.

Caflisch, R.E., 1998. Monte carlo and quasi-monte carlo methods. Acta Numerica 7, 149. doi:10.1017/S0962492900002804.

Caicedo, M., Mroginski, J.L., Toro, S., Raschi, M., Huespe, A., Oliver, J., 2019. High performance reduced order modeling techniques based on optimal energy quadrature: Application to geometrically non-linear multiscale inelastic material modeling. Archives of Computational Methods in Engineering 26, 771–792. doi:10.1007/s11831-018-9258-3.

Calleja, J., Wu, L., Nguyen, V.D., Noels, L., In Preparation. A stochastic micro-mechanics-based inverse study for ud-fiber reinforced composites failure analyzes .

Camacho, C.W., Tucker, C.L., Yalva c, S., McGee, R.L., 1990. Stiffness and thermal expansion predictions for hybrid short fiber composites. Polymer Composites 11, 229–239. doi:10.1002/pc.750110406.

Cavaliere, F., Reese, S., Wulfinghoff, S., 2020. Efficient twoscale simulations of engineering structures using the hashinshtrikman type finite element method. Computational Mechanics 65, 159 – 175. URL: https://www.springerprofessional.de/en/efficient-two-scale-simulations-of-engineering-structures-using-/17118994, doi:10.1007/s00466-019-01758-4.

Chaboche, J., Kanouté, P., Roos, A., 2005. On the capabilities of mean-field approaches for the description of plasticity in metal matrix composites. International Journal of Plasticity 21, 1409 – 1434. doi:DOI:10.1016/j.ijplas.2004.07.001.

Charmpis, D., Schuëller, G., Pellissetti, M., 2007. The need for linking micromechanics of materials with stochastic finite elements: A challenge for materials science. Computational Materials Science 41, 27 – 37. doi:10.1016/j.commatsci.2007.02.014.

Chevalier, J., Camanho, P., Lani, F., Pardoen, T., 2019. Multi-scale characterization and modelling of the transverse compression response of unidirectional carbon fiber reinforced epoxy. Composite Structures 209, 160 – 176. doi:10.1016/j.compstruct.2018.10.076.

Chiu, S.N.C., Stoyan, D., Kendall, W.S., Mecke, J., 2013. Stochastic Geometry and its Applications. Wiley Series in Probability and Statistics, John Wiley & Sons, Ltd. doi:10.1002/9781118658222.

Clarke, A.R., Eberhardt, C.N., 2002. Microscopy Techniques for Materials Science. Woodhead Publishing Series in Electronic and Optical Materials, Woodhead Publishing. doi:10.1533/9781855737501.frontmatter.

Clément, A., Soize, C., Yvonnet, J., 2012. Computational nonlinear stochastic homogenization using a nonconcurrent multiscale approach for hyperelastic heterogeneous microstructures analysis. International Journal for Numerical Methods in Engineering 91, 799–824. doi:10.1002/nme.4293.

Cohen, M.F., Shade, J., Hiller, S., Deussen, O., 2003. Wang tiles for image and texture generation. ACM Trans. Graph. 22, 287294. URL: https://doi.org/10.1145/882262.882265, doi:10.1145/882262.882265.

Corson, P.B., 1974a. Correlation functions for predicting properties of heterogeneous materials. i. experimental measurement of spatial correlation functions in multiphase solids. Journal of Applied Physics 45, 3159–3164. doi:10.1063/1.1663741.

Corson, P.B., 1974b. Correlation functions for predicting properties of heterogeneous materials. ii. empirical construction of spatial correlation functions for twophase solids. Journal of Applied Physics 45, 3165–3170. doi:10.1063/1.1663742.

Cottereau, R., 2013. A stochastic-deterministic coupling method for multiscale problems. application to numerical homogenization of random materials. Procedia IUTAM 6, 35 – 43. doi:10.1016/j.piutam.2013.01.004. iUTAM Symposium on Multiscale Problems in Stochastic Mechanics.

Daghia, F., de Miranda, S., Ubertini, F., Viola, E., 2007. Estimation of elastic constants of thick laminated plates within a bayesian framework. Composite Structures 80, 461 – 473. doi:10.1016/j.compstruct.2006.06.030.

Das, S., Ghanem, R., 2009. A bounded random matrix approach for stochastic upscaling. Multiscale Modeling & Simulation 8, 296–325. doi:10.1137/090747713.

Deodatis, G., Micaletti, R., 2001. Simulation of highly skewed non-gaussian stochastic processes. Journal of Engineering Mechanics 127, 1284–1295. doi:10.1061/(ASCE)0733-9399(2001)127:12(1284).

Der Kiureghian, A., Ke, J., 1988. The stochastic finite element method in structural reliability. Probabilistic Engineering Mechanics 3, 83 – 91. doi:10.1016/0266-8920(88)90019-7.

Doghri, I., Adam, L., Bilger, N., 2010. Mean-field homogenization of elasto-viscoplastic composites based on a general incrementally affine linearization method. International Journal of Plasticity 26, 219 – 238.

doi:10.1016/j.ijplas.2009.06.003.

Doghri, I., Brassart, L., Adam, L., Gérard, J.S., 2011. A second-moment incremental formulation for the mean-field homogenization of elasto-plastic composites. International Journal of Plasticity 27, 352 – 371. doi:DOI:10.1016/j.ijplas.2010.06.004.

Doghri, I., Ouaar, A., 2003. Homogenization of two-phase elasto-plastic composite materials and structures: Study of tangent operators, cyclic plasticity and numerical algorithms. International Journal of Solids and Structures 40, 1681 – 1712. doi:DOI:10.1016/S0020-7683(03)00013-1.

Doghri, I., Tinel, L., 2005. Micromechanical modeling and computation of elasto-plastic materials reinforced with distributed-orientation fibers. International Journal of Plasticity 21, 1919 – 1940. doi:10.1016/j.ijplas.2004.09.003.

Doghri, I., Tinel, L., 2006. Micromechanics of inelastic composites with misaligned inclusions: Numerical treatment of orientation. Computer Methods in Applied Mechanics and Engineering 195, 1387 – 1406. doi:10.1016/j.cma.2005.05.041. a Tribute to Thomas J.R. Hughes on the Occasion of his 60th Birthday.

Dvorak, G.J., 1992. Transformation field analysis of inelastic composite materials. Proceedings: Mathematical and Physical Sciences 437, 311–327.

Dvorak, G.J., Bahei-El-Din, Y.A., Wafa, A.M., 1994. Implementation of the transformation field analysis for inelastic composite materials. Computational Mechanics 14, 201–228.

Eberhardt, C.N., Clarke, A.R., 2002. Automated reconstruction of curvilinear fibres from 3d datasets acquired by x-ray microtomography. Journal of Microscopy 206, 41–53. doi:10.1046/j.1365-2818.2002.01009.x.

Eggersmann, R., Kirchdoerfer, T., Reese, S., Stainier, L., Ortiz, M., 2019. Model-free data-driven inelasticity. Computer Methods in Applied Mechanics and Engineering 350, 81–99. URL: https://www.sciencedirect.com/science/article/pii/S0045782519300878, doi:https://doi.org/10.1016/j.cma.2019.02.016.

Ernst, O.G., Ullmann, E., 2010. Stochastic galerkin matrices. SIAM Journal on Matrix Analysis and Applications 31, 1848–1872. doi:10.1137/080742282.

Eshelby, J.D., 1957. The determination of the elastic field of an ellipsoidal inclusion, and related problems. Proceedings of the Royal Society of London. Series A, Mathematical and Physical Sciences 241, pp. 376–396.

Firooz, S., Saeb, S., Chatzigeorgiou, G., Meraghni, F., Steinmann, P., Javili, A., 2019. Systematic study of homogenization and the utility of circular simplified representative volume element. Mathematics and Mechanics of Solids 24, 2961–2985. doi:10.1177/1081286518823834.

Fish, J., Nayak, P., Holmes, M.H., 1994. Microscale reduction error indicators and estimators for a periodic heterogeneous medium. Computational Mechanics 14, 323–338. doi:10.1007/BF00350003.

Fish, J., Shek, K., Pandheeradi, M., Shephard, M., 1997. Computational plasticity for composite structures based on mathematical homogenization: Theory and practice. Computer Methods in Applied Mechanics and Engineering 148, 53 – 73. doi:10.1016/S0045-7825(97)00030-3.

Fish, J., Wu, W., 2011. A nonintrusive stochastic multiscale solver. International Journal for Numerical Methods in Engineering 88, 862–879. doi:10.1002/nme.3201.

Fish, J., Yu, Q., Shek, K., 1999. Computational damage mechanics for composite materials based on mathematical homogenization. International Journal for Numerical Methods in Engineering 45, 1657–1679. doi:10.1002/(SICI)1097-0207(19990820)45:11<1657::AID-NME648>3.0.CO;2-H.

Fish, J., Yuan, Z., Kumar, R., 2018. Computational certification under limited experiments. International Journal for Numerical Methods in Engineering 114, 172–195. doi:10.1002/nme.5739.

Fish, J.F., Shek, K., 1999. Finite deformation plasticity for composite structures: Computational models and adaptive strategies. Computer Methods in Applied Mechanics and Engineering 172, 145 – 174. doi:10.1016/S0045-7825(98)00228-X.

Fritzen, F., Fernández, M., Larsson, F., 2019. On-the-fly adaptivity for nonlinear twoscale simulations using artificial neural networks and reduced order modeling. Frontiers in Materials 6, 75. doi:10.3389/fmats.2019.00075.

Fritzen, F., Hodapp, M., 2016. The finite element square reduced (fe2r) method with gpu acceleration:

towards three-dimensional two-scale simulations. International Journal for Numerical Methods in Engineering 107, 853–881. doi:10.1002/nme.5188.

Fritzen, F., Leuschner, M., 2013. Reduced basis hybrid computational homogenization based on a mixed incremental formulation. Computer Methods in Applied Mechanics and Engineering 260, 143 – 154. doi:10.1016/j.cma.2013.03.007.

Fullwood, D.T., Niezgoda, S.R., Adams, B.L., Kalilindi, S.R., 2010. Microstructure sensitive design for performance optimization. Progress in Materials Science 55, 477 – 562. doi:10.1016/j.pmatsci.2009.08.002.

Gajek, S., Schneider, M., Böhlke, T., 2020. On the micromechanics of deep material networks. Journal of the Mechanics and Physics of Solids 142, 103984. doi:10.1016/j.jmps.2020.103984.

Gao, X., Przybyla, C.P., Adams, B.L., 2006. Methodology for recovering and analyzing two-point pair correlation functions in polycrystalline materials. Metallurgical and Materials Transactions A 37, 2379–2387. doi:10.1007/BF02586212.

Geers, M., Kouznetsova, V., Brekelmans, A., 2010. Multi-scale computational homogenization: Trends and challenges. Journal of Computational and Applied Mathematics 234, 2175 – 2182. doi:10.1016/j.cam.2009.08.077.

Geißendörfer, M., Liebscher, A., Proppe, C., Redenbach, C., Schwarzer, D., 2014. Stochastic multiscale modeling of metal foams. Probabilistic Engineering Mechanics 37, 132 – 137. doi:10.1016/j.probengmech.2014.06.006.

Georgios, B., Benedikt, K., Raimund, R., 2021. Data-driven inverse uncertainty quantification in the transverse tensile response of carbon fiber reinforced composites. Composites Science and Technology 211, 108845. URL: https://www.sciencedirect.com/science/article/pii/S0266353821002013, doi:https://doi.org/10.1016/j.compscitech.2021.108845.

Ghanem, R., 1999. Ingredients for a general purpose stochastic finite elements implementation. Computer Methods in Applied Mechanics and Engineering 168, 19 – 34. doi:10.1016/S0045-7825(98)00106-6.

Ghanem, R., Brzakala, W., 1996. Stochastic finite-element analysis of soil layers with random interface. Journal of Engineering Mechanics 122, 361–369. doi:10.1061/(ASCE)0733-9399(1996)122:4(361).

Ghanem, R., Spanos, P., 1991. Stochastic Finite Elements: A Spectral Approach. Springer Verlag.

Ghanem, R.G., Kruger, R.M., 1996. Numerical solution of spectral stochastic finite element systems. Computer Methods in Applied Mechanics and Engineering 129, 289 – 303. doi:10.1016/0045-7825(95)00909-4.

Ghavamian, F., Simone, A., 2019. Accelerating multiscale finite element simulations of history-dependent materials using a recurrent neural network. Computer Methods in Applied Mechanics and Engineering 357, 112594. doi:10.1016/j.cma.2019.112594.

Gogu, C., Yin, W., Haftka, R., Ifju, P., Molimard, J., Le Riche, R., Vautrin, A., 2013. Bayesian identification of elastic constants in multi-directional laminate from moiré interferometry displacement fields. Experimental Mechanics 53, 635–648. doi:10.1007/s11340-012-9671-8.

Goldsmith, M.B., Sankar, B.V., Haftka, R.T., Goldberg, R.K., 2015. Effects of microstructural variability on thermo-mechanical properties of a woven ceramic matrix composite. Journal of Composite Materials 49, 335–350. doi:10.1177/0021998313519151.

Gorji, M.B., Mozaffar, M., Heidenreich, J.N., Cao, J., Mohr, D., 2020. On the potential of recurrent neural networks for modeling path dependent plasticity. Journal of the Mechanics and Physics of Solids 143, 103972. doi:https://doi.org/10.1016/j.jmps.2020.103972.

Goury, O., Amsallem, D., Bordas, S.P.A., Liu, W.K., Kerfriden, P., 2016. Automatised selection of load paths to construct reduced-order models in computational damage micromechanics: from dissipation-driven random selection to bayesian optimization. Computational Mechanics 58, 213–234. URL: https://doi.org/10.1007/s00466-016-1290-2, doi:10.1007/s00466-016-1290-2.

Graham-Brady, L.L., Arwade, S., Corr, D., Gutiérrez, M.A., Breysse, D., Grigoriu, M., Zabaras, N., 2006. Probability and materials: from nano- to macro-scale: A summary. Probabilistic Engineering Mechanics 21, 193 – 199. doi:10.1016/j.probengmech.2005.10.005. probability and Materials: from Nano- to Macro-Scale.

Grimmett, G., Stirzaker, D., 2001. Probability and random processes. Oxford university press. doi:10.1016/B978-0-12-172651-5.X5000-3.

Guilleminot, J., Noshadravan, A., Soize, C., Ghanem, R.G., 2011. A probabilistic model for bounded elasticity tensor random fields with application to polycrystalline microstructures. Computer Methods in Applied Mechanics and Engineering 200, 1637 – 1648. doi:10.1016/j.cma.2011.01.016.

Gupta, A., Cecen, A., Goyal, S., Singh, A.K., Kalidinhi, S.R., 2015. Structure-property linkages using a data science approach: Application to a non-metallic inclusion/steel composite system. Acta Materialia 91, 239 – 254. doi:10.1016/j.actamat.2015.02.045.

Gupta, M., Wang, K.K., 1993. Fiber orientation and mechanical properties of short-fiber-reinforced injection-molded composites: Simulated and experimental results. Polymer Composites 14, 367–382. doi:10.1002/pc.750140503.

Haario, H., Saksman, E., Tamminen, J., 1999. Adaptive proposal distribution for random walk metropolis algorithm. Computational Statistics 14, 375–395. doi:10.1007/s001800050022.

Heinze, S., Bleistein, T., Düster, A., Diebels, S., Jung, A., 2018. Experimental and numerical investigation of single pores for identification of effective metal foams properties: Experimental and numerical investigation of single pores for identification of effective metal foams properties. ZAMM - Journal of Applied Mathematics and Mechanics / Zeitschrift für Angewandte Mathematik und Mechanik 98, 682–695. doi:10.1002/zamm.201700045.

Hernández, J.A., Oliver, J., Huespe, A., Caicedo, M., Cante, J., 2014. High-performance model reduction techniques in computational multiscale homogenization. Computer Methods in Applied Mechanics and Engineering 276, 149 – 189. doi:10.1016/j.cma.2014.03.011.

Hernandez, W., Borges, F., Castello, D., Roitman, N., Magluta, C., 2015. Bayesian inference applied on model calibration of a fractional derivative viscoelastic model, in: DINAME 2015 - Proceedings of the XVII International Symposium on Dynamic Problems of Mechanics.

Hill, R., 1952. The elastic behaviour of a crystalline aggregate. Proceedings of the Physical Society. Section A 65, 349–354. doi:10.1088/0370-1298/65/5/307.

Hill, R., 1965a. Continuum micro-mechanics of elastoplastic polycrystals. Journal of the Mechanics and Physics of Solids 13, 89 – 101. doi:DOI:10.1016/0022-5096(65)90023-2.

Hill, R., 1965b. A self-consistent mechanics of composite materials. Journal of the Mechanics and Physics of Solids 13, 213 – 222. doi:DOI:10.1016/0022-5096(65)90010-4.

Hoang, T.H., Guerich, M., Yvonnet, J., 2016. Determining the size of rve for nonlinear random composites in an incremental computational homogenization framework. Journal of Engineering Mechanics 142, 04016018. doi:10.1061/(ASCE)EM.1943-7889.0001057.

Hoang, T.V., Wu, L., Golinval, J.C., Arnst, M., Noels, L., 2018. Stochastic multiscale model of mems stiction accounting for high-order statistical moments of non-gaussian contacting surfaces. Journal of Microelectromechanical Systems 27, 137–155. doi:10.1109/JMEMS.2018.2797133.

Hoang, T.V., Wu, L., Paquay, S., Golinval, J.C., Arnst, M., Noels, L., 2017. A computational stochastic multiscale methodology for mems structures involving adhesive contact. Tribology International 110, 401 – 425. doi:10.1016/j.triboint.2016.10.007.

Hobbiebrunken, T., Hojo, M., Jin, K., Ha, S., 2008. Influence of non-uniform fiber arrangement on microscopic stress and failure initiation in thermally and transversely loaded cf/epoxy laminated composites. Composites Science and Technology 68, 3107 – 3113. doi:10.1016/j.compscitech.2008.07.006.

Hojo, M., Mizuno, M., Hobbiebrunken, T., Adachi, T., Tanaka, M., Kyu Ha, S., 2009. Effect of fiber array irregularities on microscopic interfacial normal stress states of transversely loaded ud-cfrp from viewpoint of failure initiation. Composites Science and Technology 69, 1726 – 1734. doi:10.1016/j.compscitech.2008.08.032. experimental Techniques and Design in Composite Materials (ETDCM8) with Regular Papers.

Hu, N., Fish, J., McAuliffe, C., 2017. An adaptive stochastic inverse solver for multiscale characterization of composite materials. International Journal for Numerical Methods in Engineering 109. doi:10.1002/nme.5341.

Huang, D., Fuhg, J.N., Weienfels, C., Wriggers, P., 2020. A machine learning based plasticity model using proper orthogonal decomposition. Computer Methods in Applied Mechanics and Engineering 365, 113008. URL: http://www.sciencedirect.com/science/article/pii/S0045782520301924, doi:https://doi.org/10.1016/j.cma.2020.113008.

Huang, M., 2005. The n-point orientation correlation function and its application. International Journal of Solids and Structures 42, 1425 – 1441. doi:10.1016/j.ijsolstr.2004.06.037.

Huang, T., Gao, J., Sun, Q., Zeng, D., Su, X., Kam Liu, W., Chen, W., 2021. Stochastic nonlinear analysis of unidirectional fiber composites using image-based microstructural uncertainty quantification. Composite Structures 260, 113470. URL: https://www.sciencedirect.com/science/article/pii/S0263822320333997, doi:https://doi.org/10.1016/j.compstruct.2020.113470.

Huet, C., 1990. Application of variational concepts to size effects in elastic heterogeneous bodies. Journal of the Mechanics and Physics of Solids 38, 813 – 841. doi:10.1016/0022-5096(90)90041-2.

Hun, D.A., Guilleminot, J., Yvonnet, J., Bornert, M., 2019. Stochastic multiscale modeling of crack propagation in random heterogeneous media. International Journal for Numerical Methods in Engineering 119, 1325–1344. doi:10.1002/nme.6093.

Isenberg, J., 1979. Progressing from least squares to bayesian estimation, in: ASME (Ed.), Proceedings of the 1979 ASME design engineering technical conference, New York, USA. pp. 71–82.

Ito, O., Fuller, E., 1993. Computer modelling of anisotropic grain microstructure in two dimensions. Acta Metallurgica et Materialia 41, 191 – 198. doi:10.1016/0956-7151(93)90350-2.

Jang, W.Y., Kraynik, A.M., Kyriakides, S., 2008. On the microstructure of open-cell foams and its effect on elastic properties. International Journal of Solids and Structures 45, 1845 – 1875. doi:10.1016/j.ijsolstr.2007.10.008.

Jaynes, E.T., 2003. in: Bretthorst, G.L. (Ed.), Probability Theory: The Logic of Science. Cambridge University Press. doi:10.1017/CBO9780511790423.

Jelf, P., Fleck, N., 1992. Compression failure mechanisms in unidirectional composites. Journal of Composite Materials 26, 2706–2726. doi:10.1177/002199839202601804.

Jia, X., Williams, R., 2001. A packing algorithm for particles of arbitrary shapes. Powder Technology 120, 175 – 186. doi:10.1016/S0032-5910(01)00268-6.

Jiao, Y., Stillinger, F.H., Torquato, S., 2009. A superior descriptor of random textures and its predictive capacity. Proceedings of the National Academy of Sciences 106, 17634–17639. doi:10.1073/pnas.0905919106.

Jung, A., Diebels, S., 2017. Microstructural characterisation and experimental determination of a multiaxial yield surface for open-cell aluminium foams. Materials & Design 131, 252–264. doi:10.1016/j.matdes.2017.06.017.

Kalidindi, S.R., Brough, D.B., Li, S., Cecen, A., Blekh, A.L., Congo, F.Y.P., Campbell, C., 2016. Role of materials data science and informatics in accelerated materials innovation. MRS Bulletin 41, 596602. doi:10.1557/mrs.2016.164.

Kamiński, M., Kleiber, M., 1996. Stochastic structural interface defects in fiber composites. International Journal of Solids and Structures 33, 3035 – 3056. doi:10.1016/0020-7683(95)00264-2.

Kamiśki, M., 2012. Stochastic boundary element method analysis of the interface defects in composite materials. Composite Structures 94, 394 – 402. doi:10.1016/j.compstruct.2011.07.026.

Kanit, T., Forest, S., Galliet, I., Mounoury, V., Jeulin, D., 2003. Determination of the size of the representative volume element for random composites: statistical and numerical approach. International Journal of Solids and Structures 40, 3647 – 3679. doi:10.1016/S0020-7683(03)00143-4.

Kanouté, P., Boso, D., Chaboche, J., Schrefler, B., 2009. Multiscale methods for composites: A review. Archives of Computational Methods in Engineering 16, 31–75. 10.1007/s11831-008-9028-8.

Karimi, P., Malyarenko, A., Ostoja-Starzewski, M., Zhang, X., 2020. Rve problem: Mathematical aspects and related stochastic mechanics. International Journal of Engineering Science 146, 103169. doi:https://doi.org/10.1016/j.ijengsci.2019.103169.

Karkanas, P.I., Partridge, I.K., 2000. Cure modeling and monitoring of epoxy/amine resin systems. i. cure kinetics modeling. Journal of Applied Polymer Science 77, 1419–1431. doi:10.1002/1097-4628(20000815)77:7<1419::AID-APP3>3.0.CO;2-N.

Kilingar, N.G., Ehab Moustafa Kamel, K., Sonon, B., Massart, T.J., Noels, L., 2019. Computational generation of open-foam representative volume elements with morphological control using distance fields. European Journal of Mechanics - A/Solids , 103847doi:10.1016/j.euromechsol.2019.103847.

Kirchdoerfer, T., Ortiz, M., 2016. Data-driven computational mechanics. Computer Methods in Applied Mechanics and Engineering 304, 81–101. URL: https://www.sciencedirect.com/science/article/pii/S0045782516300238, doi:https://doi.org/10.1016/j.cma.2016.02.001.

Koutsourelakis, P.S., 2012. A novel bayesian strategy for the identification of spatially varying material properties and model validation: an application to static elastography. International Journal for Numerical Methods in Engineering 91, 249–268. doi:10.1002/nme.4261.

Kraynik, A.M., Reinelt, D.A., van Swol, F., 2003. Structure of random monodisperse foam. Physical Review E 67. doi:10.1103/PhysRevE.67.031403.

Krill III, C., Chen, L.Q., 2002. Computer simulation of 3-d grain growth using a phase-field model. Acta Materialia 50, 3059 – 3075. doi:10.1016/S1359-6454(02)00084-8.

Kröner, E., 1958. Berechnung der elastischen konstanten des vielkristalls aus den konstanten des einkristalls. Zeitschrift für Physik A Hadrons and Nuclei 151, 504–518. 10.1007/BF01337948.

Kugler, D., Moon, T.J., 2002. Identification of the most significant processing parameters on the development of fiber waviness in thin laminates. Journal of Composite Materials 36, 1451–1479. doi:10.1177/0021998302036012575.

Lahellec, N., Ponte Castañeda, P., Suquet, P., 2011. Variational estimates for the effective response and field statistics in thermoelastic composites with intra-phase property fluctuations. Proceedings of the Royal Society A: Mathematical, Physical and Engineering Science 467, 2224–2246. doi:10.1098/rspa.2010.0609.

Lahellec, N., Suquet, P., 2007a. On the effective behavior of nonlinear inelastic composites: I. incremental variational principles. Journal of the Mechanics and Physics of Solids 55, 1932 – 1963. doi:10.1016/j.jmps.2007.02.003.

Lahellec, N., Suquet, P., 2007b. On the effective behavior of nonlinear inelastic composites: II. a second-order procedure. Journal of the Mechanics and Physics of Solids 55, 1964 – 1992. doi:10.1016/j.jmps.2007.02.004.

Lahellec, N., Suquet, P., 2013. Effective response and field statistics in elasto-plastic and elasto-viscoplastic composites under radial and non-radial loadings. International Journal of Plasticity doi:10.1016/j.ijplas.2012.09.005.

Lai, T.C., Ip, K., 1996. Parameter estimation of orthotropic plates by bayesian sensitivity analysis. Composite Structures 34, 29 – 42. doi:10.1016/0263-8223(95)00128-X.

Le, B.A., Yvonnet, J., He, Q.C., 2015. Computational homogenization of nonlinear elastic materials using neural networks. International Journal for Numerical Methods in Engineering 104, 1061–1084. doi:10.1002/nme.4953.

Le Maitre, O., Knio, O., 2010. Spectral methods for uncertainty quantification - with applications to computational fluid dynamics. Scientific Computation, Springer. doi:10.1007/978-90-481-3520-2.

Lepage, S., Stump, F.V., Kim, I.H., Geubelle, P.H., 2011. Perturbation stochastic finite element-based homogenization of polycrystalline materials. Journal of Mechanics of Materials and Structures 6, 1153–1170. doi:10.2140/jomms.2011.6.1153.

Li, K., Gao, W., Wu, D., Song, C., Chen, T., 2018. Spectral stochastic isogeometric analysis of linear elasticity. Computer Methods in Applied Mechanics and Engineering 332, 157–190. URL: https://www.sciencedirect.com/science/article/pii/S0045782517307648, doi:https://doi.org/10.1016/j.cma.2017.12.012.

Li, Y., Chen, W., Jin, X., Xu, H., 2016. 3d representative volume element reconstruction of fiber composites via orientation tensor and substructure features, in: Davidson, B., Czabaj, M., Ratcliffe, J. (Eds.), Proceedings of the American Society for Composites - 31st Technical Conference, ASC 2016, DEStech Publications Inc., United States.

Liebscher, A., 2015. Laguerre approximation of random foams. Philosophical Magazine 95, 2777–2792. doi:10.1080/14786435.2015.1078511.

Liebscher, A., Proppe, C., Redenbach, C., Schwarzer, D., 2012. Uncertainty quantification for metal foam structures by means of image analysis. Probabilistic Engineering Mechanics 28, 143 – 151. doi:10.1016/j.probengmech.2011.08.015. computational Stochastic Mechanics CSM6.

Liebscher, A., Proppe, C., Redenbach, C., Schwarzer, D., 2013. Stochastic multiscale modeling of metal foams. Procedia IUTAM 6, 87 – 96. doi:10.1016/j.piutam.2013.01.010. iUTAM Symposium on Multiscale Problems in Stochastic Mechanics.

Liu, W.K., Belytschko, T., Mani, A., 1986. Probabilistic finite elements for nonlinear structural dynamics. Computer Methods in Applied Mechanics and Engineering 56, 61 – 81. doi:10.1016/0045-7825(86)90136-2.

Liu, Z., Bessa, M., Liu, W.K., 2016. Self-consistent clustering analysis: An efficient multi-scale scheme for inelastic heterogeneous materials. Computer Methods in Applied Mechanics and Engineering 306, 319 – 341. doi:10.1016/j.cma.2016.04.004.

Liu, Z., Fleming, M., Liu, W.K., 2018. Microstructural material database for self-consistent clustering analysis of elastoplastic strain softening materials. Computer Methods in Applied Mechanics and Engineering 330, 547 – 577. URL: http://www.sciencedirect.com/science/article/pii/S0045782517307107, doi:10.1016/j.cma.2017.11.005.

Liu, Z., Wu, C., 2019. Exploring the 3d architectures of deep material network in data-driven multiscale mechanics. Journal of the Mechanics and Physics of Solids 127, 20 – 46. doi:10.1016/j.jmps.2019.03.004.

Liu, Z., Wu, C., Koishi, M., 2019. A deep material network for multiscale topology learning and accelerated nonlinear modeling of heterogeneous materials. Computer Methods in Applied Mechanics and Engineering 345, 1138 – 1168. doi:10.1016/j.cma.2018.09.020.

Liu, Z., Yang, M., Cheng, J., Tan, J., 2021. A new stochastic isogeometric analysis method based on reduced basis vectors for engineering structures with random field uncertainties. Applied Mathematical Modelling 89, 966–990. URL: https://www.sciencedirect.com/science/article/pii/S0307904X20304352, doi:https://doi.org/10.1016/j.apm.2020.08.006.

Logarzo, H.J., Capuano, G., Rimoli, J.J., 2021. Smart constitutive laws: Inelastic homogenization through machine learning. Computer Methods in Applied Mechanics and Engineering 373, 113482. URL: https://www.sciencedirect.com/science/article/pii/S0045782520306678, doi:https://doi.org/10.1016/j.cma.2020.113482.

Lu, B., Torquato, S., 1992. Lineal-path function for random heterogeneous materials. Phys. Rev. A 45, 922–929. doi:10.1103/PhysRevA.45.922.

Lu, X., Yvonnet, J., Papadopoulos, L., Kalogeris, I., Papadopoulos, V., 2021. A stochastic fe2 data-driven method for nonlinear multiscale modeling. Materials 14. URL: https://www.mdpi.com/1996-1944/14/11/2875, doi:10.3390/ma14112875.

Lucas, V., Golinval, J.C., Paquay, S., Nguyen, V.D., Noels, L., Wu, L., 2015. A stochastic computational multiscale approach; application to mems resonators. Computer Methods in Applied Mechanics and Engineering 294, 141 – 167. doi:10.1016/j.cma.2015.05.019.

Lucas, V., Golinval, J.C., Voicu, R.C., Danila, M., Gavrila, R., Müller, R., Dinescu, A., Noels, L., Wu, L., 2017. Propagation of material and surface profile uncertainties on mems micro-resonators using a stochastic second-order computational multi-scale approach. International Journal for Numerical Methods in Engineering 111, 26–68. doi:10.1002/nme.5452.

Ma, J., Sahraee, S., Wriggers, P., De Lorenzis, L., 2015. Stochastic multiscale homogenization analysis of heterogeneous materials under finite deformations with full uncertainty in the microstructure. Computational Mechanics 55, 819–835. doi:10.1007/s00466-015-1136-3.

MacSleyne, J., Simmons, J., De Graef, M., 2008. On the use of 2-d moment invariants for the automated classification of particle shapes. Acta Materialia 56, 427 – 437. doi:10.1016/j.actamat.2007.09.039.

Madireddy, S., Sista, B., Vemaganti, K., 2015. A bayesian approach to selecting hyperelastic constitutive models of soft tissue. Computer Methods in Applied Mechanics and Engineering 291, 102 – 122. doi:10.1016/j.cma.2015.03.012.

Mahin, K.W., Hanson, K., Morris, J., 1980. Comparative analysis of the cellular and johnson-mehl microstructures through computer simulation. Acta Metallurgica 28, 443 – 453. doi:10.1016/0001-6160(80)90134-0.

Maligno, A.R., Warrior, N.A., Long, A.C., 2009. Effects of inter-fibre spacing on damage evolution in unidirectional (ud) fibre-reinforced composites. European Journal of Mechanics - A/Solids 28, 768 – 776. doi:10.1016/j.euromechsol.2008.10.009.

Malyarenko, A., Ostoja-Starzewski, M., 2016a. A random field formulation of hookes law in all elasticity classes (on line version). arXiv doi:arXiv:1602.09066v2.

Malyarenko, A., Ostoja-Starzewski, M., 2016b. Spectral expansions of homogeneous and isotropic tensor-valued random fields. Zeitschrift für angewandte Mathematik und Physik 59, 59. doi:10.1007/s00033-016-0657-8.

Malyarenko, A., Ostoja-Starzewski, M., 2016c. Tensor-valued random fields in continuum physics, in: Trovalusci, P. (Ed.), Materials with Internal Structure: Multiscale and Multifield Modeling and Simulation. Springer International Publishing, Cham, pp. 75–87. doi:10.1007/978-3-319-21494-8_6.

Malyarenko, A., Ostoja-Starzewski, M., 2017. A random field formulation of hookes law in all elasticity classes. Journal of Elasticity 127, 269–302. doi:10.1007/s10659-016-9613-2.

Mansour, R., Kulachenko, A., Chen, W., Olsson, M., 2019. Stochastic constitutive model of isotropic thin fiber networks based on stochastic volume elements. Materials 12. doi:10.3390/ma12030538.

Mariani, S., Martini, R., Ghisi, A., Corigliano, A., Beghi, M., 2011a. Overall elastic properties of polysilicon films: a statistical investigation of the effects of polycrystal morphology. International Journal for Multiscale Computational Engineering 9, 327–346.

Mariani, S., Martini, R., Ghisi, A., Corigliano, A., Simoni, B., 2011b. Monte carlo simulation of micro-cracking in polysilicon MEMS exposed to shocks. International Journal of Fracture 167, 83–101. doi:10.1007/s10704-010-9531-4.

Matous, K., Geers, M.G., Kouznetsova, V.G., Gillman, A., 2017. A review of predictive nonlinear theories for multiscale modeling of heterogeneous materials. Journal of Computational Physics 330, 192 – 220. doi:10.1016/j.jcp.2016.10.070.

Matthies, H.G., Brenner, C.E., Bucher, C.G., Soares, C.G., 1997. Uncertainties in probabilistic numerical analysis of structures and solids-stochastic finite elements. Structural Safety 19, 283 – 336. doi:10.1016/S0167-4730(97)00013-1.

McDowell, D.L., 2010. A perspective on trends in multiscale plasticity. International Journal of Plasticity 26, 1280 – 1309. doi:10.1016/j.ijplas.2010.02.008. special Issue In Honor of David L. McDowell.

Mehrez, L., Doostan, A., Moens, D., Vandepitte, D., 2012a. Stochastic identification of composite material properties from limited experimental databases, part ii: Uncertainty modelling. Mechanical Systems and Signal Processing 27, 484 – 498. doi:10.1016/j.ymssp.2011.09.001.

Mehrez, L., Fish, J., Aitharaju, V., Rodgers, W.R., Ghanem, R., 2018. A pce-based multiscale framework for the characterization of uncertainties in complex systems. Computational Mechanics 61, 219–236. doi:10.1007/s00466-017-1502-4.

Mehrez, L., Moens, D., Vandepitte, D., 2012b. Stochastic identification of composite material properties from limited experimental databases, part i: Experimental database construction. Mechanical Systems and Signal Processing 27, 471 – 483. doi:10.1016/j.ymssp.2011.09.004.

Melro, A., Camanho, P.P., Pinho, S.T., 2008. Generation of random distribution of fibres in long-fibre reinforced composites. Composites Science and Technology 68, 2092 – 2102. doi:10.1016/j.compscitech.2008.03.013.

Michel, J.C., Suquet, P., 2009. Nonuniform transformation field analysis: a reduced model for multiscale nonlinear problems in solid mechanics, in: Galvanetto, U., Aliabadi, F. (Eds.), Multiscale Modelling in Solid Mechanics - Computational Approaches. Imperial College Press, London.. Imperial College Press, pp. 159–206. doi:10.1142/p604. iSBN: 978-1-84816-307-2.

Michel, J.C., Suquet, P., 2016. A model-reduction approach in micromechanics of materials preserving the variational structure of constitutive relations. Journal of the Mechanics and Physics of Solids 90, 254 – 285. doi:10.1016/j.jmps.2016.02.005.

Mignolet, M., Soize, C., 2008. Nonparametric stochastic modeling of linear systems with prescribed variance of several natural frequencies. Probabilistic Engineering Mechanics 23, 267 – 278. doi:10.1016/j.probengmech.2007.12.027. 5th International Conference on Computational Stochastic Mechanics.

Moens, D., Vandepitte, D., 2005. A survey of non-probabilistic uncertainty treatment in finite element analysis. Computer Methods in Applied Mechanics and Engineering 194, 1527 – 1555. URL: http://www.sciencedirect.com/science/article/pii/S0045782504004049, doi:https://doi.org/10.1016/j.cma.2004.03.019. special Issue on Computational Methods in Stochastic Mechanics and Reliability Analysis.

Mohamedou, M., Zulueta, K., Chung, C.N., Rappel, H., Beex, L., Adam, L., Arriaga, A., Major, Z., Wu, L., Noels, L., 2019. Bayesian identification of mean-field homogenization model parameters and uncertain matrix behavior in non-aligned short fiber composites. Composite Structures 220, 64 – 80. doi:10.1016/j.compstruct.2019.03.066.

Molinari, A., Canova, G., Ahzi, S., 1987. A self consistent approach of the large deformation polycrystal viscoplasticity. Acta Metallurgica 35, 2983–2994.

Molinari, A., El Houdaigui, F., Tóth, L., 2004. Validation of the tangent formulation for the solution of the non-linear eshelby inclusion problem. International Journal of Plasticity 20, 291 – 307. doi:10.1016/S0749-6419(03)00038-X.

Mori, T., Tanaka, K., 1973. Average stress in matrix and average elastic energy of materials with misfitting inclusions. Acta Metallurgica 21, 571–574. Cited By (since 1996) 1814.

Most, T., 2010. Identification of the parameters of complex constitutive models: Least squares minimization vs. bayesian updating, in: Straub, D. (Ed.), Reliability and Optimization of Structural Systems.

Moulinec, H., Suquet, P., 2003. Intraphase strain heterogeneity in nonlinear composites: a computational approach. European Journal of Mechanics - A/Solids 22, 751 – 770. doi:10.1016/S0997-7538(03)00079-2.

Mozaffar, M., Bostanabad, R., Chen, W., Ehmann, K., Cao, J., Bessa, M.A., 2019. Deep learning predicts path-dependent plasticity. Proceedings of the National Academy of Sciences 116, 26414–26420. doi:10.1073/pnas.1911815116, arXiv:https://www.pnas.org/content/116/52/26414.full.pdf.

Mulay, S., Becker, G., Vayrette, R., Raskin, J.P., Pardoen, T., Galceran, M., Godet, S., Noels, L., 2015. Multiscale modelling framework for the fracture of thin brittle polycrystalline films: application to polysilicon. Computational Mechanics 55, 73–91. doi:10.1007/s00466-014-1083-4.

Nguyen, V.D., Béchet, E., Geuzaine, C., Noels, L., 2012. Imposing periodic boundary condition on arbitrary meshes by polynomial interpolation. Computational Materials Science 55, 390 – 406. doi:10.1016/j.commatsci.2011.10.017.

Nguyen, V.D., Noels, L., 2021. Interaction-based material network: A general framework for (porous) microstructured materials. Computer Methods in Applied Mechanics and Engineering , 114300URL: https://www.sciencedirect.com/science/article/pii/S0045782521005934, doi:https://doi.org/10.1016/j.cma.2021.114300.

Nguyen, V.D., Noels, L., 2022. Micromechanics-based material networks revisited from the interaction viewpoint; robust and efficient implementation for multi-phase composites. European Journal of Mechanics - A/Solids 91, 104384. doi:https://doi.org/10.1016/j.euromechsol.2021.104384.

Nguyen, V.D., Wu, L., Noels, L., 2017. Unified treatment of microscopic boundary conditions and efficient algorithms for estimating tangent operators of the homogenized behavior in the computational homogenization method. Computational Mechanics 59, 483–505. doi:10.1007/s00466-016-1358-z.

Nguyen, V.D., Wu, L., Noels, L., 2019. A micro-mechanical model of reinforced polymer failure with length scale effects and predictive capabilities. validation on carbon fiber reinforced high-crosslinked rtm6 epoxy resin. Mechanics of Materials 133, 193 – 213. doi:10.1016/j.mechmat.2019.02.017.

Nguyen, V.P., Lloberas-Valls, O., Stroeven, M., Sluys, L.J., 2010. On the existence of representative volumes for softening quasi-brittle materials a failure zone averaging scheme. Computer Methods in Applied Mechanics and Engineering 199, 3028 – 3038. doi:10.1016/j.cma.2010.06.018.

Niezgoda, S., Fullwood, D., Kalidindi, S., 2008. Delineation of the space of 2-point correlations in a composite material system. Acta Materialia 56, 5285 – 5292. doi:10.1016/j.actamat.2008.07.005.

Noels, L., Wu, L., Adam, L., Seyfarth, J., Soni, G., Segurado, J., Laschet, G., Chen, G., Lesueur, M., Lobos, M., Böhlke, T., Reiter, T., Oberpeilsteiner, S., Salaberger, D., Weichert, D., Broeckmann, C., 2016. Effective properties, in: Handbook of Software Solutions for ICME. Wiley-VCH Verlag GmbH & Co. KGaA, pp. 433–485. doi:10.1002/9783527693566.ch6.

Noshadravan, A., Ghanem, R., Guilleminot, J., Atodaria, I., Peralta, P., 2013. Validation of a probabilistic model for mesoscale elasticity tensor or random polycrystals. International Journal for Uncertainty Quantification 3, 73–100. doi:10.1615/Int.J.UncertaintyQuantification.2012003901.

Nouy, A., 1999. Recent developments in spectral stochastic methods forthenumerical solution of stochastic partial differential equations. Archives of Computational Methods in Engineering 16, 251 – 285. doi:10.1007/s11831-009-9034-5.

Novák, J., Kučerová, A., Zeman, J., 2012. Compressing random microstructures via stochastic wang tilings. Phys. Rev. E 86, 040104. URL: https://link.aps.org/doi/10.1103/PhysRevE.86.040104, doi:10.1103/PhysRevE.86.040104.

Omairey, S.L., Dunning, P.D., Sriramula, S., 2019. Multiscale surrogate-based framework for reliability analysis of unidirectional frp composites. Composites Part B: Engineering 173, 106925. doi:10.1016/j.compositesb.2019.106925.

Oskay, C., Fish, J., 2007. Eigendeformation-based reduced order homogenization for failure analysis of heterogeneous materials. Computer Methods in Applied Mechanics and Engineering 196, 1216 – 1243. doi:10.1016/j.cma.2006.08.015.

Ostoja-Starzewski, M., 1993. Micromechanics as a basis of random elastic continuum approximations. Probabilistic Engineering Mechanics 8, 107 – 114. doi:10.1016/0266-8920(93)90004-F.

Ostoja-Starzewski, M., Du, X., Khisaeva, Z.F., Li, W., 2007. Comparisons of the size of the representative volume element in elastic, plastic, thermoelastic, and permeable random microstructures. International Journal for Multiscale Computational Engineering 5, 73–82.

Ostoja-Starzewski, M., Kale, S., Karimi, P., Malyarenko, A., Raghavan, B., Ranganathan, S., Zhang, J., 2016. Chapter two - scaling to rve in random media, Elsevier. volume 49 of *Advances in Applied Mechanics*, pp. 111 – 211. doi:10.1016/bs.aams.2016.07.001.

Ostoja-Starzewski, M., Wang, X., 1999. Stochastic finite elements as a bridge between random material microstructure and global response. Computer Methods in Applied Mechanics and Engineering 168, 35 – 49. doi:10.1016/S0045-7825(98)00105-4.

Paranjape, H.M., Aycock, K.I., Bonsignore, C., Weaver, J.D., Craven, B.A., Duerig, T.W., 2021. A probabilistic approach with built-in uncertainty quantification for the calibration of a superelastic constitutive model from full-field strain data. Computational Materials Science 192, 110357. URL: https://www.sciencedirect.com/science/article/pii/S0927025621000823, doi:https://doi.org/10.1016/j.commatsci.2021.110357.

Peric, D., de Souza Neto, E.A., Feijóo, R.A., Partovi, M., Molina, A.J.C., 2010. On micro-to-macro transitions for multi-scale analysis of non-linear heterogeneous materials: unified variational basis and finite element implementation. International Journal for Numerical Methods in Engineering 87, 149 – 170. doi:10.1002/nme.3014.

Perrin, G., Soize, C., Duhamel, D., Funfschilling, C., 2012. Identification of polynomial chaos representations in high dimension from a set of realizations. SIAM Journal on Scientific Computing 34, A2917–A2945. doi:10.1137/11084950X.

Pettermann, H.E., Plankensteiner, A.F., Böhm, H.J., Rammerstorfer, F.G., 1999. A thermo-elasto-plastic constitutive law for inhomogeneous materials based on an incremental Mori-Tanaka approach. Computers & Structures 71, 197 – 214. doi:DOI:10.1016/S0045-7949(98)00208-9.

Phoon, P., Huang, H., Quek, S., 2005. Simulation of strongly non-gaussian processes using karhunenloeve expansion. Probabilistic Engineering Mechanics 20, 188 – 198. doi:10.1016/j.probengmech.2005.05.007.

Pierard, O., Doghri, I., 2006. An enhanced affine formulation and the corresponding numerical algorithms for the mean-field homogenization of elasto-viscoplastic composites. International Journal of Plasticity 22, 131 – 157. doi:10.1016/j.ijplas.2005.04.001.

Pitz, E., Pochiraju, K., 2019. Quasi monte carlo simulations for stochastic failure analysis in composites, in: Proceedings of the American Society for Composites - 34th Technical Conference, ASC 2019. doi:10.12783/asc34/31406.

Pivovarov, D., Oberleiter, T., Willner, K., Steinmann, P., 2018a. Fuzzy-stochastic fembased homogenization framework for materials with polymorphic uncertainties in the microstructure. International Journal for Numerical Methods in Engineering 116, 633–660. doi:10.1002/nme.5947.

Pivovarov, D., Steinmann, P., 2016. Modified sfem for computational homogenization of heterogeneous materials with microstructural geometric uncertainties. Computational Mechanics 57, 123–147.

Pivovarov, D., Steinmann, P., Willner, K., 2018b. Two reduction methods for stochastic fem based homogenization using global basis functions. Computer Methods in Applied Mechanics and Engineering 332, 488 – 519. doi:10.1016/j.cma.2018.01.002.

Pivovarov, D., Zabihyan, R., Mergheim, J., Willner, K., Steinmann, P., 2019. On periodic boundary conditions and ergodicity in computational homogenization of heterogeneous materials with random microstructure. Computer Methods in Applied Mechanics and Engineering 357, 112563. doi:10.1016/j.cma.2019.07.032.

Ponte Castañeda, P., 1991. The effective mechanical properties of nonlinear isotropic composites. Journal of the Mechanics and Physics of Solids 39, 45–71. doi:DOI:10.1016/0022-5096(91)90030-R.

Ponte Castañeda, P., 1992. A new variational principle and its application to nonlinear heterogeneous systems. SIAM Journal on Applied Mathematics 52, 1321–1341.

Ponte Castañeda, P., 1996. Exact second-order estimates for the effective mechanical properties of nonlinear composite materials. Journal of the Mechanics and Physics of Solids 44, 827 – 862. doi:DOI:10.1016/0022-5096(96)00015-4.

Ponte Castañeda, P., 2002a. Second-order homogenization estimates for nonlinear composites incorporating field fluctuations: I - theory. Journal of the Mechanics and Physics of Solids 50, 737 – 757. doi:10.1016/S0022-5096(01)00099-0.

Ponte Castañeda, P., 2002b. Second-order homogenization estimates for nonlinear composites incorporating field fluctuations: II - applications. Journal of the Mechanics and Physics of Solids 50, 759 – 782. doi:10.1016/S0022-5096(01)00098-9.

Ponte Castañeda, P., Willis, J., 1995. The effect of spatial distribution on the effective behavior of composite materials and cracked media. Journal of the Mechanics and Physics of Solids 43, 1919 – 1951. doi:10.1016/0022-5096(95)00058-Q.

Popescu, R., Deodatis, G., Prevost, J., 1998. Simulation of homogeneous non-gaussian stochastic vector fields. Probabilistic Engineering Mechanics 13, 1 – 13. doi:10.1016/S0266-8920(97)00001-5.

Pruchnicki, E., 1998. Hyperelastic homogenized law for reinforced elastomer at finite strain with edge effects. Acta Mechanica 129, 139–162. doi:10.1007/BF01176742.

Rao, C., Liu, Y., 2020. Three-dimensional convolutional neural network (3d-cnn) for heterogeneous material homogenization. Computational Materials Science 184, 109850. URL: https://www.sciencedirect.com/science/article/pii/S0927025620303414, doi:https://doi.org/10.1016/j.commatsci.2020.109850.

Rappel, H., Beex, L., 2019. Estimating fibres material parameter distributions from limited data with the help of bayesian inference. European Journal of Mechanics - A/Solids 75, 169 – 196. doi:10.1016/j.euromechsol.2019.01.001.

Rappel, H., Beex, L., Hale, J., Noels, L., Bordas, S., 2019a. A tutorial on bayesian inference to identify material parameters in solid mechanics. Archives of Computational Methods in Engineering doi:10.1007/s11831-018-09311-x.

Rappel, H., Beex, L., Noels, L., Bordas, S., 2019b. Identifying elastoplastic parameters with bayes theorem considering output error, input error and model uncertainty. Probabilistic Engineering Mechanics 55, 28 – 41. doi:10.1016/j.probengmech.2018.08.004.

Rappel, H., Beex, L.A.A., Bordas, S.P.A., 2018. Bayesian inference to identify parameters in viscoelasticity. Mechanics of Time-Dependent Materials 22, 221–258. doi:10.1007/s11043-017-9361-0.

Rappel, H., Wu, L., Noels, L., Beex, L.A.A., 2019c. A Bayesian Framework to Identify Random Parameter Fields Based on the Copula Theorem and Gaussian Fields: Application to Polycrystalline Materials.

Journal of Applied Mechanics 86. doi:10.1115/1.4044894. 121009.

Reccia, E., De Bellis, M.L., Trovalusci, P., Masiani, R., 2018. Sensitivity to material contrast in homogenization of random particle composites as micropolar continua. Composites Part B: Engineering 136, 39 – 45. doi:10.1016/j.compositesb.2017.10.017.

Redenbach, C., 2009. Microstructure models for cellular materials. Computational Materials Science 44, 1397 – 1407. doi:10.1016/j.commatsci.2008.09.018.

Reuss, A., 1929. Berechnung del fliessgrenze von mischkristallen auf grund der plastizitätbedingung für einkristalle. Z Angew Math Mech 9, 49 – 58.

Rocha, I., Kerfriden, P., van der Meer, F.P., 2020. Micromechanics-based surrogate models for the response of composites: A critical comparison between a classical mesoscale constitutive model, hyper-reduction and neural networks. European Journal of Mechanics - A/Solids 82, 103995. doi:10.1016/j.euromechsol.2020.103995.

Rosi, B., Matthies, H.G., 2008. Computational approaches to inelastic media with uncertain parameters. Journal of the Serbian Society for Computational Mechanics 2, 28–43.

Rossol, M.N., Fast, T., Marshall, D.B., Cox, B.N., Zok, F.W., 2015. Characterizing in-plane geometrical variability in textile ceramic composites. Journal of the American Ceramic Society 98, 205–213. doi:10.1111/jace.13275.

Sakata, S., Ashida, F., 2011. Hierarchical stochastic homogenization analysis of a particle reinforced composite material considering non-uniform distribution of microscopic random quantities. Computational Mechanics 48, 529–540. doi:10.1007/s00466-011-0604-7.

Salem, A.A., Shaffer, J.B., Satko, D.P., Semiatin, S.L., Kalidindi, S.R., 2014. Workflow for integrating mesoscale heterogeneities in materials structure with process simulation of titanium alloys. Integrating Materials and Manufacturing Innovation 3, 322–343. doi:10.1186/s40192-014-0024-6.

Salmi, M., Auslender, F., Bornert, M., Fogli, M., 2012. Apparent and effective mechanical properties of linear matrix-inclusion random composites: Improved bounds for the effective behavior. International Journal of Solids and Structures 49, 1195 – 1211. doi:10.1016/j.ijsolstr.2012.01.018.

Sankaran, S., Zabaras, N., 2007. Computing property variability of polycrystals induced by grain size and orientation uncertainties. Acta Materialia 55, 2279 – 2290. doi:10.1016/j.actamat.2006.11.025.

Savvas, D., Papaioannou, I., Stefanou, G., 2020. Bayesian identification and model comparison for random property fields derived from material microstructure. Computer Methods in Applied Mechanics and Engineering 365, 113026. doi:10.1016/j.cma.2020.113026.

Savvas, D., Stefanou, G., 2017. Assessment of the effect of microstructural uncertainty on the macroscopic properties of random composite materials. Journal of Composite Materials 51, 2707–2725. doi:10.1177/0021998316677333.

Savvas, D., Stefanou, G., Papadrakakis, M., 2016. Determination of rve size for random composites with local volume fraction variation. Computer Methods in Applied Mechanics and Engineering 305, 340 – 358. doi:10.1016/j.cma.2016.03.002.

Saylor, D.M., Fridy, J., El-Dasher, B.S., Jung, K.Y., Rollett, A.D., 2004. Statistically representative three-dimensional microstructures based on orthogonal observation sections. Metallurgical and Materials Transactions A 35, 1969–1979. doi:10.1007/s11661-004-0146-0.

Schröder, J., Labusch, M., Keip, M.A., 2016. Algorithmic two-scale transition for magneto-electro-mechanically coupled problems: Fe2-scheme: Localization and homogenization. Computer Methods in Applied Mechanics and Engineering 32, 253–280. doi:10.1016/j.cma.2015.10.005.

Scott, D.W., 2015. Multivariate density estimation: theory, practice, and visualization. John Wiley & Sons.

Segurado, J., Lebensohn, R.A., LLorca, J., 2018. Chapter one - computational homogenization of polycrystals, in: Hussein, M.I. (Ed.), Advances in Crystals and Elastic Metamaterials, Part 1. Elsevier. volume 51 of *Advances in Applied Mechanics*, pp. 1–114. URL: https://www.sciencedirect.com/science/article/pii/S0065215618300012, doi:https://doi.org/10.1016/bs.aams.2018.07.001.

Sena, M.P., Ostoja-Starzewski, M., Costa, L., 2013. Stiffness tensor random fields through upscaling of planar random materials. Probabilistic Engineering Mechanics 34, 131 – 156. doi:10.1016/j.probengmech.2013.08.008.

Sepahvand, K., 2016. Spectral stochastic finite element vibration analysis of fiber-reinforced composites with random fiber orientation. Composite Structures 145, 119 – 128. doi:10.1016/j.compstruct.2016.02.069.

Shabir, Z., Van der Giessen, E., Duarte, C.A., Simone, A., 2019. On the applicability of linear elastic fracture mechanics scaling relations in the analysis of intergranular fracture of brittle polycrystals. International Journal of Fracture 220, 205–219. doi:10.1007/s10704-019-00381-x.

Shinozuka, M., 1971. Simulation of multivariate and multidimensional random processes. The Journal of the Acoustical Society of America 49, 357–368. doi:10.1121/1.1912338.

Shinozuka, M., Jan, C.M., 1972. Digital simulation of random processes and its applications. Journal of Sound and Vibration 25, 111 – 128. doi:10.1016/0022-460X(72)90600-1.

Soize, C., 2000. A nonparametric model of random uncertainties for reduced matrix models in structural dynamics. Probabilistic Engineering Mechanics 15, 277 – 294. doi:10.1016/S0266-8920(99)00028-4.

Soize, C., 2005. Random matrix theory for modeling uncertainties in computational mechanics. Computer Methods in Applied Mechanics and Engineering 194, 1333 – 1366. doi:10.1016/j.cma.2004.06.038. special Issue on Computational Methods in Stochastic Mechanics and Reliability Analysis.

Soize, C., 2006. Non-gaussian positive-definite matrix-valued random fields for elliptic stochastic partial differential operators. Computer Methods in Applied Mechanics and Engineering 195, 26 – 64. doi:10.1016/j.cma.2004.12.014.

Soize, C., 2017. Uncertainty Quantification; An Accelerated Course with Advanced Applications in Computational Engineering. Interdisciplinary Applied Mathematics 47, Springer Nature. doi:10.1007/978-3-319-54339-0.

Soize, C., Ghanem, R., 2016. Data-driven probability concentration and sampling on manifold. Journal of Computational Physics 321, 242 – 258. doi:10.1016/j.jcp.2016.05.044.

Sokołowski, D., Kamiński, M., 2020. Probabilistic homogenization of hyper-elastic particulate composites with random interface. Composite Structures 241, 112118. doi:10.1016/j.compstruct.2020.112118.

Soldner, D., Brands, B., Zabihyan, R., Steinmann, P., Mergheim, J., 2017. A numerical study of different projection-based model reduction techniques applied to computational homogenisation. Computational Mechanics 60, 613–625. doi:10.1007/s00466-017-1428-x.

Sonon, B., Fran cois, B., Massart, T., 2012. A unified level set based methodology for fast generation of complex microstructural multi-phase rves. Computer Methods in Applied Mechanics and Engineering 223-224, 103 – 122. doi:10.1016/j.cma.2012.02.018.

Sonon, B., François, B., Massart, T.J., 2015. An advanced approach for the generation of complex cellular material representative volume elements using distance fields and level sets. Computational Mechanics 56, 221–242. doi:10.1007/s00466-015-1168-8.

Stafford, D., Jackson, T.L., 2010. Using level sets for creating virtual random packs of non-spherical convex shapes. Journal of Computational Physics 229, 3295 – 3315. doi:10.1016/j.jcp.2010.01.003.

Stefanou, G., 2009. The stochastic finite element method: Past, present and future. Computer Methods in Applied Mechanics and Engineering 198, 1031 – 1051. doi:10.1016/j.cma.2008.11.007.

Stefanou, G., Savvas, D., Papadrakakis, M., 2015. Stochastic finite element analysis of composite structures based on material microstructure. Composite Structures 132, 384 – 392. doi:10.1016/j.compstruct.2015.05.044.

Stefanou, G., Savvas, D., Papadrakakis, M., 2017. Stochastic finite element analysis of composite structures based on mesoscale random fields of material properties. Computer Methods in Applied Mechanics and Engineering 326, 319 – 337. doi:10.1016/j.cma.2017.08.002.

Strelen, J.C., Nassaj, F., 2007. Analysis and generation of random vectors with copulas, in: Proceedings of the 39th Conference on Winter Simulation: 40 Years! The Best is Yet to Come, IEEE Press, Piscataway, NJ, USA. pp. 488–496. doi:10.1109/WSC.2007.4419639.

Sudret, B., Der Kiureghian, A., 2000. Stochastic finite element methods and reliability, in: of Civil & Environmental Engineering, D. (Ed.), Structural Engineering, Mechanics and Materials, Report No UCB/SEEM-2000/08. Logos Verlag.

Suquet, P., 1995. Overall properties of nonlinear composites: A modified secant moduli theory and its link with ponte castañeda's nonlinear variational procedure. Comptes Rendus de l" Académie des Sciences 320, 563–571.

Székely, G.J., Rizzo, M.L., Bakirov, N.K., 2007. Measuring and testing dependence by correlation of distances. Ann. Statist. 35, 2769–2794. doi:10.1214/009053607000000505.

Tal, D., Fish, J., 2016. Generating a statistically equivalent representative volume element with discrete defects. Composite Structures 153, 791 – 803. doi:10.1016/j.compstruct.2016.06.077.

Talbot, D., Willis, J., 1992. Some simple explicit bounds for the overall behaviour of nonlinear composites. International Journal of Solids and Structures 29, 1981 – 1987. doi:DOI:10.1016/0020-7683(92)90188-Y.

Talbot, D.R.S., Willis, J.R., 1985. Variational principles for inhomogeneous non-linear media. IMA Journal of Applied Mathematics 35, 39–54. doi:10.1093/imamat/35.1.39.

Talbot, D.R.S., Willis, J.R., 1987. Bounds and self-consistent estimates for the overall properties of nonlinear composites. IMA Journal of Applied Mathematics 39, 215–240. doi:10.1093/imamat/39.3.215.

Tootkaboni, M., Graham-Brady, L., 2010. A multi-scale spectral stochastic method for homogenization of multi-phase periodic composites with random material properties. International Journal for Numerical Methods in Engineering 83, 59–90. doi:10.1002/nme.2829.

Torquato, S., 2002. Microstructural Descriptors. Springer New York, New York, NY. pp. 23–58. doi:10.1007/978-1-4757-6355-3_2.

Trovalusci, P., De Bellis, M.L., Ostoja-Starzewski, M., Murrali, A., 2014. Particulate random composites homogenized as micropolar materials. Meccanica 49, 2719–2727. doi:10.1007/s11012-014-0031-x.

Trovalusci, P., Ostoja-Starzewski, M., De Bellis, M.L., Murrali, A., 2015. Scale-dependent homogenization of random composites as micropolar continua. European Journal of Mechanics - A/Solids 49, 396 – 407. doi:10.1016/j.euromechsol.2014.08.010.

Tu, S.T., Cai, W.Z., Yin, Y., Ling, X., 2005. Numerical simulation of saturation behavior of physical properties in composites with randomly distributed second-phase. Journal of Composite Materials 39, 617–631. doi:10.1177/0021998305047263.

Vanaerschot, A., Cox, B.N., Lomov, S.V., Vandepitte, D., 2013a. Stochastic framework for quantifying the geometrical variability of laminated textile composites using micro-computed tomography. Composites Part A: Applied Science and Manufacturing 44, 122 – 131. doi:10.1016/j.compositesa.2012.08.020.

Vanaerschot, A., Cox, B.N., Lomov, S.V., Vandepitte, D., 2013b. Stochastic multi-scale modelling of textile composites based on internal geometry variability. Computers & Structures 122, 55 – 64. doi:10.1016/j.compstruc.2012.10.026. computational Fluid and Solid Mechanics 2013.

Vanaerschot, A., Cox, B.N., Lomov, S.V., Vandepitte, D., 2014. Simulation of the cross-correlated positions of in-plane tow centroids in textile composites based on experimental data. Composite Structures 116, 75 – 83. doi:10.1016/j.compstruct.2014.05.017.

Vanaerschot, A., Panerai, F., Cassell, A., Lomov, S.V., Vandepitte, D., Mansour, N.N., 2017. Stochastic characterisation methodology for 3-d textiles based on micro-tomography. Composite Structures 173, 44 – 52. doi:10.1016/j.compstruct.2017.03.107.

Vaughan, T., McCarthy, C., 2010. A combined experimental-numerical approach for generating statistically equivalent fibre distributions for high strength laminated composite materials. Composites Science and Technology 70, 291 – 297. doi:10.1016/j.compscitech.2009.10.020.

Vecchio, I., Redenbach, C., Schladitz, K., Kraynik, A.M., 2016. Improved models of solid foams based on soap froth. Computational Materials Science 120, 60–69. doi:10.1016/j.commatsci.2016.03.029.

Verhoosel, C.V., Remmers, J.J.C., Gutiérrez, M.A., de Borst, R., 2010. Computational homogenization for adhesive and cohesive failure in quasi-brittle solids. International Journal for Numerical Methods in Engineering 83, 1155–1179. doi:10.1002/nme.2854.

Verpoest, I., Lomov, S.V., 2005. Virtual textile composites software wisetex: Integration with micro-mechanical, permeability and structural analysis. Composites Science and Technology 65, 2563 – 2574. doi:10.1016/j.compscitech.2005.05.031. 20th Anniversary Special Issue.

Vigliotti, A., Csányi, G., Deshpande, V., 2018. Bayesian inference of the spatial distributions of material properties. Journal of the Mechanics and Physics of Solids 118, 74 – 97. doi:10.1016/j.jmps.2018.05.007.

Vincent, M., Giroud, T., Clarke, A., Eberhardt, C., 2005. Description and modeling of fiber orientation in injection molding of fiber reinforced thermoplastics. Polymer 46, 6719 – 6725. doi:10.1016/j.polymer.2005.05.026. polymer Blends, Composites and Hybrid Polymeric Materials.

Voigt, W., 1889. über die beziehung zwischen den beiden elastizitätskonstanten isotroper körper. Wied Ann 38, 573 – 587.

Vořechovský, M., 2008. Simulation of simply cross correlated random fields by series expansion methods. Structural Safety 30, 337 – 363. URL: http://www.sciencedirect.com/science/article/pii/S0167473007000422, doi:https://doi.org/10.1016/j.strusafe.2007.05.002.

Doškář, M., Novák, J., Zeman, J., 2014. Aperiodic compression and reconstruction of real-world material systems based on wang tiles. Phys. Rev. E 90, 062118. URL: https://link.aps.org/doi/10.1103/PhysRevE.90.062118, doi:10.1103/PhysRevE.90.062118.

Williams, S.R., Philipse, A.P., 2003. Random packings of spheres and spherocylinders simulated by mechanical contraction. Physiscal Review E 67, 051301. doi:10.1103/PhysRevE.67.051301.

Wirtz, D., Karajan, N., Haasdonk, B., 2015. Surrogate modeling of multiscale models using kernel methods. International Journal for Numerical Methods in Engineering 101, 1–28. doi:10.1002/nme.4767.

Wu, L., Adam, L., Doghri, I., Noels, L., 2017. An incremental-secant mean-field homogenization method with second statistical moments for elasto-visco-plastic composite materials. Mechanics of Materials 114, 180 – 200. doi:10.1016/j.mechmat.2017.08.006.

Wu, L., Adam, L., Noels, L., 2021. Micro-mechanics and data-driven based reduced order models for multi-scale analyses of woven composites. Composite Structures 270, 114058. URL: https://www.sciencedirect.com/science/article/pii/S0263822321005183, doi:https://doi.org/10.1016/j.compstruct.2021.114058.

Wu, L., Chung, C.N., Major, Z., Adam, L., Noels, L., 2018a. From SEM images to elastic responses: A stochastic multiscale analysis of UD fiber reinforced composites. Composite Structures 189, 206 – 227. doi:10.1016/j.compstruct.2018.01.051.

Wu, L., Lucas, V., Nguyen, V.D., Golinval, J.C., Paquay, S., Noels, L., 2016. A stochastic multi-scale approach for the modeling of thermo-elastic damping in micro-resonators. Computer Methods in Applied Mechanics and Engineering 310, 802 – 839. doi:10.1016/j.cma.2016.07.042.

Wu, L., Nghia Chung, C., Major, Z., Adam, L., Noels, L., 2018b. A micro-mechanics-based inverse study for stochastic order reduction of elastic ud-fiber reinforced composites analyzes. International Journal for Numerical Methods in Engineering 115, 1430 – 1456. doi:10.1002/nme.5903.

Wu, L., Nguyen, V.D., Adam, L., Noels, L., 2019. An inverse micro-mechanical analysis toward the stochastic homogenization of nonlinear random composites. Computer Methods in Applied Mechanics and Engineering 348, 97 – 138. doi:10.1016/j.cma.2019.01.016.

Wu, L., Nguyen, V.D., Kilingar, N.G., Noels, L., 2020a. A recurrent neural network-accelerated multi-scale model for elasto-plastic heterogeneous materials subjected to random cyclic and non-proportional loading paths. Computer Methods in Applied Mechanics and Engineering 369, 113234. doi:10.1016/j.cma.2020.113234.

Wu, L., Noels, L., 2022. Recurrent neural networks (rnns) with dimensionality reduction and break down in computational mechanics; application to multi-scale localization step. Computer Methods in Applied Mechanics and Engineering 390, 114476. URL: https://www.sciencedirect.com/science/article/pii/S0045782521006940, doi:https://doi.org/10.1016/j.cma.2021.114476.

Wu, L., Noels, L., Adam, L., Doghri, I., 2013a. A combined incremental–secant mean–field homogenization scheme with per–phase residual strains for elasto–plastic composites. International Journal of Plasticity 51, 80–102. doi:10.1016/j.ijplas.2013.06.006.

Wu, L., Noels, L., Adam, L., Doghri, I., 2013b. An implicit-gradient-enhanced incremental-secant mean-field homogenization scheme for elasto-plastic composites with damage. International Journal of Solids and Structures 50, 3843 – 3860. doi:10.1016/j.ijsolstr.2013.07.022.

Wu, L., Tjahjanto, D., Becker, G., Makradi, A., Jérusalem, A., Noels, L., 2013c. A micromeso-model of intra-laminar fracture in fiber-reinforced composites based on a discontinuous galerkin/cohesive zone method. Engineering Fracture Mechanics 104, 162 – 183. doi:10.1016/j.engfracmech.2013.03.018.

Wu, L., Zulueta, K., Major, Z., Arriaga, A., Noels, L., 2020b. Bayesian inference of non-linear multiscale model parameters accelerated by a deep neural network. Computer Methods in Applied Mechanics and Engineering 360, 112693. doi:10.1016/j.cma.2019.112693.

Wulfinghoff, S., Cavaliere, F., Reese, S., 2018. Model order reduction of nonlinear homogenization problems using a hashinshtrikman type finite element method. Computer Methods in Applied Mechanics and Engineering 330, 149 – 179. doi:10.1016/j.cma.2017.10.019.

Xu, H., Dikin, D.A., Burkhart, C.B., Chen, W., 2014. Descriptor-based methodology for statistical characterization and 3d reconstruction of microstructural materials. Computational Materials Science 85, 206 – 216. doi:10.1016/j.commatsci.2013.12.046.

Xu, R., Yang, J., Yan, W., Huang, Q., Giunta, G., Belouettar, S., Zahrouni, H., Ben Zineb, T., Hu, H., 2020. Data-driven multiscale finite element method: From concurrence to separation. Computer Methods in Applied Mechanics and Engineering 363, 112893. URL: https://www.sciencedirect.com/science/article/pii/S004578252030075X, doi:https://doi.org/10.1016/j.cma.2020.112893.

Xu, T., Li, M., 2009. Topological and statistical properties of a constrained voronoi tessellation. Philosophical Magazine 89, 349–374. doi:10.1080/14786430802647065.

Xu, T., Li, M., 2010. Geometric methods for microstructure rendition and atomic characterization of poly- and nano-crystalline materials. Philosophical Magazine 90, 2191–2222. doi:10.1080/14786431003630843.

Xu, X., Graham-Brady, L., 2005. A stochastic computational method for evaluation of global and local behavior of random elastic media. Computer Methods in Applied Mechanics and Engineering 194, 4362 – 4385. doi:10.1016/j.cma.2004.12.001.

Yabansu, Y.C., Steinmetz, P., Hötzer, J., Kalidindi, S.R., Nestler, B., 2017. Extraction of reduced-order process-structure linkages from phase-field simulations. Acta Materialia 124, 182 – 194. doi:10.1016/j.actamat.2016.10.071.

Yang, H., Guo, X., Tang, S., Liu, W.K., 2019. Derivation of heterogeneous material laws via data-driven principal component expansions. Computational Mechanics 64, 365–379. doi:10.1007/s00466-019-01728-w.

Yang, S., Yu, S., Ryu, J., Cho, J.M., Kyoung, W., Han, D.S., Cho, M., 2013. Nonlinear multiscale modeling approach to characterize elastoplastic behavior of cnt/polymer nanocomposites considering the interphase and interfacial imperfection. International Journal of Plasticity 41, 124 – 146. doi:10.1016/j.ijplas.2012.09.010.

Yang, Z., Yabansu, Y.C., Al-Bahrani, R., Liao, W.k., Choudhary, A.N., Kalidindi, S.R., Agrawal, A., 2018. Deep learning approaches for mining structure-property linkages in high contrast composites from simulation datasets. Computational Materials Science 151, 278 – 287. doi:10.1016/j.commatsci.2018.05.014.

Yeong, C.L.Y., Torquato, S., 1998. Reconstructing random media. Phys. Rev. E 57, 495–506. doi:10.1103/PhysRevE.57.495.

Yin, X., Chen, W., To, A., McVeigh, C., Liu, W., 2008. Statistical volume element method for predicting microstructureconstitutive property relations. Computer Methods in Applied Mechanics and Engineering 197, 3516 – 3529. doi:10.1016/j.cma.2008.01.008.

Yin, X., Lee, S., Chen, W., Liu, W.K., Horstemeyer, M.F., 2009. Efficient random field uncertainty propagation in design using multiscale analysis. Journal of Mechanical Design 131. doi:10.1115/1.3042159.

Yuan, Z., Fish, J., 2009. Multiple scale eigendeformation-based reduced order homogenization. Computer Methods in Applied Mechanics and Engineering 198, 2016 – 2038. doi:10.1016/j.cma.2008.12.038. advances in Simulation-Based Engineering Sciences Honoring J. Tinsley Oden.

Yun, G.J., Shang, S., 2016. A new inverse method for the uncertainty quantification of spatially varying random material properties. International Journal for Uncertainty Quantification 6, 515–531. doi:10.1615/Int.J.UncertaintyQuantification.2016018673.

Yvonnet, J., 2019. Solid mechanics and its applications, in: Computational Homogenization of Heterogeneous Materials with Finite Elements. Springer International Publishing.

Yvonnet, J., He, Q.C., 2007. The reduced model multiscale method (r3m) for the non-linear homogenization of hyperelastic media at finite strains. Journal of Computational Physics 223, 341 – 368. doi:10.1016/j.jcp.2006.09.019.

Yvonnet, J., Monteiro, E., He, Q.C., 2013. Computational homogenization method and reduced database model for hyperelastic heterogeneous structures. International Journal for Multiscale Computational Engineering 11, 201–225. doi:10.1615/IntJMultCompEng.2013005374.

Zhang, A., Mohr, D., 2020. Using neural networks to represent von mises plasticity with isotropic hardening. International Journal of Plasticity , 102732doi:https://doi.org/10.1016/j.ijplas.2020.102732.

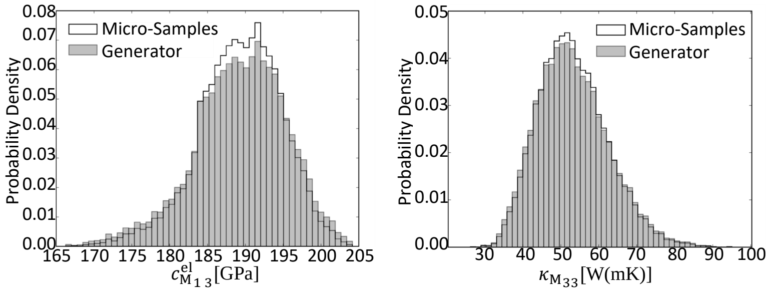

(a) $\{C^{\mathrm{el}}_{\mathrm{M}_{11}}(\omega^l) : \omega^l \in \mathcal{W}\}$ *vs.* $\{c^{\mathrm{el}^p}_{\mathrm{M}_{11}};\ p = 1,\ 2,\ ...\}$ (b) $\{\mathrm{K}_{\mathrm{M}_{33}}(\omega^l) : \omega^l \in \mathcal{W}\}$ *vs.* $\{\kappa^p_{\mathrm{M}_{33}};\ p = 1,\ 2,\ ...\}$

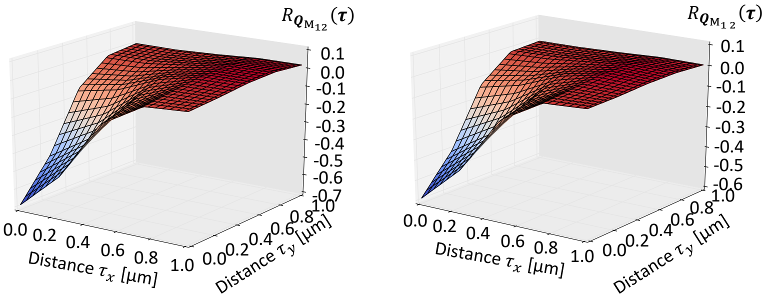

(c) $R_{\boldsymbol{Q}_{\mathrm{M}_{12}}}(\boldsymbol{\tau})$; Observations (d) $R_{\boldsymbol{Q}_{\mathrm{M}_{12}}}(\boldsymbol{\tau})$; Generated

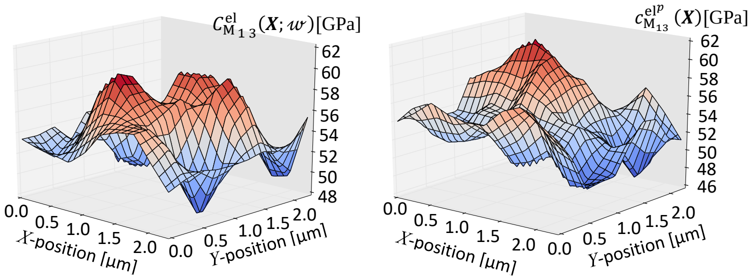

(e) $C^{\mathrm{el}}_{\mathrm{M}_{13}}(\omega^l)$ (f) $c^{\mathrm{el}^p}_{\mathrm{M}_{13}}$

Figure 35: Extraction and pseudo-samples generation using the high-number of parameters approach combined with a spectral generator for non-Gaussian random field of thermo-mechanical properties by Wu et al. (2016); The micro structure consists in a columnar poly-silicon of average grain size of about $l_{\text{micro}} \simeq 200$ nm: (a) and (b) Comparison of the distribution of respectively an elasticity tensor $\mathbf{c}^{\mathrm{el}}_{\mathrm{M}}$ component (1 1) and a thermal conductivity tensor $\boldsymbol{\kappa}_{\mathrm{M}}$ component (3 3) extracted from the observations $\omega^l \in \mathcal{W}$ with $l = 1..n^{\text{observation}}$ obtained by the window technique with an SVE size $l_{\text{SVE}} = 0.5\mu$m and from the generated pseudo-samples; (c) and (d) Comparison of the cross correlation of the random field $\{\boldsymbol{Q}_{\mathrm{M}}(\boldsymbol{X},\ \omega) : \boldsymbol{X} \in \Omega,\ \omega \in \mathcal{W}\}$ (295) obtained by, respectively, the window technique and the pseudo-samples generator; and (e) and (f) Illustrations of a random field realisation of an elasticity tensor $\mathbf{c}^{\mathrm{el}}_{\mathrm{M}}$ component (1 2) obtained by, respectively, the window technique and the pseudo-samples generator; Modified from Computer Methods in Applied Mechanics and Engineering 310, Wu, L., Lucas, V., Nguyen, V.D., Golinval, J.C., Paquay, S., Noels, L., A stochastic multi-scale approach for the modeling of thermo-elastic damping in micro-resonators, 802-839. Copyright (2016).

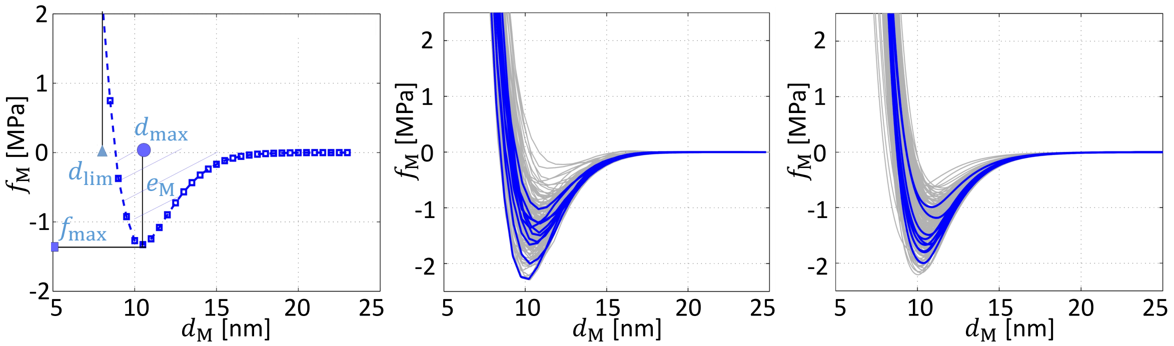

(a) Schematics

(b) Observations $\{F_{\mathrm{M}}(d_{\mathrm{M}};\, \boldsymbol{X},\, \mathfrak{w}^k) : \mathfrak{w}^k \in \mathcal{W}\}$

(c) Pseudo-samples $\{f^p_{\mathrm{M}}(d_{\mathrm{M}};\, \boldsymbol{X}) : p = 1,\, 2,\, \ldots\}$

Figure 36: Generation by Hoang et al. (2017) of stochastic adhesive contact forces accounting for the roughness of the surface: (a) Identification of adhesive force features; (b) 200 observations $\{F_{\mathrm{M}}(d_{\mathrm{M}};\, \boldsymbol{X},\, \mathfrak{w}^k) : \mathfrak{w}^k \in \mathcal{W}\}$ obtained by MC of the micro-mechanics model, 10 of which are highlighted; and (c) 200 pseudo-samples $\{f^p_{\mathrm{M}}(d_{\mathrm{M}};\, \boldsymbol{X}) : p = 1,\, 2,\, \ldots\}$ obtained by the PCE, 10 of which are highlighted; Modified from Tribology International 110, Hoang, T.V., Wu, L., Paquay, S., Golinval, J.C., Arnst, M., Noels, L., A computational stochastic multiscale methodology for mems structures involving adhesive contact, 401-425. Copyright (2017).

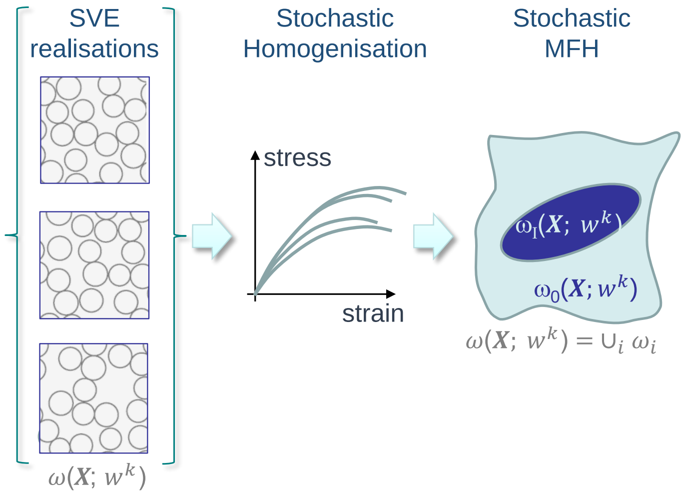

Figure 37: MFH-based multi-fidelity: Extraction of stochastic equivalent MFH problems $\omega(\boldsymbol{X};\, \mathfrak{w}^k)$ from direct computational homogenisation performed on virtual SVEs.

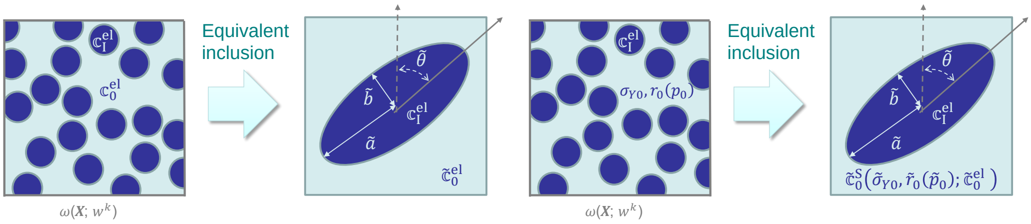

(a) Elastic identification

(b) Elasto-plastic law identification

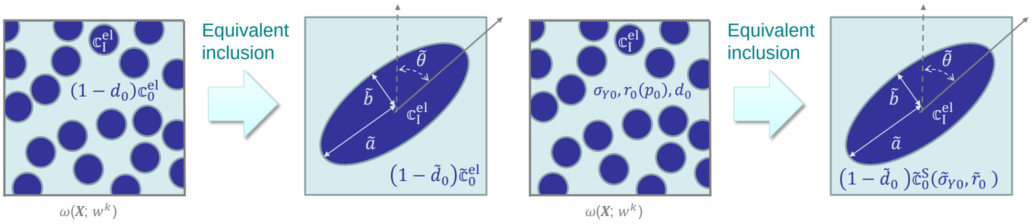

(c) Damage law identification

(d) Elasto-plastic law identification of damage-enhanced matrix

Figure 38: Equivalent MFH problem defintion for each SVE realisation $\omega(\boldsymbol{X}; \mathfrak{w}^k)$: (a) Identification of the equivalent inclusion of equivalent semi-axes $\tilde{a}$ and $\tilde{b}$ and equivalent orientation $\tilde{\theta}$ and of the equivalent elastic matrix of equivalent elastic tensor $\tilde{\mathbb{C}}_0^\mathrm{el}$; (b) Case of elastic inclusions embedded in an elasto-plastic matrix with the identification of the equivalent matrix yield stress $\tilde{\sigma}_{Y0}$ and equivalent matrix hardening law $\tilde{r}_0(\tilde{p}_0)$; (c) Case of elastic inclusions embedded in a damage-enhanced elasto-plastic matrix with the identification of the equivalent damage law $\tilde{d}_0(\tilde{p}_0)$ during a virtual elastic unloading; and (d) Case of elastic inclusions embedded in a damage-enhanced elasto-plastic matrix with the identification of the equivalent matrix yield stress $\tilde{\sigma}_{Y0}$ and equivalent matrix hardening law $\tilde{r}_0(\tilde{p}_0)$ upon reloading.

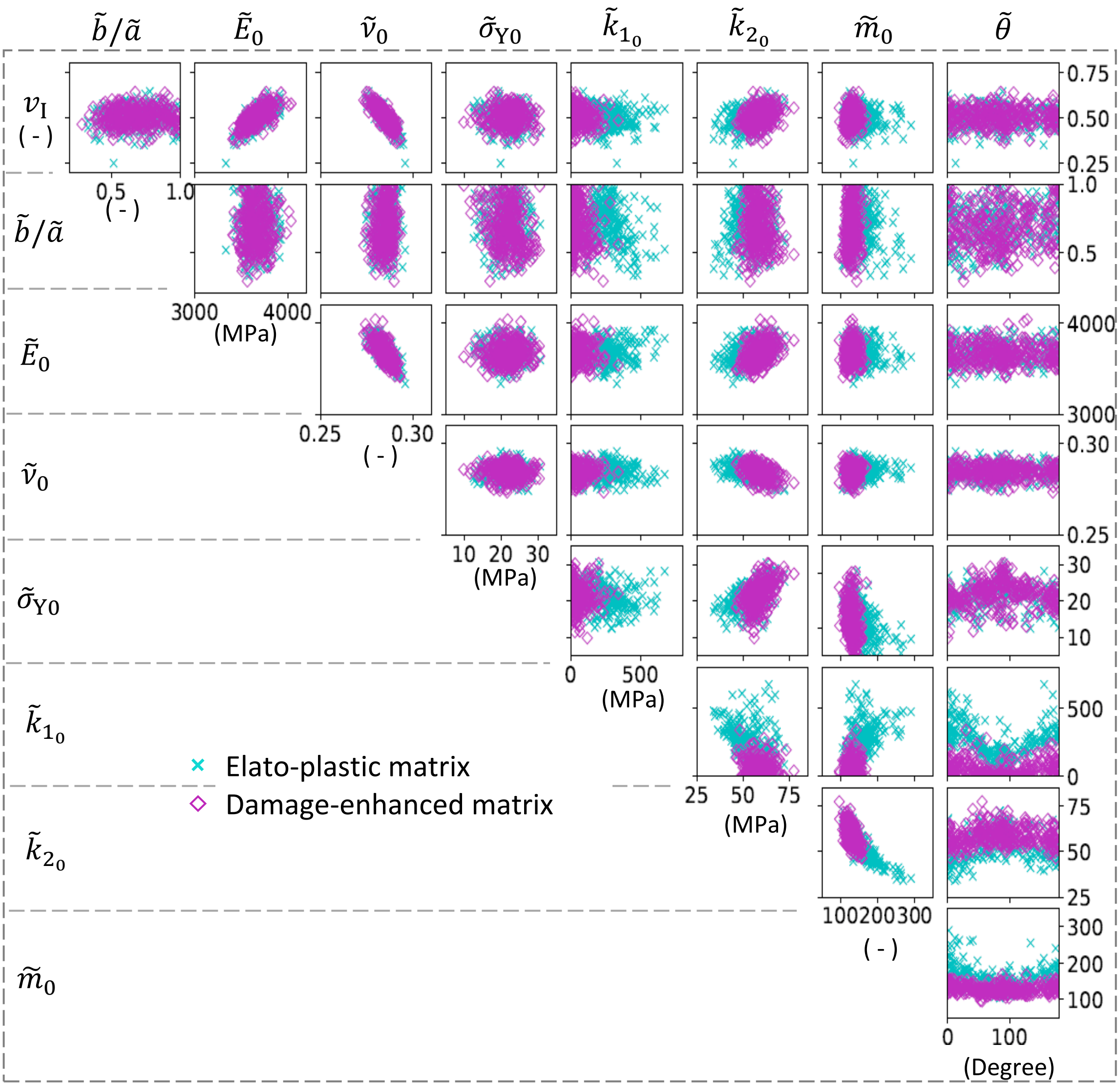

Figure 39: Equivalent parameters distributions and dependencies for the different SVE realisations $\omega(\boldsymbol{X};\,w^k)$ with $w^k \in \mathcal{W}$ as identified by Wu et al. (2019) in the case of elastic inclusion of volume fraction v_{I} embedded either in an elasto-plastic matrix or in a damage-enhanced elasto-plastic matrix: equivalent inclusion of equivalent semi-axes $\tilde{a}$ and $\tilde{b}$ and equivalent orientation $\tilde{\theta}$; equivalent matrix Young's modulus $\tilde{E}_0$ and Poisson ratio $\tilde{\nu}_0$; equivalent matrix yield stress $\tilde{\sigma}_{Y0}$ and equivalent matrix hardening law $\tilde{r}_0(\tilde{p}_0) = \tilde{k}_{1_0}\tilde{p}_0 + \tilde{k}_{2_0}\left(1 - e^{-\tilde{m}_0\tilde{p}_0}\right)$; equivalent damage parameters not shown for conciseness; Modified from Computer Methods in Applied Mechanics and Engineering 348, Wu, L., Nguyen, V.D., Adam, L., Noels, L., An inverse micro-mechanical analysis toward the stochastic homogenization of nonlinear random composites, 97-138. Copyright (2019).

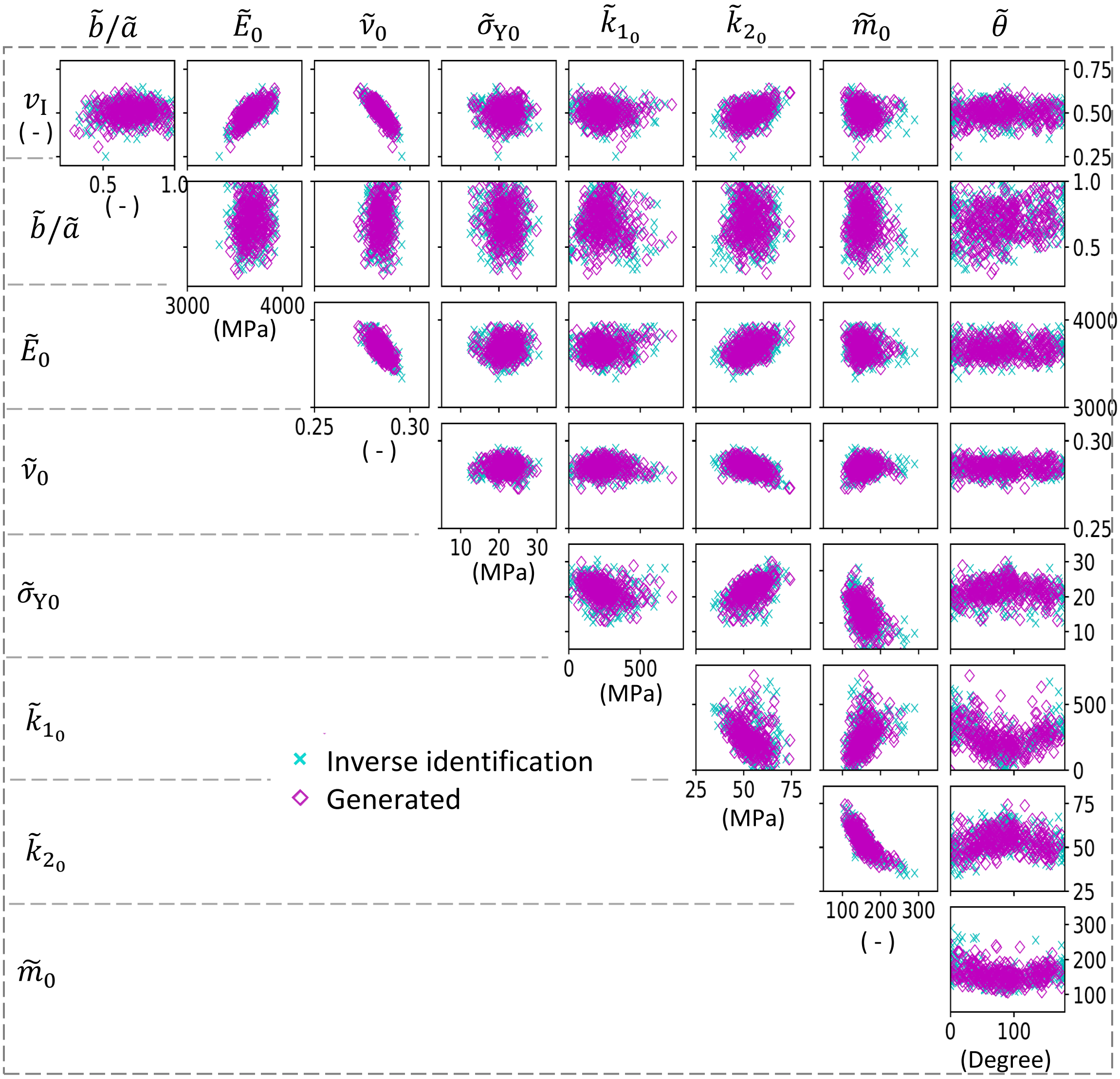

Figure 40: Generation of the identified parameters distributions and dependencies by Wu et al. (2019) of the stochastic MFH described in Section 5.4.2 and illustrated in Fig. 39 in the case of elastic inclusion of volume fraction v_{I} embedded in an elasto-plastic matrix: equivalent inclusion of equivalent semi-axes $\tilde{a}$ and $\tilde{b}$ and equivalent orientation $\tilde{\theta}$; equivalent matrix Young's modulus $\tilde{E}_0$ and Poisson ratio $\tilde{\nu}_0$; equivalent matrix yield stress $\tilde{\sigma}_{Y0}$ and equivalent matrix hardening law $\tilde{r}_0(\tilde{p}_0) = \tilde{k}_{1_0}\tilde{p}_0 + \tilde{k}_{2_0}\left(1 - e^{-\tilde{m}_0\tilde{p}_0}\right)$; Modified from Computer Methods in Applied Mechanics and Engineering 348, Wu, L., Nguyen, V.D., Adam, L., Noels, L., An inverse micro-mechanical analysis toward the stochastic homogenization of nonlinear random composites, 97-138. Copyright (2019).